



THE UNIVERSITY OF  
**WAIKATO**  
*Te Whare Wānanga o Waikato*

Research Commons

<http://researchcommons.waikato.ac.nz/>

## Research Commons at the University of Waikato

### Copyright Statement:

The digital copy of this thesis is protected by the Copyright Act 1994 (New Zealand).

The thesis may be consulted by you, provided you comply with the provisions of the Act and the following conditions of use:

- Any use you make of these documents or images must be for research or private study purposes only, and you may not make them available to any other person.
- Authors control the copyright of their thesis. You will recognise the author's right to be identified as the author of the thesis, and due acknowledgement will be made to the author where appropriate.
- You will obtain the author's permission before publishing any material from the thesis.

**Strata Movement Study Using a 250 m Deep  
Inclinometer Borehole  
Huntly East Coalmine, New Zealand**

A thesis  
submitted in partial fulfilment  
of the requirements for the degree  
of

**Master of Science in Earth Sciences**

at  
**The University of Waikato**

by  
**ZHAODONG DU**



THE UNIVERSITY OF  
**WAIKATO**  
*Te Whare Wānanga o Waikato*

The University of Waikato  
2012



# Abstract

Strata movement has adverse impacts on structures located on the surface and in the subsurface within a subsidence basin or affected area. Damages to a mine shaft may result from lateral movement and/ or vertical subsidence of the strata at a depth when the resultant stress is larger than the strength of the lining.

My study was developed in collaboration with Solid Energy NZ Limited. My research concentrated on monitoring a 250 m deep borehole to assess changes of strata movement that occurred as underground mining approached the inclinometer borehole. The borehole was a simulation of a proposed shaft. The objectives of my research were to study strata movement characteristics above and adjacent to the North 5 coal mining area by monitoring the inclinometer and interpreting the reading data collected from the inclinometer borehole as the underground mining advanced; develop a model of subsidence using Phase2 software; then compare the modelling subsidence with what we have measured to identify any correlation or difference.

The inclinometer borehole was located west of Te Ohaki Road, 300 m from the location of a proposed shaft in the adjacent panel in the Huntly East Mine. A total of 13 sets of inclinometer measurements were undertaken over two years from March 2009. Measurement stopped on 11 March 2011 because the probe could not be lowered through a depth of approximately 38 m in the borehole.

My study uses ‘extraction vector’, and ‘movement trajectory of the borehole’ for analysing and interpreting the deep borehole movement in underground mining, and addresses the far field subsidence movement as to its potential impact on structures on the surface or in the subsurface. This thesis also introduces the concept of negative vertical additional friction, developed in China, which is a potentially helpful concept for this study, and the proposed shaft project.

Three major movement zones were identified, two ‘shear zones’ from 135.0 to 135.5 m and from 166 to 170 m, and one ‘creeping zone’ from the surface to 115 m. The borehole movement was presented by the trajectory of the intersection of the borehole at depths of surface (1 m), 135 m, and 166 m. The two shear zones occurred on the bedding planes in Te Kuiti Group, the creeping zone occurred in the weak strata of the Tauranga Group and upper Te Kuiti Group. The borehole movements were non-linear, and the borehole lateral movement trajectories varied with depth. Three polynomial equations were developed from regression and modelling for indicating the relationship and predication between the nearest extraction distance and the induced lateral movement.

The installation of an inclinometer borehole deeper than 120 m was not found in around 100 literature articles reviewed. No reports of use of inclinometer monitoring of ground movement induced by underground extraction were found in the literature reviewed. According to ASTM (2005), no standards are available yet for evaluation against precision and bias issues arising from use of borehole inclinometer. Therefore, the inclinometer borehole in this study may be one of the most complicated cases for monitoring and measurement of strata movement induced by the underground extraction in New Zealand.





# Acknowledgements

First and foremost I would like to thank my supervisors, Dr. Megan Balks and Dr. Vicki Moon, for all of their advice, help, support and everything they had done for me during my research and thesis writing, and for being so approachable. Megan initiated the research project, helped me revise my drafts and optimising the thesis structure. Vicki assisted me with the modelling, data error correction and interpretation, advised me the option of modelling software and strength criterion, and organising the codes. I greatly enjoyed the discussions with you two on inclinometer monitoring, the data analysis and related topics. We were excited for and cheered up for every achievement and process during the research!

I would like to thank Priscilla Page and Ross Winter, my mentors at Solid Energy. Thank Ross so much to have initiated the project, and provided me data CD. Huge appreciations go to Cilla for her work together in inclinometer measurements, probe calibration, discussions on research, thesis revision, and her provision of all the mining data and literature. Cilla, we had the enjoyable and impressive field work time.

I would like to attribute my research and thesis to the Joint Project Team members: Megan, Vicki, Priscilla, Ross, Lachlan, and myself. The success is from the team work!

Acknowledgement to Solid Energy for the logistics and sharing part of the trip cost. Thanks to Heather, Arthur, Lachlan, Wendy, Bill, and Survey Team for their support and hospitality during my stay at Huntly.

Thanks to Sydney, Jenny, Willem, Errol, and Renat for their assistance and support. Thanks to my fellows Kerri, Ying, Cathy, Alice, Doreen and Varvara for their help and laugh together to relax for a spell in the busy research work.

Finally I would like to thank my family, especially my son Tian, my nephew Si, for their support and company, mentally and physically, in my busy study time. Thanks to my friends, particularly Guangping, the Songs, the Liangs, Lan, Lisa, Amy, and Chunli for their support, and keeping me sane, and occasionally and friendly distracting me from the addictive data work and thesis writing.





# Table of Contents

Abstract

Acknowledgements

Table of Contents

List of Figures

List of Tables

Table of Contents

Chapter 1	Introduction .....	1
1.1	Considerations in Coal Mining Practice .....	1
1.2	Huntly East Mine .....	3
1.2.1	Location and Establishment .....	3
1.2.2	Geology and Subsidence at Huntly East Mine.....	4
1.2.3	Current Mining Method .....	6
1.3	Current Development at Huntly East Mine.....	8
1.4	Objectives of Study.....	10
Chapter 2	Literature Review.....	11
2.1	Introduction .....	11
2.2	Literature on subsidence .....	11
2.2.1	Mechanism of subsidence .....	12
2.2.2	Dynamic Subsidence and Final Subsidence .....	15
2.2.3	Subsidence Impacts at the Surface and in Subsurface.....	16
2.2.4	Previous Investigations for the Huntly East Mine.....	17
2.2.5	Prediction of Subsidence.....	19
2.2.5.1	Introduction .....	19
2.2.5.2	Theoretical numerical techniques .....	21
2.3	Literature Review on Shaft Sinking .....	25
2.3.1	Objectives.....	25
2.3.2	Mine Shaft.....	26
2.3.3	The Negative Additional Vertical Friction.....	27
2.4	Literature on Inclinometer .....	28
2.4.1	Principle and Technique .....	28
2.4.2	Application and Aims of Inclinometer Measurements .....	30
2.4.3	Inclinometer Types.....	31
2.4.4	Current Inclinometer Developments .....	32

2.4.4.1 Major Inclinometer Expertise and Software.....	32
2.4.4.2 Literature on Inclinometer Borehole Monitoring.....	34
2.4.5 Plot Types .....	35
2.4.5.1 Plot Type and Relationships.....	35
2.4.5.2 Incremental displacement plots .....	37
2.4.5.3 Cumulative Displacement Plot.....	38
2.4.5.4 From Incremental Plots to Cumulative Plots .....	41
2.4.5.5 Rate of Displacement (Displacement vs. Time) .....	42
2.4.5.6 Cumulative Deviation Plot .....	44
2.4.5.7 Incremental Deviation Plots.....	44
2.4.5.8 Checksums and Difference Checksum Plot.....	45
2.4.5.9 Absolute Position plot .....	47
2.5 Summary and Conclusion .....	47
2.5.1 Subsidence Review .....	48
2.5.2 Review on Shaft Sinking.....	51
2.5.3 Literature on Inclinometer.....	52
Chapter 3    Huntly Geology, Hydrology, and Geotechnical Characteristics .....	55
3.1 Introduction.....	55
3.2 Geology.....	55
3.2.1 Regional Setting .....	55
3.2.1.1 Waikato Coal Region.....	55
3.2.1.2 Tauranga Group .....	57
3.2.1.3 Te Kuiti Group.....	57
3.2.1.4 Waikato Coal Measures.....	58
3.2.1.5 Coal resources .....	59
3.2.1.6 Regional faulting .....	59
3.2.2 Local Geology .....	60
3.2.2.1 Current exploration .....	60
3.2.2.2 Local geological Vulcan model.....	62
3.2.2.3 Local basement ridges and domes .....	62
3.2.2.4 Local faults and coal seams .....	64
3.2.2.5 Local combined Renown and Kupakupa seam dip.....	67
3.2.3 Geology in the Inclinometer Borehole (20091) .....	68
3.2.3.1 Basic data from the Borehole .....	68
3.2.3.2 Stratigraphy.....	70
3.3 Hydrological characteristics.....	72
3.3.1 Regional Hydrogeology.....	72

3.3.1.1 Overview .....	72
3.3.1.2 Hydrogeologic units.....	72
3.3.1.3 Tauranga Group hydro-geologic units .....	74
3.3.2 Ground water level in the pilot borehole.....	75
3.3.3 Geographic and Surface Water.....	75
3.3.3.1 Geography.....	75
3.3.3.2 Subsidence and surface water .....	77
3.3.4 Local Hydrology (borehole 20097).....	78
3.3.4.1 Drilling observations .....	78
3.3.4.2 Water level data.....	78
3.3.4.3 Lugeon values .....	79
3.3.4.4 Slug testing and permeability .....	80
3.3.5 Okowhao Lake.....	80
3.4 Geotechnical Characteristics of Pilot Borehole .....	80
3.4.1 Introduction .....	80
3.4.2 Pilot Borehole (20097) Geology Summary .....	81
3.4.3 Geotechnical Investigations.....	81
3.4.4 Geotechnical Conditions .....	82
3.4.4.1 Lithology .....	82
3.4.4.2 Soil Classification .....	82
3.4.4.3 Rock Types.....	83
3.4.4.4 Weathering.....	83
3.4.4.5 Broken zones.....	84
3.4.4.6 Rock Quality Designation (RQD) .....	84
3.4.4.7 Rock Defects.....	86
3.4.4.8 Intact Rock Properties .....	87
3.4.4.9 Soil Material Properties.....	92
Chapter 4    Inclinometer and Phase2 Modelling Investigation Methods .....	97
4.1 Introduction.....	97
4.2 Borehole Inclinometer Method .....	98
4.2.1 Location of the Borehole.....	98
4.2.2 Methods and Objectives on the Borehole.....	100
4.2.3 The Structure of the Boreholes .....	100
4.2.4 Operation of Inclinometer .....	102
4.2.5 Inclinometer Data Error Correction .....	104
4.2.5.1 Data errors and inclinometer accuracy .....	104
4.2.5.2 Checksums of readings .....	107

4.2.5.3 Bias-shift error .....	111
4.2.5.4 Rotation error.....	114
4.2.5.5 Depth error .....	117
4.2.5.6 Orientation corrections for casing.....	120
4.2.5.7 Spiral correction for casing.....	120
4.2.6 Inclinometer Calibration.....	122
4.2.6.1 Introduction.....	122
4.2.6.2 Inclinometer calibration in laboratory.....	122
4.2.6.3 Results and conclusions .....	123
4.3 Inclinometer Borehole (20091) Descriptions .....	126
4.3.1 Borehole Coring .....	126
4.4 Numerical Modelling and Phase2 (RocScience).....	127
4.4.1 Introduction.....	127
4.4.2 Overview of Modelling of Subsidence .....	127
4.4.2.1 Modelling principles .....	127
4.4.2.2 SCT’s modelling work using FLAC at Huntly East Coalmine .....	128
4.4.3 Option of the Modelling Code.....	129
4.4.3.1 Principle of option of software .....	129
4.4.3.2 Choice of modelling software .....	129
4.4.4 General project settings in Phase2 .....	130
4.4.4.1 Analysis type.....	130
4.4.4.2 Solver type .....	132
4.4.4.3 Axisymmetric models.....	132
4.4.4.4 Restrictions on axisymmetric modelling .....	133
4.4.4.5 Convergence type .....	133
4.4.4.6 Tensile failure reduces shear strength to residual.....	134
4.4.4.7 Tensile failure reduces ‘Hoek-Brown Tensile Strength’ to zero .....	135
4.4.4.8 Groundwater method .....	135
4.4.4.9 Use effective stress analysis .....	135
4.4.4.10 Probabilistic analysis .....	136
4.4.5 Boundaries .....	136
4.4.5.1 Excavation boundary .....	136
4.4.5.2 External boundary .....	137
4.4.5.3 Material boundary .....	137
4.4.5.4 Piezometric line .....	137
4.4.6 Loading overview .....	137
4.4.6.1 Field stress .....	138



4.4.6.2 Use ‘Actual Ground Surface’ .....	138
4.4.6.3 Use ‘Effective Stress Ratio’ .....	138
4.4.6.4 Stress ratio .....	140
4.4.7 Initial Element Loading .....	141
4.4.7.1 Initial stress and body force .....	141
4.4.7.2 Unit weight .....	141
4.4.7.3 Unit weight vs. unit weight of overburden (Gravity Field Stress) ....	142
4.4.8 Elastic Properties.....	142
4.4.9 Strength Parameters .....	143
4.4.9.1 Material type.....	143
4.4.9.2 Failure (strength) criterion.....	144
4.4.9.3 Dilation Parameter .....	147
4.4.10 Apply shear strength reduction (SSR).....	148
4.4.11 Define hydraulic properties.....	148
4.4.12 Mesh Generation .....	149
4.5 Summary and Conclusions.....	150
4.5.1 Borehole Inclinometer Method .....	150
4.5.2 Inclinometer Data Error Correction .....	150
4.5.3 Inclinometer Calibration .....	150
4.5.4 Numerical Modelling and Phase2 .....	151
Chapter 5 Inclinometer Data Analysis and Error Corrections.....	153
5.1 Introduction.....	153
5.2 Main Observations of Inclinometer Monitoring .....	153
5.2.1 Water Level Changes in Borehole .....	153
5.2.2 Traversing of Probe Stopped.....	155
5.2.3 Traversing of Probe via the B Axis Grooves.....	156
5.3 Inclinometer Data for the Borehole .....	157
5.3.1 Raw Data.....	157
5.3.2 The Absolute Position of the Borehole Prior to Error Correction.....	159
5.3.2.1 The Absolute Position of the Borehole on 27/03/2009 .....	159
5.3.2.2 The Absolute Position of the Borehole on 13 surveys .....	161
5.3.3 The Cumulative Displacement Plots.....	161
5.4 Data Corrections .....	163
5.4.1 Introduction .....	163
5.4.2 Mean Checksums.....	163
5.4.3 Instrument Constant Unification .....	166
5.4.4 Extreme Checksum Analysis.....	168

5.4.4.1	Checksum plots .....	168
5.4.4.2	Extreme reading edit .....	174
5.4.5	Bias Error Correction.....	175
5.4.6	Rotation Error.....	177
5.4.7	Depth Error .....	179
5.4.8	Spiral Correction for Casing.....	184
5.5	Summary and Conclusions.....	185
5.5.1	Discussions .....	185
5.5.1.1	Probe kicking.....	185
5.5.1.2	Probe jamming .....	186
5.5.1.3	Comprehensive analysis of 3 events.....	187
5.5.1.4	Shortcoming of traversing inclinometer method.....	187
5.5.1.5	Replication of measurement.....	188
5.5.1.6	Determining the causes of probe jamming and water level changes	188
5.5.2	Conclusions.....	189
5.5.3	Recommendations .....	191
5.5.3.1	Continuing the monitoring.....	191
Chapter 6	Borehole Movement Interpretation and Extraction Outlays.....	193
6.1	Introduction.....	193
6.2	Inclinometer Plots Analysis.....	194
6.2.1.	Approach and Aim.....	194
6.2.2	Incremental Displacement.....	194
6.2.3	Resultant Cumulative Displacement .....	197
6.2.4	Strata Movement Trajectory at 135 m (Shear zone 1) .....	200
6.2.5	Shear Displacement at Shear Zone 1 (at 135 m) .....	203
6.2.6	Strata Movement Trajectory at 166 m.....	205
6.2.7	Shear Movement at 166 m.....	208
6.2.8	Creeping Zone from Surface to 115 m .....	210
6.2.9	Comparison of Strata Movement at 1 m, 135 m, 166 m .....	213
6.3	Extraction Advancing and Outlays .....	217
6.3.1	Introduction.....	217
6.3.2	Extraction Time Series Data .....	218
6.3.3	Simplification of the Multiple Extraction Locations.....	220
6.4	Movement of the Borehole Opening.....	223
6.5	Movement Zones vs. Stratigraphy.....	224
6.5.1	Introduction.....	224
6.5.2	Geophysical Log from 43 to 135 m .....	226

6.5.3 Geophysical Log from 120 to 145 m .....	227
6.5.4 Geophysical Log from 155 to 182 m .....	228
6.6 Discussions .....	229
6.6.1 Movement Data of the Borehole Opening .....	229
6.6.2 Principle of the Trajectory of Borehole Movement.....	230
6.6.3 Main Borehole Observations and Movement Interpretation.....	231
6.7 Conclusions .....	232
<b>Chapter 7 Model Development and Numerical Modelling of Strata Movement</b>	<b>235</b>
7.1 Introduction .....	235
7.2 Model Development of Strata Movement .....	235
7.2.1 Introduction .....	235
7.2.2 Delay Time between Extraction and Subsidence.....	236
7.2.3 Calculation of Extraction Volumes Contributing to Subsidence .....	238
7.2.4 Extraction Parameters (Vector).....	239
7.2.5 Correlation between Horizontal Movement and Nearest Edge Distance	240
7.2.5.1 Introduction .....	240
7.2.5.2 Eight separate subsidence events and rectangle conversion to circle	240
7.2.5.3 Calculation of weighted stope centre location and nearest distance.	241
7.2.5.4 Delay time identification.....	243
7.2.5.5 Correlation equation between the lateral movement and extraction	247
7.2.6 Borehole Movement Trajectory and Extraction Vectors .....	250
7.3 Numerical Modelling of Strata Movement .....	254
7.3.1 Geological Model for Software Modelling .....	254
7.3.2 Establishment for Software Modelling.....	256
7.3.2.1 Project settings.....	256
7.3.2.2 Material properties .....	257
7.3.2.3 Creating the model boundary .....	259
7.3.2.4 Strata settings .....	261
7.3.2.5 Boundary conditions .....	262
7.3.2.6 Loading conditions .....	263
7.3.2.7 Mesh generation .....	263
7.3.2.8 Strength (failure) parameters.....	263
7.3.3 Initial Trials to Choose Failure Criterion .....	264
7.3.4 Combination and Running Trial .....	267
7.3.4.1 Combinations.....	267
7.3.4.2 Model running for 24 combinations .....	268

7.3.5 Model Running Using Elastic Material Method .....	269
7.3.6 Final Modelling and Validation .....	270
7.3.6.1 Final modelling.....	270
7.3.6.2 Final modelling analysis .....	272
7.4 Summary and Conclusions.....	279
7.4.1 Model Development and Regression Equations .....	279
7.4.2 Numerical Modelling .....	280
7.4.3 Discussions .....	282
Chapter 8 Summary and Conclusions.....	283
8.1 Summary of Literature Review .....	283
8.1.1 Findings and Implications from the Literature Review .....	283
8.1.2 Potential Outstanding Features of This Study .....	284
8.2 Discussion.....	285
8.2.1 Main Borehole Observations and Movement Interpretation.....	285
8.2.2 Shortcoming of Traversing Inclinometer Method .....	286
8.2.3 Replication of Measurement .....	287
8.2.4 Suggestions for Further Work.....	287
8.2.4.1 Alternative software options .....	287
8.2.4.2 Inclinometer calibration .....	288
8.2.4.3 Continuing the monitoring.....	288
8.2.4.4 Attention to the Far Field Subsidence Movements .....	289
8.2.4.5 Vertical movement data of the Borehole opening .....	289
8.3 Conclusions.....	290
8.3.1 Conclusions on Data Error Correction .....	290
8.3.2 Conclusions on Movement Interpretation .....	291
8.3.3 Conclusions on Movement Modelling .....	292
8.4 Limitations.....	293
8.4.1 Limitations of Monitoring Operation.....	293
8.4.2 Limitation of Literature on Inclinometer Monitoring.....	294
8.4.2 Limitation on Inclinometer Calibration in Laboratory.....	294
8.4.3 Modelling Limitation .....	295
8.4.3.1 “All Models Are Wrong But Some Are Useful” (Box, 1979).....	295
8.4.3.2 Limitation of option of software .....	295
8.4.4 Insufficient Vertical Subsidence Data .....	296
8.4.5 The 0.336 m Outstanding Casing above the Ground Surface.....	296
8.5 Epilogue .....	297
References.....	299

<b>1</b>	<b>Appendix A: Literature Review Supplements .....</b>	<b>315</b>
	<b>A-1 Subsidence Deformation Indices and Concepts .....</b>	<b>315</b>
	<b>A-2 Factors Affecting Mine Subsidence .....</b>	<b>319</b>
	<b>A-3 Empirical Prediction Method of Subsidence - Graphical method.....</b>	<b>325</b>
	<b>A-4 Empirical Prediction Method of Subsidence - Profile functions.....</b>	<b>328</b>
	<b>A-5 Empirical Prediction Method of Subsidence - Influence functions .....</b>	<b>332</b>
	<b>A-6 Prediction Method of Subsidence - Numerical Techniques .....</b>	<b>335</b>
	<b>A-7 Physical Models.....</b>	<b>341</b>
	<b>A-8 State of Art on Prediction of Subsidence .....</b>	<b>347</b>
	<b>A-9 In-Situ Horizontal Stress, Yassien’s Study (2003) .....</b>	<b>354</b>
	<b>A-10 Prevention of Subsidence.....</b>	<b>354</b>
	<b>A-11 Far Field Subsidence Movements.....</b>	<b>357</b>
	<b>A-12 Safety Pillars for Shaft.....</b>	<b>359</b>
<b>2</b>	<b>Appendix B: The Negative Additional Vertical Stress.....</b>	<b>366</b>
	<b>B-1 Introduction.....</b>	<b>366</b>
	<b>B-2 Rupture Characteristics .....</b>	<b>367</b>
	<b>B-3 Negative Additional Vertical Friction .....</b>	<b>372</b>
	<b>B-4 Examples for Calculations.....</b>	<b>376</b>
	<b>B-5 Prevention, Protection and Repair of Shaft Lining.....</b>	<b>384</b>
	<b>B-6 Contribution and Supports .....</b>	<b>388</b>
	<b>B-7 Interesting Finding – Novikov’s paper.....</b>	<b>390</b>
	<b>B-8 Discussions .....</b>	<b>391</b>
	<b>B-9 Conclusions .....</b>	<b>393</b>
<b>3</b>	<b>Appendix C: Precautions for Minimising the Data Errors .....</b>	<b>394</b>
<b>4</b>	<b>Appendix D: Original Inclinometer Measurement Data (CD copy).....</b>	<b>395</b>
<b>5</b>	<b>Appendix E: The Inclinometer Data after Data Error Correction (CD file)...</b>	<b>396</b>
<b>6</b>	<b>Appendix F: Calculations for the Weighted Extraction Parameters (CD file)</b>	<b>397</b>
<b>7</b>	<b>Appendix G: Cross Sections of Strata across the Inclinometer Borehole (CD file)</b>	<b>398</b>

# List of Figures

Figure 1.1 Location of Huntly East Coalmine (After Solid Energy, 2009). .....	3
Figure 1.2 Location of current underground mining and main entrance in the Huntly Underground mine (adopted from Google, 2011). .....	4
Figure 1.3 Typical geological section of Huntly Coalmine (Solid Energy, 2006). .....	5
Figure 1.4 Idealised panel frameworks by Bord and Pillar mining (Gale, 2007)... ..	7
Figure 1.5 ‘As built’ Bord and Pillar mining layout for N51 (Gale, 2003). .....	7
Figure 1.6 The location of the Huntly North Project (Solid Energy, 2007).....	9
Figure 2.1 Subsidence over coal seam withdrawal (after Crowell, 2010). .....	12
Figure 2.2 Typical subsidence profile (from Debono, 2007). .....	14
Figure 2.3 Development of a subsidence trough in exaggerated vertical scale (from Debono, 2007). .....	16
Figure 2.4 Subsidence over the south headings, Huntly at 29th July 1985 (from Kelsey, 1986). .....	18
Figure 2.5 The locations of the point P and excavation underground (From Li et al., 2010). .....	23
Figure 2.6 Lateral movements monitoring with inclinometer (from Cornforth, 2005). .....	28
Figure 2.7 (a) Inclinometer casing showing internal longitudinal grooves. (b) Inclinometer traversing in casing (from Machan & Bennett, 2008). .....	29
Figure 2.8 Measurement principles of Inclinometer (from Machan & Bennett, 2008). .....	29
Figure 2.9 (a), Principles of configuration of inclinometer equipment; (b), Illustration of inclinometer operation in cumulative displacement (from Stark and Choi, 2008). .....	30
Figure 2.10 Plan view of inclinometer casing showing groove directions (from SOIL, 2008). .....	32
Figure 2.11 The relationships between deviation and displacement and their differences. .....	36
Figure 2.12 Inclinometer data plots: a. cumulative deviation plot; b. cumulative displacement plot (from Mikkelsen, 2001). .....	37
Figure 2.13 Incremental displacements and spikes (from Slope Indicator, 2001). .....	38
Figure 2.14 Cumulative displacements in horizontal large scale (from Machan & Bennett, 2008). .....	39
Figure 2.15 Effects of different scales to display lateral cumulative displacement (Slope Indicator, 2001). .....	40
Figure 2.16 Comparison of data sets using incremental and cumulative displacement profiles (from Slope Indicator Company, 2006, p9). .....	41
Figure 2.17 Example of inclinometer data for determining shear zone (from Cornforth, 2005). .....	42
Figure 2.18 Example of a displacement vs. time plot (from Slope Indicator, 2001). .....	43
Figure 2.19 Example of a cumulative deviation of casing (from Slope Indicator, 2001). .....	44
Figure 2.20 Example of an incremental deviation plot showing the offset to vertical (from Slope Indicator, 2001). .....	45
Figure 2.21 Example of a checksum plot and difference checksum plot (from Slope Indicator, 2001). .....	46

Figure 2.22 Example of an extreme value of displayed readings presented in GTILT (from Mitre Software, 2003).....	47
Figure 3.1 The 13 coalfields extending from Drury near Auckland to Mangapehi near Te Kuiti in the western central North Island (from Ministry of Economic Development, 2011). .....	56
Figure 3.2 Location Plan of North 5, North 6 and North 7 mining areas (from Solid Energy, 2007).....	60
Figure 3.3 Location Plan of Drillholes – highlighted in red (from Solid Energy, 2006).....	61
Figure 3.4 Kupakupa Seam Floor Contours in Vulcan Geological Model (from Solid Energy, 2006).....	63
Figure 3.5 Major fault structures (from Solid Energy, 2006).....	64
Figure 3.6 Fault dips, Section A-A’ from Figure 3.3 (from Solid Energy, 2006). 65	
Figure 3.7 The samples of the chips from wash drilling in the Borehole 20091(from Solid Energy, 2009a).....	69
Figure 3.8 The location of the Huntly North Project and existing catchment (from Golder Kingett Michell, 2007). .....	76
Figure 3.9 Plot of water level change over borehole depth (from PDP, 2009). ....	79
Figure 3.10 RQD values over depth (from Page, 2009).....	85
Figure 3.11 Summary plot of structure from Acoustic scanner interpretation (from Page, 2009). .....	86
Figure 3.12 Stress VS Depth for the Huntly Region (from Larratt et al., 2010, p8). .....	90
Figure 4.1 Location of the Inclinometer Borehole, Huntly (image from Google, 2011).....	98
Figure 4.2 The location of inclinometer borehole (from Solid Energy, 2011a)....	99
Figure 4.3 Structure of borehole 20091, Huntly East Mine (Not in scale).....	101
Figure 4.4 Inclinometer monitoring photo one (Photo: Page, 2011).....	102
Figure 4.5 Inclinometer monitoring photo two (Photo: Page, 2011).....	102
Figure 4.6 Digital Inclined Inclinometer system (from SOIL, 2008).....	103
Figure 4.7 Operation of the inclinometer. (a) the probe; (b) the plan view of the probe; (c) the plan view of the probe in casing (from Slope Indicator Co., 2006). .....	103
Figure 4.8 Total error and random errors in inclinometer data (from Machan & Bennett, 2008). .....	105
Figure 4.9 Typical bias shift errors (from Mikkelsen, 2003). .....	111
Figure 4.10 The typical patterns of bias-shift errors in plots (from Slope Indicator Co., 2000). .....	112
Figure 4.11 Results of tests using three probes in a single borehole on the same day. (a) lateral displacement on the A axis; (b) deviation on the B axis; (c) lateral displacement on the A axis after correction. Similarity between the A and B profiles indicates rotation error (from Slope Indicator Co., 2003; Cornforth, 2005). .....	115
Figure 4.12 One typical plot containing depth errors (Slope Indicator Co., 2000). .....	117
Figure 4.13 Plots before & after depth error correction (Slope Indicator Co., 2000) .....	117
Figure 4.14 Plots of incremental deviation & cumulative displacement in J shaped casing (Slope Indicator Co., 2000).....	118

Figure 4.15 An example of depth error in J-shaped casing (Slope Indicator Co., 2000).	118
Figure 4.16 Plots of incremental deviation and cumulative displacement in S-shaped casing (Slope Indicator Co., 2000).	119
Figure 4.17 An example of depth error in S-shaped casing (Slope Indicator Co., 2000).	119
Figure 4.18 Influence of spiral error on plots of displacement (from Slope Indicator Co., 2002).	121
Figure 4.19 The setup of the inclinometer calibration on 13 July 2011 at Huntly.	123
Figure 4.20 Correlations between the smart level and the inclinometer for tilt values in the A axis.	125
Figure 4.21 Correlations between the two types of tilt values, the A axis vs. the B Axis of the probe showing a high R <sup>2</sup> value and small slope.	125
Figure 4.22 The analysis method option in Phase2 modelling for Huntly strata movement.	131
Figure 4.23 Axisymmetric Analysis models, left representing sphere, right for cylinder (from RocScience, 2011).	132
Figure 4.24 Effect of Gradation Factor on the mesh – a. gradation factor = 0.1 and b. gradation factor = 0.3. (The Expansion Factor of the External Boundary is equal to 1 in this case) (from RocScience, 2011).	149
Figure 5.1 Water level changes in the Borehole, Huntly East Mine.	154
Figure 5.2 Inclinometer data displayed in PDA in the B 180 axis reading.	158
Figure 5.3 Example In-Site programme data display for inclinometer data measured on 27 March, 2009.	159
Figure 5.4 The absolute position of the Borehole on 27/03/2009 prior to error correction.	160
Figure 5.5 The absolute plan view of the Borehole (from top to bottom) on 27/03/2009.	160
Figure 5.6 The absolute positions of the Borehole on 13 surveying days, the two graphs use the same vertical scale and the same horizontal scale.	161
Figure 5.7 The cumulative displacement plots of 13 surveys of the Borehole, the curved lines on 12/11/2010 and 18/01/2011 showing abnormal from the other 11 curved lines.	162
Figure 5.8 Cumulative displacement plots for the A axis and the B axis from the 11 ‘useful’ datasets.	165
Figure 5.9 Checksums in the A axis and the B axis: (a) small scale, (b) large scale.	169
Figure 5.10 Checksum plot on 27/03/2009.	170
Figure 5.11 Checksum plot on 27/05/2009.	170
Figure 5.12 Checksum plot on 25/06/2010.	170
Figure 5.13 Checksum plot on 31/08/2010.	170
Figure 5.14 Checksum plot on 24/09/2010.	171
Figure 5.15 Checksum plot on 14/10/2010.	171
Figure 5.16 Checksum plot on 28/10/2010.	171
Figure 5.17 Checksum plot on 31/11/2010.	171
Figure 5.18 Checksum plot on 21/12/2010.	172
Figure 5.19 Checksum plot on 03/02/2011.	172
Figure 5.20 Checksum plot on 22/02/2011.	172
Figure 5.21 a, the A axis cumulative displacement after checksum editing; b, the B axis cumulative displacement after checksum editing.	176



Figure 5.22 The A axis cumulative displacements vs. the B axis cumulative deviation showing no major rotation error. ....	178
Figure 5.23 The B axis Cumulative displacement vs. the A axis cumulative deviation showing no major rotation error. ....	178
Figure 5.24 Comparison of the incremental deviations and cumulative displacements in the A axis for J-shape casing, showing no major depth error..	180
Figure 5.25 Comparison of the incremental deviations and cumulative displacements in the B axis for J-shape casing, showing no major depth error..	181
Figure 5.26 Comparison of the incremental deviations and cumulative displacements in the A axis for S-shape casing, showing no major depth error.	182
Figure 5.27 Comparison of the incremental deviations and cumulative displacements in the B axis for S-shape casing, showing no major depth error.	183
Figure 5.28 The spiral sign is 'false' representing no spiral data available in the datasets. ....	185
Figure 5.29 Different magnitudes of probe kicks on inconsistent joint in different directions. ....	186
Figure 6.1 Incremental displacement plots for the 11 surveys, a. in the A axis; b. in the B axis (data corrected see Chapter 5 for details). ....	195
Figure 6.2 Resultant cumulative displacements showing three movement zones. ....	198
Figure 6.3 Two shear zone locations and thickness in resultant cumulative displacement plot from 100 to 245 m section. ....	199
Figure 6.4 Plan view of borehole movement trajectory, 11 continuous locations at 135 m. ....	201
Figure 6.5 Magnitude of movement rate along trajectory at 135 m. ....	203
Figure 6.6 The shear zone and shear distance at 135 m depth for a survey. ....	203
Figure 6.7 Shear movement rate at 135 m for the 11 inclinometer surveys.....	205
Figure 6.8 Plan view of trajectory of the Borehole at 166 m. ....	206
Figure 6.9 Movement rates along the borehole trajectory between 11 surveys at 166 m depth. ....	207
Figure 6.10 The shear zone and shear distance at 166 m depth for one survey. .	209
Figure 6.11 Magnitudes of shear movement rate at 166 m depth. ....	210
Figure 6.12 Plan view of the movement trajectory of the Borehole opening at 1 m depth below the ground surface where the final measurement was taken.....	212
Figure 6.13 Surface movement rate along the trajectory (at 1 m). ....	213
Figure 6.14 Comparison of the three movement trajectories of the Borehole at 3 depths (both axes have the same scale in each graph).....	215
Figure 6.15 Comparison of strata movement rates along trajectory at 1m, 135 m and 166 m, all was showing a major trend of rising over time, and decreasing with depth. ....	217
Figure 6.16 Comparison of the strata shear movement rates at 135 m and 166 m. ....	217
Figure 6.17 Extraction outlay and advancing direction from extraction centre in 2005 (2006) to extraction centre in 2011 showing an S shape of the advancement (adapted from Solid Energy, 2011a). ....	219
Figure 6.18 Theoretical diagram showing inclinometer borehole and the scope of subsidence (from Kelsey, 1986). ....	220
Figure 6.19 Extraction centres determined by simplifying the monthly multiple locations of extraction (adapted from Figure 6.17). ....	222
Figure 6.20 Main trends of ground vertical movement (to reference) at collar opening, measured using GPS. ....	224

Figure 6.21 The whole geophysical log from surface to 250 m taken when borehole was installed in 2009 (from Solid Energy, 2009d). .....	225
Figure 6.22 Geophysical log from 40 to 135 m, showing no bedding planes from 115 m to surface (from Solid Energy, 2009d) .....	226
Figure 6.23 Geophysical log from 120 to 145 m showing the bedding plane at 135 m (Solid Energy, 2009d). .....	227
Figure 6.24 Geophysical log from 155 to 182 m showing the bedding planes at 166 to 170 m (Solid Energy, 2009d). .....	228
Figure 6.25 The trajectory of the borehole movement in an intersection plane at a depth by the borehole locations from inclinometer measurements following extraction location change.....	230
Figure 7.1 The calculation using method of Equilibrium of the Centre of Gravity. ....	241
Figure 7.2 Graph of the correlation coefficient values (from Table 7.2) for time delay from zero months to 20 months for identifying the best negative correlation. ....	245
Figure 7.3 Weighted nearest distance from the nearest edge of extraction to the Borehole (left axis) for delay times of 1 month, 12 months, and 18 months delay; and the lateral movement magnitudes at depths of 1 m, 135 m and 166 m (right axis). .....	246
Figure 7.4 Scatter plot of the horizontal movement and nearest edge distance from extraction to the borehole for 18 month delay pattern. ....	248
Figure 7.5 Scatter plots of the horizontal movement at 1 m depth with the nearest edge distance from extraction to the borehole for 18 month delay pattern.....	248
Figure 7.6 Comparison of the borehole movement trajectories a, b, c (from section 6.2.9) with the extraction pattern d - showing weighted extraction vectors from no. 1 to no. 8 in the 18 month time delay, representing the 8 weighted locations of the extraction centres from each 6 induction months (Table 7.4). The zero at origin is the location of the inclinometer borehole. ....	253
Figure 7.7 The full 2D model representing the 9 geological layers of the inclinometer monitoring region (created in Phase2, data source from Table 3.6 in Section 3.3.2). ....	255
Figure 7.8 Sketches of an axisymmetric extraction 2D (upper) and 3D (lower) model with square stope that was idealised into cylinder for axisymmetric type modelling. ....	259
Figure 7.9 The model boundary sizing 500 m times 1500 m, including an extraction cylinder of 4.55 m effective height and $x=200$ m radius, which was created in Phase2.....	260
Figure 7.10 The model with nine strata profile and groundwater piezometer lines (half of the axisymmetric model profile in Figure 7.7).....	261
Figure 7.11 Meshed Model with 1500 nodes on External Boundary, model boundary size 1500 m wide times 500m high.....	262
Figure 7.12 The one layer model for initial trials to choose the failure criterion. ....	264
Figure 7.13 The model interpretation screen, with 8 vertical lines and 3 horizontal lines. ....	271
Figure 7.14 The plots of the displacement from measurement, modelling and calculation at surface (1 m depth). ....	273
Figure 7.15 Correlation between the measured & modelled lateral displacements at 1 m.....	274

Figure 7.16 Correlation between the modelled & calculated lateral displacements at 1 m. ....	274
Figure 7.17 The plots of the displacement from measurement, modelling and calculation at 135 m depth. ....	275
Figure 7.18 Correlation between the measured and modelled lateral displacements at 135 m. ....	276
Figure 7.19 Correlation between the calculated and modelled lateral displacements at 135 m. ....	276
Figure 7.20 The plots of the displacement from measurement, modelling and calculation at 166 m depth. ....	277
Figure 7.21 Correlation between the measured and modelled lateral displacements at 166 m. ....	278
Figure 7.22 Correlation between the calculated and modelled lateral displacements at 166 m. ....	278

## List of Tables

Table 2.1 Determination of ground movement (after Stark and Choi, 2008; Cornforth, 2005). ....	31
Table 2.2 Summary of the major inclinometer software and function. ....	33
Table 2.3 Major literature on inclinometer borehole monitoring. ....	34
Table 2.4 Plot type and their functions (Slope Indicator, 2001). ....	36
Table 3.1 Acoustic Scanner Interpretation of Coal Seam Boundary Dip and Dip Direction (from Solid Energy, 2006). ....	68
Table 3.2 The striplog of inclinometer borehole 20091 (from Solid Energy, 2009b). ....	70
Table 3.3 The formation tops and thickness in the Borehole 20091 (from Solid Energy, 2009). ....	72
Table 3.4 Hydro-geological Units and hydro-geological characteristics (from Crampton, 2010). ....	73
Table 3.5 Hydraulic conductivity of Tauranga Group hydrogeological unit (from PDP, 2006). ....	74
Table 3.6 Groundwater level in the borehole 20097 (Larratt et al., 2009). ....	75
Table 3.7 Lugeon values for borehole 20097 (from PDP, 2009). ....	79
Table 3.8 The Slug testing and permeability values (from PDP, 2009). ....	80
Table 3.9 Profile of drill hole 20097 (from Page, 2009). ....	81
Table 3.10 Summary of Geology via drill exploration (from Page, 2009). ....	81
Table 3.11 Lithology intersected in the pilot borehole (from Page, 2009). ....	82
Table 3.12 Soil classification from surface to 36.95 m in 20097 (from Page, 2009). ....	83
Table 3.13 Rock types in borehole 20097 (from Page, 2009). ....	83
Table 3.14 weathering of rock in 20097 (from Page, 2009). ....	84
Table 3.15 Major broken zones distribution in rock strata (from Page, 2009). ....	84
Table 3.16 RQD analysis per lithology for borehole 20097 (from Page, 2009). ..	85
Table 3.17 UCS, Modulus of Elasticity & Poisson's Ratio (from Page, 2009, p10). ....	88
Table 3.18 Typical values of coefficient of earth pressure at rest (RocScience, 2011). ....	89

Table 3.19 The results of the average $\sigma_h$ and average $\sigma_h/\sigma_v$ stress ratio, for the Borehole 20091, calculated using Equations 3.1 and 3.2. ....	91
Table 3.20 Results of point load index test for borehole 20097 (from Page, 2009). ....	91
Table 3.21 Summary of Slake durability test results for borehole 20097 (from Page, 2009).....	92
Table 3.22 Summary of consolidated-undrained triaxial tests (from Page, 2009).92	
Table 3.23 Summary of Atterberg limit test results (from Page, 2009).....	93
Table 4.1 Sources of errors of inclinometer (after Mikkelsen, 2007 and Slope Indicator Co., 2000). ....	106
Table 4.2 Summary of data errors and correction methods (after Mikkelsen, 2003, 2007; Stark & Choi, 2008).....	107
Table 4.3 Checksum and instrument constant, calculations for the A axis measurement. ....	110
Table 4.4 Mean checksum variations from project samples by the Specialist software. ....	110
Table 4.5 Inclinometer calibration results and accuracy.....	124
Table 4.6 Smart Level reading VS probe result (degree).....	124
Table 4.7 Typical values of coefficient of earth pressure at rest (from RocScience, 2011). ....	140
Table 5.1 Checksums, Standard Deviations and Coefficients of Variation (CV) before correction, the shadings showing the CV values are larger than 10% for the A axis, 20% for the B axis. ....	164
Table 5.2 Checksums, Standard Deviations and CV with unified instrument constants 25000. ....	168
Table 5.3 Depths of the extreme checksums having CV values larger than 10% for the A axis and 20% for the B axis.....	173
Table 5.4 Checksums, standard deviations and CV values after edit of extreme readings. ....	175
Table 5.5 The investigation of methods for extending the capability of inclinometer casing (after Machan and Bennet, 2008). ....	190
Table 6.1 The incremental displacement data for the A and B axes. Data larger than 2.5 mm are shaded.....	196
Table 6.2 Inclinometer data and movement features of shear zone 1 at 135 m..	200
Table 6.3 Movement distances and rates along borehole trajectory at 135 m. ...	202
Table 6.4 The cumulative displacements in the both A and B axes, and the resultant cumulative displacement at depth of 35 m and 135.5 m. ....	204
Table 6.5 Shear movement features of shear zone 1 at 135 m of the Borehole (BH). ....	204
Table 6.6 Inclinometer data and strata movement features at a depth of 166 m.	206
Table 6.7 Movement distance, rates along the borehole trajectory at 166 m.....	207
Table 6.8 The cumulative displacements in the both A and B axes, and the resultant cumulative displacement at depth of 166 m and 170 m. ....	208
Table 6.9 Shear movement features at depths of 166 m, calculated from Table 6.7. ....	209
Table 6.10 Surface movement features of the creeping zone (from surface to 115 m deep).....	211
Table 6.11 Surface movement distance, rate along the trajectory (1 m depth)...	211

Table 6.12 Movement distance and rate of the Borehole between measurements along movement trajectories, at depths of 1m, 135 m and 166 m, on 11 surveys. ....	216
Table 6.13 The area, distance, and bearing of the summated monthly extraction cells, average seam thickness 7 m (Solid Energy, 2011a).....	221
Table 6.14 GPS data on the borehole ground reduced level (m) (from Solid Energy, 2011a). ....	223
Table 7.1 Theoretical time relationship between extraction and lateral subsidence that would be expected in May 2010 following extraction commencing in November 2008, (i.e. Assumed delay time was 18 months). ....	237
Table 7.2 The distance from the nearest edge of the weighted extraction cylinder to the Borehole (m) in delay times varying from zero to 20 months.....	244
Table 7.3 Some cut-off distances of extraction and cut-off horizontal movement of strata at surface, 135 m and 166 m, in linear and nonlinear correlations, North 5, Huntly East Coalmine.....	250
Table 7.4 Samples of the extraction vectors and extraction duration for 11 surveys in 8 measurement months, 18 months delay time. ....	251
Table 7.5 Parameters as input into Phase2 modelling, Huntly East Coalmine. ..	258
Table 7.6 The coordinates of geological settings for the 9 layers in modelling..	261
Table 7.7 Coordinates for plotting groundwater piezometer lines for modelling (from Larratt et al., 2009 and Table 7.6 in section 7.3.2.2).....	262
Table 7.8 Averages of parameters for 9 layers for determining failure criterion. (G)-H-B: (Generalised Hoek Brown criterion; D-P: Drucker Prager criterion; M-C: Mohr Coulomb criterion. ....	265
Table 7.9 The outcomes of initial trials to choose the failure criterion, using one layer model by inputting the average parameters from Table 7.8, measurement distances of 438 m and 472 m. ....	266
Table 7.10 Variables used for trials of subsidence modelling using Phase2.....	267
Table 7.11 The 24 Combinations of modelling trials with varying factors from Table 7.8. ....	267
Table 7.12 The modelling results for 24 combinations, modelled using Phase2, with average Young's Modulus. Iteration /tolerance: 500/0.001; Lateral displacement measured (mm) : 27.9 mm/19.2 mm at distances of 438 m/472 m. ....	268
Table 7.13 Variables and constants used for trials of subsidence modelling using Phase2.....	269
Table 7.14 The failure criterion and the suitable strata to assign (from Section 4.4.7.2).....	270
Table 7.15 The modelling results for eight combinations, modelled using Phase2, by inputting average Young's Modulus. Iteration /tolerance: 500/0.001 .....	270
Table 7.16 Variables used for the final modelling of strata movement using Phase2.....	271
Table 7.17 The final results of modelling using Phase2 with parameters from Table 7.16, all tests were convergent. No corresponding measured vertical data available.....	272
Table 7.18 Some cut-off distances of extraction and cut-off horizontal movement of strata at surface, 135 m, and 166 m, North 5, the Huntly East Coalmine. ....	279





# Chapter 1 Introduction

## 1.1 Considerations in Coal Mining Practice

The environmentally responsible development of New Zealand's mineral resources has been scheduled as one priority in the six main policy drivers in the Economic Growth Agenda (The New Zealand Government, 2010). Coal is a significant natural resource and will bring benefits to New Zealand by means of more exploration, more extraction, and high extraction ratio of coal to meet requirements from overseas and the domestic needs of New Zealand economic development (Brownlee, 2009).

To improve the contribution of mineral resources, we need to concentrate not only on quantity of exploration and extraction, but also on the extraction ratio. A higher extraction ratio plays a significant role in leaving less mineral resources underground, and meanwhile maximising the resource recovered for a given environmental impact. It is important to understand the mechanisms of land subsidence and to optimise the extraction layout, especially in thick coal seams, to maximise the coal extraction ratio and minimise the adverse environmental effects (Howard L. et al., 1992).

Ground subsidence is one of the effects resulting from underground mining, which impacts on society, ecology, and environments. The United States Geological Survey estimates that land subsidence, and resulting flooding and structural damage, costs \$125 million annually and \$400 million is spent annually in the USA to control subsidence (New York State, 2007). Every year in China, approximately 120,000 ha of agricultural land are ruined by subsidence and associated changes of land water regime, induced by coal extraction. In north-west



of China, 2000 residents have to migrate out the mine area for every 10 million tonnes of coal extraction (He et al., 2003). Little information on the cost of mine-induced subsidence is available in New Zealand. However, the cost of the subsidence damage to the New Zealand Electricity Division (NZED) Hostel in 1983 above the Huntly East Mine was estimated at approximately \$450,000 (Kelsey, 1986). In 2002, eighty-three properties were evaluated in high and medium risk zones of potential ground collapses above, and adjacent to, the Martha Gold Mine at Waihi. For safety reasons the properties were vacated (Hauraki District Council, 2002).

In recent years, with the rapid development in mining, expansion of urbanization and increasing concerns for the environment, mining companies and associated research agents have devoted attention to the subject of subsidence and studied it in a more methodical manner across the world. Appropriate regulations and specifications related to ground subsidence have also been enforced by government agencies (Li et al., 2010).

In New Zealand, Sections 2, 106 and 220 in the Resource Management Act (RMA) regulate land management including land subsidence hazards (New Zealand Government, RMA, 1991). Good mining practices must be reconciled with respect to the environment. The efforts of Oceana Gold at Macraes Flat and Reefion, Newmont Waihi Gold at Waihi, and Solid Energy at Stockton have demonstrated that mining and good environmental practice can 'sit side by side' (Brownlee, 2009). Through good practice it is proved that mining and the environment can co-exist together (Brownlee, 2009).

## 1.2 Huntly East Mine

### 1.2.1 Location and Establishment

Huntly East Underground Mine commenced production in 1978 from Huntly East. East Mine is one of Solid Energy's major coal mine sites and is located just north of Huntly Township, approximately 80 km south of Auckland (Figure 1.1). The main entrance of Huntly Underground Mine is located in the east side of Huntly Town (Figure 1.2) (Solid Energy, 2009).

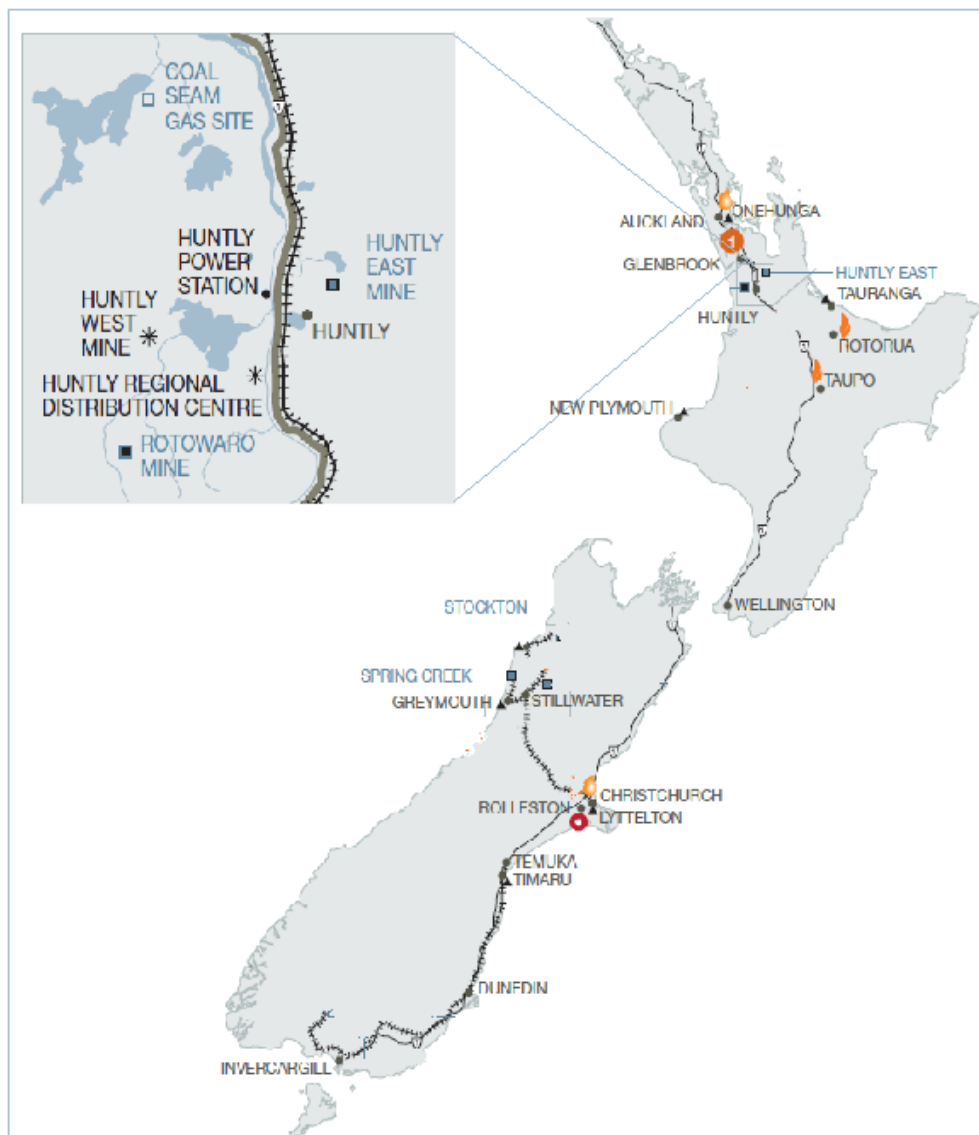
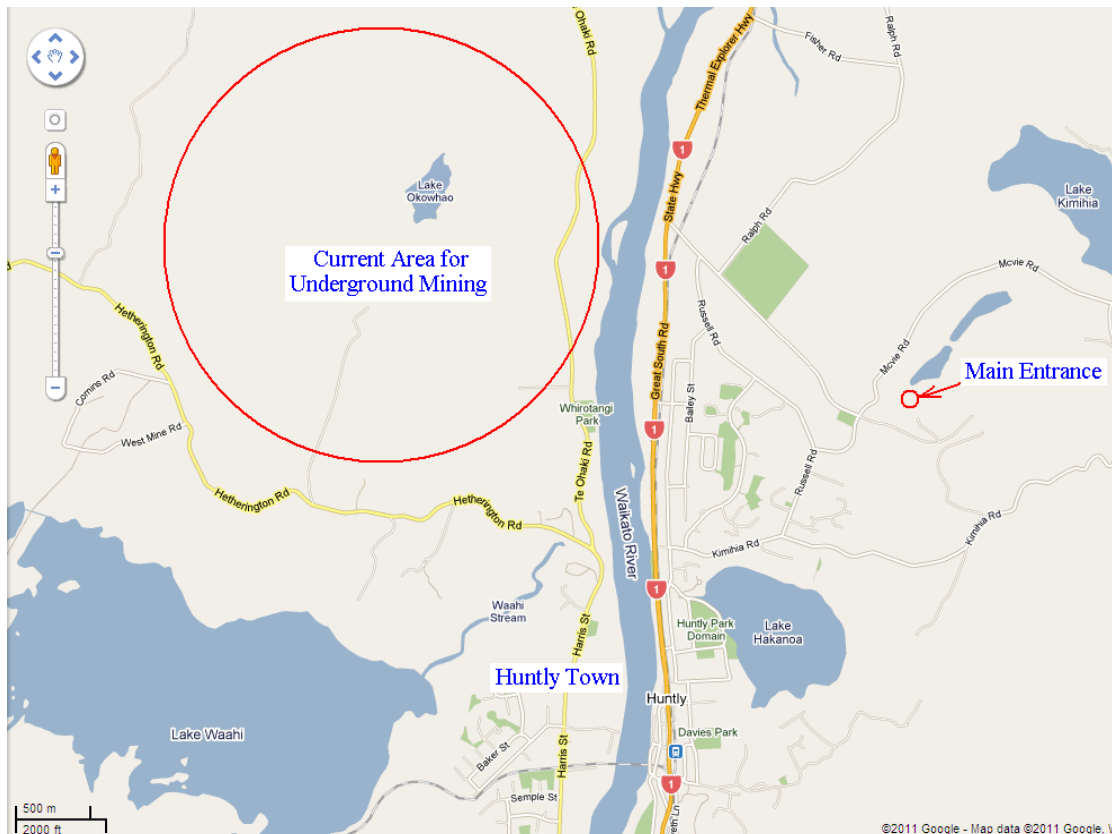


Figure 1.1 Location of Huntly East Coalmine (After Solid Energy, 2009).

Now all the mine development and coal extraction are being undertaken underground on the north-west side out of Huntly Township. The currently mined area is reached by an underground passage beneath the Waikato River (Figure 1.2). The depth of mining ranges from approximately 150 to 400 m (Solid Energy, 2007).



**Figure 1.2 Location of current underground mining and main entrance in the Huntly Underground mine (adopted from Google, 2011).**

### **1.2.2 Geology and Subsidence at Huntly East Mine**

The Huntly East Mine area consists of a sequence of mudstones and coal seams of the Te Kuiti Group with a thickness ranging from 25 m to 250 m, which is overlain by a succession of saturated sands, silts, and gravels of the Tauranga Group with a thickness from 25 to 70 m. The coal seam is typically 20 m thick (Figure 1.3) (Solid Energy, 2006).

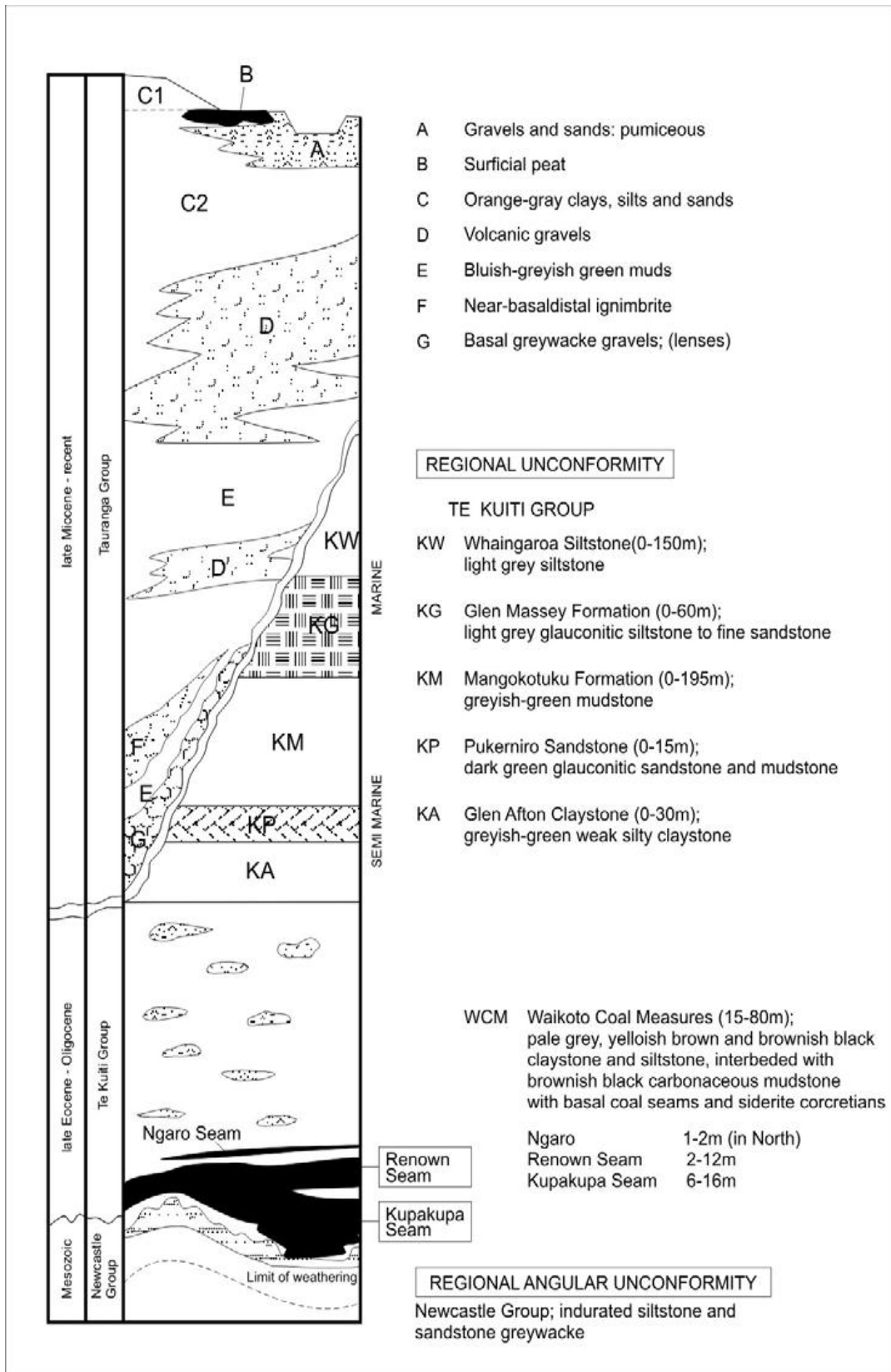


Figure 1.3 Typical geological section of Huntly Coalmine (Solid Energy, 2006).

Land subsidence was first noticed just five years after the initial production of the Huntly East Coalmine in early 1983. A sinking area of 7 hectares had a maximum

settlement of 800 mm. The subsidence impacted on NZED Hostel (Kelsey, 1986). The Huntly Coalmine area has been suffering ground subsidence for decades. In 2006, planned and managed subsidence over the north mine panels 51 and 52 ranged approximately from 1 to 1.2 m (Guy et al., 2006).

The first study of Huntly ground subsidence was undertaken by Kelsey in 1986. He researched the cause and mechanism of subsidence above the south heading of the Huntly East Mine, developed an engineering model of the subsidence and provided a numerical analysis of the model and at the end provided the suggestions for the future mining work (Kelsey, 1986). Following changes to mining zones, mining methods, seam depth, and geological and hydrological features, subsidence varies in respect to its extent, control measures and predictability. My study will investigate the relationship between subsidence and mining above the Huntly East N55 panel in the North 5 (N5) Extension area.

### **1.2.3 Current Mining Method**

In the Huntly East Mine, extraction is currently by a partial system – ‘Bord and Pillar’ mining methods (also called Room and Pillar mining) whereby some coal is purposefully left to ensure that subsidence is minimised and the coal extraction rate is maximised within the settlement control to meet environmental requirements (Gale, 2001) (Figure 1.4). Small coal pillars (fenders) are left within the extracted zone and the mined width is controlled. Large “barrier” pillars (chain pillars) are left to provide support to the overburden. The chain pillars and the panel extraction layouts are designed to manage subsidence. Figure 1.4 illustrates the normal design layouts of the extraction to manage inter-connection risk and subsidence in Hunt East Underground Mine (Gale, 2007). Figure 1.5 shows the as-built layout of the N51 panel (Gale, 2003).

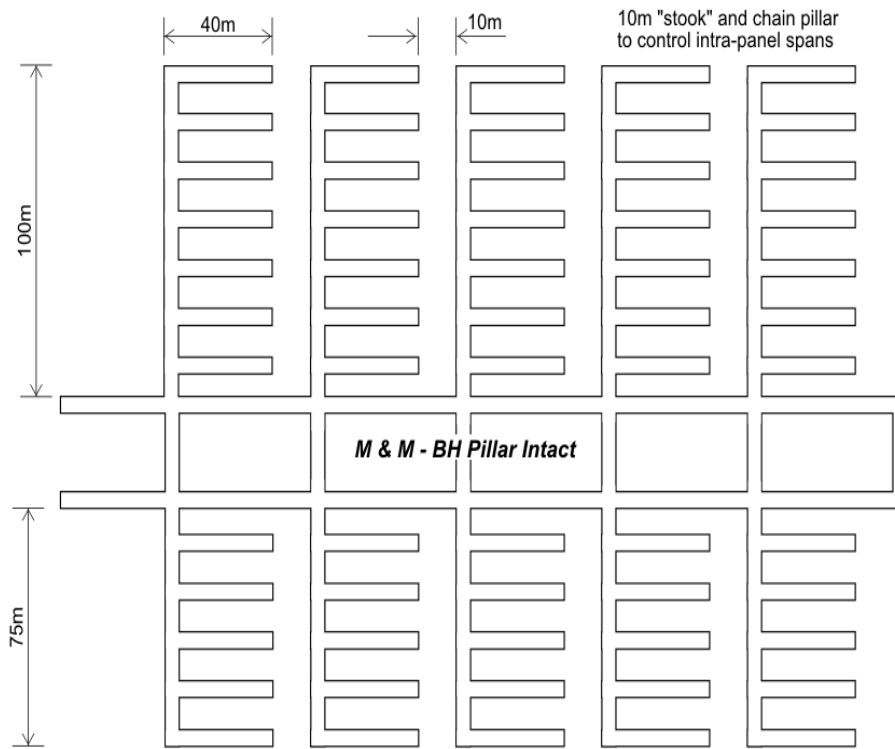


Figure 1.4 Idealised panel frameworks by Bord and Pillar mining (Gale, 2007).

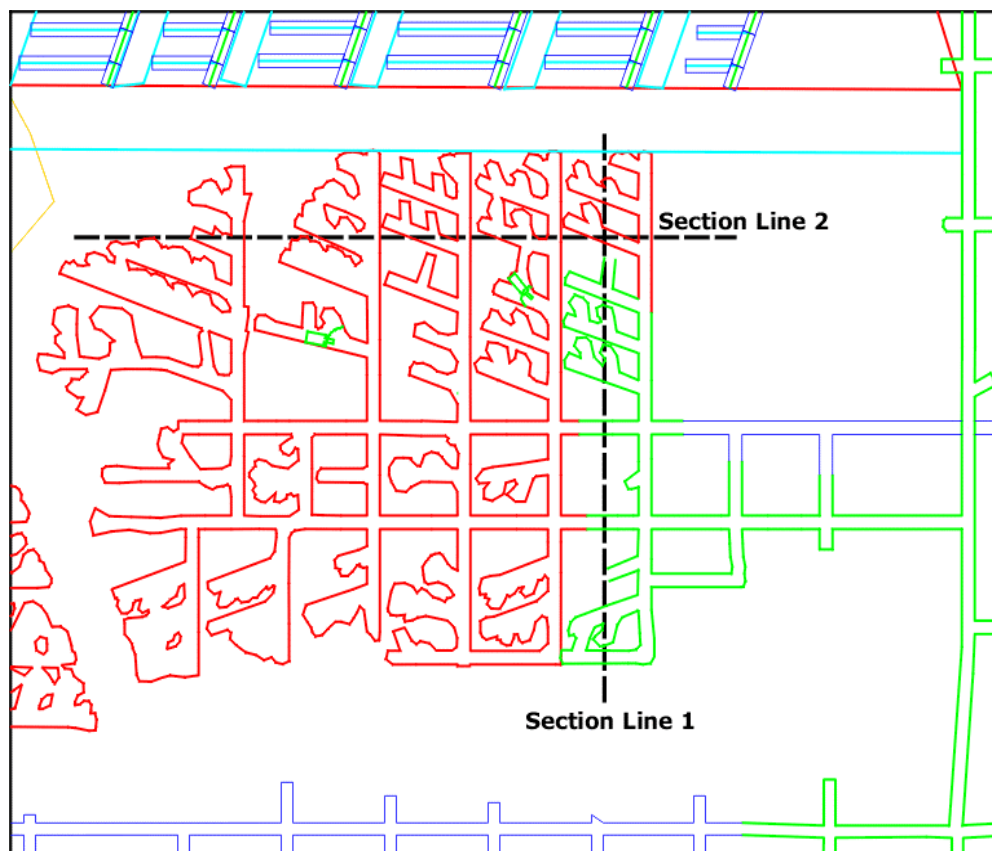


Figure 1.5 'As built' Bord and Pillar mining layout for N51 (Gale, 2003).

### **1.3 Current Development at Huntly East Mine**

Solid Energy New Zealand (SENZ) currently extracts coal from the Huntly East Underground Coal Mine in areas named the North 5, North 5 Extension, and North 6 areas (Figure 1.6). To meet continuing demand for coal both domestically and internationally, SENZ has planned to expand its underground operations into an area referred to as the Huntly North Project area (HNP). Current coal extraction at the Huntly East Mine is approximately 450,000 tonnes per year. The proposed extension of the underground mine into the HNP would necessitate an extensive increase in the length of underground access roadways. SENZ, therefore, suggested sinking a ventilation shaft between the surface and the underground workings of the HNP. The Huntly North Project (HNP) area is located to the west of the Waikato River, approximately 4 km north of Huntly Township, which is next to the existing North 5 Extension (Figure 1.6). Solid Energy expects coal extraction from the HNP will continue for a period of about 15 years (Larratt et al., 2009; Golder Kingett Mitchell, 2007).

The proposed vertical shaft has an internal diameter of 4 meters and depth of 300 meters (Larratt et al., 2009). The lateral movement and vertical subsidence of strata will impact on shaft safety. Therefore, the major aim of this study is to research the mechanism linking underground seam extraction to ground subsidence by monitoring the changes of strata around inclinometer borehole 20091 (referred as 'the Borehole' in this thesis) as a simulation of the large shaft. The study results may contribute to the design of protection pillars beneath the shaft site, in order to control the subsidence and strata horizontal movement, and ensure the safety of the shaft while maximising the extraction of coal around the protection pillars.



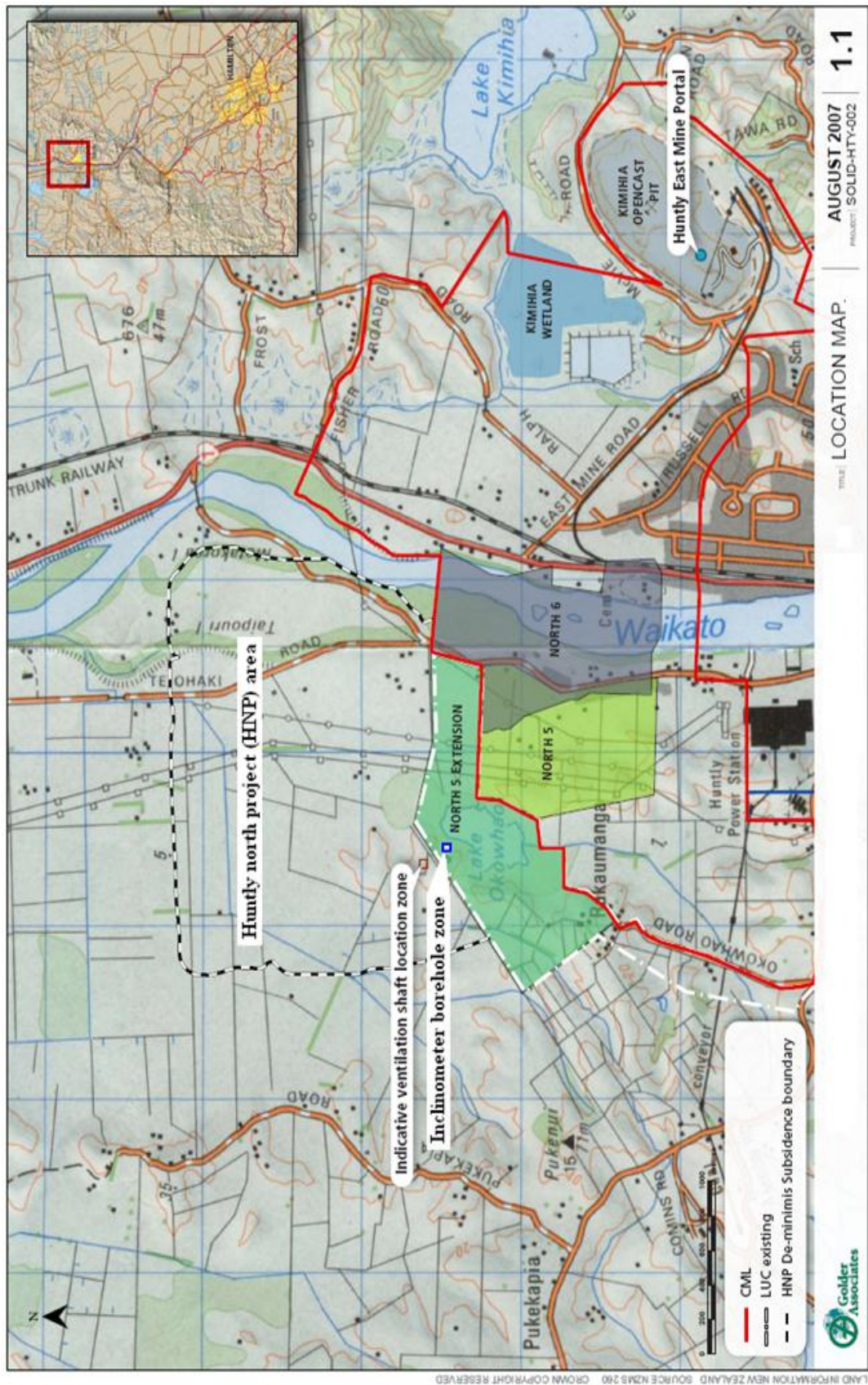


Figure 1.6 The location of the Huntly North Project (Solid Energy, 2007).



## **1.4 Objectives of Study**

My study is developed in collaboration with Solid Energy North. My research concentrates on monitoring a 250 meter deep inclinometer borehole to assess changes of strata horizontally and vertically that occur as underground mining approaches the inclinometer shaft.

The research will provide information on how close to the shaft we can plan to extract coal without inducing strata movement. Horizontal movement along bedding planes and strata vertical settlement along lining may cause damage to the proposed shaft lining. The information from the project will be a direct input into what the pillars pattern and how large the barrier (safety) pillar around the shaft needs to be, that is, how far is the extraction to the protection pillar. The larger is the barrier pillar, the lower the overall resource utilisation for the mine.

Therefore, the objectives of this study are summarised as the following:

- To study subsidence characteristics above and adjacent to the N55 panel by monitoring the inclinometer and interpreting the data collected from the inclinometer borehole as the underground mining advances.
- To develop a model of subsidence adjacent to the inclinometer drill hole.
- To compare the modelled subsidence with what we have measured, are they correlated or different?

# Chapter 2 Literature Review

## 2.1 Introduction

There is considerable literature on the topics of subsidence, inclinometer monitoring and shaft sinking. The literature may deal with one or several aspects such as the mechanism, models, formulae, and effects of ground subsidence; subsidence control and pillar design; shaft and subsidence; and the negative vertical force acting on shaft lining from strata subsidence.

This chapter includes three main areas: subsidence, shaft sinking, and inclinometer monitoring, which are briefly reviewed. Some specific or detailed reviews in particular sub topics are attached in Appendix A.

Of the literature reviewed, some are directly related to the research of the geology and subsidence at Huntly East Mine, such as Tan and St. George (1989), Moon and Roy (2004), and Guy et al. (2006).

## 2.2 Literature on subsidence

Mine subsidence was recognised in the 1850s in Belgium and France. However, only from 1950s were efforts started in predicting the magnitudes of subsidence and its effect on the environment (Keilich, 2009). Thus, ground subsidence has been researched for more than half a century.

Subsidence is a natural or man-made phenomenon of the land surface sinking, and occurs in response to underground mining area throughout the world. Subsidence is mostly produced by the loss of subsurface support from withdrawal of underground resources, solid, liquid, or gas, as non-metal minerals, metal ores, geo-liquids and gas, and groundwater (Figure 2.1). The occurrence of land sinking

may be immediate and sudden or gradual to be delayed for many years with little or no horizontal displacement (Blodgett & Kuipers, 2002).

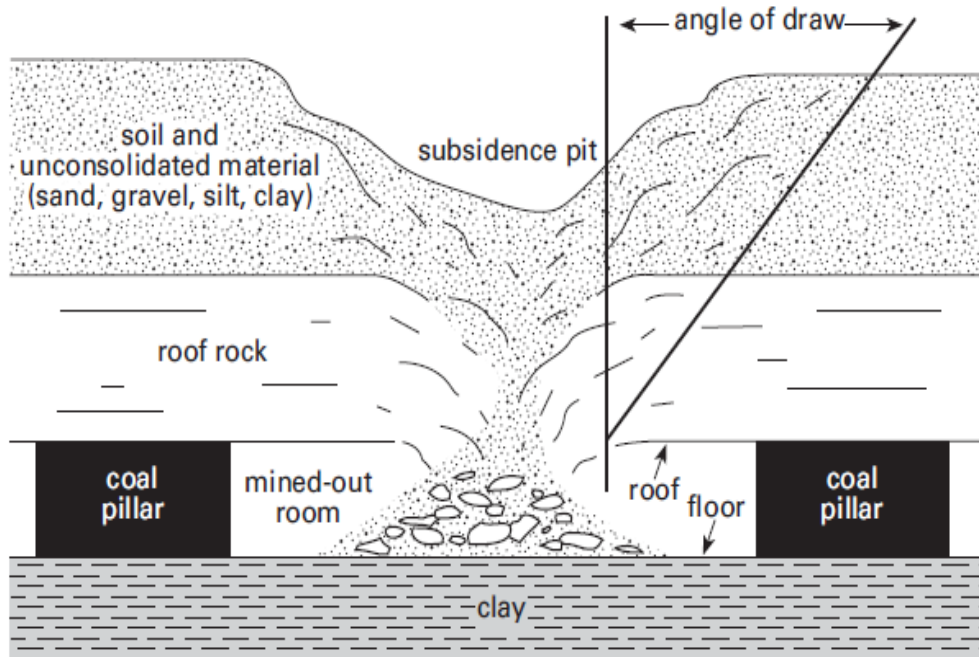


**Figure 2.1 Subsidence over coal seam withdrawal (after Crowell, 2010).**

Depending on the location of land subsidence, subsidence can pose significant risks in terms of health and safety, interruption to transportation, damage to infrastructure, and impacts on hydrological regimes (New York State, 2007; Johnson 1991; Karmis et al., 2008).

### **2.2.1 Mechanism of subsidence**

When a void is created underground the stress state in the surrounding strata becomes unbalanced (Keilich, 2009; Howard et al., 1992). The disturbed stress leads to deformations and displacements of the surrounding materials. The scale of deformation and displacement relies on the 'magnitude of the stresses and the cavity dimensions' (Howard et al., 1992).

Depending on the roof bridging capacity, the pillar stability, and strata arching strength, the deformation and displacement may move and extend to the surface,

to form a ground surface depression, which is commonly called subsidence. Therefore, the mine subsidence mechanism can be summarised as: mine subsidence is the ground movement above mine panels, that occurs in response to the overlying strata caving and ground movement which refills the mine voids to replace the extracted minerals. The space produced by mineral extraction is filled up by the caved rocks, by small amounts of dilation of the interlocked strata above, and by a little bulking of the caved rock. Therefore, land subsidence is the end result of the ground movement into the extracted zone (Gale, 2006). Land subsidence is a dynamic, spatial and temporal process (Cao et al., 2008).

Subsidence includes both vertical displacement, and horizontal displacement of materials (Whittaker and Reddish, 1989). The horizontal area of deformed ground is, therefore, larger than the area of the mined out panel itself (Figure 2.2). The majority of the subsidence happens over the centre of the extraction panel and tapers off around the perimeter of the panel. The vertical settlement at the surface is mostly smaller than the extracted coal thickness due to voids left in the collapsed strata and the bulking effect of caving materials (Whittaker and Reddish, 1989; Mine Subsidence Engineering Consultants, 2007).

A typical mine always has more than one panel. Thus, the areas of effects of adjacent panels have overlapping zones and consequently differential subsidence is expected above a panel when an adjacent panel is being mined. Therefore, the overlapping subsidence is larger than for a single extracted panel (Mine Subsidence Engineering Consultants, 2007; Gutierrez et al., 2010).

It is usually accepted that vertical subsidence of less than 20 mm has negligible effect on surface infrastructure and it is 'generally adopted as the cut-off point for determination of the angle of draw' (Debono, 2007). In the Coalfields of New

South Wales (NSW), the angle of draw is taken as 26.5 degrees when local data is not available, i.e. a point on the surface at a distance of half the depth of cover from the goaf edge.

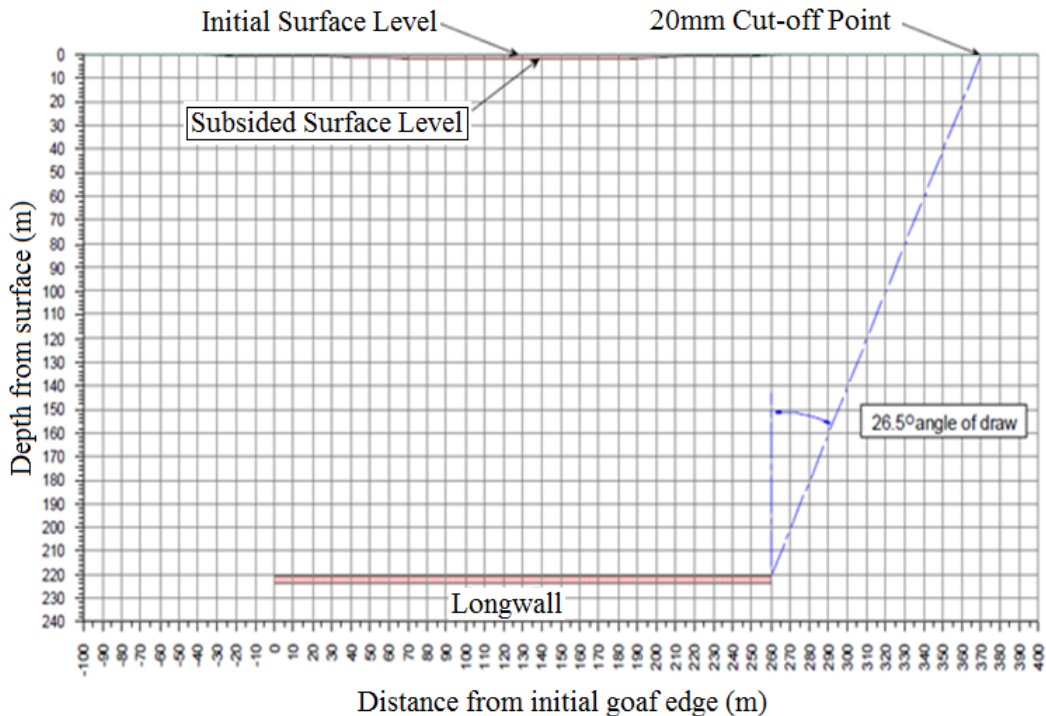


**Figure 2.2 Typical subsidence profile (from Debono, 2007).**

If the extracted panel is narrow in width and the strata above the seam are strong enough, the roof may not collapse and thence no surface subsidence occurs. However, in order to maximise the utilisation of coal resources, wide panels of coal are mined mostly, hence, the roof is prone to collapse. This threshold panel width is named the critical width and is generally used as ‘1.4 times depth of cover. It does, however, depend upon the nature of the strata’ (Debono, 2007).

Where great super-critical areas are mined, the maximum possible subsidence may range from 55% to 65% of the extracted seam height. By leaving chain pillars in place providing some support, the maximum subsidence is then normally less than the range 55% to 65% of the extracted seam height (Debono, 2007).

Due to the overlapping effects of subsidence induced from neighbouring panels, the incremental subsidence of a second or subsequent panel adjacent is larger than the subsidence of an individually separated panel of the same geometry. As further adjacent panels are under extraction, additional subsidence occurs above the previously mined panel or panels. The subsidence effect spreads across the ground as wave at approximately the same speed as the longwall face advances within the panel. ‘The development of subsidence at any point on the surface of the ground can be seen to be a very complex mechanism and the cumulative effect of a number of separate movements’ (Debono, 2007).

### **2.2.2 Dynamic Subsidence and Final Subsidence**

Dynamic subsidence is the subsidence movement occurring as mining advances toward, beneath, and past a point of interest in the strata and on the surface. Final subsidence is the degree and profile of subsidence after the extraction has passed that point of interest and ‘no further subsidence-related movements are expected to occur’ (Karmis et al, 2008; Liu, 2010).

Both dynamic and static subsidence need to be assessed in terms of their different damage potential to the structures on the surface and in the subsurface. The final, static subsidence troughs have permanent impacts on surface structures located near the edges of the subsidence basin from tensional strains. However, dynamic subsidence applies both tensile and compressive strains to the structures as mining progresses, so structures in the subsidence domain may be damaged by both tension and compression (Karmis et al., 2008; Liu, 2010).

### 2.2.3 Subsidence Impacts at the Surface and in Subsurface

The most significant impacts on surface and subsurface structures occur during the development of the subsidence trough as maximum ground movements occur. During the ground movement horizontal tensile strains build from zero up to a maximum over the length of convex curvature (Figure 2.3) (Debono, 2007).

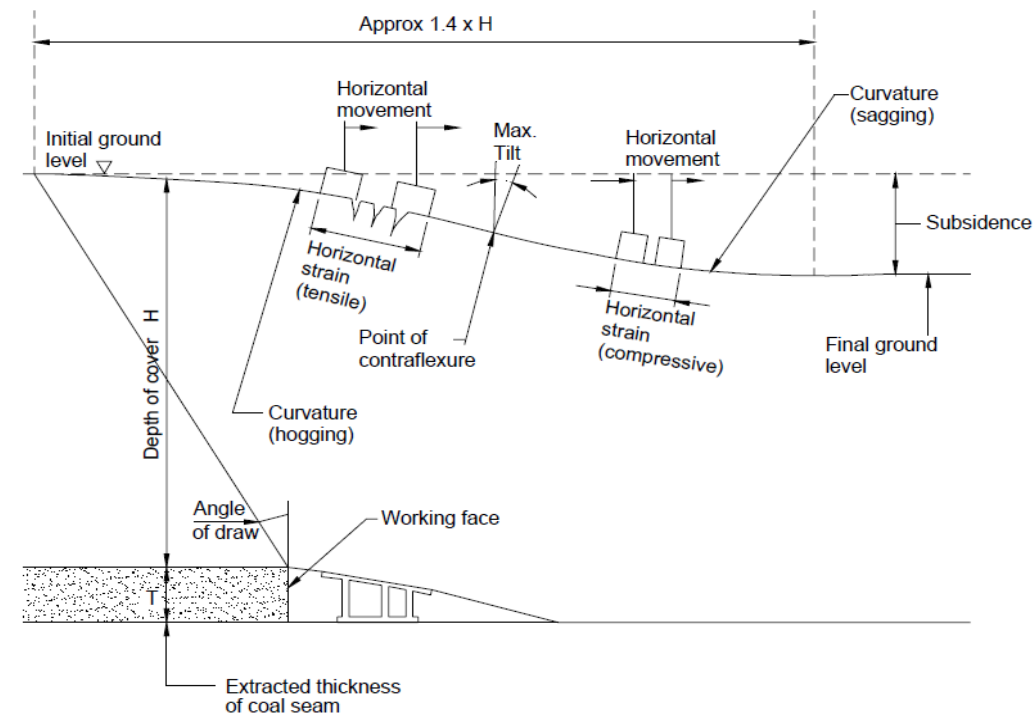


**Figure 2.3** Development of a subsidence trough in exaggerated vertical scale (from Debono, 2007).

Most of the points on the ground and in the subsurface suffer three-dimensional movements with changing tilt, curvature, and strain in both transverse and longitudinal directions. The impacts of subsidence on structures therefore depend upon the location of the structures within the trough. Surface features at the positions with maximum curvature and strain generally suffer the largest damage (Debono, 2007). A structure, i.e. a shaft lining, in the ground within a subsidence zone may suffer bending, shear, compressive, and tensile forces.

## **2.2.4 Previous Investigations for the Huntly East Mine**

Investigation of subsidence of the Huntly East Mine started in 1978 by the establishment of survey network by the Department of Lands and Survey to monitor relative ground movement above the underground mining. From the observation of the benchmarks that were not influenced by the mining activity, Bradley (1982) reported that the seasonal vertical settlement in the Huntly East Mine from natural causes is generally less than 5 mm (cited by Kelsey, 1986). Until 1985 the subsidence with settlement greater than 100 mm was noticed at three sites (Figure 2.4) (Kelsey 1986).

Subsidence features at Huntly East were (Kelsey 1986):

- The subsidence was characterised into two phases: rapid phase and slow phase. Rapid settlement reached 10 to 36 mm per day; slow subsidence was averaged approximately 0.1 to 0.7 mm /day (Figure 2.4).
- 75% of total subsidence occurred within 7.7% and 15% of total settlement time period for the E91 and E53 panels respectively in the rapid phase.

In 1983 State Coal Mines (S. C. M.) undertook a surface investigation by mapping the compressive and tensile subsidence characteristics around the NZED Hostel and installing 10 piezometers to monitor the upper aquifer in the Tauranga Group. Up to 1986 no significant decline in water level had been measured i.e. no major water interconnection resulted from the underground mining (Kelsey 1986).



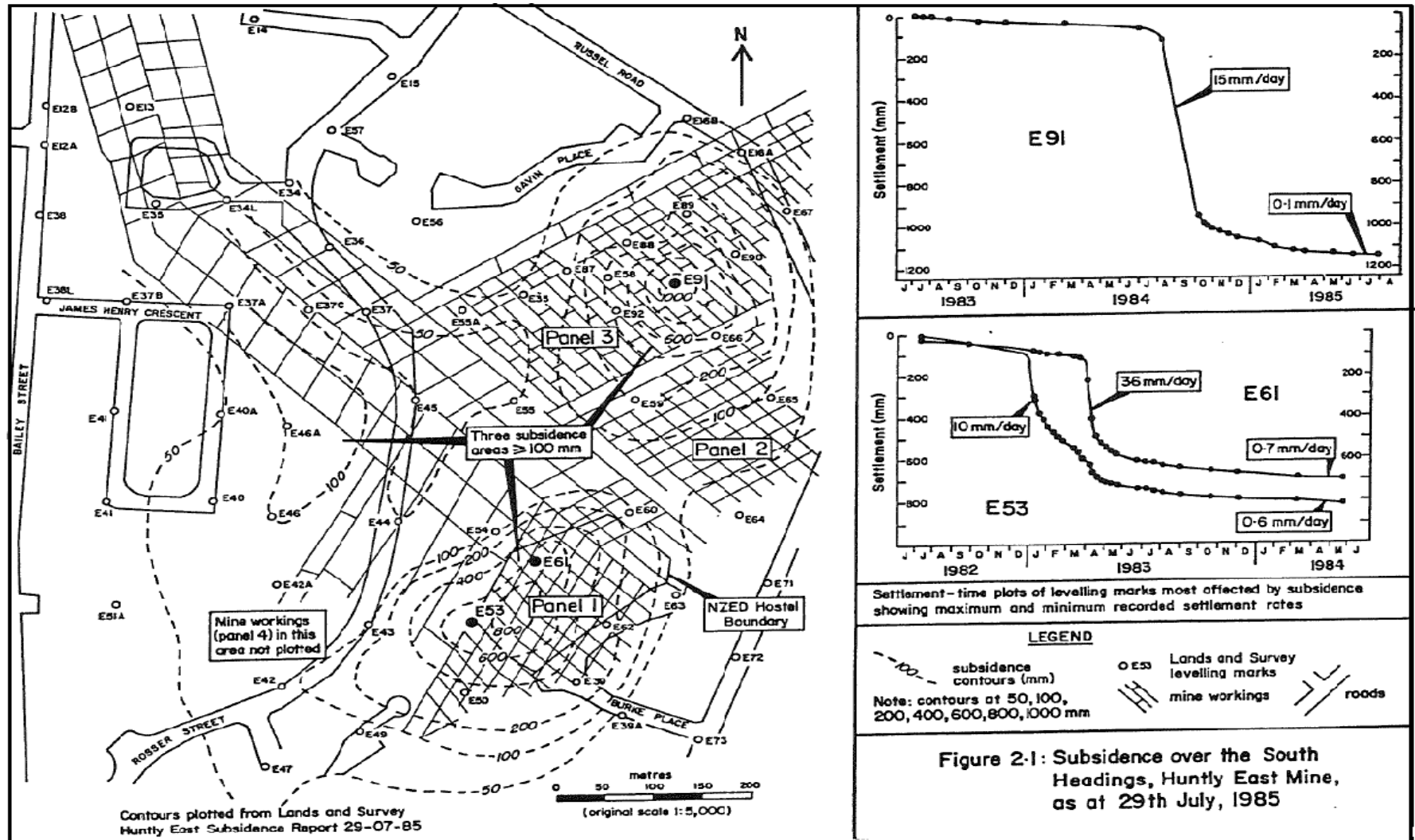


Figure 2.4 Subsidence over the south headings, Huntly at 29th July 1985 (from Kelsey, 1986).

Kelsey (1986) pointed out that the engineering geological model of the subsidence is most likely to be mine roof collapse leading to void migration to near the top of the Te Kuiti Group sequence causing drainage and depressurisation of aquifers at the bottom of the Tauranga Group. Aquifer depressurisation causes consolidation within both the aquifer and aquitards by dewatering due to drainage (Kelsey, 1986).

Guy et al. (2006) studied the interaction between underground mining and overlying aquifers at Huntly. They found that ‘the overburden rocks, whether clay rich or not, have a significant joint fabric which allows flow at rates greater than intact clay units.’

Strata Control Technology (SCT) (an Australia based geotechnical consultant and instrumentation company) has collaborated with Solid Energy in coal mine extraction consultation since 2001. SCT submits their consultation in designs of extraction outlay, mine thickness, subsidence prediction, pillar design and relative reviews, mostly using the FLAC code to simulate the subsidence and the underground coal extraction at Huntly East Mine. There are nearly 20 geotechnical reports submitted over the ten years, which are summarised in Section 4.4.2.5.

## **2.2.5 Prediction of Subsidence**

### **2.2.5.1 Introduction**

Subsidence control measures can be taken in the following three stages: (1) Prediction; (2) Prevention; and (3) Protection. In many cases the occurrence of ground subsidence induced by mine extraction is predictable, but, sometimes, there are some uncertainties to predict the subsidence (Whittaker and Reddish,

1989). The effectiveness of preventative and protective measures on subsidence depend on the predictive accuracy of subsidence and its associated parameters, such as vertical subsidence, horizontal displacement, tilt, curvature and associated tensile and compressive strains needed to assess the possible damage to surface or in-ground structures. Once the maximum subsidence and the profile of the subsidence curve are predicted, other parameters can be calculated. Therefore, prediction of subsidence is of significance in underground mining (Bahuguna et al, 1991).

Various authors have suggested a number of ways to classify the prediction methods of subsidence (Bahuguna et al., 1991; Puertas, 2010; Aston et al., 1987; Haciosmanoglu 2004; Whittaker and Reddish, 1989). In this thesis, the methods for prediction of the ground subsidence are classified into 4 types: (a) empirical techniques, (b) numerical modelling, (c) physical models, and (d) artificial neural networks (ANNs). This section mainly focuses on introducing the numerical modelling method. A review of the other three methods is attached in Appendix A.

Empirical methods, mainly including graphical methods, profile functions, and influence functions, are derived from experience obtained from a number of field measurements and past projects. Empirical methods are fast, simple to apply and present ‘fairly satisfactory results’ (Bahuguna et al., 1991).

Numerical or theoretical methods use analytical or mechanistic characteristics and based on the rheology and mechanics of subsiding materials and their response to changing extraction geometries (Bahuguna et al., 1991). Numerical methods work on modelling principles by using mathematical representation of idealized materials in the application of continuum mechanics (Blodgett & Kuipers, 2002).

The prediction work by both empirical methods and numerical methods can be computer-based or handwriting-paper-based. The choice of subsidence prediction models depends primarily on the mining 'situations being simulated and on the information sought' (Whittaker and Reddish, 1989).

#### **2.2.5.2 Theoretical numerical techniques**

Numerical models are also called theoretical models (UWA, 2010). Numerical modelling is the process of solving the equations representing a mechanical process by a step-wise approximation, to reach the final satisfying solutions (Minerals Council of Australia, 1997). Numerical methods have the advantage that, once the model is established, then a number of associated scenarios may be investigated by simulation. However, it must be remembered that numerical models may create wrong judgement in application.

There has been significant development in numerical methods as powerful tools for solving complex problems, such as geological, mechanic and, hydrological questions, following the development of computer technology. A number of commercial numerical analysis codes have become relatively user friendly in recent times, such as ABAQUS, ADINA, ANSYS, FLAC, RocScience and UDEC (Kumar et al., 2010).

Several theoretical or numerical techniques have been utilised for problems in subsidence prediction. The computerized numerical modelling methods include the Finite Element Method (FEM), Boundary Element Method (BEM), Distinct (or discrete) Element Method (DEM), and Finite Difference Method (FDM) (UWA, 2010).

Numerical models are based on statistical and mechanistic rules treating the material of the overburden as a ‘model of either a cohesionless stochastic or elastic, or even plastic, isotropic or anisotropic medium’ (Bahuguna, et al., 1991). The numerical modelling methods are used in modelling overburden and simulation of mine geometry to predict subsidence over mine panels. Finite difference (FDM) and finite element (FEM) models are currently popular. FEM models are more suitable for problems with complicated boundaries, but the methods are somewhat more complicated than FDM models (Bahuguna, et al., 1991).

Calibration and verification is an integral part of numerical modelling because of the simplifications, formulations, and assumptions used in describing the physical processes (UWA, 2010). By verification the modeller can tune the parameters and indices against an observed event. The practicability of simpler models should be scrutinized first because complex models may have a larger opportunity for errors both judgementally and numerically. Finally, the restrictions of the model should always be clearly understood (UWA, 2010; Minerals Council of Australia, 1997, Mine-site Water Management Handbook MWMH Fact Sheet 12).

### **Theoretical analysis methods**

Theoretical analysis methods are mainly based on continuum mechanics principles for prediction of the magnitude of subsidence. A number of behavioural models for immediate roof and strata above, such as elastic, plastic, visco-elastic, and elasto-plastic ones, have been used for predicting the surface subsidence in different situations. Szpetkowski (1972) introduced a theoretical model for

calculation of surface subsidence at point P(x, y) when excavating an area A at a depth of H and thickness of m (Figure 2.5) (Li et al, 2010).

$$S = \frac{am}{4\pi BH} \int_a^b \exp\left[\frac{-(x-\xi)^2}{4BH}\right] d\xi \times \int_c^d \exp\left[\frac{-(y-\eta)^2}{4BH}\right] d\eta$$

Where, a is the subsidence factor, symbols  $\xi$  and  $\eta$  are coefficients of the working conditions, and B can be calculated from

$$\frac{1}{\sqrt{2B}} = \frac{k\sqrt{2\pi}}{1000}$$

Where, k is a characteristic quantity of the overburden strata (Li et al, 2010).

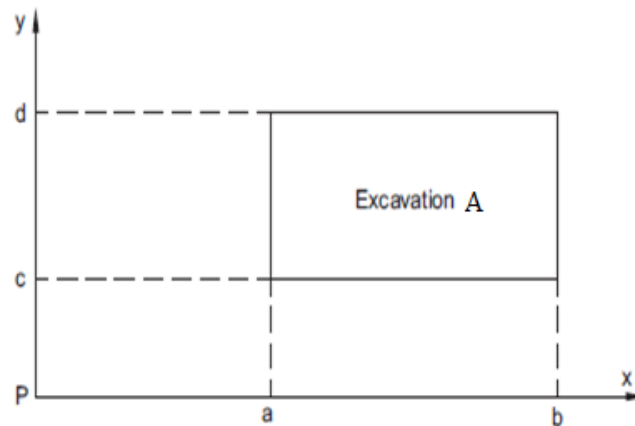


**Figure 2.5** The locations of the point P and excavation underground (From Li et al., 2010).

### **FEM: Finite element method**

The finite element method (FEM) is the most widely used numerical method for geological mechanics and rock engineering, as it does not need detailed programming experience to make efficient use of the finite element approach to problem solving in rock mechanics (UWA, 2010).

FEM undertakes the structural analysis of the overburden and gob (goaf) by dividing and subdividing it into a set of finite individual structural elements, also

called sub-domains (UWA, 2010; Haciosmanoglu, 2004). Under the stresses in the overburden body, the nodes of the mesh, as elements of strata, suffer strains and get displaced.

The magnitudes of displacement of each element are dependent on the values of stress and material properties of each element. The factors of geological discontinuities such as joints, faults, bedding planes, and different types of overlying layers, can be put into FEM for prediction of the subsidence.

In FEM the element mesh is spread all over the body of the overburden. Handling very large scale and complex equation systems will make the FEM method more voluminous and time consuming (Haciosmanoglu, 2004). The FEM software currently used are Phase2, ANSYS, Plaxis (Lawless et al, 2003) ADINA, Abaqus FEA (formerly ABAQUS) (Brown University, 2011).

### **BEM: Boundary element method**

The boundary element method (BEM) is much simpler to use. In the BEM of subsidence simulation, the element mesh is 'not spread all over the body of the overburden but only at the boundary' (Bahuguna et al., 1991; Haciosmanoglu, 2004). Therefore, BEM is more useful for situations where geological discontinuities are comparatively less as it is simpler than FEM. The BEM treats the rock mass as a 'discontinuous system of interacting blocks' (Bahuguna et al, 1991). This method is mainly suitable for modelling a jointed rock mass with deformation mechanism of separation of blocks, rotation of mass, or slip associated with large relative movements. Boundary element method has yet to develop its credit in confident subsidence prediction. A commonly used BEM software is LAMODEL (Kennedy, 2008).

## **FDM: Finite differential method**

In the finite differential method (FDM), the problem domain, such as a geological feature or manmade structure, is discretised into a set of sub-domains or elements. FDM demands physical or mathematical approximations made throughout an enclosed region. The solution procedure works on ‘numerical approximations of the governing equations, i.e. the differential equations of equilibrium, the strain displacement relations and stress-strain equations, as in classical finite difference methods’ (UWA, 2010). FDM may also use approximations to the connectivity of the elements, and continuity of displacements and stresses between elements, as in the finite element method (UWA, 2010).

Itasca International Incorporated has developed numerical modelling codes for solving problems in geomechanics and hydrology for the past 30 years. The finite difference, advanced continuum modelling codes (FLAC and FLAC3D) are suitable for geotechnical analysis of rock, soil, and structural support in two and three dimensions (Itasca, 2011).

## **2.3 Literature Review on Shaft Sinking**

### **2.3.1 Objectives**

Because the results of my inclinometer monitoring research may finally serve the shaft sinking project, the literature review on shaft sinking will help with scoping what the study should focus on. Aspects of subsidence monitoring include, such as, whether the movement directions of the strata studied should include lateral and vertical displacements; what data needs to be collected; and the extent of the ground area to study needs to be decided.



### **2.3.2 Mine Shaft**

Mine shafts are the most important infrastructure of deep mines, which supply all access and exit services to underground operations, including transport of ore and supplies, personnel traffic, fresh air, power, communications, water supply, and drainage (Unrug, 1998, cited by Queen's University, 2009). In 2012 Solid Energy North is to sink a vertical shaft as the main ventilation entrance over the N55 Panel that has a diameter of 4 meters and depth of 300 meters. The shaft will be sunk through the coal seam and will sit on the solid greywacke bedrock (Larratt, 2009). The lateral movement and vertical subsidence of strata may have major effects on shaft integrity and safety.

The shaft, firstly, must be located at a point where supported structures and mine working is in close proximity. Special concerns and considerations must be taken when the mine is to be very close to or located under waterbodies, such as a lake or close to major faults (Queen's University, 2009).

Secondly, the properties of the in-situ strata around the proposed shaft should be investigated. Drilling and coring are the most reliable measure to get the required geological information. Thus hydro-geological testing on core recovered and borehole logging reveal the aquifer characteristics, such as water levels, aquifer thickness, and hydrostatic heads. Geo-mechanical testing is necessary for measuring porosity, rock quality designation (RQD), inclination of strata, rock modulus, Poisson ratio, etc.

The investigation boreholes should be close enough to the proposed shaft axis (10 to 30 meters) to make sure the test results are representative of the shaft sinking conditions (Unrug, Location and Design of Vertical Shafts, 1992, cited by

Queen's University, 2009). If a pilot borehole will be used in shaft sinking (as in the designed method) then the pilot hole is ideal to use as an investigation drill hole.

The location of the shaft is also a trade-off between development costs, haulage distance and mineral recovery. For ore bodies with flat seam, constructing the shaft in the centre of the ore body is the most efficient solution. This reduces haulage distances, ventilation facility and airflows. However construction in the centre of the mined area may require use of safety pillars for shaft protection, consequently decreasing the recovery rate of the mineral resource. The alternative option, to increase the ore recovery, is to locate the shaft outside of the ore body. However, haulage and ventilation distances to the shaft go up remarkably, for instance, by an increase of 50%, compared to the central placement option (Queen's University, 2009).

### **2.3.3 The Negative Additional Vertical Friction**

The concept of 'Negative Additional Vertical Friction (stress)' originated from shaft lining rupture in Xinhua region, China and largely published in the Chinese literature. However over ten of the papers on the negative additional vertical friction (stress) have been published in International Journals or presented in International Conferences in English (such as Bi et al., 1997; Liang et al., 2009; Tobar and Meguid, 2010; Wang et al., 2010; Zhao et al., 2009; Zhou et al., 2009).

It is evident that the negative additional friction is an essential part of adverse effects from the ground subsidence onto the shaft lining. It is possible that we can use the negative additional friction concept to benefit us in this research project in help with the proposed shaft project, as a guidance and reference for the design,

construction and even later maintenance and protection in the duration of mining production. The geology at Huntly has similarity with the Xuhuai region. Up to July 2011, none of the reports, designs or documents on this Shaft has mentioned the negative additional friction and its impacts. Therefore, this review could be likely to be of some assistance and experience for the shaft sinking project above N55 panel.

The literature review on the negative additional vertical friction is attached in Appendix B.

## 2.4 Literature on Inclinometer

### 2.4.1 Principle and Technique

Lateral movement of the ground at depth can be measured by an inclinometer system. At first, the inclinometer casing is installed in an inclinometer borehole which is drilled into stable strata (Figure 2.6).

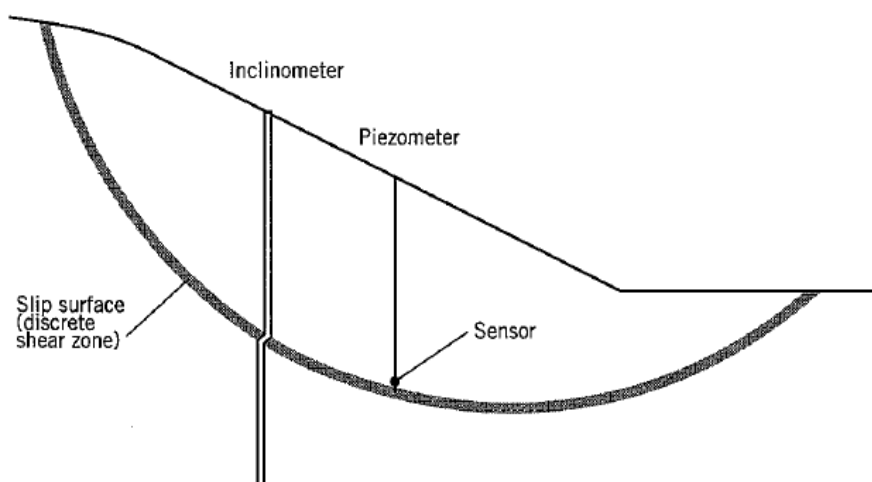


**Figure 2.6 Lateral movements monitoring with inclinometer (from Cornforth, 2005).**

The casing has four longitudinal grooves at 90 degrees, where the inclinometer's wheels can track along during the measurement (Figure 2.7). Accelerometers in the probe measure the tilt of the probe and casing at any depth along its traversing

length. The tilt supplies information about lateral movement through the sine function, tilt angle, and the hypotenuse of a right triangle (Figures 2.8, 2.9).

The distance between two wheels  $L$  is generally 500mm. the probe accelerometer detects the tilt angle change  $\theta$  from the absolute vertical, so the horizontal deflection per reading is calculated as  $(L \times \sin \theta)$ . A plot of data from summing up the deviations from the bottom provides a profile of the casing.

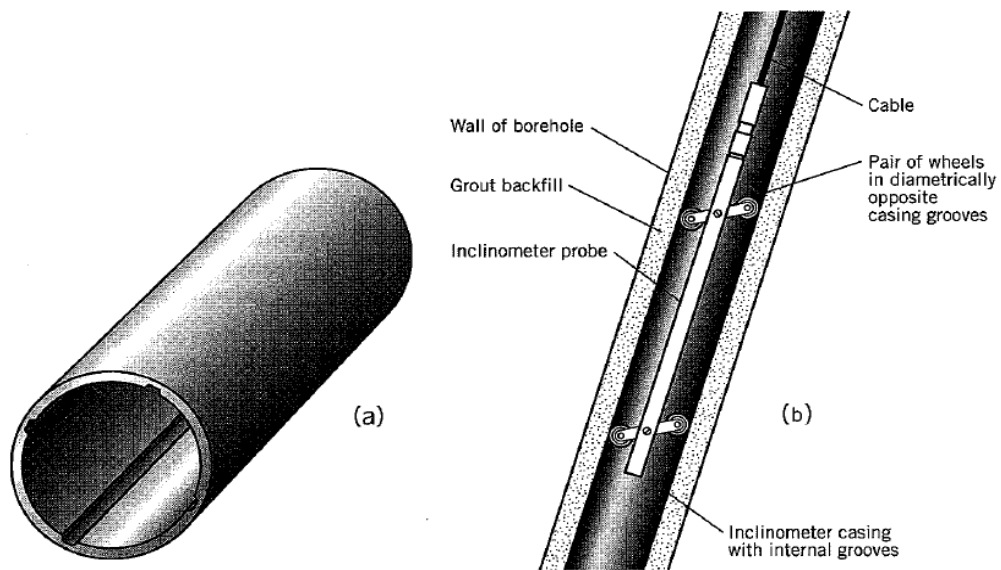


**Figure 2.7 (a) Incliner casing showing internal longitudinal grooves. (b) Incliner traversing in casing (from Machan & Bennett, 2008).**

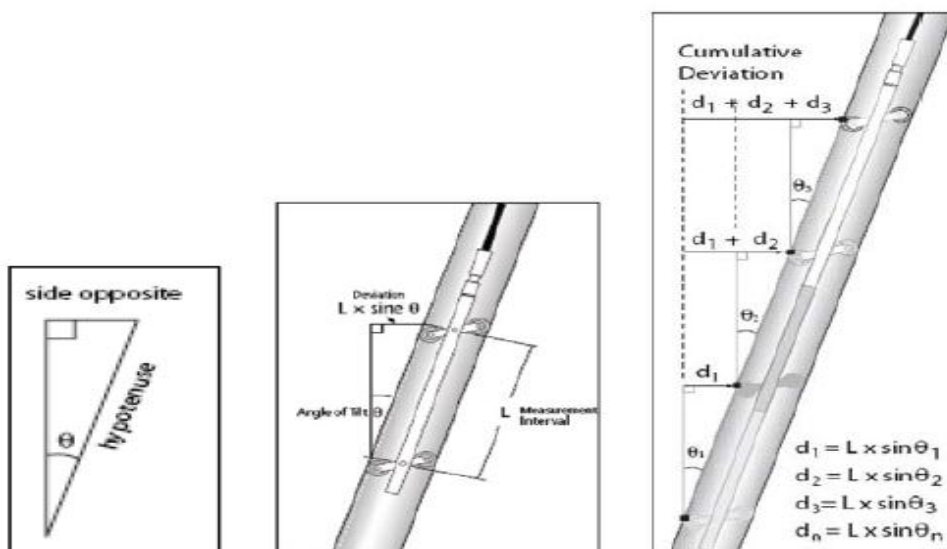


**Figure 2.8 Measurement principles of Incliner (from Machan & Bennett, 2008).**

Plotting curve lines from data sets from different site visits of measurement can tell whether changes in the shape of the casing in 2D or 3D have occurred, which can imply ground movement or displacement (Machan & Bennett, 2008). Comparison of successive casing profiles indicates the location, depth, direction, magnitude and rate of change in movement and type of ground movement (SOIL, 2008; Slope Indicator Company, 2006; Stark and Choi, 2008).

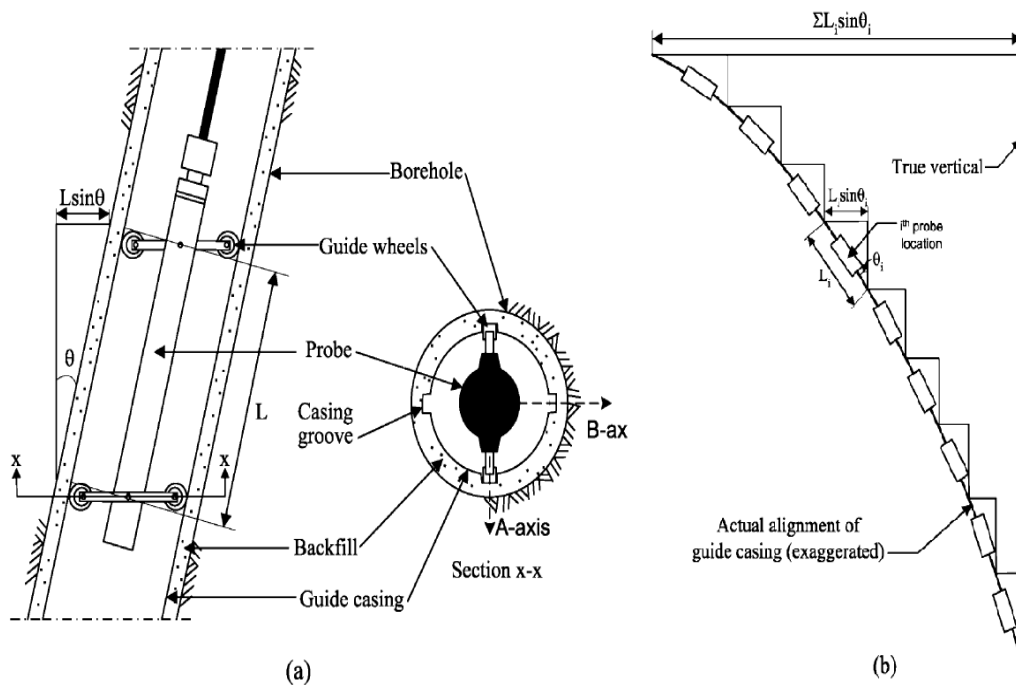


**Figure 2.9 (a), Principles of configuration of inclinometer equipment; (b), Illustration of inclinometer operation in cumulative displacement (from Stark and Choi, 2008).**

## 2.4.2 Application and Aims of Inclinometer Measurements

The inclinometer is a valuable instrument for analysing subsurface lateral movement. The incremental displacement (also referred to ‘deflection’) and cumulative horizontal displacement profiles are typically ‘the most reliable means to determine the zone of the shear movement’ (Stark and Choi, 2008) (Table 2.1).

Inclinometer monitoring can supply information of the depth of landslide movements; the thickness of a shear zone; the magnitude of the movement; the rate of the movement; and the direction of movement. The inclinometer can be used in areas: measuring lateral movement of earthworks or structure; landslides; stability adjacent to extraction or underground workings; and deflection of piles, piers, abutments or retaining walls (RST Instruments Ltd, 2010).

**Table 2.1 Determination of ground movement (after Stark and Choi, 2008; Cornforth, 2005).**

Determination of the Ground Movement and Trajectory		
Factors		On surface and In Subsurface
Borehole locations to initial	mm	Determined in the plot of resultant horizontal cumulative displacement
Movement magnitude	mm	Identified from resultant plot of cumulative displacement at certain depth(s)
Movement rate	mm/y or m/y inch/y	Distance between measurement divided by time of movement
Movement direction	Degree (bearing)	By $\text{ATAN}(D_b/D_a)$ at a depth
Zone thickness	(m)	Thickness of the creeping zone or shear zone

$D_a, D_b$ : the horizontal cumulative displacement in the A axis and B axis

Inclinometer data obtained can be used in modelling of movement, design of the retaining work, design of the structure, i.e. shaft, in ground with potential movement, and slide prediction work (Cornforth, 2005).

### 2.4.3 Inclinometer Types

There are two major types of accelerometers now being used in inclinometer probes: the most widely used servo-accelerometer or the recently introduced MEMS (Micro-Electro-Mechanical Systems) accelerometer. MEMS inclinometer probes have been used since 2005. The main advantages of the MEMS probe are

‘low power consumption, durability, wireless transmission and low cost’ (Machan & Bennett, 2008). Limitations include temperature sensitivity, signal noise, and low resolution from vertical. MEMS inclinometer systems need to be independently evaluated and demonstrated (Machan & Bennett, 2008).

One single probe may contain one or two biaxial accelerometers, which measure two horizontal deflections known as the A and B axes (Figure 2.10). The B sensor data measured are less accurate and more sensitive to curvature of the casing than those of the A sensor because the size of the casing groove controls the B-axis sensor alignment (Stark & Choi, 2008). The A axis, therefore, should be oriented with the direction of strata movement, while the B axis is at right angles to the A axis. The A0 axis is usually installed pointing in the expected movement direction of the ground so deformation corresponds to a positive value of change (Stark & Choi, 2008).

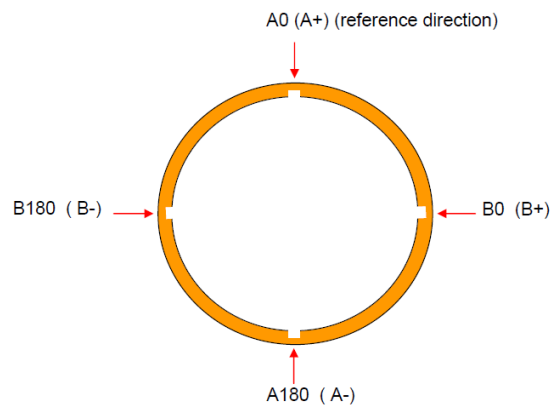


**Figure 2.10 Plan view of inclinometer casing showing groove directions (from SOIL, 2008).**

## **2.4.4 Current Inclinometer Developments**

### **2.4.4.1 Major Inclinometer Expertise and Software**

The currently available and efficient commercial inclinometer software packages are DigiPro®, DataMate Manager (DMM)®, Gtilt®, In-Site® and Inclinalysis®

(referred as ‘the 5 inclinometer software’ in this thesis) from the USA, Canada and UK (Table 2.2).

**Table 2.2 Summary of the major inclinometer software and function.**

Company name	SOIL UK	Slope Indicator (SI)		RST	Mitre Software
Inclinometer software	In-Site®	DigiPro®	DMM®	Inclinalysis®	GTILT®
Version, year	v2.92, 2010	v1.34.1(3) 2006	v2.9.1 2008	v 2.43, 2010	v2.18a, 2003
File Format Imported	RPP, MDB, GTILT, etc	RPP, MDB, GTILT,PCSLIN etc		RPP, CSV, GI, TXT, etc	RPP, MDB, RPX, etc.
Software Function	Import file	√	√	√	√
	Export file	√ (need Dongle)	√	√	√
	Borehole log data	√	x	x	√
	Validate	√	√	√	x
	Compare	√	√	√	√
	Alert monitoring	√	x	x	x
	Orientation edit	√	√	x	x
	Depth adjustment	√	x	x	x
	Plot deviation	√	√	√	√
	Plot displacement	√	√	√	√
	Absolute position	√	x	√	√
	Plot Checksum	x	√	√	√
	Reading Editor	√	√	√	√
	Bias correction	x	√	√	√
	Rotation correction	x	√	x	x
	Depth correction	x	√	x	x
	Spiral correction	x	√	x	√
	Strain vs. time	x	x	x	x
	displacement vs. time	x	x	x	√
	Plan view	√	x	x	√
	Absolute plan	√	x	√	√
	Report output	√	√	√	√
Settlement profile	x	x	√	x	
Angle & resultant	x	√	x	x	



#### 2.4.4.2 Literature on Inclinometer Borehole Monitoring

A considerable body of literature exists regarding case studies of inclinometer installations, with approximately 100 contributions reviewed in preparation of this thesis. Of these, some 14 recent papers and manuals represent the current state of research. These are summarised in Table 2.3.

**Table 2.3 Major literature on inclinometer borehole monitoring.**

	Author & year	Short Title	Max. Depth	Movement type	Data correction
Inclinometer Papers and reports	Mikkelsen, 2007	Inclinometer data and recognition of system errors	80m	slope	mentioned
	Machan & Bennett, 2008	Use of Inclinometer for Geotech Instrumentation	50 m	slope	mentioned
	Cornforth, 2005	Landslides in practice: investigation & analysis	90 m	slope	mentioned
	Mikkelsen, 2003	Advance in Inclinometer data analysis.	90m	slope	mentioned
	Sargand, 2004	Inclinometer – TDR Comparative Study	15m	slope	-
	Ryan & Berloger, 2007	Slope inclinometer installation and monitoring	40m	slope	-
	Forlati, et al., 2001	FE Analysis of a Deep-seated Slope Deformation	120 m	slope	-
Training documents	SI*, 2000	Data reduction; graph types; probe accuracy, Error corrections	90m	slope	mentioned
Inclinometer manuals	SI, 2011	DMM for Windows User Manual, pp48	70m	slope	mentioned
	SI, 2006	Digitilt Inclinometer Probe 50302599, pp13	100m	slope	mentioned
	SI, 2004	DigiPro for Windows User Manual, pp 38	100m	slope	mentioned
	SOIL, 2009	In-Site Inclinometer Data Software Manual	13m	slope	mentioned
	RST, 2010	RST MEMs Digital Inclinometer system manual	26.6m	slope	no
FBG sensor	Chai et al., 2010	Deformations in uncompacted strata by sensors (FBG)	181 m	Strata beside shafts induced by extraction	no

\*SI: Slope Indicator Company

Some key features from my review of the literature are:

- Installation of an inclinometer borehole deeper than 120 m were not found in the literature reviewed;
- only a few applications (one listed in Table 2.3) of inclinometer used for monitoring movement induced by underground extraction have been found;
- all reviewed cases have the bottom of the casing in stable strata below the movement zone; and
- no standards are available yet for evaluation against precision and bias issues arising (ASTM, 2005, cited by Machan & Bennett, 2008, p31).

In contrast, the inclinometer monitoring borehole in my research was 250 m deep, and the bottom of the casing was installed 50 m above the coal seam roof, i.e., the bottom section of the borehole had potential for displacement.

## **2.4.5 Plot Types**

### **2.4.5.1 Plot Type and Relationships**

In data reduction and error correction (Slope Indicator, 2001) the graph types are grouped into two categories of standard plots and diagnostic plots (Table 2.4). The difference between the displacement and the deviation is that deviation shows the casing profile in the ground, and displacement indicates the casing movement (Figures 2.11 and 2.12).

The difference between the zero and subsequent readings indicates a change in the shape and position of the casing from its initial position (Stark and Choi, 2008). The relationships between deviation and displacement, and the differences between them are illustrated in Figures 2.11 and 2.12.

**Table 2.4 Plot type and their functions (Slope Indicator, 2001).**

	Standard Plots	Diagnostic Plots
Use	Used to report ground behaviours.	Used to determine the potential for systematic errors and to help calculate corrections.
Plot Types	• Incremental Displacement vs. depth	• Cumulative Deviation
	• Cumulative Displacement vs. depth	• Incremental Deviation
	• Displacement vs. Time	• Checksums and Difference Checksum

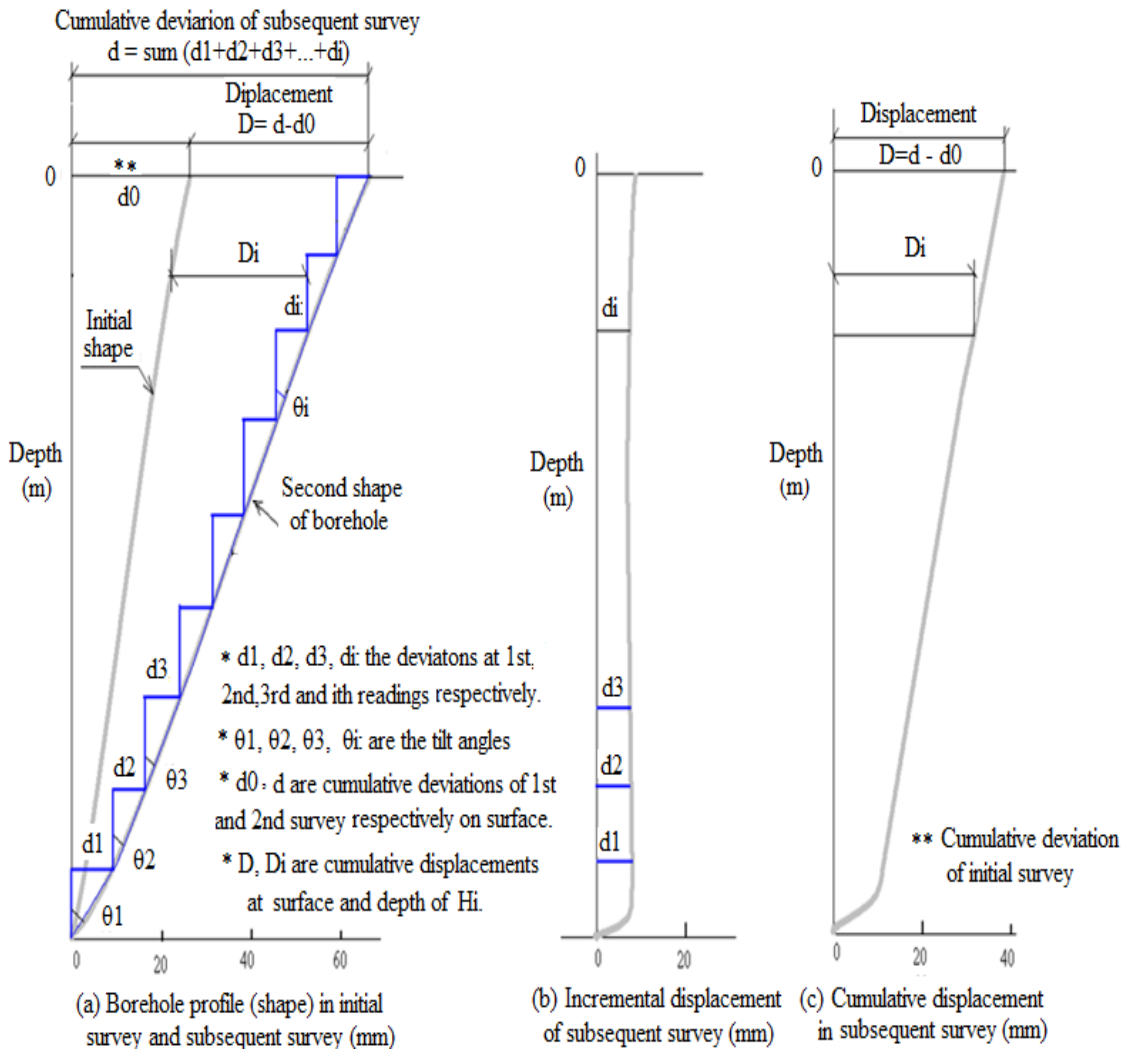


**Figure 2.11 The relationships between deviation and displacement and their differences.**

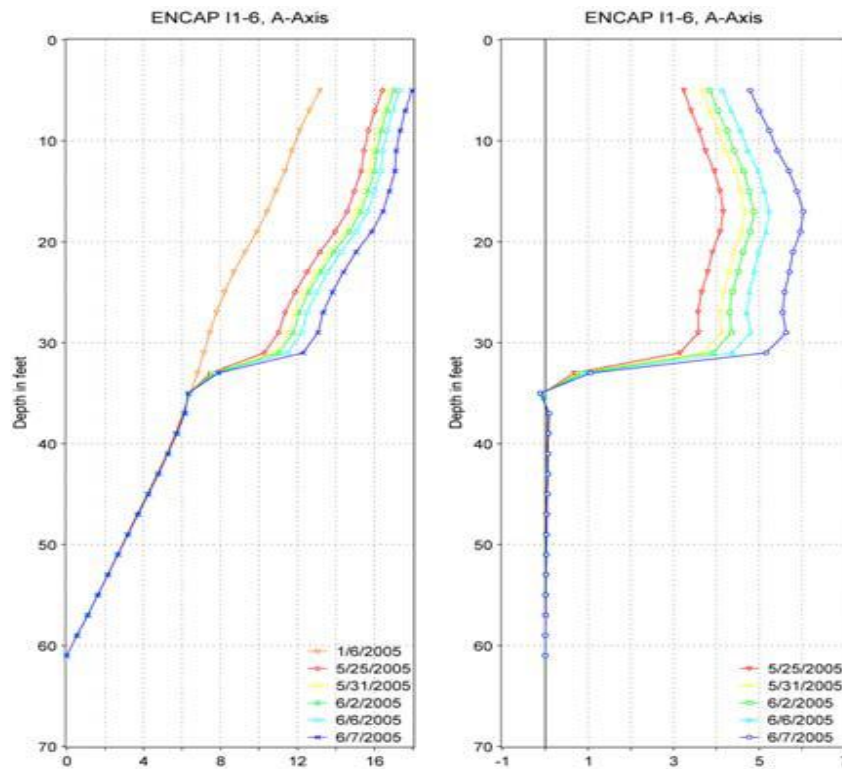


**Figure 2.12** Incliner data plots: a. cumulative deviation plot; b. cumulative displacement plot (from Mikkelsen, 2001).

#### 2.4.5.2 Incremental displacement plots

Incremental displacement (Figure 2.13) is one form of inclinometer data presentation, indicating displacement over each reading point (generally at 0.5m intervals i.e. probe length), during the time since the initial reading sets. Apparently errors by users and or instrument malfunction do not accumulate in incremental plotting, because the incremental data are ‘plotted from reading to reading, i.e. delta previous not delta datum’ (SOIL, 2009, p7).

Incremental displacement plots (Figure 2.13) indicate movement at each reading interval generally of 0.5 m. The plot is theoretically a straight vertical line if there is no ground movement, providing there are no measuring errors. A spike indicates significant movement. Growth in the spike over separated measurement intervals means a continuing movement.

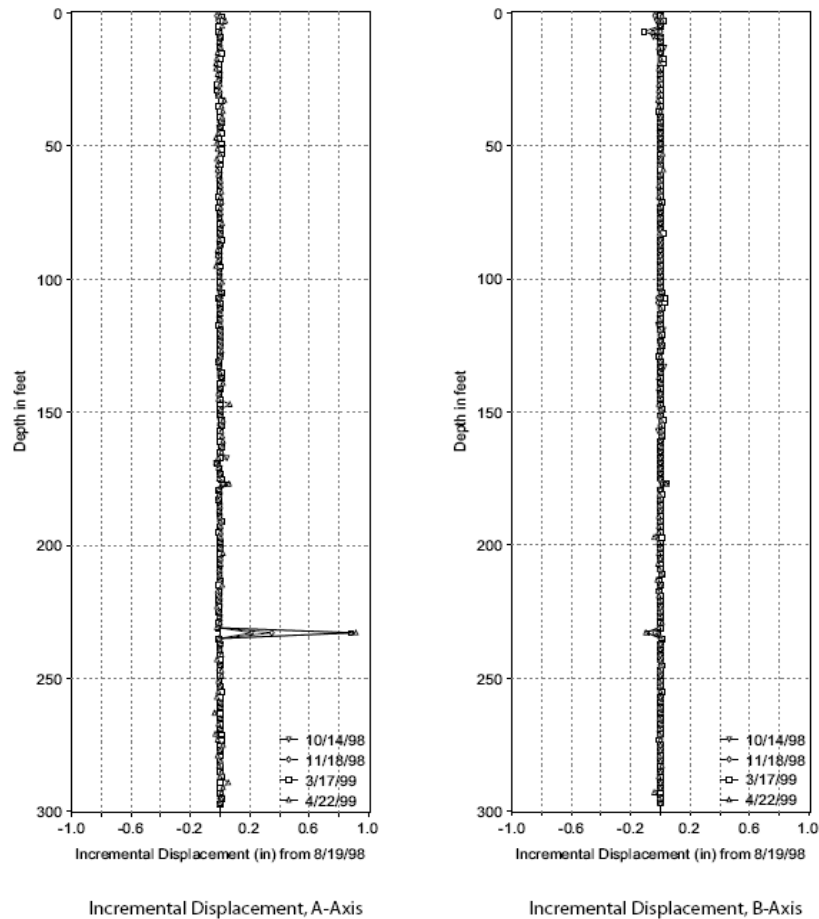


**Figure 2.13 Incremental displacements and spikes (from Slope Indicator, 2001).**

The spike and growth of spike are illustrated at 235 feet in Figure 2.13. The incremental displacement plot ‘minimizes any systematic error, because each plotted point contains only one instance of the error’ (Slope Indicator, 2001). So the relevant plots such as rate of displacement plot can be calculated from the incremental displacement plot, not from cumulative displacement plots, to minimise the effects of data errors.

### 2.4.5.3 Cumulative Displacement Plot

Cumulative displacement plots are the most commonly used plot type that displays a displacement profile of the borehole in the A axis and the B axis. The resultant can give the shape of the borehole in 3 dimensions in the ground. This plot presents the changes in the position of the casing since the initial set of reading(s) as reference. In cumulative displacement the probe errors could be

added up cumulatively if user errors have occurred in measuring. In this circumstance the data can be checked with the method of incremental displacement function that will be discussed in data correction in Section 4.2.5.

In Figure 2.14, the cumulative displacement plot looks rough because the horizontal scale is generally much larger than the vertical scale as the monitored casing is some meters to some hundred meters in depth or length, but the lateral movement is normally quite small with a magnitude of some millimetres to some hundred millimetres. Therefore the shear displacement can be identified easily in larger scale (Figure 2.14) (Slope Indicator, 2001; Machan & Bennett, 2008).

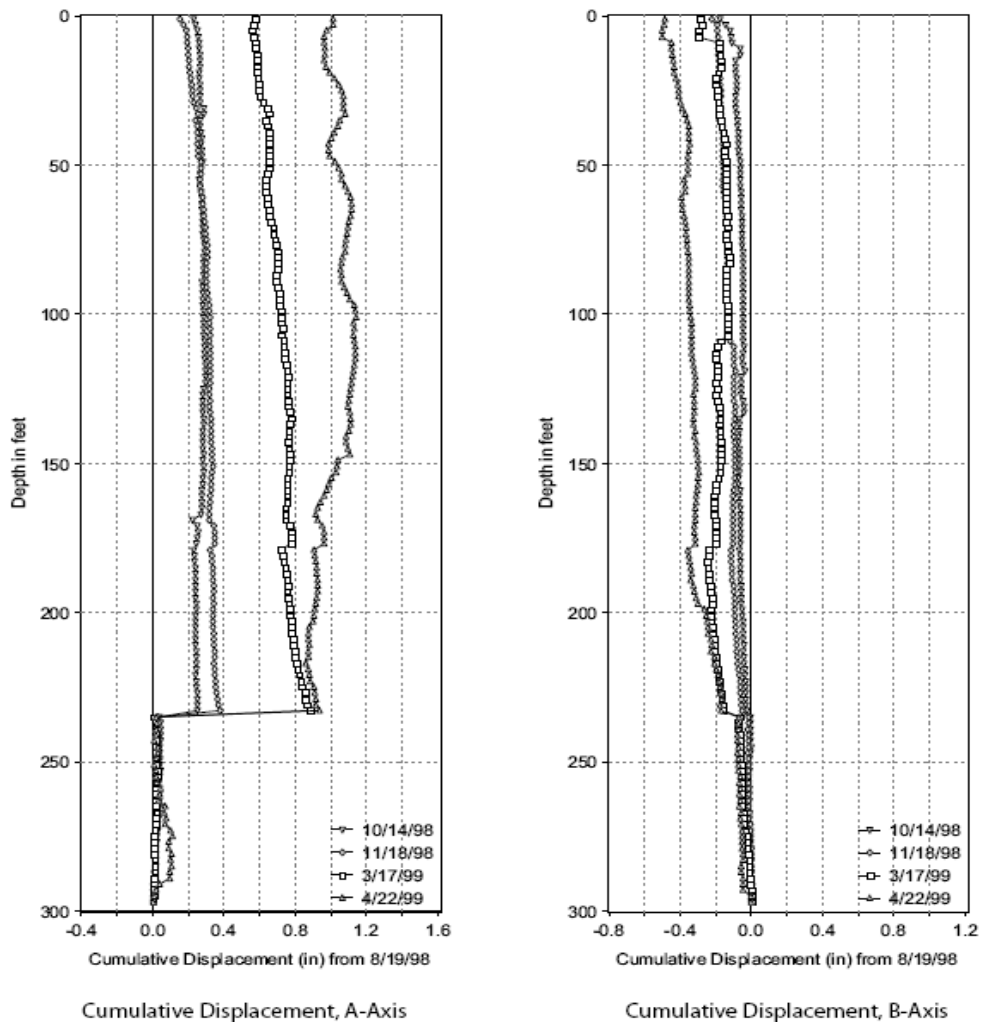


**Figure 2.14 Cumulative displacements in horizontal large scale (from Machan & Bennett, 2008).**

The scales should be chosen that reveal appropriate information of strata movement and hide noise in data (Mikkelsen, 2007). Figure 2.15 shows the effects of the different scales of the plot of the same data set. The left graph in Figure 2.15 is auto-scaled, it is difficult to interpret. The standard accuracy for a normal inclinometer monitoring is  $\pm 0.25$  mm per meter ( $\pm 0.3/100$  feet) (Slope Indicator, 2001).

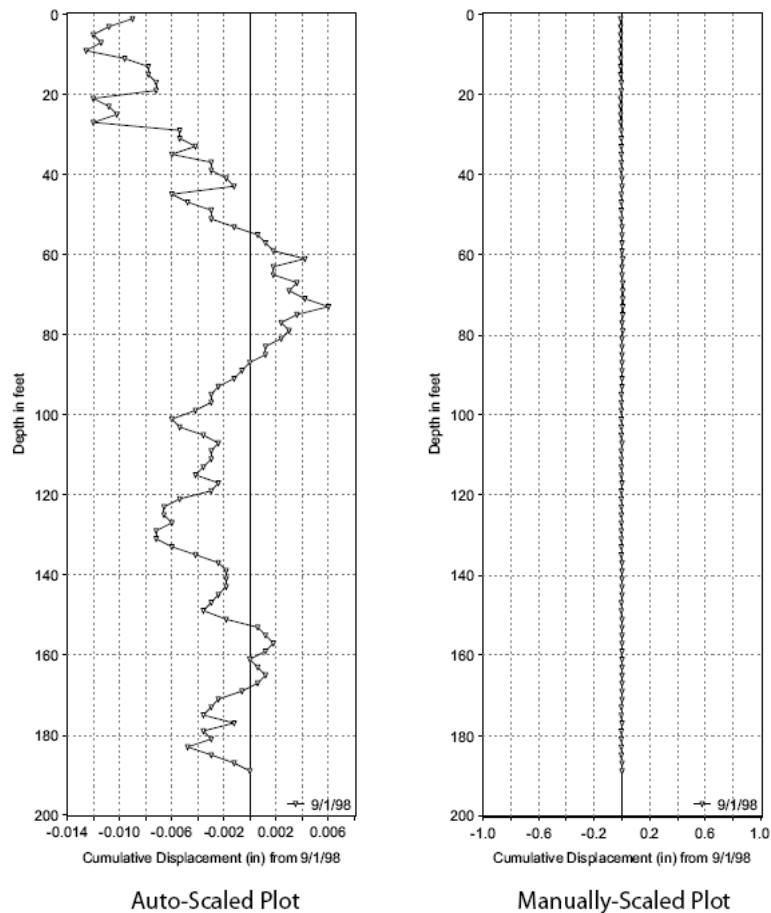


**Figure 2.15 Effects of different scales to display lateral cumulative displacement (Slope Indicator, 2001).**

The maximum reading in the left graph is only 0.3556 mm (0.014 inches) but the depth is 58 m (190 feet). Therefore, the left plot shows 100% noise. The plot on the right presents the same data in an appropriate scale where all the noise has been terminated, then it can be clearly interpreted that there is no movement in this survey (Slope Indicator, 2001).

#### 2.4.5.4 From Incremental Plots to Cumulative Plots

Where the end of the casing is inserted into stable strata, there is assumed to be no lateral displacement occurring at the base of the borehole. The cumulative displacement is generally obtained by summing increments of displacement at each measured interval from the bottom up to the ground surface in the A axis and B axis respectively. The lateral displacement of one set of readings is calculated by subtracting the initial set of tilt readings from this reading. This plot presents the changes in the position of the casing since the initial set of readings as reference. SOIL (2009) recommends the first three readings, since the probe casing has been installed, as a reference for higher accuracy. Figure 2.16 shows how the cumulative graph is plotted from an incremental graph.

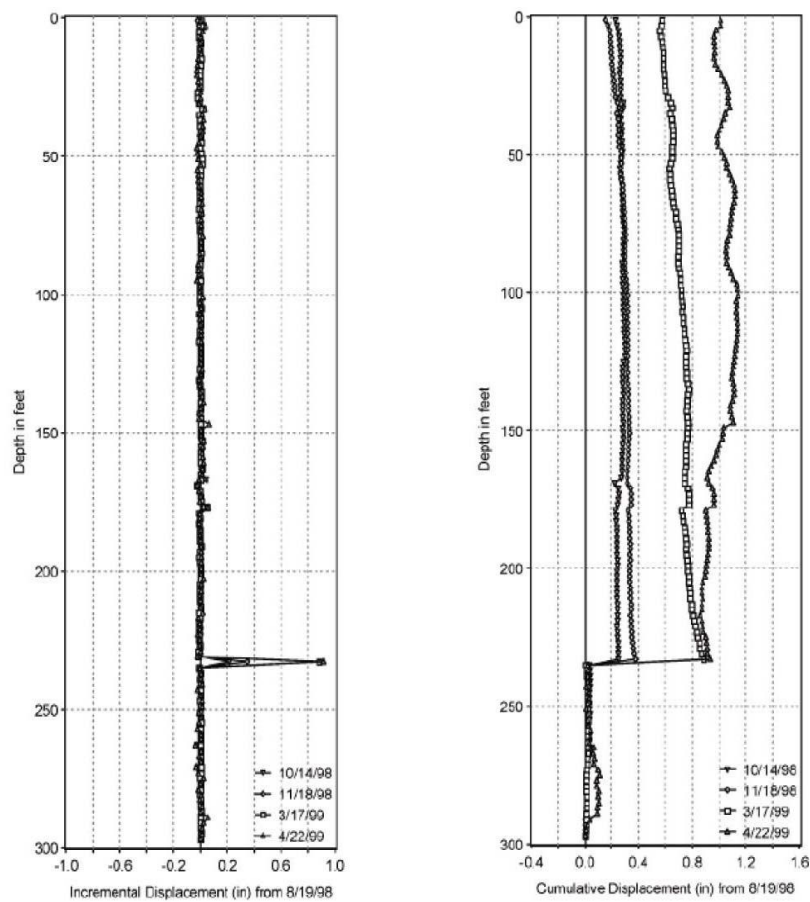


**Figure 2.16 Comparison of data sets using incremental and cumulative displacement profiles (from Slope Indicator Company, 2006, p9).**



For highlighting and emphasizing the movements between surveys, when plotting, the initial readings are reset to zero; the initial reading plot overlaps with the vertical axis. The lateral movement plot from the second time readings will, assuming movement has occurred, be offset from the vertical axis as for example presented in Figure 2.17b.

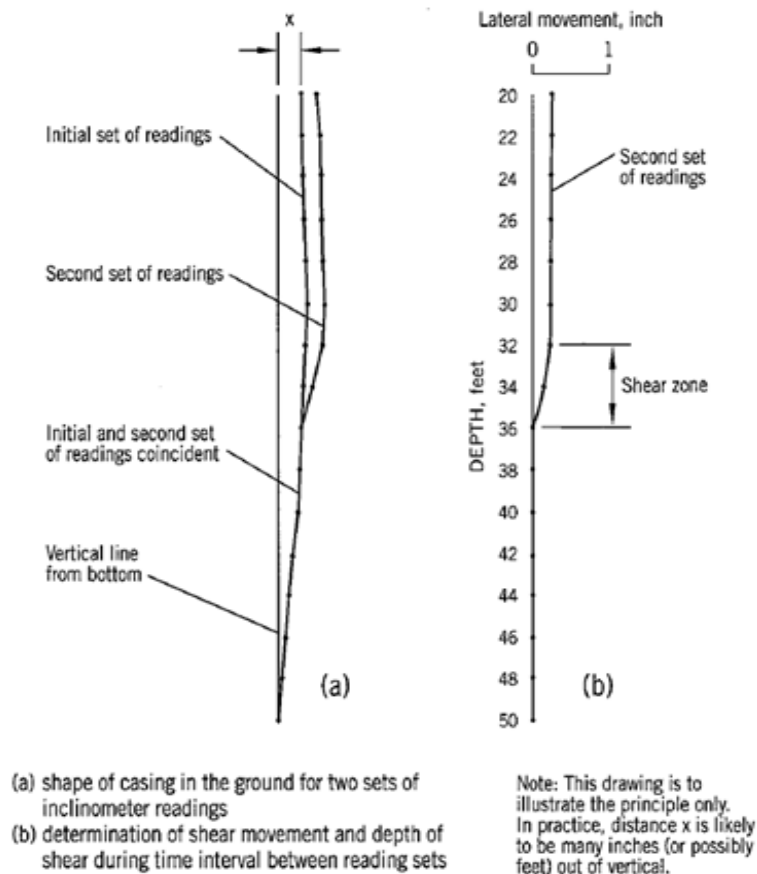


**Figure 2.17 Example of inclinometer data for determining shear zone (from Cornforth, 2005).**

Therefore, the plotted cumulative graphs show the shape of the inclinometer casing relative to the initial condition drawn from the first inclinometer measurement.

#### 2.4.5.5 Rate of Displacement (Displacement vs. Time)

In the situation where underlying extraction is occurring, a time series of displacement plots show the changes or deformation of the strata varying with the

advancement of underground working. A displacement rate graph shows the discrete deformation over the displacement time. Such graphs can help with determining whether ground deformations are accelerating, decelerating or coming to the end, or keeping the same rate (Mikkelsen, 1996, cited by Machan & Bennett, 2008).

Rates of ground movement are calculated from the inclinometer incremental data, as only the deformations occurring at the discrete depths in the incremental graphs are analysed rather than in cumulative displacement graphs because the latter may contain cumulative systematic errors and consequently multiply or diminish the actual ground displacement (Machan & Bennett, 2008).

In a time plot, a line with rising up, dipping down, or horizontal slopes means accelerating, decelerating and even-speed movement. The rate of displacement could be correlated with underground extraction advancing in time series and other time-based parameters if available in strata movement monitoring (Slope Indicator, 2001). Figure 2.18 shows the rate of displacement calculated from the incremental value at 233 - 235 feet in Figure 2.16.

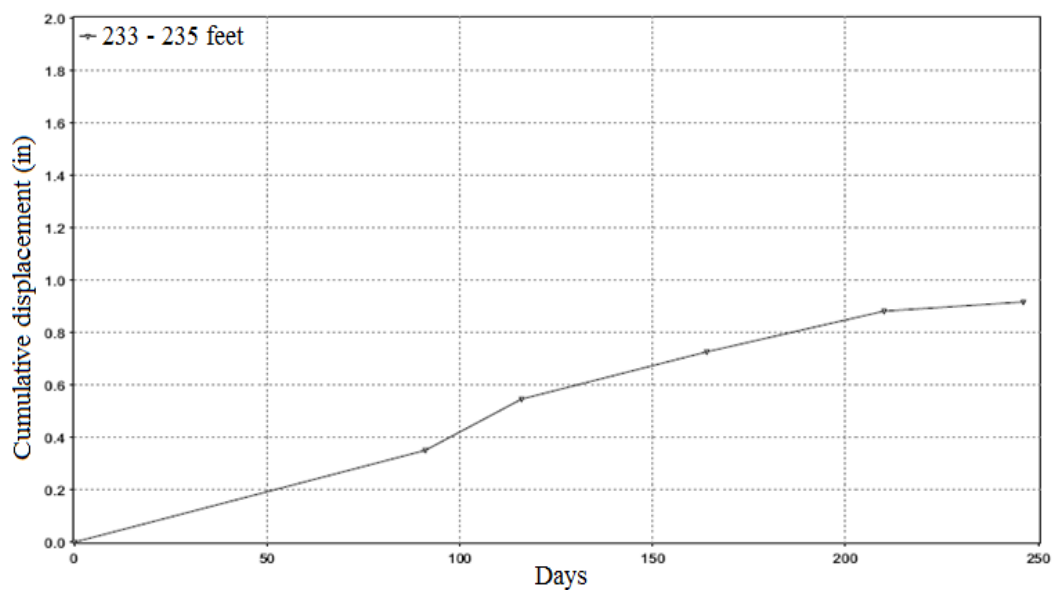


**Figure 2.18 Example of a displacement vs. time plot (from Slope Indicator, 2001).**

### 2.4.5.6 Cumulative Deviation Plot

A cumulative deviation plot illustrates the absolute position and profile of the casing relative to the vertical (Figure 2.19). Since inclination of the casing may result in errors, the cumulative deviation plot is helpful for ‘diagnosing and correcting rotation errors’ (Slope Indicator, 2001).

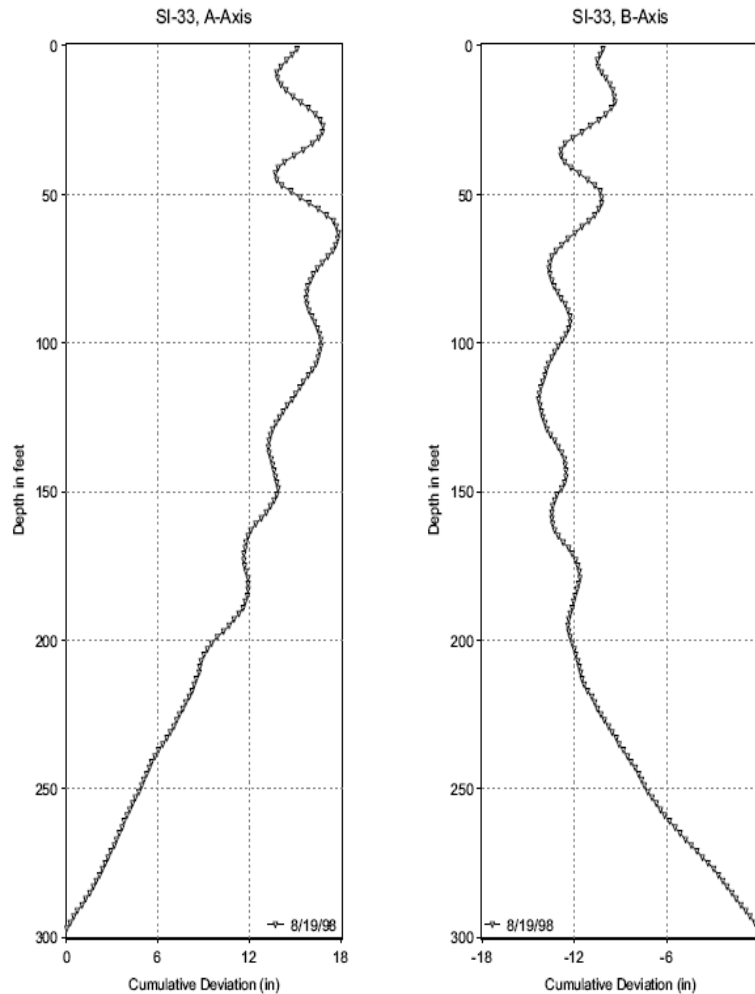
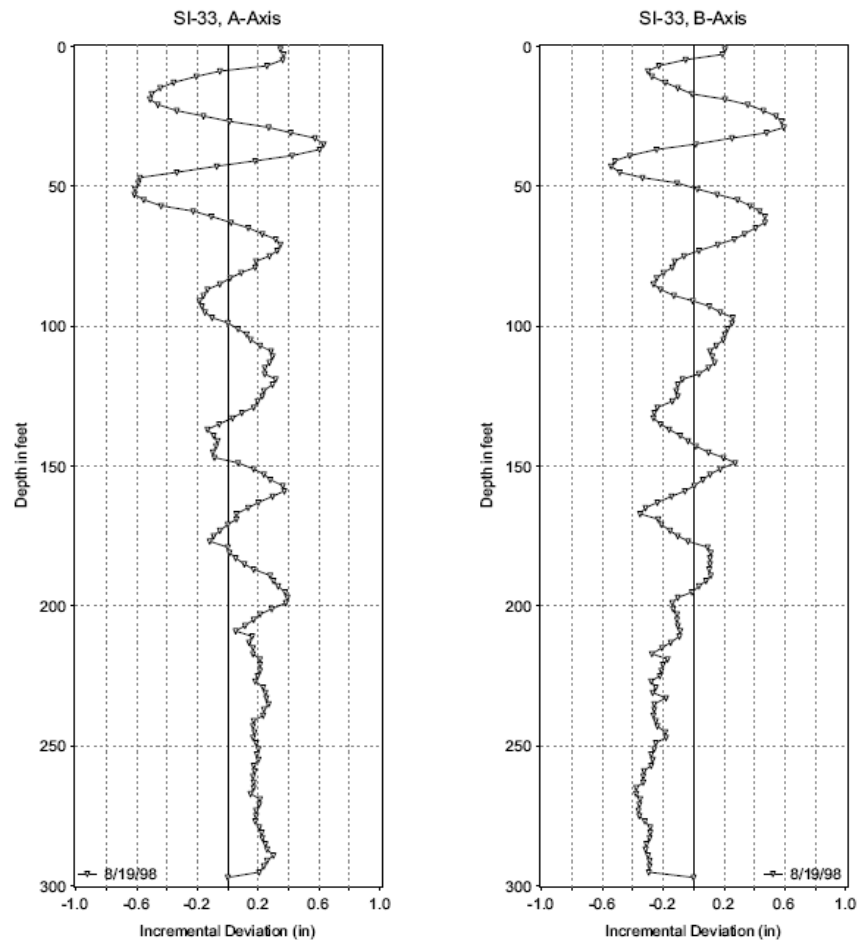


Figure 2.19 Example of a cumulative deviation of casing (from Slope Indicator, 2001).

### 2.4.5.7 Incremental Deviation Plots

Incremental deviation is a simple plot of the probe readings, displaying lateral offset to vertical at each reading interval with depth (Figure 2.20). Theoretically, the ‘casing should be installed as straight as possible’ (Slope Indicator, 2001). The more variations in readings with depth indicate the more bends and curves in

the probe casing. Curvatures in the casing may lead to displacement error due to ‘changes in the depth positioning of the probe’ (Slope Indicator, 2001). Therefore Incremental Deviation plots are used in diagnosing depth error.



**Figure 2.20 Example of an incremental deviation plot showing the offset to vertical (from Slope Indicator, 2001).**

#### **2.4.5.8 Checksums and Difference Checksum Plot**

A checksum is the sum of a “0” reading and a “180” reading at the same depth, so checksum in the A axis equals  $A_0 + A_{180}$ ; checksum in the B axis equals to  $B_0 + B_{180}$ . A checksum graph plots checksums for each reading and is used for checking the quality of the datasets.

Spikes in the checksum plot may represent faulty readings or result from a characteristic of the casing (the left plot in Figure 2.21). Checksum plot lines may not overlay each other because the bias shift of the probe often varies. Frequent

changes in the plot may 'indicate a weak probe and the potential for bias-shift errors' (Slope Indicator, 2001). A tilted checksum line implies a drifting sensor.

The plot for difference of checksums shows the difference of checksum of current readings minus the initial checksum, thus 'eliminating casing signatures and reveals only changes in checksums' (Slope Indicator, 2001). The right plot in Figure 2.21 shows the difference of the checksums between the checksums at two different dates.

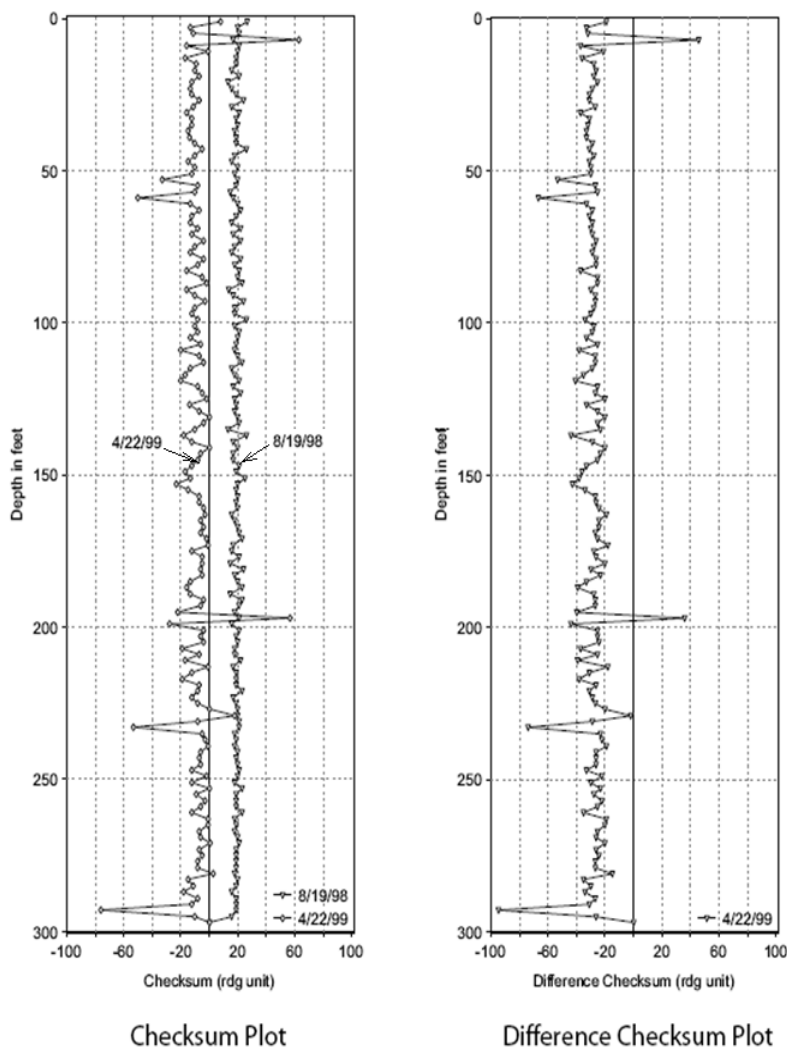
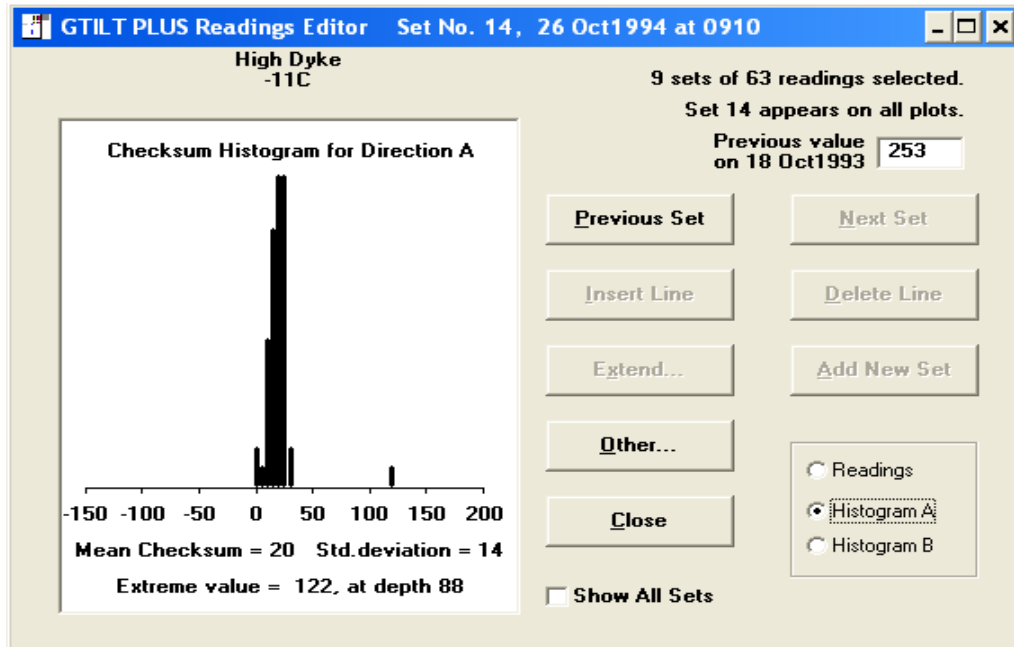


Figure 2.21 Example of a checksum plot and difference checksum plot (from Slope Indicator, 2001).

Rougher plotted lines generally imply a lower data quality. There are several spikes in each graph. The spikes indicate the ‘extreme values of readings’ (Figure 2.22) (Mitre Software, 2003) in the A axis and the B axis.



**Figure 2.22** Example of an extreme value of displayed readings presented in GTILT (from Mitre Software, 2003).

#### 2.4.5.9 Absolute Position plot

An absolute position plot is produced by plotting the initial inclinometer data and shows the absolute position and shape of the probe casing and will present the verticality, twists, and spiral shapes of the casing installation. It does not stand for any movement, but can be useful for assessing installation error against designed borehole structure (SOIL, 2009). The absolute position plot from the inclinometer data can be validated with a polar plot created by borehole geophysical logging.

## 2.5 Summary and Conclusion

This chapter has briefly reviewed three main areas: subsidence, shaft sinking, and inclinometer monitoring (some specific or detailed reviews in particular subtopics

are attached in Appendices A and B). The highlights of this chapter are summarised as below.

### **2.5.1 Subsidence Review**

The common mechanism of subsidence is described as: mine subsidence is the ground movement above mine panels, that occurs in response to the overlying strata caving and ground movement which refills the mine voids to replace the extracted minerals. The space produced by mineral extraction is filled up by the caved rocks, by small amounts of dilation of the interlocked strata above, and by a little bulking of the caved rock. Therefore, land subsidence is the end result of the ground movement into the extracted zone.

Land subsidence is a dynamic, spatial and temporal process. Subsidence includes both vertical displacement, and horizontal displacement of materials.

Vertical subsidence of less than 20 mm has negligible effect on surface infrastructure and it is commonly accepted as the cut-off point for determination of the angle of draw.

The critical width and is generally used as 1.4 times depth of cover. It does, however, depend upon the nature of the strata.

Where great super-critical areas are mined, the maximum possible subsidence may range from 55% to 65% of the extracted seam height. By leaving chain pillars in place providing some support, the maximum subsidence is then normally less than the above range.

There is an overlapping effect of subsidence induced from neighbouring panels; the incremental subsidence of a second or subsequent panel adjacent is larger than the subsidence of an individual separated panel of same geometry.

The development of subsidence at any point of the ground may have a very complex mechanism and can be seen to be the composite effect of a number of separate movements.

Both dynamic and static subsidence need to be assessed in terms of their different damage potential to the structures on the surface and in the subsurface.

The most significant impacts on surface and subsurface structures occur during the development of the subsidence trough as maximum ground movements occur.

Most of the points on the ground and in the subsurface suffer three-dimensional movements with changing tilt, curvature, and strain in both transverse and longitudinal directions.

The impacts of subsidence on structures depend upon the location of the structures within the trough. Surface features at the positions with maximum curvature and strain generally suffer the largest damage.

A structure, i.e. a shaft lining, in the ground within a subsidence zone may suffer bending, shear, compressive, and tensile forces.

The seasonal vertical settlement in the Huntly East Mine from natural causes was generally less than 5 mm.

The subsidence at Huntly East was characterised into two phases: rapid phase (10 to 36 mm/ day) and slow phase (0.1 to 0.7 mm/day).



75% of total subsidence occurred within about 10% of total settlement time period for the E91 and E53 panels respectively.

Subsidence mechanism in the Huntly East Mine was analysed by Kelsey (1986) as: the engineering geological model of the subsidence is most likely to be mine roof collapse leading to void migration to near the top of the Te Kuiti Group sequence causing drainage and depressurisation of aquifers at the bottom of the Tauranga Group. Aquifer depressurisation causes consolidation within both the aquifer and aquitards by dewatering due to drainage.

The methods for prediction of the ground subsidence include (a) empirical techniques, (b) numerical modelling, (c) physical models, and (d) artificial neural networks (ANNs).

Empirical methods are fast, simple to apply and present fairly satisfactory results. Numerical methods have the advantage that, once the model is established, then a number of associated scenarios may be investigated by simulation. However, it must be remembered that numerical models may create wrong judgement in application.

Calibration and verification is an integral part of numerical modelling because of the simplifications, formulisations, and assumptions used in describing the physical processes

The finite element method (FEM) is the most widely used numerical method for geological mechanics and rock engineering. The FEM software currently used are Phase2, ANASYS, Plaxis, ADINA, Abaqus FEA.

The finite difference, advanced continuum modelling codes (FLAC and FLAC3D) are suitable for geotechnical analysis of rock, soil, and structural support in two and three dimensions.

### **2.5.2 Review on Shaft Sinking**

Mine shafts are the most important infrastructure of deep mines. Mine shaft supplies all access and exit services to underground operations, including transport of ore and supplies, personnel traffic, fresh air, power, communications, water supply, and drainage.

The properties of the in-situ strata around the proposed shaft should be investigated. Thus hydro-geological testing Geo-mechanical testing should be undertaken.

The investigation boreholes should be close enough to the proposed shaft axis (10 to 30 meters) to make sure the test results are representative of the shaft sinking conditions.

Constructing the shaft in the centre of the ore body is the most efficient solution, however, may require use of safety pillars for shaft protection, consequently decreasing the recovery rate of the mineral resource. The alternative option, to increase the ore recovery, is to locate the shaft outside of the ore body. However, haulage and ventilation distances to the shaft go up remarkably.

The negative additional vertical friction acting on the external surface of the lining may cause vertical downwards stress within shaft lining and damage the lining at a depth when the resultant stress is larger than the strength of the lining. Considering the geological features of Hunlty East, review of the negative

additional vertical friction could be of some importance for the shaft sinking project above N55 panel (also see Appendix B).

### **2.5.3 Literature on Inclinometer**

The inclinometer is a valuable instrument for analysing subsurface lateral movement. The incremental displacement and cumulative horizontal displacement profiles are typically the most reliable means to determine the zone of the shear movement.

The inclinometer plots comprise standard plots and diagnostic plots. Standard plots include incremental displacement vs. depth, cumulative displacement vs. depth, and displacement vs. time. Diagnostic plots include cumulative deviation, incremental deviation, and checksums and difference checksum.

Strata Movement factors monitored by inclinometer in-situ and needed in design include the magnitude, rate, direction, depth, and type of ground movement.

A considerable body of literature exists regarding case studies of inclinometer installations, with approximately 100 contributions reviewed in preparation of this thesis. Some key features from my review of the literature are:

- Installation of an inclinometer borehole deeper than 120 m were not found in the literature reviewed;
- only a few applications (one sample listed in Table 2.3) of inclinometer used for monitoring movement induced by underground extraction have been found;
- all reviewed cases have the bottom of the casing in stable strata below the movement zone; and

- no standards are available yet for evaluation against precision and bias issues arising (ASTM (2005) also supports this statement).

In contrast, the inclinometer monitoring borehole in my research was 250 m deep, and the bottom of the casing was installed 50 m above the coal seam roof, i.e., the bottom section of the borehole had potential for displacement. The inclinometer borehole, in my project, may be one of the most complicated cases for monitoring and measurement of the strata movement induced by the underground extraction.



# **Chapter 3 Huntly Geology, Hydrology, and Geotechnical Characteristics**

## **3.1 Introduction**

This chapter introduces the Huntly geology, hydrology, geotechnical characteristics and some geographic features relevant to this research. The geology and hydrology are described from the regional scale, the local scale, and for the specific boreholes. The geotechnical conditions are based on two boreholes; the inclinometer borehole (20091) and a shaft pilot borehole (20097), which were used in analysing the mechanism of ground movement, and used for inputs into modelling, using the Phase2 software in Chapter 7. The region includes the area from Drury to Te Kuiti in the western North Island including Huntly Coal Mine. The local area includes the area covered by Huntly East Mine.

## **3.2 Geology**

### **3.2.1 Regional Setting**

#### **3.2.1.1 Waikato Coal Region**

The Waikato Coal Region is New Zealand's major coal producing region including some 13 coalfields and extending approximately 180 km from Drury near Auckland to Mangapehi near Te Kuiti in the western central North Island (Figure 3.1) (Moon and Joy, 2004; Ministry of Economic Development, 2011). Huntly is one of the 13 major coalfields, some others are Maramarua, Waikare, Rotowaro, and Kawhia, Tihiroa and Mangapehi (Ministry of Economic Development, 2011).

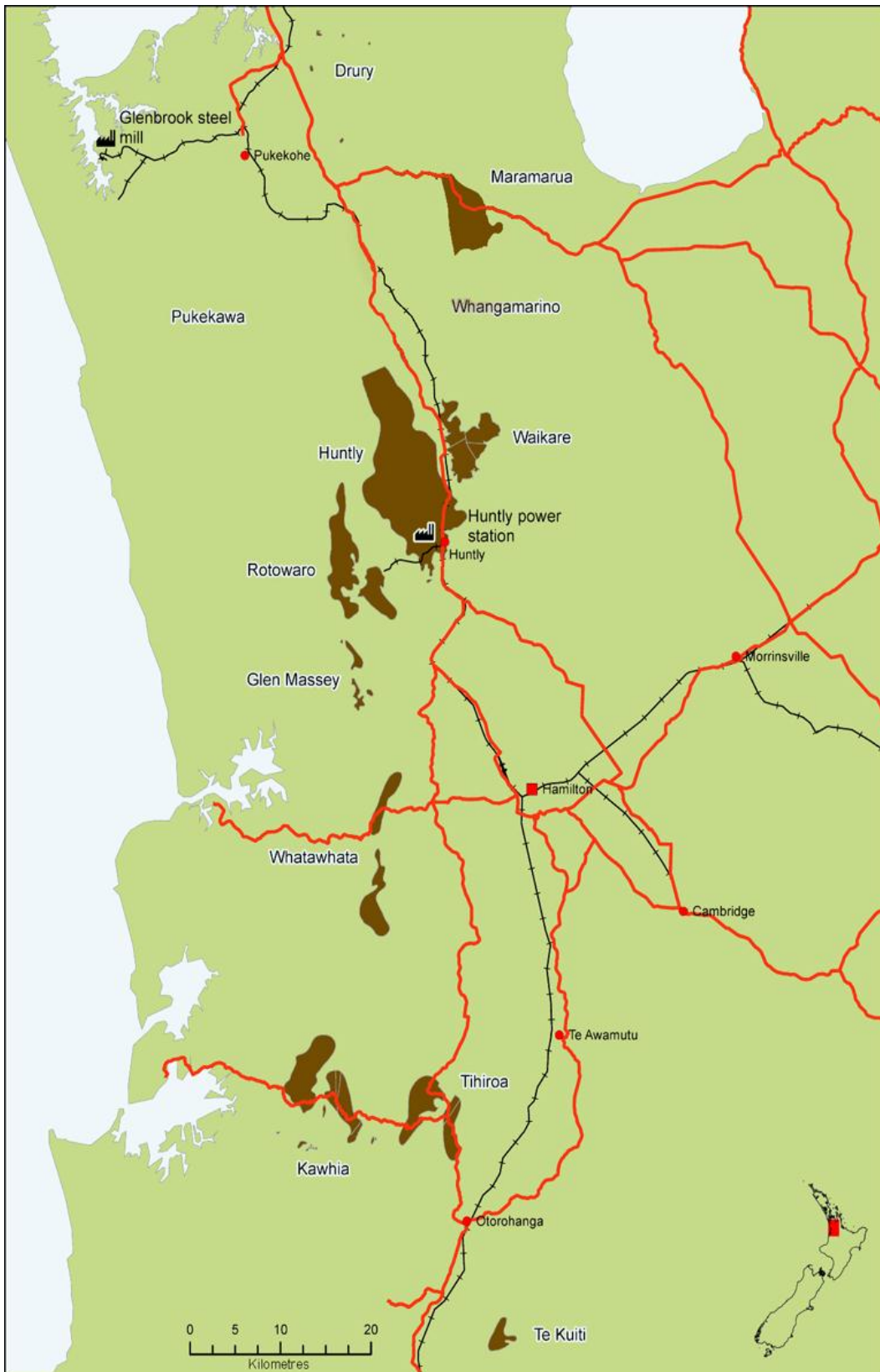


**Figure 3.1** The 13 coalfields extending from Drury near Auckland to Mangapehi near Te Kuiti in the western central North Island (from Ministry of Economic Development, 2011).

The Tauranga Group forms the upper 25 to 70 metres of the 350m or so of overburden that overlies the coal in the Huntly North mine area. Geological formations underlying the Tauranga Group, from new to old, are the Te Kuiti Group, Waikato Coal Measures, and greywacke basement (see Figure 1.3, page 5) (PDP, 2006).

### **3.2.1.2 Tauranga Group**

The Tauranga Group includes a varied group of Quaternary silts, clays, gravels, and weathered volcanic ash deposits. The Tauranga Group has an erosional and unconformable contact surface with the underlying Te Kuiti Group across ages from the Miocene to Pliocene (Figure 1.3) (Solid Energy, 2006).

In Huntly Coalfield, hilly topography is formed largely by Pleistocene gravels overlain by the Hamilton Ash Formation. Holocene peat deposits occur locally in the eastern end of Lake Okowhao, in topographical lows and in the North 65 project area (Solid Energy, 2006).

### **3.2.1.3 Te Kuiti Group**

The Te Kuiti Group overburden unit underlies the upper Tauranga Group and comprises a ‘transgressive sequence of sandstones, mudstones, siltstones and the basal Waikato Coal Measures’ (Solid Energy, 2006) (Figure 1.3).

The Te Kuiti overburden serves as a potential “rock head” between the coal seam and the overlying Tauranga aquifer and protects the seams against the interconnection between the Tauranga aquifer and coal seams. The protection level that Te Kuiti supplies correlates with the quantity of subsidence. Latest modelling suggests that where subsidence is larger than 1.6m the “rock head” fails and interconnection from the Tauranga aquifer is likely to occur (Solid Energy, 2006).



### **3.2.1.4 Waikato Coal Measures**

At the base of the Te Kuiti Group, coal seams are located within the late Eocene Waikato Coal Measures (WCM). The WCM has a varying thickness from 30 to 100 m and overlies Mesozoic basement greywacke, with an unconformable erosional surface (Figure 1.3). With gradual marine intrusion, the coal measures were overlain by a succession of marginal marine and fluvial sediments, and an unconformable sequence of much younger sedimentary and volcanic deposits forming the Te Kuiti Group (Moon and Joy, 2004; Ministry of Economic Development, 2011).

The WCM contain two economic coal seams: Renown and Kupakupa, which are widespread and commonly mined (Solid Energy, 2006). The Kupakupa seam is usually 3-10 m thick, but may reach 20 m in parts of the Huntly and Waikare coalfields (Ministry of Economic Development, 2011). The two major coal seams are located at the base of the coal measures and are overlain by shales, siltstones and claystones. In some parts of the Huntly East mine, such as in panels of North 55, North 57 and North 65, the two coal seams may coalesce into a thickness of up to 21 m.

The coal measures are deposited in regional natural basins over a rolling contact surface, with minor contemporary faulting and ‘widespread compactional effects’ (Ministry of Economic Development, 2011). Subsequent block faulting and erosion have impacted the present distribution, depth, and structure of coal seams (Ministry of Economic Development, 2011).

Huntly East Mine is part of the Huntly Coalfield which covers an area about 20 km long and 9 km wide. The Kupakupa and Renown seams are two major seams in the Huntly East Mine. The Kupakupa seam is the main extraction seam in

thickness from approximately 6 to 10 m, the Renown is the upper seam with a thickness from 0.5 to 5 m. The depth of the coal is normally 150 to 300 m below the surface. Floor and roof rocks have a lower strength ( $2\text{--}5 \text{ MN m}^{-2}$ ) than coal strength ( $5\text{--}25 \text{ MN m}^{-2}$ ) (Moon and Joy, 2004).

### **3.2.1.5 Coal resources**

Waikato coal, particularly from the northern part of the region, is a high quality thermal coal covering the full sub-bituminous rank range, from sub-bituminous C to sub-bituminous A. Coal resources in the region are about 2 billion tonnes presenting one of the country's most important energy resources (Ministry of Economic Development, 2011). The depth of the coal resource varies considerably, from more than 300 m deep, to an opencastable depth (Solid Energy, 2011).

Coal production commenced in the Waikato in the late 1840s. In the 1950s, production was over 1 million tonnes per year, and now yields about 2.5 million tonnes a year, which is about 50% of New Zealand's total production and 70% of coal production for domestic use. The Huntly East mine produces over 400,000 tonnes a year and is the last remaining underground mine in the North Island (Ministry of Economic Development, 2011).

### **3.2.1.6 Regional faulting**

The general geological structure in the Waikato Region is block faulting with normal steep-dip faults. The most frequent fault set is orientated northeast-southwest. The regional faulting dip is 10 degrees northwest, with a depth-of-cover close to 600m around the northern boundary of the coalfield. Mining environments are stable in the un-faulted areas at a mean cover of 200m. The seam has moderate methane levels demanding cautious ventilation control. The

fault throw ranges from 5m to 25m having been intersected in the existing workings (Solid Energy, 2011).

### 3.2.2 Local Geology

#### 3.2.2.1 Current exploration

The inclinometer borehole is in the North 55 panel (in North 5 Extension area) and the proposed shaft is located in North 7 area (the Huntly North Project Area ) (Figure 3.2, also see Figure 1.6 in Page 9). The North 5, North 5 and North 6 areas were previously explored through NZ Coal Resources Survey (“NZCRS”) drilling with drill-hole spacing offsets between 500 and 800m. Additional infill drilling was conducted in 2004 (Figure 3.3) (Solid Energy, 2006).

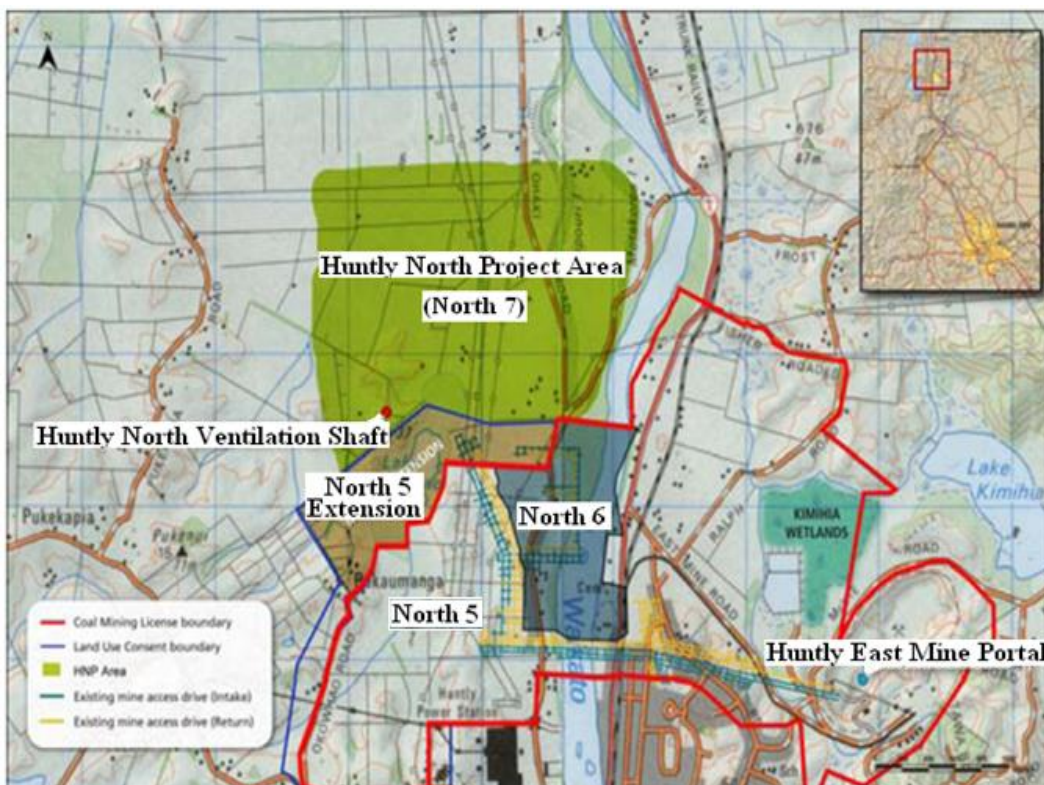
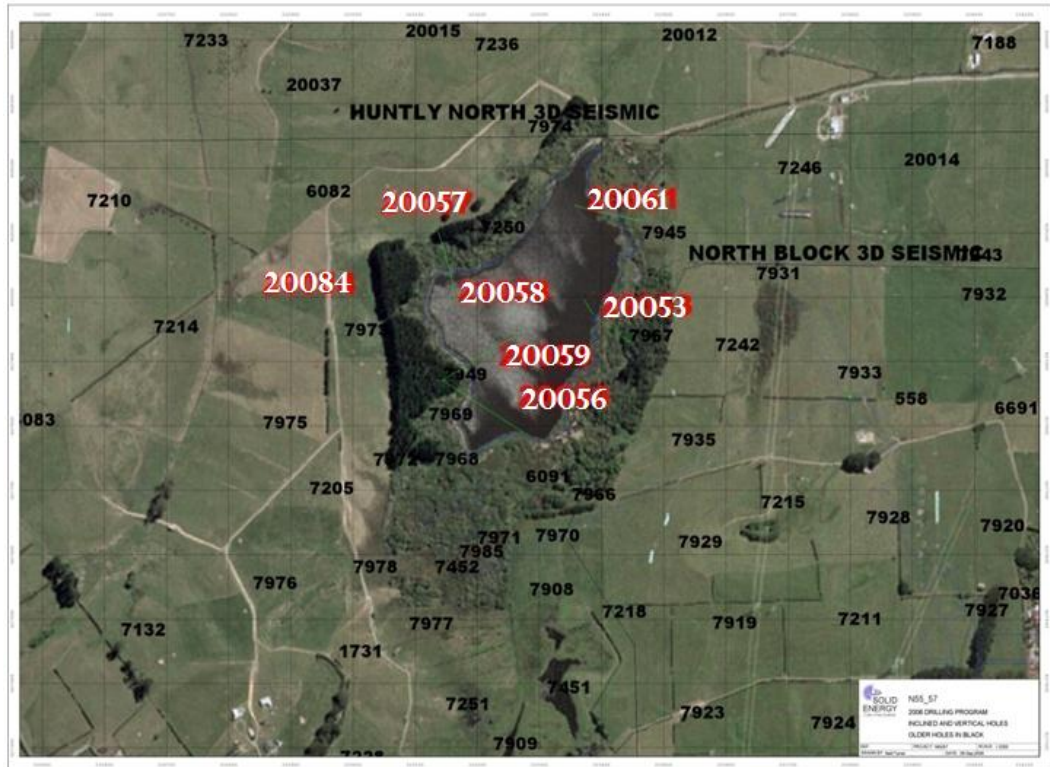


Figure 3.2 Location Plan of North 5, North 6 and North 7 mining areas (from Solid Energy, 2007).



**Figure 3.3 Location Plan of Drillholes – highlighted in red (from Solid Energy, 2006).**

Four inclined infill holes and three vertical infill holes were drilled in 2005 under the bed of Lake Okowhao and the area immediately to north and northwest of the lake (Figures 3.3). The seven drill-holes have provided detailed seam geometry, coal quality data, and geotechnical analysis (Solid Energy, 2006).

Specifications for all the boreholes included:

- Wash drilling sample intervals every 5m (3m in the Tauranga Group).
- Touch coring of coal, coring of mid-burden and adjacent basement in all holes.
- Geophysical logging of all holes (coal combination, sonic, acoustic scanner, dipmeter) by Weatherford Ltd.
- Detailed coal analyses – ply by ply proximate, sulphur, calorific value and density.
- Installation of deep and shallow piezometers for water quality and water pressure testing (Solid Energy, 2006).

### **3.2.2.2 Local geological Vulcan model**

The geological data were input into the Vulcan computer model by Solid Energy. The local Vulcan geological model displays the geological formations including the Renown and Kupakupa coal horizons in three dimensions. The coal horizons were interplotted 'by points in x,y,z format at the intersections of drillholes with the seams and overburden horizons, seismic control where applicable, roof and floor points from underground drilling and fault strings were mapped from underground exposures or geologic interpretations' (Solid Energy, 2006).

The Vulcan model presents a near real structural interpretation integrating the geophysical Acoustic data, underground mapping exposures, drilling information (mainly RQD, joint/shear zone mapping), 3D seismic data, and geologic interpretation. The Vulcan model guides the mining operation and requires update following an increase of data points from further seismic shotholes, underground mapping and reconciliation (Solid Energy, 2006).

### **3.2.2.3 Local basement ridges and domes**

The basement ridges and domes are outlined in the North 55 and North 57 area, immediately north and south of the mining panels (three circled areas in Figure 3.4).

Roadways developed over basement ridges have typically suffered horizontal stress concentrations more than twice the typical horizontal stress for that depth. Basement ridges re-orientate *in situ* stresses perpendicular to the longitudinal axis of the ridge structure, consequently leading to hazards that fast deteriorate mining conditions over basement ridges. Thus secondary reinforcement and even tertiary support are required (Solid Energy, 2006).



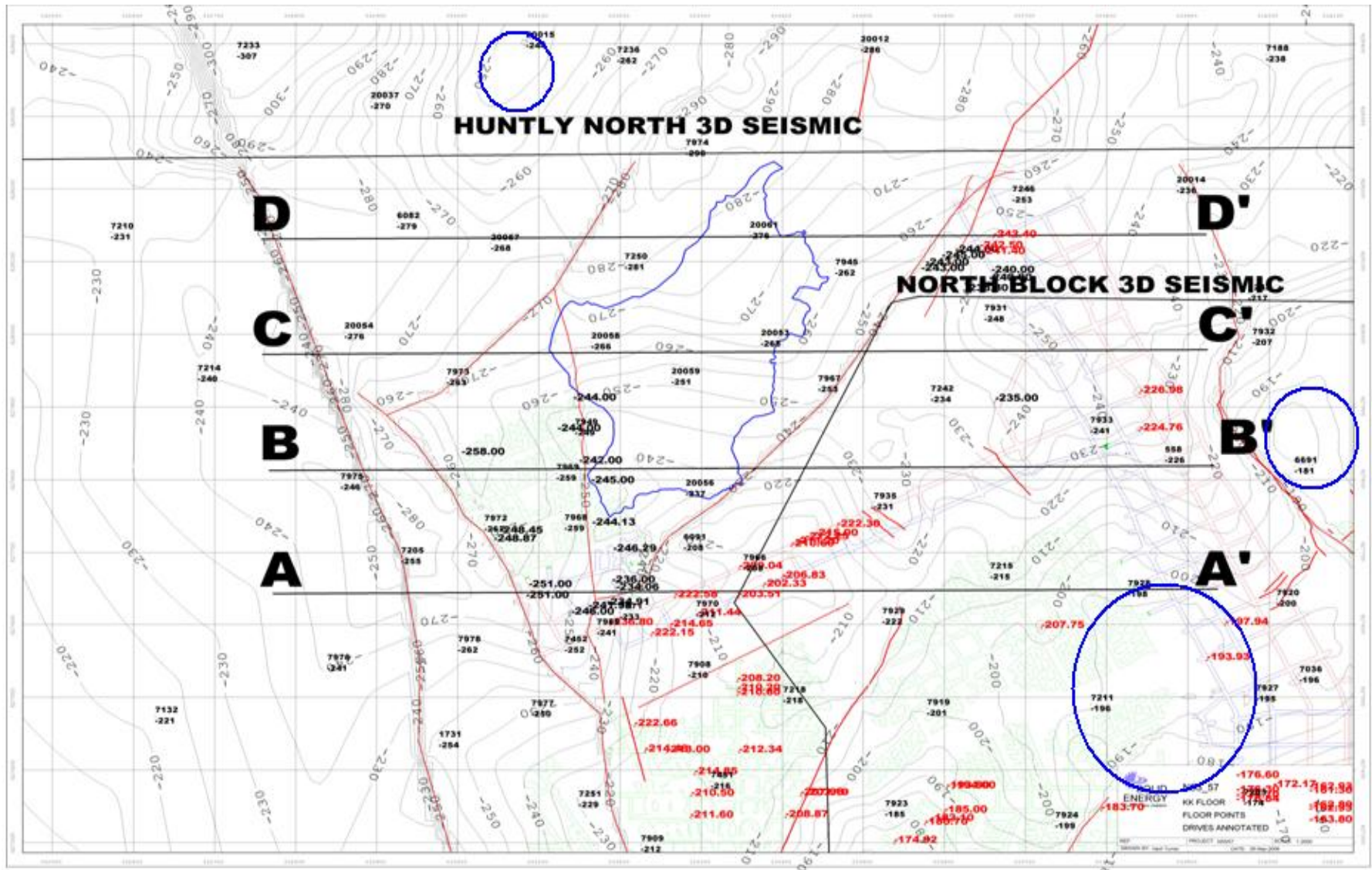


Figure 3.4 Kupakupa Seam Floor Contours in Vulcan Geological Model (from Solid Energy, 2006).

A topographic high, semi-circular basement dome has been proven in the north of the North 55 and 57 area with a fully cored drill hole 20015, recovering just 5.75m of Combined Seam coal. There is a wide basement plateau around DH 7935 to 7242 with a reduced level at -231 to -234 m in the southwest. The drillhole 20056 on the downthrown side of the splay fault revealed the thin coal and shearing observed on a basement high. This area may have adverse stress conditions (Figure 3.4) (Solid Energy, 2006).

### 3.2.2.4 Local faults and coal seams

Five major faults have been defined and mapped through the N55/57 area using drillhole offsets, roof and floor points from drilling, fault mapping, downhole geophysical surveys and poor RQD/core recovery (Figure 3.5).

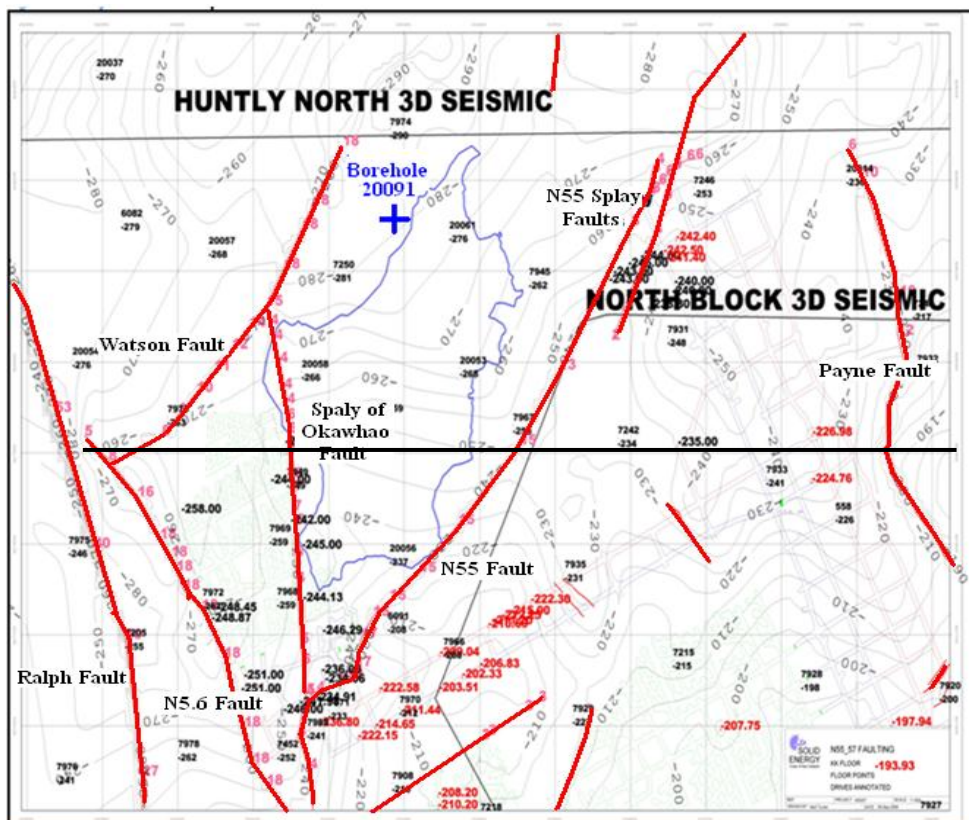
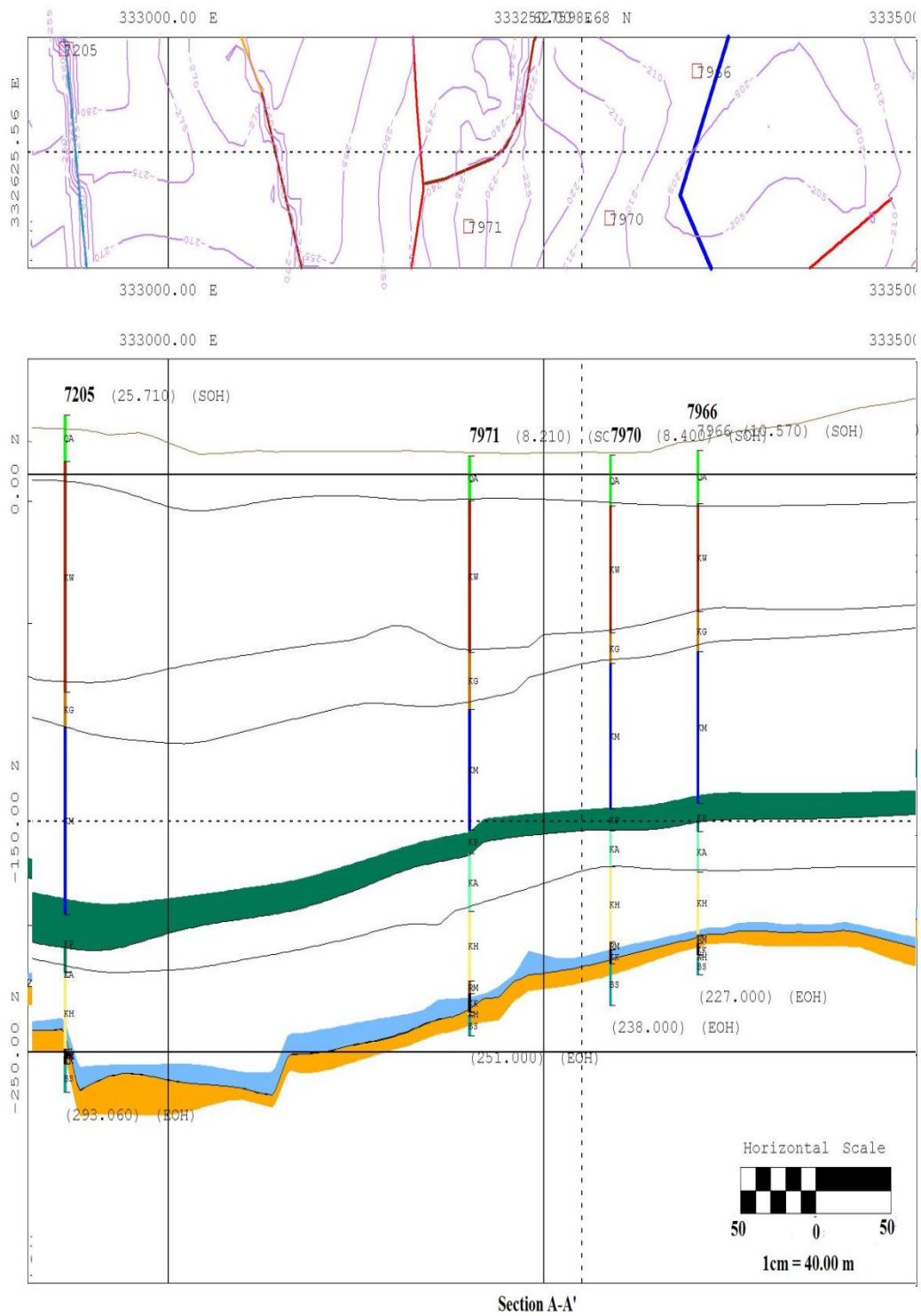


Figure 3.5 Major fault structures (from Solid Energy, 2006).

The five major faults are the Ralph Fault, Okowhao Splay fault, the North 5.6 Fault and its splay in the west, Watson fault, and Payne fault in the far east. The cross section of A – A’ shows the fault dips in Figure 3.6.



**Figure 3.6 Fault dips, Section A-A’ from Figure 3.3 (from Solid Energy, 2006).**



The large faults in the N55/57 area orientate approximately north to NNW. The Ralph fault is a major regional structure which has a throw of 30-55m. The Payne Fault has a curved fault outline, roughly parallel with the Ralph fault trending from NNW in the south to NE in the north with a throw of 25-30m, the throw dies out to 6m in the north. N56 Fault has a throw of 15-18m and Splay Okawhao fault has a throw of 4-10m. Both faults are 'considered to be synthetic to the Ralph Fault plane' (Solid Energy, 2006, p32).

Smaller faults (<5 metre throw) are usually aligned northeast to southwest, have been mapped underground in the N56 development roads, and are parallel to the larger N55 fault and Watson fault. The smaller faults do not offset horizons because of the small magnitude of the throw. Further small faults may be presented but not evident 'in the current Vulcan model due to the resolution of the current drillhole spacing' (Solid Energy, 2006).

- N55 Fault – New Fault Interpretation

N55 fault was found in Vulcan model between 20056 and 6091 after completion of exploration of drillhole 20056. The fault throw is conservatively approximated 15 metres in the centre of the N55 panel fading out to 6m throw towards the N56 Fault and Okawhao Splay Faults in the southwest. The N55 Fault splays into a 8 m main fault mapped in the N55 development drives and a synthetic 4m splay fault underground mapped in the main trunk drives (Solid Energy, 2006).

- Watson Fault

The Watson fault was orientated from the Ralph fault to north along the west side of the Okowhao Lake in a NNE trend. The throw of the fault is 18m. The Watson Fault has a dip of 60-70 degrees with a dip direction of 130 degrees.

- Faults in Huntly North Project area

None of the known faults are within 50 metres of the proposed shaft in the Huntly North Project area. There are two known major faults beyond the 50 m scope, they are steeply dipping normal faults intersecting coal seam level.

The more significant fault has a 15-20 m throw in the south-east corner, trending NE-SW with a SE direction of dip. It is likely that this fault intersects the overlying Te Kuiti Group.

The smaller fault has an approximately 5 m throw and lies northwest of the ventilation shaft. Even though this fault has been detected through the Te Kuiti formation, it has not yet been determined if it extends through the whole lithological set (Solid Energy, 2006).

### **3.2.2.5 Local combined Renown and Kupakupa seam dip**

The N65 panel area has two coal seams, the Renown and Kupakupa Seams which banded together into a combined seam at 20062, have a total thickness 20.35 m and a range from 8-21m within the 500m horizontal distance. The Kupakupa Seam averages 9.5m, but thins over basement highs to less than 4 metres in confined areas (Solid Energy, 2006).

The dip of the seam base is equivalent to basement relief rather than seam dip. The seam dip varies from 1.72 degrees to 27 degrees (Table 3.1). The dip direction is mostly NNW with localised dip of the coal seam towards faults such as in 20057 and 7972 (Solid Energy, 2006).

**Table 3.1 Acoustic Scanner Interpretation of Coal Seam Boundary Dip and Dip Direction (from Solid Energy, 2006).**

Acoustic Scanner Defect Interpretation - Defect Listing					
HOLE_ID	Seam	Depth m	Dip degree	Dip direction Azimuth, degree	Defect type
7931	RM_TOP	239.7	19	110	Coal seam boundary
7933	RM_TOP	232.01	10	23	Coal seam boundary
7945	RM_TOP	255.09	19.14	327.03	Coal seam boundary
7949	RM_TOP	252.372	15.33	324	Coal seam boundary
7968	RM_TOP	248.79	2.5	106.96	lithology change
7969	RM_TOP	249.39	1.99	229.68	lithology change
7970	RM_TOP	211.34	5.72	290.41	lithology change
7971	RM_TOP	227.44	5.66	258.96	lithology change
7972	RM_TOP	252.99	7.13	243.47	lithology change
7973	RM_TOP	272.82	2.48	339.99	lithology change
7974	RM_TOP	293.01	2.7	285.54	lithology change
7975	RM_TOP	249.97	9.69	35.84	lithology change
7977	RM_TOP	245.53	45	276.77	lithology change
7978	RM_TOP	253.37	1.29	250.6	lithology change
20012	RM_TOP	277.97	27	350	Coal seam boundary
20014	RM_TOP	225.95	25	260	bedding
20053	RM_TOP	275.74	9	340	Coal seam boundary
20054	RM_TOP	274.6	6.84	343	Coal seam boundary
20056	RM_TOP	289.5	9.65	262	Coal seam boundary
20057	RM_TOP	265	14.57	184	Coal seam boundary
20058	RM_TOP	285.6	6.84	314	Coal seam boundary
20059	RM_TOP	286.3	4.02	325	Coal seam boundary
20061	RM_TOP	283.8	1.72	331	Coal seam boundary

### 3.2.3 Geology in the Inclinometer Borehole (20091)

#### 3.2.3.1 Basic data from the Borehole

The Borehole 20091 was drilled by Drillforce NZ Ltd using a ‘wash drilling’ method, in February 2009, with a total depth of 250 m. The primary role for this borehole was to provide for inclinometer monitoring; as well as for geophysical logging and chip sampling for obtaining stratigraphic, lithologic, and geotechnical

data as it relates to the modelling of the strata movement linking with the underground extraction.

The chip samples brought from the borehole by circulation to surface were collected and logged every 5 meters (Figure 3.7). The geology retrieved from the chip samples and combined down-hole geophysics survey is illustrated in Table 3.2.

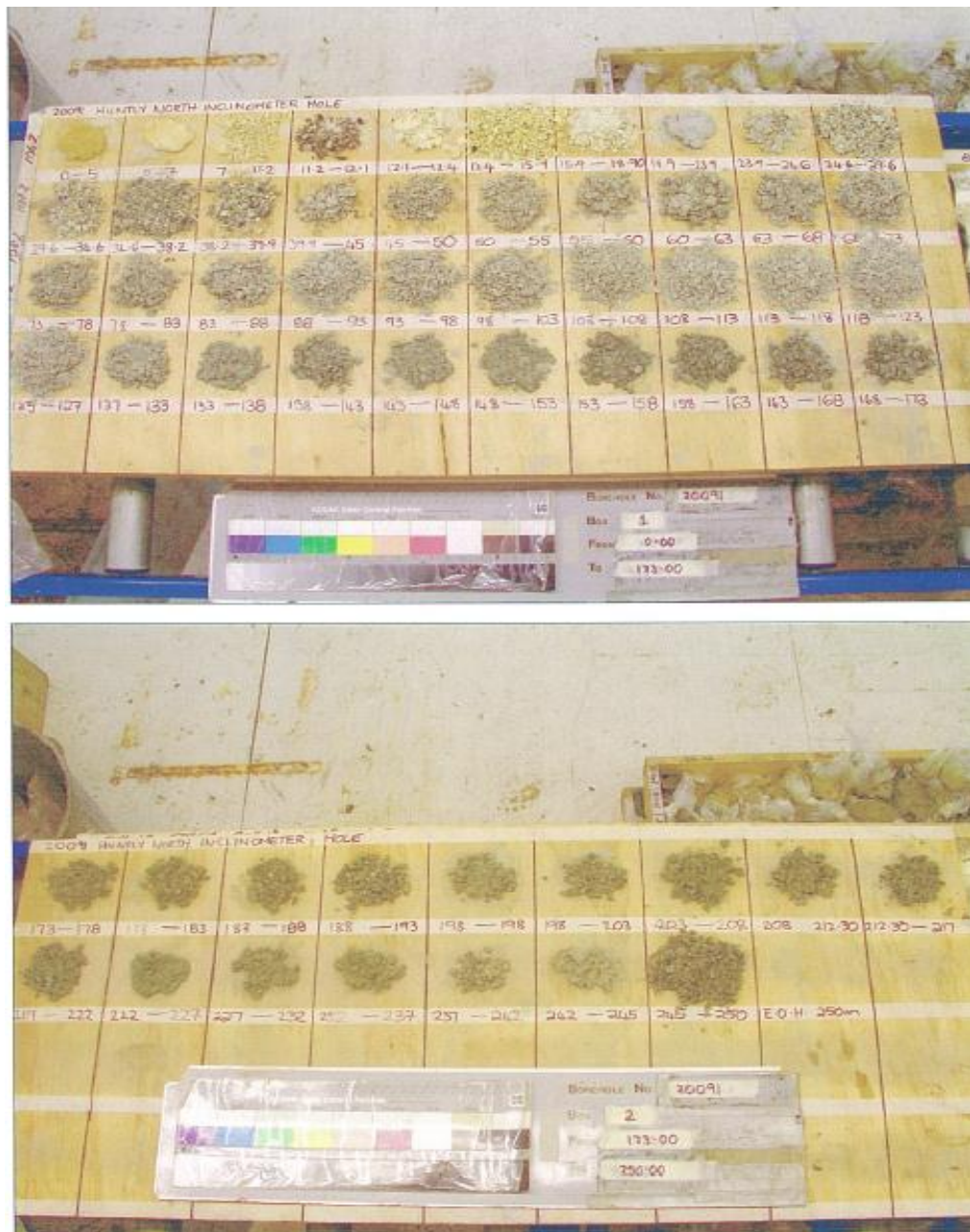
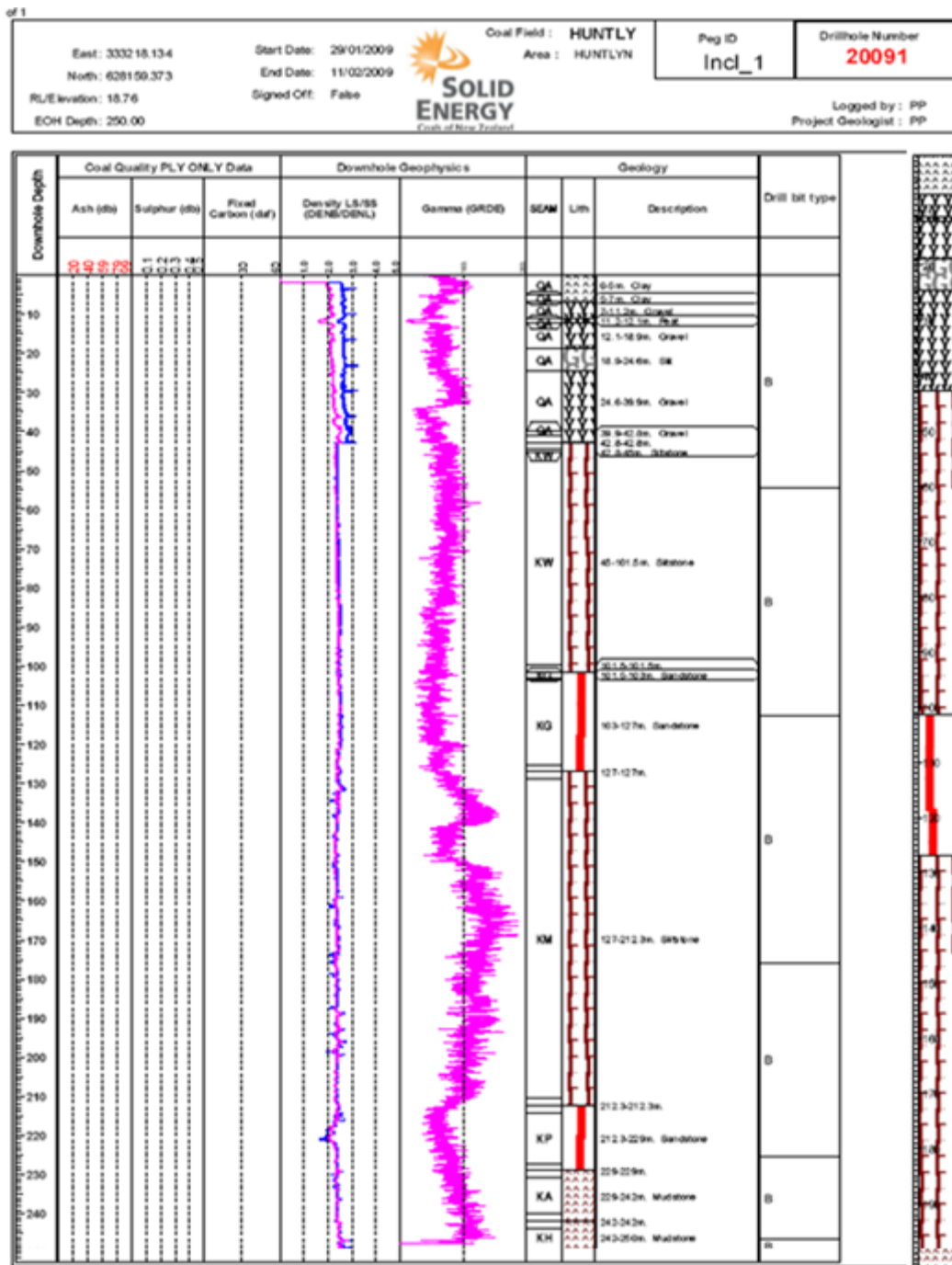


**Figure 3.7** The samples of the chips from wash drilling in the Borehole 20091(from Solid Energy, 2009a).

Table 3.2 The striplog of inclinometer borehole 20091 (from Solid Energy, 2009b).



### 3.2.3.2 Stratigraphy

The stratigraphy from surface to the borehole bottom includes 42.8 m of Tauranga Group at the top, and 207.2 m of Te Kuiti Group at the bottom (Table 3.3). Casing was extended to a depth of 42.7 m to reach the contact between the Tauranga Group and the Te Kuiti Group at 42.8 m. Using data from the Borehole chip

samples and the geophysical logging data, the stratigraphy is explained as below (Solid Energy, 2009) :

The Tauranga Group contains first 7 meters clay, then 34.9 m of gravels, parted with 0.9 m of peat at a depth of 11.2 to 12.1 m.

The Te Kuiti Group encloses six formations exposed in the Borehole. They are Whaingaro Formation (KW); Glen Massey Formation (KG); Mangakotuku Formation (KM); Mangakotuku – Pukemiro Mbr (KP); Pukemiro – Glen Afton (KA); and WCM (KH). The Whaingaro Formation (KW) has a thickness of 58.7 m from a depth of 42.8 to 101.5 m and consists mostly of siltstone.

Contact between the KW and Glen Massey Formation (KG) is gradationally fining upwards. The KG was 25.5 m thick and consists of lower medium - grained, glauconitic, calcareous sandstone.

The KG – KM contact was located 127 m deep. The KM formation has a thickness of 85.3 m, and consists largely of dark grey, slightly calcareous mudstone; shells are common.

The Mangakotuku (KM) – Pukemiro Mbr. (KP) contact at 212.3 m was defined by a change from very fine to fine-grained glauconitic sandstone. The KP formation comprised 16.7 m of sandstone.

Contact between the Pukemiro (KP) – Glen Afton (KA) is at 229 m depth. The KA is of mostly dark grey mudstone; thin shell layers are common. The contact between KA and KH is at 242 m. KH has a thickness of 8 m investigated of mudstone.

**Table 3.3 The formation tops and thickness in the Borehole 20091 (from Solid Energy, 2009).**

Group Name	Formation name	Depth (thickness), m
Tauranga Group	QA	1 – 42.8 m (42.8 m)
	Erosional unconformity	42.8 m (58.7 m)
	Whaingaro Fm (KW)	101.5 m (25.5 m)
	Glen Massey Fm (KG)	127.0 m (85.3 m)
Te Kuiti Group	Mangakotuku Fm (KM)	212.3 m (16.7 m)
	Pukemiro Mbr (KP)	229.0 m (13.0 m)
	Glen Afton Mbr (KA)	242.0 m (8.0 m)
	WCM (KH)	
	Coal Seams	not drilled into
EOH		250 m measured

### 3.3 Hydrological characteristics

#### 3.3.1 Regional Hydrogeology

##### 3.3.1.1 Overview

The overall groundwater flows eastwards towards the Waikato River, most flow occurs in the upper approximately 40m in the Tauranga Group (TG) where coarse grained sediments are predominant. Investigations reveal a differing degree of interconnection between the TG groundwater and the Waikato River (PDP, 2006).

Groundwater levels in the TG investigation holes vary from approximately 7 m to 8.7 m above sea level (RL). The minimum groundwater flow is inferred in the fines-dominated Whangamarino Formation at 40 m below the ground surface (PDP, 2006).

##### 3.3.1.2 Hydrogeologic units

PDP (2009) summarized the hydrogeology of the sequence in the Huntly North Mine area (Table 3.4). There are five aquifers intersected by three aquitards, all vary in thickness. The Tauranga Group aquifer has the largest conductivity, transmissivity, and storability.

**Table 3.4 Hydro-geological Units and hydro-geological characteristics (from Crampton, 2010).**

Aquifer/aquitard	Aquifer						Hydrogeological Units
	Nature of	Thickness range (m)	Hydraulic Conductivity K (m/day)	Transmissivity (m <sup>2</sup> /day)	Aquifer Storability	Confined/unconfined	
Tauranga Group Aquifer	Sand & gravel sediment – lensed & channelised. Interfigering with silt & clay sediment	<5.0	0.43 – 17.3	10 - 300	0.001 – 0.2	Semi-confined to unconfined	Tauranga Group Aquifer
Whaingaroa Siltstone Aquitard		0 – 200					Aquitard
Ahirau Sandstone Aquifer	Fractured sandstone	~30 – 50 (total)	0.001	0.01	0.0001	Confined	Glen Massey Aquifer
Dunphail Siltstone Aquitard							
Elgood Limestone Aquifer	Fractured limestone						
Rotowaro Siltstone Aquitard		50 – 80					Aquitard
Pukemiro Sandstone Aquifer	Fractured sandstone	May-25	0.01	0.1	0.0001	Confined	Pukemiro Aquifer
Glen Afton/WCM Claystone Aquitard		25 - 60					Aquitard
Coal Seams aquifer	Fractured coal seams	<0.3 – 19.5	0.001 – 0.02	0.01 – 0.2	0.0001	Confined	Coal seam aquifer
WCM Claystone and Siltstone (Fireclay) / Weathered Greywacke Aquitard		~0.5 – 10					
Greywacke Aquifer	Fractured siltstone and sandstone	>1000	0.001 – 0.01	>5	nd	Confined	



### 3.3.1.3 Tauranga Group hydro-geologic units

The significance of the Tauranga Group is that it behaves as a single aquifer which is hydrologically connected to the Waikato River. Recent work for assessing the risk of interconnection between the underground mine workings and the Tauranga aquifer has dictated a detailed hydro-stratigraphic subdivision of this Group for modelling the recharge potential (Solid Energy, 2006). Based on grainsize/textural based Hydraulic Conductivity (K) values, the TG can be divided into 5 hydrogeological units (HU) for hydrogeological interpretation and 2D groundwater modelling (Table 3.5) (PDP, 2006).

**Table 3.5 Hydraulic conductivity of Tauranga Group hydrogeological unit (from PDP, 2006).**

Sediment Grain Size	Hydrogeological Unit	Representative K (m/s)
Gravel	K1	$3.7 \times 10^{-3}$
Sand gravel	K2	$4.1 \times 10^{-4}$
Sand	K3	$5.9 \times 10^{-5}$
Mud sand gravel	K4	$6.4 \times 10^{-6}$
Sand silt		
Peat		
Sand gravel mud	K5	$4.0 \times 10^{-9}$
Mud		

HUs were allocated based on geology from seismic shot-hole and previous investigation hole, then were used for the TG investigation hole and infill hole geology to complement the database and present a QA check on the ‘grainsize-HU correlation used for the shot-holes’ (PDP, 2006). The high K - low K margin is  $1 \times 10^{-7} \text{ m.s}^{-1}$  for the inflow assessment. This cut-off value is ‘based on there being marginal contribution to inflow from sediments with a K of less than  $1 \times 10^{-7} \text{ m.s}^{-1}$ ’ (PDP, 2006).

### 3.3.2 Ground water level in the pilot borehole

The groundwater reduced level and the water level depth from the surface in the borehole 20097 are listed in Table 3.6.

**Table 3.6 Groundwater level in the borehole 20097 (Larratt et al., 2009).**

Parameters	Tauranga Group (TG soils)	TK 1 Siltstone	TK2 Sandstone	TK3 Mudstone	TK4 Sandstone
	1	2	3	4	5
Ground water reduced level (undr,rl, m)	12	12	-5	-5	-12
Ground ware depth from surface (RL:12m)	0	0	17	17	24
borehole 20091 (m)	0-43	43-102	102-127	127-212	212-229
borehole 20097 (m)	0-37	37-98	98-123	123-205	205-215

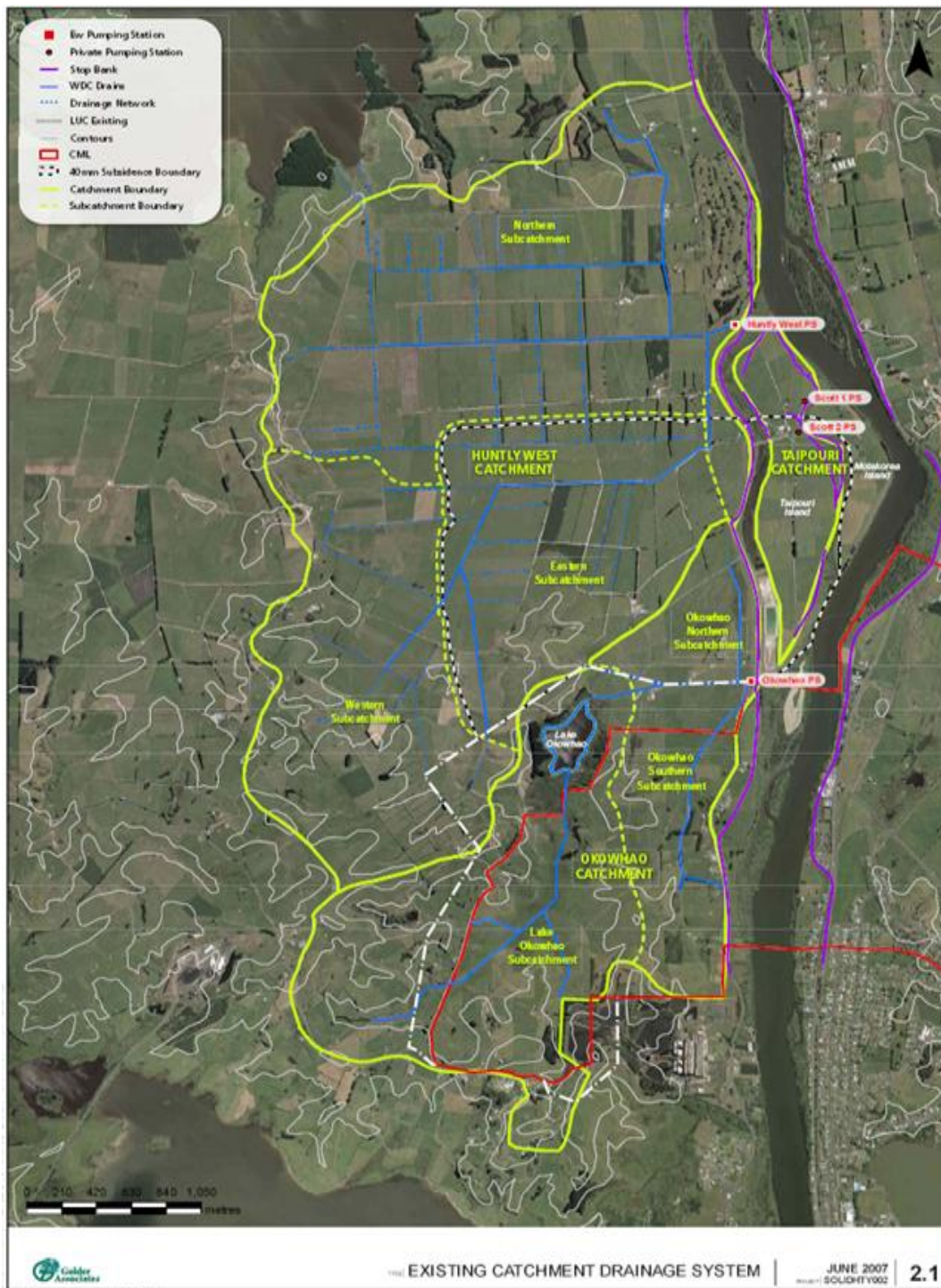
  

Parameters	TK5 Claystone /Mudstone	TK6 Mudstone Claystone	TK7 coal seam	Greywacke	Source
	6	7	8	9	
Ground water reduced level (undr,rl, m)	-12	-140	-140	-140	Larratt et al., 2009
Ground ware depth from surface (RL:12m)	24	152	152	152	
borehole 20091 (m)	229-242	242-262	262-272	272-350	Solid Energy, 2009)
borehole 20097 (m)	215-229	229-262	262-272	272-350	

### 3.3.3 Geographic and Surface Water

#### 3.3.3.1 Geography

The Huntly North Project (HNP) area has an alluvial terrace dominantly used for intensive dairy production, with exceptions in areas of the Hukanui Amuri marae, the Te Ohaki Road reserve and the Waikato River oxbows and flood plain (Figure 3.8).



**Figure 3.8** The location of the Huntly North Project and existing catchment (from Golder Kingett Michell, 2007).

The drainage system is maintained through the operation of active two pumpstations to maintain an artificially lowered groundwater level beneath the alluvial terrace and to provide drainage of stormwater (Golder Kingett Michell, 2007).

The HNP area is relatively flat and low-lying with an elevation varying from around 8 m RL to 20 m RL. Stop banks along the banks of the Waikato River to prevent flooding. Farm drains release water to trunk drainage channels. The drainage network finally discharges water to the Waikato River by two pump stations, Okowhao in the south and Huntly West in the north (Golder Kingett Michell, 2007).

### **3.3.3.2 Subsidence and surface water**

During 15 years of extraction in the HNP area, subsidence induced in mining is anticipated to increasingly have an impact on the surface topography. The maximum projected subsidence is controlled to be up to 1.5 m (1.3 m  $\pm$  200 mm). Consequently, current topographic basins within this area will be expected to become larger and deeper, with consequent affects on the related drainage networks and surface water drainage pattern. If no measures are taken the impacted drainage systems will not function to discharge the water into the Waikato River, then the pastures will be nonproductive, more seriously the ponding problem will further lead to higher potential of increase of subsidence and result in more risk to cause shaft problems (Golder Kingett Michell, 2007).

Golder Kingett Michell (2007) suggested that it may be possible to maintain most of the HNP area in productive pasture with little or no raise in ponding above what currently happens through a combination of mitigation measures carried out prior to coal extraction. The preferred mitigation approaches are:

- to clear the existing channels of intruding vegetation and to enlarge and re-grade the drains.

- If the hydraulic efficiency of the above measures is too low to guarantee the occurrence of ponding retained at its current level, modifying the switching levels on the existing Pump Station.
- or constructing a new pump station within the subsidence area.

### **3.3.4 Local Hydrology (borehole 20097)**

This section is mostly extracted from ‘the Huntly North Shaft Borehole Testing – Factual Report’, by PDP (2009) from Pattle Delamore Partners Ltd.

#### **3.3.4.1 Drilling observations**

The only significant zone of circulation fluid loss observed by the drillers in 20097 was within the coal seam. This indicates low permeability in all formations but the coal seam (PDP, 2009).

Another major observation was the occurrence of ‘rod rattling’ at around 117 m depth (adjacent to the base of the Glen Massey Formation). This may indicate plenty of rock fracturing at that depth (PDP, 2009).

#### **3.3.4.2 Water level data**

Start and end of day water levels recorded throughout the drilling period shows the influence of permeability variations down the hole (Figure 3.9).

Figure 3.9 also shows the expected hydraulic inclination derived from the piezometric levels recorded in nearby borehole 20015. In the highest permeability formation water levels may ‘equilibrate close to the piezometric level, and remain at well head level for low permeability formations’ (PDP, 2009). Water level shows slow decline while drilling through the Pukemiro Formation indicating low permeability (PDP, 2009). Once drilling advanced into the coal, the water level declined comparatively rapidly indicating higher permeability (PDP, 2009).

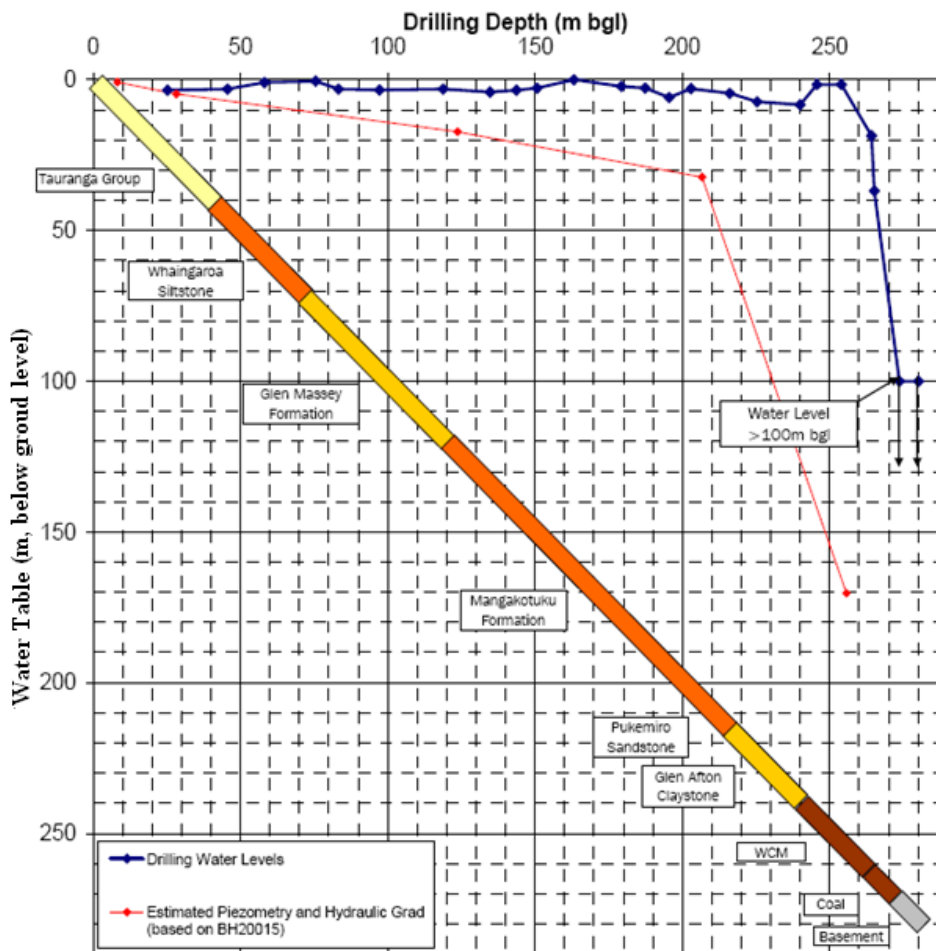


Figure 3.9 Plot of water level change over borehole depth (from PDP, 2009).

### 3.3.4.3 Lugeon values

Lugeon value indicates the loss of water, in litres per minute, and per meter borehole, at an over-pressure of 1 MPa. The loss indicates the water absorption capacity of the strata surrounding the borehole section. The maximum Lugeon values in 20097 are summarised in Table 3.7.

Table 3.7 Lugeon values for borehole 20097 (from PDP, 2009).

Unit and Lithology	Lugeon ( $\mu\text{L}$ )
Whaingaroa siltstone (Silt/mudstone)	0.6 (max)
Glen Massey formation (Silt)	0.7 (max)
Glen Massey formation (Sandstone)	0.5 (max)
Mangakotuku formation (Mudstone)	0.9-3.7 (max)
Pukemiro sandstone (Sandstone)	1.2-6.8 (max)
Waikato coal measures (Mudstone/coal)	5.7 (max)
Renown/Kupakupa seam (Coal)	0.7 (max)

### 3.3.4.4 Slug testing and permeability

The Slug Test is one of several different methods to assess the permeability (or hydraulic conductivity) of an aquifer. The process involves quickly adding or removing a quantity of water from a well, then making a series of water-level measurements to assess the rate of water-level recovery (<http://www.geologicresources.com>, 2011). Slug testing of the piezometers in 20097 and a nearby Tauranga Group piezometer (20033) was carried out, the results are summarised in Table 3.8.

**Table 3.8 The Slug testing and permeability values (from PDP, 2009).**

Piezometer	Permeability (m/s)
Tauranga Group (20033 and 20032)	$1.2 \times 10^{-8}$ to $3.1 \times 10^{-5}$
Whaingaroa Siltstone (20097-3)	$<6 \times 10^{-9}$
Glen Massey formation (20097-2)	$2.7 \times 10^{-9}$

### 3.3.5 Okowhao Lake

Okowhao Lake is around 70 meters south of the inclinometer borehole. The depth of this lake is unknown. It covers an area of 2 square kilometres.

## 3.4 Geotechnical Characteristics of Pilot Borehole

### 3.4.1 Introduction

The Pilot Borehole (20097) was located at the site of the proposed shaft and drilled at a depth of 280.3 m completed during August and September 2009. The aim of the investigation to the borehole was to obtain the geotechnical features at this site by conducting testing and analyses to ‘provide input to the baseline geotechnical report for the shaft’ (Page, 2009) and supplying input to the ground movement modelling. The profile of drill hole 20097 is summarised in Table 3.9.

**Table 3.9 Profile of drill hole 20097 (from Page, 2009).**

Hole	Northing (m)	Easting (m)	RL(m)	Depth (m)	Geotechnical log
20097 (HNS2009)	628482.063	333225.1	12.02	280.3	0-280.3m

### **3.4.2 Pilot Borehole (20097) Geology Summary**

A summary of the geology revealed in the borehole 20097 is summarised in Table 3.10 The detailed geological log and photographs of the cores are referred to the Geotechnical Information Report for 20097 (Page, 2009).

**Table 3.10 Summary of Geology via drill exploration (from Page, 2009).**

Group	Formation	Depth (m)
Tauranga	(Quaternary)	0 – 36.95
Te Kuiti	Whaingaroa Siltstone	36.95 – 98.34
	Glen Massey Sandstone	98.34 – 123.00
	Mangakotuku Formation	123.00 – 205.12
	Pukemiro Sandstone	205.12 – 214.66
	Glen Afton Claystone	214.66 – 229.10
	Waikato Coal Measures	229.10 – 272.80
Newcastle		272.80 – 280.30

### **3.4.3 Geotechnical Investigations**

The quaternary soil overburden has a thickness of 36.95m. In this section seven Standard Penetration Tests (SPT) were accomplished, three samples were retrieved for Triaxial testing, and five samples were taken for Atterburg Limit testing. From 36.95 m to borehole bottom (280.3 m) cores were sampled for Uni-axial compressive strength test (UCS), point load index and slake durability tests (Page, 2009).



### 3.4.4 Geotechnical Conditions

#### 3.4.4.1 Lithology

The general lithology intersected in the pilot borehole includes three groups from new to old as Tauranga, Te Kuiti and Newcastle. Tauranga group is 36.95 m thick of soil overburden. Te Kuiti group is 235.85 m thick. Newcastle group was not drilled through (Table 3.11).

**Table 3.11 Lithology intersected in the pilot borehole (from Page, 2009).**

Depth		Lithology	Description
From	To		
0	36.95	Tauranga Group	Unconsolidated sands, silts and clays with some peat layers
36.95	98.34	Whaingaroa Siltstone (Te Kuiti Group)	Light grey calcereous SILTSTONE
98.34	123	Glen Massey Sandstone (Te Kuiti Group)	Light grey glauconitic fine SANDSTONE with some siltstone layers
123	205.12	Mangakotuku Formation (Te Kuiti Group)	Greyish-green MUDSTONE
205.12	214.66	Pukemiro Sandstone (Te Kuiti Group)	Dark green glauconitic SANDSTONE
214.66	229.1	Glen Afton Claystone (Te Kuiti Group)	Greyish-green weak silty CLAYSTONE/MUDSTONE
229.1	272.8	Waikato Coal Measures	Yellowish brown and brownish black MUDSTONE/CLAYSTONE/SILTSTONE interbedded with brownish black and carbonaceous mudstone, siderite concretions and basal coal seams 262.00-262.20 Renown Rider Seam 263.85-272.20 Renown and Kupakupa Seam
272.8	280.3	Newcastle Group	Indurated siltstone and sandstone GREYWACKE

#### 3.4.4.2 Soil Classification

The soil materials in the upper 36.95 m consist of mainly clay and sand (fine to coarse) (Table 3.12). Others are volcanic tephra, peat, silt and mud. Nearly 12.3% i.e. 4.55m of core was lost in drilling of this 36.95 m.

**Table 3.12 Soil classification from surface to 36.95 m in 20097 (from Page, 2009).**

Soil Type	Percentage in upper 36.95m interval of borehole 20097
Clay	37.40%
Tephra	16.90%
Sand Fine-medium grained	13.30%
Sand Coarse, pebbly, gritty	10.50%
Other (peat, mud, silt, soil)	9.60%

#### **3.4.4.3 Rock Types**

Mudstone makes up to 65% of the section between 36.95m and 280.3m (Table 3.13). Sandstone comprises 13.4% with siltstone at 12%. A total of 5.95m (2.5%) of core was lost in this section (Page, 2009).

**Table 3.13 Rock types in borehole 20097 (from Page, 2009).**

Rock Type	Percentage between 36.95m and 280.3m in borehole 20097
Mudstone	33.0%
Mudstone, silty	32.7%
Sandstone	13.4%
Siltstone	12.0%
Coal	3.1%
Greywacke	2.9%
Siderite	0.4%
Core Loss	2.5%

#### **3.4.4.4 Weathering**

The majority (nearly 84%) of the rocks were unweathered or slightly weathered. Weathered soils take up 13.2% of the entire depth of 280.30 m, highly weathered rocks are minor (less than 1%), (Table 3.14).

**Table 3.14 weathering of rock in 20097 (from Page, 2009).**

Depth (m)	Degree of Weathering	%
0.00-36.95	Soils, Completely-moderated weathered	13.2
36.95-215.04	Slightly Weathered	63.5
215.04-272.20	Unweathered	20.4
272.20-273.95	Highly weathered	0.6
273.95-280.30	Moderately weathered	2.3

### 3.4.4.5 Broken zones

Table 3.15 presents the thicker, more significant faulted/sheared /broken zones logged in the 20097 cores that might cause instability in a shaft (Page, 2009).

**Table 3.15 Major broken zones distribution in rock strata (from Page, 2009).**

Depth (m)		Total Length (m)	Comments
From	To		
46.75	47.05	0.30	Crushed
48.12	48.30	0.18	
48.30	48.55	0.25	
57.00	57.25	0.25	
59.30	61.00	0.70	Broken core with some crushed zones
85.54	86.54	1.00	Partly sheared
88.83	90.52	1.69	Sheared and crushed
112.30	112.45	0.15	Crushed
116.90	117.15	0.25	
134.72	134.90	0.18	
177.23	177.64	0.41	
234.60	235.00	0.40	Broken core
264.56	272.20	7.64	Cleated/broken coal seam

### 3.4.4.6 Rock Quality Designation (RQD)

Figure 3.10 shows the RQD vs. depth. Table 3.16 indicates the RQD vs. lithology.

The Rock Quality Designation (RQD) values increase over depth except the coal seam section having a very poor RQD (Page, 2009).

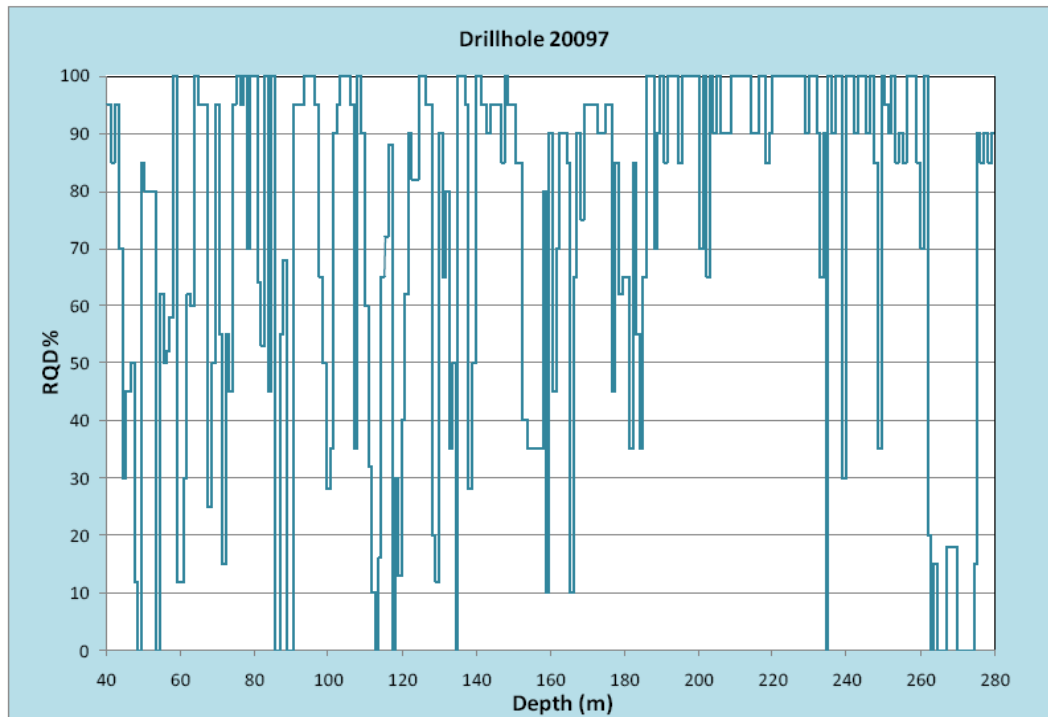


**Figure 3.10 RQD values over depth (from Page, 2009).**

Rock Quality Designation are usually Very Good (80%-100%) to Good (60%-80%), with several sections of Very Poor values (0% - 20%), which naturally stand for the broken, sheared and faulted zones. The coal seam has the lowest RQD values, 100% are very poor due to its well cleated structures (Page, 2009).

**Table 3.16 RQD analysis per lithology for borehole 20097 (from Page, 2009).**

Lithology	RQD %				
	Very poor	Poor	Fair	Good	Very good
	0-20	20-40	40-60	60-80	80-100
Whaingaroa Siltstone	13.2%	5.1%	20.0%	12.7%	49.0%
Glen Massey Sandstone	14.0%	21.1%	7.9%	16.2%	40.8%
Mangakotuku Formation	4.0%	10.8%	7.9%	12.5%	<b>64.7%</b>
Pukemiro Sandstone	0.0%	0.0%	0.0%	0.0%	<b>100.0%</b>
Glen Afton Claystone	0.0%	0.0%	0.0%	0.0%	<b>100.0%</b>
Waikato Coal Measures (above coal seam)	4.1%	8.1%	0.0%	5.8%	<b>82.0%</b>
Waikato Coal Measures Coal Seam	<b>100.0%</b>	0.0%	0.0%	0.0%	0.0%
Newcastle Group	32.0%	0.0%	1.7%	0.0%	<b>66.3%</b>

### 3.4.4.7 Rock Defects

The rock defects include joints, beddings, faults, sheared zones, joints, face cleats, butt cleats, open fractures and terminating joints. Rock defects were evaluated by two methods: structural logging of the core and interpretation of the down-hole acoustic scanner log. Defect orientations, per defect type, analysed from the acoustic scanner data are plotted in Stereonets (Figure 3.11).

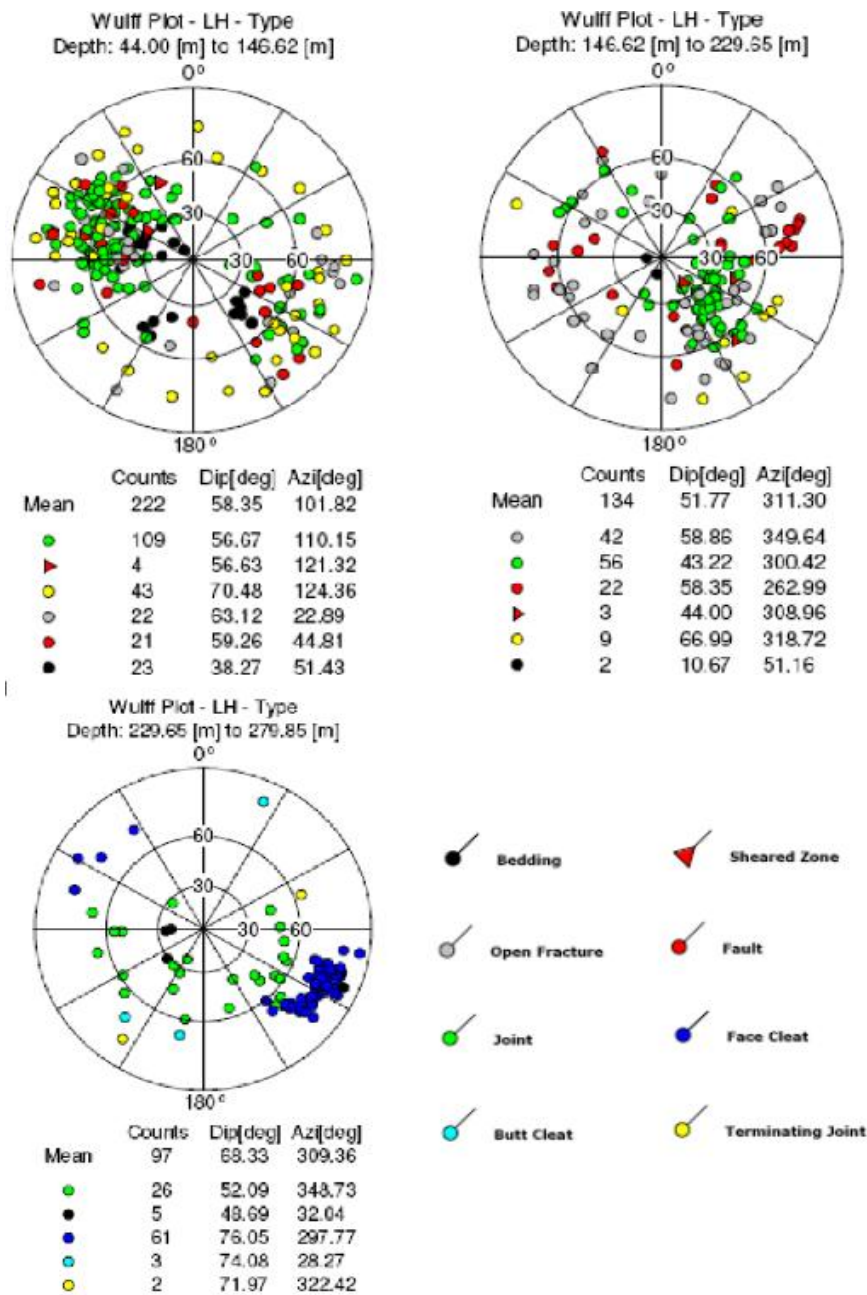


Figure 3.11 Summary plot of structure from Acoustic scanner interpretation (from Page, 2009).

In section 44-146.62 m, there were 222 defects. Joints take up to 109 over 222 counts, which have an average dip of 56.67 degrees in a azimuth of 110.15 degrees. There are only four shear zones with a dip of 56.63 degrees in azimuth of 121.32. Other defects have 21 to 43 counts (Page, 2009).

From 146.62 m to 229.65 m, a total of 134 defects were found. There were 56 joints dipping 43.22 degrees in average orientating 300.42 degree in azimuth. Beddings have the least counts of 2 dipping 10.67 degree with an azimuth of 51.16 degrees (Page, 2009).

In section 229.65 m to 279.85 m, there were 97 defects. Face cleats have the most counts of 61. Joints have 26 counts dipping 52.09 degrees and orientating 343.73 degree in azimuth (Page, 2009).

#### **3.4.4.8 Intact Rock Properties**

- **Unconfined Compressive Strength (UCS), Modulus of Elasticity (E) and Poisson's Ratio ( $\nu$ )**

UCS samples were chosen from the drill core below 36.95m for laboratory testing. A total of 28 samples were tested by Geotechnics Ltd. Te Kuiti lithologies have the average UCS values between 1 and 26.6 MPa (Very Weak to Weak rock) (Table 3.17).

Elastic Modulus (E) defines the relationship between stress and strain for intact rock and is required for estimation of ground deformation due to stress. The average E values are between 0.47 and 3.8 G Pa.

Poisson's Ratio ( $\nu$ ) is a measure of rock expansion when compressed and is also used for stress/deformation modelling purposes. The average  $\nu$  values are between 0.11 and 0.22.

**Table 3.17 UCS, Modulus of Elasticity & Poisson's Ratio (from Page, 2009, p10).**

Depth (m)		Lithology	UCS (Mpa)	Modulus of Elasticity (GPa)	Poisson's Ratio (V)
From	To				
41.28	41.40	Whaingaroa Siltstone	7.503	0.635	0.14
42.85	43.04	Whaingaroa Siltstone	2.847	0.469	0.13
44.70	44.89	Whaingaroa Siltstone	4.316	0.505	0.15
46.23	46.36	Whaingaroa Siltstone	4.782	0.601	0.14
49.87	50.05	Whaingaroa Siltstone	4.700	0.598	0.15
51.44	51.60	Whaingaroa Siltstone	4.510	0.706	0.12
52.04	52.20	Whaingaroa Siltstone	5.741	0.521	0.11
52.78	52.94	Whaingaroa Siltstone	4.497	0.643	0.16
56.20	56.35	Whaingaroa Siltstone	8.767	1.201	0.14
56.61	56.80	Whaingaroa Siltstone	7.152	0.689	0.11
62.52	62.72	Whaingaroa Siltstone	7.463	0.865	0.13
64.29	64.53	Whaingaroa Siltstone	8.157	0.865	0.12
65.27	65.40	Whaingaroa Siltstone	4.470	1.146	0.17
66.56	66.75	Whaingaroa Siltstone	11.675	1.092	0.13
69.82	69.98	Whaingaroa Siltstone	10.428	1.005	0.14
70.17	70.30	Whaingaroa Siltstone	8.294	1.014	0.15
85.36	85.52	Whaingaroa Siltstone	8.060	0.960	0.14
101.96	102.12	Glen Massey Sandstone	19.175	2.082	0.15
110.05	110.23	Glen Massey Sandstone	26.622	2.500	0.14
202.77	202.98	Mangakotuku Formation	12.958	1.298	0.22
202.98	203.09	Mangakotuku Formation	15.996	3.556	0.12
205.41	205.60	Pukemiro Sandstone	13.014	2.106	0.12
206.32	206.47	Pukemiro Sandstone	34.650	3.857	0.11
218.89	219.01	Glen Afton Claystone	7.185	1.831	0.14
228.11	228.27	Glen Afton Claystone	7.178	0.875	0.11
237.14	237.27	Waikato Coal Measures	11.910	1.358	0.11
242.75	242.86	Waikato Coal Measures	15.190	2.551	0.18
253.77	253.92	Waikato Coal Measures	10.359	1.006	0.12

- **Rock stress**

The ratio of horizontal to vertical effective stresses in soil is defined as the coefficient of earth pressure at rest,  $K_0$ . Typical  $K_0$  values are listed in Table 3.18 (Phase2 Theory, RocScience, 2011).

**Table 3.18 Typical values of coefficient of earth pressure at rest (RocScience, 2011).**

No.	Soil Type	$K_0$
1	Dense sand	0.35
2	Loose sand	0.6
3	Normally consolidated clays	0.5 – 0.6
4	Lightly overconsolidated clays	1.0
5	Heavily overconsolidated clays	3.0

My modelling might use the coefficient of earth pressure at rest,  $K_0 = 0.55$  as the TG consists of saturated clayey soils.

According to Gale (CNZ2543, 2003) ‘The stress system modelled is one considered to be typical of the field stresses measured in the mine and anticipated in the N5 mining area. The vertical stress is due to lithostatic load and the total horizontal stress is based on a tectonic strain component (0.7) and a lithostatic component. The model couples water flow and water depressurisation due to inflow into the mine, together with strata movement and rock fracture’. The effective stress ratio used for the other eight strata may be chosen as 0.7.

However, measurements in the Huntly region have shown that horizontal stresses are a function of depth (Figure 3.12). Larratt et al. (2010) presents two equations for calculating the horizontal stress and vertical stress in-situ in Huntly East Coalmine. The vertical stress is computed by and equal to the overburden stress:

$$\sigma_v = \frac{\rho * g * H}{10^6} \quad (3-1, \text{ adapted from Larratt et al., 2010})$$

The horizontal stress is as indicated by the likely  $\sigma_H$  range vales shown in Figure 3.12. The value of horizontal stress is calculated by:



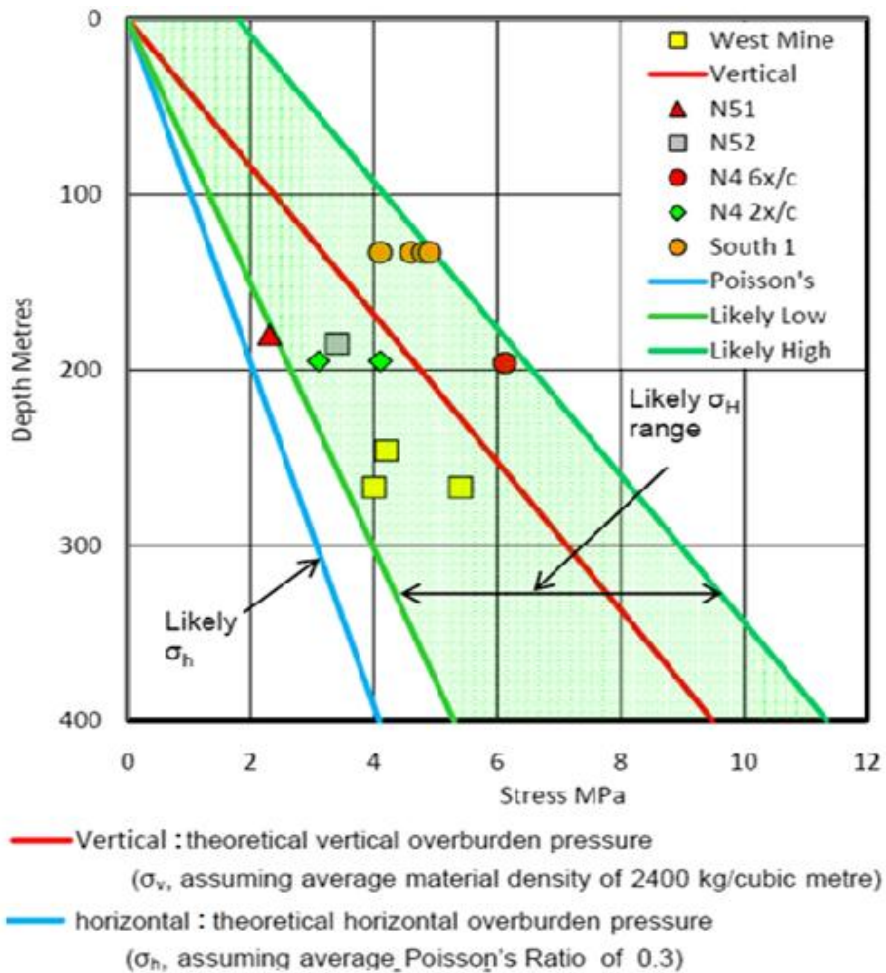


Figure 3.12 Stress VS Depth for the Huntly Region (from Larratt et al., 2010, p8).

$$\sigma_H = 1.75 + \sigma_v \quad (3-2, \text{ adapted from Larratt et al., 2010})$$

Where: H = Depth below surface, m

$\sigma$  = Stress, MPa

$\rho$  = the average material density, kg/m<sup>3</sup>.

To be conservative, it is supposed that the minor horizontal stress is equal to the major horizontal stress. The calculated results of the average  $\sigma_h$  and average  $\sigma_H/\sigma_v$  stress ratio, for the Borehole 20091, are listed in Table 3.19, which are to be used in modelling in Chapter 7.

**Table 3.19 The results of the average  $\sigma_h$  and average  $\sigma_h/\sigma_v$  stress ratio, for the Borehole 20091, calculated using Equations 3.1 and 3.2.**

Formation type	Depth	Average density	Vertical stress, $\sigma_v$	Average $\sigma_v$	Horizontal stress, $\sigma_h$	Average $\sigma_h$	Average $\sigma_h / \sigma_v$ stress ratio	
							by Larratt et al. 2010	**
	m	kg/m <sup>3</sup>	Mpa	Mpa	Mpa	MPa		
Tauranga Group (TG): soils	1	1700	0.0167	0.37	1.752	1.787	4.9	0.55
	43	TG only	0.7164		1.823			
Te Kuiti Group & Base: rocks	44	2210	0.952952	0.95	1.84724	2.351	2.5	0.7
	500	includes TG	10.829		2.855			

\*\* by Gale, 2003; RocScience, 2011

The results from calculation by equations 3.1 and 3.2 are much larger than the method by Gale (2003) and RocScience (2011). The calculation results by Lattatt et al. (2010) equations were used in my thesis because they were verified by the field measurements.

- **Point Load Index**

Point load index tests were used to provide an indirect estimate of uniaxial compressive strength and were conducted at several lengths of the cores. The test results are presented in Table 3.20.

**Table 3.20 Results of point load index test for borehole 20097 (from Page, 2009).**

Lithology	No. of tests	Is (50)			Standard Deviation
		Min	Average	Max	
Whaingaroa Siltstone	19	0.36	0.55	0.84	0.14
Glen Massey Sandstone	2	1.28	1.55	1.81	0.37
Mangakotuku Formation	3	0.46	0.57	0.65	0.09
Pukemiro Sandstone	3	0.52	0.70	0.98	0.25
Glen Afton Claystone	3	0.57	0.62	0.66	0.05
Waikato Coal Measures	10	0.38	0.70	1.50	0.35
Basement	1	1.82	1.82	1.82	0.00

- **Slake Durability Tests**

Slake durability is a test to estimate the resistance of rocks, mainly clayey rocks such as shales, to a combination of wetting and abrasion. Test results are expressed as a slake-durability index that represents the percentage of dry mass of the fragments retained by a drum of 2.0 mm square-mesh after two cycles of oven drying and 10 minutes of mixing in water, under the effect of deterioration and abrasion (ASTM D4644, 2008).

Slake durability tests were conducted by samples from several intervals along the length of the drill cores. Detailed test results in Table 3.21 indicate that the Waikato Coal Measures have very low Durability (less than 50).

**Table 3.21 Summary of Slake durability test results for borehole 20097 (from Page, 2009).**

Lithology	No. of tests	Average Slake Durability Index (%)
Whaingaroa Siltstone	7	94.3
Glen Massey Sandstone	1	96.7
Pukemiro Sandstone	1	81.5
Glen Afton Claystone	1	71.5
Waikato Coal Measures	1	23.3

#### 3.4.4.9 Soil Material Properties

- **Consolidated-undrained Triaxial Compression Tests**

Consolidated-undrained triaxial compression tests on three samples from the pilot borehole showed the friction angles and cohesion values in Table 3.22.

**Table 3.22 Summary of consolidated-undrained triaxial tests (from Page, 2009).**

Depth (m)		Description	f'	C'
From	To		( <sup>o</sup> )	(kPa)
26.75	26.87	Tauranga Group	29	169
32.77	32.89		19	120
35.8	35.91		11	88

- **Atterberg Limits**

Atterberg Limit tests on five samples obtained from the clay or clayey layers (Table 3.23) indicated high plasticity (20-40) for the samples from first three depths, very high plasticity (>40) for samples from the last two depths.

**Table 3.23 Summary of Atterberg limit test results (from Page, 2009).**

Depth (m)		Description	Water content (%)	Liquid Limit	Plastic Limit	Plasticity Index
From	To					
2.7	3.15	Clayey SILT	43.9	57	31	26
5.7	6.15	Clayey SILT	67.2	69	44	25
11.7	12.15	Clayey SILT	57.2	65	37	28
14.7	15.15	Clayey SILT	54.3	87	34	53
17.7	18.15	Clayey SILT	53.5	86	34	52

### 3.5 Climate

This area has warm summers and cool winters. The regional westerly and south westerly winds normally bring mild, humid conditions from the Tasman Sea. Rainfall and evaporation reveal the seasonal variations. Average annual rainfall is approximately 1,200 mm, and winter has a higher rainfall than summer. Evaporation is obviously seasonal and is high in the summer and low in the winter (Golder Kingett Michell, 2007).

### 3.6 Summary

The Waikato Coal Region is New Zealand's major coal producing region including some 13 coalfields and extending approximately 180 km in the western central North Island. Huntly is one of the 13 major coalfields.

The stratigraphy in the Huntly Coalfield area from surface to the borehole bottom includes Tauranga Group, Te Kuiti Group, and Greywacke as the base. The WCM contain two economic coal seams: Renown and Kupakupa that are located at the

bottom of Te Kuiti Group and overlies on the Greywacke basement. The depth of the coal is normally 150 to 300 m below the surface. Floor and roof rocks have a lower strength ( $2\text{--}5 \text{ MN m}^{-2}$ ) than coal strength ( $5\text{--}25 \text{ MN m}^{-2}$ ).

The overall groundwater flows eastwards towards the Waikato River, most flow occurs in the upper approximately 40m in the Tauranga Group (TG). Groundwater level in the TG investigation holes is approximately 8 m above sea level (RL).

The drainage system in the Huntly North Project (HNP) area is maintained through the operation of active two pumpstations to maintain an artificially lowered groundwater level beneath the alluvial terrace and to provide drainage of stormwater, therefore the groundwater level remains relatively stable.

### **The Tauranga Group**

- The Tauranga Group (TG) has a thickness of approximately 25 to 70 metres including saturated Quaternary clays, sands, gravels and weathered volcanic ash deposits. The TG has an erosional and unconformable contact with the underlying Te Kuiti Group. The TG behaves as a single aquifer which is hydrologically connected to the Waikato River.
- The Tauranga Group materials have a high to very high plasticity index.
- Average stress ratio ( $\sigma_h / \sigma_v$ ) of TG materials is approximately 4.9.

### **The Te Kuiti Group**

- In the Te Kuiti Group mudstone makes up to approximately 65% of the section, others materials are sandstone, siltstone, and coal. 84% of the rocks were unweathered or slightly weathered. Highly weathered rocks are less than 1%.

- The Te Kuiti overburden serves as a potential “rock head” between the coal seam and the overlying Tauranga aquifer and protects the seams against the interconnection between the Tauranga aquifer and coal seams. When subsidence is larger than 1.6m the “rock head” may fail and interconnection from the Tauranga aquifer is likely to occur (section 3.2.1.3).
- At the base of the Te Kuiti Group, coal seams have a varying thickness from 30 to 100 m and overlie Mesozoic basement greywacke, with an unconformable erosional surface. The coal seam is the only significant zone of high permeability above basement formation.
- The Majority of the Te Kuiti rocks have higher Rock Quality Designation as Very Good (80%-100%) to Good (60%-80%). The coal seams have the lowest RQD values, 100% are very poor having well cleated structures.
- Te Kuiti lithologies have the average uniaxial compressive strength (UCS) values between 1 and 26.6 MPa classed as Very Weak to Weak rock. The average Elastic Modulus (E) values are between 0.47 and 3.8 GPa. The average Poisson’s Ratio ( $\nu$ ) values are between 0.11 and 0.22.
- Average  $\sigma_h/\sigma_v$  stress ratio of materials in Te Kuiti Group is approximately 2.5.

### **Fault structures**

- In the N55/57 area, there are five major faults mainly orientating approximately north to NNW. The majority of the five faults have a throw larger than 10 m, up to 55 m for Ralph Fault.



# Chapter 4 Inclinometer and Phase2 Modelling Investigation Methods

## 4.1 Introduction

To study the strata movement linking with the coal seam extraction underground, I undertook borehole inclinometer monitoring. Data from GPS levelling and surveying, borehole logging and sampling, down-hole geophysical survey, and groundwater monitoring were provided to me by Solid Energy. I undertook software plotting and modelling. The borehole 20091 was used to supply inclinometer monitoring, coring, down-hole loggings, and casing top surveying.

The research methods and their objectives were:

- Borehole inclinometer monitoring was used to measure lateral ground movement.
- GPS surveying was used to investigate and profile vertical subsidence of the ground surface.
- Borehole investigation and logging were used to obtain the geological, hydrological and hydraulic information of the strata, and the geotechnical parameters of the cores;
- Inclinometer software packages were used to plot graphs and for analysis of data to interpret the casing movement in 2 D and or 3 D.
- Groundwater data were used in the modelling.
- The Phase2 code was used to model the movement of the strata above the coal seam extraction in panels around the inclinometer borehole.



## 4.2 Borehole Incliner Method

### 4.2.1 Location of the Borehole

The inclinometer borehole is located in the west of the Te Ohaki Road, at the north edge of the Lake Okowahao, 322 m away from the location of the proposed shaft in the adjacent panel in Huntly East Mine (Figure 4.1). Therefore there are significant similarity, correlation, and relevance between the inclinometer borehole and the proposed shaft hole in terms of geology, hydrology, and topography.

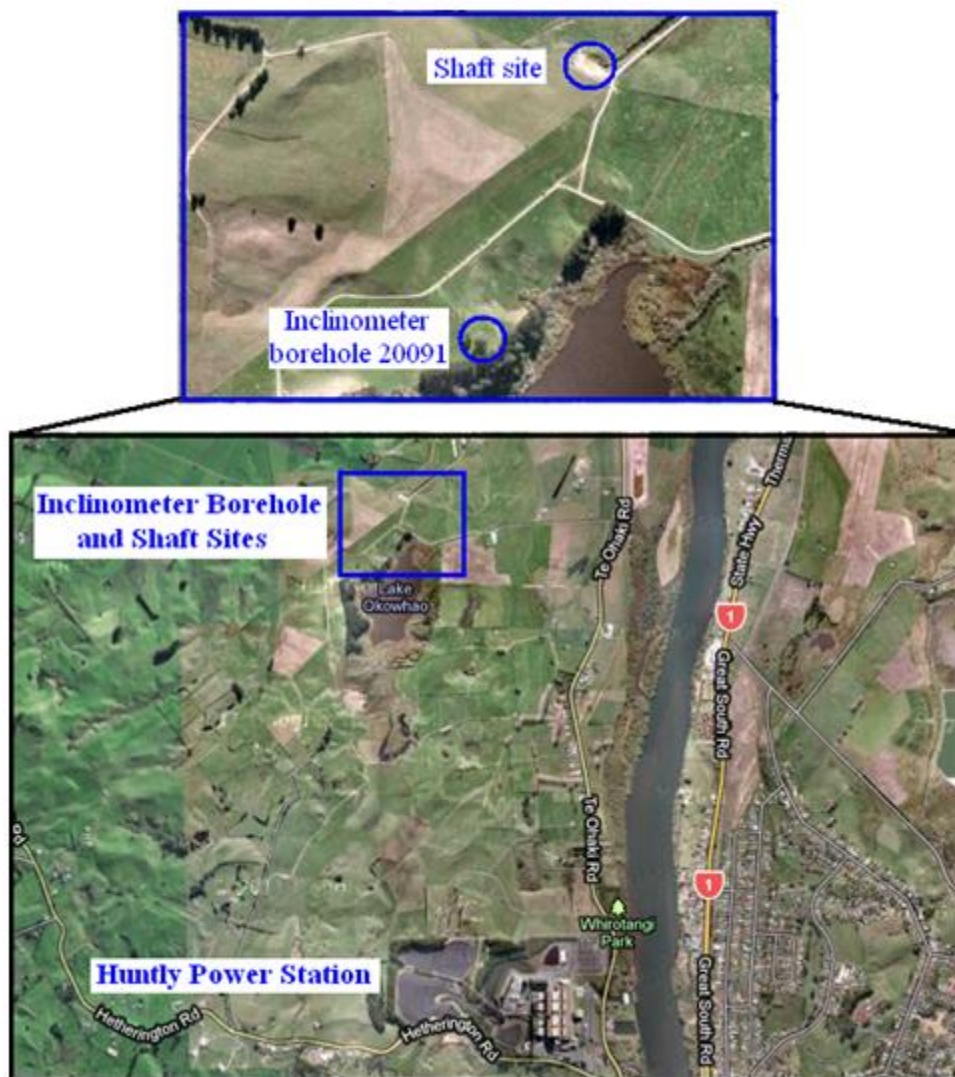


Figure 4.1 Location of the Inclinometer Borehole, Huntly (image from Google, 2011).

The inclinometer borehole was drilled on a slope that leans southeast down to the Lake Okowahao. The location of the Borehole opening is approximately 9 m higher than both east and west side low land. The road on the north side of the Borehole is approximately 5 m above the collar elevation and is the crest point of the local area. The Borehole is situated at the north edge of the N55 Panel of the Huntly East Mine (Figure 4.2). The north coal seam from the Borehole was left as a protective pillar for the shaft. The south coal seam was mined by the ‘bord and pillar’ method and by April 2011 the southwest part has been extracted and the mining operation was heading towards the final southeast part.

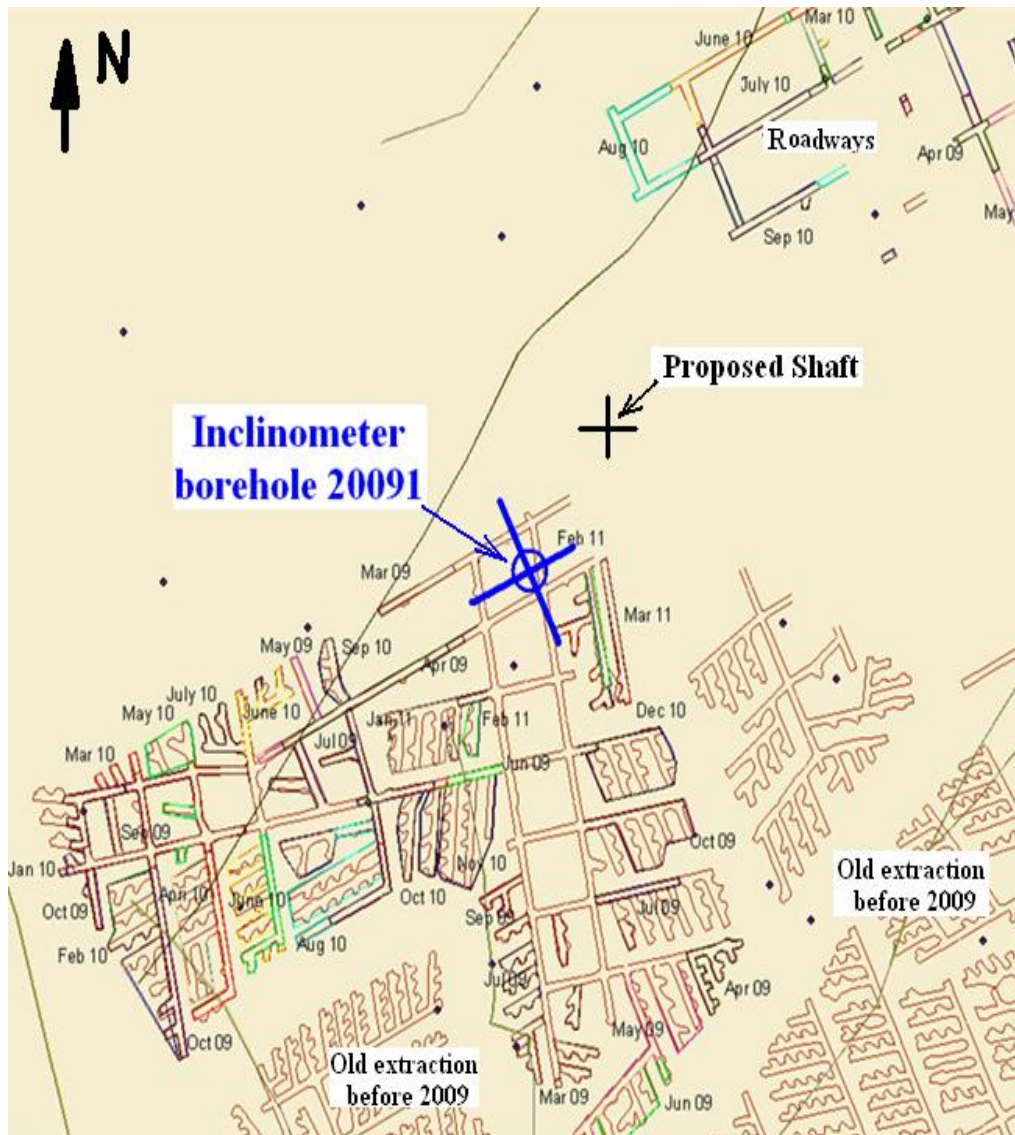


Figure 4.2 The location of inclinometer borehole (from Solid Energy, 2011a).

## **4.2.2 Methods and Objectives on the Borehole**

The Borehole is the focus of this research:

- The use of traversing inclinometer to monitor and measure lateral ground movement in the Borehole. From the inclinometer data the magnitude, rate, direction, depth, and type of ground movement may be determined.
- The Borehole investigation and logging were used to obtain the geological, hydrological and hydraulic information of the strata and aquifers and the geotechnical parameters of the cores;
- Observation of groundwater in the Borehole to monitor the changes of water level.

## **4.2.3 The Structure of the Boreholes**

The Borehole structure had two layers of casing (Figure 4.3). The outer casing is Ø150 mm BSP (British Standard Pipe, a steel pipe) casing inserted to 42.7 m below the ground surface to hold the loose and unstable soil overburden. The inner casing is the inclinometer casing made of an OD Ø 70 mm PVC high press casing (ID 59 mm) with key-grooves premade in it. The annulus gap between the outer and inner casing is approximately 35 mm. The inclinometer casings normally have a constant modulus length of 3 m, assembled using couplings, rivets, and sealing tape, ensuring strong joints. The assembled casing was descended to 250 m into the Borehole and had 0.336 m standing above the ground surface. The annulus between the two casings was grouted with a cement - sodium bentonite - water mixture. The Borehole and casing were enclosed to prevent groundwater exchange between the water in the Borehole and the groundwater beyond the Borehole (Solid Energy, 2009c).

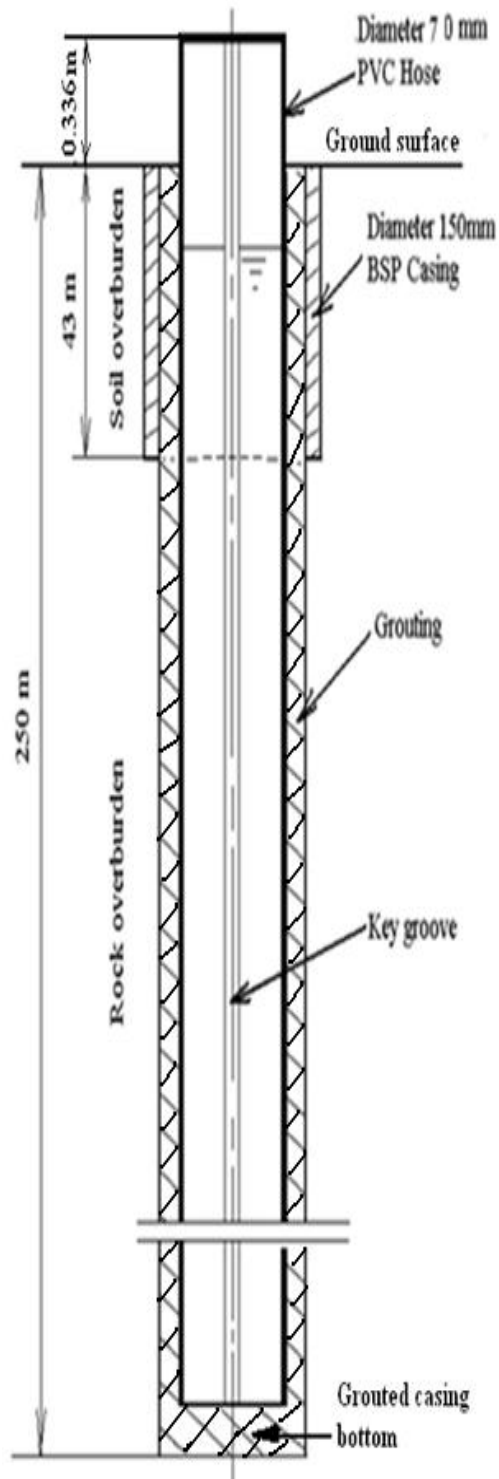


Figure 4.3 Structure of borehole 20091, Huntly East Mine (Not in scale).



## 4.2.4 Operation of Inclinator

The initial or ‘zero’ inclinometer reading was undertaken shortly after the installation of the casing on 27/03/2009 to determine the initial shape of the casing. Figure 4.4 shows Priscilla and Zhaodong are waiting for 5 minutes for the probe to equilibrate at the bottom of the Borehole before readings, and Figure 4.5 shows Zhaodong is lowering the inclinometer into the Borehole.



**Figure 4.4 Inclinometer monitoring photo one (Photo: Page, 2011).**



**Figure 4.5 Inclinometer monitoring photo two (Photo: Page, 2011).**

The main procedures for traversing the probe and taking readings in situ are summarised as follows:

1. A ‘dummy’ probe was first lowered into the Borehole to ‘verify adequate guide casing conditions for monitoring, rather than risking damage to the more expensive inclinometer probe’ (Machan and Bennet, 2008). The ‘dummy’ probe has the same length, shape and weight with the inclinometer probe tied and lowered through a rope.

2. The main on – off switch was turned on the Hub (or probe reel) (Figure 4.6) to energise the accelerometers, making them less susceptible to shock;



**Figure 4.6 Digital Inclined Inclinometer system (from SOIL, 2008).**

3. The probe was inserted into the casing with the lower wheels (Figure 4.7) in the A0 groove.

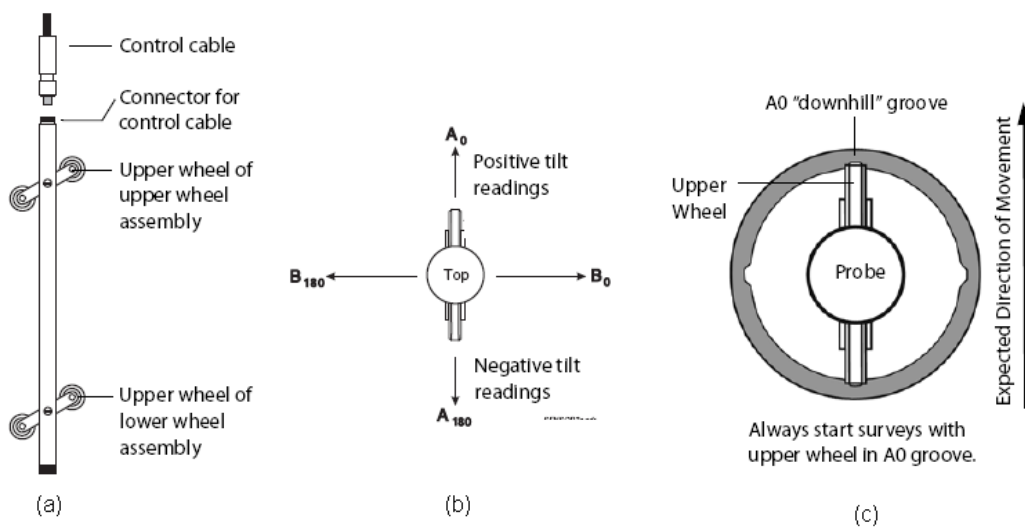


**Figure 4.7 Operation of the inclinometer. (a) the probe; (b) the plan view of the probe; (c) the plan view of the probe in casing (from Slope Indicator Co., 2006).**

4. The probe was slowly (about 30 m per minute) lowered to the bottom of the measurement section of the casing. We lowered it to 245 m depth to avoid striking the bottom of the probe.
5. The probe was allowed to equilibrate at the bottom of the Borehole to adjust to the temperature inside the casing for 5 minutes.
6. The probe was lifted to the starting depth. The operator then waited for the numbers of A and B on the Digital Readout (PDA, Personal Digital Assistant) to stabilize and recorded the A and B readings by pressing the Enter button on the remote control.
7. The probe was then raised to the next depth at intervals of 0.5 m. Waited for a stable reading, and then recorded it. The process was repeated until the probe got to the top of the casing.
8. The probe was then lifted out of the collar and rotated 180 degrees when being hold uptight, so that the lower wheels were inserted into the A180 groove.
9. Again the probe was lowered to the starting depth, and the survey continued as above.

## **4.2.5 Inclinometer Data Error Correction**

### **4.2.5.1 Data errors and inclinometer accuracy**

Inclinometer data errors include random errors and systematic errors (Figure 4.8). Random errors come from the sensors, reducing the precision of the probe measurement. Systematic errors result from user's operations that influence the working of the probe (Machan & Bennett, 2008), which include bias-shift errors, rotation errors and depth positioning errors (Cornforth, 2005).

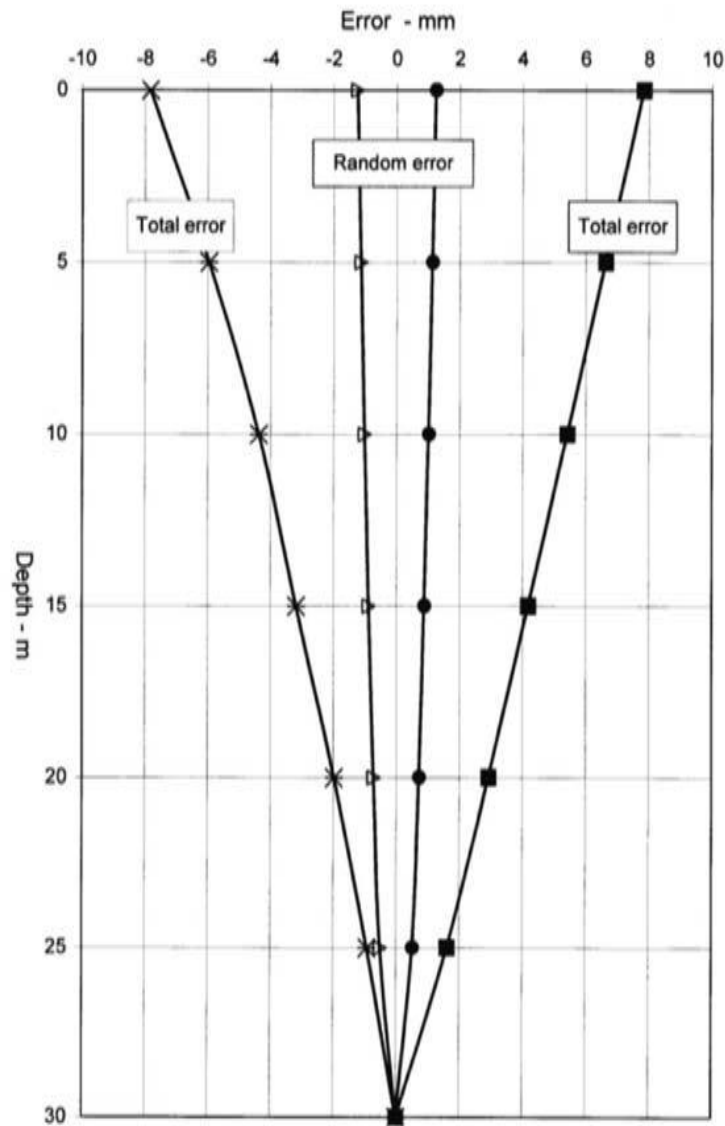


**Figure 4.8 Total error and random errors in inclinometer data (from Machan & Bennett, 2008).**

Cornforth (2005) stressed that the accuracy of inclinometer measurements decreases with increasing deviation from vertical. The largest potential for systematic errors exists at the deepest depth of a probe casing because of four causes: (1) instrument warm-up drift being most acute, (2) more probable calibration hysteresis, (3) more tendency of the borehole to drift from vertical, and (4) the largest distance from the top reference point (Slope Indicator Co., 2000; Mikkelsen, 2003). Sources of errors are mainly the probe, cable, PDA and casing (Table 4.1).



**Table 4.1 Sources of errors of inclinometer (after Mikkelsen, 2007 and Slope Indicator Co., 2000).**

Equipment	Errors or error source
Probe	Sensor Bias shift
	Rotation (sensor alignment shift)
	Connectors, Wheels
Cable	Depth control, Poor storage, Aging
Readout (PDA)	Set up, Operation
Casing	Inclination, Curvature, Backfill
	Grooves, Coupling

The Slope Indicator Company (2000, 2001, and 2006) training manual and technical papers on inclinometer monitoring provide detailed instructions for verifying and evaluating data measured. According to ASTM (2005), no standards are available yet for evaluation against precision and bias issues (cited by Machan & Bennett, 2008). System field accuracy of an inclinometer is normally  $\pm 7.8$  mm of displacement per 30 m of casing, which combines both random and systematic errors (Figure 4.8) (Slope Indicator Co., 2000; Mikkelsen, 2003; Machan & Bennett, 2008).

‘All errors look like displacement, and can lead to costly, false engineering conclusions by the unaware’ (Mikkelsen, 2003). Error correction, therefore, is a vital stage in data collection and processing for assuring the correct data for interpretation, but it is not a simple phase. Undertaking corrections appropriately demands knowledge and experience. In this chapter, a brief introduction to some aspects of error correction in data collection by inclinometer measuring and monitoring is discussed. More details and knowledge about error correction may be found in literature such as Slope Indicator Company (2006); Mikkelsen (2003); and Cornforth (2005).

Generally there are five types of error corrections in analysis and interpretation of the inclinometer data. They are: checksum correction; orientation correction for casing; spiral correction for casing; bias-shift error; and rotation errors. Before introducing the details of data errors, Table 4.2 summarises the data errors types and correction methods. Non-zero checksum readings may result from any of the errors listed in Table 4.2.

**Table 4.2 Summary of data errors and correction methods (after Mikkelsen, 2003, 2007; Stark & Choi, 2008).**

	Data Errors	Detailed Types	Error Features	Error Causes	Correction Methods	Procedures for Error Correction
System Field Accuracy  * 7.8mm per 30 m or * 0.26 mm/m	Random Errors * limit 1.24 mm / 30 m or 0.041 mm / m	Random Errors	Less influential; relatively constant; Can not be corrected	Random errors	minimised with better installation and precise reading procedures	Can not be corrected.
	Systematic Errors  * limit 6.6 mm/30m; * may vary with each survey; * +/-0.22mm / m, very small * can be corrected * at casing bottom, the highest potential of errors	Bias-shift errors (BSE)	Most common; small value; may changes with each survey; Identified as leaning straight lines	bias-change; slight jarring; Warm-up drift.	Evaluated by checksums Mean checksum plot should be vertical in one dataset. Easy to correct by calibration value 'b'. BSE=0.01 mm x b x N	Identify; Quantify; Manually correct or put correction factors into software for correction (i.e. Gtilt, DigiPro, and In-Site).
		Sensitivity drift errors	Least common; simplest; most devious to notice	The drift in amplifier.	Easy to correct using calibrated instrument constant 'k'.	
		Rotation errors	Combination of casing inclination & sensor axis alignment shift. Identified as similar graphs in A and B	Too big inclination of casing and probes change.	Trial and Error corrections; Rotation error angle: $\Delta = \arcsine(r/s)$ , small within physical limit of sensor and wheel behaviours.	
Depth-positioning errors	Combination of the casing curvature and vertical placement errors. Not common.	change in cable reference, length, casing settlement & compression	Easy to identify, but most hard to quantify and correct. The collar of casing should be surveyed to identify elevation changes.			
Others	Mistakes	Mistakes or gross errors	Detected in checksum; when (k = 25000), A & B axis: 10 & 20units	Inclinometer or operator mistakes	Once detected, the dataset should be errors corrected or rejected.	Check checksums; try to correct; discarded if not corrected.
	Spiral errors (the last correction after above systematic error corrections)	Spiral errors	Cause errors in resultant direction of move, but not in its magnitude. Identified as crossing of plots.	Groove spiral from pre made or later twisted in movement	Should be measured when: Casing is 60 m deeper and casing is not esp. made with spiral controls from factory.	Measure spiral by spiral sensor; Input the skew into GTILT, In-Site or DigiPro.

#### 4.2.5.2 Checksums of readings

Inclinometer measurements generally are recorded as the pairs of readings in the A0 and A180, and B0 and B180 axes. The first evaluation of the data quality is checking the checksums of data, by summing the two values measured in

diametrically opposite directions of the A0 and A180, and B0 and B180 at the same depth. Ideally, the checksums should be zero because the probe readings have opposite signs but equal absolute values. However, in practice, any errors can cause the checksum to be non-zero, i.e. have a constant and generally small value because of bias in probe, variation in grooves, and positional error in probe and irregularity in casing, where a low standard deviation will represent data accuracy (Machan & Bennett, 2008; Slope Indicator Co., 2003; Stark and Choi, 2008).

The checksums at each depth should be:

- roughly the same, and
- consistent along the length of the borehole

Checksums should only be a problem, whatever their actual numeric values, if they fall outside the parameters above. However, it is quite normal that if readings are taken about a casing joint, then checksums for these readings might never stabilise, even though all of the other checksums are consistent (SOIL, 2008).

When non-zero checksums are constant for all depths in a dataset, then it is easy to eliminate. If, however the checksums are not constant and a large checksum difference occurs at one depth, the reading data can be corrected by the mean of the neighbouring readings (Machan & Bennett, 2008, p32). If large checksums and variations are detected in a dataset, the measurement should be repeated until satisfactory checksums are obtained (Mikkelsen, 2003; Cornforth, 2005; Machan & Bennett, 2008). But if checksums are not constant, that is, the checksum plots are displayed as leaning or curved lines the probe should be recalibrated before subsequent measurement.

Small checksums are not a problem, but it becomes a problem when the standard deviation is over ‘5 to 10 units of the mean checksum for the primary axis (A)’ (Machan & Bennett, 2008). Cornforth (2005) and Slope Indicator Co. (2000) indicated that the standard deviation of checksums measures the random errors in the survey. Generally, the standard deviation of checksums should not be bigger than 10 for the A axis and 20 for the B axis. Unfortunately, the above references have not further discussed what the instrument constants are for the inclinometer used, which determine the magnitude of readings and value of the checksums for the cited limits of 10 to 20 units and what casing depths are dependent on to create these limits of units.

The inclinometers may use constants such as 5000 (used by SOIL Co.), 25000 (used by RST in GTilt, and Slope Indicator Co. in In-Site), or 50000 (used by SOIL Co.) that are for metric system and 20000 used by all probes with English unit system. Instrument constant is not required for data calculation, but is used for controlling decimal of the displayed readings only in the format of ‘ $\sin \theta \times k$ ’ (SOIL, 2010, p24). When the tilt  $\theta$  remains the same, different instrument constants yield different displayed readings, consequently yield different standard deviations.

Table 4.3 clearly explains the correlation between the checksum and the instrument constants. For instance, when the instrument constant changes from 5000 to 50000 the readings in both A and B axis will be amplified 10 times, and the checksums and standards deviations increase 10 times as well.

**Table 4.3 Checksum and instrument constant, calculations for the A axis measurement.**

	Tilt	Measure intervals	Sine function	Instrument constant		Display reading	Incremental deviation	Bias	Bias reading	A0 reading	A180 reading	Checksum	Combined reading
Symbol Formula	$\theta$	L	$\sin \theta$	K		$R = K \cdot \sin \theta$	$d = L \cdot \sin \theta = L \cdot (R/K)$	b	b	R + b	-R + b	A0 + A180	$(A0 - A180)/2$
Unit	deg.	mm	unitless	unitless		Units	mm	deg.	Units	Units	Units	Units	Units
Example in the A axis	1	500	0.0175	25000	Metric	436	8.726		13.1	449	-423	26	436
				20000	English	349	8.726	0.03	10.5	360	-339	21	349
				5000	Metric	87	8.726		2.6	90	-85	5	87
				50000	Metric	873	8.726		26.2	899	-846	52	873
Note				Also it is called Data type.	Supposing no bias in probe.						Varies on different K values.	Bias removed.	

More importantly the mean checksums cited in the samples packaged in the specialist software packages, namely, GTILT®, In-Site®, Inclinalysis®, DMM®, are not always in compliance with the theoretical limit of 10 and 20 units (Table 4.4). Therefore, in this thesis the Coefficient of Variation (CV) was used to evaluate the checksum quality. Here, the CV is the ratio of standard deviation over mean of checksum. The threshold CV values in this study are 10% and 20% for the A axis and the B axis checksum. If big checksums and variations exist in a dataset, the measurement should be repeated until satisfactory checksums are obtained (Mikkelsen, 2003; Cornforth, 2005) or the correction of readings for abnormal checksums may be conducted.

**Table 4.4 Mean checksum variations from project samples by the Specialist software.**

	In Site®	GTilt®	DMM®	DigiPro®
Unit system	English	English	English	English
Data type	20000; 25000	20000	20000	20000
Probe sensitivity	10000 units/30degs			
A axis	Instalation1-1	Instalation1-2	Instalation1-3	Instalation1-4
	3.0, 3.2	3 to 40	3.0, 4.2	0.6 to 5.1
B axis	9.5, 10.4	9 to 13	8.2, 10.4	0.6 to 11.8
	Instalation2-1	Instalation2-2	Instalation2-3	Instalation2-4
A axis	2.6 to 9.5	2 to 16	-9 to 3	3.0 to 3.6
B axis	7.3 to 13.6	6 to 11	-9 to -46	8.2 to 11.6

#### 4.2.5.3 Bias-shift error

If the inclinometer probe is held absolutely vertical, the reading is typically a non-zero value that is the probe's bias. Bias with a constant value in a survey is normally neutralised during data reduction when the A0 (or B0) readings are coupled with the A180 readings (or B180). But if the bias changes during a monitoring run, it cannot be neutralised during the data reduction process. The remaining value is called 'the Bias-Shift Error' that is embedded in the reduced data (Figure 4.9).

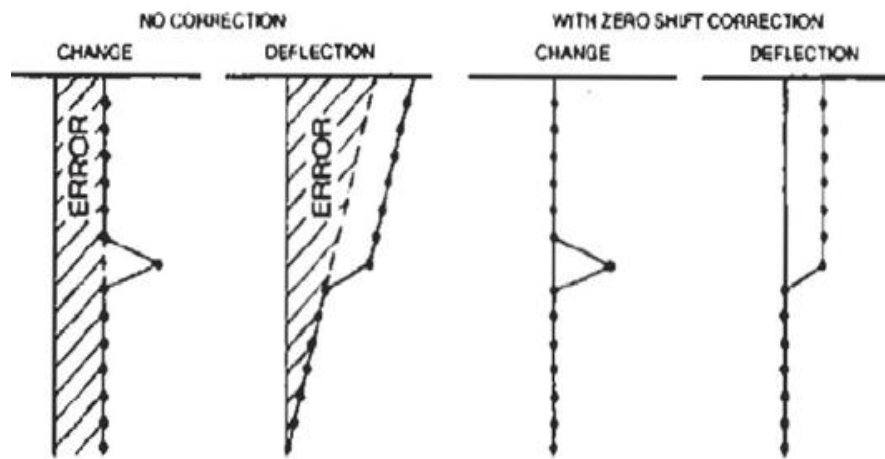


**Figure 4.9 Typical bias shift errors (from Mikkelsen, 2003).**

The bias shift is a function of the 'probe calibration and performance' (Machan & Bennett, 2008); it is the most common type of systematic error. The Bias-Shift error is relatively simple to correct, and is the first type of correction to the data set (Machan & Bennett, 2008).

Main causes of Bias-shift errors include:

- (1) Bumping the probe by rushed operation or due to the irregularity of the casing: it is certain that dropping the probe changes the bias, and bumping the probe may change the bias as well.
- (2) Warm-Up Drift: the probe should be powered up first, and then lowered to the bottom of the casing, with a 5 to 10 minutes waiting time

before starting measurement so that the probe can adjust to the temperature of the water and stabilize.

If the probe cannot get well stabilized, readings taken during the first 5 or 10 minutes of the survey may include drifting bias values or extreme values. The abnormal readings with the drifting bias and extreme values will show an apparent false movement at the lower part of the borehole where the bottom of the casing is usually fixed in stable strata (Slope Indicator Co., 2000).

Figure 4.10 shows the typical patterns caused by bias-shift error when incremental and cumulative displacements are plotted. Checksums have the same trend with incremental displacements.

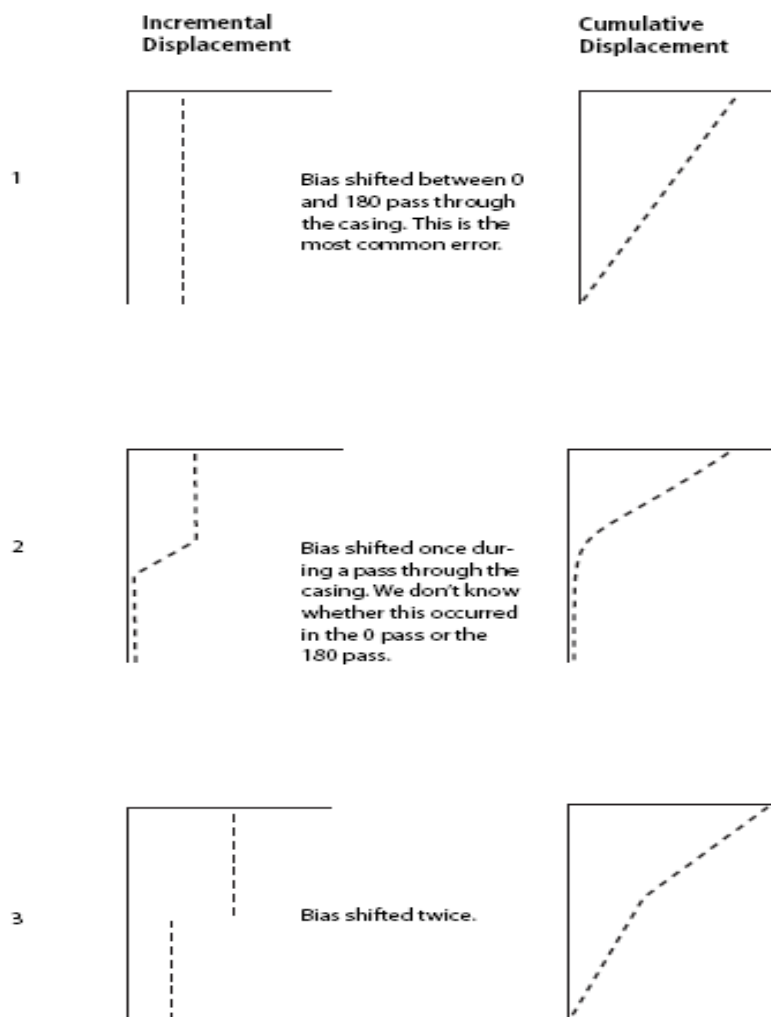


**Figure 4.10** The typical patterns of bias-shift errors in plots (from Slope Indicator Co., 2000).

The mean checksum in type 1 remains relatively constant, which is the most common pattern and is easy to correct. The checksum in type 2 drifts once and then keeps constant. For type 3, the checksum varies twice. In the cumulative displacement, the plot is typically a straight line leaning right or left in type 1, a straight leaning line plus a curve in type 2, and two straight tilting lines in type 3 (SI, 2000). These typical patterns help distinguish bias-shift errors in the data (Slope Indicator Co., 2003).

Systematic bias-shift is easy to correct by using inclinometer graphing software to correct the error visually in a 'trial and error' (Mikkelsen, 2003, p7) way or to determine a displacement value for computing a correction factor. Correction factors are different for A and B readings because they are measured by two separate accelerometers. Generally correction values also vary for different datasets.

Visual Correction:

- a). in a cumulative displacement plot, identify displacements that are produced by bias-shift error. For example, if the bottom 10 m of the casing is fixed in stable strata, any displacement there is actually from bias-shift error, which typically shows a straight line tilting away from vertical;
- b) In presentation software, input a value (typically less than 20, using a positive value if the tilt is positive or entering a negative value if the tilt is negative;
- c) apply the correction and check the redrawn plot; and
- d) The tilted line becomes vertical when the bias-shift error has been removed (Slope Indicator Co., 2000).



Calculated Correction:

- a) in a cumulative displacement plot as above, for each affected dataset, identify displacements that are from bias-shift error;
- b) find the depth with the largest cumulated bias-shift error;
- c) find the exact displacement value for the depth obtained above;
- d) calculate the number of intervals up to and including this depth;
- e) compute a bias correction value by Formula 2.1 and input it to the specialist software; and
- f) The plot is corrected off the bias-shift errors. Formula 2.1 is used for correcting displayed readings on the In-Site platform. Formula 2.2 can be used for correcting incremental displacement data in Excel file.

$$B_s = BSE / (N \times C) \quad \text{(Formula 2.1) (Mikkelsen, 2003)}$$

Where:

$B_s$  is bias-shift correction per interval, no unit

BSE is the total bias-shift error over zone considered, (mm)

$N$  is the number of reading intervals, no unit

$C$  = reading intervals distance/2K (mm or inch)

For metric unit,  $C = 500\text{mm} / (2 \times 25000) = 0.01$  mm;

For English unit,  $C = 2 \times 12 \text{ inches} / (2 \times 20000) = 0.0006$  inch

$$B_s (\text{mm}) = BSE (\text{mm}) / \text{number of intervals} \quad \text{(Formula 2.2) (Slope Indicator Co., 2000)}$$

#### 4.2.5.4 Rotation error

Rotation is a small change in the alignment of the axis of the probe, usually less than one degree. Theoretically, the probe is aligned so that the A-axis accelerometer measures inclination only in the A-plane. If the mechanics of the probe is rotated somewhat towards the B plane, the A-axis accelerometer

becomes slightly sensitive to tilts in the B-plane too' (Slope Indicator Co., 2003).

Rotation error, therefore, is the cross-axis component in a reading.

Rotation error can be identified by inspection of the cumulative displacement and deviation graphs as follows:

- The cumulative displacement is plotted in a curved line, which should be straight (such as two lines in Figure 4.11 a in the A axis).

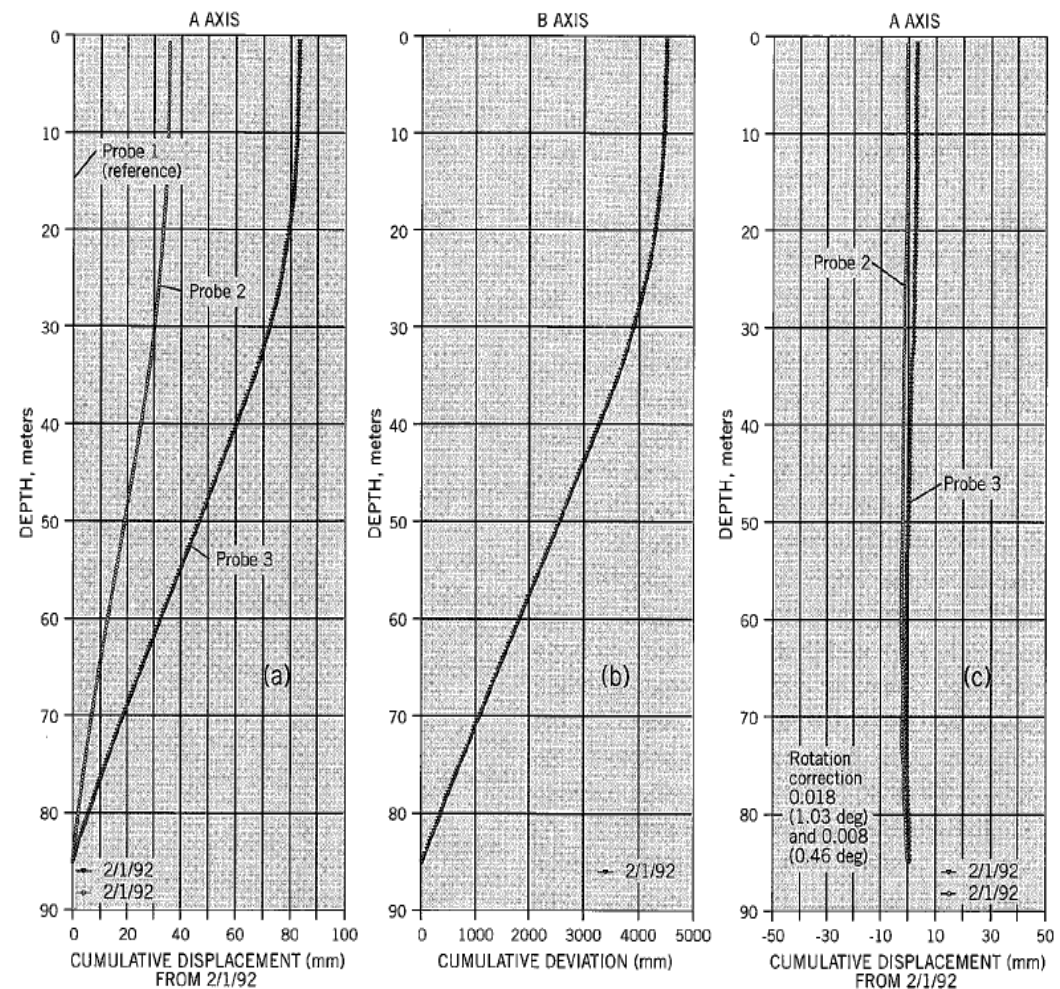


**Figure 4.11 Results of tests using three probes in a single borehole on the same day. (a) lateral displacement on the A axis; (b) deviation on the B axis; (c) lateral displacement on the A axis after correction. Similarity between the A and B profiles indicates rotation error (from Slope Indicator Co., 2003; Cornforth, 2005).**

- The cumulative deviation line shows significant tilt in the cross axis (Figure 4.11b).
- The two plots in (a) and (b) have the similar shape (Figure 4.11).

The casing declined approximately 4 degrees in the B-axis (Figure 4.11b). The corrected displacement is displayed on right graph (c) and shows the significant difference between the non-corrected and corrected (Slope Indicator Co., 2003).

Conditions leading to rotation error include:

- Significant inclination in the cross axis;
- An alignment change of the probe occurring after the initial set was taken.

The change in the alignment may result from:

- Wear and tear on wheel yokes and bearings.
- Bumps to the probe causing sensor movement affect A and B axis readings separately.
- Changes in the alignment of the accelerometer within the probe during repair.
- Using different probes to survey the same inclinometer casing (Slope Indicator Co., 2000).

Correcting rotation error can be applied using a ‘trial and error procedure’ (Machan & Bennet, 2008; Mikkelsen, 2003) with expertise. Rotation errors are easy to correct by using an inclinometer graphing program. Slope Indicator (2000) suggests:

- Draw a cumulative displacement plot with datasets that contain the error.
- Identify rotation error; find the depth of the maximum error.
- Plot a cumulative deviation graph of the cross axis of the reference survey, find the deviation value at the same depth.
- Divide the displacement value by the deviation value. The result is a starting value for correcting rotation.
- In a specialist program (DigiPro), enable rotation corrections and enter the rotation value.

- Apply the correction and inspect the redrawn plot. The curve in the line should straighten.

#### 4.2.5.5 Depth error

The probe should be positioned consistently at each depth in the survey to assure that readings can be compared reliably. However, if the probe is ‘positioned above or below the proper depth the reading will change, even if there is no movement’ (Slope Indicator Co., 2011). This change of reading is defined as the depth error (Figure 4.12). In a straight casing the change is small, and can be neglected. However, when the casing is not straight the error might be significant. Figure 4.13 shows the displacement is - 0.35 inches before correction, and approximately -0.04 after (Slope Indicator Co., 2011).

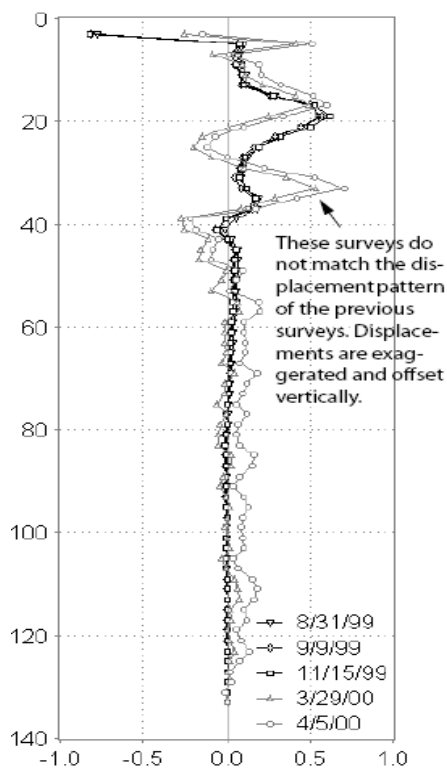


Figure 4.12 One typical plot containing depth errors (Slope Indicator Co., 2000).

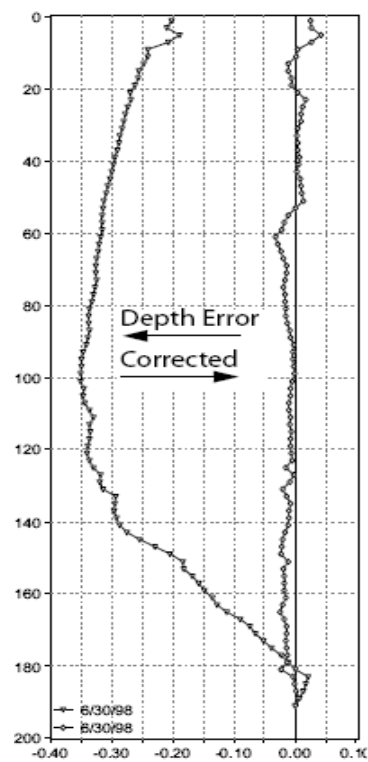
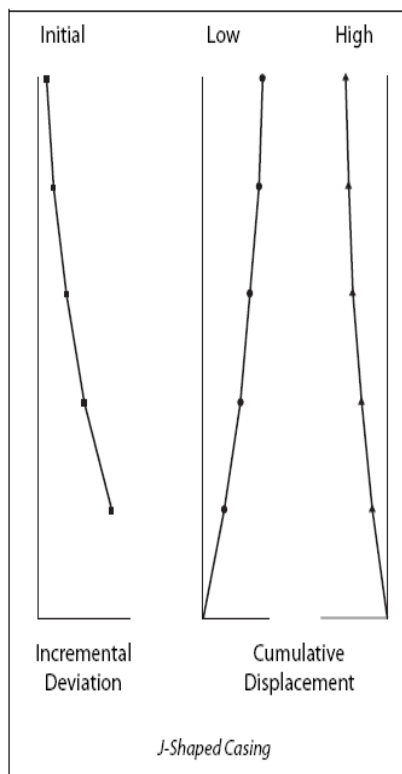


Figure 4.13 Plots before & after depth error correction (Slope Indicator Co., 2000)

If the casing collar reference changes, every reading in the survey will be influenced. If the casing length changes due to being compressed by subsidence, the probe will be positioned deeper at every interval. Readings will be affected.

When cable length changes by shrinking, stretching over time, or cable replacement, readings are affected also. Depth errors can be corrected by specialist software in the settlement correction function. Random positioning mistakes may lead to the wrong measuring depth and take a wrong reading. This cannot be adjusted by specialist software, and must be corrected manually instead (Slope Indicator Co., 2011). A detailed example of depth error correction is explained in Slope Indicator Co. (2011).

Systematic depth errors can be distinguished by comparison of displacement plots to the incremental deviation plot of the reference survey. A systematic depth error exists if a similar shape is identified. Figures 4.14 and 4.16 show two types of casing shape, J-shaped and S-shaped casing, Figures 4.15 and 4.17 show two questionable surveys for identifying depth error (Slope Indicator Co., 2000).



**Figure 4.14** Plots of incremental deviation & cumulative displacement in J shaped casing (Slope Indicator Co., 2000).

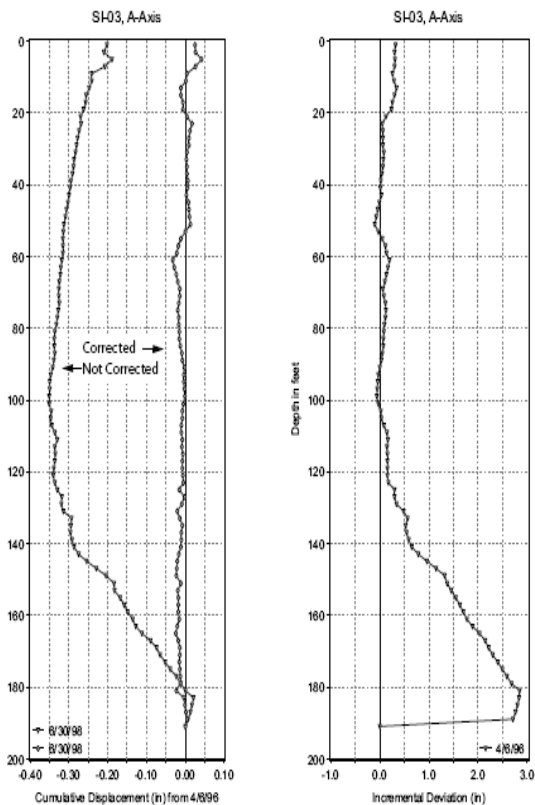


**Figure 4.15** An example of depth error in J-shaped casing (Slope Indicator Co., 2000).

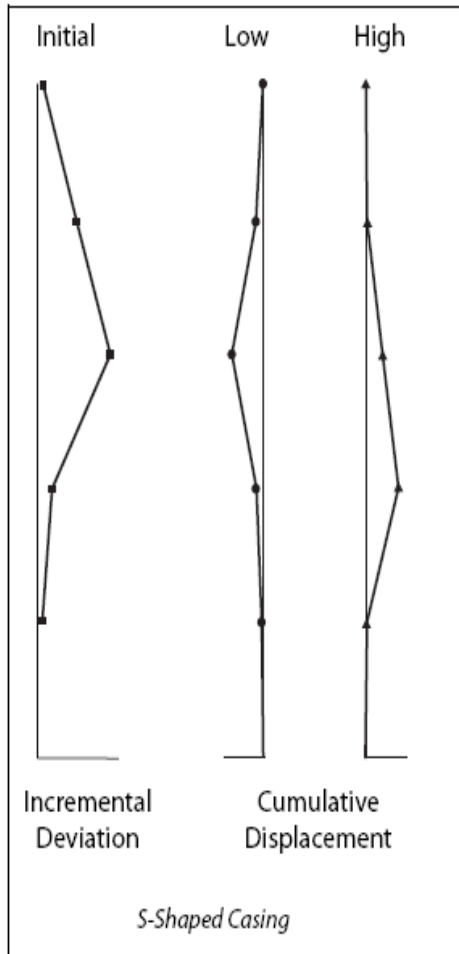


**Figure 4.16** Plots of incremental deviation and cumulative displacement in S-shaped casing (Slope Indicator Co., 2000).

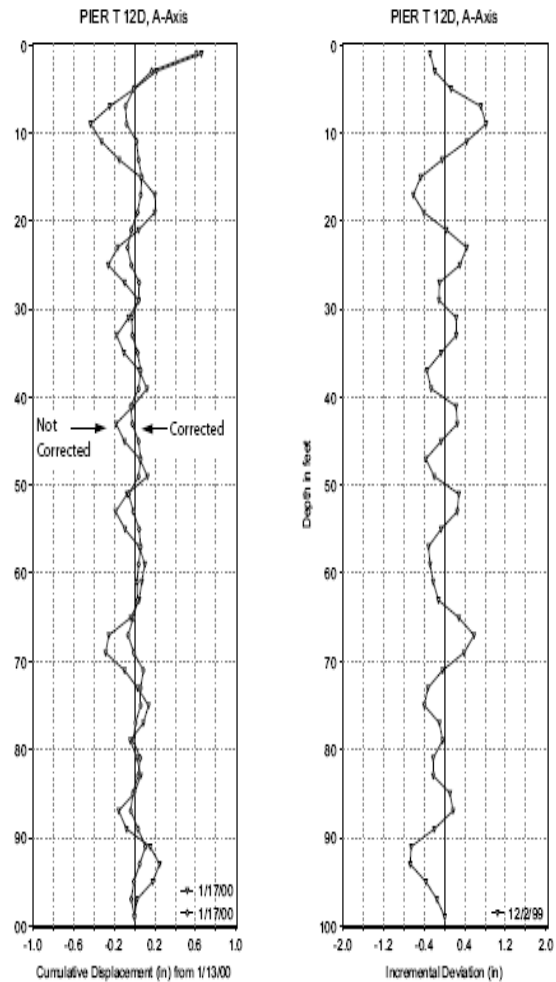


**Figure 4.17** An example of depth error in S-shaped casing (Slope Indicator Co., 2000).

When the depth error is identified, a new dataset of corrected readings can be computed by the following calculation (Slope Indicator Co., 2000):

For each depth,

Corrected reading = Current reading + correction

Correction = Curvature x (Depth Error/Interval)

Curvature = Reading above – Current reading, probe too deep

Or

Curvature = Reading Below – Current reading, probe too shallow

Depth error = [Distance from correct depth]

Interval = The reading interval used, typically 2 feet or 0.5 m.

The detailed contents of depth error identification and correction are referred to Slope Indicator Co. (2000).

#### **4.2.5.6 Orientation corrections for casing**

If the A0 groove in a casing exactly faces the movement direction, there will be no reading of movement in B axis when the movement remains in the same direction over an entire depth. When key grooves are not directly lined up with the direction of movement, the measured angle between the A axis and direction of displacement can be put into the inclinometer software, to compensate the orientation difference (Slope Indicator Co., 2003; SOIL, 2010). After rotating the orientation of the 'two measuring axes into the axis (plane) of the movement, then there is no need to plot the B plane component' (Conforth, 2005, p78).

Casing orientation correction may be helpful for final presentation in a resultant displacement plot; however, it must not be conducted before systematic error corrections are applied. Also, A and B readings are mixed in the reorientation of the axes (Slope Indicator Co., 2000).

#### **4.2.5.7 Spiral correction for casing**

Casing spiral may exist in casing products and may be produced during installation. The spiral is generally minor in short lengths but may be significant in deeper installations, which can cause problems with interpretation of readings. The spiral can be measured by a spiral sensor and the spiral value can be used to correct each set of inclinometer readings.

Correction of spiral errors is not normally required. However, it is a 'good practice to measure spiral in inclinometers deeper than 200 feet long or in access

pipe that is not controlled for spiral by the manufacturer' (Slope Indicator Co., 2000, p31).

Spiral errors may be displayed as the crossing of plot lines of data in different survey visits (Figure 4.18) (Slope Indicator Co., 2002). The spiral values are accumulated from the bottom to the top, so the maximum values occur at the bottom of the curves.

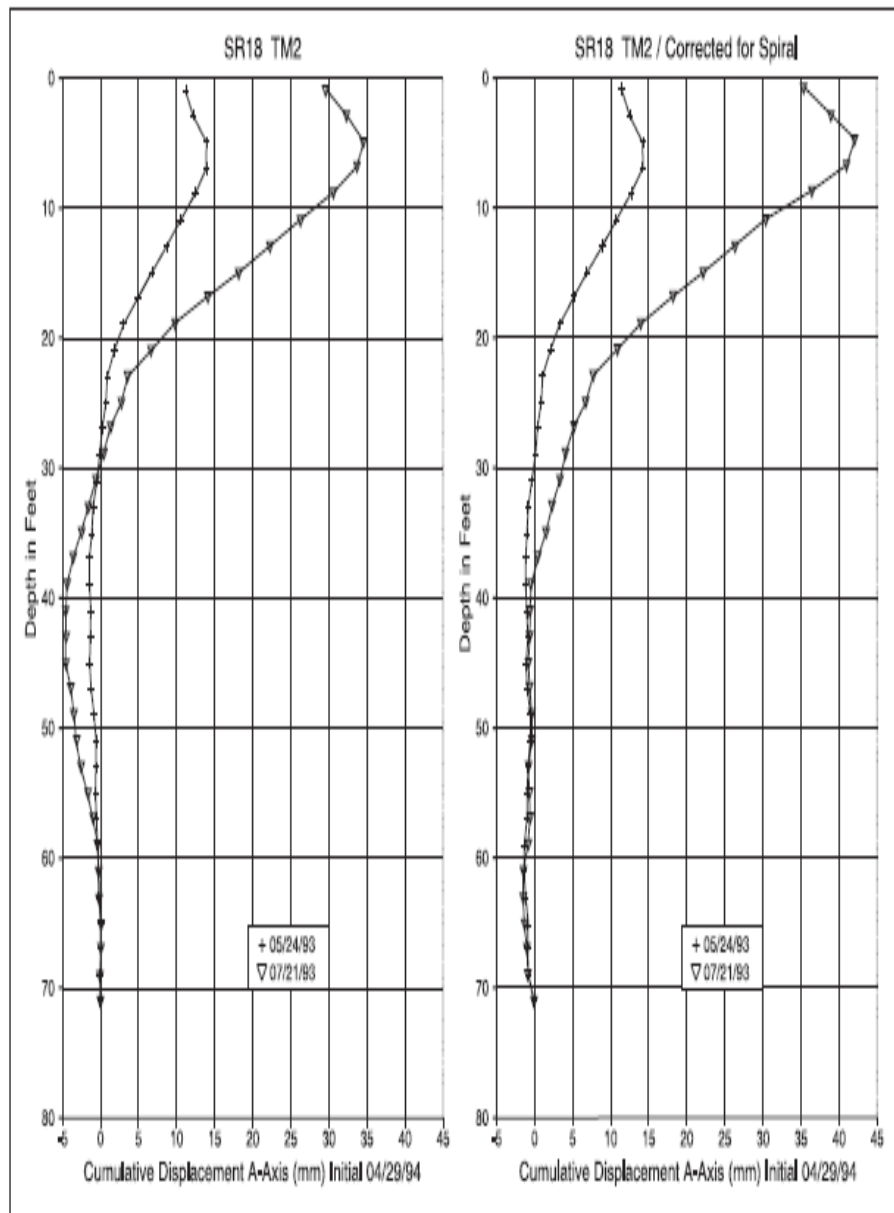


**Figure 4.18 Influence of spiral error on plots of displacement (from Slope Indicator Co., 2002).**



A spiral survey on a twisted casing is processed and stored in the DMM® (DataMate Manager) database. DigiPro® automatically finds the spiral data if it exists in DMM® (Slope Indicator Co., 2004). If the accumulated spiral is less than 20 degrees, it can be ignored in analysis (Slope Indicator Co., 2011).

## **4.2.6 Inclinometer Calibration**

### **4.2.6.1 Introduction**

The inclinometer system should be regularly calibrated to ensure that the readings taken with the system are accurate. Soil Instruments recommends calibration on a yearly basis by the inclinometer manufacturer or the inclinometer expert (SOIL, 2009). The inclinometer system used for the inclinometer borehole monitoring is number 1678 that is also used for slope monitoring in Rotowaro Opencast Mine weekly. The time spending on trip and for calibration will take nearly 6 weeks if sending to the UK headquarters of SOIL Company. The 1678 inclinometer was not sent to UK for calibration timely.

### **4.2.6.2 Inclinometer calibration in laboratory**

To ensure the accurate readings and consistent work state of the inclinometer system, inclinometer calibration was undertaken in laboratory at Huntly on 13 July 2011 (Figure 4.19). The tilt angles were measured using a Digital Smart level, and were compared with the tilt angles from the inclinometer (probe number 1678). The Digital Smart level has accuracy of  $\pm 0.1$  degree, and the system accuracy of the probe is 2 mm over 25 m, that is 0.005 degree. Thus, only gross errors could be checked for using this system.

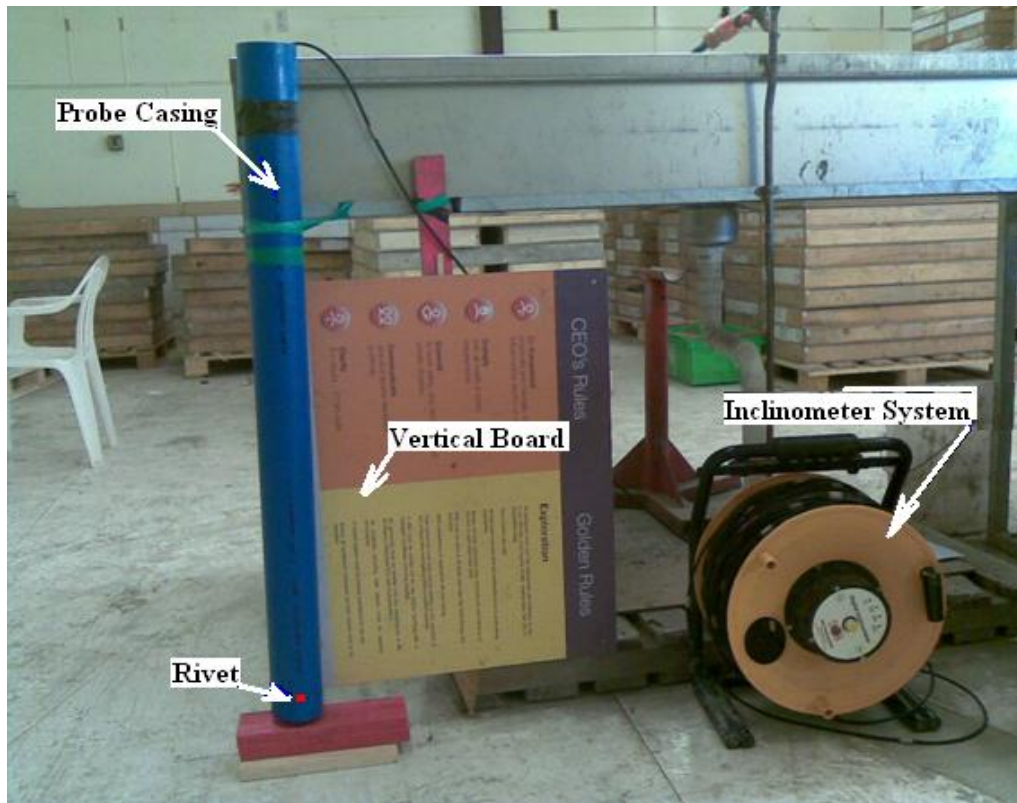


**Figure 4.19** The setup of the inclinometer calibration on 13 July 2011 at Huntly.

The installation is that the vertical board is always having a 0 degree tilt. The probe casing was turning around a rivet to supply with the required angle for the casing and probe in the vertical plane. The B axis was perpendicular to the vertical board, the A axis was parallel with the vertical board.

#### **4.2.6.3 Results and conclusions**

Table 4.5 records the tilts measured by the digital smart level with the average tilts measured by the inclinometer in seven surveys and datasets. Table 4.6 summarises and compares the Smart Level reading VS probe result. Figures 4.20 and 4.21 are the scattered plots from data in Table 4.6 to show the correlations between the types of two tilt values.

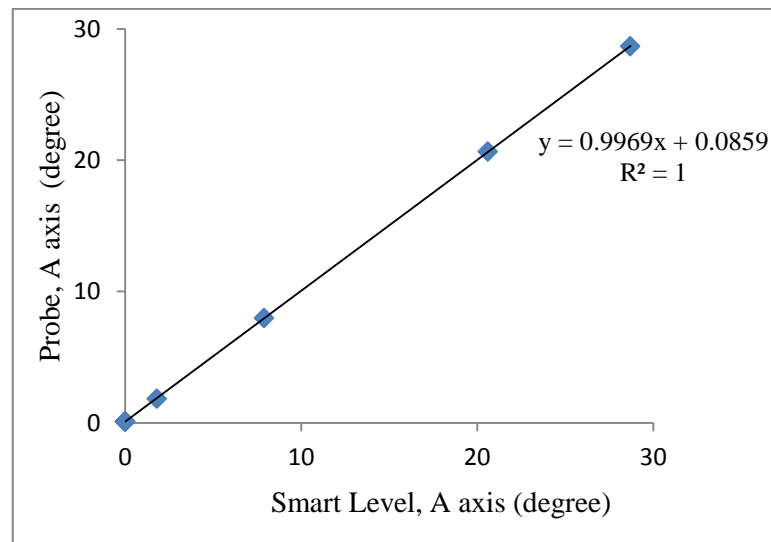
**Table 4.5 Inclinometer calibration results and accuracy.**

Tester: Priscilla Page; David DU		Probe No. 1678	
Location: Core Shed, Solid Energy, Huntly		Time: 13 July 2011	
Measurement number	Smart Level Reading (degree)	Probe Reading (degree)	Accuracy
1	A Tilt 0	A Tilt 0.092	A Accuracy % 99.898
	B Tilt 0	B Tilt 0.195±0.0006	B Accuracy % 99.783
2	A Tilt 0	A Tilt 0.114	A Accuracy % 99.874
	B Tilt 0	B Tilt 0.200	B Accuracy % 99.778
3	A Tilt 0	A Tilt 0.082	A Accuracy % 99.909
	B Tilt 0	B Tilt 0.192	B Accuracy % 99.787
4	A Tilt 2	A Tilt 1.832	A Accuracy % 99.964
	B Tilt 0	B Tilt 0.373	B Accuracy % 99.586
5	A Tilt 20.6	A Tilt 20.660	A Accuracy % 99.913
	B Tilt 0	B Tilt 1.482	B Accuracy % 98.353
6	A Tilt 28.7	A Tilt 28.672	A Accuracy % 100.046
	B Tilt 0	B Tilt 1.762	B Accuracy % 98.042
7	A Tilt 7.8	A Tilt 7.969	A Accuracy % 99.916
	B Tilt 0	B Tilt 0.244	B Accuracy % 99.729

**Table 4.6 Smart Level reading VS probe result (degree).**

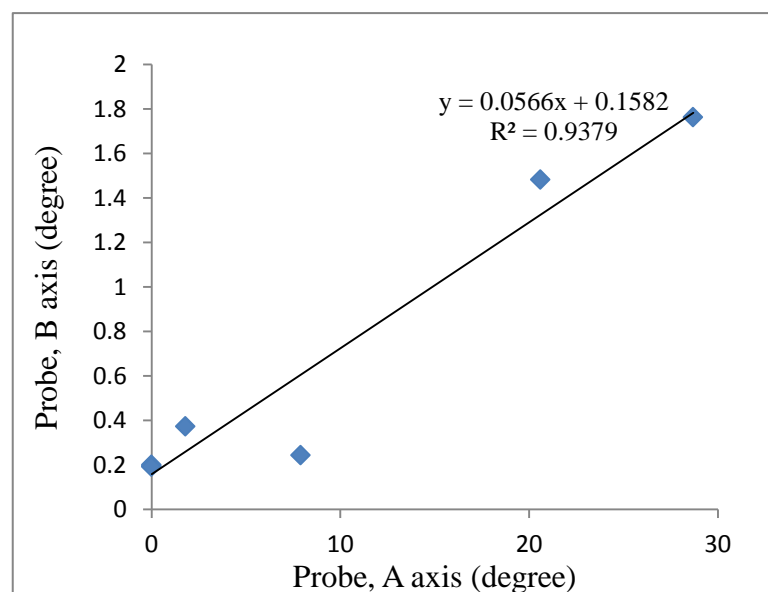
A axis, Smart Level Reading (degree);	A axis, Probe Result (degree)	B axis, Smart Level Result (degree)	B axis, Probe Result (degree)
0	0.0918	0	0.195
0	0.1135	0	0.2002
0	0.082	0	0.1916
1.8	1.8319	0	0.3728
20.6	20.6603	0	1.4824
28.7	28.672	0	1.7622
7.9	7.9691	0	0.2435

Figure 4.20 shows a very good correlation between the smart level A axis readings and probe A axis measurements by giving a  $R^2=1$  and a slope of 0.996.



**Figure 4.20 Correlations between the smart level and the inclinometer for tilt values in the A axis.**

Figure 4.21 is used to identify the cross axis correlation between the probe A axis and the probe B axis. Though there is a high correlation value ( $R^2 = 0.937$ ), the slope of 0.056 is very small. Therefore the influence between the probe A axis and the probe B axis exists, but is minor.



**Figure 4.21 Correlations between the two types of tilt values, the A axis vs. the B Axis of the probe showing a high R2 value and small slope.**

From Table 4.5, and Figures 4.20 and 4.21 it can be concluded that:

- The probe readings of the tilt are consistent and stable
- All accuracy of tilt readings in the A axis is higher than 99.8%, 5 of 7 datasets have accuracy larger than 99.9%.
- All accuracy in the B axis is higher than 98%, 4 of 7 datasets are larger than 99.7%
- When the tilt in the A axis is bigger, the accuracy in the B axis becomes lower. This is in accordance with the theory in literature.
- There is a very good correlation between the smart level A axis readings and probe A axis measurements by giving a  $R^2=1$  and a slope of 0.996.
- The influence between the smart A axis and probe B axis is minor because the slope of the correlation line is 0.056.
- Through the calibration it is concluded that the inclinometer is in reliable condition to use in the borehole monitoring.
- The accuracy could be higher if the calibration was carried out over a larger distance and with a more accurate independent measurement system.

## **4.3 Inclinometer Borehole (20091) Descriptions**

### **4.3.1 Borehole Coring**

The Borehole was drilled by wash coring by Drillforce NZ Ltd in February 2009, ended at the depth of 250 m. The chip samples brought by circulation was collected and logged every 5 meters on surface.

All chips samples were logged as recovered (Figure 3.7 in page 69). The borehole was opened by a  $\Phi 150$  mm blade bit, drilled to 43 m depth, and then the  $\Phi 150$  mm BSP casing was emplaced to 42.7 m deep. The geophysical borehole logs for

the Borehole 20091 were used in Section 6.5 for analysing the movement zone vs. stratigraphy.

## **4.4 Numerical Modelling and Phase2 (RocScience)**

### **4.4.1 Introduction**

Due to the availability of the software, and computer facility, time requirements, and software characteristics, Phase2, a powerful finite element modelling software package, was chosen for modelling strata movement in this study. This section introduces the modelling methods and significant requirements that are needed for Phase2 modelling. The theoretical contents in this chapter are mostly extracted from manuals and documents from RocScience in 2011.

### **4.4.2 Overview of Modelling of Subsidence**

#### **4.4.2.1 Modelling principles**

“All Models Are Wrong But Some Are Useful” (George Box, 1979).

The numerical modelling of geological and geotechnical problems have uncertainties, not only about the selection of the model and modelling code but also the option of the input parameters and ‘quite often assumptions made without proper justification’(Keilich, 2009). The development of numerical modelling methods for longwall panels and the block movement model relies on the principles of modelling. Hudson et al. in 2005 (cited in Keilich, 2009) specified the principles of the numerical modelling that ‘numerical modelling itself is not the most important aspect, but the conceptualisation of the problem, material properties and parameters should be paramount in any investigation’.

A review of models that are commonly used in the mining industries is included in Appendix A-5.

#### **4.4.2.2 SCT's modelling work using FLAC at Huntly East Coalmine**

Within the past over ten years, SCT (Strata Control Technology Operations Pty Ltd, Australia) has been providing Solid Energy with the specialist services in optimising the extraction options of the coal seam to improve the recovery of coal resources.

SCT mostly uses the FLAC computer code for modelling subsidence for design of the extraction layouts at Huntly because the complex pillar geometries and extraction layouts need to be assessed for a variety of depths outside the current experience base. The objectives of the modelling may be to:

- simulate the caving and settlement process;
- assess the influence of panel width and pillar geometries left unmined;
- assess the effect of varying geology and depth;
- assess the potential for water connection from the Tauranga Formation to the mine via the fracture network formed (Gale, 2007);
- predict and quantify the in situ strength of pillars created to support the overburden;
- quantify the fracture distribution and potential for induced permeability within the overburden which may interact with the Tauranga Formation;
- predict surface subsidence, tilts and strains (Gale, 2003).

Part of the criteria employed for assessing the feasibility of a layout is:

- The factor of safety for ground support and long term pillars must not be less than 2.5 under conditions of partial extraction.

- Surface subsidence is less than 150mm.
- Surface horizontal strain is less than 2mm/m.
- Surface tilt is less than 3mm/m (Gale, 2003).

The application within the past 10 years for prediction of the vertical subsidence and optimising the extraction layouts have given very good agreement with the measured data. However, no attempts at the prediction of the horizontal displacement have been undertaken or discussed with modelling in the FLAC code by SCT.

### **4.4.3 Option of the Modelling Code**

#### **4.4.3.1 Principle of option of software**

The principles for choosing suitable software for modelling in this research are:

- The usability and suitability of the software characteristics for subsidence modelling induced by underground extraction.
- The availability of the software and computer facility from own organization or being outsourced at a low cost.
- The time requirements should be reasonable in the research timeframe, which include time to get familiarity with the software and time for running and adjusting the modelling to achieve the attempted results.

#### **4.4.3.2 Choice of modelling software**

ABAQUS was initially chosen as the modelling code, but was found too much time-consuming because it is advanced software having large software package and thick user manual. Phase2 is available in University Laboratory and is simple to use. Also, on UWA (2010) and Minerals Council of Australia (1997), the practicability of simpler models should be scrutinized first because complex



models may have a larger opportunity for errors both judgementally and numerically. Considering the time limit of the research work as well, the Phase2 model was finally selected for the modelling work in this study.

#### **4.4.4 General project settings in Phase2**

##### **4.4.4.1 Analysis type**

Phase2 only includes Plane Strain and Axisymmetric analysis type. Plane Strain analysis supposes that the excavation(s) are of infinite length normal to the plane section of the analysis. In most cases a Plane Strain analysis is used. Tunnel or longwall mining can be modelled by a Plane Strain method (RocScience, 2011).

If the out-of-plane excavation dimension is less than approximately five times the largest cross-sectional dimension, the stress changes calculated using Plane Strain conditions may show some exaggeration since the stress flow around the "ends" of the excavation is not considered. The overestimation becomes more noticeable as the out-of-plane dimension approaches the same magnitude as the in-plane dimensions (RocScience, Plane Strain Analysis.htm, 2011).

The Axisymmetric analysis allows analysing a 3-dimensional excavation which is rotationally symmetric about an axis. The input is 2-dimensional, but because of the rotational symmetry, the analysis is dealing with a symmetrical 3-dimensional problem (RocScience, 2011).

The 22 monthly extraction cells of the underground coal seams at North 5 area of Huntly East Coalmine had an average length/width ratio of 1.5, 73% of stopes have a ratio less than 2, 27% stopes have a ratio from 2 to 3 (Figure 4.22). Therefore, neither method of Plane Strain and Axisymmetric analysis type could be directly used for my model.

The Analysis Method Option for Modelling by Phase2

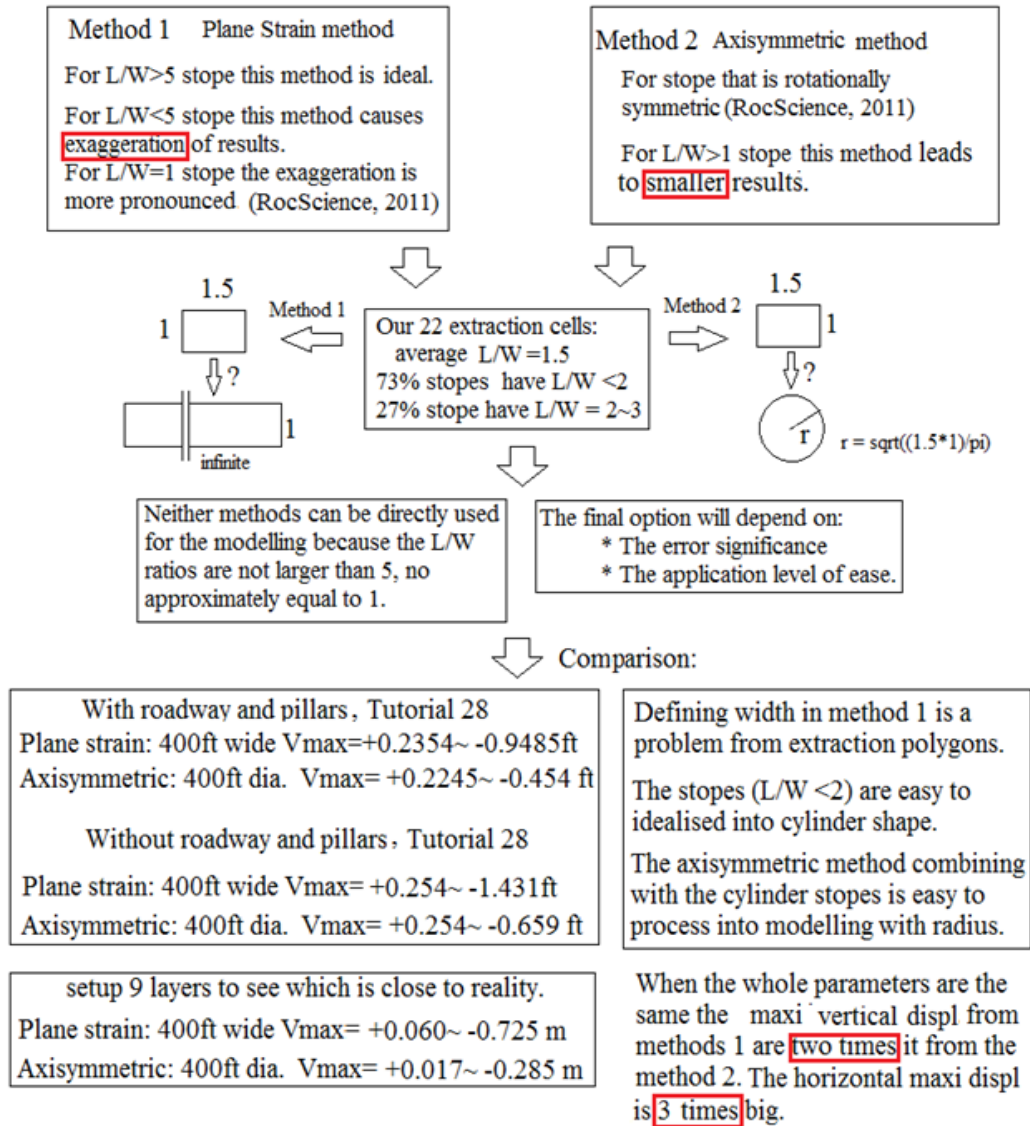


Figure 4.22 The analysis method option in Phase2 modelling for Huntly strata movement.

Through consideration of the two methods (Figure 4.22), the Axisymmetric Type was chosen to analyse the excavation 3-dimensional model in this research because the monthly extraction stope  $L/W$  ratio is at an average of 1.5 and the results from the trial calculation by axisymmetric model were more representative of the real scenario.

#### 4.4.4.2 Solver type

Phase2 has three methods of calculation: Gaussian Elimination, Conjugate Gradient Iteration, and Pre-Conditioned Conjugate Gradient Iteration. Conjugate Gradient solution technique was used for solving large problems, since disk swapping is enabled with the Conjugate Gradient methods. When all materials are elastic, the solution will be quicker with the Conjugate Gradient techniques (RocScience, 2011).

#### 4.4.4.3 Axisymmetric models

In axisymmetric models, only an external boundary is required, the shape of the external boundary implicitly defines the excavation. In Figure 4.23 the left edge of each mesh is coincident with the  $X = 0$  axis, the model on the left represents a *sphere* and the model on the right represents a *cylinder*, in three dimensions. In this modelling the stope from extracted coal seams will be idealised into the *cylinder shape* to meet the axisymmetric model requirement in Phase2.

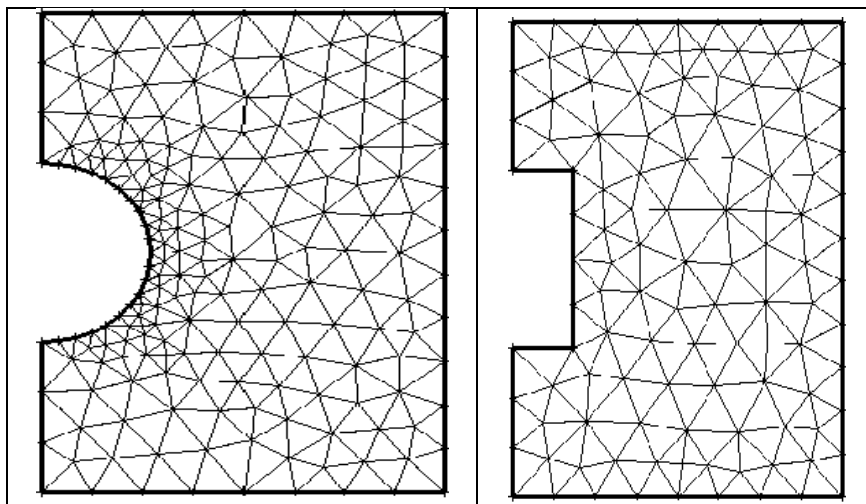


Figure 4.23 Axisymmetric Analysis models, left representing sphere, right for cylinder (from RocScience, 2011).

#### **4.4.4.4 Restrictions on axisymmetric modelling**

There are several restrictions on the use of Axisymmetric modelling in Phase2 on RocScience (2011):

- The field stress must be axisymmetric.
- Cannot be used with bolts, however, liners are permitted.
- Cannot be used with joints (discontinuity).
- All materials must have isotropic elastic properties, i.e. of the parameters of Young's modulus, and Poisson ratio.
- The true orientation of the excavation can be horizontal, vertical or at any inclination. However, the Phase2 Axisymmetric analysis requires the operator to map coordinates so that the model is symmetric about the  $X = 0$  axis (i.e. a vertical axis located at  $X = 0$ ), since all finite elements are rotated about this axis.
- To form a closed excavation, one edge of the mesh must be coincident with the  $X = 0$  (vertical) axis. If this is not the case, the excavation will be "open-ended".

The modelled geological body has a size of approximately 1000 m times 1000 m times 500 m. The geological materials in each layer were assumed to be isotropic elastic. The shear movement in two shear zones at depths of 135 m and 166 m could not be modelled by Phase2. Detailed analysis will be discussed in Chapter 7.

#### **4.4.4.5 Convergence type**

Phase2 provides for two convergence types: Absolute Energy or Square Root Energy as the convergence criterion used for the finite element stress analysis, which are defined by the following equations in vector notation (RocScience, 2011).

### Square Root Energy Criterion

---

Energy convergence is satisfied when:

$$\frac{\sqrt{\sum_{j=1}^N \left( (P_{(n),j} - f_{(i),j}) \Delta u_{(i),j} \right)^2}}{\sqrt{\sum_{j=1}^N \left( (P_{(n),j} - f_{(0),j}) \Delta u_{(0),j} \right)^2}} < (\text{specified energy tolerance})$$

where  $P_{(n),j}$ ,  $f_{(i),j}$ ,  $f_{(0),j}$ ,  $\Delta u_{(i),j}$  and  $\Delta u_{(0),j}$  are the components (N in total) of  $\mathbf{P}_{(n)}$ ,  $\mathbf{F}_{(i)}$ ,  $\mathbf{F}_{(0)}$ ,  $\Delta \mathbf{U}_{(i)}$  and  $\Delta \mathbf{U}_{(0)}$ , respectively.

### Absolute Energy Criterion

---

Energy convergence is satisfied when:

$$\left\| \frac{\Delta \mathbf{U}_{(i)}^T (\mathbf{P}_{(n)} - \mathbf{F}_{(i)})}{\Delta \mathbf{U}_{(0)}^T (\mathbf{P}_{(n)} - \mathbf{F}_{(0)})} \right\| < (\text{specified energy tolerance})$$

These criteria mean that, for a given load step, iterations can cease when the energy difference of a current state becomes a minor fraction of the initial energy imbalance. If this condition is not satisfied during a specified maximum amount of iterations, the solution process is deemed not to have converged (RocScience, 2011). No further comparison is available from the literature. In my modelling I ran both options.

#### 4.4.4.6 Tensile failure reduces shear strength to residual

Phase2 uses two probable failure styles of a solid element: tensile or shear. Either or both of these types may occur in a given element.

If ‘the Tensile failure reduces shear strength to residual’ is selected in Project Settings, then if tensile failure occurs at a point in a material (and shear failure has not already occurred), the shear strength of the material at that point will be automatically reduced to the residual shear strength parameters for that material. This is a realistic assumption to make, particularly for *brittle materials*. This option is only valid for materials where the material type = *Plastic*, and the

residual strength parameters are less than the peak strength parameters. So this option has NO effect for materials with the following parameters: material type = Elastic, or material type = Plastic, but the residual strength parameters are equal to the peak strength parameters (i.e. perfectly plastic material properties) (RocScience, 2011).

If ‘the Tensile failure reduces shear strength to residual’ is NOT selected, the shear strength parameters will NOT be reduced when tensile failure happens in a material, i.e. the tensile and shear failure modes will be self-governing. In this modelling I tried to run both options.

#### **4.4.4.7 Tensile failure reduces ‘Hoek-Brown Tensile Strength’ to zero**

In using the Hoek-Brown or Generalized Hoek-Brown failure criterion, tensile failure of a solid element will automatically decrease the tensile strength to zero (RocScience, 2011). In this modelling I ran both options.

#### **4.4.4.8 Groundwater method**

Options of Groundwater parameters in the Project Settings are used to specify how pore water pressures will be modelled if pore pressure is included in the stress analysis in terms of effective stress analysis (RocScience, 2011).

My modelling used piezometric lines as groundwater method as the piezometric data were available.

#### **4.4.4.9 Use effective stress analysis**

With the option of ‘Use Effective Stress Analysis’, material deformation is a result of changes in effective stress. This is a partly-coupled analysis where ‘changes in pore pressure, and thus effective stress, affect deformation but

changes in deformation or loading do not affect pore pressure' (RocScience, 2011).

Without this option deformation is only a result of changes in total stress by uncoupled analysis where changes in pore pressure do not affect deformation and changes in loading or deformation do not affect pore pressure (RocScience, 2011).

I used the option of 'Use Effective Stress Analysis' because the groundwater method is chosen with piezometric lines.

#### **4.4.4.10 Probabilistic analysis**

Probabilistic analysis can be carried out in Phase2 (8.0) using the Rosenblueth point estimate method where two "point estimates" are made for each random variable at fixed values of one standard deviation on either side of the mean (mean + standard deviation, mean - standard deviation). The finite element analysis is carried out for each possible combination of point estimates (RocScience, 2011).

The random variables for material properties, joint properties, and field stress can be defined using the options in the Statistics menu. My modelling did not use the Probabilistic Analysis because the materials were assumed even in a layer.

#### **4.4.5 Boundaries**

To create the boundaries is the first step in creating a Phase2 model after setting the Project Settings. The major different boundary types defined in Phase2 that may be used in this modelling are:

##### **4.4.5.1 Excavation boundary**

Excavation boundaries use the closed polylines representing excavations. In a case of staged excavations, an Excavation boundary usually represents its final stage or

maximum extent of an excavation. Intermediate boundaries within the excavation are denoted by Stage or Material boundaries (RocScience, 2011).

#### **4.4.5.2 External boundary**

External boundary also uses the closed polyline, outlining the extent of the finite element mesh, and containing all other boundaries. An External boundary is required for every Phase2 model and only one External boundary can be defined for a model. As stated in Section 7.2.3 in axisymmetric models, only an External boundary is required, the shape of the External boundary implicitly defines the excavation of a CYLINDER; therefore, no excavation boundary is needed in this modelling (RocScience, 2011).

#### **4.4.5.3 Material boundary**

Material boundaries are represented by open or closed polylines, used to define boundaries between different material types. Material boundaries are used to define the rock and soil mass layers in this modelling to illustrate nine strata.

#### **4.4.5.4 Piezometric line**

A polyline representing a water table or Piezometric surface is used to calculate pore pressures for an effective stress analysis. Piezometric Lines is only available when the Groundwater Method = Piezometric Lines. In this modelling four piezometric lines were input to represent groundwater conditions (RocScience, 2011).

#### **4.4.6 Loading overview**

The various types of loads defined in a Phase2 model, include: Field Stress; Load Split; Seismic Load; Distributed Loads and Line Loads.



#### **4.4.6.1 Field stress**

Field Stress is an in-situ stress condition prior to excavation; which includes Constant field stress and Gravity field stress options.

The Constant field stress option is used to define an in-situ stress field (prior to excavation) which does not vary with position or depth, which is not applicable to this modelling.

The Gravity field stress is used to define an in-situ stress field which varies linearly with depth. The depth can be measured from either: a user-specified Ground Surface Elevation or the actual ground surface of a model (RocScience, 2011). My modelling used the 'Gravity Field Stress' option.

#### **4.4.6.2 Use 'Actual Ground Surface'**

The initial vertical stress at a given point in strata is calculated using the depth below the Actual Ground Surface of the model, and the unit weight of the overlying material(s) as entered in the Define Material Properties dialog.

Using this option, Phase2 automatically determines the ground surface elevation above every finite element and defines its vertical stress based on the weight of material overlying it.

The Use Actual Ground Surface option provides the best initial estimate of the vertical in-situ stress (RocScience, 2011). In my modelling I used the 'Use Actual Ground Surface' option.

#### **4.4.6.3 Use 'Effective Stress Ratio'**

The effective stress ratio option allows specifying whether the Horizontal/Vertical stress ratios are applied to the Total vertical stress or the Effective vertical stress, when calculating the horizontal stress. By default the horizontal/vertical stress

ratio  $K$  is a constant value, i.e. horizontal stress is directly proportional to the vertical stress.

If the Use Effective Stress Ratio checkbox is NOT selected, then the horizontal stress is calculated from the total vertical stress, as follows:

$$\sigma_H = K \sigma_V \quad (\text{RocScience, 2011})$$

Where:  $\sigma_H$  = total horizontal stress

$\sigma_V$  = total vertical stress

$K$  = horizontal/vertical stress ratio (total stress)

If the Use Effective Stress Ratio checkbox IS selected, then the horizontal stress is calculated from the effective vertical stress, as follows:

$$\sigma'_H = K' \sigma'_V$$

$$\sigma_H = \sigma'_H + u = K' \sigma'_V + u = K'(\sigma_V - u) + u \quad (\text{RocScience, 2011})$$

Where:  $\sigma_H$  = total horizontal stress

$\sigma'_H$  = effective horizontal stress

$\sigma'_V$  = effective vertical stress

$\sigma_V$  = total vertical stress

$u$  = pore pressure

$K'$  = horizontal/vertical stress ratio (effective stress)

My modelling used the Effective Stress Ratio in Tauranga Group (TG) because the soils in TG are saturated.

#### 4.4.6.4 Stress ratio

In geotechnical modelling, determination of in-situ stresses is of ultimate importance. For soils, vertical stresses can be readily defined, but horizontal stresses are much more difficult to establish.

The ratio of horizontal to vertical effective stresses in soil is defined as the coefficient of earth pressure at rest,  $K_0$ . Typical  $K_0$  values are listed in Table 4.7 (Phase2 Theory, RocScience, 2011). The ratio of horizontal to vertical effective stresses in rocks is not discussed in the above literature.

**Table 4.7 Typical values of coefficient of earth pressure at rest (from RocScience, 2011).**

No.	Soil Type	$K_0$
1	Dense sand	0.35
2	Loose sand	0.6
3	Normally consolidated clays	0.5 – 0.6
4	Lightly overconsolidated clays	1.0
5	Heavily overconsolidated clays	3.0

The average coefficient of earth pressure at rest is  $K_0 = 0.55$  for the TG consists of saturated clayey soils.

However, in section 3.4.4.8, the calculation by equation (Larratt et al., 2010) gave the ratio of horizontal to vertical effective stresses in Tauranga Group soils as 4.6, and in rocks as 1.4.

By trial running of modelling the later results were more practicable. Therefore, my thesis used 4.9 for soils and 2.5 for rocks in the lateral movement modelling in Chapter 7.

## **4.4.7 Initial Element Loading**

### **4.4.7.1 Initial stress and body force**

In Finite Element model an element can have two initial internal loadings, initial stress and body force. Body force is just self-weight. An initial stress is like compressing the sponge; if confinement on one edge of the sponge is released it expands in that direction. This is basically what happens when opening up an excavation in a material with an initial stress. Body force and initial stress work to balance each other out to equilibrium. Four options are available as: field stress only; field stress & body force; body force only; and none (RocScience, 2011).

Field Stress loading is derived from the values entered in the Field Stress dialog. Body Force loading represents the self-weight of the elements, and is derived from the Unit Weight of the material entered in the Define Material Properties dialog (RocScience, 2011).

If using a constant field stress, then the default Initial Element Loading for each material will be Field Stress Only. If using a Gravity field stress, then the default Initial Element Loading for each material will be Field Stress and Body Force (RocScience, 2011). My modelling worked under Field Stress and Body Force.

### **4.4.7.2 Unit weight**

Unit Weight is only enabled if Initial Element Loading is either Field Stress & Body Force or Body Force Only. If applicable, the Unit Weight is used to determine the Body Force applied to each finite element. Unit Weight is disabled if Initial Element Loading = either Field Stress or None (RocScience, 2011). Therefore my modelling used the Unit Weight for defining the Body Force.

#### **4.4.7.3 Unit weight vs. unit weight of overburden (Gravity Field Stress)**

The distinction between the Unit Weight of a material entered in the Define Material Properties dialog, and the Unit Weight of Overburden entered in the Field Stress dialog is:

- ‘The Unit Weight of a material in the Define Material Properties dialog is used to determine the Body Force applied to each finite element of a given material type.
- The Unit Weight of Overburden in the Field Stress dialog is used to determine the Gravity Field Stress for all finite elements in the model.
- For a multiple material model, these two unit weights will not necessarily be the same.
- For a single material model, the Unit Weight should be the same as the Unit Weight of Overburden’ (RocScience, 2011).

Both Unit Weight and Unit Weight of Overburden were used in my modelling.

#### **4.4.8 Elastic Properties**

Four elastic models are available for defining material elastic properties: Isotropic; Transversely Isotropic; Orthotropic and Duncan-Chang Hyperbolic. Only Isotropic and Duncan-Chang Hyperbolic are applicable for Axisymmetric Analysis.

My modelling chose axisymmetric type (Section 4.4.4.1). All materials, therefore, must have Isotropic elastic properties. The elastic properties of an Isotropic material are delineated by a single value of Young’s Modulus and a single value of Poisson’s Ratio.

## 4.4.9 Strength Parameters

In the Define Material Properties dialog, the Strength Parameters option allows the user to define:

- the failure (strength) criterion for a material
- the material type (elastic or plastic)

### 4.4.9.1 Material type

Material Type may be selected as either Elastic or Plastic.

- Elastic Material

With Material Type = Elastic, the failure criterion parameters entered will only be used for calculation and plotting of the strength factor within the material. Although an Elastic material cannot "fail", the failure envelope allows a degree of overstress to be calculated (RocScience, 2011).

- Plastic Material

With Material Type = Plastic, the strength parameters entered will be used in the analysis if yielding occurs. This is unlike Elastic materials, where the strength parameters are only used to obtain values of the strength factor, but do not affect the analysis results (i.e. stresses and displacements are not affected).

When defining a material as Plastic the residual strength parameters and a dilation parameter also need to be defined, depending on the strength criterion.

- If the residual strength parameters are equal to the peak parameters, it is an "ideally" elastic-plastic material.

- The dilation is a measure of the increase in volume of the material when sheared (RocScience, 2011).

My modelling tried both Elastic and Plastic material types.

#### **4.4.9.2 Failure (strength) criterion**

The strength criteria in Phase2 for defining the strength of rock mass or soil include: Mohr-Coulomb, Hoek-Brown, Drucker-Prager, Generalized Hoek-Brown, and Cam-Clay, Modified Cam-Clay, and Discrete Function (RocScience, 2011).

Cam-Clay, Modified Cam-Clay, and Discrete Function are not discussed in this chapter. For the Mohr-Coulomb, Hoek-Brown or Generalized Hoek-Brown criteria, RocData or RocLab were directly linked with Phase2 to help determine values of input parameters.

- Mohr-Coulomb

Mohr-Coulomb law is widely used in soil engineering where it appears to give a good estimate of actual strength variation, particularly over relatively small stress ranges (Brady and Brown, 2004, p107). In my modelling the Mohr-Coulomb criterion were used in the eight strata except the Greywacke basement.

Mohr-Coulomb criterion needs the following parameters in the analysis: cohesion; friction angle and tensile strength. If considering pore pressure, then cohesion and friction angle are effective stress parameters. If the Material Type is Plastic, the following values also need to be defined: Dilation Angle and Residual values of cohesion, friction angle and tensile strength (RocScience, 2011).

- Hoek-Brown and Generalized Hoek-Brown

The original Hoek-Brown criterion has been found to work well for most rocks of good to reasonable quality in which the rock mass strength is controlled by tightly interlocking angular rock pieces. For lesser quality rock masses like in Huntly East Mine, the Generalized Hoek-Brown criterion can be used (RocScience, 2011).

Generalized Hoek-Brown criterion requires the following parameters:

- The intact uniaxial compressive strength (UCS) of the rock.
- parameters  $m_b$ ,  $s$  and  $a$

If the Material Type = Plastic, also need to define:

- Dilation parameter
- Residual values of  $m_b$ ,  $s$  and  $a$

The Generalized Hoek-Brown strength criterion is described by the following equation:

$$\sigma_1' = \sigma_3' + \sigma_{ci} \left( m_b \frac{\sigma_3'}{\sigma_{ci}} + s \right)^a \quad (\text{RocScience, 2011})$$

where:

- $m_b$  is a reduced value (for the rock mass) of the material constant  $m_i$  (for the intact rock)
- $s$  and  $a$  are constants which depend upon the characteristics of the rock mass
- $\sigma_{ci}$  is the uniaxial compressive strength (UCS) of the intact rock pieces
- $\sigma_1'$  and  $\sigma_3'$  are the axial and confining effective principal stresses respectively



When it is practically impossible to carry out triaxial or shear tests on rock masses to obtain direct values of the parameters, some practical approaches of estimating the material constants  $m_b$ ,  $a$  and  $s$  are required. According to Hoek, Carranza-Torres & Corkum (2002) (cited by RocScience, 2011), the parameters of the Generalized Hoek-Brown criterion can be determined from the following equations:

$$m_b = m_i \exp\left(\frac{GSI - 100}{28 - 14D}\right)$$

$$s = \exp\left(\frac{GSI - 100}{9 - 3D}\right)$$

$$a = \frac{1}{2} + \frac{1}{6}\left(e^{-GSI/15} - e^{-20/3}\right)$$

where:

- GSI is the Geological Strength Index
- $m_i$  is a material constant for the intact rock
- Parameter D is a "disturbance factor" which depends upon the degree of disturbance to which the rock mass has been subjected by blast damage and stress relaxation. It varies from 0 for undisturbed in situ rock masses to 1 for very disturbed rock masses.

The Generalized Hoek-Brown strength criterion is one of the main strength criteria used in my modelling.

- Drucker-Prager

The Drucker–Prager yield criterion is a pressure-dependent method for defining whether a material has failed or undergone plastic yielding. The criterion was developed to model the plastic deformation of soils (Wikipedia, 2011).

The simplification of Mohr-Coulomb model where the hexagonal shape of the failure cone was substituted by a simple cone is known as the Drucker-Prager model (Drucker & Prager, 1952, cited by RocScience, 2011). Generally, the Drucker-Prager model has the same advantages and limitations with the Mohr-Coulomb model but the latter model was preferred over the Mohr-Coulomb model (Ti et al., 2009). Therefore, the Drucker-Prager model was one of the major methods in my modelling.

The Drucker-Prager strength parameters are: tensile strength; q parameter and k parameter.

#### **4.4.9.3 Dilation Parameter**

A dilation parameter can be defined for Mohr-Coulomb, Hoek-Brown and Drucker-Prager materials, if the Material Type = Plastic. Dilatancy is a measure of how much volume increase occurs when the material is sheared.

- For a Mohr-Coulomb material, dilatancy is an angle that generally varies between zero (non-associative flow rule) and the friction angle (associative flow rule).
- For (Generalised) Hoek-Brown materials, dilatancy is defined using a dimensionless parameter that generally varies between zero and  $m_b$ .

Low dilation angles/parameters (i.e. zero) are generally associated with soft rocks while high dilation angles/parameters (i.e.  $\phi$  or  $m_b$ ) are associated with hard brittle rock masses. A good starting estimate is to use  $0.333*m_b$  or  $0.333*\phi$  for soft rocks and  $0.666*m_b$  or  $0.666*\phi$  for hard rocks (RocScience, 2011).

#### **4.4.10 Apply shear strength reduction (SSR)**

In the Define Material Properties dialog, the Apply SSR option allows the user to turn the SSR analysis on or off for individual materials. NOTE: this option is only available if carrying out a Shear Strength Reduction (SSR) analysis (i.e. the Determine Strength Reduction Factor checkbox is selected in the Project Settings dialog), and is only enabled if the Material Type = Plastic.

The Apply SSR option for materials has the following purpose:

- By default, if carrying out an SSR analysis with Phase2, the Apply SSR checkbox is turned on for all materials, so that the SSR analysis will be applied to all plastic materials.
- If turning the Apply SSR checkbox OFF for a material, the material will retain its original plastic strength parameters without being subjected to the SSR strength reduction. In other words, an SSR model is allowed to simultaneously have plastic materials which are NOT subjected to strength reduction, and plastic materials which are subjected to strength reduction.

Shear Strength Reduction is an advanced user option, and in most cases this checkbox should be left on for all materials (RocScience, 2011).

#### **4.4.11 Define hydraulic properties**

The Define Hydraulic Properties option is used to specify the groundwater and or hydraulic parameters for each material. This option is only used when considering pore pressure in Phase2 analysis (RocScience, 2011).

In my modelling the Groundwater Method = Piezometric Lines was chosen, then Piezometric Lines were assigned to each material.

#### 4.4.12 Mesh Generation

The graded mesh type produces a good graded mesh for most models, using a quadtree nodal insertion technique. In this case a Graded mesh type is used.

The Number of Excavation Nodes directly determines the discretisation of the Excavation boundaries. The Number of Excavation Nodes in conjunction with the Gradation Factor determines the discretisation of all other boundaries in the model. The Gradation Factor, in conjunction with the Number of Excavation Nodes, determines the discretisation of all other boundaries in the model.

The Gradation Factor is the ratio of 'the average length of discretisation on Excavation boundaries, to the length of discretisation on the External boundary, at the maximum distance from the Excavation boundaries' (RocScience, 2011).

If Gradation Factor is the default 0.1, which implies that, the average length of the External boundary discretisation will be (approximately) 10 times the average length of the Excavation discretisation (Figure 4.24) (RocScience, 2011).

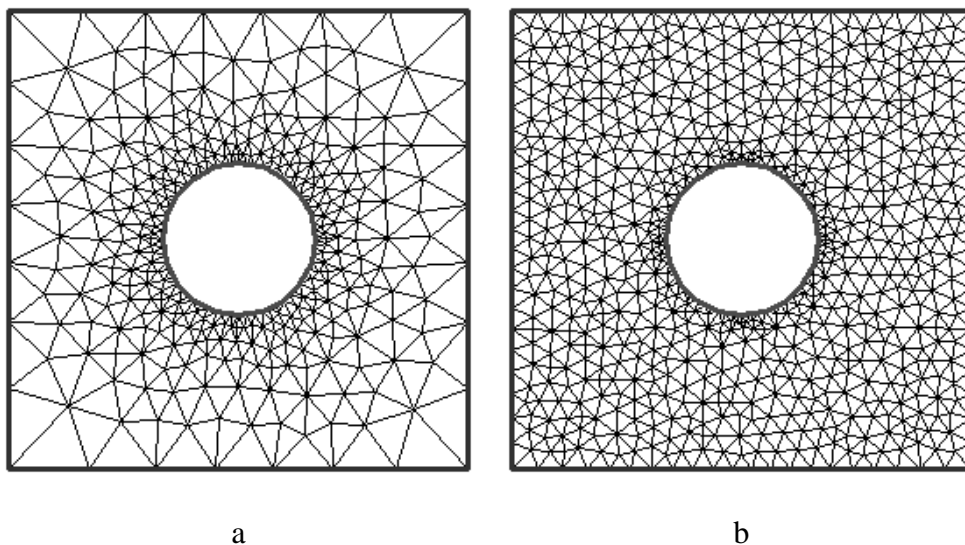


**Figure 4.24 Effect of Gradation Factor on the mesh – a. gradation factor = 0.1 and b. gradation factor = 0.3. (The Expansion Factor of the External Boundary is equal to 1 in this case) (from RocScience, 2011).**

## **4.5 Summary and Conclusions**

This chapter introduced the investigation methods including borehole inclinometer monitoring, the inclinometer data error correction, and modelling methods.

### **4.5.1 Borehole Inclinometer Method**

The inclinometer borehole 20091 is 300 m away from the location of the proposed shaft in the adjacent panel in Huntly East Mine. Therefore there are significant similarity, correlation and relevance between the two boreholes.

The Borehole structure had two layers of casing: the outer casing is Ø150 mm BSP inserted to 42.7 m below the ground surface. The inner casing is the inclinometer casing made of an OD Ø 70 mm PVC high press casing installed to the bottom of the borehole at 250 m.

### **4.5.2 Inclinometer Data Error Correction**

Generally there are five types of error corrections in analysis and interpretation of the inclinometer data. They are: checksums correction; orientation correction for casing; spiral correction for casing; bias-shift error; and rotation errors. Every type of errors has its appearance in the plots, identification method, and correction measures.

### **4.5.3 Inclinometer Calibration**

The inclinometer used in the borehole monitoring was not timely sent to UK for regular calibration because it was used weekly but the total time spent on way and for calibration in UK would be around 6 weeks. To ensure the accurate readings

and consistent work state of the inclinometer system, the inclinometer calibration was undertaken in laboratory at Huntly as provisional measures on 13 July 2011. Through the calibration it is concluded that the inclinometer was in reliable condition to use in the borehole monitoring.

#### **4.5.4 Numerical Modelling and Phase2**

Through overview of modelling of subsidence, due to the availability of the software, and computer facility, time requirements, and software characteristics, Phase2 was chosen for modelling strata movement in this study. The numerical modelling of the geological and geotechnical problems has uncertainties, 'so the modelling should be subjected to 'soft' and 'hard' audits.

The main requirements to establish a Phase2 model for modelling strata subsidence in inclinometer project area in the Huntly Coalmine were summarised as below:

- The voids of periodically extracted coal seams are idealised into the *cylinder shape of stope* to meet the axisymmetric model requirement.
- All materials used isotropic elastic properties.
- Use piezometric lines as groundwater method and tick the option of 'Use Effective Stress Analysis' because the groundwater method is chosen with piezometric lines.
- Use 'gravity field stress' option, and 'Actual Ground Surface' option.
- My modelling chose 'Field Stress & Body Force' in initial element loading, therefore used the Unit Weight for defining the Body Force.
- This model doesn't use the residual Young's modulus because when the material yields the load state does not change.

- With Material Type = Elastic, the failure criterion parameters will only be used for calculation and plotting of the strength factor within the material. Although an Elastic material cannot "fail", the failure envelope allows a degree of overstress to be calculated
- With Material Type = Plastic, the strength parameters entered will be used in the analysis if yielding occurs.
- Criteria of Mohr-Coulomb, Drucker–Prager model, and Generalized Hoek-Brown strength were the main strength criteria used in my modelling.
- Low dilation angles/parameters (i.e. zero) are generally associated with soft rocks. A starting estimate is to use  $0.333 \cdot m$  or  $0.333 \cdot \phi$  for rocks in my modelling.
- The Unsaturated Shear Strength option was not chosen in this study.
- ‘Apply Shear Strength Reduction’ option should be chosen for all materials.

# **Chapter 5 Inclinometer Data Analysis and Error Corrections**

## **5.1 Introduction**

This chapter scrutinises the inclinometer borehole datasets, explains the error corrections that were undertaken. The data error correction and analysis were undertaken on the datasets measured on the A axis and the B axis separately because the measurements on the A axis and the B axis were separate with different potential sources of errors, magnitudes of offset of casing to vertical, and varying accuracy.

Data errors may include bias-shift error, rotation error, depth error or spiral error (Cornforth, 2005; Machan & Bennett, 2008; Mikkelsen, 2007 in Section 4.2.5). The error corrections of data were conducted prior to its analysis and interpretation. The data correction commenced with checksum analysis, followed by discussions on bias-shift, and consideration of rotation errors, depth errors, and finally spiral correction of the datasets for both the A axis and B axes.

## **5.2 Main Observations of Inclinometer Monitoring**

### **5.2.1 Water Level Changes in Borehole**

From the Borehole installation day (27/03/2009) to 18/01/2011 the water level observed in the casing remained at 9 m below the ground level, and then it rose up to 2.5 m below the ground surface by 03/02/2011 (Figure 5.1). On 22/02/2011 the water level was found around 20 cm above the ground level in the casing. The Borehole was watertight as it was enclosed by a PVC casing and grout sealing.



The rising water level is most likely to indicate that the probe casing and grouting somewhere in the Borehole were broken.

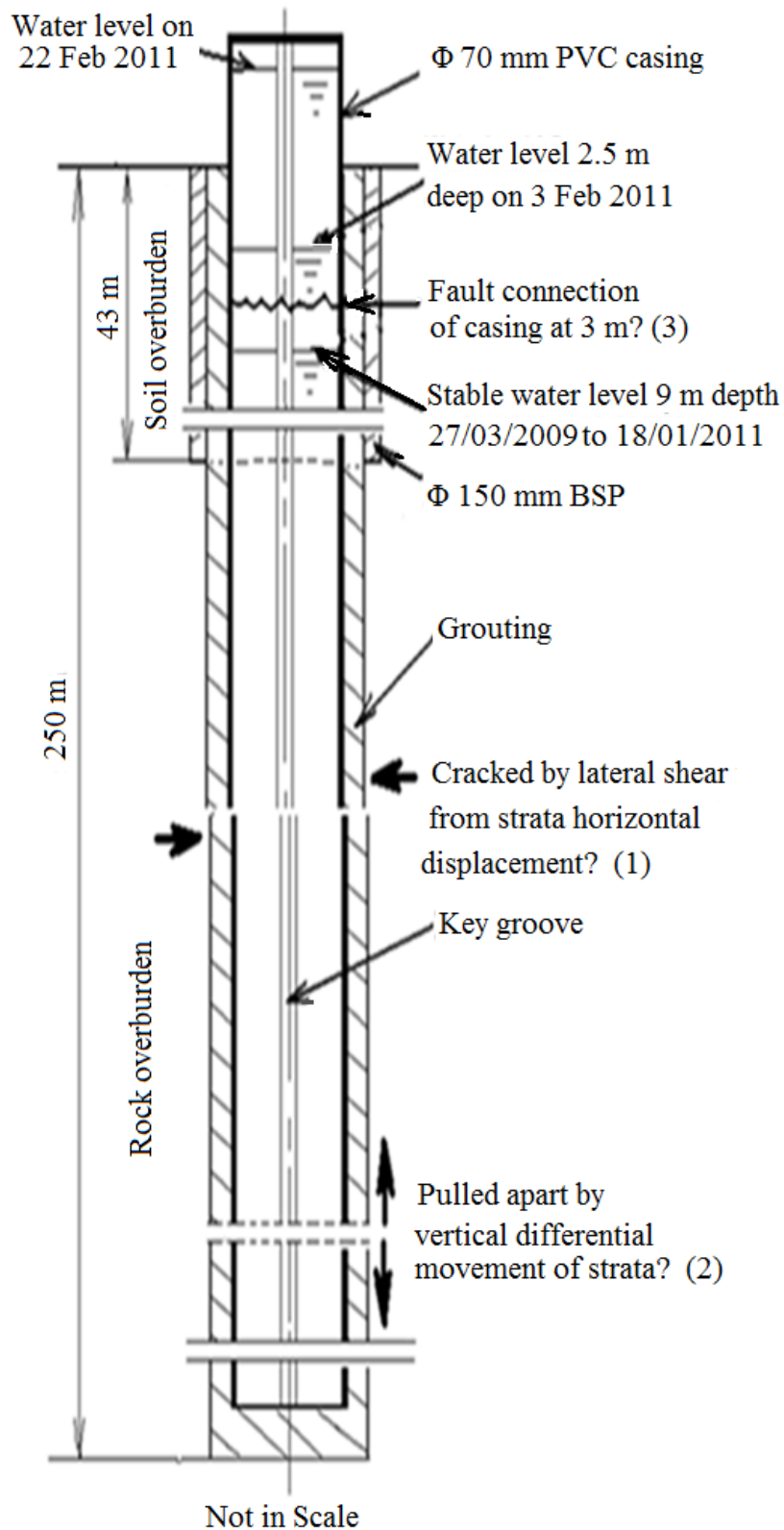


Figure 5.1 Water level changes in the Borehole, Huntly East Mine.

There are three possible causes for a casing break.

1. The casing and grout may have been ruptured by shear force induced by lateral strata movement at one or several depths. Any shear displacement must be small as the probe traversed down without obvious resistance and the monitoring was continued successfully from 27/03/2009 to 22/02/2011.

2. The casing and grout were pulled apart to form a fractured gap by tensile force due to vertical differential displacement of formations. A pulling-apart gap creates less resistance to movement of the probe because the two parts of the casing still have the same axis.

3. A break of the joint connection within 42.7 m was unlikely to occur because the Ø 150 mm outer steel casing was installed to the depth of 42.7 m from the surface to protect the internal probe casing.

Thus, the most likely cause of the rising water level in the casing was due to casing and grouting ruptures resulting from shearing or tensional force in the strata movement below 42.7 m.

### **5.2.2 Traversing of Probe Stopped**

On 11 March 2011, the dummy probe stopped at a depth of 38.53 m in the A axis. During the following one hour, lowering of the dummy probe was attempted seven times; every time the situation got worse, and the dummy probe stopped at progressively shallower depths from 38.53 m to approximately 38 m, 37 m, and 36 m. We decided not to lower the digital inclinometer probe in case the probe was lost. Thus, monitoring at the Borehole ceased.

### **5.2.3 Traversing of Probe via the B Axis Grooves**

On 02/06/2011, a trial of lowering the dummy probe along the A axis was jammed at 33.45 m deep. Then a trial along the B axis was successful without any resistance over the whole borehole depth.

Following this trial, an inclinometer reading on 14 June 2011 was not very successful. Firstly lowering the dummy probe by the B axis, it smoothly traversed to the bottom of the casing, but it was lifted out with the wheels tracing from the A axis! Who knew at what depth the wheels changed their tracks! It was guessed that somewhere in the casing there might be a big gap or serious deformation to let the wheels leave the B axis and swap into the A axis. There was no obvious resistance to the dummy probe during traversing down and up.

Then we lowered down the inclinometer along the B axis. The readings appeared to be normal. However the probe did not track along the grooves as the wheels were seen between the A and B grooves when it reached the top of the borehole.

The probe was turned 180 degrees and lowered down to the bottom for a second reading trip. When starting reading at 245.5m, a warning message on the PDA screen was noticed over the 'checksum sign' as 'face errors at 245.5m'. As the measurement was continued, the error message stayed there. The probe wheels might be not in the right grooves, so the reading checksums were beyond the alert limits, therefore the warning was given. The probe was not in the groove track again this time when pulled out of the casing

It was hard to know how the wheels changed grooves or jumped out of the grooves and where in the Borehole the wheels started altering their tracks.

Therefore, the measurements on 14 June 2011 were not used and no further measurement was attempted.

## **5.3 Inclinometer Data for the Borehole**

### **5.3.1 Raw Data**

A total of 13 inclinometer surveys were successfully conducted using the same inclinometer probe (Series Number 1678) on 13 separate days: 27/03/2009, 27/05/2010, 25/06/2010, 31/08/2010, 24/09/2010, 14/10/2010, 28/10/2010, 12/11/2010, 30/11/2010, 21/12/2010, 18/01/2011, 03/02/2011, and 22/02/2011.

The monitoring duration was approximately 2 years. I assisted with inclinometer measurement from 28/10/2010 onwards. The first survey on 27 March 2009 is the reference or initial baseline for this research. The comparison and calculations were all undertaken based on the initial borehole measurement. The system accuracy of the probe 1678 is 2 mm over 25 m, i.e. 0.04 mm per 0.5 m length gauge (SOIL, 2010).

The 13 datasets were stored in PDA (Personal Digital Assistant) as raw data in RPP format. Every per-depth reading contained seven columns: 'depth; A0, A180, A checksum; B0, B180 and B checksum'. The inclinometer measurement started from 245 m and ended at 1 m from the collar top in each survey. There is no data for the tilt at depth zero, since it was not measured (RST Instruments Ltd, 2010).

During measurement the PDA displayed the deviations in the A and B axes by  $(A0-A180)/2$ , for the A axis and  $(B0-B180)/2$  for the B axis for each per-depth reading (Figure 5.2). The 'Face Error' warning message (in red in Figure 5.2) appeared if the deviation was larger than 5 mm per gauge to remind the operator to check if the probe was lowered to the right depth or in the right groove.



**Figure 5.2 Inclinometer data displayed in PDA in the B 180 axis reading.**

The raw data in RPP format stored in the PDA was then downloaded into computer either, by using Microsoft's free tool, ActiveSync, or by means of a Compact Flash Card (SOIL Manual, 2008). The raw data were transferred from the PDA to computer in RPP format. The RPP file was read and reduced by the In-Site software into the installation files in Access Database format (MDB). The data file in spreadsheet format (Excel® format) could be obtained through the output function of the In-Site specialist software.

The dataset file was provided by Solid Energy in the Access database format (MDB), not in RPP format. Therefore all the analysis and interpretation were conducted based on the supplied MDB format data file. The data samples are displayed in the program In-Site® (Figure 5.3). The whole datasets are listed in Appendix D (attached in CD as an electronic copy).

The readings of A0, A180, B0, and B180 are the product of  $\sin(\theta) \times$  (instrument constant k) (Section 4.2.5.2 and Table 4.3). Checksum A is the sum of the A0 and A180, checksum B is the sum of B0 and B180.

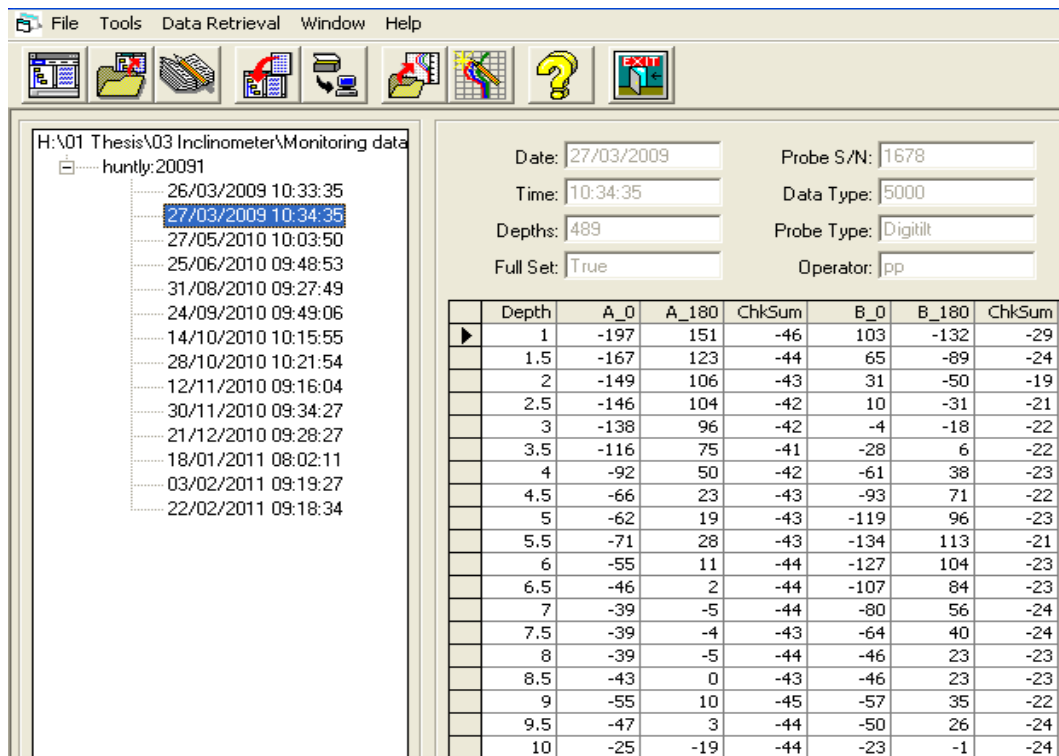


**Figure 5.3 Example In-Site programme data display for inclinometer data measured on 27 March, 2009.**

The inclinometer borehole was 250 m deep with a monitoring depth of 245 m. The interval of measurement was 0.5 m. The measurement section was from 1 m to 245 m. Therefore, there were 489 measurement intervals from 1 m to 245 m, so there are 489 groups of per-depth readings within one survey.

### **5.3.2 The Absolute Position of the Borehole Prior to Error Correction**

#### **5.3.2.1 The Absolute Position of the Borehole on 27/03/2009**

The data of the first survey on 27/03/2009 (Figure 5.4) is plotted as the initial absolute position in the A and B axes. Figure 5.4 shows that the borehole was not straight, it spiralled down. The offset to vertical was approximately 3.5 m in the A axis vertical plane at borehole bottom, and 0.39 m in the B axis vertical plane at 174 m. Figure 5.5 shows the resultant plan view of the Borehole.

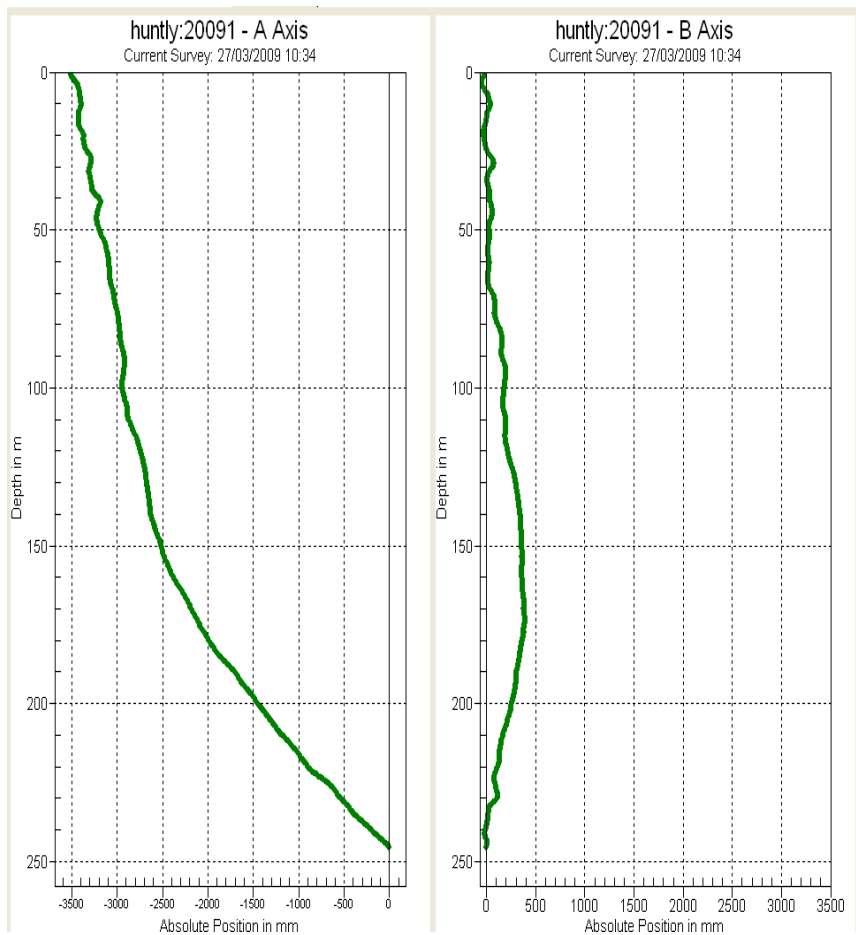


Figure 5.4 The absolute position of the Borehole on 27/03/2009 prior to error correction.

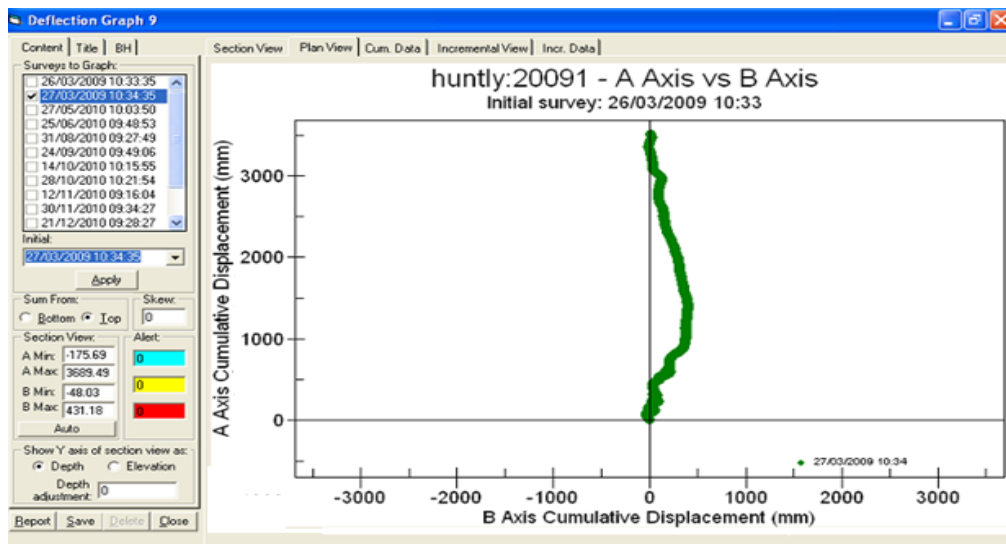
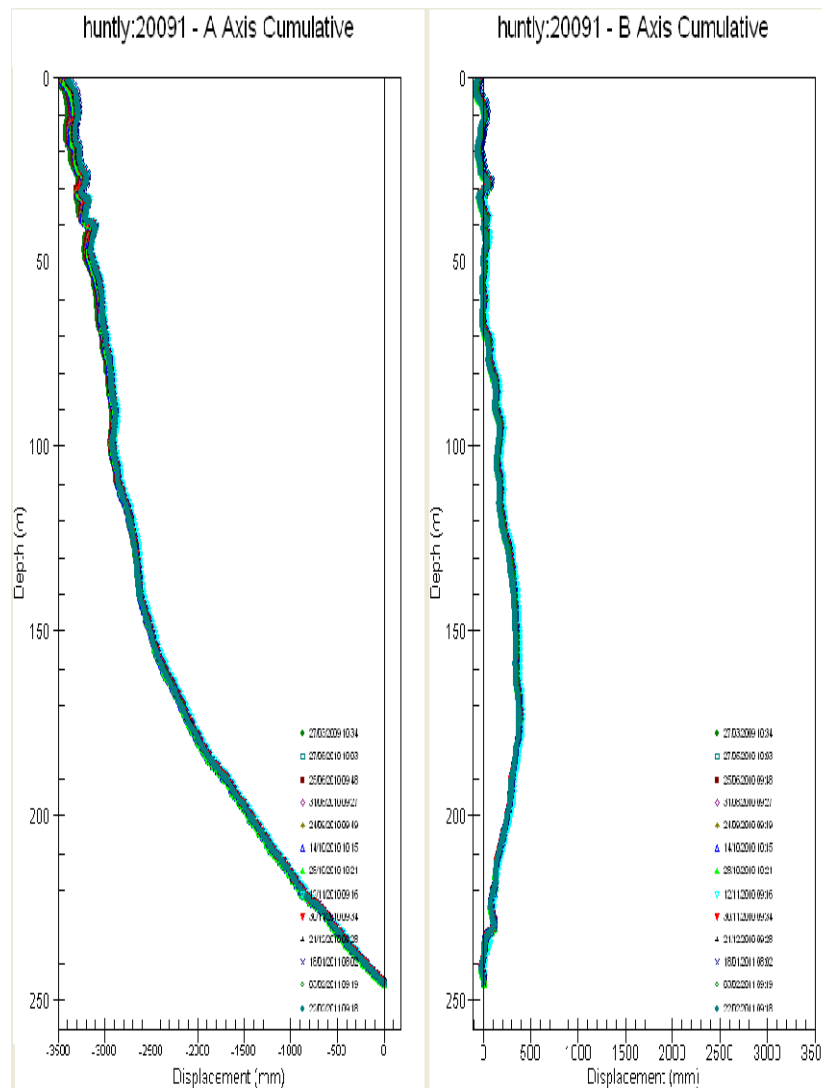


Figure 5.5 The absolute plan view of the Borehole (from top to bottom) on 27/03/2009.

Figure 5.5 shows that the borehole projection on the horizontal plane was not straight. The offset to the A axis was approximately 0.40 m at approximately 1.5 m away along the A axis.

### 5.3.2.2 The Absolute Position of the Borehole on 13 surveys

The absolute positions projected on vertical planes of the A axis and B axis for the 13 surveys (Figure 5.6) display the actual shapes in ground of the Borehole on the 13 days. The gaps between the plot lines are very small compared to the Borehole depth. All the 13 shapes surveyed are close to the initial shape on 27/03/2009.



**Figure 5.6** The absolute positions of the Borehole on 13 surveying days, the two graphs use the same vertical scale and the same horizontal scale.

### 5.3.3 The Cumulative Displacement Plots

For convenience of analysing and highlighting the movement of the ground, displacement plots are normally used in inclinometer monitoring, instead of



absolute position plots (as described in Section 2.4.5). The 13 surveys were reduced and plotted in cumulative displacement graphs (Figure 5.7) in both the A and B axes, based on the calculation by subtracting the cumulative deviation (measured on each day) from the initial cumulative deviation measured immediately after installation on 27/03/2009 (see Section 2.4.5.1).

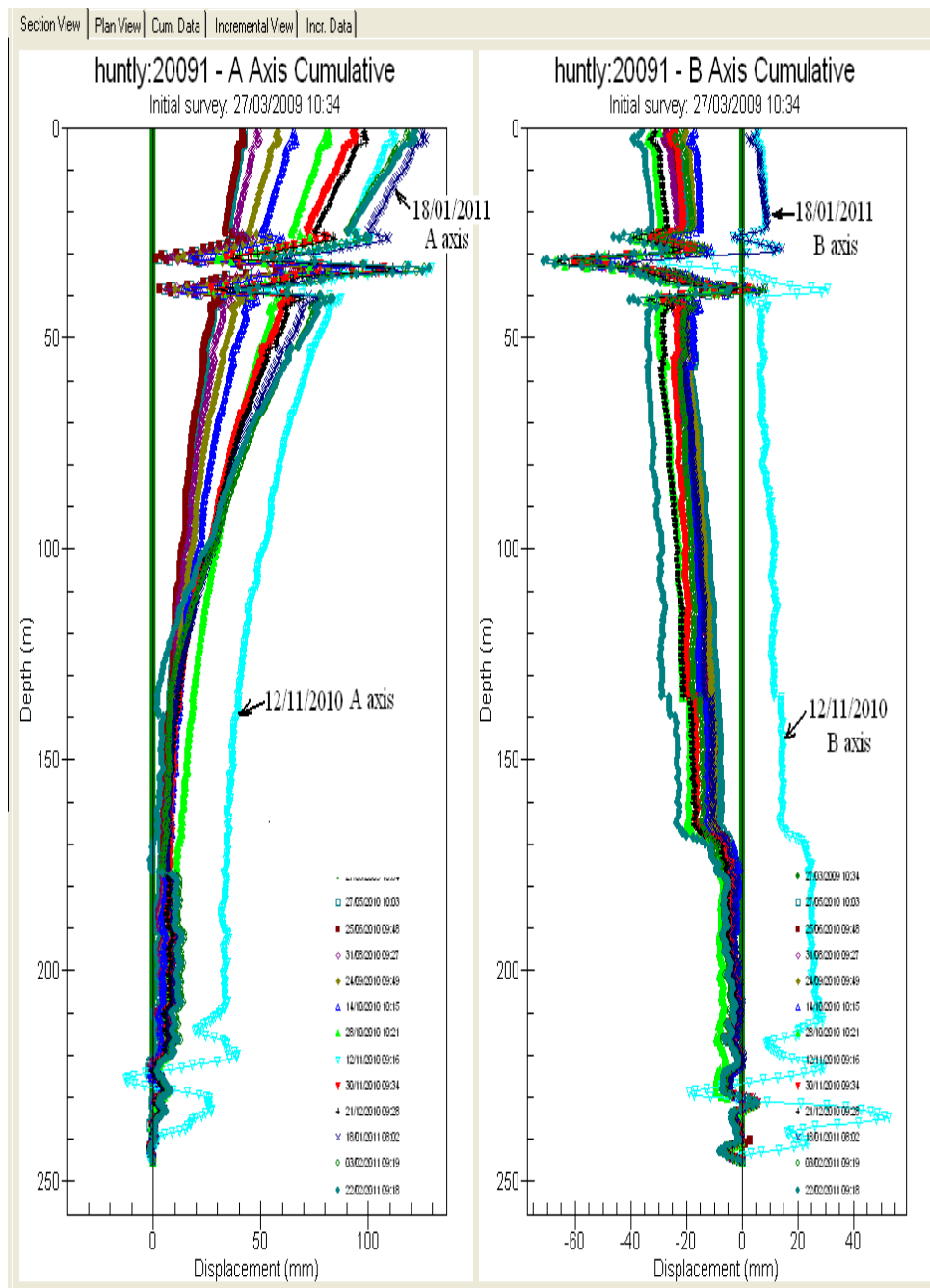


**Figure 5.7 The cumulative displacement plots of 13 surveys of the Borehole, the curved lines on 12/11/2010 and 18/01/2011 showing abnormal from the other 11 curved lines.**

## **5.4 Data Corrections**

### **5.4.1 Introduction**

There are straight leaning lines, curved lines and cross lines in Figure 5.7. That means there may be data errors in the 13 datasets, which may include bias-shift error, rotation error, depth error or spiral error, according to the literature review (Section 4.2.5.3). These potential errors should be identified and corrected. The error corrections of data were undertaken prior to its analysis and interpretation for strata movement. The correction will start with checksum analysis, followed by bias-shift, rotation errors, depth errors, and finally spiral correction of the datasets for both the A axis and B axes.

### **5.4.2 Mean Checksums**

The checksums for the 13 surveys are summarised in Table 5.1. The Coefficient of Variation (CV) was used to evaluate the checksum quality (Section 4.2.5.3).

While most CVs were less than 10% for the A axis, and less than 20 % for the B axis, and thus acceptable, there were three days on which measurements exceeded the acceptable thresholds. The CV values (shaded data in Table 5.1) were 38% for the A axis and 72% for the B axis on 12 November 2010, and 45% for the A axis and 30% for the B axis on 18 January 2011, which are much larger than 10% and 20% thresholds respectively. Also from Figure 5.7 the plots for those two surveys are obviously out of normal range. Therefore the two surveys on 12 November 2010 and 18 January 2011 were discarded from further data analysis. The 11 remaining ‘useful’ surveys are plotted in Figure 5.8.

**Table 5.1 Checksums, Standard Deviations and Coefficients of Variation (CV) before correction, the shadings showing the CV values are larger than 10% for the A axis, 20% for the B axis.**

Date	A Checksums			B Checksums			
	Mean	Standard Deviation	Coefficient of Variation	Mean	Standard Deviation	Coefficient of Variation	Instrument constant*
27/03/2009	-47.5	3.2	6.70%	-25.2	3.3	13.10%	5000
27/05/2010	-61.3	4.2	6.90%	-39.9	3.5	8.80%	5000
25/06/2010	-63	4.3	6.80%	-40.1	4.8	12%	5000
31/08/2010	-632.6	41.1	6.50%	-410.8	36.8	9.00%	50000
24/09/2010	-638.2	41.3	6.50%	-411.8	38.8	9.40%	50000
14/10/2010	-606.6	41.1	6.80%	-420	36.2	8.60%	50000
28/10/2010	-589.9	50.6	8.60%	-428.1	69.9	16.30%	50000
12/11/2010	-594.4	225.4	38.00%	-435.6	320.6	71.90%	50000
30/11/2010	-557.7	42.6	7.60%	-438.6	41.7	9.50%	50000
21/12/2010	-556.3	41.9	7.50%	-435	40.1	9.00%	50000
18/01/2011	-525.3	237.5	45.20%	-423.8	127.6	30.10%	50000
3/02/2011	-550.3	45.7	8.30%	-432.4	43.2	10.00%	50000
22/02/2011	-560.1	72.8	13.00%	-436.5	48.8	11.00%	50000

The plot on 12/11/2010 started offset off the other 11 surveys from the bottom (Figure 5.7). That meant the probe was not stabilized at start measurement at 245 m due to less waiting time for probe warm-up.

The plot on 18/01/2011 started offset off the other 11 surveys from about 22m to the surface in the cumulative displacement graph (Figure 5.7). That meant that the probe ‘kicked’ a rupture or deformed point as results of the irregularity of the casing at 22 m, leading to the instability of the probe. The possible reason for causing the two abnormal surveys was the instability of the probe.

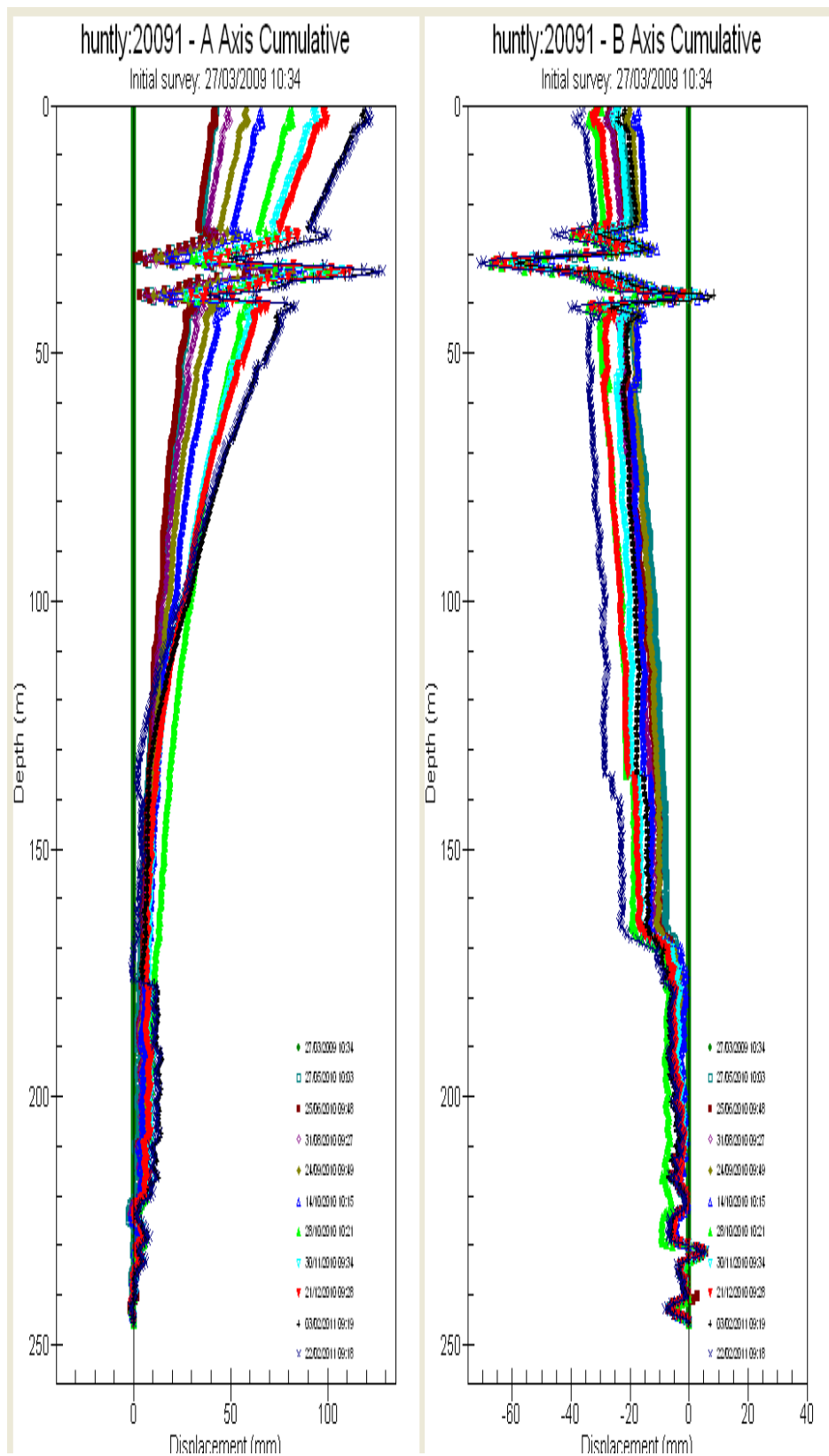


**Figure 5.8 Cumulative displacement plots for the A axis and the B axis from the 11 ‘useful’ datasets.**

Of the remaining CV values (Table 5.1), only the CV value of the A axis on 22/02/2011 at 13%, was more than 10%, and the values for the B axis were all less than 20%. The CV values may decrease following error correction.

### **5.4.3 Instrument Constant Unification**

In the first three surveys the instrument constant that was used, by the inclinometer system for measurement and reduction of data, was 5000 ( $k_1$ ) for the In-Site software version 2.01 and below (Table 5.1), afterwards the constant 50000 ( $k_2$ ) was used for version 2.70 and above for the remaining nine surveys.

For efficient analysis, easy comparison and being able to utilise other standard software resources such as GTILT®, Inclinalysis® and DigiPro® in data analysis, the 11 survey datasets were converted with the instrument constant 25000 ( $k_0$ ) that is the worldwide inclinometer metric standard, instead of  $k_1$  and  $k_2$  being used in the current datasets measured by SOIL Inclinometer. If not converted, the datasets of the Borehole will be misread in other inclinometer programmes (Section 4.2.5.3). The conversion process and equation are:

- During measurement by the probe, the raw data ‘ $\sin(\theta)$ ’ was taken by the In-Port program, then processed and stored into the PDA as ‘ $\sin(\theta)$ ’ in the A and B axes. Where  $\theta$  is the tilt angle of the casing to vertical.
- The data stored in the PDA were downloaded to computer by use of Microsoft ActiveSync to form the RPP format file of inclinometer data.
- The RPP data file was imported into In-Site program to plot the displacement graphs and incremental graphs, and create the Access database format file (file extension ‘.MDB’). The data in MDB file were in the reading unit as ‘ $\sin(\theta) \times k_1$  (or  $k_2$ )’, where  $k_1 = 5000$ , and

$k_2 = 50000$ . The Excel file was created by exporting the MDB data through the In-Site program. Then the displacement graphs and incremental graphs were produced in Excel programme as well as in the In-Site program.

- In Excel®, the displayed SOIL incremental reading ‘ $\sin(\theta) \times k_1$  (or  $k_2$ )’ was divided by the factor  $k_1$  (5000) for the first three surveys and  $k_2$  (50000) for the remaining nine surveys, the raw data ‘ $\sin(\theta)$ ’ were then recovered.
- The recovered raw data were multiplied by the standard instrument constant 25000 ( $k_0$ ) to give the new displayed readings ‘ $\sin(\theta) \times k_0$ ’ and saved as a new MDB file.
- The new MDB file with the standard instrument constant was then imported into all the popular inclinometer software, including the In-Site® programme, for analysis.

Through the conversion, only the displayed readings, their checksums and standard deviations changed with the applied standard metric instrument constant 25000. The conversion didn’t alter any of the raw data  $\theta$ ,  $\sin(\theta)$ , the reduced deviations and displacements because the deviations were computed from the equation  $d = L \times \sin(\theta)$  without the instrument constant in it (refer to Table 4.3 in section 4.2.5.2). Here  $L$  is the probe interval length  $L = 500$  mm.

The new checksums, standard deviations and coefficients of variation are summarized in Table 5.2. Comparing to Table 5.1, the checksums and standard deviations have been changed with the new instrument constant 25000. However the CV values remain constant.

**Table 5.2 Checksums, Standard Deviations and CV with unified instrument constants 25000.**

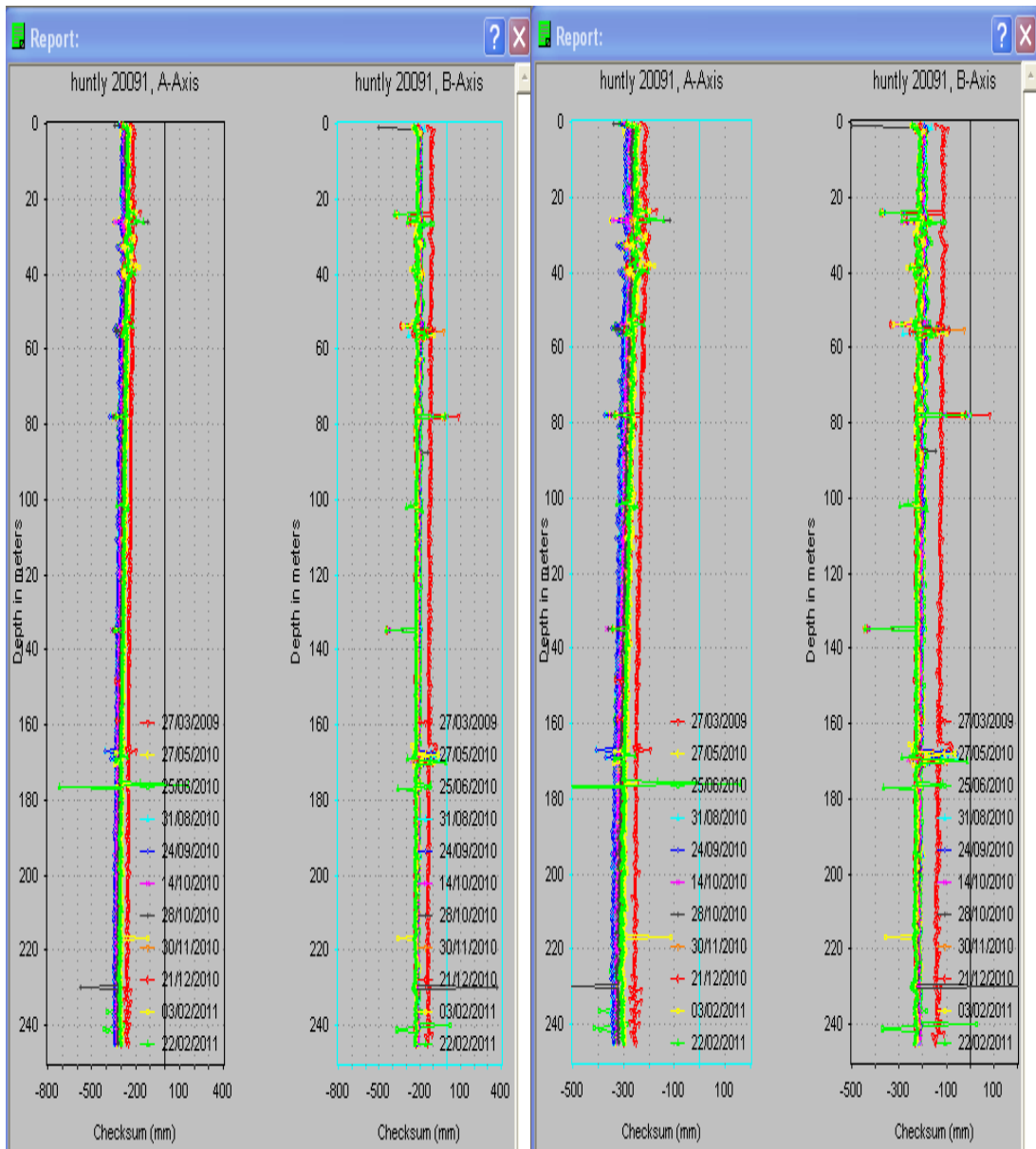
Date	A Checksums			B Checksums			
	Mean	Standard Deviation	Coefficient variation	Mean	Standard Deviation	Coefficient variation	Instrument constant
27/03/2009	-237.5	16.0	6.80%	-126.2	16.5	13.10%	25000
27/05/2010	-306.7	21.0	6.80%	-199.5	17.5	8.80%	25000
25/06/2010	-314.9	21.7	6.90%	-200.5	24.0	12.00%	25000
31/08/2010	-316.3	20.6	6.50%	-205.4	18.4	9.00%	25000
24/09/2010	-319.1	20.6	6.50%	-205.9	19.4	9.40%	25000
14/10/2010	-303.2	20.6	6.80%	-210	18.1	8.60%	25000
28/10/2010	-295.0	25.3	8.60%	-214.1	34.9	16.30%	25000
30/11/2010	-278.9	21.3	7.60%	-219.3	20.9	9.50%	25000
21/12/2010	-278.2	21.0	7.50%	-222.5	20.1	9.00%	25000
03/02/2011	-275.2	22.9	8.30%	-221.2	22.1	10.00%	25000
22/02/2011	-280.0	36.4	13.00%	-223.2	24.4	10.90%	25000

#### 5.4.4 Extreme Checksum Analysis

##### 5.4.4.1 Checksum plots

Figure 5.9 presents the assembly plots of the checksums of the 11 surveys in the A and B axes. The checksums on the reference date (March, 2009) were consistent down the length of the Borehole in both axes (red lines on Figure 5.9). The checksums for the monitoring from May 2010 to February 2011 were generally consistent, but of a somewhat greater magnitude than the initial checksums showing the accelerometer B gradually differing over time.

Figures from 5.10 to 5.20 give 11 separate plots comparing the checksums of the 11 surveys in DigiPro®. There were several spikes on the checksum plot in each survey, their impacts on the plots were significant, because the cumulative displacement data come from the sum-up of the incremental data from the bottom (see Figures 2.11 and 2.12 in Section 2.4.5.1).



a.

b.

**Figure 5.9 Checksums in the A axis and the B axis: (a) small scale, (b) large scale.**

The cumulative displacement plot lines will become apparently abnormal in both magnitude and shape once these ‘extreme’ readings are added in. Incorrect extreme readings, therefore, had to be corrected.

The extreme checksums were picked out from the inclinometer dataset if their CV values are larger than 10% for the A axis, and 20% for the B axis (Section 5.4.2).



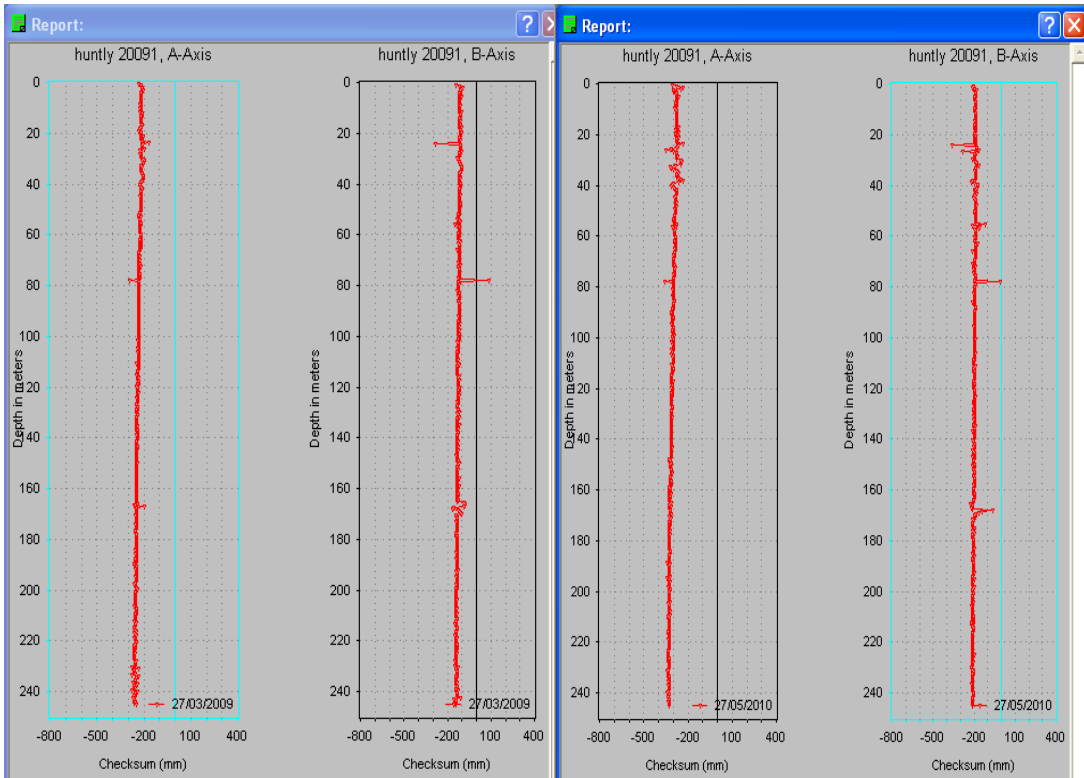


**Figure 5.10** Checksum plot on 27/03/2009.

**Figure 5.11** Checksum plot on 27/05/2009.

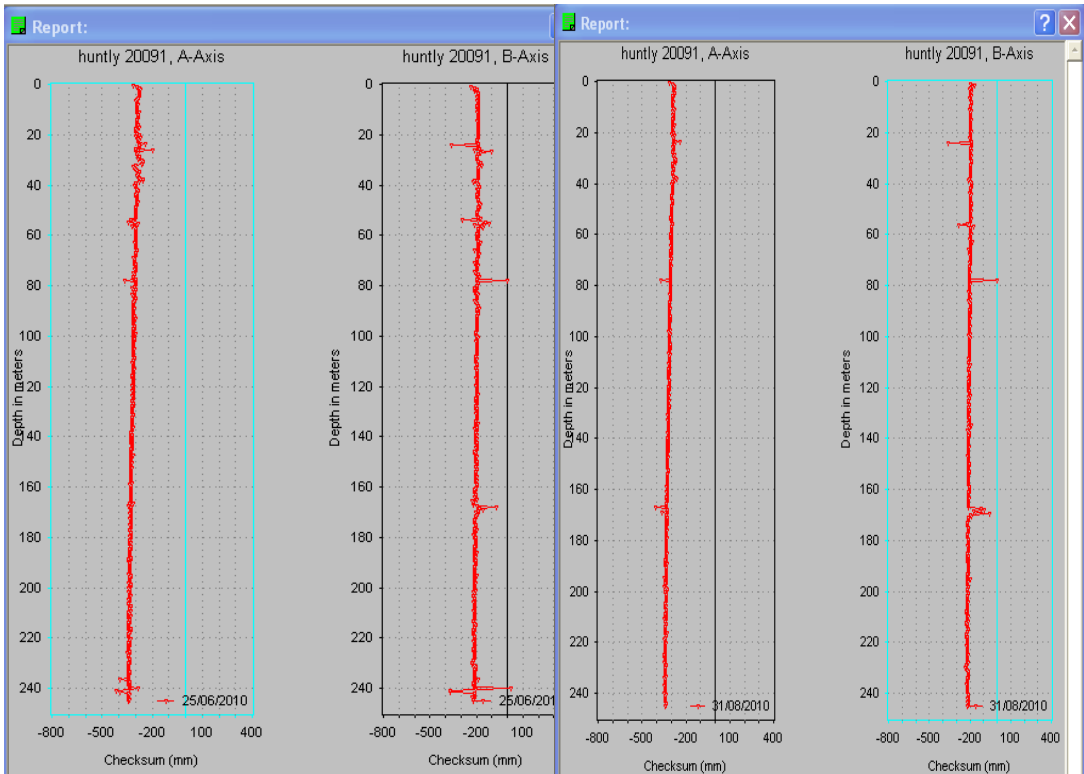


**Figure 5.12** Checksum plot on 25/06/2010.

**Figure 5.13** Checksum plot on 31/08/2010.

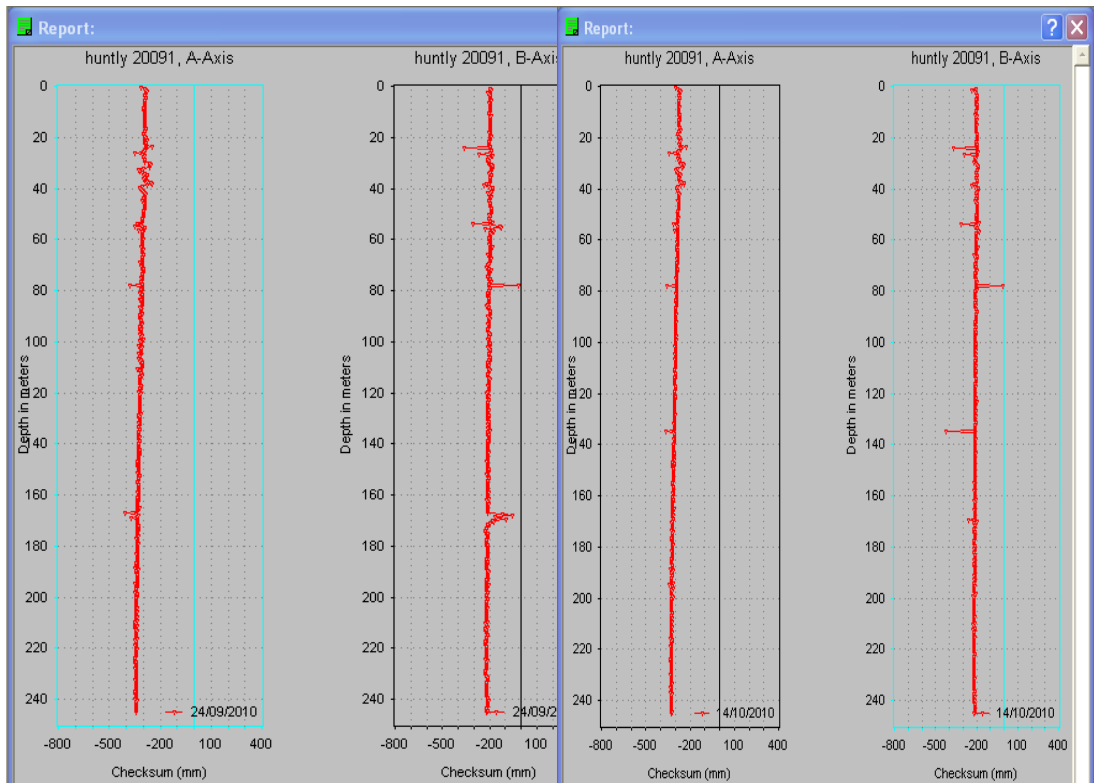


**Figure 5.14 Checksum plot on 24/09/2010. Figure 5.15 Checksum plot on 14/10/2010.**

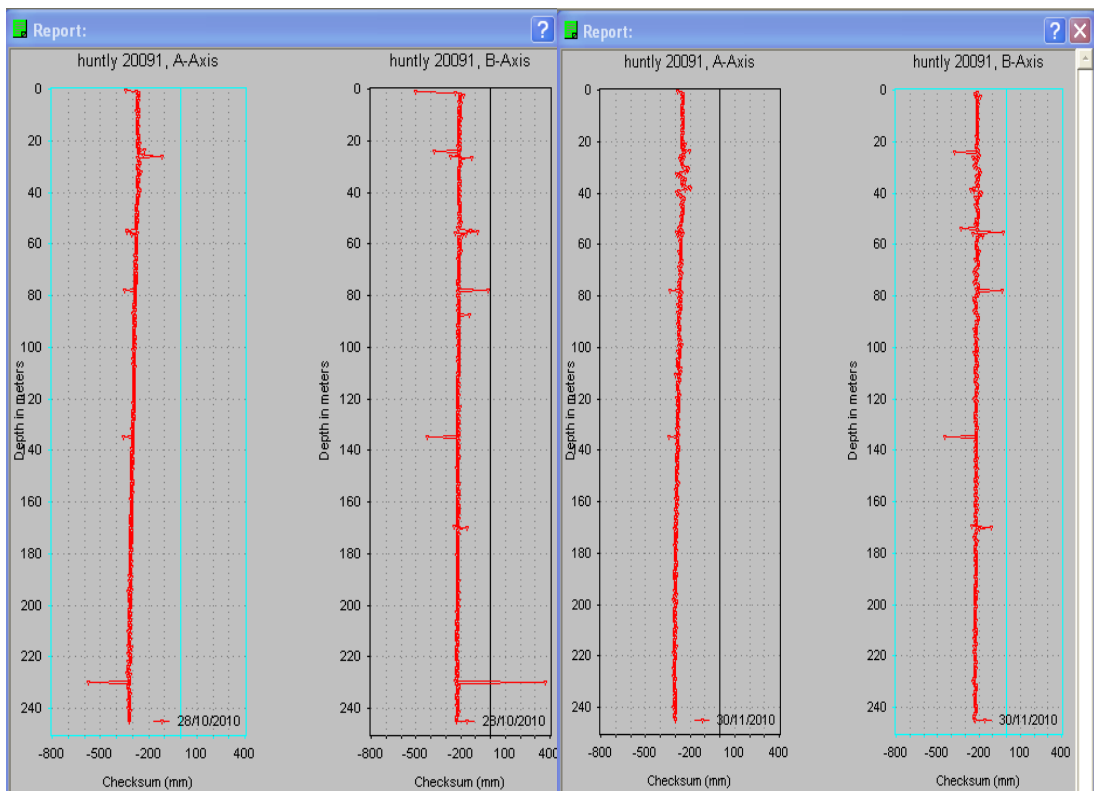


**Figure 5.16 Checksum plot on 28/10/2010. Figure 5.17 Checksum plot on 31/11/2010.**

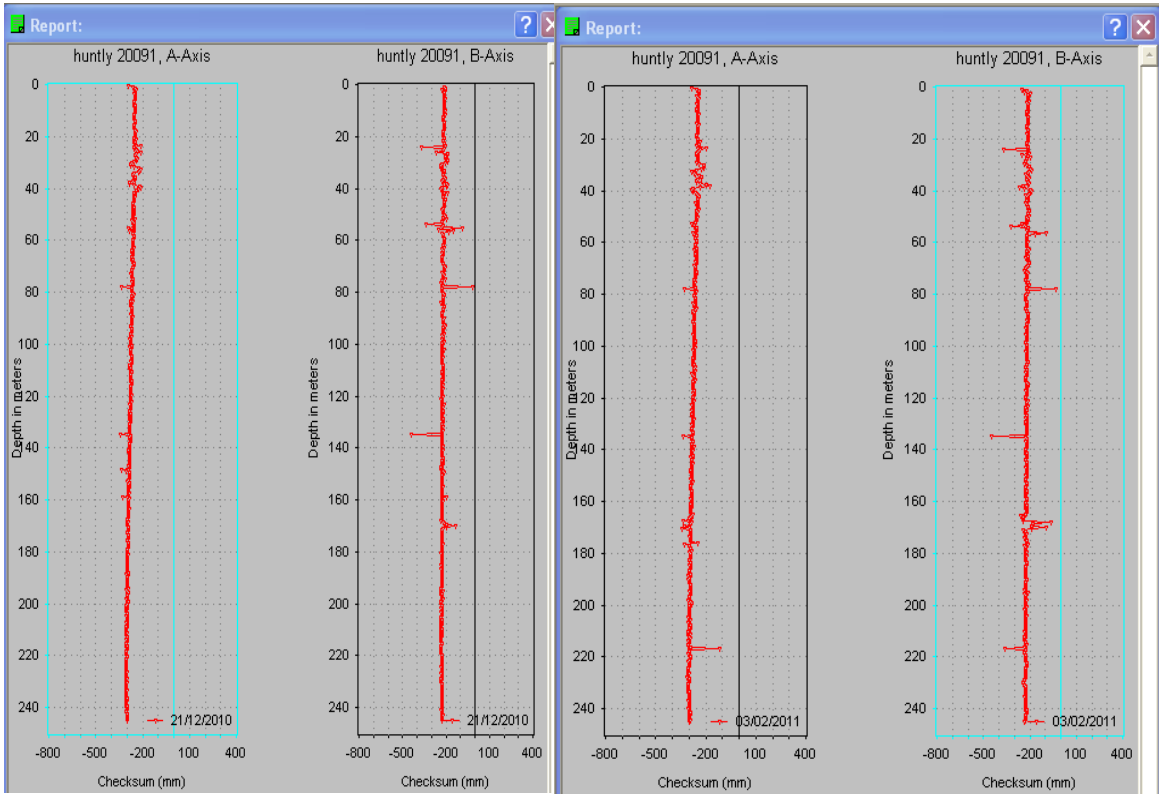


**Figure 5.18** Checksum plot on 21/12/2010.

**Figure 5.19** Checksum plot on 03/02/2011.

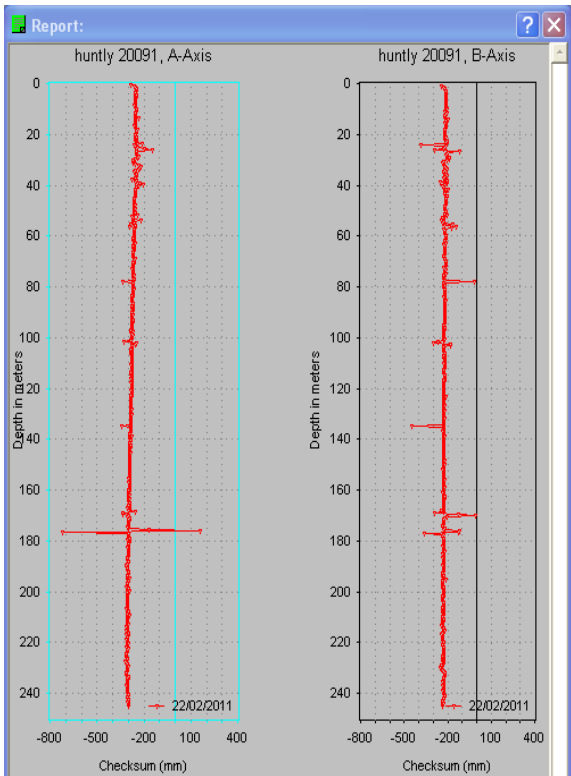


**Figure 5.20** Checksum plot on 22/02/2011.

- **Checksum plots and regular occurrences of spikes**

Looking through the above 11 checksum plots (Figure 5.10 to Figure 5.20) and the inclinometer dataset the depths of extreme checksums occurrence are summarised in Table 5.3. There are some regular occurrences to be noticed:

- All the plots for the B axis are vertical or near-vertical with a slight tilt, and more straight and vertical than the A axis plots that mostly are slightly curved.
- The depths of spikes are summarised in Table 5.3. The extreme checksums occurred mostly at depths of 24 m, 56m, 78 m, 135 m, 167 m and 169.5 m (or 170 m).
- At 24 m, 56 m and 78 m abnormal readings occurred every time in both axes, leading to extreme checksums.

**Table 5.3 Depths of the extreme checksums having CV values larger than 10% for the A axis and 20% for the B axis.**

Survey No.	Survey dates	Depth (m)							
		24	26.5	56	78	135	167	169.5	Others
0	27/03/2009	24		56	78		165.5-167		
1	27/05/2010	24	26.5	55.5	78		168		
2	25/06/2010	24	26.5	54; 55.5	78		168		240
3	31/08/2010	24		56.5	78		167.5-168	169.5	1.5
4	24/09/2010	24		54-55.5	78		167.5-168	169.5	
5	14/10/2010	24		54	78	135		169.5	
6	28/10/2010	24	26.5	55-56.5	78	135	167-	170	230; 87.5;
7	30/11/2010	24		55.5	78	135		170	
8	21/12/2010	24		55.5	78	135		170	
9	3/02/2011	24		56.5; 57	78	135	168	169.5	38-38.5, 217
10	22/02/2011	24	26.5	55.5-57	78	135		169.5; 170	102; 176-177

- At 135 m depth abnormal checksums occurred from 14/10/2010 onwards. At 169.5 m (or 170 m) abnormal checksums were noticed from 31/08/2010 onwards. At other depths listed in Table 5.3 the spikes occurred randomly.

- **Interpretations of the occurrence**

- The curved A axis plots might be due to the larger offset of the Borehole from vertical in the A axis direction, maximum 3.3 m compared to the B axis offset at maximum of 0.39 m, the further from vertical, the lower the accuracy of the inclinometer.
- At depths of 24 m, 56 m, 78 m, 135 m and 167 m the spikes occurred frequently, where there were possibly the casing joints or adjacent below or above the joints that had irregularity or deformations. The probe kicked the deformed joints with its upper or lower wheels.
- At depths of 24 m, 56 m, and 78 m every time there were abnormal differential readings in both the A and B axes.
- At 135 m, 169.5 m (or 170 m) depths the joints “kicked” the probe presumably because the strata movement and the casing deformation had caused larger curvature or irregularity there after 14/10/2010 at 135 m and 31/08/2010 at 169.5 m.
- The variations around 56 m, 167 m and 169.5 m may be from strong bumping of the probe to the irregularity of the casing joints. The bumping impact lasted longer than other depths to have influenced several measurements close to the three depths.

#### **5.4.4.2 Extreme reading edit**

If the checksums show a large checksum difference occurring at one depth, the reading data can be corrected using the mean of the neighbouring readings (Machan & Bennett, 2008). This thesis uses the average of adjacent readings from below and above to replace the extreme readings. Here it is supposed that the value of tilt in a 0.5 m interval should smoothly link the inclinations from

readings 0.50 m above and below the extreme reading to allow the probe to successfully traverse through.

The In-Site software was used to edit the extreme reading values to smooth the spikes of checksums. This resulted in amended mean checksums, and gave CV values of the corrected readings for each axis all less than 10% (Table 5.4).

**Table 5.4 Checksums, standard deviations and CV values after edit of extreme readings.**

Survey date	A Checksums			B Checksums			Instrument constant
	Mean	Standard Deviation	Coefficient variation	Mean	Standard Deviation	Coefficient variation	
27/03/2009	-237.6	15.5	6.52%	-126.6	10.6	8.37%	25000
27/05/2010	-306.5	20.6	6.72%	-199.8	10.3	5.16%	25000
25/06/2010	-314.8	19.7	6.26%	-200.9	11.5	5.72%	25000
31/08/2010	-316.0	19.8	6.27%	-205.9	10.3	5.00%	25000
24/09/2010	-319.0	19.8	6.21%	-206.6	10.3	4.99%	25000
14/10/2010	-302.9	20.0	6.60%	-209.1	7.7	3.68%	25000
28/10/2010	-294.4	19.6	6.66%	-215.8	14.5	6.72%	25000
30/11/2010	-278.8	20.4	7.32%	-219.5	8.9	4.05%	25000
21/12/2010	-277.8	20.2	7.27%	-222.2	9.5	4.28%	25000
03/02/2011	-275.6	19.9	7.22%	-221.3	8.9	4.02%	25000
22/02/2011	-280.3	20.4	7.28%	-223.7	8.5	3.80%	25000

Comparison of the new plots after correction (Figure 5.21 a and b) with the plots before correction (see Figure 5.8) indicates that there are fewer lines crossing and the lines are easier to distinguish (the gaps between lines are greater) after editing.

#### **5.4.5 Bias Error Correction**

Figure 5.21 shows the cumulative displacement plots in the A and B axes for the Borehole before bias correction. For the A axis from 245 to 139 m, and for the B axis from 245 to 170 m, the plots are leaning in nearly straight lines.



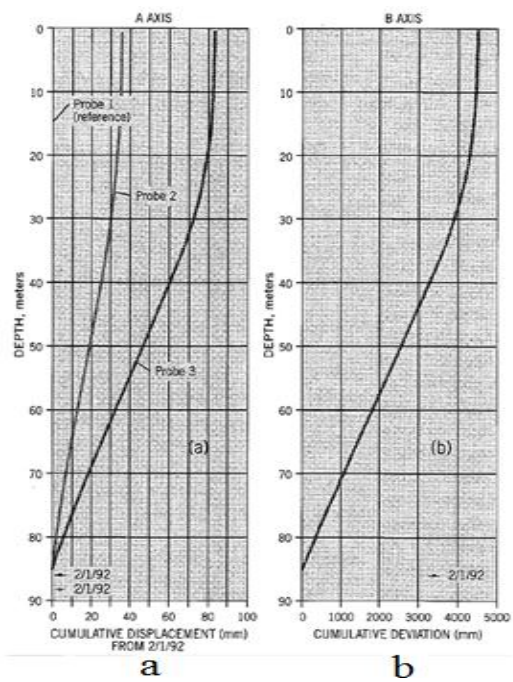
For the A axis from 245 to 139 m, and for the B axis from 245 to 170 m, the leaning lines might stand for the strata movement induced by the extraction 50 m underneath the borehole, also might be caused by bias-shift errors. Considering 50 m distance from borehole bottom to the coal seam roof, the leaning line was estimated affected by the seam extraction as a major factor, and by bias-shift error as a minor factor. Furthermore, there was no measures available to identify each weight of the two factors, the bias shift error was not analysed further in this study.

#### **5.4.6 Rotation Error**

Figures 5.22 and 5.23 are the plots for identifying the rotation errors. Figures 5.22 a, b are the typical plot pattern containing rotation error. Figures 5.23 c, d are the current plot for the Borehole, which were produced by DigiPro®. By comparing the two groups of plots, the following features were found:

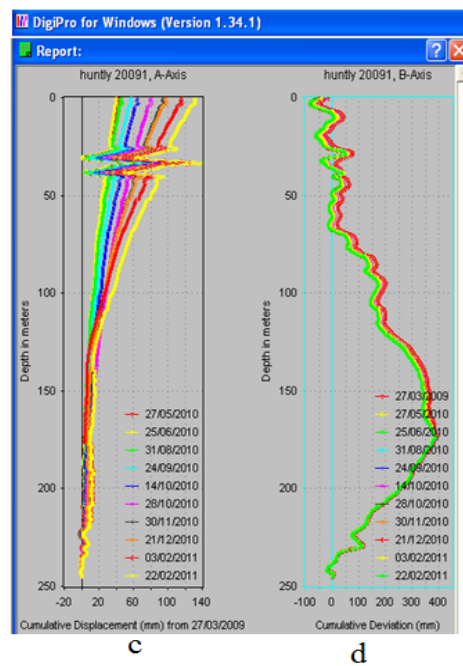
- There are some slight curves at 70 m and 130 m, but no significant curved lines in the A axis cumulative displacement plot (Figure 5.22 c). There are no curves in the B axis cumulative displacement plot (Figure 5.23 c).
- In the B axis cumulative deviation graph (Figure 5.22 d) the offset of the borehole at 173 m is 0.4 m, crossing the section from 175 m to 238 m, and then the largest tilt is 0.36 degree, i.e.  $\text{ATAN}(0.4 \text{ m} / (175 \text{ m} - 238 \text{ m}))$ . In the A axis cumulative deviation plot (Figure 5.23 d), the offset at 245.5 m is 3.3 m over the borehole depth 245.5 m, then, the largest tilt is 0.77 degree, i.e.  $\text{ATAN}(3.3 \text{ m} / 245.5 \text{ m})$ . The two tilts of 0.36 and 0.77 degrees are less than 4 degrees (Section 4.2.5.4). Thus, the current cumulative deviation lines in the A and B axes may not show significant tilt.
- Figure 5.22 c doesn't have the similar shape with Figure 5.22 d, and Figure 5.23 c doesn't have the similar shapes with Figure 5.23 d (Section 4.2.5.4).



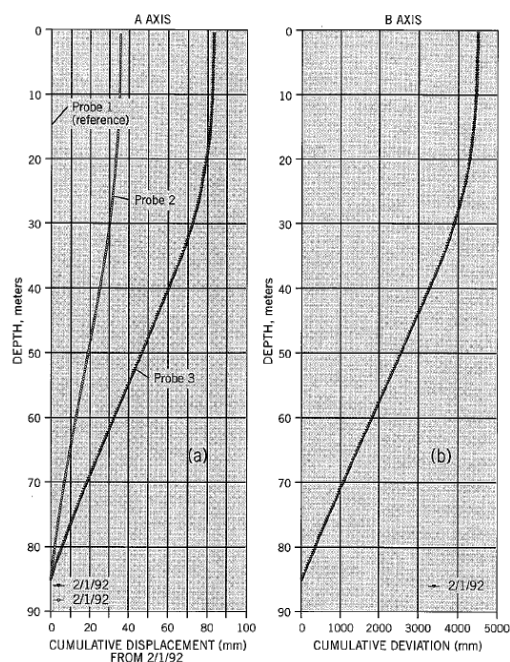


a and b: Typical plot pattern containing rotation error, the casing tilts  $4^{\circ}$  in b (Section 4.2.5.4).

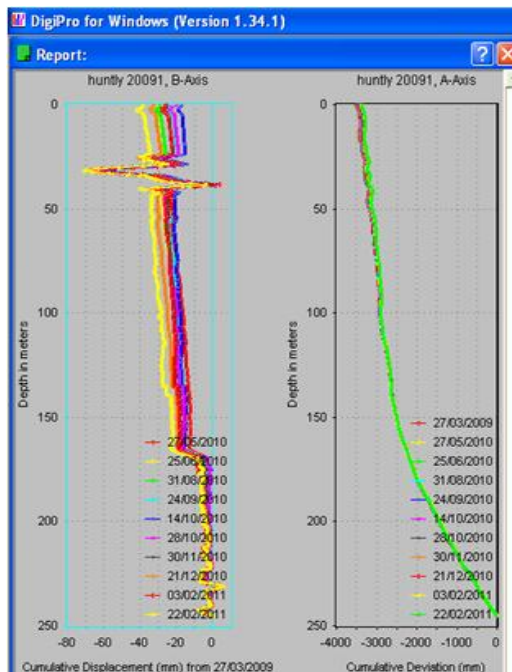
**Figure 5.22 The A axis cumulative displacements vs. the B axis cumulative deviation showing no major rotation error.**



c and d: Current plot of the A axis cumulative displacement, the casing tilts  $0.36^{\circ}$  in d.



a and b: Typical plot pattern containing rotation error, the casing tilts  $4^{\circ}$  in b (Section 4.2.5.4).



c and d: Current plot of the B Axis cumulative displacement, the casing tilts  $0.77^{\circ}$  in d.

**Figure 5.23 The B axis Cumulative displacement vs. the A axis cumulative deviation showing no major rotation error.**

Therefore, there may be no major rotation errors in the datasets.

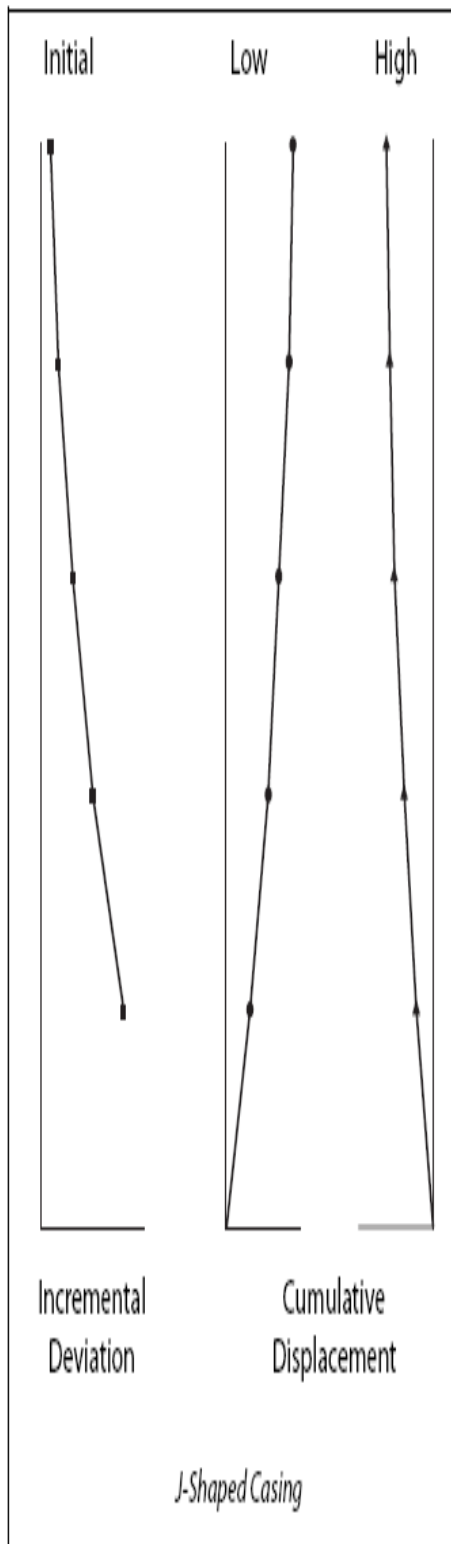
However, there are small inclinations in the cross axis at approximately 0.3 and 0.77 degree in Figures 5.22 d and 5.23 d respectively. Also, it was observed that an alignment change of the probe possibly occurred after the initial dataset was taken, which typically results from:

- Wear and tear on wheel yokes and bearings;
- Bumps to the probe causing sensor movement to affect the A and B axis readings separately (Section 4.2.5.4; Slope Indicator Co., 2000).

Therefore, rotation errors might exist in the dataset, but their impacts are not more than minor, consequently rotation errors were considered negligible, and not corrected for in this study.

#### **5.4.7 Depth Error**

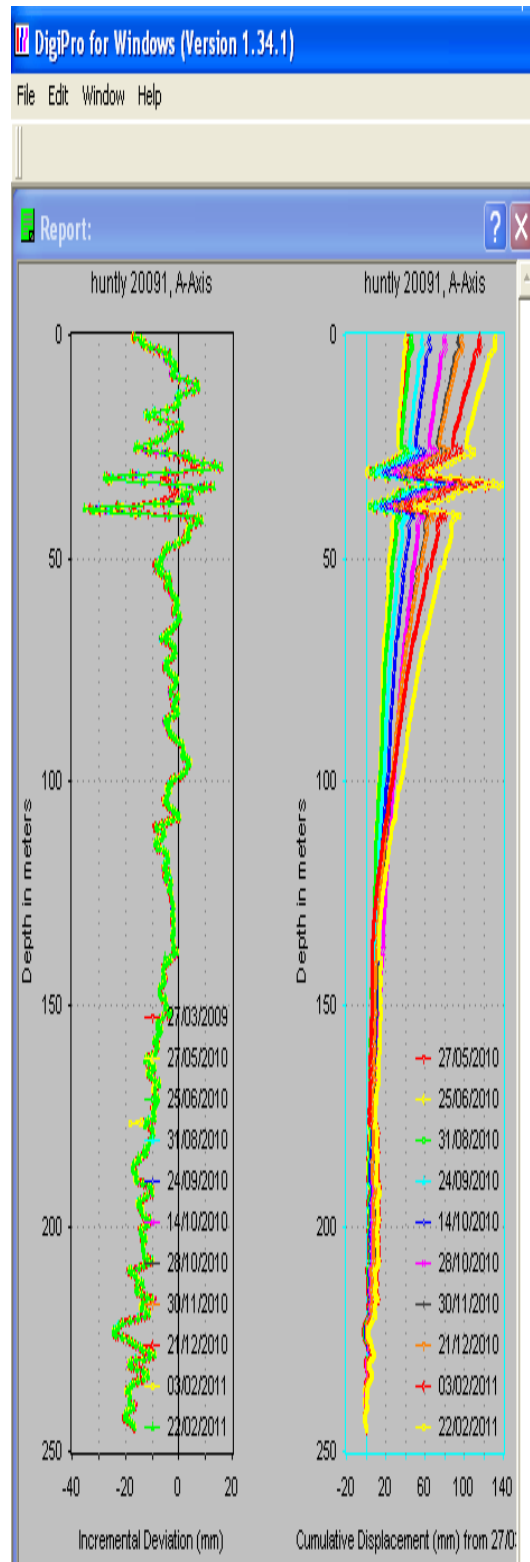
Systematic depth errors can be identified by comparison of cumulative displacement plots of a questionable survey to the incremental deviation plot of the reference survey for the same axis, instead of the cross axis (Section 4.2.5.4). A systematic depth error exists if a similar shape between cumulative displacement and incremental deviation, such as a and b graphs in Figures 5.24, 5.25, 5.26, and 5.27 as the four reference figures, is identified (Slope Indicator Co., 2000). Plots c and d in Figures 5.24, 5.25, 5.26, and 5.27 are the inclinometer plots drawn in DigiPro® for identifying depth errors. From the comparison of the four pairs of graphs, no obvious or significant similarities between the plots c and d could be seen, so major depth errors were not identified.



a

b

a and b: the schematics of the depth errors in J-shaped casing (Section 4.2.5.5) .

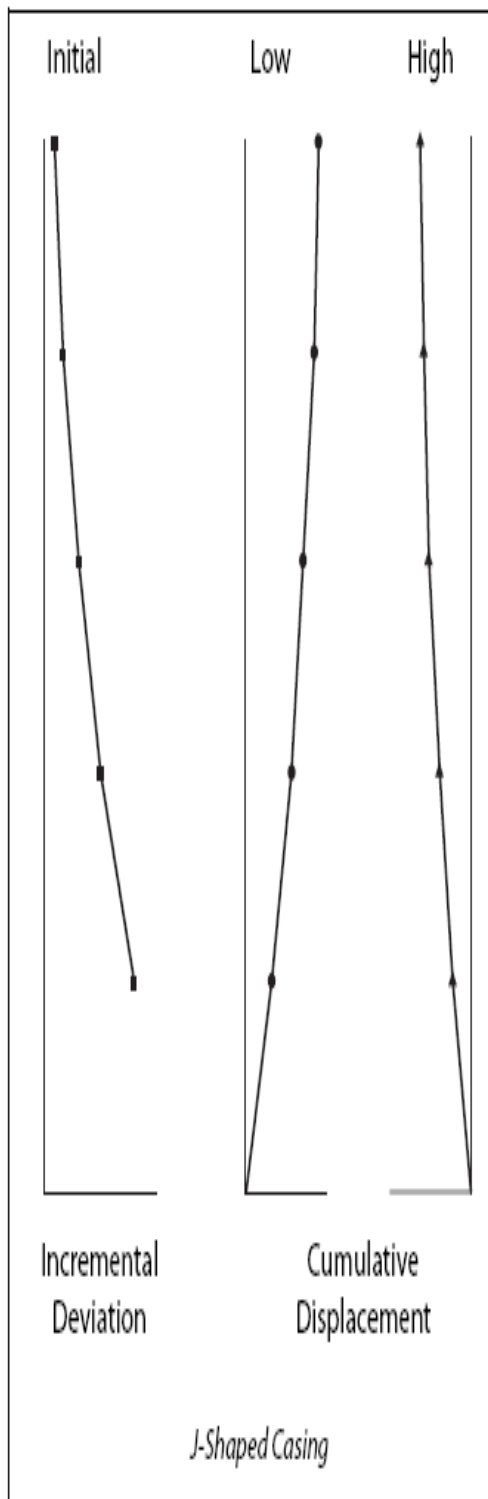


c

d

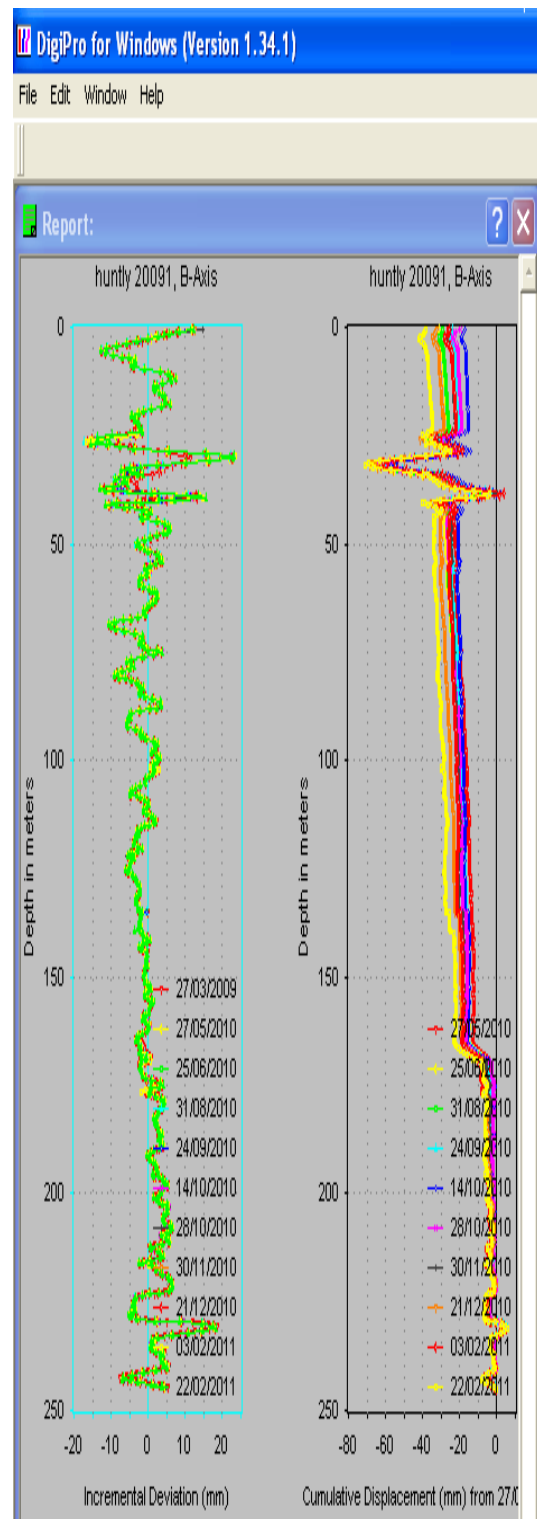
c and d: the plots of incremental deviation and cumulative displacement in the A axis of the Borehole.

**Figure 5.24 Comparison of the incremental deviations and cumulative displacements in the A axis for J-shape casing, showing no major depth error.**



a

b



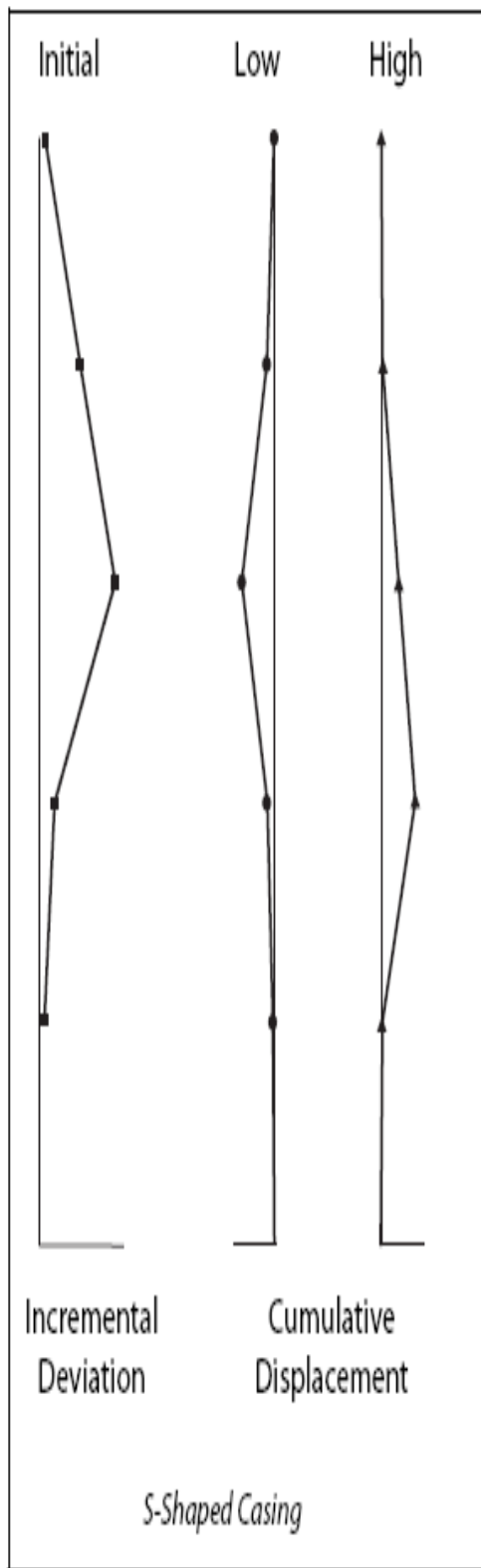
c

d

a and b: the schematics of the depth errors in J-shaped casing (Section 4.2.5.5).

c and d: the plots of incremental deviation and cumulative displacement in the B axis of the Borehole.

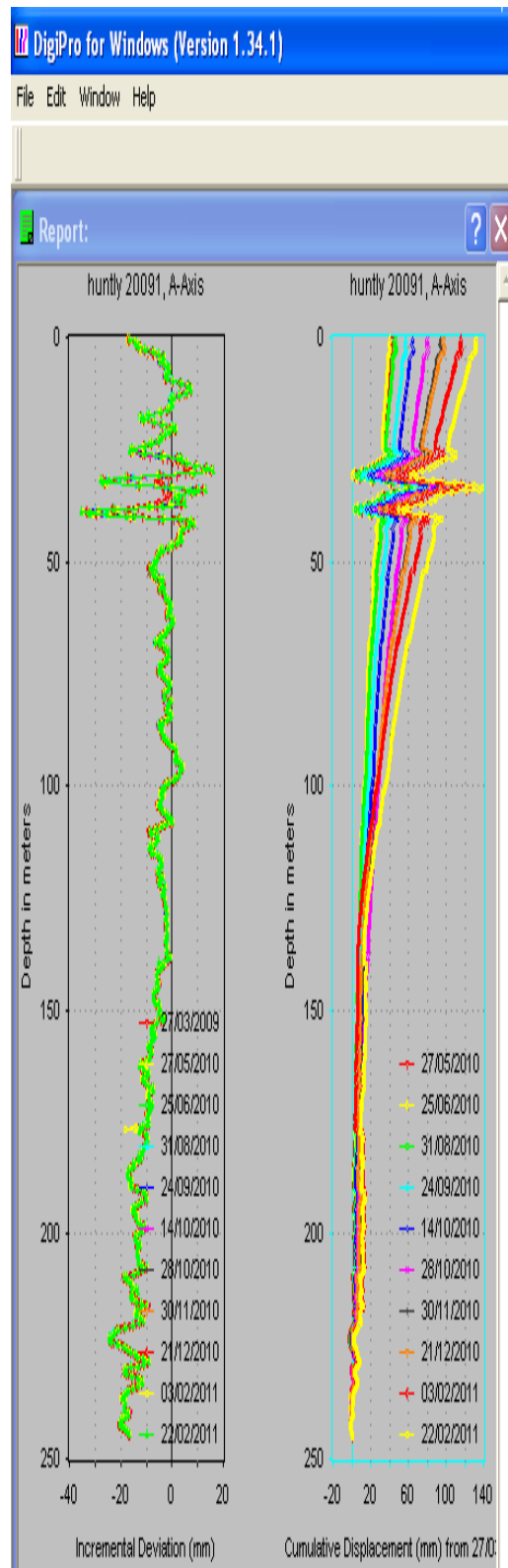
**Figure 5.25 Comparison of the incremental deviations and cumulative displacements in the B axis for J-shape casing, showing no major depth error.**



a

b

a and b: the schematics of the depth errors in S-shaped casing (Section 4.2.5.5).

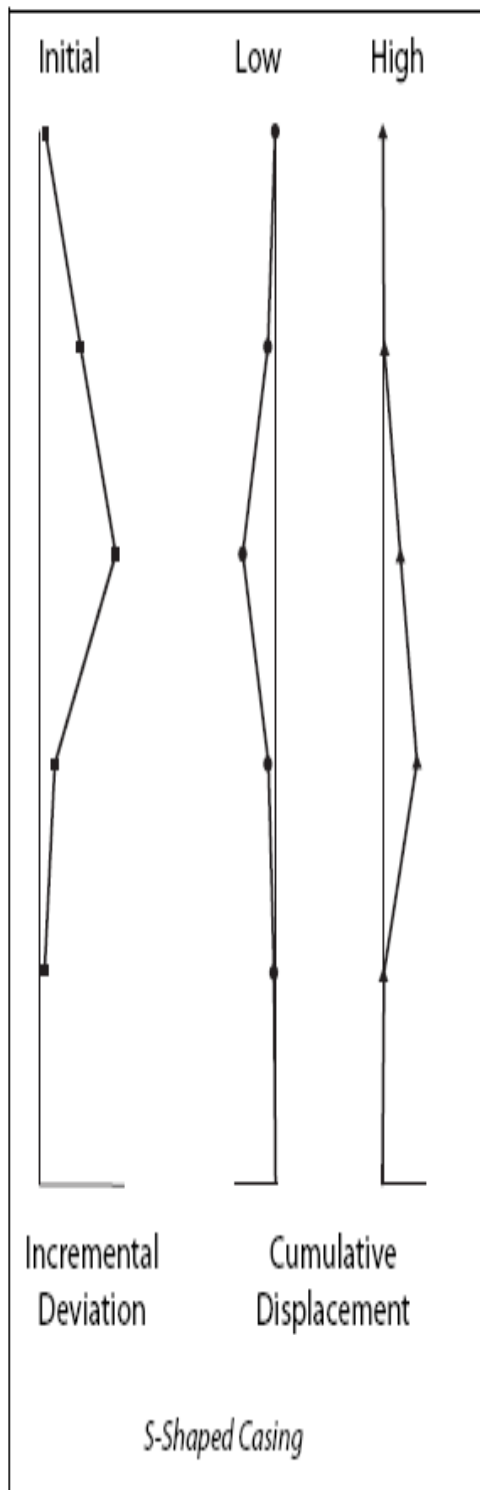


c

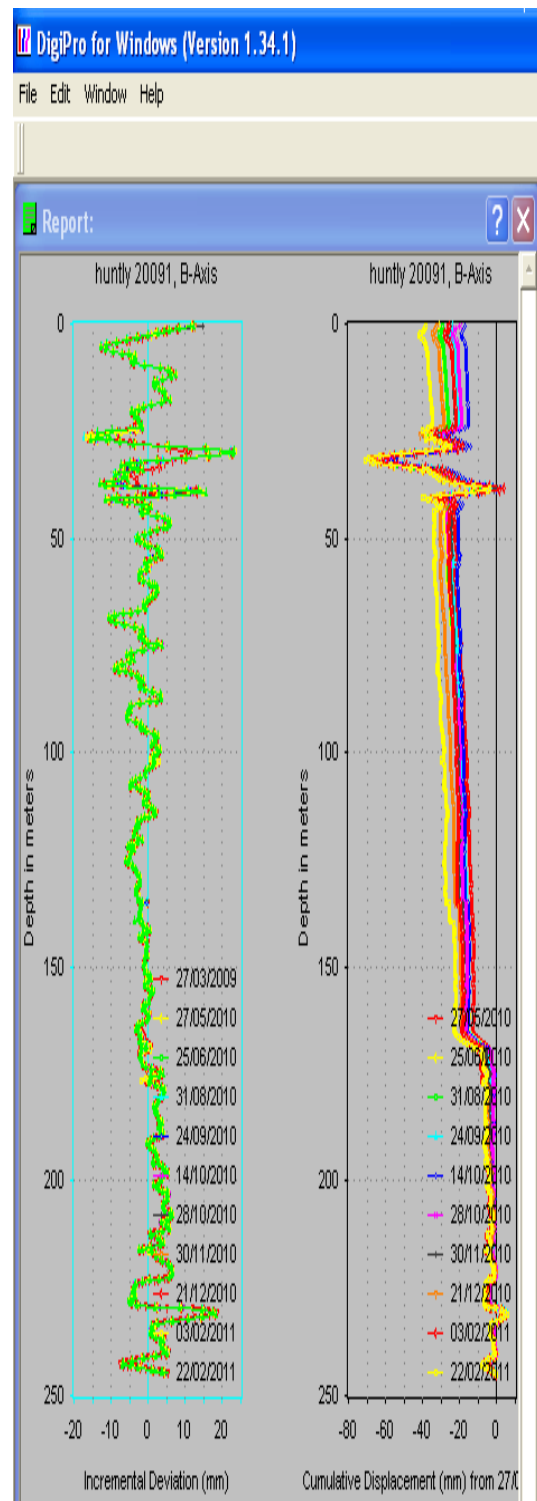
d

c and d: the plots of incremental deviation and cumulative displacement in the A axis of the Borehole.

**Figure 5.26 Comparison of the incremental deviations and cumulative displacements in the A axis for S-shape casing, showing no major depth error.**



a and b: the schematics of the depth errors in S-shaped casing (Section 4.2.5.5).



c and d: the plots of incremental deviation and cumulative displacement in the B axis of the Borehole.

**Figure 5.27 Comparison of the incremental deviations and cumulative displacements in the B axis for S-shape casing, showing no major depth error.**

However, minor depth errors may exist because the following conditions had been encountered in the measurements (Section 4.2.5.5):

- The casing collar might slightly rise and drop through surveys using GPS (to be reported in section 6.4); so the ground heaved and settled causing the casing length changed as the nine layers had different properties, hence, had differential vertical settlement, the probe was positioned a little bit deeper at every interval while the ground subsided.
- The cable length might change by possible shrinking or stretching due to seasonal temperature changes.

The above changes were small; every reading in the survey might be slightly influenced. Comparing the Borehole depth of 245 m to the span of small subsidence or slight collar level change at a maximum of approximately 147 mm (74 - (-73)), the influence of the depth error would be minor, and so was not taken into account in this study. Random positioning mistakes were not evident in the plots, thus were not concerned in this study.

#### **5.4.8 Spiral Correction for Casing**

The groove spiral accuracy used in this borehole is less than  $0.5^{\circ}$  per 3 m length according to the product manual by SOIL (2007). If the accumulated spiral is less than 20 degrees, it can be ignored in analysis (Slope Indicator Co., 2011). The spiral errors may exist in the datasets, but there may be no spiral survey data available for the Borehole casing because Figure 5.28 shows the spiral sign is false representing no spiral sensor inserted or activated in the SOIL inclinometer during the measurements for the Borehole. Therefore the spiral errors were not discussed in this thesis.

H:\01 Thesis\03 Incliner\Monitoring data\MMV03-1 kill extreme, 25000 of new K b4 average no two days.mdb

Installation Header Survey List

Date	Time	Depths	Full Set	Constant	Spiral	Operator	Sensor
27/03/2009	10:34:35	489	True	25000	False	pp	1678
27/05/2010	10:03:50	489	True	25000	False	pp	1678
25/06/2010	09:48:53	489	True	25000	False	pp	1678
31/08/2010	09:27:49	489	True	25000	False	pp	1678
24/09/2010	09:49:06	489	True	25000	False	pp	1678
14/10/2010	10:15:55	489	True	25000	False	pp	1678
28/10/2010	10:21:54	489	True	25000	False	pp	1678
30/11/2010	09:34:27	489	True	25000	False	pp	1678
21/12/2010	09:28:27	489	True	25000	False	pp	1678
03/02/2011	09:19:27	489	True	25000	False	pp	1678
22/02/2011	09:18:34	489	True	25000	False	pp	1678

Figure 5.28 The spiral sign is ‘false’ representing no spiral data available in the datasets.

## 5.5 Summary and Conclusions

### 5.5.1 Discussions

#### 5.5.1.1 Probe kicking

Why the extreme checksum readings (Table 5.3) occurred at the joints or  $\pm 0.5$  m nearby joints? Figure 5.29 explains one of the possible mechanisms that may have caused the extreme readings. The Borehole is very deep of 245 m and the offset and curvature of the Borehole may have been enough to cause the inconsistency and irregularity of the joint connections from the beginning at depths of 24, 56 and 78 m, and following the strata movement, the deformation of the casing increased, then the number of irregularity rose at the other depths in Table 5.3.

As the wheel was traversing up and facing the inconsistency at an acute angle the probe will kick the joint harder than where the lower wheel faces the inconsistency. The A0 and A180 readings, therefore, were different from the readings at smooth joints or in sections between the joints.



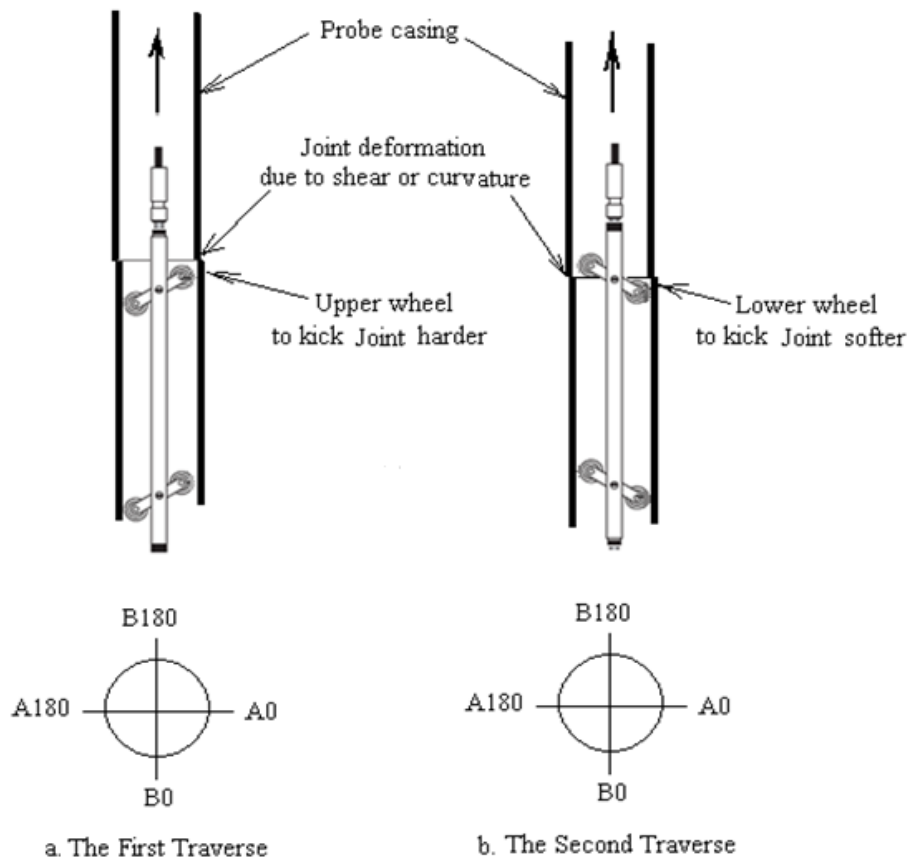


**Figure 5.29 Different magnitudes of probe kicks on inconsistent joint in different directions.**

Thus the combined readings,  $(A0-A180)/2$  and the checksums,  $(A0+A180)$  become extreme in this circumstance; the same problem exists in the B axis as well. The above inference is in agreement with the statement that: ‘if readings are taken about a casing joint, then checksums for these readings may never stabilise, if all of the other checksums are consistent, then this also quite normal’ (SOIL manual, 2008).

### 5.5.1.2 Probe jamming

Jamming of the probe at approximately 38 m depths, and at and after 11 March 2011 was likely caused by bending of the Borehole and the probe casing. RST Instruments (2010) states that the minimum radius that a 0.5 m long probe can negotiate is 3.12m when using  $\text{Ø}70$  mm probe casing (ID  $\text{Ø} 59$  mm). Initial

calculations, however, suggest that the radius at approximately 38.53m is around 10.5 m, which is large enough to pass the probe. However, when the section of casing just beneath the bend is twisted 90 degrees spatially to this bending plane, it may be easy for the lower deformation of the casing to jam the probe.

#### **5.5.1.3 Comprehensive analysis of 3 events**

Considering the water level changes and traversing of probe stopped in the Borehole, and the discarded two surveys described in Section 5.4.2, it is anticipated that the three issues may be resulted from one casing rupture problem at a depth of about 38 m in the borehole. The rupture might start from the lateral differential movement of the layers, and or the vertical stretching or compression due to the differential layer subsidence and upsidence. Firstly the significant differential deformation at around 38 m contributed to the tangled cumulative displacement plot before 03/02/2011, then the casing rupture occurred, but was small leading to groundwater out the enclosed borehole entering the casing, raising water levels observed from 03/02/2011; meanwhile the rupture resisted the probe traversing or even kicked the probe leading to the occurrence of the two abnormal surveys on 12/11/2010 and 18/01/2011. As the rupture increased to a level, the probe was not able to traverse through and got jammed on 11 March 2011. The rupture kept increasing and became large enough to let the probe shift between A and B grooves in the casing in the trials of dummy probe and lowering on 02/06/2011.

#### **5.5.1.4 Shortcoming of traversing inclinometer method**

Compared with embedded in-place multi-probes, a traversing method using one probe can save investment. However, when the deformation rises to a level where the probe cannot be lowered through, continued use of the probe become

impossible. Therefore the traversing method often cannot measure for as long as desired.

Nearly 2/3 of the mining area had been extracted around inclinometer borehole up to March 2011 when the probe traversing was stopped at 38.53 m. The north half part was left intact for the shaft protection pillar. The southeast part was just commenced of extraction up to March 2011. In fact the strata movement was in its early stage considering that 2/3 of the area had been extracted, and the delay characteristics of ground movement vs. the extraction advancing (90% of subsidence usually occurs in first 6 months from notice of the subsidence). Therefore, the data measured might be approximately half of what the inclinometer research project should get.

#### **5.5.1.5 Replication of measurement**

The inclinometer manual only recommends repetition of measurement when the checksums are beyond the 5 mm limitation. If the measurement was repeated 3 times on one day the more accurate and reliable results would have been obtained. However, the repetition would have cost more and consumed more time.

#### **5.5.1.6 Determining the causes of probe jamming and water level changes**

A suggestion for a possible measure to locate the casing cracks and depth is to undertake an investigation by CCTV camera down the probe casing. Its aims and benefits will be as follows:

- Determine the reason of the water level changes in borehole.
- Determine the crack characteristics and locations in probe casings.
- Validate the inclinometer probe workability as evidence collaterally due to lack of probe validation information from the SOIL Company

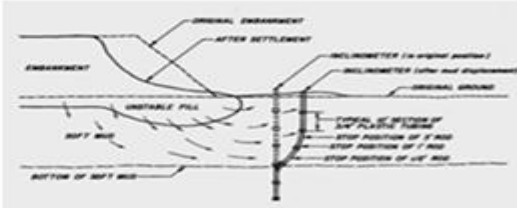
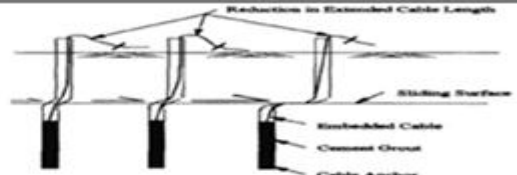
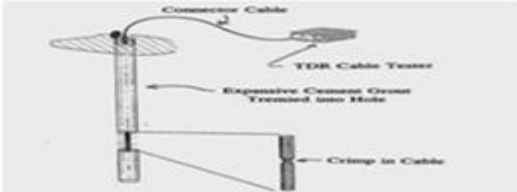

- Help determine further methods to continue the monitoring of underground extraction. For instance if the CCTV inspection is stopped at a depth say 150m by sharp bent or serious rupture of casing. Then the extensometer may be unable to be inserted below that depth (Table 5.5).

## 5.5.2 Conclusions

This chapter has scrutinised the datasets, and undertaken the error corrections.

- The data errors in the 13 inclinometer datasets include the extreme checksum values, bias-shift error, rotation error, depth error and spiral error.
- Evaluation of the checksum quality by the Coefficient of Variation (CV) led to the two surveys on 12 November 2010 and 18 January 2011 being discarded from the data analysis due to their abnormal checksums and CV values. The other 11 surveys were used in the data interpretation.
- Several spikes (extreme values) on the checksum plot in each survey have been corrected by averaging the neighbouring readings. The resulting amended mean checksums gave CV values of the corrected readings for each axis all less than 10%.
- Because the Borehole bottom was not installed in a stable stratum, the extraction induced movement and the Bias-shift error both contributed to the leaning lines at the bottom section in the cumulative plot.
- There were no major rotation errors, depth errors, and spiral errors in the datasets. However, small errors of the above three error types might exist, but their impacts were considered not more than minor, and consequently not corrected in this study.

Table 5.5 The investigation of methods for extending the capability of inclinometer casing (after Machan and Bennet, 2008).

Method Name	Features	Surface or In-hole method?	Applied pre or post Bent?	Used in New Zealand?	Suitable for BH20091?	Picture
<b>Poor Man's Inclinometer Method</b>	A short section of pipe attached to a wire cable can be left or traversed into borehole to detect bent and depths	In-hole	All the time for detecting depths of bents in shallow borehole	Easy, simple, inaccurate method	No, borehole is too deep.	
<b>Survey Method</b>	Measure collar changes in x, y, z	Surface	All time	Common	Yes, carry on.	
<b>Extensometer Method</b>	When casing is very distorted, the wire cable is anchored to the bottom of casing with a grout plug.	In-hole or on slope surface	Pre-buried or Later applied	Yes	Most likely	
<b>TDR Method</b>	A coaxial cable for TDR can be inserted into casing to measure strata movement. It is a developing method.	In-hole	Pre-buried or Later applied	No available information (mostly used in USA)	Probable one, have not found NZ agent of this method.	
<b>Fixed-in-place Inclinometer Probe</b>	To collect real time continuous data with remote system. Probes costly but saving time and labour	In-hole or on surface of slope	Pre-buried or Later applied if borehole diameter permits	Yes	No, borehole diameter is small. No probe can be buried in now.	

- Therefore, Figure 5.21 gives the final cumulative displacement graphs in the A axis and B axis.

To conclude, the useful 11 inclinometer datasets contained the extreme checksum readings, and possible bias-shift errors, minor rotation errors, depth errors, and spiral errors. Extreme checksum readings were corrected. The other three errors were minor and not corrected in this thesis.

### **5.5.3 Recommendations**

#### **5.5.3.1 Continuing the monitoring**

The inclinometer monitoring was stopped in March when the seam extraction was just underneath the inclinometer borehole. Considering the requirement of further data and the Borehole continuous use as a costly structure, the recommendation for extending capacity of the inclinometer method in the Borehole is listed in Table 5.5. So the further monitoring of strata movement may be required for obtaining the complete measurement and good understanding of ground displacement characteristics. In the following 6 months from March 2011, further monitoring of the inclinometer borehole was: to carry on the borehole opening survey of the x, y, z by Survey Team, Solid Energy, and attention had been noticed to mark a permanent spot on the opening of the borehole to get further accurate GPS data.



# Chapter 6 Borehole Movement

## Interpretation and Extraction Outlays

### 6.1 Introduction

This chapter interprets the strata movement in terms of movement rate, direction, shear zones, shear depth, movement vs. timing of coal extractions, and type of ground movement. The interpretation is based on the datasets after data error correction and analysis described in Chapter 5. The results of the interpretation are utilised to discuss the mechanism of the ground vertical and horizontal movement observed and infer the implications for the proposed shaft project.

The interpretation of the movement characteristics mostly relied on the resultant data of the A axis and B axis because the resultant movement is the actual movement of the strata. The trajectories used to describe the borehole movement at 1 m, 135 m and 166 m were developed from the 11 successful inclinometer surveys.

The zones of the shear movement were determined by incremental displacement and cumulative horizontal displacement plots that are typically ‘the most reliable means to determine the zone of the shear movement’ (Stark and Choi, 2008).

The monthly extraction cells had an average length/width ratio of 1.5, but had varying area and distance to the inclinometer borehole (Section 4.4.2.1).

The historic delay time between completion of extraction and the start of the subsidence was approximately 1 to 2 years in the Huntly East area (Kelsey, 1986).

The delay time in the North 5 area was identified in this study by analysing the correlation between the borehole lateral movement and the distance from extraction edge to the Borehole.



## **6.2 Inclinometer Plots Analysis**

### **6.2.1. Approach and Aim**

After the error corrections (in Section 5.4), the datasets were analysed and interpreted through the plots of the data using five inclinometer software packages, and the Excel spread sheet that have particular graphing and analysing functions (Section 4.2.5). The major movement parameters include the magnitude, rate, direction, depth, and type of ground movement.

### **6.2.2 Incremental Displacement**

The incremental displacement data after data error correction, for the 11 inclinometer measurements are listed in Appendix E. The incremental displacement plots on the A and B axes are illustrated in Figure 6.1. The probe system accuracy was 2 mm over 25 m (SOIL, 2010).

Spikes larger than 2.5 mm occurred at depths of 139.5 m, 176.5 m, 177 m, and 230 m in the A axis, and 135 m, 229.5-230 m, and 241- 241.5 m in the B axis (Table 6.1).

There were a cluster of spikes, at approximately 166 to 170 m in the B axis, which were less than 2.5 mm, but occurred on the negative side of the vertical axis, mostly varying from -1 mm to -2 mm, which might indicate a thick shear zone in a cumulative displacement plot.

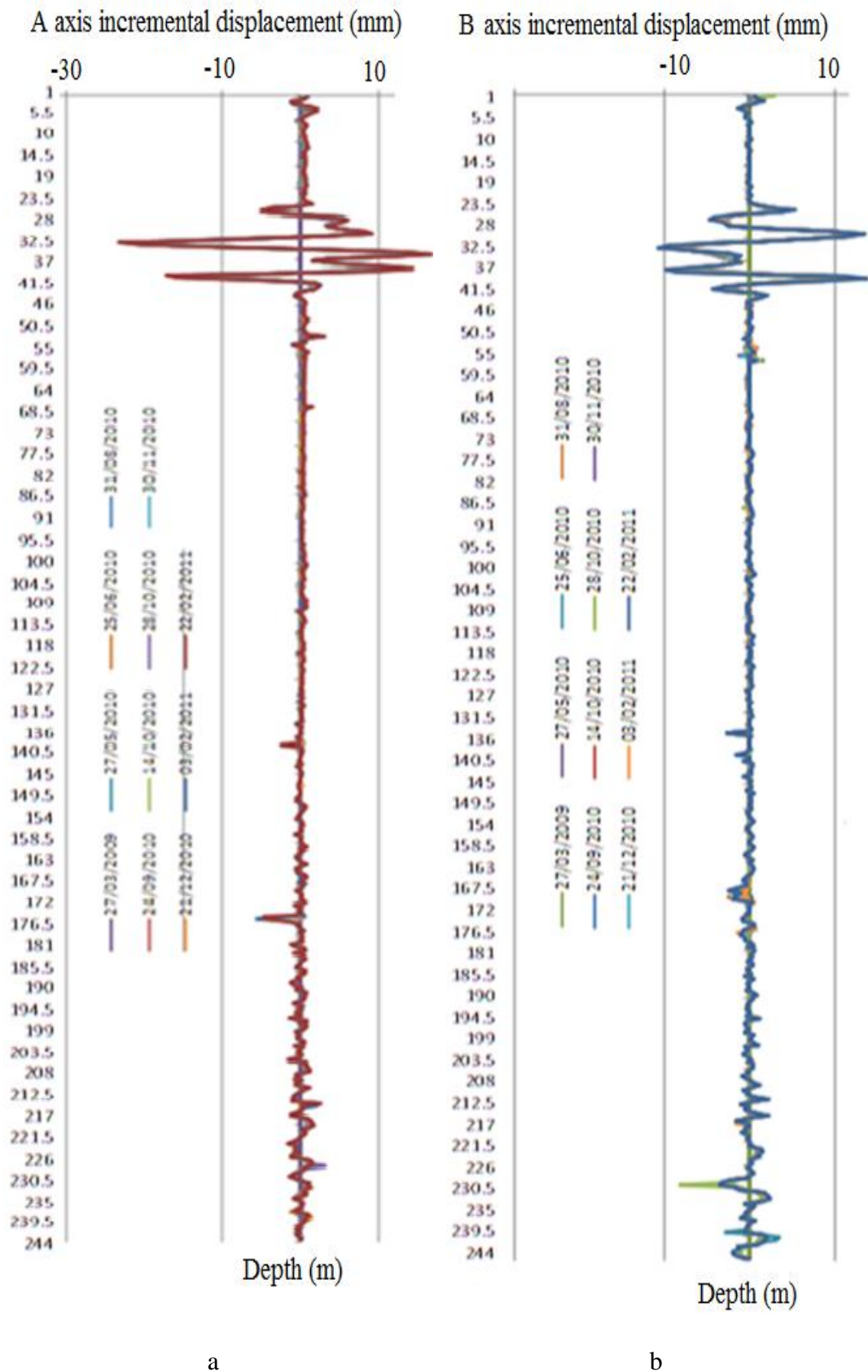


**Figure 6.1 Incremental displacement plots for the 11 surveys, a. in the A axis; b. in the B axis (data corrected see Chapter 5 for details).**

**Table 6.1 The incremental displacement data for the A and B axes. Data larger than 2.5 mm are shaded.**

Incremental Deflection Data in the A axis (mm):

Depth (m)	27/03/2009	27/05/2010	25/06/2010	31/08/2010	24/09/2010	14/10/2010	28/10/2010	30/11/2010	21/12/2010	3/02/2011	22/02/2011
139.5	0	0.2	0.3	0.3	0.2	0.2	0.2	0.2	0.2	-0.2	-2.5
176.5	0	0.4	0.5	0.5	0.5	0.4	0.3	0.3	0.1	-1.3	-4.8
177	0	0	-0.1	0	-0.1	-0.1	-0.1	-0.3	-0.6	-5.5	-4.5
230	0	0.8	1	0.9	0.9	0.7	3.2	1	0.9	1	1.2

Incremental Deflection Data in the B axis (mm):

Depth (m)	27/03/2009	27/05/2010	25/06/2010	31/08/2010	24/09/2010	14/10/2010	28/10/2010	30/11/2010	21/12/2010	3/02/2011	22/02/2011
135	0	-0.3	-0.3	-0.3	-0.2	-2.5	-2.3	-2.5	-2.4	-2.5	-2.6
229.5	0	-2.6	-2.9	-2.8	-2.8	-2.3	-2	-2.8	-2.7	-2.9	-3.3
230	0	-2.8	-3.2	-3	-3	-2.6	-8.1	-3	-2.9	-3.2	-3.6
241	0	1.5	3.5	1.7	1.6	1.4	1.2	1.7	1.6	1.8	2
241.5	0	1.2	3.1	1.4	1.4	1.2	1.1	1.5	1.4	1.6	1.7

What we are concerned with are the spikes of incremental values that are separate, discrete and larger than 2.5 mm (referred to as a ‘significant spike’ in Section 2.4.3) that might indicate significant shear movement. The spikes separate, discrete and larger than 2.5 mm are at depths of 139.5 m, 176.5 m, 177 m in the A axis, and 135 m in the B axis (Table 6.1). Other spikes are not in the separate, discrete mode, such as the spikes from 24.5 to 42 m, and from 230 m to 245.5 m in both axes (Figure 6.1). Those spikes would be diminished and or neutralised in the cumulative summation calculation.

The plot lines fluctuated significantly around the vertical axis with a magnitude range -23.2 mm to +16.7 mm, in section 25 m to 40 m in the A axis, and -10.7 mm to 13.9 mm, in section 24.5 m to 42 m in the B axis (Figure 6.1). The changes from 24.5 m to 42 m in both axes may not rise from the deformation of the strata movement because:

- The Ø70 probe PVC casing was installed into the borehole through a pre-installed 42.7 m long, Ø150 mm outer steel casing (Figure 4.3 in Section 4.2.3). The 35 mm wide annulus between the two casings was cement grouted. There was little possibility for steel casing having that tangled movement in the Tauranga soil strata, that is, the tangled plot lines from 22 m to 40 m may not be representative of the real ground lateral movement.
- The grout cement in that section may be weak and porous due to poor grouting performance or the casing may have bulged or been partially disconnected due to layers with differential subsidence or upsidence. Consequently the inclinometer could have irregular and random movements in the 22 to 40 m zone. As this probe casing movement might not correspond to the ground lateral deformation; the spikes from 22 to 40 m may not be the direct result of strata movement.

The section from 230 m to 245.5 m was the bottom section of the Borehole. With the displacement mostly less than 2.5 mm, the small tangled plots may indicate the mixture of effects of potentially porous and weak grout, the irregularity of the casing joints, and lower measurement accuracy at bottom due to the 3.3 m offset of the casing from vertical (Section 5.3.2). The effect of the right and left tangled spikes off the vertical axis was diminished in summing up for computing cumulative displacement.

### **6.2.3 Resultant Cumulative Displacement**

Figure 6.2 is the resultant cumulative displacement plots from summation of the A axis and B axis components (as in Figure 5.21, Section 5.4.5). There are three

zones presented, one 'creeping zone' from 0 m to 115 m, and two 'shear zones' at approximately 135 m and 166 m .

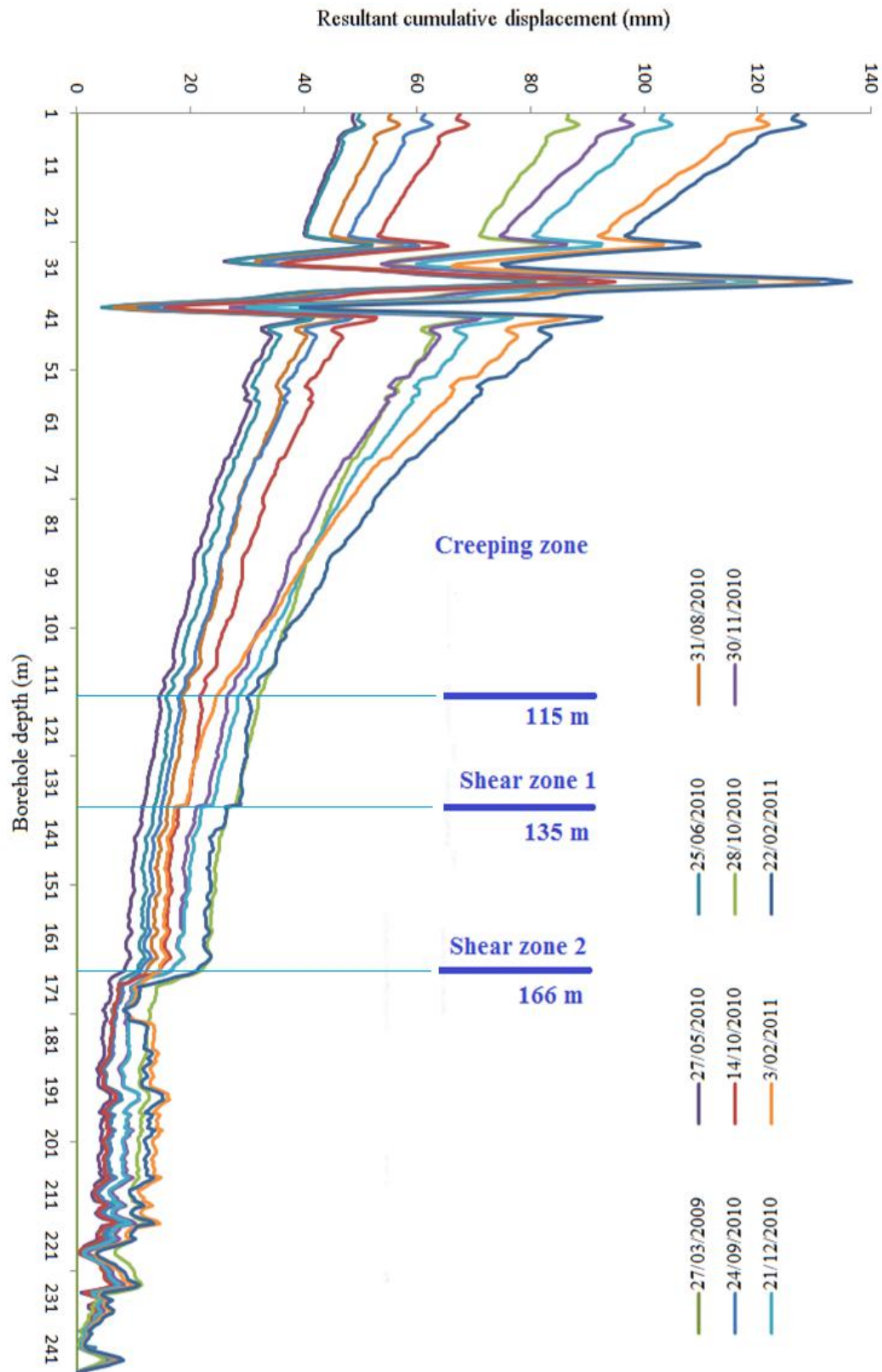


Figure 6.2 Resultant cumulative displacements showing three movement zones.



The displacement at depths from 166 to 170 m may be a thick shear zone (shear zone 2) with a thickness of 4 m, occurring from 27/03/2009 to 22/02/2011 (Figure 6.3).

It should be pointed out that there were two types of movement of the strata in a shear zone: the absolute strata movement along the borehole trajectory and the relative shear movement of the shear zone roof against the shear zone floor. The roof at 135 m moved absolutely against the initial borehole shape and moved relatively against the shear zone floor at 135.5 m (Figure 6.3).

#### 6.2.4 Strata Movement Trajectory at 135 m (Shear zone 1)

The strata at 135 m had an absolute displacement relative to the initial borehole. The movement at 135 m had a varying displacement from 12 to 29 mm (Table 6.2).

**Table 6.2 Inclinator data and movement features of shear zone 1 at 135 m.**

Survey Date	Displ. (mm)	Cumul. time (day)	Cumul. time (year)	A axis 135 m	B axis 135 m	Location No.	Bearing degree
27/03/2009						0	
27/05/2010	11.8	426	1.17	7.7	-9	1	101
25/06/2010	13.9	455	1.25	8.3	-11.2	2	97
31/08/2010	16.3	522	1.43	9.5	-13.2	3	96
24/09/2010	15.1	546	1.5	10.4	-10.9	4	104
14/10/2010	19.6	566	1.55	12	-15.4	5	98
28/10/2010	28	580	1.59	18.5	-21.1	6	101
30/11/2010	22.9	613	1.68	11.7	-19.6	7	91
21/12/2010	24	634	1.74	11.7	-21	8	89
3/02/2011	19.4	678	1.86	8	-17.7	9	84
22/02/2011	29	697	1.91	1.9	-28.9	10	64

In any horizontal intersection plane across the inclinometer borehole in the ground there is a borehole trajectory that consists of the 11 borehole locations and

represents the borehole movement changes. The trajectory is illustrated by plotting the borehole displacement in the A axis and B axis in 11 different surveys.

The Borehole movement trajectory at 135 m depth for the 11 surveys (Figure 6.4) indicates that the borehole movement at 135 m was a nonlinear, dynamic movement. 7 over 10 locations have bearings larger than  $90^{\circ}$ . The final location, No. 10 has a displacement of 29.0 mm from the origin (the reference location of the borehole) with a bearing of  $64^{\circ}$  i.e. towards the ENE (or  $94^{\circ}$  to the A180).

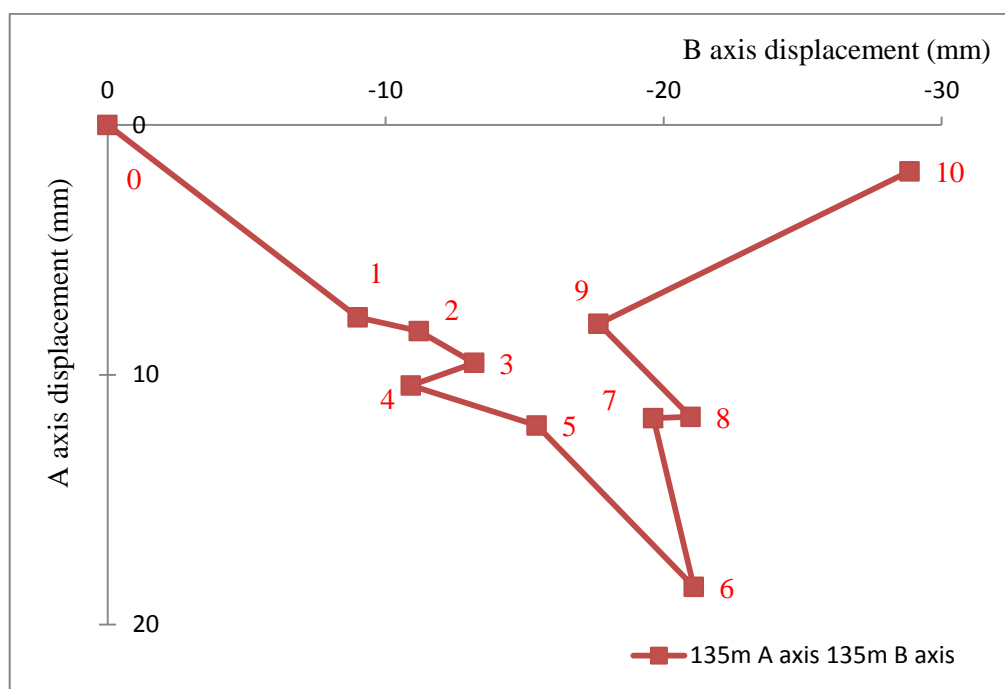


**Figure 6.4 Plan view of borehole movement trajectory, 11 continuous locations at 135 m.**

The cumulative displacement (Figure 6.2) is not the information that is of most concern. The actual movement of the casing and the ground around the casing was represented by the movement trajectory that consisted of the borehole locations from 0 to 10 (Figure 6.4). The movement distance and the movement rate along the trajectory represent the actual movement of the borehole at 135 m depth (Figure 6.4). Taking the trajectory section from 8 to 9 as the example for movement calculation, the distance between the two measurements were obtained



by Formula 6.1 and all calculated distances along trajectory are summarised in Table 6.3:

**Distance between 8 & 9 measurement**

$$= \text{SQRT} ((A9 - A8)^2 + (B9 - B8)^2) \quad (6-1)$$

Where:

A8 and B8 are the A axis and B axis displacements at location 8 at 135 m depth;

A9 and B9 are the A axis and B axis displacements at location 9 at 135 m depth;

**Table 6.3 Movement distances and rates along borehole trajectory at 135 m.**

Date	Measure Number	Move from to	Distance (mm)	Time gap (year)	Movement Rate (mm/month)
27/03/2009	0				
27/05/2010	1	0-1	11.8	1.17	0.8
25/06/2010	2	1-2	2.3	0.08	2.3
31/08/2010	3	2-3	2.4	0.18	1.1
24/09/2010	4	3-4	2.5	0.07	3.1
14/10/2010	5	4-5	4.8	0.05	7.2
28/10/2010	6	5-6	8.6	0.04	18.4
30/11/2010	7	6-7	6.9	0.09	6.3
21/12/2010	8	7-8	1.3	0.06	1.9
3/02/2011	9	8-9	5.0	0.12	3.4
22/02/2011	10	9-10	12.7	0.05	20.1
Sum			58.3	1.91	

The magnitudes of the movement rates along the trajectory at 135 m were plotted in Figure 6.5. The movement rate had two peaks of 18.4, and 20.1 mm/month during stages of 5-6 and 9-10 (Figure 6.5).

The strata movement at 135 m was nonlinear with a varying movement rate of 0.8 to 20.1 mm/month (Table 6.3). The summing displacement along the trajectory

was 58.4 mm over approximately 2 years, while the overall final displacement at No. 10 relative to No. 0 was 29.0 mm with a bearing of  $64^{\circ}$  to the true north.

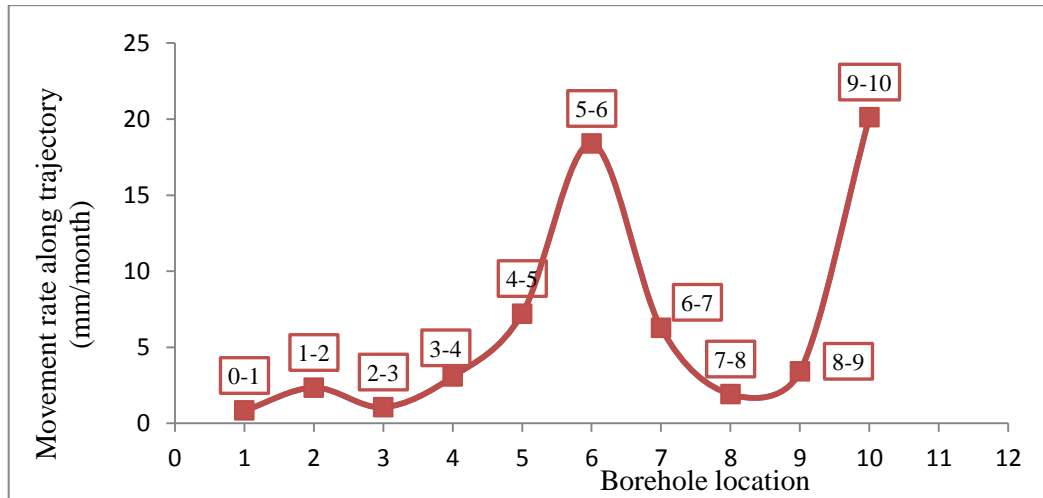


Figure 6.5 Magnitude of movement rate along trajectory at 135 m.

### 6.2.5 Shear Displacement at Shear Zone 1 (at 135 m)

The roof of the shear zone at 135 m had not only an absolute displacement, but also a relative shear movement over the shear zone floor at 135.5 m.

The shear distance is calculated by the Equation 6.2 (refer to Figure 6.6).

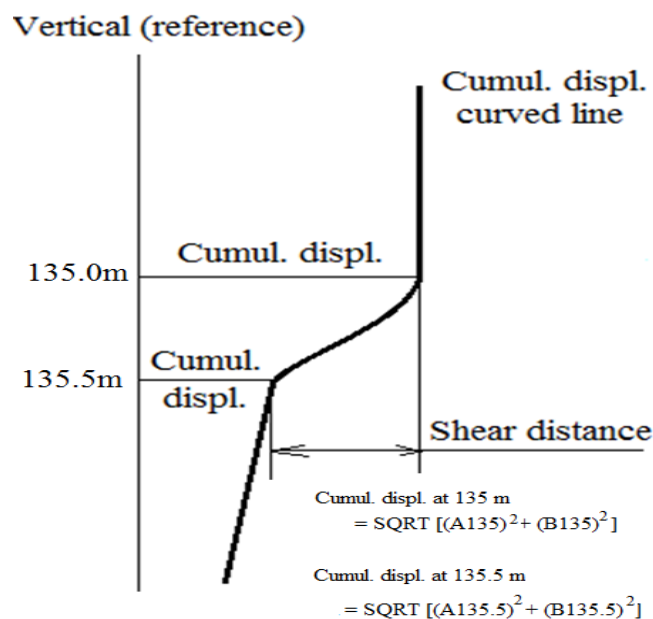


Figure 6.6 The shear zone and shear distance at 135 m depth for a survey.

**Shear distance at 135 m = Cumulative displacement at 135 m**

**- Cumulative displacement at 135.5 m (6-2)**

Shear deformations and the rates of the shear were calculated from Table 6.4 and summarised in Table 6.5, and were plotted in Figure 6.6. The movement at 135 m had a varying shear displacement from 0.2 mm to 2.7 mm. The maximum shear change of 1.3 mm was measured during stage 4-5. The maximum was 2.7 mm measured on 22/02/2011 (Table 6.5).

**Table 6.4 The cumulative displacements in the both A and B axes, and the resultant cumulative displacement at depth of 35 m and 135.5 m.**

	Cumul displ. at 135 m		Cumul. Displ. at 135.5 m		Resultant		Shear distance
	mm		mm		mm		mm
	A axis	B axis	A axis	B axis	at 135 m	at 135.5 m	
27/03/2009	0	0	0	0	0	0	0
27/05/2010	7.7	-9	7.65	-8.7	11.8	11.6	0.3
25/06/2010	8.25	-11.2	8.2	-10.9	13.9	13.6	0.3
31/08/2010	9.53	-13.19	9.47	-12.8	16.3	15.9	0.3
24/09/2010	10.43	-10.91	10.34	-10.7	15.1	14.8	0.2
14/10/2010	12.03	-15.44	12.51	-12.9	19.6	18.0	1.6
28/10/2010	18.49	-21.09	18.97	-18.7	28.0	26.7	1.4
30/11/2010	11.74	-19.63	12.2	-17.1	22.9	21.0	1.9
21/12/2010	11.69	-20.97	12.12	-18.5	24.0	22.1	1.9
3/02/2011	7.96	-17.66	8.39	-15.2	19.4	17.3	2.0
22/02/2011	1.86	-28.85	2.28	-26.2	28.9	26.3	2.7

**Table 6.5 Shear movement features of shear zone 1 at 135 m of the Borehole (BH).**

Date	Shear distance (mm)	Shear difference (mm)	Shear time (year)	Shear Rate (mm/month)	Move from to
27/03/2009					
27/05/2010	0.3	0.3	1.17	0.02	0-1
25/06/2010	0.3	0.1	0.08	0.05	1-2
31/08/2010	0.3	0.0	0.18	0.01	2-3
24/09/2010	0.2	-0.1	0.07	-0.11	3-4
14/10/2010	1.6	1.3	0.05	2.00	4-5
28/10/2010	1.4	-0.2	0.04	-0.41	5-6
30/11/2010	1.9	0.5	0.09	0.45	6-7
21/12/2010	1.9	0.0	0.06	0.04	7-8
3/02/2011	2.0	0.1	0.12	0.09	8-9
22/02/2011	2.7	0.6	0.05	0.96	9-10

Figure 6.7 shows the plot of the shear rate at 135 m. The shear was slow before section 3-4 (09/2010), and suddenly reached a peak of 2.0 mm/month on 4-5 (14/10/2010). The shear then slowed down in the following three surveys. The shear movement changed reversely in survey from 6-7 to 8-9, and then increased to a rate of 0.96 mm/month on section 9-10.

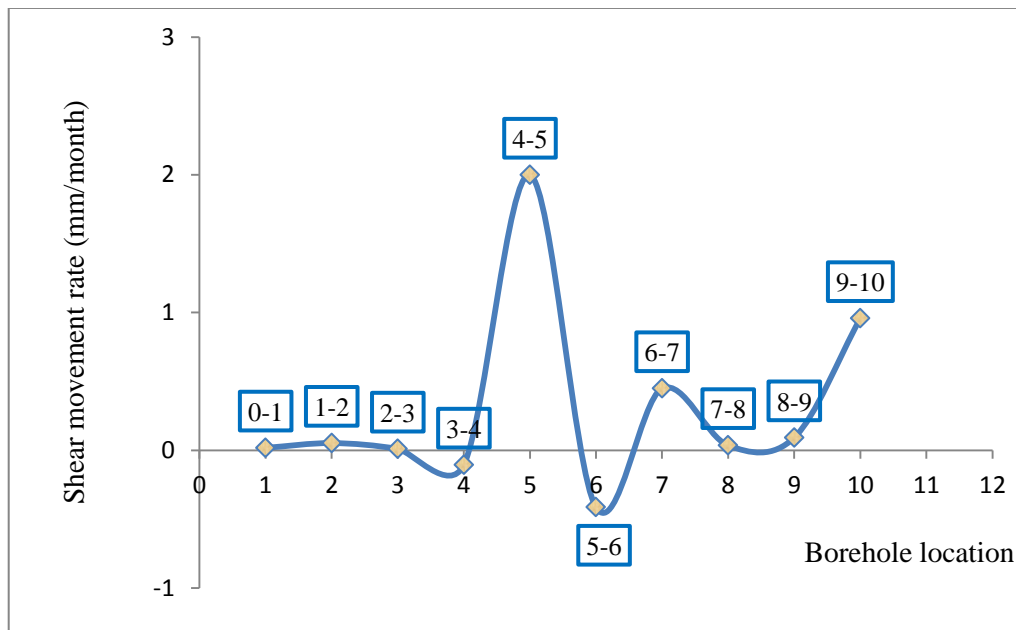


**Figure 6.7 Shear movement rate at 135 m for the 11 inclinometer surveys.**

Therefore, the shear zone 1 was a narrow shear zone with a thickness approximately 0.5 m from 135 to 135.5 m with small (<3 mm) shear deformation. The shear rates were not stable and not larger than 2 mm/month.

### 6.2.6 Strata Movement Trajectory at 166 m

The strata at 166 m also had an absolute displacement relative to the initial borehole shape. The movement at 166 m had a varying displacement from 3.7 mm to 12.8 mm. The movement features are listed in Table 6.6.

The movement trajectory of the Borehole at depth of 166 m for the 11 surveys are illustrated in Figure 6.8 showing that the strata movement at 166 m was a

nonlinear, dynamic movement. The results of distance changes between the continuous surveys along the trajectory were calculated from Formula 6.01 and are listed in Table 6.7.

**Table 6.6 Inclinator data and strata movement features at a depth of 166 m.**

Date	Displacement (mm)	Cumulative time (year)	A axis displ. (mm)	B axis displ. (mm)	Location No.	Bearing (degree)
27/03/2009	0	0	0	0	0	
27/05/2010	9.0	1.17	4.1	-8	1	87
25/06/2010	11.2	1.25	5.1	-10.1	2	87
31/08/2010	13.3	1.43	5.3	-12.2	3	83
24/09/2010	12.1	1.5	6.2	-10.4	4	91
14/10/2010	15.6	1.55	8.2	-13.3	5	92
28/10/2010	22.9	1.59	13.1	-18.8	6	95
30/11/2010	17.9	1.68	7.7	-16.1	7	86
21/12/2010	17.8	1.74	6.9	-16.5	8	83
3/02/2011	15.2	1.86	5.8	-14	9	83
22/02/2011	22.8	1.91	1.6	-22.7	10	64

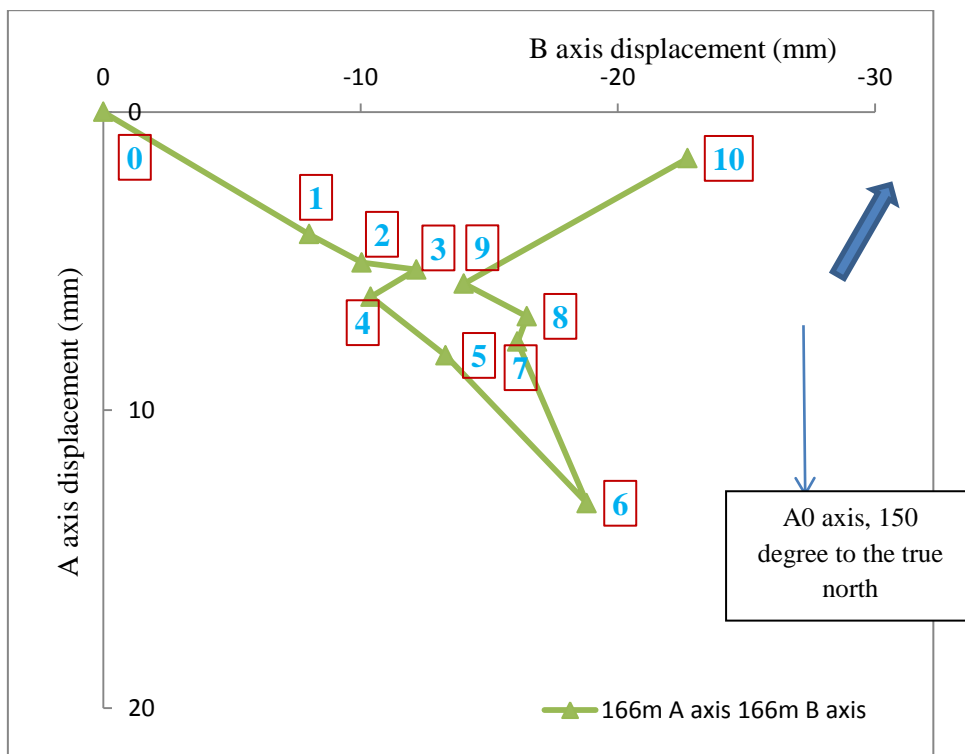


**Figure 6.8 Plan view of trajectory of the Borehole at 166 m.**

**Table 6.7 Movement distance, rates along the borehole trajectory at 166 m.**

Date	Location Number	Move from to	Distance (mm)	Time gap (day)	Time gap (year)	Movement Rate (mm/month)
27/03/2009	0					
27/05/2010	1	0-1	9.0	426	1.17	0.6
25/06/2010	2	1-2	2.3	29	0.08	2.3
31/08/2010	3	2-3	2.1	67	0.18	1.0
24/09/2010	4	3-4	2.0	24	0.07	2.5
14/10/2010	5	4-5	3.5	20	0.05	5.3
28/10/2010	6	5-6	7.4	14	0.04	15.9
30/11/2010	7	6-7	6.1	33	0.09	5.5
21/12/2010	8	7-8	0.9	21	0.06	1.3
03/02/2011	9	8-9	2.7	44	0.12	1.8
22/02/2011	10	9-10	9.7	19	0.05	15.2
Sum			45.6		1.91	

The movement rates along the trajectory (Figure 6.9) show an increase trend and the peak rate reached 15.9 mm per month in 5-6 section. The second highest 15.2 mm/month occurred on 9-10. Other movement rates remained less than 6 mm/month. The final measurement at No. 10 had a displacement of 22.8 mm to No.0 with a bearing of 64° to the true north (Figure 6.7).

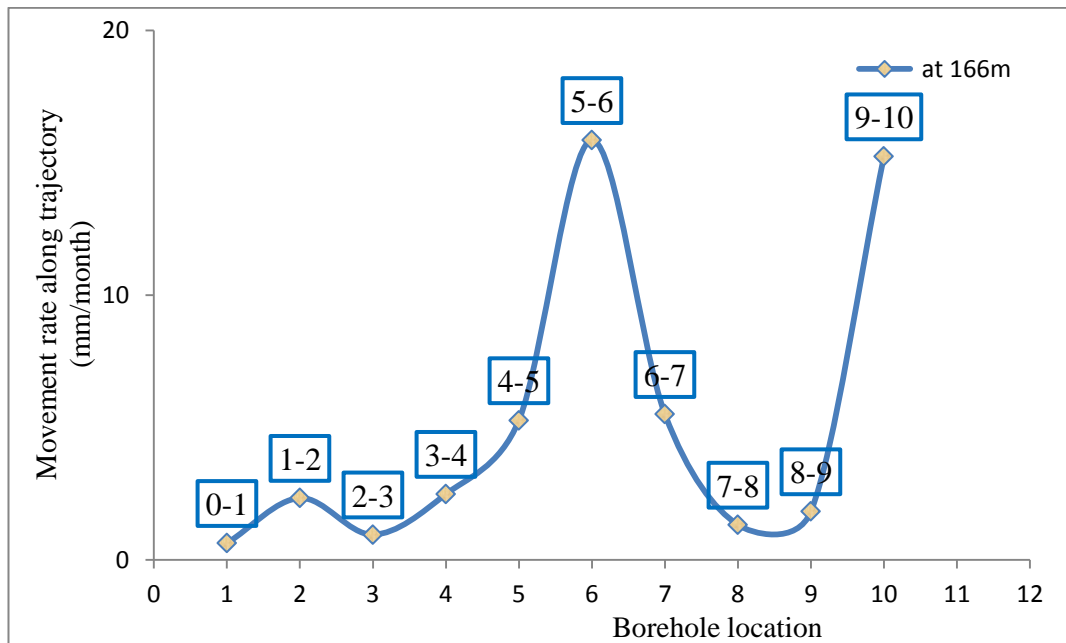


**Figure 6.9 Movement rates along the borehole trajectory between 11 surveys at 166 m depth.**

To conclude, the strata movement at a depth of 166 m was dynamic in both direction and rate, and had a rising trend. The largest strata movement rates reached 15.9 mm/month from number 5 to 6 measurements in 10/2010. The cumulative displacement along the trajectory was 45.6 mm over 1.91 years.

### 6.2.7 Shear Movement at 166 m

Shear zone 2 (at 166 m) had a thickness of 4 m from 166 to 170 m and occurred from 27/03/2009 to 22/02/2011 (Figure 6.3). The cumulative displacement in both the A and B axes, and the resultant cumulative displacement at depth of 166 m and 170 m are listed in Table 6.8.

**Table 6.8 The cumulative displacements in the both A and B axes, and the resultant cumulative displacement at depth of 166 m and 170 m.**

Survey		Cumul. displ., A axis		Cumul. displ., B axis		Resultant Cumul. Displ.	
Date	No.	mm	mm	mm	mm	mm	mm
		166 m	170 m	166 m	170 m	166 m	170 m
27/03/2009	0	0.0	0.0	0.0	0.0		
27/05/2010	1	4.1	3.8	-8.0	-4.5	9.0	5.9
25/06/2010	2	5.1	5.2	-10.1	-5.5	11.2	7.5
31/08/2010	3	5.3	5.4	-12.2	-6.0	13.3	8.1
24/09/2010	4	6.2	6.3	-10.4	-5.4	12.1	8.3
14/10/2010	5	8.2	6.8	-13.3	-3.2	15.6	7.5
28/10/2010	6	13.1	11.5	-18.8	-9.3	22.9	14.8
30/11/2010	7	7.7	7.5	-16.1	-7.3	17.9	10.5
21/12/2010	8	6.9	6.6	-16.5	-8.7	17.8	10.9
3/02/2011	9	5.8	5.8	-14.0	-10.0	15.2	11.5
22/02/2011	10	1.6	0.3	-22.7	-12.9	22.8	12.9

The shear distance is calculated by the Equation 6.3 (refer to Figure 6.10).

$$\text{Shear distance at 166 m} = \text{Cumulative displacement at 166 m} -$$

$$\text{Cumulative displacement at 170 m} \quad (6-3)$$

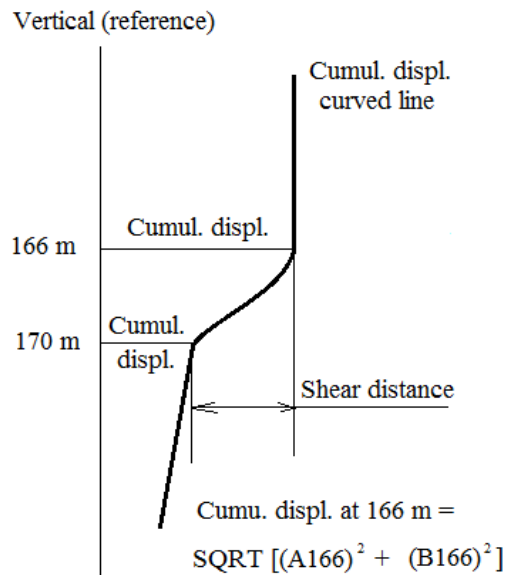


**Figure 6.10 The shear zone and shear distance at 166 m depth for one survey.**

Shear deformations and the rates of the shear were calculated and summarised in Table 6.9, and were plotted in Figure 6.11. The movement at 166 m had a varying shear displacement from 3.1 mm to 9.9 mm. The maximum shear change of 6.3 mm was measured during stage 9-10.

**Table 6.9 Shear movement features at depths of 166 m, calculated from Table 6.7.**

Survey	Shear from to	Shear distance	Shear change	Shear time	Shear rate
Date		mm	mm	month	mm/month
		between roof & floor per survey	between survey		
27/03/2009					
27/05/2010	0-1	3.1	3.1	14.04	0.22
25/06/2010	1-2	3.7	0.6	0.96	0.67
31/08/2010	2-3	5.2	1.4	2.16	0.64
24/09/2010	3-4	3.8	-1.3	0.84	-1.67
14/10/2010	4-5	8.1	4.3	0.60	6.40
28/10/2010	5-6	8.1	0.0	0.48	0.08
30/11/2010	6-7	7.4	-0.8	1.08	-0.69
21/12/2010	7-8	7.0	-0.4	0.72	-0.57
03/02/2011	8-9	3.6	-3.4	1.44	-2.29
22/02/2011	9-10	9.9	6.3	0.60	9.93

The largest shear rate of 9.93 mm/month occurred from 03/02/2011 to 22/02/2011.

The shear rate at other times varied between -1.67 to 6.40 mm/month.



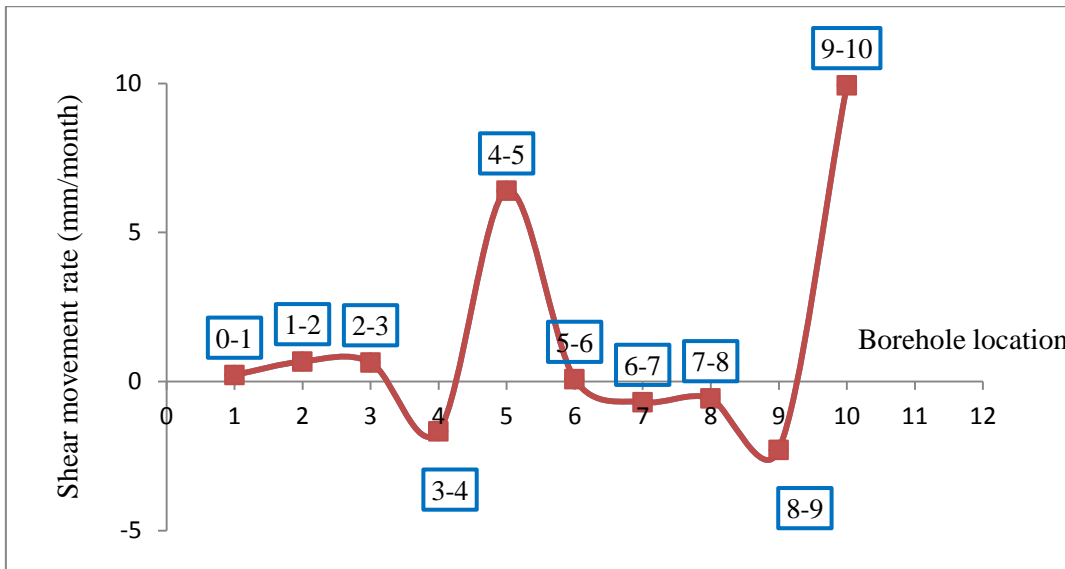


**Figure 6.11 Magnitudes of shear movement rate at 166 m depth.**

To conclude, shear zone 2 (at 166 m) was a major shear zone. Strata movement of shear zone 2 at a depth of 166 m was dynamic in both direction and rate. Shear movement rate at 166 m reached a peak of 9.93 mm/month measured during the last interval from number 9 to 10 measurements.

### **6.2.8 Creeping Zone from Surface to 115 m**

No shearing movement was apparent from the surface to 115 m; however this section was a creeping movement zone. The creeping extended to 115 m depth and the movement rate was greatest towards the top of the borehole. The inclinometer measurement ended at 1 m depth in casing in each survey, so the calculations for surface displacement and rates were all based on the readings at 1 m depth (Section 5.3.1). The creeping cumulative displacement and rates were calculated and summarized in Table 6.10. The final creeping cumulative displacement was 127.2 mm measured on 22/02/2011 having a bearing of 134° to the true north.

**Table 6.10 Surface movement features of the creeping zone (from surface to 115 m deep).**

Date	Cumul. Displ. (mm)	Cumul. time (year)	Displ. at 1 m A axis	Displ. at 1 m B axis	Location No.	Bearing (degree)
27/03/2009					0	
27/05/2010	48.9	1.17	42.5	-24.3	1	120
25/06/2010	49.9	1.25	42	-27	2	117
31/08/2010	55.5	1.43	48.9	-26.2	3	122
24/09/2010	61.4	1.5	58	-20.2	4	131
14/10/2010	67.7	1.55	65.5	-17	5	135
28/10/2010	86.6	1.59	81.5	-29.5	6	130
30/11/2010	96.8	1.68	93.8	-23.6	7	136
21/12/2010	103.5	1.74	98.8	-30.8	8	133
3/02/2011	121.1	1.86	119.1	-21.5	9	140
22/02/2011	127.2	1.91	122	-35.9	10	134

The trajectory with locations and bearings of the Borehole profile in creeping movement at the surface for the 11 surveys were illustrated in Figure 6.12 showing that the creeping movement was a nonlinear, dynamic movement.

Using the formula 6.01, the movement distance, rate and direction changes between the 11 continuous surveys on surface were obtained in Table 6.11.

**Table 6.11 Surface movement distance, rate along the trajectory (1 m depth).**

Date	No.	Move from to	Distance (mm)	Time gap (year)	Move rate (mm/month)
27/03/2009	0				
27/05/2010	1	0-1	48.9	1.17	3.4
25/06/2010	2	1-2	2.8	0.08	2.9
31/08/2010	3	2-3	7	0.18	3.1
24/09/2010	4	3-4	10.9	0.07	13.6
14/10/2010	5	4-5	8.2	0.05	12.3
28/10/2010	6	5-6	20.2	0.04	43.4
30/11/2010	7	6-7	13.7	0.09	12.5
21/12/2010	8	7-8	8.8	0.06	12.5
3/02/2011	9	8-9	22.4	0.12	15.3
22/02/2011	10	9-10	14.7	0.05	23.2
Sum			<b>157.6</b>	1.91	

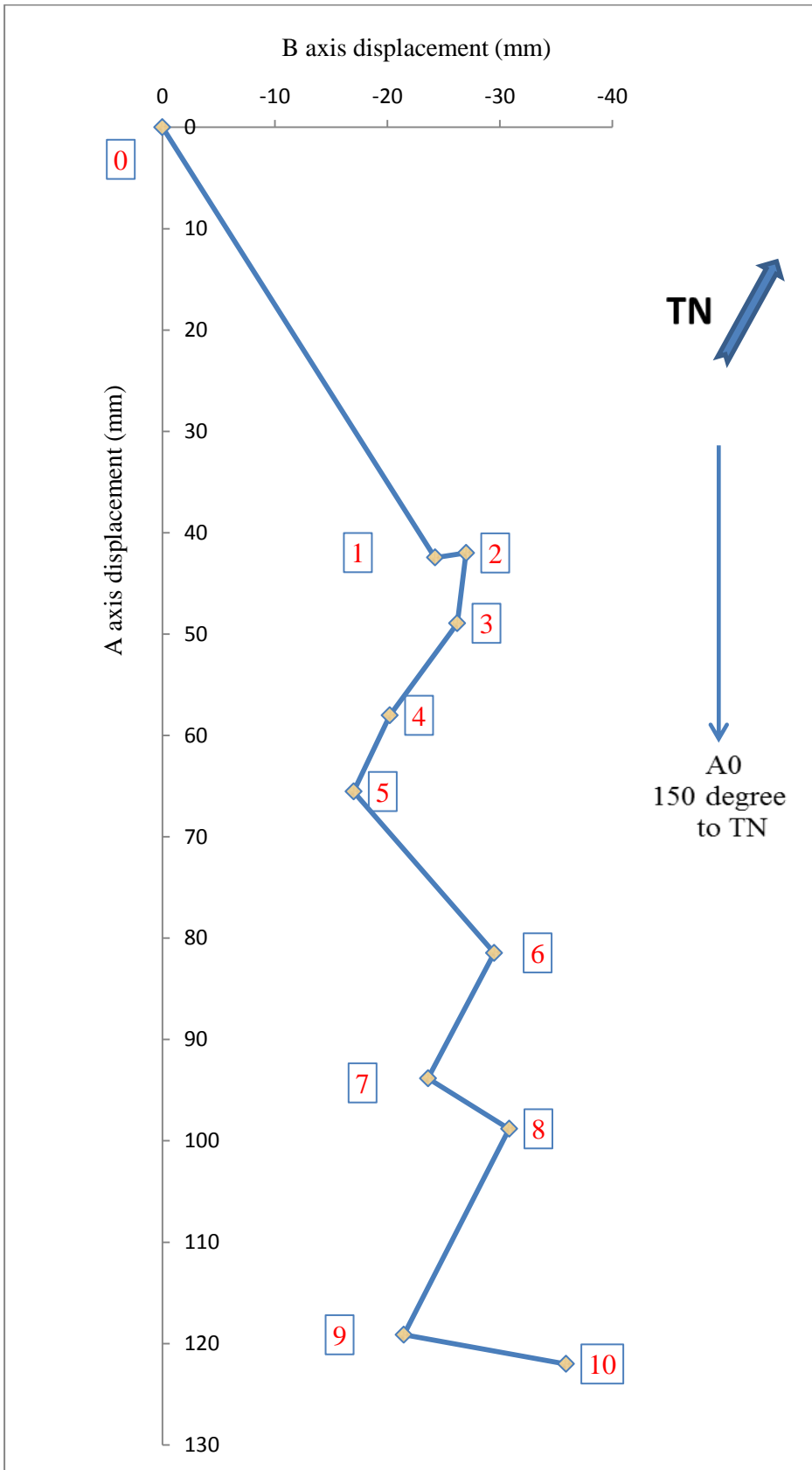


**Figure 6.12 Plan view of the movement trajectory of the Borehole opening at 1 m depth below the ground surface where the final measurement was taken.**

The magnitudes of the movement rate were plotted in Figure 6.13. The main trend of the rate of the surface movement fluctuated and rose. The rate started at 3.4 mm/month in stage 0-1, gradually increased to the maximum of 43.4 mm/month in stage 5-6, and then fell to approximately 12 to 15 mm/month in the following three survey stages. The rate reached 23.2 mm/month in the last section from number 9 to 10 measurements.

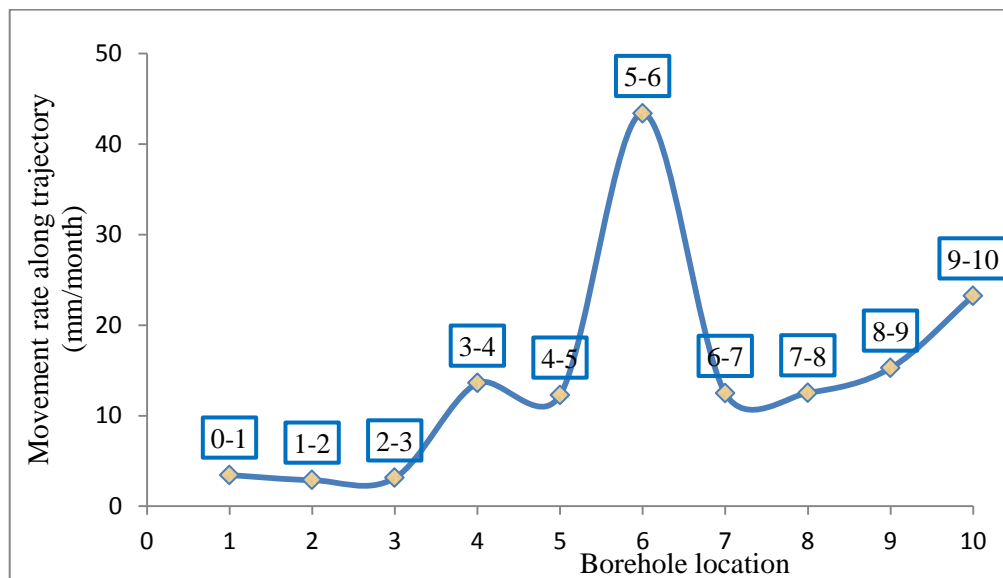


**Figure 6.13 Surface movement rate along the trajectory (at 1 m).**

Therefore, the movement of the creeping zone from 115 m to the surface was dynamic in both direction and rate, the Borehole opening showed a non-linear movement. The cumulative displacement along the trajectory was 157.6 mm or a total linear displacement from initial location (No.0) of about 130 mm over 1.91 years.

### **6.2.9 Comparison of Strata Movement at 1 m, 135 m, 166 m**

Three borehole trajectories at three depths (Figure 6.14) display some similarities between the three curved lines:

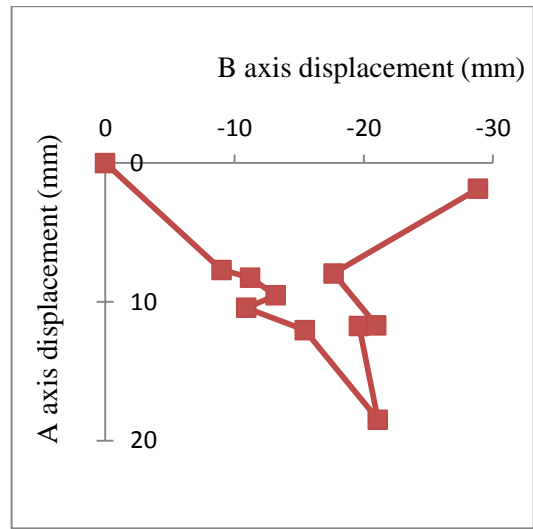
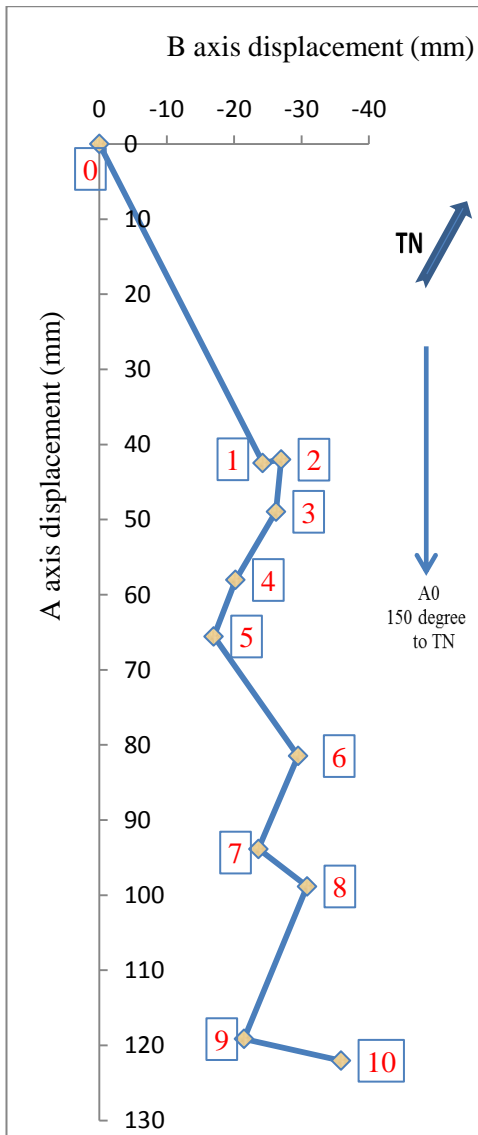
- They are all non-linear curved lines. The movements were all non-linear.

- Large similarity of the movement patterns at 135 m and 166 m were observed.
- The three movements from the borehole to the first location had a similar bearing direction to the true north at  $120^{\circ}$ ,  $101^{\circ}$ , and  $87^{\circ}$  in the 4<sup>th</sup> Cartesian.
- The trajectory at surface (1 m) had a near straight movement.
- From 0 to 7 the movement trajectories were in a near-straight line in three plots.

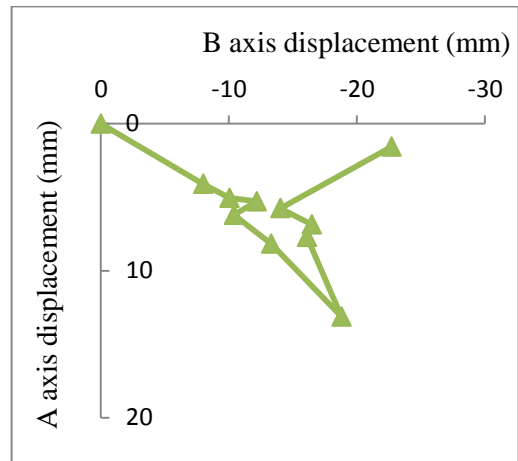
The major reasons causing the difference between trajectories at surface and trajectories at depth (two trajectories at 135 m and 166 m are similar) were estimated as:

- The inclinometer borehole was located on a steep slope, the collar opening was approximately 10 m above the gully on the east and west sides.
- There was a lake (the Lake Okowahao) south adjacent to the inclinometer borehole. The edge of lake water is approximately 70 m away from the borehole opening. The depth of the lake is unknown. The borehole opening might have a vertical distance of several tens of meters to the lake bottom.

Therefore it was estimated that after the initiation of the strata movement the lateral movement of the upper several ten meters section of the borehole above Lake Bottom may be controlled by the superposition of the movement down slope to the lake (situated south of the borehole) and by the induction of the extraction of the coal seam underground.



b, Trajectory at 135 m (from Figure 6.5).



a, Trajectory at 1 m (from Figure 6.13).

c, Trajectory at 166 m (from Figure 6.10).

**Figure 6.14 Comparison of the three movement trajectories of the Borehole at 3 depths (both axes have the same scale in each graph).**

The movement rate at the surface (1 m), 135 m and 166 m varied over time (Table 6.12).

Figure 6.14 and Table 6.12 show that the strata movement rate at the three depths fluctuated. The three varying patterns of the movement rates were similar, and reached peaks at the same measurement during measurements 5-6 and 9-10.

**Table 6.12 Movement distance and rate of the Borehole between measurements along movement trajectories, at depths of 1m, 135 m and 166 m, on 11 surveys.**

Survey Date	Borehole Location		Move distance (mm)			Rate (mm/month)		
	No.	Move from to	1 m (surface)	135 m	166 m	1 m (surface)	135 m	166 m
27/03/2009	0							
27/05/2010	1	0-1	48.9	11.8	9	3.4	0.8	0.6
25/06/2010	2	1-2	2.8	2.3	2.3	2.9	2.3	2.3
31/08/2010	3	2-3	7	2.4	2.1	3.1	1.1	1
24/09/2010	4	3-4	10.9	2.5	2	13.6	3.1	2.5
14/10/2010	5	4-5	8.2	4.8	3.5	12.3	7.2	5.3
28/10/2010	6	5-6	20.2	8.6	7.4	43.4	18.4	15.9
30/11/2010	7	6-7	13.7	6.9	6.1	12.5	6.3	5.5
21/12/2010	8	7-8	8.8	1.3	0.9	12.5	1.9	1.3
3/02/2011	9	8-9	22.4	5	2.7	15.3	3.4	1.8
22/02/2011	10	9-10	14.7	12.7	9.7	23.2	20.1	15.2
Average			16	6	5	creeping 14	shear 6	shear 5

The movement rate at 1 m reached a maximum of 43 mm/month in the 5-6 stage. The movement rate at 166m reached a maximum of 15.9 mm/month in the 5-6 interval. Then movement rate at 135 m reached a maximum of 20.1 mm/month at the end of the measurement period 9-10. All three movements showed a major trend of rising over time, and decreasing with depth, however the rate for 135 m depth was only slightly higher than at depth of 166 m (Figure 6.15).

The shear movements of the two shear zones at the depth of 135 m and 166 m also had different movement features in terms of directions and movement rates (Figure 6.16).

The shear rate at 166 m (shear zone 2) varied more remarkably than 135 m (shear zone 1), and the rate at 166 m was 3 times the rate at 135 m in stage 4-5, and 10 times in stage 9-10.

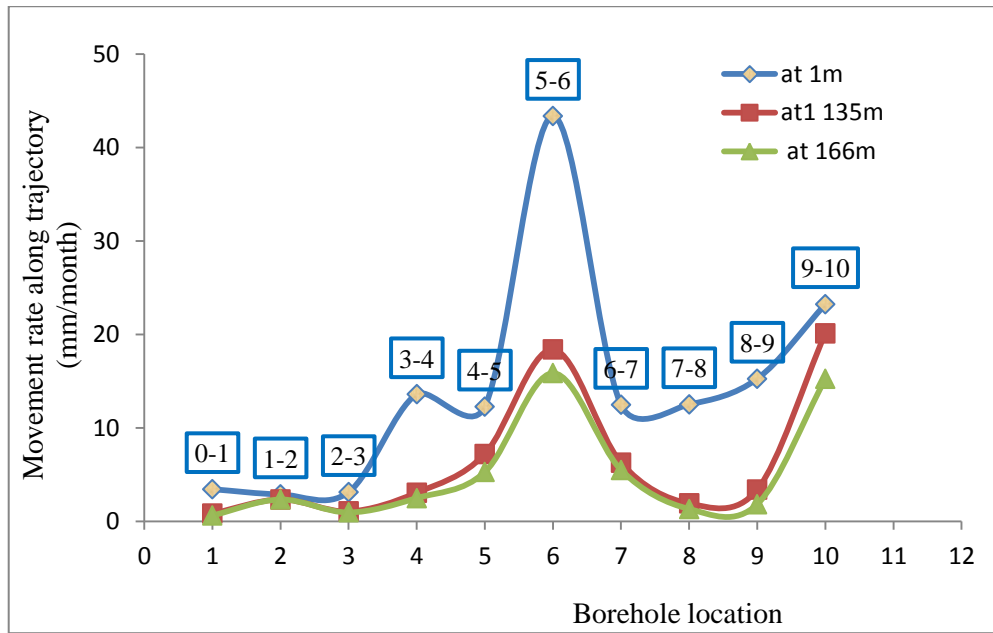


Figure 6.15 Comparison of strata movement rates along trajectory at 1m, 135 m and 166 m, all was showing a major trend of rising over time, and decreasing with depth.

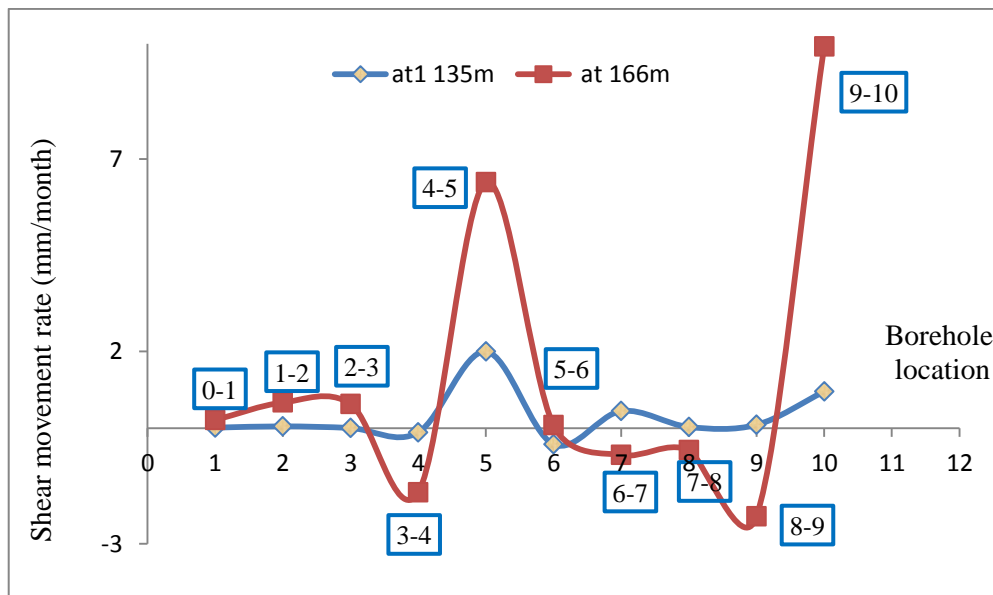


Figure 6.16 Comparison of the strata shear movement rates at 135 m and 166 m.

## 6.3 Extraction Advancing and Outlays

### 6.3.1 Introduction

In study of the correlation between underground extraction and strata movement, it is easy to identify the extraction features and the induced subsidence profile parameters and, to determine their correlation for a ‘one to one event’, that is, for



a separate extracted panel the subsidence induced is certain and clear, the subsidence parameters could be simply and clearly measured and determined. However in this inclinometer monitoring project, the underground extraction is continuous and linked in a time series, there is no obvious and complete panel boundary between monthly workings in relation to induction to the subsidence. Therefore, there is no clear match between the inclinometer measured dataset and the extraction outlays mined below. To determine the mechanism of the subsidence and the correlation between the extraction and displacement, the time relationship between the extraction completions, start of the pillar collapse, commencement of the subsidence, and the duration of the subsidence should be determined first.

### **6.3.2 Extraction Time Series Data**

The extraction map in the North 5 mining area (Figure 6.17) shows the approximate shapes of the monthly underground advancement of coal seam mining in 2009 -2011 and yearly mining outlays in 2005, 2006, 2007, and 2008. The monthly panel dimension had a typical average size of 45 m by 65 m. A length/width ratio of mined cells varied, but not by more than two, with an average ratio of 1.5.

In the northeast corner the blue and red profiles are the planned roadways. Around the Borehole, mainly in the southwest side, the green polygon patterns (marked with month and year) were the recently mined area.

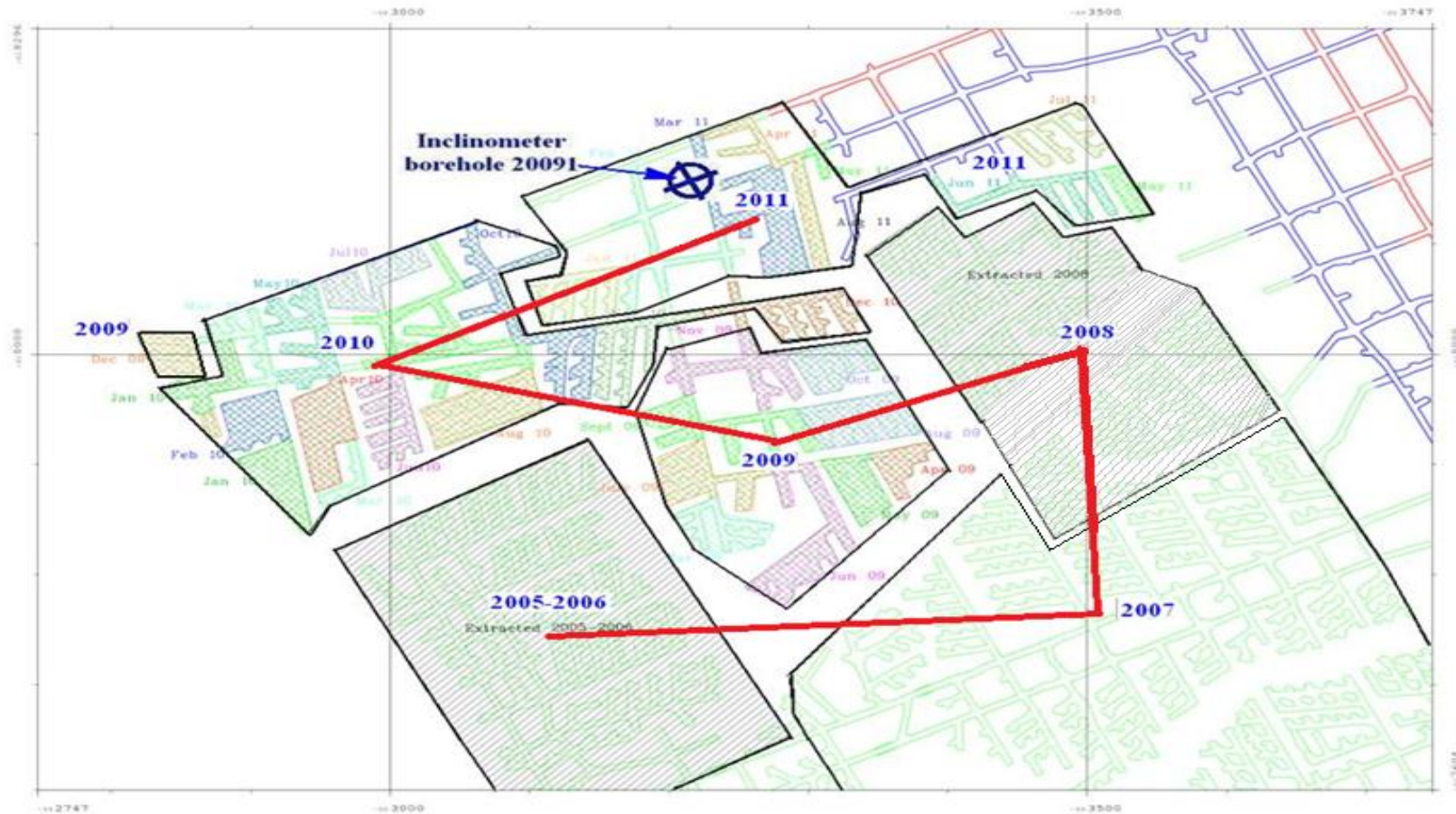


Figure 6.17 Extraction outlay and advancing direction from extraction centre in 2005 (2006) to extraction centre in 2011 showing an S shape of the advancement (adapted from Solid Energy, 2011a).

The map (Figure 6.17) represents an area of 1000 m long by 692 m wide. Within this 692 000 m<sup>2</sup> area extraction was undertaken in a large S shape pattern during 2005 to 2011. Within each year the monthly extraction was also not in a direct straight line order under a harmonic mining method.

According to statistical data of the angle of draw in Huntly East Mine by Kelsey (1986) and SCT (2003 to 2010), the angles of draw had a range between 37<sup>0</sup> and 63<sup>0</sup> for the 5 mm subsidence contour in the Huntly East Mine (Figure 6.18).

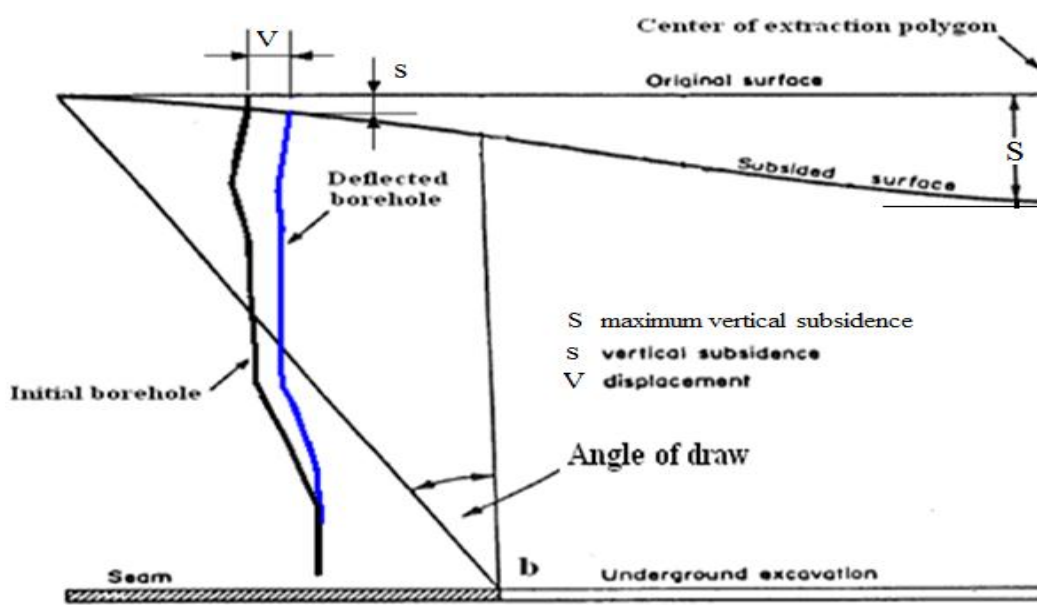


Figure 6.18 Theoretical diagram showing inclinometer borehole and the scope of subsidence (from Kelsey, 1986).

Therefore, only the extractions that had a distance within 500 m from the extraction edge to the borehole were chosen for analysis ( $250 \text{ m} * \text{TAN} (37^{\circ} \sim 63^{\circ}) = 188\sim 491 \text{ m}$ , there, 250 m is the average depth of the coal seam). The mapped extraction area (1000 m x 692 m) in Figure 6.17 is larger than 500x500 m, and therefore, conservatively meets the theoretical area to obtain a measureable effect on the borehole as a result of the coal extraction.

### 6.3.3 Simplification of the Multiple Extraction Locations

There might be several extraction locations in a month, i.e. there were two extraction locations in January 2010, separated by the polygon that was extracted in February 2010 (Figure 6.17, the left corner). To analyse correlation between extraction and movement, multiple locations for each month were summarised into one by the method of Equilibrium of the Centre of Gravity (Texas A&M University, 2011). Extraction data are summarised monthly in Table 6.13 from 2008 to 2011 and displayed in Figure 6.19. Only yearly extraction data from 2005 to 2007 was available. The distances of the extracted area centre to the Borehole are mostly less than 500 m except data in 09/2008, 08/2008 and 04/2008.

**Table 6.13 The area, distance, and bearing of the summated monthly extraction cells, average seam thickness 7 m (Solid Energy, 2011a).**

Coal seam extraction cells				Coal seam extraction cells			
Time	Centre Distance* m	Area Extracted m <sup>2</sup>	Centre Azimuth degree	Time	Centre Distance* m	Area Extracted m <sup>2</sup>	Centre Azimuth degree
Jul-11	261	1445	83	Sep-09	224	2679	174
Jun-11	284	1730	93	Aug-09	252	3031	149
May-11	241	956	80	Jul-09	267	2319	180
Apr-11	77	1897	79	Jun-09	346	3090	166
Mar-11	73	3844	120	May-09	307	1711	156
Feb-11	40	1920	194	Apr-09	298	1093	150
Jan-11	131	1701	217	Mar-09	319	1956	176
Dec-10	147	2167	147	Feb-09	0	0	0
Nov-10	170	1886	196	Jan-09	0	0	0
Oct-10	179	3223	228	Dec-08	298	1751	115
Sep-10	239	3789	234	Nov-08	286	1332	133
Aug-10	262	3233	215	Oct-08	272	1854	122
Jul-10	245	2137	248	Sep-08	517	2423	127
Jun-10	309	1907	224	Aug-08	623	1004	130
May-10	304	2309	241	Jul-08	605	1136	128
Apr-10	349	2799	229	Jun-08	498	1797	124
Mar-10	257	2447	223	May-08	461	2667	133
Feb-10	385	1841	234	Apr-08	543	1450	134
Jan-10	392	3389	228	Mar-08	447	2342	132
Dec-09	404	1788	245	Feb-08*	447	2022	132
Nov-09	171	2243	169	Jan-08*	457	2340	139
Oct-09	197	1852	149	<b>Average</b>	285	2052	159

\*Not included in the average.

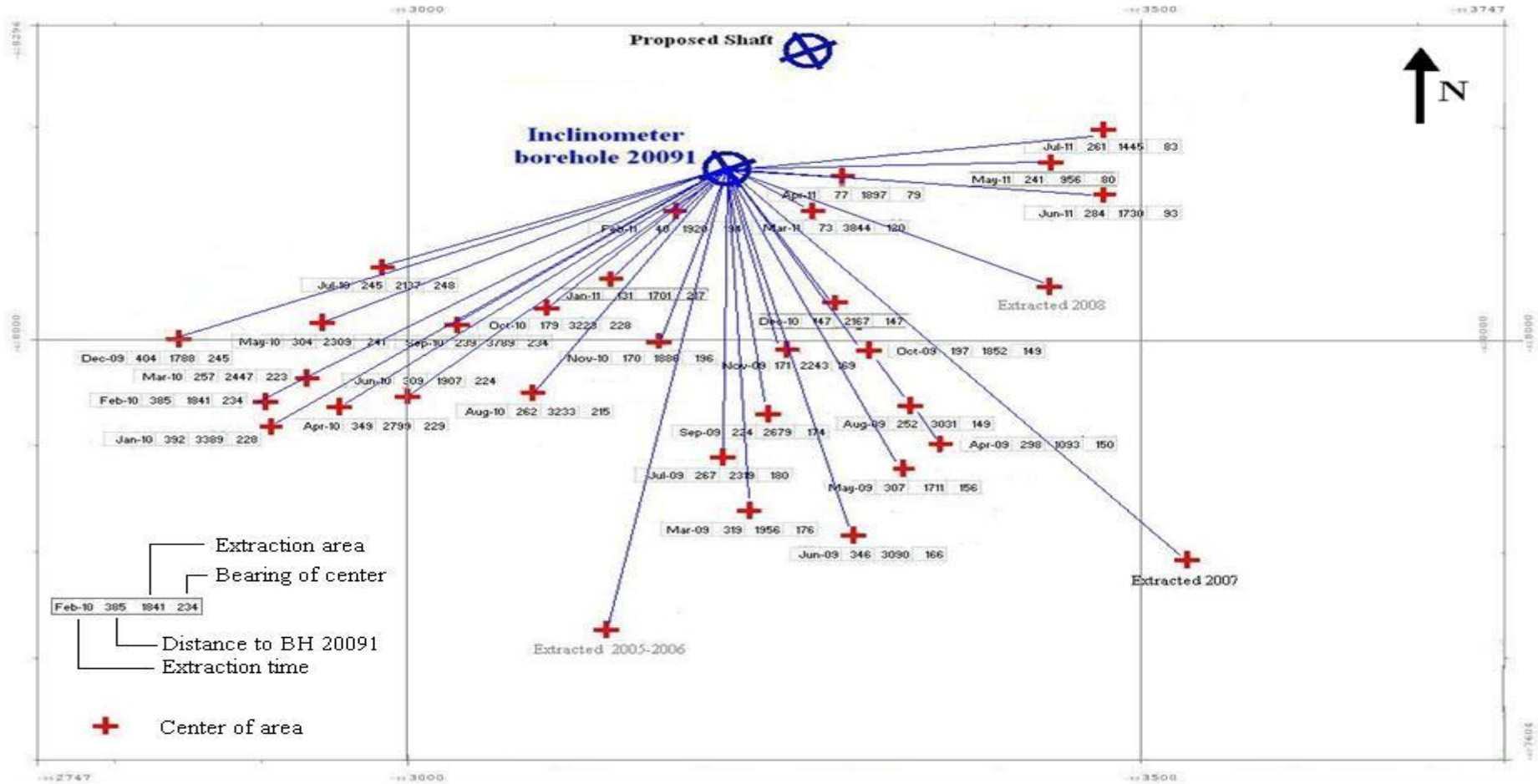


Figure 6.19 Extraction centres determined by simplifying the monthly multiple locations of extraction (adapted from Figure 6.17).

## 6.4 Movement of the Borehole Opening

Ground surface reduced level was surveyed by GPS for monitoring the ground vertical movement that was contributed to the underground coal extraction. The GPS survey data on the inclinometer borehole ground Reduced Level (RL) change is listed in Table 6.14. GPS had an accuracy of  $\pm 40$  mm for vertical measurement.

**Table 6.14 GPS data on the borehole ground reduced level (m) (from Solid Energy, 2011a).**

Survey No.	Date surveyed	Ground RL (m) ( $\pm 40$ mm)	Drop/raise (mm) to reference	Drop/raise (mm) delta	Time difference (day)	Subsiding rate (mm/month)	Survey Interval
1	27/09/2009	18.425	0	0	0	0	
2	04/11/2010	18.478	53	53	403	4	1-2
3	24/11/2010	18.499	74	21	20	31	2-3
4	10/01/2011	18.434	9	-65	47	-41	3-4
5	28/02/2011	18.428	3	-6	49	-4	4-5
6	28/03/2011	18.416	-9	-12	28	-13	5-6
7	15/06/2011	18.393	-32	-23	79	-9	6-7
8	10/08/2011	18.352	-73	-41	56	-22	7-8
9	21/09/2011	18.380	-45	28	42	20	8-9

Following with the underground extraction the casing top level was fluctuating (Figure 6.20). The maximum range in vertical movement from the peak on 24/11/2010 to the bottom of the curved line on 10/08/2011 was 147 mm.

The drainage system in this region is maintained through the operation of two active pump stations to maintain an artificially lowered groundwater level beneath the alluvial terrace and to provide drainage of stormwater (Golder Kingett Michell, 2007) (Section 3.3.3). Therefore the groundwater level is relatively stable, thus the ground surface reduced level is unlikely to be influenced by hydrological factors. The ground reduced level varied with the composite effects of the underground extraction as major factor and the seasonal temperature change as the minor factor

because the seasonal vertical settlement from natural causes is likely to be less than 5 mm (Kelsey, 1986).

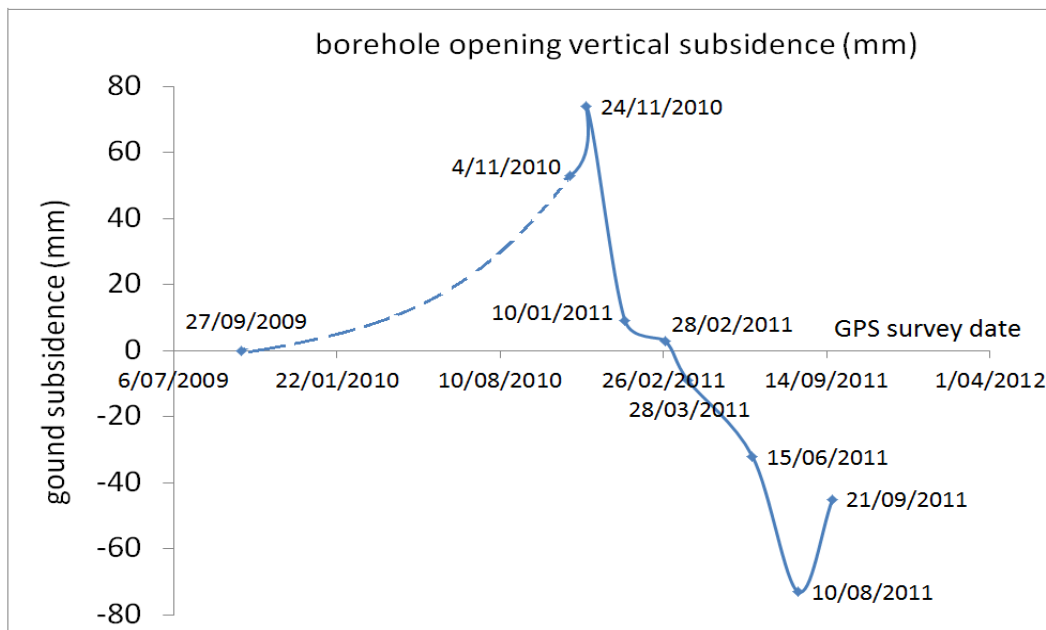


**Figure 6.20 Main trends of ground vertical movement (to reference) at collar opening, measured using GPS.**

## 6.5 Movement Zones vs. Stratigraphy

### 6.5.1 Introduction

There may be a correlation between the geological features with the movement zones observed from the Borehole inclinometer monitoring; for example, creeping movement normally may occur in the soil layers or weak rock; shear zones generally exist in bedding or joints where the movement of the overlaying strata slide over the lower strata because the bedding plane separates beds and is an area easily fractured. The thickness of a shear zone may vary from less than one meter to several meters (Section 4.3.2).

The geophysical Acoustic log in small scale from surface to 250 m is displayed in Figure 6.21 with density, Gamma grade and Acoustic Amplitude over depth (Solid Energy, 2009). From the surface to 128 m there was no obvious bedding



plane, but from 130 to 250 m the bedding was well developed. The darker colour in Acoustic Amplitude over depth indicates a longer Acoustic travel time representing joints or beddings.

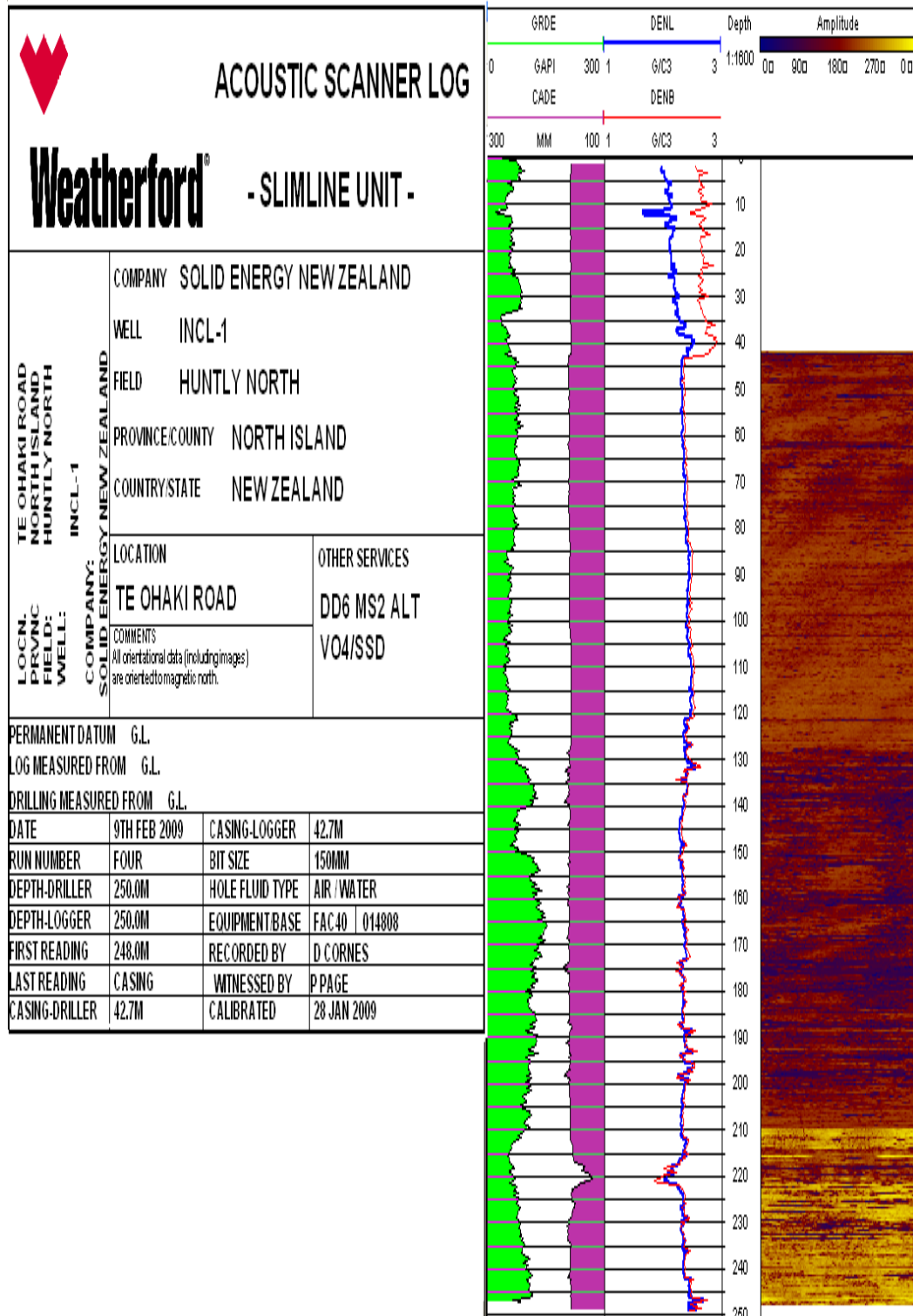


Figure 6.21 The whole geophysical log from surface to 250 m taken when borehole was installed in 2009 (from Solid Energy, 2009d).



## 6.5.2 Geophysical Log from 43 to 135 m

The geophysical log from 43 to 135 m is displayed in Figure 6.22 with density, grade and Acoustic Amplitude over depth. There is no obvious bedding or jointing in this section. The creeping movement occurred from 115 m upwards to surface. Section from the surface to 43 m is sealed with  $\Phi 125$  mm steel casing, no geophysical logging available.

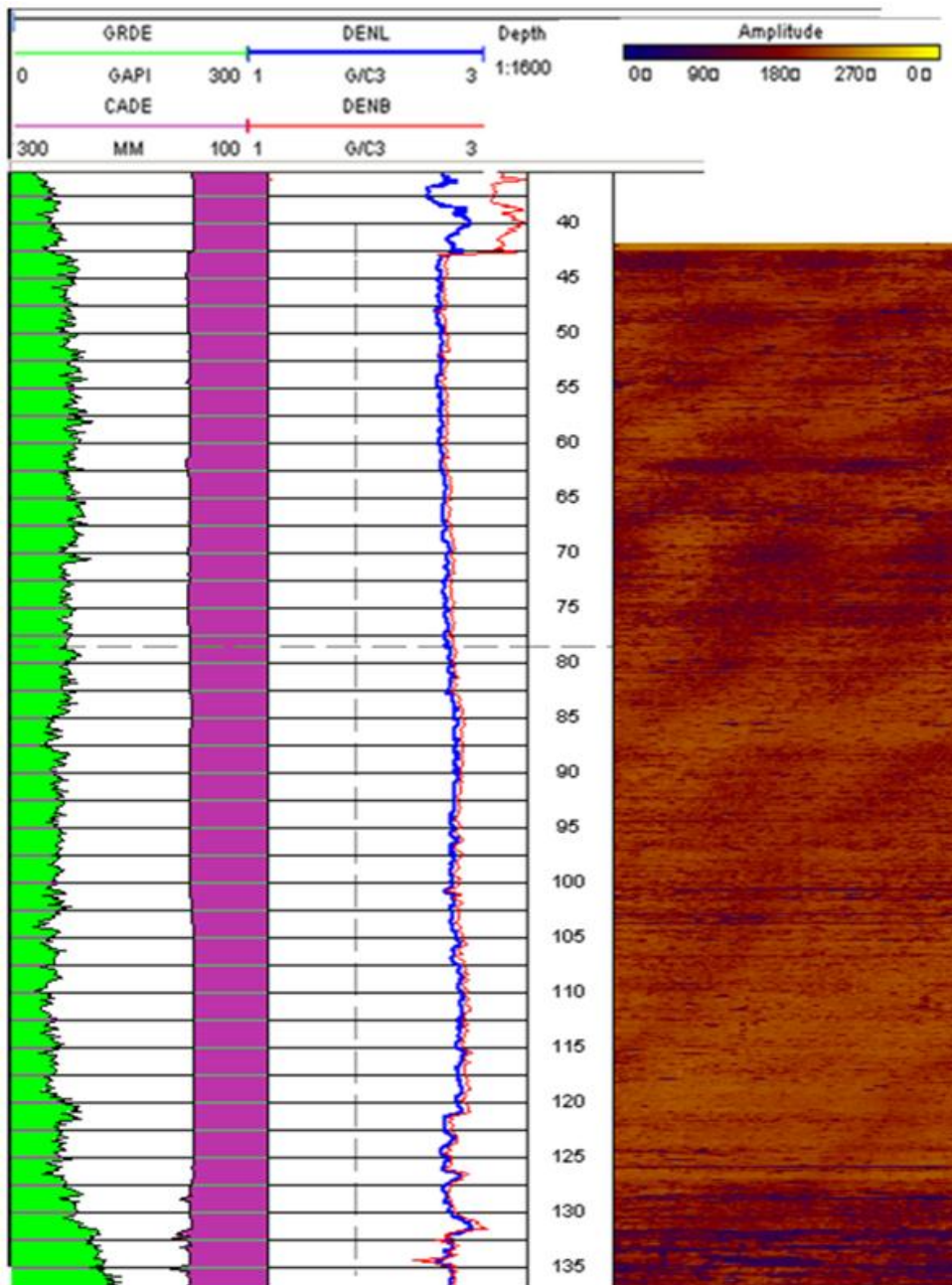


Figure 6.22 Geophysical log from 40 to 135 m, showing no bedding planes from 115 m to surface (from Solid Energy, 2009d)

### 6.5.3 Geophysical Log from 120 to 145 m

The geophysical log from 120 to 145 m is displayed in Figure 6.23 with density, grade and Acoustic Amplitude over depth. There exists near-horizontal bedding at 135 m; its thickness is less than 0.5 m. The bedding dips at 26.6 degrees; azimuth of dip is 288.1 degrees, that is, the bearing is 266.8 degrees (Solid Energy, 2011a). The shear zone 1 at 135 m coincided well with the bedding at 135 m.

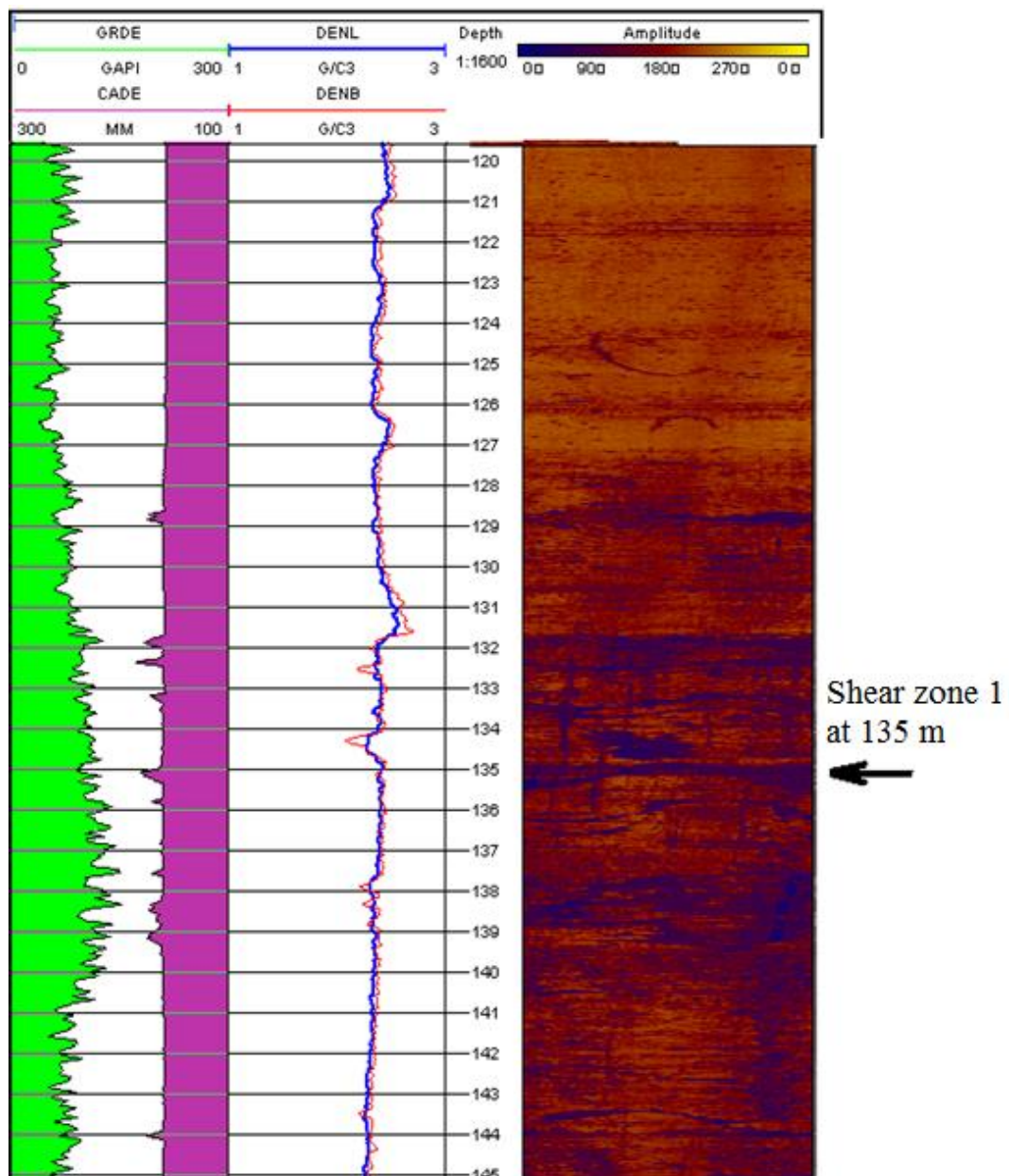


Figure 6.23 Geophysical log from 120 to 145 m showing the bedding plane at 135 m (Solid Energy, 2009d).

### 6.5.4 Geophysical Log from 155 to 182 m

The geophysical log from 155 to 182 m is displayed in Figure 6.24 with density, grade and Acoustic Amplitude over depth.

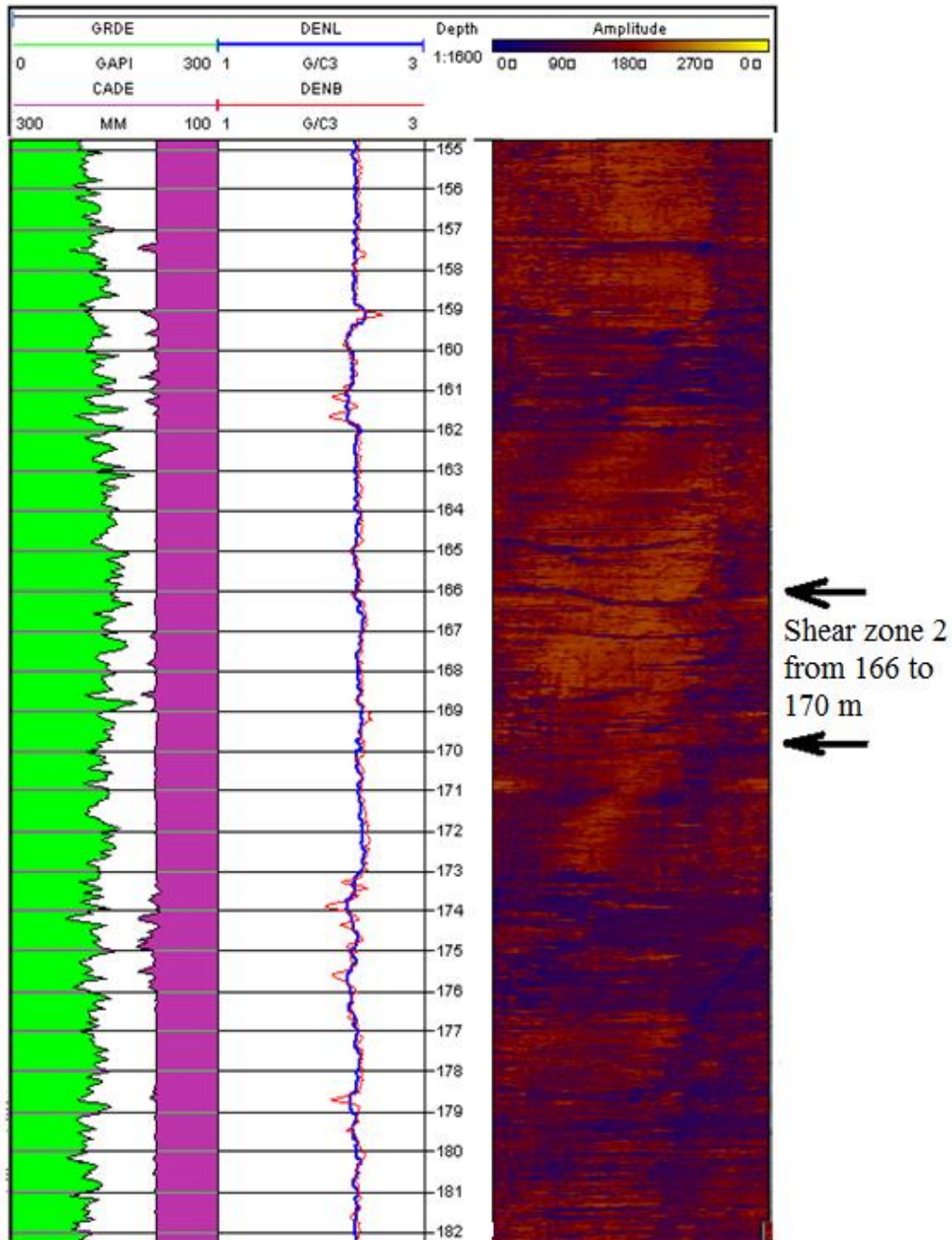


Figure 6.24 Geophysical log from 155 to 182 m showing the bedding planes at 166 to 170 m (Solid Energy, 2009d).

There are two near-horizontal bedding planes from at 166 and 170 m where the Sear zone 2 took place and had a 4 m thickness. The shear zone 2 coincided well with the bedding structure.

## 6.6 Discussions

### 6.6.1 Movement Data of the Borehole Opening

In assessing the GPS data for the height of the top of the inclinometer borehole the measurement error needs to be taken into account and corrected through the calculation of difference between measurements. On the error analysis equation for addition and subtraction  $x = a + b - c$  (Widener University, 2012), the uncertainty in result will be:

$$s_x = \sqrt{s_a^2 + s_b^2 + s_c^2 + \dots}$$

Where, x: result of calculation

a, b & c: numbers used for calculation

$s_x$ : uncertainty in result

$s_a$ ,  $s_b$  &  $s_c$ : uncertainty in numbers used for calculation

Therefore, the uncertainty in calculating the raise and drop in Table 6.14 from GPS data will be:

$$s_x = \text{SQRT } ((\pm 40)^2 + (\pm 40)^2) = \pm 56.7 \text{ mm}$$

There were only two (out of eight) results larger than 56.7 mm in Table 6.14. Therefore, GPS data of the Borehole opening were insufficient for analysing the

vertical movement. More datasets were required from continuous monitoring to determine the strata vertical movement.

However, the available data initially showed that the strata might have heaved and subsided following the extraction of the underground coal seam. The analysis of correlation between the extraction and vertical subsidence needs more data from further monitoring work.

### 6.6.2 Principle of the Trajectory of Borehole Movement

Figure 6.25 shows the principle of the trajectory of borehole movement in an intersection plane at a depth in the harmonic mining method (Section 2.2.5). The data suggest that when the extraction location changed the induced subsidence varied in its direction and magnitude.

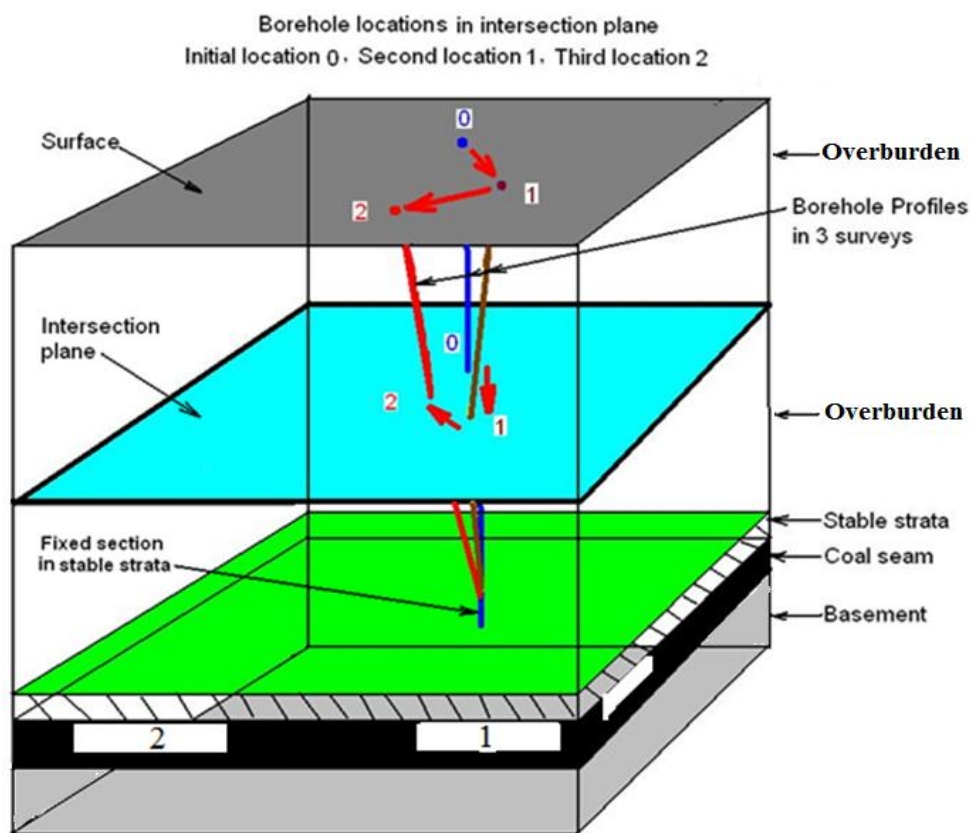


**Figure 6.25** The trajectory of the borehole movement in an intersection plane at a depth by the borehole locations from inclinometer measurements following extraction location change.



The model described by Figure 6.25 assumes that the base of the borehole has not moved. It should be recognised that this may not be the case in our situation and there is some potential for movement in the lower strata which may have influenced the veracity of the subsequent calculations.

### **6.6.3 Main Borehole Observations and Movement Interpretation**

In sections 5.5.1, three major events, such as probe kicking, probe jamming, borehole water level changes, were discussed and analysed. Those events were mostly to have the related connections with the inclinometer measurements, and influence the veracity of the interpretation results of the strata movements. For example, the extreme checksum readings occurred at the joints or  $\pm 0.5$  m nearby joints and or at a depth where the casing deformation rose to a certain level.

The three issues may be resulted from one casing rupture problem at a depth of about 38 m in the borehole. At first, the casing at around 38 m might have a large lateral differential movement in the weak and porous grout cement, which was induced by the vertical stretching and compression due to the differential layer subsidence and upsidence. Consequently, the significant differential deformation at around 38 m contributed to the tangled cumulative displacement plot before 03/02/2011, then the casing rupture occurred when deformation increased, but was small leading to groundwater out the enclosed borehole entering the casing, raising water levels observed from 03/02/2011; meanwhile the rupture resisted the probe traversing or even kicked the probe leading to the occurrence of the two abnormal surveys on 12/11/2010 and 18/01/2011. As the rupture increased to a level, the probe was not able to traverse through and got jammed on 11 March 2011. The rupture kept increasing and became large enough to let the probe shift

between A and B grooves in the casing in the trials of dummy probe and lowering on 02/06/2011.

Nearly 2/3 of the mining area had been extracted around inclinometer borehole up to March 2011 when the probe traversing was stopped at 38.53 m. The data measured might be approximately half of what the inclinometer research project should get.

It is expected that more measurements may yield more accurate interpretation results of strata movement; the repetition of inclinometer measurement can provide more accurate and reliable results.

## **6.7 Conclusions**

This chapter has interpreted the inclinometer data into strata movement. The zones of the movement were determined using incremental displacement and resultant cumulative horizontal displacement plots.

- There were three movement zones presented, two 'shear zones' from 135.0 to 135.5 m and from 166.0 to 170 m, and one 'creeping zone' from surface (1 m) to 115 m.
- The borehole movement was presented using the trajectory of the intersection of the borehole at depths of surface, 135 m, and 166 m.
- The trajectories of the borehole movement show that the movement was non-linear, and the trajectories varied with depth, but showed a similar overall pattern.
- From 0 to 115 m, the creeping started at a depth of 115 m and was highest near the surface. The maximum creeping rate was 43 mm per month

measured on 28/10/2010. It is clearly shown that the displacement rate had a rising trend and fluctuated.

- From 135.0 to 135.5 m there was a thin, minor, shear zone with the highest shear rate of 2.0 mm per month measured on 14/10/2010.
- The shear zone at depths from 166 to 170 m was the major shear zone seen in the inclinometer data with a largest shear rate of 9.93 mm/month measured on 22/02/2011.
- The cumulative displacements along the trajectory of borehole movement were 58.3 mm at 135 m depth, 45.6 mm at 166 m depth, and 157.6 mm near the ground surface (1 m depth). However, the cumulative displacements between the initial measurement (No.0, undertaken on 29/03/2009) and the final measurement (No. 10, undertaken on 22/02/2011) were 29 mm at 64<sup>0</sup> (ENE) at 135 m depth, 22.8 mm at 64<sup>0</sup> (ENE) at 166 m depth, and 127.2 mm at 134<sup>0</sup> (ESE) at 1 m depth. So the casing top was moving towards general direction of coal extraction, but at depths of 135 m and 166 m the overall movement was towards ENE. The detailed discussion is undertaken in Chapter 7 using the comparison between the borehole movement trajectories and the extraction trajectory.
- The trajectory of the extraction advancing was not in a straight line. Correspondingly the trajectory of the borehole lateral movement was also a non-linear movement having a varying movement rate and direction.
- The two shear zones were located on strata bedding planes of the Te Kuiti formation. The creeping movement occurred in the soft Tauranga formation and across the upper Te Kuiti formation.
- The ground at the borehole location might have vertical raise and drop movement according to insufficient data. The maximum range in vertical



raise and drop might be 147 mm from March 2009 to February 2011.

Further monitoring work was required for analysing the correlation between the extraction and vertical subsidence.

To conclude, the three movement zones had different movement directions and rates along depth and over time. Therefore the three zones had different movement behaviours over depth which may have been responding to dynamic extraction locations in the mining operation.

# **Chapter 7 Model Development and Numerical Modelling of Strata Movement**

## **7.1 Introduction**

This chapter firstly determines the delay times between the extraction and the subsidence by using the monthly extraction areas that correspond to the measured strata movement. Regression equations are then developed indicating the correlations between the extraction distance and the lateral movement, allowing prediction of how close the extraction edge can be allowed to approach the proposed shaft to retain control of subsidence.

This chapter then defines the input parameters for numerical modelling using Phase2 (Section 4.4). The regression equations were verified and corrected in the numerical modelling, and developed into three new modelled equations that might be used to calculate the cut-off distance between the extraction and the proposed shaft.

## **7.2 Model Development of Strata Movement**

### **7.2.1 Introduction**

Lateral and vertical movements of the casing in the Borehole were possibly the result of subsidence induced from the nearby multiple extraction locations within the angle of draw in the corresponding mining period. The resultant ground movement was the superimposition of the subsidence resulting from scattered locations of the extraction within a certain period of time.

### **7.2.2 Delay Time between Extraction and Subsidence**

Subsidence doesn't arise at the same time as extraction advances because the pillars remain in place for some time; after the pillars collapse the caving of the head-rock and overburden also take time to spread upwards to the surface. Therefore, the total delay time between completion of extraction and completion of subsidence is the sum of the pillar standing time plus the pillar collapse time plus the time for layers to carve up to the surface. We don't know this actual delay time for the inclinometer project area.

It has been observed by several authors (Mitchell, 2007; Solid Energy AEE, 2007) that 90% of the subsidence takes place during the first 6 months from the first observation to the finish of subsidence at the surface. For simplifying the study, this thesis assumes that 100% of subsidence develops within the first 6 months following initiation of surface subsidence. Kelsey (1986), in a study of the Huntly East Coalmine around the NZED Hotel, commented on the total delay time between panel extraction completion and observed finish of surface subsidence, of approximately 1 to 2 years. This also suggests a likely delay time of about 6 to 18 months between extraction finish to the first observation of subsidence on the ground surface.

Table 7.1 illustrates the principle of the time relationship between extraction and subsidence in a sample of 18 months delay time.

**Table 7.1 Theoretical time relationship between extraction and lateral subsidence that would be expected in May 2010 following extraction commencing in November 2008, (i.e. Assumed delay time was 18 months).**

Extraction month	Hysteresis time (month)						Subsidence start	Subsidence development			Subsidence expected in May-10	Contribution to May 2010 subsidence		Assumed effective volume m <sup>3</sup>
	12 months							6 months				weight	%	
Nov-08 1000 m <sup>3</sup>	→						Nov-09	→			yes	6/6	100	1000
Dec-08 1000m <sup>3</sup>	→						Oct-09	→			yes	5/6	83.3	833
Jan-09 1000m <sup>3</sup>	→						Jan-10	→			yes	4/6	66.7	667
Feb-09 1000m <sup>3</sup>	→						Feb-10	→			yes	3/6	50	500
Mar-09 1000m <sup>3</sup>	→						Mar-10	→			yes	2/6	33.3	333
Apr-09 1000m <sup>3</sup>	→						Apr-10	→			yes	1/6	16.7	167
May-09 1000m <sup>3</sup>	→						May-10	→			no	0	0	0
Assumptions:														
100% subsidence occurred in the first months from observation of subsidence, and subsidence has an even speed in the 6 months.														
Therefore, subsidence measured in May 2010 was induced by the extraction during Nov 2008 and April 2009.														
Monthly extraction magnitude from Nov 2008 to May 2009 was all 1000 cubic meters as assumption for this example.														
											SUM	3.5	350	3500

For a theoretical movement in May 2010, it is estimated that the subsidence would have started 6 months earlier (in November 2009); the extraction would have finished 18 months before May 2010 if the time delay of subsidence is one year and a half. That means the subsidence induced by the extraction earlier than 18 months before May 2010 was completed. Subsidence induced by the extraction later than 12 months before May 2010 has not started. Therefore, to simplify the analysis and interpretation work, extractions before November 2008 and after April 2009 were assumed not to influence the theoretical movement of the borehole in May 2010 (Table 7.1).

### **7.2.3 Calculation of Extraction Volumes Contributing to Subsidence**

The extraction in November 2008, therefore, would have fully contributed (at a weight of 6/6) its influence to the induced movement at the borehole measured in May 2010; extraction in December 2008 would have contributed 83.3% (5/6) to the measured movement in May 2010; and so on to the extraction in April 2009 which is estimated to have contributed 16.7% (1/6) to the movement. This will sum up to a theoretical total effective volume of 3500 m<sup>3</sup>, assuming each extraction was 1000 m<sup>3</sup> (Table 7.1).

Consequently, extractions in 2005, 2006 and 2007 were more than 18 months prior to March 2009 when the first inclinometer measurement was taken. Extractions after February 2010 were later than 12 months from February 2011 when the final measurement was undertaken. Thus, only extraction data in 2009, and parts of 2008, and 2010 were used for movement analysis (Table 6.13 in Section 6.3.3) if the delay time is chosen as 18 months.

The total effective volume will remain the same for other delay time patterns assuming the subsidence development (from observed start to finish) remains 6 months, just pillar standing time and carving development time vary. The effective extraction volume to cause movement over one month will be 3.5 times the monthly average volume:

$$\text{Effective extraction volume} = 350\% * \text{monthly average volume (m}^3\text{)}$$

When the extracted seam height is stable the effective extraction area to cause movement over one month will be 3.5 times the monthly average area.

The following sections will try to determine the best estimate of delay time using inclinometer borehole data.

#### **7.2.4 Extraction Parameters (Vector)**

Similar to a vector definition in physics or mathematics, a new concept, the extraction vector, was used to define the extraction characteristics that control the subsidence. The extraction vector to a measurement point includes extraction stope volume, stope shape, and axis direction, extraction centre distance, and bearing direction from the extraction centre to the measurement point.

As the extraction seam height was relatively stable at approximately 6 to 8 m, 7 m was used as the average extracted seam thickness. Then the extraction volume could be represented by extraction area (m<sup>2</sup>) times 7 (m). The measurement point is the borehole location in the inclinometer project area. The extraction location bearing is the orientation of the extraction centre from the inclinometer borehole.

## **7.2.5 Correlation between Horizontal Movement and Nearest Edge Distance**

### **7.2.5.1 Introduction**

Because the extraction cells (blocks) in the North 5 mining area are adjacent (Figure 6.17), the total mining area exceeds any critical width required for maximum subsidence to occur. Likewise, in a single panel to cause the maximum subsidence the extraction width must be larger than the critical width (refer to Appendix A-2). Development of subsidence in the North 5 area, thus, follows mining advancement whether the extraction advance was large or small. Therefore, the magnitude of the borehole movement may have a direct correlation with the only significant varying factor – the distance from the nearest edge of the extraction to the Borehole.

### **7.2.5.2 Eight separate subsidence events and rectangle conversion to circle**

To simplify the analysis, the subsidence was approximated as eight separate subsidence events, relating to the strata lateral displacement measurements in May, June, August, September, October, November, December 2010, and February 2011. Each monthly measurement was assumed to be the final static subsidence of the strata, which was induced by the 6 continuous months of extraction between 12 and 18 months prior to each measurement time, with weights from 6/6 to 1/6 as described in Table 7.1.

To simplify studying the correlation problems, the weighted extraction volumes were simplified from a cuboid of voids (having a rectangle base with an approximately length/width ratio = 1.5) into an equivalent cylinder of the void. The radius of the circle is computed using  $\pi r^2 = \text{area}$ , and centered at the centre of the rectangle.

### 7.2.5.3 Calculation of weighted stope centre location and nearest distance

The weighted stope cylinder area and location was calculated by the method of Equilibrium of the Centre of Gravity (Texas A&M University, 2011) (Figure 7.1, calculation details refer to Appendix F).

In this method, two separate cylinders with base areas  $a_1$  and  $a_2$ , centred at locations  $o_1$  and  $o_2$  at distances  $d_1$  and  $d_2$  from the borehole, are simplified to a single volume of cylinder (base area  $A$ , location  $O$  and distance  $D$ ). The area ( $A$ ) will be given by  $A = (a_1 * w_1) + (a_2 * w_2)$

Where,  $w_1$  is the weight factor of extraction month for area1;

$w_2$  is the weight factor of extraction month for area2.

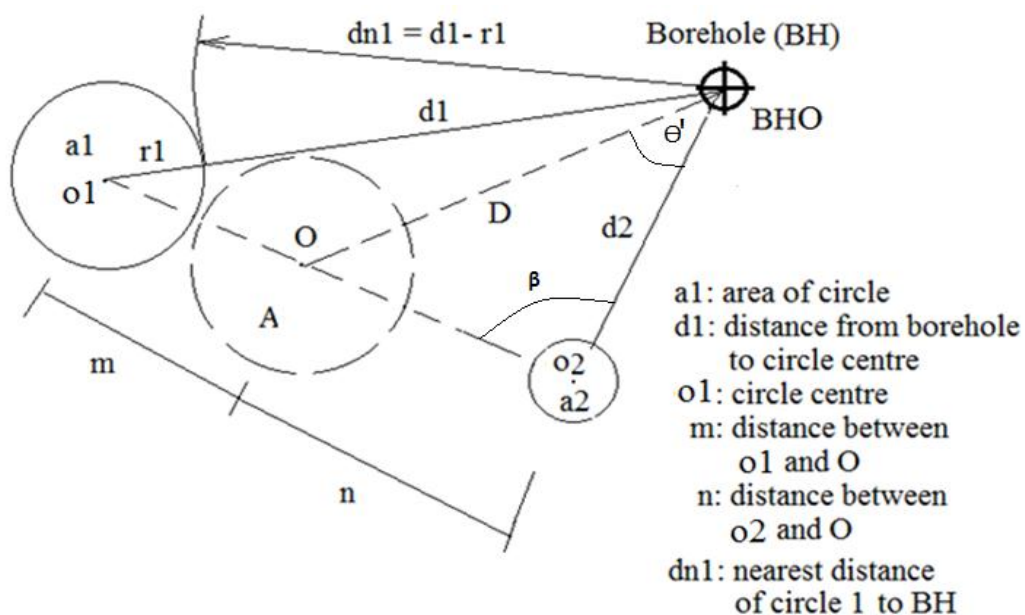


**Figure 7.1** The calculation using method of Equilibrium of the Centre of Gravity.

The location  $O$  is determined by the calculations below, using Scalene Triangle equation the distance  $(m + n)$  from  $o_1$  to  $o_2$  is:

$$(m + n)^2 = (d_1)^2 + (d_2)^2 + 2 * (d_1) * (d_2) * \text{COS}(\theta_1 - \theta_2) \quad (7-1)$$

Where,  $\theta_1, \theta_2$  are the bearing of distance  $d_1$  and  $d_2$ ;



m and n are the distance from O to o1 and o2.

Then by the equation of Equilibrium of the Centre of Gravity:

**(a1) \* m = (a2) \* n, thus, the distance from o1 to O:**

$$m = (a1/a2)* n$$

On Scalene Triangle equation:

$(d1)^2 = (d2)^2 + (m + n)^2 + 2*(m + n)*(d2)*\text{COS}(\beta)$ , then angle  $\beta$  can be obtained.

The distance D then can be computed by:

$$D = (d2)^2 + n^2 + 2*(d2)*n * \text{COS} (\beta),$$

Also the bearing of distance D can be given by the same equation:

$$n^2 = D^2 + (d2)^2 + 2*D*(d2)*\text{COS} (\theta')$$

$$\theta = \theta' + \theta 2$$

For each 6 month period considered, for example, Nov. 2008, Dec. 2008, Jan. 2009, Feb. 2009, Mar. 2009, and Apr. 2009, the calculations are:

Months 1 + 2: an average weighted extraction area was obtained using addition computation, assuming 100% of area for month 1, 83% for month 2 by undertaking a mass equilibrium calculation (assuming a constant density). This calculation will give an equivalent location (D1) and area (A1) for these two months.

Months 3 + 4: repeating above addition calculation using 67% for month 3, and 50% for month 4, obtaining an equivalent location (D2) and area (A2) for these two months.

Months 5 + 6: repeating above addition calculation using 33% for month 5, and 17% for month 6, obtaining an equivalent location (D3) and area (A3) for these two months.

Then adding up A1 and A2 with equal weight gives equivalent location (D4) and area (A4). Finally adding up A4 and A3 gives the equivalent location (D) and area (A), which are the final results consisting of weighted area, the distance from borehole to the extraction centre, and the bearing of the extraction centre to the borehole.

The distance of the nearest edge of the coal stope cylinder to the Borehole is the the centre distance to the borehole minus the radius of the stope circle. The nearest distance, weighted area, and the bearing of the circle centre to the borehole for assumed delay times of zero to 20 months are summarised in Table 7.2 for the eight inclinometer survey months.

#### **7.2.5.4 Delay time identification**

Table 7.2 lists all the correlation coefficients (R) representing the relationship between the lateral movement at three depths, and the nearest extraction edge for delay times from zero to 20 months. The R values for an 18 month delay are the minima of -0.84 at 1m, -0.69 at 135 m, and -0.68 at depths of 166 m.

**Table 7.2 The distance from the nearest edge of the weighted extraction cylinder to the Borehole (m) in delay times varying from zero to 20 months.**

Measure date	*Lateral movement			The weighted nearest distance from nearest stope edge to the borehole at each delay time #																				
	at 3 depths (mm)			Delay time (months)																				
	1m	135m	166m	0	1	2	3	4	5	6	7	8	9	10	11	12	13	14	15	16	17	18	19	20
May-10	3.4	0.8	0.6	241	207	119	167	162	214	219	246	245	272	236	263	260	21	336	382	412	460	<b>448</b>	468	437
Jun-10	2.9	2.3	2.3	309	241	207	119	167	162	214	219	246	245	272	272	263	94	237	336	382	412	<b>460</b>	448	468
Aug-10	3.1	1.1	1	265	284	309	241	207	119	167	162	214	219	246	245	272	272	263	255	237	336	<b>382</b>	412	460
Sep-10	13.6	3.1	2.5	221	265	284	309	241	207	119	167	162	214	219	246	245	272	272	263	255	238	<b>336</b>	382	412
**Oct-10	27.9	12.3	10.7	242	221	265	284	309	241	207	119	167	162	214	219	246	245	272	272	263	255	<b>238</b>	336	382
Nov-10	12.5	6.3	5.5	210	242	221	265	284	309	241	207	119	167	162	214	219	246	245	272	272	263	<b>255</b>	238	336
Dec-10	12.5	1.9	1.3	89	210	242	221	265	284	309	241	207	119	167	162	214	219	246	245	272	272	<b>263</b>	255	237
**Feb-11	19.2	11.8	8.5	125	14	89	210	242	221	265	284	309	241	207	119	167	162	214	219	246	245	<b>272</b>	272	263
Correlation coefficient			1m	-0.41	-0.4	0.01	0.6	0.85	0.49	0.15	-0.28	-0.21	-0.48	-0.47	-0.55	-0.53	0.43	-0.27	-0.55	-0.55	-0.76	<b>-0.84</b>	-0.59	-0.53
		at	135m	-0.25	-0.61	-0.25	0.34	0.66	0.34	0.2	-0.1	0.04	-0.18	-0.28	-0.57	-0.6	0.22	-0.41	-0.47	-0.43	-0.59	<b>-0.69</b>	-0.52	-0.43
			166m	-0.16	-0.5	-0.17	0.36	0.68	0.34	0.15	-0.2	-0.05	-0.22	-0.26	-0.47	-0.51	0.25	-0.38	-0.42	-0.41	-0.57	<b>-0.68</b>	-0.49	-0.36

\* Lateral movement data from Table 6.12 in Section 6.2.9.

\*\*Horizontal movement data in October 2010 and February 2011 are the average of two measurements in each month.

# The weighted nearest distances were calculated as per section 7.2.5.3

Figure 7.2 is plotted for the 21 correlation coefficient values at depths of 1 m, 135 m and 166 m (from Table 7.2) and used for further identifying the best appropriate negative correlation between lateral movement and the nearest edge to the Borehole. By inspection of the 3 lines (Figure 7.2), the correlation R plots had three negative peaks at 1 month, 12 months, and 18 months delay time for the three depths of 1 m, 135 m, and 166 m, but the lowest correlation R values are found in the 18 months delay.

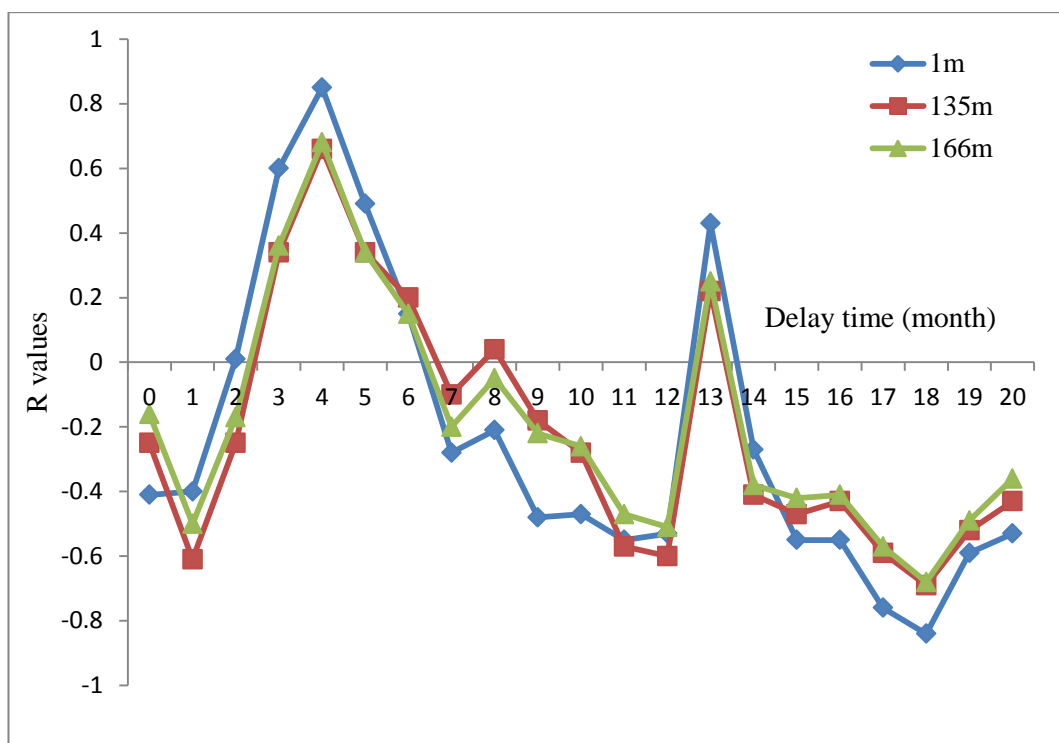


**Figure 7.2 Graph of the correlation coefficient values (from Table 7.2) for time delay from zero months to 20 months for identifying the best negative correlation.**

Figure 7.3 shows the relationship between the weighted nearest distances and the lateral movements for the 1 month, 12 months, and 18 months delay. According to the engineers' experience of mining operations in Huntly East Coalmine, the delay time of the subsidence is estimated at approximately one year from completion of extraction to first subsidence noticed at the ground surface. However, no accurate data for delay time was available for one-to-one extraction-subsidence events. The 1 month delay time plot (Figure 7.3) doesn't make sense

as it does not fall within the 6 – 18 month range of observed subsidence commencement (Section 7.2.2) , and the line for 12 months delay time is relatively flat compared to the 18 month one. Therefore, the 18 months delay time shows the best negative correlation between the lateral movement and the nearest distances.

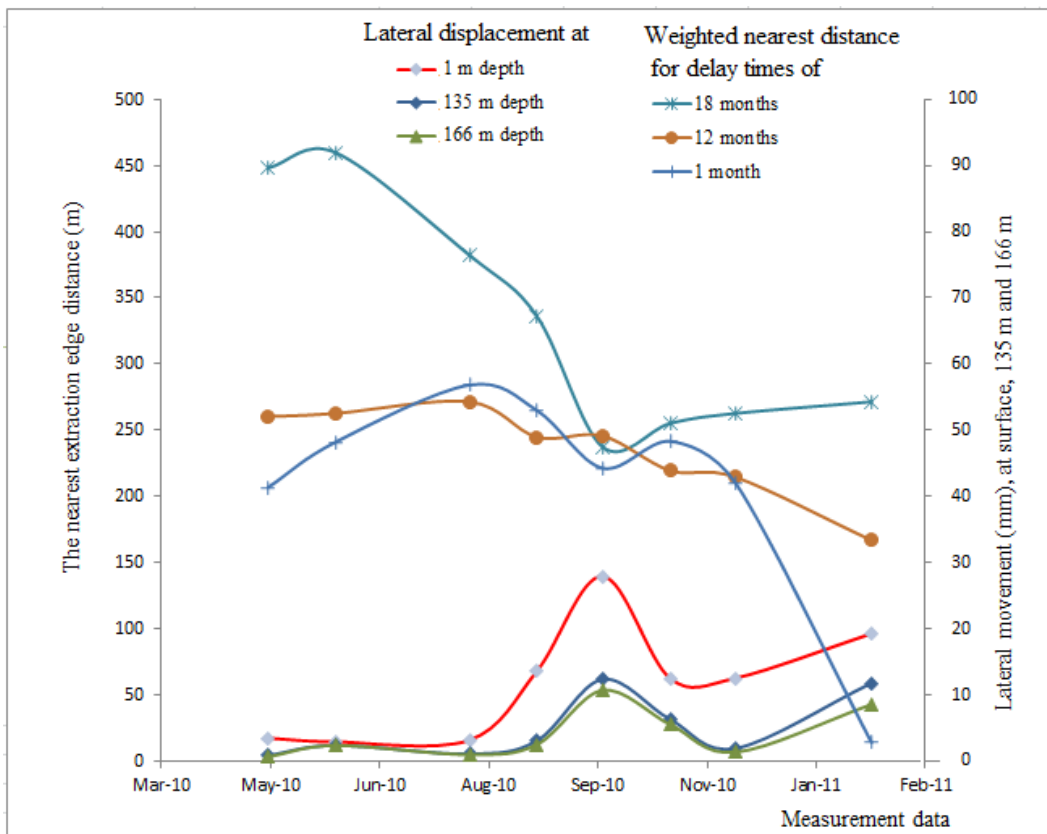


**Figure 7.3** Weighted nearest distance from the nearest edge of extraction to the Borehole (left axis) for delay times of 1 month, 12 months, and 18 months delay; and the lateral movement magnitudes at depths of 1 m, 135 m and 166 m (right axis).

The best estimate of the delay time from the completion of extraction to the completion of surface subsidence used in the modelling was finally determined as 18 months. The subsidence development in my research area was thus delineated as: surface subsidence began one year after completion of extraction, and developed during the following 6 months to reach the maximum subsidence. The first one year time includes a pillar standing period, then pillar collapse time, and

stope caving spreading up to the surface. In the 6 month development, dynamic subsidence was influenced by the 6 different extraction vectors. The monthly measured magnitude of subsidence was the final resultant of influence of the 6 extraction cells which had varying locations, distance to the borehole, and different bearing, with changing area weights from 6/6 to 1/6.

#### **7.2.5.5 Correlation equation between the lateral movement and extraction**

The horizontal movement at three depths and the nearest edge distances from extraction to the borehole for an 18 month delay pattern are highlighted in Table 7.2 (bolded column).

A correlation equation could be obtained by plotting the shaded data with the horizontal movement at three depths (in Table 7.2). Several trend line types in plots, including exponential, linear, logarithmic, polynomial and power regression, can be inspected to find the best suitable regression type for describing relationship between the lateral movement and the extraction.

Figure 7.4 is the linear trend-lines of the Scatter plot of horizontal movement at three depths and the corresponding nearest edge distances from extraction to the borehole (Table 7.2).

From the Scatter plots the linear Equations 7.2, 7.3 and 7.4 are obtained,

$$y = -8.4833x + 432.66 \quad R^2 = 0.7033 \quad \text{at surface} \quad (7.2)$$

$$y = -13.069x + 396.38 \quad R^2 = 0.4734 \quad \text{at 135 m} \quad (7.3)$$

$$y = -15.954x + 396.42 \quad R^2 = 0.4582 \quad \text{at 166 m} \quad (7.4)$$

Where: x, the movement distance of the Borehole at a depth over a month, mm

y, the nearest distance from extraction edge to the Borehole, m.

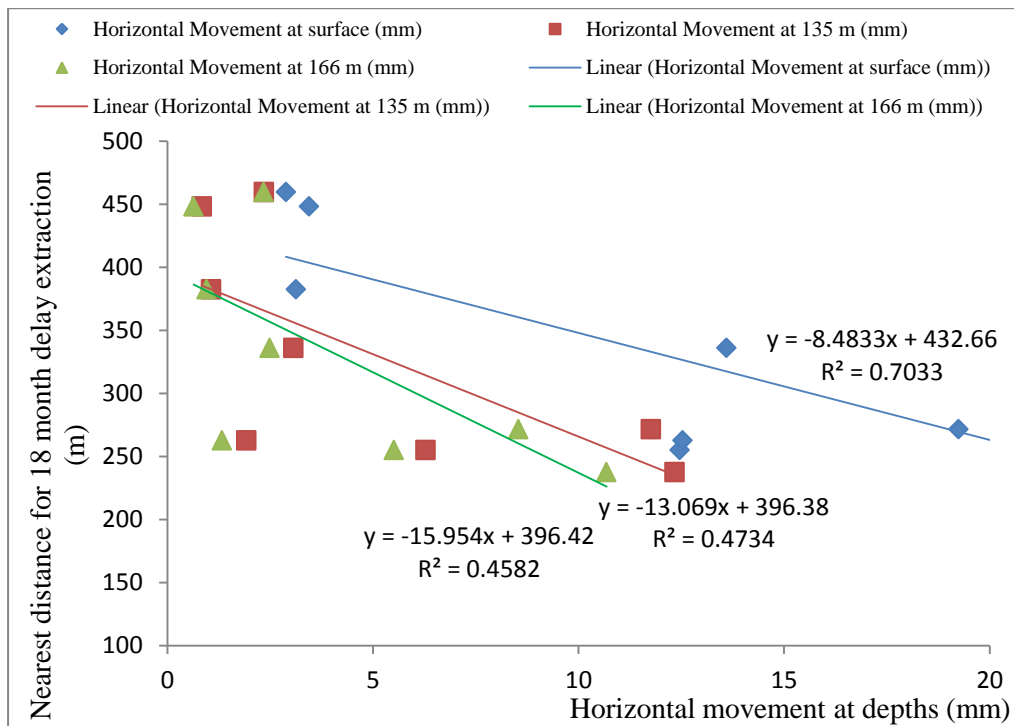


**Figure 7.4 Scatter plot of the horizontal movement and nearest edge distance from extraction to the borehole for 18 month delay pattern.**

Figure 7.5 shows the nonlinear trend-lines of the Scatter plots of horizontal movement at 1 m, and the nearest edge distances from extraction to the borehole (from Table 7.2).

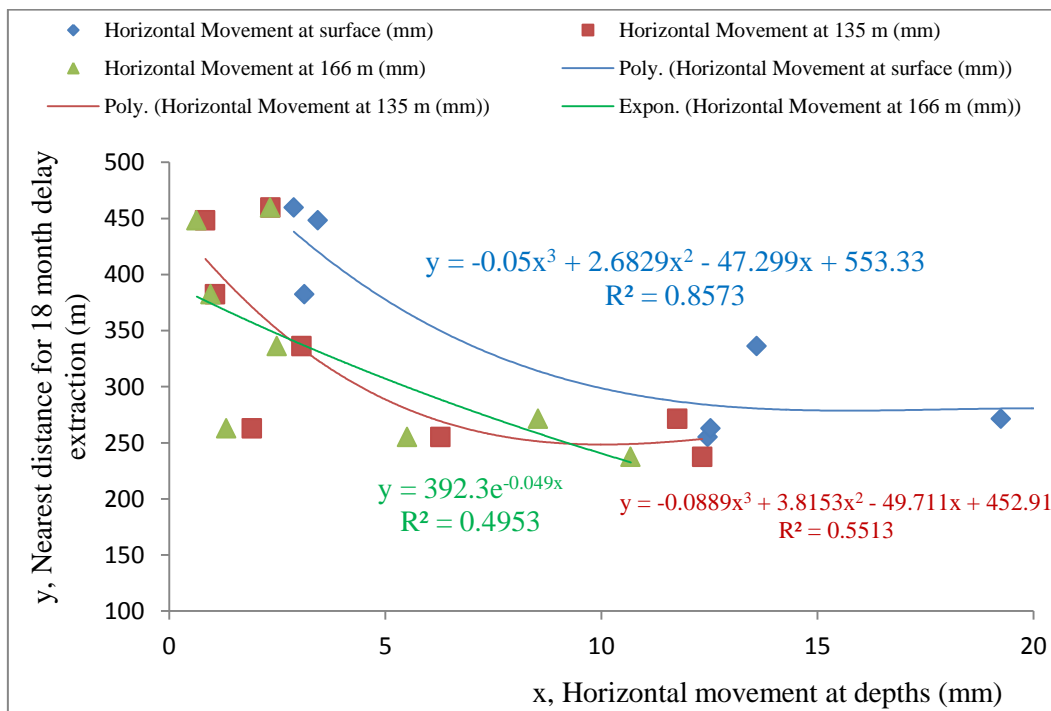


**Figure 7.5 Scatter plots of the horizontal movement at 1 m depth with the nearest edge distance from extraction to the borehole for 18 month delay pattern.**

The non-linear Equations 7.5, 7.6 and 7.7 are obtained,

$$y = -0.05x^3 + 2.6829x^2 - 47.299x + 553.33 \quad R^2 = 0.8573 \quad \text{at 1m} \quad (7.5)$$

$$y = -0.0889x^3 + 3.8153x^2 - 49.711x + 452.91 \quad R^2 = 0.5513 \quad \text{at 135 m} \quad (7.6)$$

$$y = 392.3e^{-0.049x} \quad R^2 = 0.4953 \quad \text{at 166 m} \quad (7.7)$$

Where,

x and y are the same as above in Equations 7.2, 7.3 and 7.4.

This formula shows the nonlinear correlation between the horizontal movement at 1 m depth, and the nearest edge distance from extraction to the Borehole.

By comparing Figures 7.5 and 7.4, the  $R^2$  values are higher in Figure 7.5 than Figure 7.4 for the 1 m depth plot, representing better matching of the extraction with the measured movements. Therefore, the non-linear equation 7.5 is recommended as the formula to describe the correlation between the extraction and the lateral movement at 1 m depth.

For instance, the cut-off distance for determining the impact of subsidence on a structure in a subsidence bowl in a design, can be obtained using the Equations 7.5, 7.6 and 7.7 (Table 7.3). The data does not give a good prediction for the 135 m and 166 m depths because their  $R^2$  values are not significant.

To conclude, the best estimate of the delay time was 18 months. The cut-off distance to avoid 5 mm lateral displacement at 1 m depth was computed as 376 m (Table 7.3).



**Table 7.3 Some cut-off distances of extraction and cut-off horizontal movement of strata at surface, 135 m and 166 m, in linear and nonlinear correlations, North 5, Huntly East Coalmine.**

	Borehole horizontal movement (mm)		Extraction nearest distance to borehole To avoid each horizontal movement			
			nonlinear m	linear m	Difference* m	
At surface (1m)	X=	0	Y=	553	433	120
	X=	2	Y=	468	416	52
	X=	5	Y=	376	390	-14
	X=	10	Y=	295	348	-53
at 135 m	X=	0	Y=	453	396	57
	X=	2	Y=	368	370	-2
	X=	5	Y=	289	331	-42
	X=	10	Y=	248	266	-18
at 166 m	X=	0	Y=	392	396	-4
	X=	2	Y=	356	365	-9
	X=	5	Y=	307	317	-10
	X=	10	Y=	240	237	3

\*difference between distances calculated using nonlinear equations (7.8, 7.9, 7.10) and linear equations (7.5, 7.6, 7.7).

## 7.2.6 Borehole Movement Trajectory and Extraction Vectors

Table 7.4 shows extraction parameters (vectors) and extraction duration contributing to induction of subsidence measured over 8 months for the 11 surveys, with 18 months delay time.

From Table 6.13 the average monthly extraction area is  $2052 \text{ m}^2$ , and then the average effective area will be  $2052 \times 3.5 = 7182 \text{ m}^2$ , which has a radius of 48 m for the shape of an approximated cylinder bottom. Therefore the average distance from the nearest edge of the cylinder (the weighted extraction stope) to the Borehole is  $285 - 48 = 237 \text{ m}$  during March 2008 to July 2011 (285 m is the average distance from cylinder centre to the Borehole, Table 6.13).

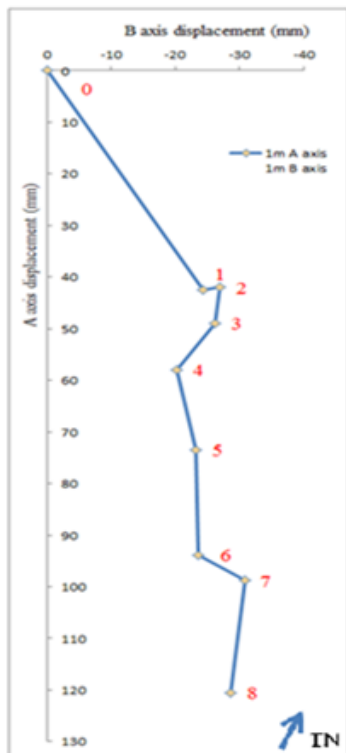
**Table 7.4 Samples of the extraction vectors and extraction duration for 11 surveys in 8 measurement months, 18 months delay time.**

		Extraction vector					Extraction duration 6 months					
Inclinom. survey	Inclinometer survey	Centre distance	Weighted area	Azimuth	Radius	Nearest edge distance	Weight % of extraction area					
Number	Month	m	m <sup>2</sup>	degree	m	m	100	83	67	50	33	17
1	May-10	494	6541	107	46	448	Oct-08	Sep-08	Aug-08	Jul-08	Jun-08	May-08
2	Jun-10	501	5465	124	42	459	Nov-08	Oct-08	Sep-08	Aug-08	Jul-08	Jun-08
3	Aug-10	424	5509	93	42	382	Jan-09	Dec-08	Nov-08	Oct-08	Sep-08	Aug-08
4	Sep-10	379	5732	97	43	336	Feb-09	Jan-09	Dec-08	Nov-08	Oct-08	Sep-08
5	Oct-10	275	4458	127	38	237	Mar-09	Feb-09	Jan-09	Dec-08	Nov-08	Oct-08
6	Nov-10	289	3626	112	34	255	Apr-09	Mar-09	Feb-09	Jan-09	Dec-08	Nov-08
7	Dec-10	296	3380	126	33	263	May-09	Apr-09	Mar-09	Feb-09	Jan-09	Dec-08
8	Feb-11	310	4632	156	38	272	Jul-09	Jun-09	May-09	Apr-09	Mar-09	Feb-09

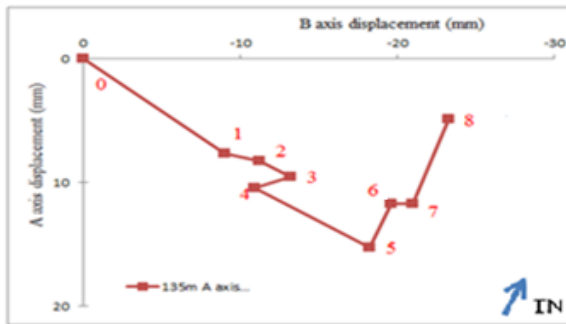
Figure 7.6 compares the borehole movement trajectories (Figure 7.6 a, b, and c) with extraction trajectory (Figure 7.6 d) for an 18 month delay time. The extraction patterns show some similarities with the borehole movement trajectory:

- All borehole movement trajectories and the extraction trajectory are non-linear (Figure 7.6 a, b, c, and d).
- All the weighted extraction locations from 1 to 8 are to the southeast of the borehole except No. 8 which is south (Figure 7.6 d).
- All the measured borehole movement locations from 1 to 8 range from  $64^{\circ}$  to  $140^{\circ}$  (Figure 7.6 a, b, and c) (Sections 6.2.4, 6.2.6, and 6.2.8).
- The measured movement sections from No. 0 to No. 1 (in Figure 7.6 a, b, and c) had a bearing from the true north at  $120^{\circ}$  at 1 m depth,  $101^{\circ}$  at 135 m depth, and  $87^{\circ}$  at 166 m depth, with the section from No. 0 to No. 1 in the weighted extraction trajectory with a bearing of  $107^{\circ}$  (in Figure 7.6 d).
- There was similar length feature observed in the four plots: section distances of 0-1, 4-5, and 7-8 are long, the other section distances are relatively short. That means the extraction moved further (larger extraction vector) from last extraction, resulting in a bigger lateral movement than some amount of extraction close to last extraction area.

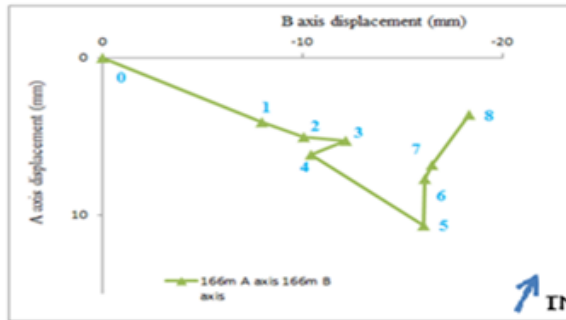
The strata movement induced are not only determined by the extraction characteristics, but also controlled by the geological and hydrological properties of the strata, and the geotechnical parameters of the rocks and soils, which all varied over the borehole depth and over horizontal distances.



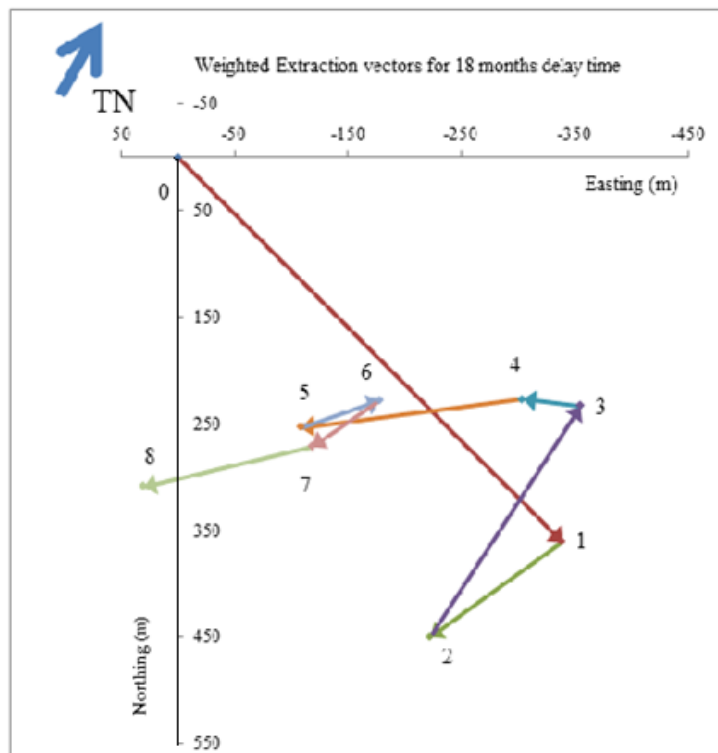
a. Trajectory at surface (from Figure 6.13)



b. Trajectory at 135 m (from Figure 6.5)



c. Trajectory at 166 m (from Figure 6.10)



d. Weighted extraction trajectory (from Figure 7.5)

Figure 7.6 Comparison of the borehole movement trajectories a, b, c (from section 6.2.9) with the extraction pattern d - showing weighted extraction vectors from no. 1 to no. 8 in the 18 month time delay, representing the 8 weighted locations of the extraction centres from each 6 induction months (Table 7.4). The zero at origin is the location of the inclinometer borehole.

Also, the inertia of the movement caused by extraction will last in a certain period in a direction even though that extraction ceased and a new extraction started in a new location in a different bearing. Therefore, it may be understandable that no exact or direct correlation could be observed between the extraction patterns and the borehole movement trajectories. The difference between the extraction plot and the borehole movement plots may result from the data errors, measurement errors, or all the limitations discussed in Chapters 5 and 6. More accurate matching of the extraction trajectory and the borehole movement trajectories may be found via future work from inclinometer dataset analysis, error correction, and movement interpretation.

The geological, hydrological and geotechnical characteristics of the strata in this North 5 project area were relatively constant in each strata. The coal seam depth and extraction height did not change much, so the changing parameters inducing borehole movement should be the extraction area, extraction centre distance to the Borehole and its bearing to the Borehole (refer to Appendix A-1 and Figure A-1).

## **7.3 Numerical Modelling of Strata Movement**

### **7.3.1 Geological Model for Software Modelling**

Numerical modelling requires a 2D geological model of the extracted seams and neighbouring zone, including geology, stratigraphy, groundwater and geotechnical characteristics, which are compiled from literature review and the borehole log information.

In verification all the modelling parameters and indices were tuned against the measured movement, until the modelled subsidence agrees with the interpretation of the measured subsidence using the inclinometer monitoring. If the modelling

has a good agreement with the measured subsidence then the model can be used as guidance in the related design and prediction of the subsidence.

Figure 7.7 shows the geometry of coal field layers in the North 5 mining area where the inclinometer borehole is located.

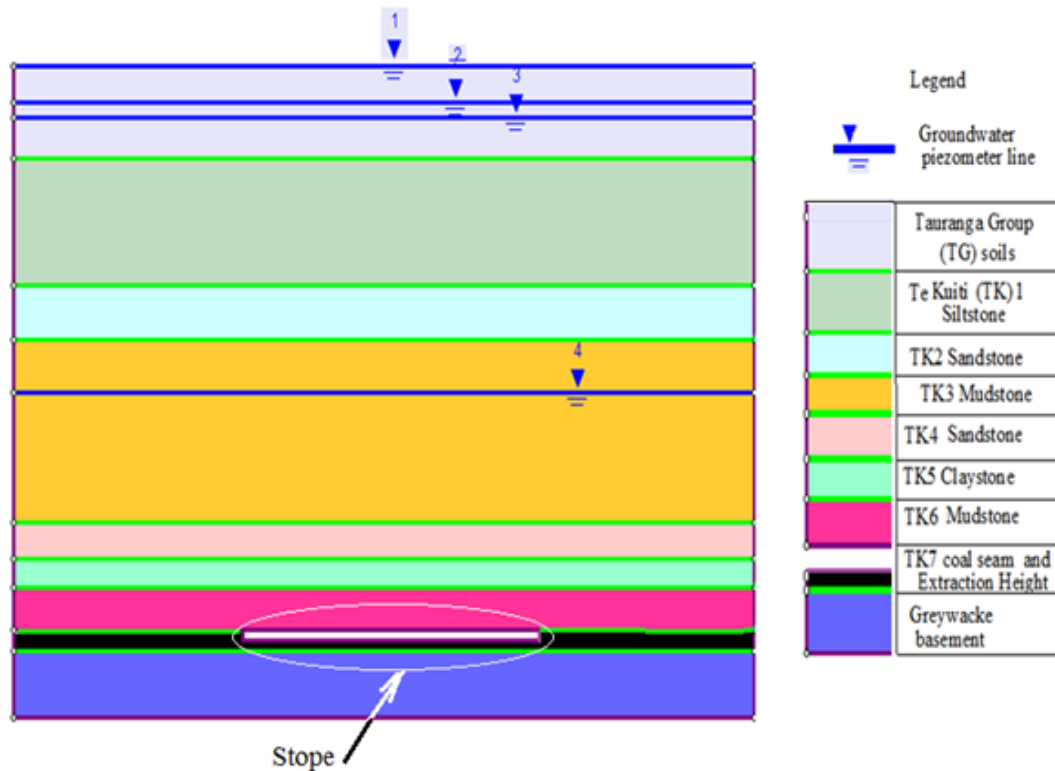


**Figure 7.7** The full 2D model representing the 9 geological layers of the inclinometer monitoring region (created in Phase2, data source from Table 3.6 in Section 3.3.2).

The cross sections of geological formations across the inclinometer borehole are listed in Appendix G showing the strata are relatively flat and the thickness of the strata within the model were assumed as even.

The geological model provides part of the inputs essential for a geo-mechanical finite element analysis in Phase2.

The borehole monthly lateral movement distances will be modelled in Phase2 against the monthly lateral displacement (Section 6.6.2.9, Table 6.12). The borehole vertical subsidence is to be modelled as well; though the measured

vertical subsidence data were insufficient to fully assess vertical displacement (Section 6.3, Table 6.14). The only varying subsidence induction factor in the modelling will be the distance between the borehole location and the nearest edge of the extraction stope (the cylinder) where the subsidence occurred within the relevant 6 continuous months (See Section 7.2.2, Table 7.1). In the field measurement the extraction locations of the mining cells were changing in a harmonic mining area, the borehole location was relatively stable though the borehole had a slight lateral displacement. In the modelling the extraction nearest edge was fixed.

### **7.3.2 Establishment for Software Modelling**

#### **7.3.2.1 Project settings**

The general project settings for Phase 2 modelling were chosen as follow:

- An Axisymmetric model was chosen to analyse the excavation in this research (Section 4.4.4.1).
- The Conjugate Gradient technique was chosen for the Solver type.
- I tried both the convergence types: Absolute Energy criterion and Square Root Energy criterion in my modelling.
- The ‘Tensile failure reduces shear strength to residual’ option is not used because it is for brittle rocks.
- Both of the options: with and without Tensile Failure Reduces ‘Hoek-Brown Tensile Strength’ to Zero in using the Hoek-Brown or Generalized Hoek-Brown failure criteria were tried.
- Piezometric lines were used as the groundwater method and the option of ‘Use Effective Stress Analysis’ was selected.

### 7.3.2.2 Material properties

The 'Define Material Properties' selected in my modelling were chosen as below:

- In initial element loading, my model worked under Field Stress & Body Force. Therefore Unit Weight was used for defining the Body Force.
- As the modelling uses an axisymmetric analysis all materials were limited to having isotropic elastic properties.
- The residual Young's modulus was not used because when the material yields the load state does not change.
- Duncan-Chang Hyperbolic constitutive model is not usable for axisymmetric analysis; the isotropic elastic model was trialled.
- Options of the 'Unsaturated Shear Strength', and 'Apply Shear Strength Reduction' were not chosen in this study.

Chapter 3 detailed the geological, hydrological and geotechnical characteristics of the strata in the inclinometer project area. The parameters of material properties of the soils and rocks are summarized in Table 7.5 as input parameters for subsidence modelling. Basic parameters i.e. Unit weight, Young's modulus, tensile strength, compressive strength, friction angle, cohesion are data from testing or field measurements (sources of these data are referenced in Table 7.5). The other parameters are computed from the basic parameters using the RocData software or by the relative calculations in Table 7.5.



**Table 7.5 Parameters as input into Phase2 modelling, Huntly East Coalmine.**

Parameters	Unit/sign		TG soils	TK 1	TK2	TK3	TK4	TK5	TK6	TK7	Basement	
Materials			soils	Siltstone	Sandstone	Mudstone	Sandstone	Claystone /Mudstone	Mudstone Claystone	coal seam	Grey-wacke	
Unit weight	MN/m <sub>3</sub>		0.017	0.0225	0.0238	0.0228	0.026	0.023	0.0237	0.013	0.027	Geotechnics Co., 2009
Young's modulus	MPa	Axial	-	795	2291	2320	3857	1353	1638	2700 <sup>#</sup>	8000 <sup>#</sup>	Geotechnics, 2009; <sup>#</sup> Tan & George, 1989
Young's modulus	MPa	Transverse	-	5824	15693	18303	36244	10622	11744		10000 <sup>#</sup>	
Young's modulus	MPa	= axial	41**	795	2291	2427	2982	1353	1638	-	-	Page, 2009
H/V ratio			4.6	1.4	1.4	1.4	1.4	1.4	1.4	1.4	1.4	SCT, 2003
Tensile strength	peak, MPa	0.58*UCS/10	0.058	0.696	1.334	1.276	1.334	0.464	1.334	0.58	1.624	SCT, 2001
Poisson's ratio			0.3	0.15	0.25	0.15	0.2	0.1	0.1	0.1	0.15	Larratt et al., 2009
Intact comp strength	MPa	Range	0-1	4-20	15-30	3-20	10-35	1--15	15-30	5-15	20-35	
Intact comp strength	MPa	Average	1	12	23	22	23	8	23	10	28	
Mohr rock constant	mi			3	3	3	7	2	4	2	3	
Groundwater level	undr,RL, m		12	12	-5	-5	-12	-12	-140	-140	-140	
Depth from surface	RL:12m, m		0	0	17	17	24	24	152	152	152	Calculated from groundwater level
Geologic strength index	(GSI)		5	35	45	40	40	30	45	20	70	RocData, GSI values
D =/ m <sub>i</sub> =			0/1	0/7	0/17	0/7	0/17		0/4	0.8/7	0/18	From RocData calculation
Friction angle	peak, deg.		20(4.7)	23.26	33.57	24.69	32.06	17.83	21.77	18.82	41.53	
Cohesion	peak, MPa		126 (0.004)	0.411	1.25	0.826	1.159	0.2	0.789	0.24	2.246	
m <sub>b</sub> parameter	peak		0.034	0.687	2.384	0.821	1.994	0.328	0.561	0.402	6.165	
s parameter	peak		0.000026	0.0007	0.0022	0.0013	0.0013	0.0004	0.0022	0.0001	0.0357	
Dilation parameter.	a		0.619	0.516	0.508	0.511	0.511	0.522	0.508	0.544	0.501	
q parameter	peak, MPa		0.34	0.39	0.55	0.42	0.53	0.31	0.37	0.32	0.66	Calculated from formula (RocScience, 2011)
k parameter	peak		118.4	0.38	1.04	0.75	0.98	0.19	0.73	0.23	1.68	
Dilation parameter	(in Plastic only)	(G)-H-B; D-P: 0.333mb	0.0113	0.2288	0.7939	0.2734	0.664	0.1092	0.1868	0.1339	2.0529	
		M-C:0.333phi	6.66	7.746	11.179	8.222	10.676	5.937	7.249	6.267	13.829	

\*\* From Larratt, 2010, the weighted calculation.

(G)-H-B: (Generalised) Hoek-Brown.

D, disturbance factor

M-C: Mohr-Coulomb

m<sub>i</sub>: material constant for intact rock.

### 7.3.2.3 Creating the model boundary

The model size should be adequately stretched so that the boundary conditions imposed do not affect the simulation results (Capasso and Mantica, 2006). In accordance with Section 6.3, and geological settings information from the boreholes 20091 and 20097 (Chapter 3), the model boundary in the initial modelling trial using Phase2 was firstly defined as 500 m thick by 1500 m wide as an axisymmetric analysis model.

The stopes from periodically extracted coal seams were idealised into *cylindrical voids* to meet the axisymmetric model requirement in Phase2 (Section 6.3.2). The extraction shape of *cylinder* was implicitly enclosed by the left edge of the model with the  $X = 0$  axis of the model. The axisymmetric 2D and 3D sketches of the model (Figure 7.8) indicate that at the  $X = 0$  point the strata only has a vertical settlement, no lateral movement is allowed by the model.

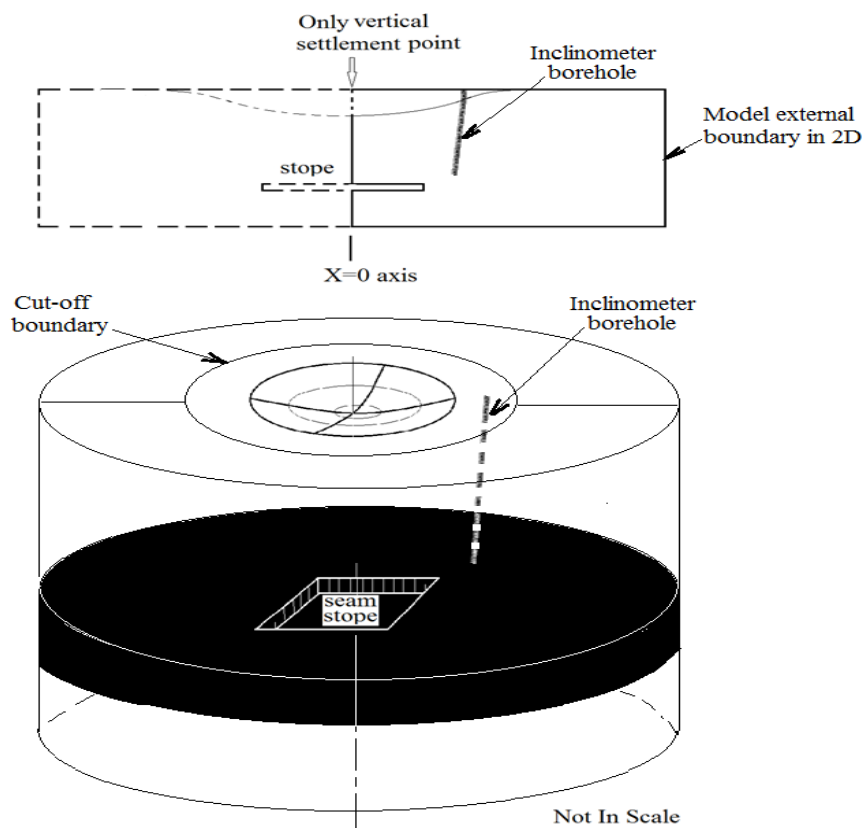


**Figure 7.8** Sketches of an axisymmetric extraction 2D (upper) and 3D (lower) model with square stope that was idealised into cylinder for axisymmetric type modelling.

The borehole location was relatively stable compared with the changing monthly extraction cells (Figure 6.17), though it had a small lateral displacement less than 200 mm (Section 6.28). In modelling, the extraction nearest edge is fixed, and the borehole location changed to reflect the different monthly nearest edge distances.

The model external boundary is illustrated in Figure 7.9. The extraction height was at an average of 7 m (Section 7.2.2), and the extraction ratio was approximately 65%, so the effective void height after extraction was 4.55 m ( $7 \text{ m} \times 65\% = 4.55 \text{ m}$ ). The radius of the stope cylinder for modelling was assumed  $x = 200 \text{ m}$ , larger than the half of critical width in Huntly East Mine (Critical width =  $1.4 \times 250 = 350 \text{ m}$ , Section 2.2.1). Thus, the extraction nearest edge is fixed at  $x = 200 \text{ m}$  from the model origin, while the borehole locations or the inclinometer measurement points vary from 237, 255, 263, 272, 336, 382, 448, to 459 m from the nearest edge of the weighted extraction stope (Table 7.4) in Figure 7.8.

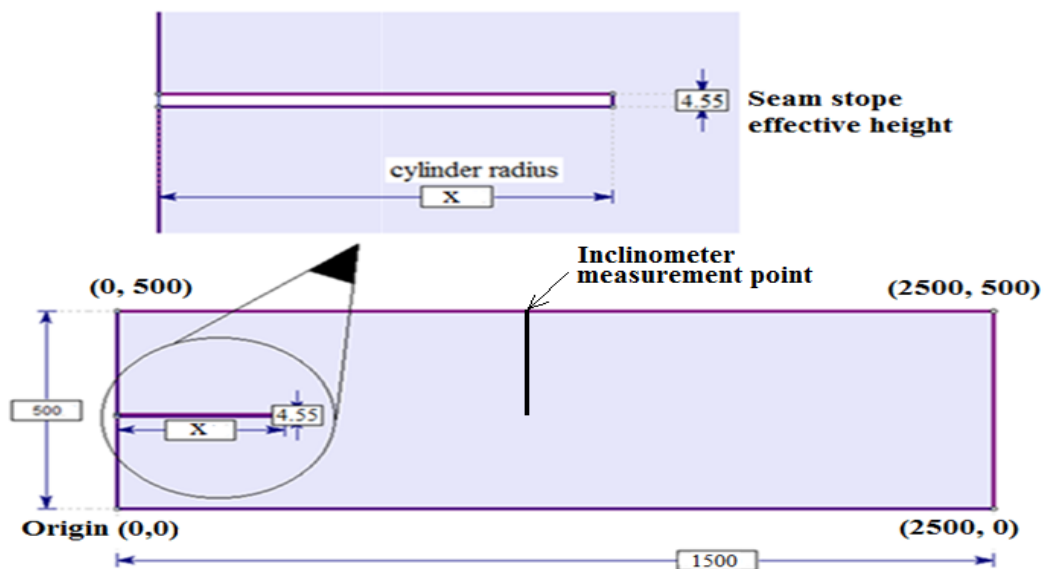


**Figure 7.9** The model boundary sizing 500 m times 1500 m, including an extraction cylinder of 4.55 m effective height and  $x=200 \text{ m}$  radius, which was created in Phase2.

As stated in Section 7.3.2 in axisymmetric models, only an External boundary is required, the shape of the External boundary implicitly defines the excavation of a *cylinder*; therefore, no excavation boundary is needed in this modelling.

### 7.3.2.4 Strata settings

The nine strata are established by the material boundary function (Figure 7.10). Nine geological settings are established for the model by the Material Boundary Function through inputting the strata profile coordinates (Table 7.6), and the groundwater piezometer line coordinates (Table 7.7).

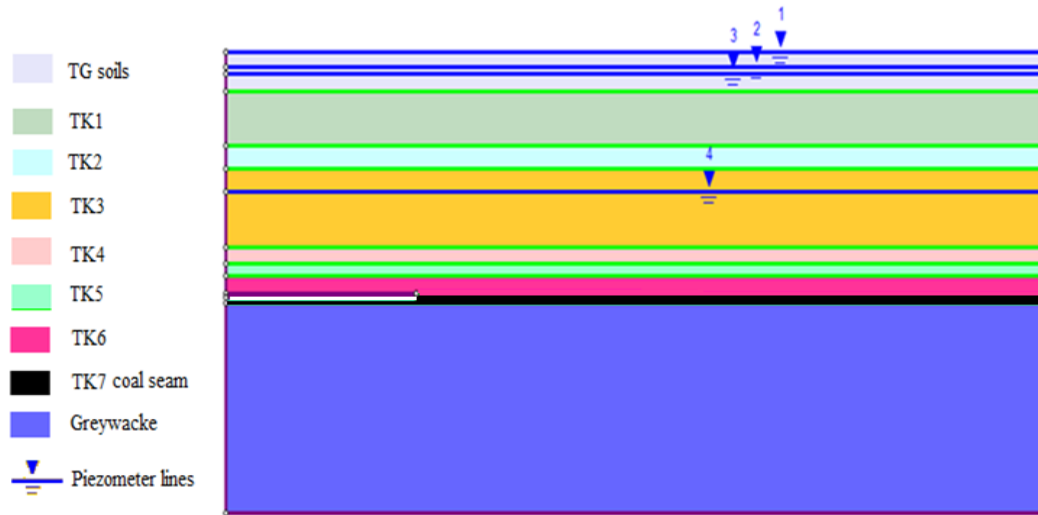


**Figure 7.10** The model with nine strata profile and groundwater piezometer lines (half of the axisymmetric model profile in Figure 7.7).

**Table 7.6** The coordinates of geological settings for the 9 layers in modelling.

Model Dimensions 1500 m x 500 m									
Ground surface elevation: 500m							Extraction ratio: 65%		
Coal seam thickness: 10 m			Extraction height: 7 m				Effective Extracted Thickness: 4.55 m		
Strata	x	y					x	y	
Tauranga Group	0	500	Tauranga Group				2500	500	
TK1	0	457	TK1				2500	457	
TK2	0	398	TK2				2500	398	
TK3	0	373	TK3				2500	373	
TK4	0	288	TK4				2500	288	
TK5	0	271	TK5				2500	271	
TK6	0	258	TK6				2500	258	
TK7 ( coal)	0	238	TK6				2500	238	
TK7 ( coal)	0	233.5	TK7 (extrac ted coal)	TK&(coal)			2500	233.5	
TK&(coal)	0	228	TK&(coal)				2500	228	
Greywacke	0	0	Greywacke				2500	0	

**Table 7.7 Coordinates for plotting groundwater piezometer lines for modelling (from Larratt et al., 2009 and Table 7.6 in section 7.3.2.2).**

From (left side coordinates)		To (right side coordinates)		Strata that the piezometer lines are assigned to
X, m	Y, m	X, m	Y, m	
0	500	1500	500	TG, TK1
0	483	1500	483	TK2, TK3
0	476	1500	476	TK4, TK5
0	348	1500	348	TK6, TK7 and Greywacke

### 7.3.2.5 Boundary conditions

The boundary conditions assigned to the model are composed of null displacement at the right boundary, and bottom boundary of the model, and no horizontal displacement at the left side because it is the centre axis of the axisymmetric model where  $X = 0$  (Figure 7.11, also refer to Figure 7.8).

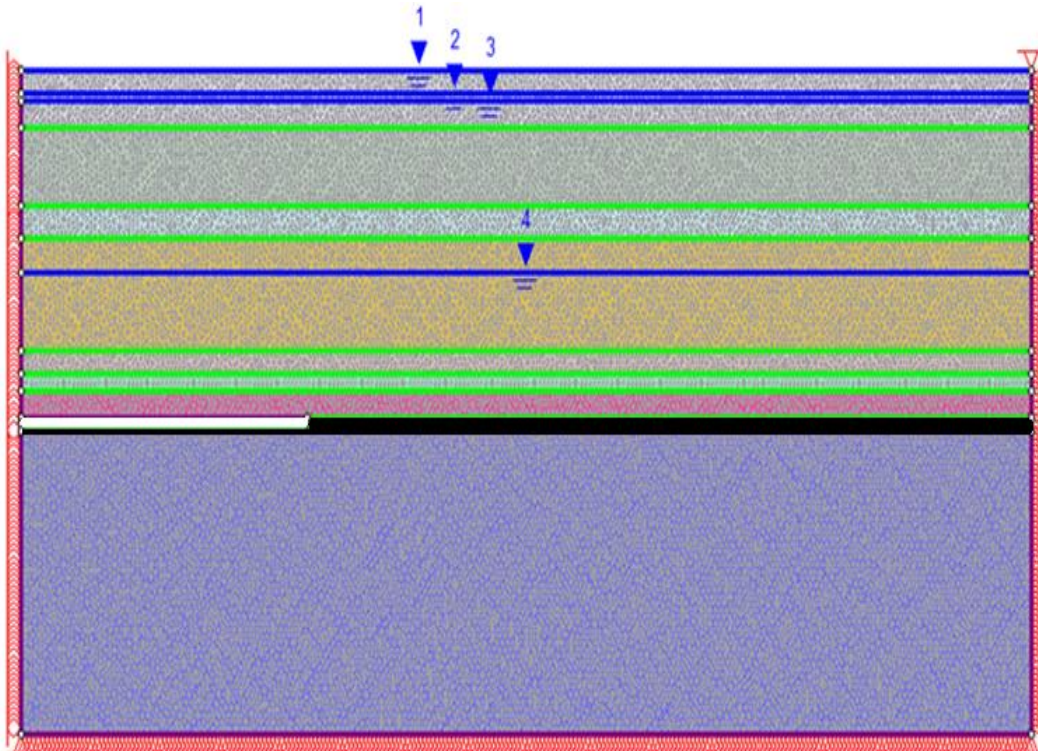


**Figure 7.11 Meshed Model with 1500 nodes on External Boundary, model boundary size 1500 m wide times 500m high.**

### **7.3.2.6 Loading conditions**

My modelling used the ‘Gravity Field Stress’ option to define an in-situ stress field which varies linearly with depth. The Use Actual Ground Surface option was selected to estimate the vertical in-situ stress. Therefore, the Unit Weight of Overburden option is not applicable.

From section 3.4.4.8, the ratio of horizontal to vertical effective stresses in Tauranga Group soils is 4.9, and for rocks it is 2.5.

### **7.3.2.7 Mesh generation**

In this case a Graded mesh type is used. The number of external nodes is 1500; the mesh diagram of the model is illustrated in Figure 7.11. This model has a total of 54,520 nodes, and 107,540 elements. Each element is 11.6 m<sup>2</sup>.

### **7.3.2.8 Strength (failure) parameters**

In the Strength Parameters option the material type (elastic or plastic) and the failure (strength) criterion for a material were described as below.

My modelling tried both Elastic and Plastic material types:

- with elastic materials, the failure criterion parameters entered are only used for calculation of the strength factor within the material;
- with plastic materials, the strength parameters entered are used in the analysis if yielding occurs.

Three main failure (strength) criteria for a material used in my modelling were the Mohr-Coulomb criterion, the Hoek-Brown and Generalized Hoek-Brown strength criteria, and the Drucker–Prager yield criterion. For plastic materials, dilation parameters were also defined for each criterion. The dilation parameters were

calculated by using  $0.333 \cdot m_b$  in the Hoek-Brown criteria or  $0.333 \cdot \phi$  in the Mohr-Coulomb criterion for soft rocks (see Section 4.4.9).

### 7.3.3 Initial Trials to Choose Failure Criterion

A one layer model was initially established (Figure 7.12) by inputting the average parameters (Table 7.8, obtained from Table 7.5). This one layer model was used for initial trials to choose the most suitable failure criterion. In this initial modelling just two horizontal distances (438 m and 472 m) were used, these being the distances from the origin of the model to the two sampled measurement points in 10/2010 and 02/2011, i.e. the nearest edge distance (from Table 7.2) plus 200 m (Figure 7.8). The results of these trials are listed in Table 7.9.

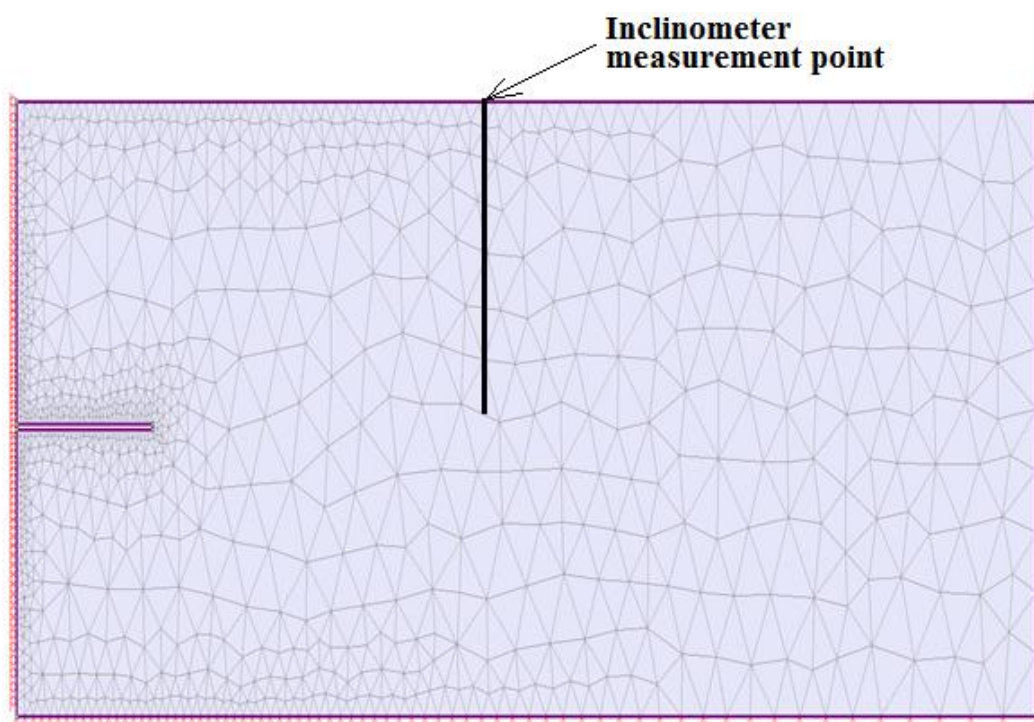


**Figure 7.12 The one layer model for initial trials to choose the failure criterion.**

**Table 7.8 Averages of parameters for 9 layers for determining failure criterion. (G)-H-B: (Generalised Hoek Brown criterion; D-P: Drucker Prager criterion; M-C: Mohr Coulomb criterion.**

Parameters	Average value	Note
Unit weight MN/m <sup>3</sup>	0.022	
Young's modulus (MPa), axial	2555	Axial
Young's modulus (MPa), transverse	12352	Transverse
Young's modulus (MPa), average	7454	Average
Poisson's ratio	0.17	
Intact comp strength(MPa)	17	
Mohr rock constant mi	3	
Groundwater level (undrained, RL, m)	-48	
Depth from surface (RL:12m)	60	
GSI(geologic strength index)	37	
D= / mi=	0/17	
Tensile strength (peak, MPa)	1.0	
Friction angle (peak, degree)	26	
Cohesion(peak, MPa)	15	
H/V ratio	1.4	
m <sub>b</sub> parameter(peak)	1.49	
s parameter(peak)	0.005	
dilation parameter a	0.53	
q parameter (peak, MPa)	0.4	
k parameter (peak)	14	
Dilation parameter (in Plastic only)	0.49	(G)-H-B; D-P: 0.333mb
Dilation parameter (in Plastic only)	8.64	M-C:0.333phi

For elastic material type (Table 7.9), all the four criteria of Mohr-Coulomb, Heok-Brown (H-B), Generalised H-B and Drucker-Prager give the same horizontal displacements of 52.3 mm at 438 m, and 43.6 mm at 472 m, and the same vertical subsidence of 34 mm at 438 m, and 25 mm at 472 m from the nearest extraction edge. For the plastic material type, all four criteria give different horizontal displacements and vertical subsidence compared to the elastic material method. The results from plastic method are a little bit larger than the elastic method, however the modelling for plastic method ‘may not be convergent and the iterations exceeded the maximum number allowable’ (message popup on screen after modelling finish). Therefore, in further modelling the trails were mainly focused on the elastic method.



Considering that the criteria of Hoek-Brown (H-B) and Generalised H-B gave the same initial modelling results, and rock masses in the Huntly East Mine had the lesser quality (Section 4.4.4), the Hoek-Brown criterion was discarded and the Generalised H-B was used in following modelling.

**Table 7.9 The outcomes of initial trials to choose the failure criterion, using one layer model by inputting the average parameters from Table 7.8, measurement distances of 438 m and 472 m.**

Failure criterion	Displacement modelled (mm)*		Iteration /tolerance	Convergent	Comment
	Lateral	Vertical			
Mohr-Coulomb, elastic	52.3/43.6	34/25	500/0.001	yes	same results
	52.3/43.6	34/25	500/0.01	yes	
	52.3/43.6	34/25	500/0.1	yes	
Mohr-Coulomb, plastic	55.1/46.3	35/26	500/0.001	May be not, iterations exceeded	results vary, a little bit larger than results from elastic method
	52.7/43.9	35/25	500/0.01		
	53.3/44.5	35/25	500/0.1		
Hoek-Brown (H-B), elastic	52.3/43.6	34/25	500/0.001	yes	same results
	52.3/43.6	34/25	500/0.01	yes	
	52.3/43.6	34/25	500/0.1	yes	
Hoek-Brown (H-B), plastic	55.1/46.3	35/26	500/0.001	May be not, iterations exceeded	results vary, a little bit larger than results from elastic method
	52.7/43.9	35/25	500/0.01		
	53.3/44.5	35/25	500/0.1		
Generalised H-B, elastic	52.3/43.6	34/25	500/0.001	yes	same results
Generalised H-B, plastic	44.8/36.0	30/22	500/0.001	May be not, iterations exceeded	results vary, smaller than results from elastic method
	45.7/36.9	32/23	500/0.01		
	44.4/35.8	32/23	500/0.1		
Drucker-Prager, elastic	52.3/43.6	34/25	500/0.001	yes	same results
Drucker-Prager, plastic	55.1/46.3	35/26	500/0.001	May be not, iterations exceeded	results vary, a little bit larger than results from elastic method
	52.7/43.9	35/25	500/0.01		
	53.3/44.5	35/25	500/0.1		

\* Lateral and vertical displacement on surface at 438 m and 472 m from the origin or 238 m and 272 m from the nearest extraction edge in model (Figure 7.9).

## 7.3.4 Combination and Running Trial

### 7.3.4.1 Combinations

The full nine geological units are used in modelling from this section. Table 7.10 lists the constants and variables for establishing the models in addition to the data in Table 7.5. Twenty four modelling trials were run (as in Table 7.11) for optimising the best combination.

**Table 7.10 Variables used for trials of subsidence modelling using Phase2.**

Constants: every run uses the same.		Variables: each is tried in a run combination.		Factor	
Analysis type	Axisymmetric analysis (cylinder)	Convergence type	Absolute Energy criterion	1	
Solver type	Conjugate gradient Iteration		Square Root Energy criterion	2	
Elastic material type	Isotropic elastic property	Tensile Failure reduces Hoek-Brown tensile strength to 0	tick	3	
Effective stress	Soil: 4.9; Rocks: 2.5		not tick	4	
Groundwater	Piezometer lines	Strength parameters	Mohr-Coulomb	5	
Field stress	Gravity stress		Failure criterion	Drucker-Prager	6
Initial element loading	Field stress and Body force		Generalised Hoek-Brown	7	
		Material type	Elastic	8	
			Plastic	9	

**Table 7.11 The 24 Combinations of modelling trials with varying factors from Table 7.8.**

Combination	Factor number				Combination	Factor number			
1	1	3	5	8	13	2	3	5	8
2	1	3	5	9	14	2	3	5	9
3	1	3	6	8	15	2	3	6	8
4	1	3	6	9	16	2	3	6	9
5	1	3	7	8	17	2	3	7	8
6	1	3	7	9	18	2	3	7	9
7	1	4	5	8	19	2	4	5	8
8	1	4	5	9	20	2	4	5	9
9	1	4	6	8	21	2	4	6	8
10	1	4	6	9	22	2	4	6	9
11	1	4	7	8	23	2	4	7	8
12	1	4	7	9	24	2	4	7	9

### 7.3.4.2 Model running for 24 combinations

Table 7.12 summarises the results of the 24 model trials.

**Table 7.12 The modelling results for 24 combinations, modelled using Phase2, with average Young's Modulus. Iteration /tolerance: 500/0.001; Lateral displacement measured (mm) : 27.9 mm/19.2 mm at distances of 438 m/472 m.**

Combination	Factor number	Lateral displacement modelled (mm)	Convergent
1	1 3 5 8	25.7/19.7	yes
2	1 3 5 9	10.9/7.2	May be not, iterations exceeded
3	1 3 6 8	25.7/19.7	yes
4	1 3 6 9	0/0	May be not, iterations exceeded
5	1 3 7 8	25.7/19.7	yes
6	1 3 7 9	46.9/17.2	May be not, iterations exceeded
7	1 4 5 8	25.7/19.7	yes
8	1 4 5 9	43.1/5.8	May be not, iterations exceeded
9	1 4 6 8	25.7/19.7	yes
10	1 4 6 9	0/0	May be not, iterations exceeded
11	1 4 7 8	25.7/19.7	yes
12	1 4 7 9	4.2/3.3	May be not, iterations exceeded
13	2 3 5 8	25.7/19.7	yes
14	2 3 5 9	17.9/1.2	May be not, iterations exceeded
15	2 3 6 8	25.7/19.7	yes
16	2 3 6 9	0/0	May be not, iterations exceeded
17	2 3 7 8	25.7/19.7	yes
18	2 3 7 9	22.3/10.4	May be not, iterations exceeded
19	2 4 5 8	25.7/19.7	yes
20	2 4 5 9	19.6/4.1	May be not, iterations exceeded
21	2 4 6 8	25.7/19.7	yes
22	2 4 6 9	0/0	May be not, iterations exceeded
23	2 4 7 8	25.7/19.7	yes
24	2 4 7 9	3.3/3.0	May be not, iterations exceeded
		All '8's give same result.	

For elastic materials (having 8 as the 4<sup>th</sup> factor number in Table 7.10), all trials gave the same modelled horizontal displacements of 25.7 mm at 438 m, and 19.7 mm at 472 m from the model origin. For plastic materials, all trials give horizontal displacements varying from 0/0 to 46.9/17.2 mm, however all the modelling using

plastic materials ‘may not be convergent and the iterations exceeded the maximum number allowable’ (message popup on screen after finish of modelling). The combinations using Drucker-Prager criterion (with two end factor numbers 6 and 9) yielded a zero/zero mm displacement in the plastic model.

Therefore, elastic material type was used in the further modelling, that is, the entire geological model was regarded to be consisted of an elastic mass because the strain was small and within the range of the elastic deformation. This is due to the large model dimension and small strata movement induced by the small slope over the deformed geological body. Therefore, the nine strata displaced in an elastic manner after extraction in my modelling.

There was no difference in the modelled results by choosing either of the two convergence types, 1 or 2 in Table 7.11. Also, no difference was obtained for ticking option ‘Tensile Failure reduces Hoek-Brown tensile strength to 0’ or not. So the factors 1, 2, 3, and 4 were not used in the following modelling work.

### 7.3.5 Model Running Using Elastic Material Method

After trials from sections 7.3.4, the narrowed factors are listed in Table 7.13. The failure criteria include Mohr-Coulomb, Drucker-Prager and Generalised Hoek-Brown. The eight combinations of trials are listed in Table 7.14.

**Table 7.13 Variables and constants used for trials of subsidence modelling using Phase2.**

Constants: every run uses the same.		Variables: each is tried in a run.		
Analysis type	Axisymmetric analysis		Criterion	Factor
Solver type	Conjugate gradient iteration	Failure criterion	Mohr-Coulomb	5
Elastic material type	Isotropic elastic property		Drucker-Prager	6
Effective stress	Soil: 4.9, rocks: 2.5		Generalised Hoek-Brown	7
Groundwater	Piezometer lines			
Initial element loading	Field stress and body force			
Material type	Elastic			

**Table 7.14 The failure criterion and the suitable strata to assign (from Section 4.4.7.2).**

Strata	Failure criterion to assign	
	Criteria name	Factor
TG soils	Mohr-Coulomb or	5
	Drucker-Prager	6
TK1 to TK6	Mohr-Coulomb or	5
	Generalised Hoek Brown	7
TK7 coal seam	Mohr-Coulomb or	5
	Generalised Hoek Brown	7
Greywacke	Generalised Hoek Brown	7

The modelled results (Table 7.15) show that the three failure criteria have presented the same modelling results in the eight trials. Comparison with measured surface displacements show 2.2 mm (8%)/ 0.5 mm (3%) difference between measured and modelled at the 2 distances considered.

**Table 7.15 The modelling results for eight combinations, modelled using Phase2, by inputting average Young's Modulus. Iteration /tolerance: 500/0.001**

Combination	Factor number	Lateral displacement at surface		Convergent
		modelled (mm)	measured (mm)	
1	5 5 5 7	25.7/19.7*	27.9/19.2	yes
2	6 5 5 7	25.7/19.7	27.9/19.2	yes
3	5 7 5 7	25.7/19.7	27.9/19.2	yes
4	6 7 5 7	25.7/19.7	27.9/19.2	yes
5	5 5 7 7	25.7/19.7	27.9/19.2	yes
6	6 5 7 7	25.7/19.7	27.9/19.2	yes
7	5 7 7 7	25.7/19.7	27.9/19.2	yes
8	6 7 7 7	25.7/19.7	27.9/19.2	yes

25.7/19.7\*: 25.7 mm is the lateral displacement modelled on surface at of 238 m from nearest edge (or 438 m from origin) to the borehole, 19.7 mm is the lateral displacement modelled on surface at 272 from nearest edge (or 472 m from origin) to the borehole.

## 7.3.6 Final Modelling and Validation

### 7.3.6.1 Final modelling

The final modelling was conducted using the parameters in Table 7.16. The modelling results were requested by plotting the query lines in the model (Figure 7.13). The eight vertical lines are at distances of 238, 255, 263, 272, 336, 382, 448,

460 m from the extraction edge, or 438, 455, 463, 472, 536, 582, 648, and 660 m from the ORIGIN of the model (refer to Table 7.2 the bolded column for 18 month delay time dataset). The three horizontal lines are on three planes at depths of 1, 135 m and 166 m which were the three discussed depths from strata movement interpretation in Chapter 6, which represent the near ground surface (at 1 m), the shear zone 1 (at 135 m), and the shear zone 2 (at 166 m). The modelled lateral displacements and vertical displacements were read from the 24 cross points by the eight vertical lines and three horizontal lines in the model, and summarised in Table 7.17.

**Table 7.16 Variables used for the final modelling of strata movement using Phase2.**

Analysis Type	Axisymmetric analysis (cylinder)	
Solver Type	Conjugate gradient Iteration	
Elastic Material Type	Isotropic elastic property	
Effective stress analysis	Soil: 4.9; Rocks: 2.5	
Groundwater	Piezometer lines	
Field stress	Gravity field stress	
Initial element loading	Field stress and Body force	
Convergence Type	Absolute Energy criterion	
Young's Modulus	averages from Table 7.5	
Other Parameters	refer to Table 7.5	
Material type	Elastic	
Failure criterion and layers to assign	Mohr-Coulomb	TG soils
	Mohr-Coulomb	TK1 to TK6
	GHB	TK7- coal seam
	GHB	Greywacke

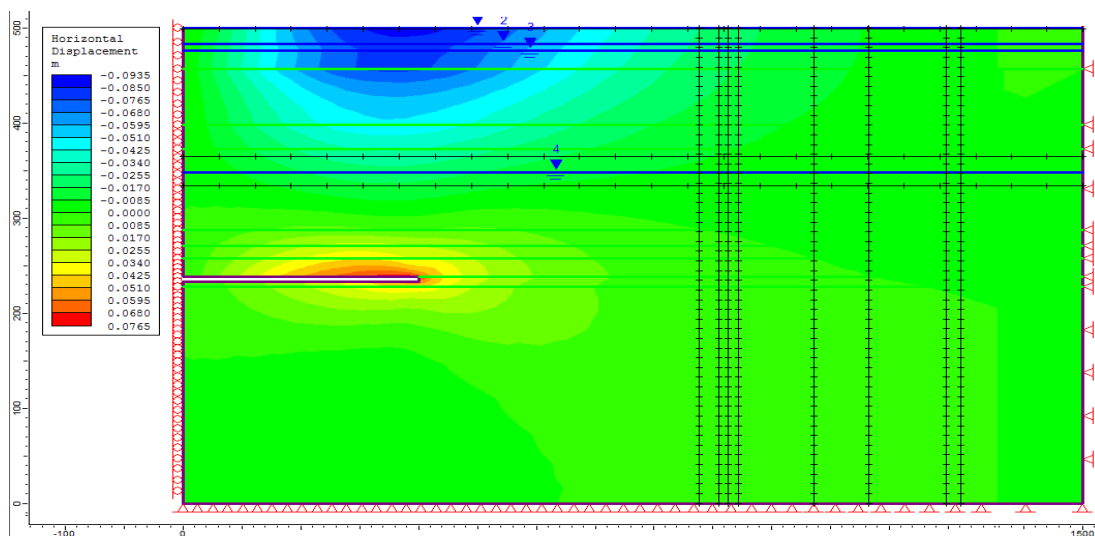


**Figure 7.13 The model interpretation screen, with 8 vertical lines and 3 horizontal lines.**

**Table 7.17 The final results of modelling using Phase2 with parameters from Table 7.16, all tests were convergent. No corresponding measured vertical data available.**

No.	Depth	Distance from EDGE	Distance from CENTRE	H displ. modelled	H displ. measured	Difference	V displacement modelled
	m	m	m	mm	mm	mm	mm
1-1	at 1 m	238	438	-25.7	-27.9	2.2	-11
1-2		255	455	-22.5	-12.5	-10	-9
1-3		263	463	-21.2	-12.5	-8.7	-8
1-4		272	472	-19.7	-19.2	-0.5	-7
1-5		336	536	-11.7	-13.6	1.9	-4
1-6		382	582	-8.2	-3.1	-5.1	-2
1-7		448	648	-4.5	-3.4	-1.1	0
1-8		460	660	-4	-2.9	-1.1	0
2-1	at 135 m	238	438	-9.2	-12.3	3.1	-8
2-2		255	455	-8.3	-6.3	-2	-6
2-3		263	463	-8.1	-1.9	-6.2	-5
2-4		272	472	-7.6	-11.8	4.2	-5
2-5		336	536	-5.5	-3.1	-2.4	-2
2-6		382	582	-4.3	-1.1	-3.2	-1
2-7		448	648	-3	-0.8	-2.2	0
2-8		460	660	-2.8	-2.3	-0.5	0
3-1	at 166 m	238	438	-5.2	-10.7	5.5	-7
3-2		255	455	-5.1	-5.5	0.4	-6
3-3		263	463	-4.8	-1.3	-3.5	-5
3-4		272	472	-4.7	-8.5	3.8	-5
3-5		336	536	-3.6	-2.5	-1.1	-2
3-6		382	582	-3.1	-1	-2.1	-1
3-7		448	648	-2.4	-0.6	-1.8	0
3-8		460	660	-2.3	-2.3	0	0

### 7.3.6.2 Final modelling analysis

- **Angle of Draw**

To establish the angle of draw from the modelled data for the inclinometer project area, the coordinate corresponding to a 20 mm vertical displacement was identified as (384.5, 500.0), where 20 mm of vertical subsidence is the cut-off value for determination of the angle of draw (Debono, 2007). Then the surface distance to the origin from that point was 384.5 m minus 200 m, equals to 184.5

m,. The stope right top had a coordinate (200.0, 238.0). Therefore, the angle of draw was calculated as below:

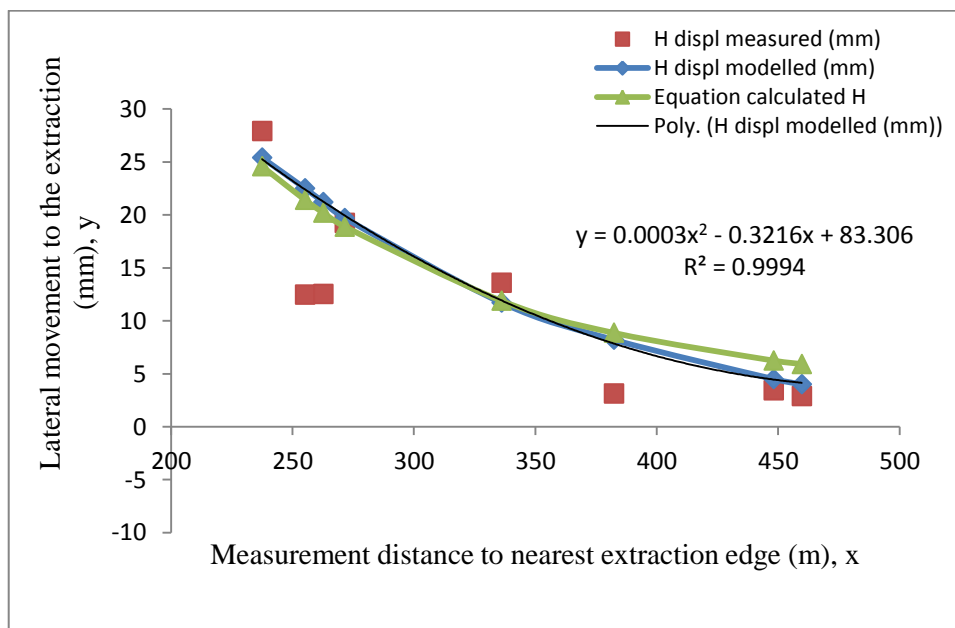
$$\gamma = \text{ATAN} (384.5-200.0)/(500.0-238.0) = 35^{\circ}$$

From the third column in Table 7.17, all the distances from EDGE are larger than 184.5 m, thus the eight points were all outside angle of draw, but notable horizontal displacements were still evident. The modelled vertical subsidence was all less than 11 mm.

- **Displacement plots at surface (1 m)**

Figure 7.14 compares the displacement plots of data from modelling, and calculation by equation:  $y = -0.05x^3 + 2.6829x^2 - 47.299x + 553.33$  (from Equation 7.5 that is a regression equation from measured data at 1 m). The trend lines from the calculation and modelled data agree well. The equation from the modelled trend line was obtained as Equation 7.8.

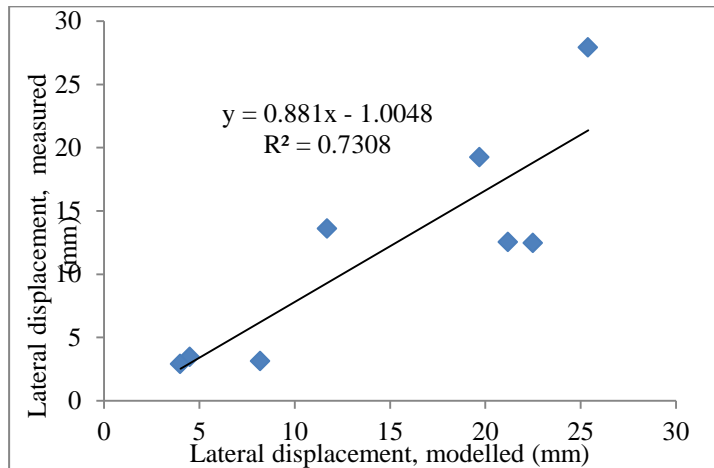
$$y = 0.0003x^2 - 0.3216x + 83.306 \quad R^2 = 0.9994 \quad (7.8)$$



**Figure 7.14 The plots of the displacement from measurement, modelling and calculation at surface (1 m depth).**

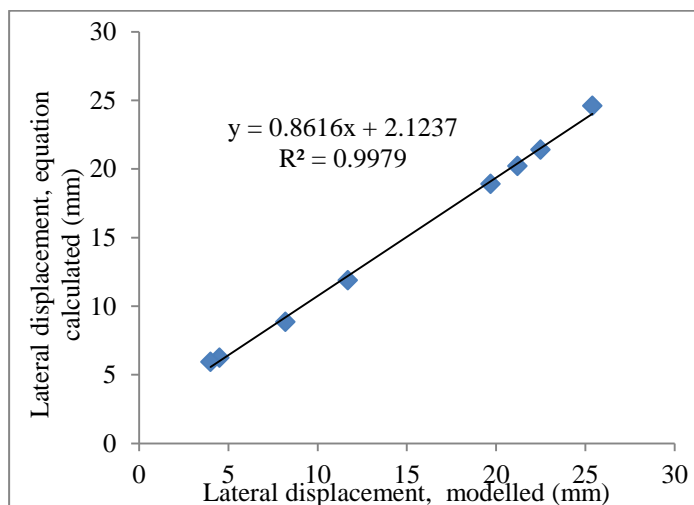


Figure 7.15 indicates the correlation between the modelled data and measured data. The somewhat lower  $R^2$  of 0.738 is possibly due to the two equal measured lateral displacements of -12.5 mm for the number 1-2 and 1-3 measurements that were measured at two different distances of 255 m and 263 m in Table 7.17.



**Figure 7.15 Correlation between the measured & modelled lateral displacements at 1 m.**

Figure 7.16 shows the correlation between the modelled data and the calculated data using the regression Equation 7.5. The trend line gives a high  $R^2 = 0.9979$ . Therefore, the Equation 7.8 may be used as the predication equation for determining the distance between the measurement locations to the nearest extraction edge at the ground surface (1 m depth).



**Figure 7.16 Correlation between the modelled & calculated lateral displacements at 1 m.**

- **Displacement plots at 135 m**

Figure 7.17 compares the displacement plots of data from modelling and calculation by equation:  $y = -0.0889x^3 + 3.8153x^2 - 49.711x + 452.91$  (Equation 7.6 that is the regression equation from measured data at 135 m). The curved lines by calculation and modelling agree well. The equation from the modelled trend line were obtained as Equation 7.9, having a high  $R^2=0.9993$ .

$$y = 7E-05x^2 - 0.0759x + 23.284 \quad R^2 = 0.9993 \quad (7.9)$$

Figure 7.18 indicates the correlation between the modelled data and measured data. The lower  $R^2$  of 0.5112 is possibly due to the too small measured lateral displacements of -1.9 mm (The modelled is -8.1 mm) for the number 2-3 measurements at 135 m depth, which was measured at a distance of 263 m from the nearest edge (Table 7.17).

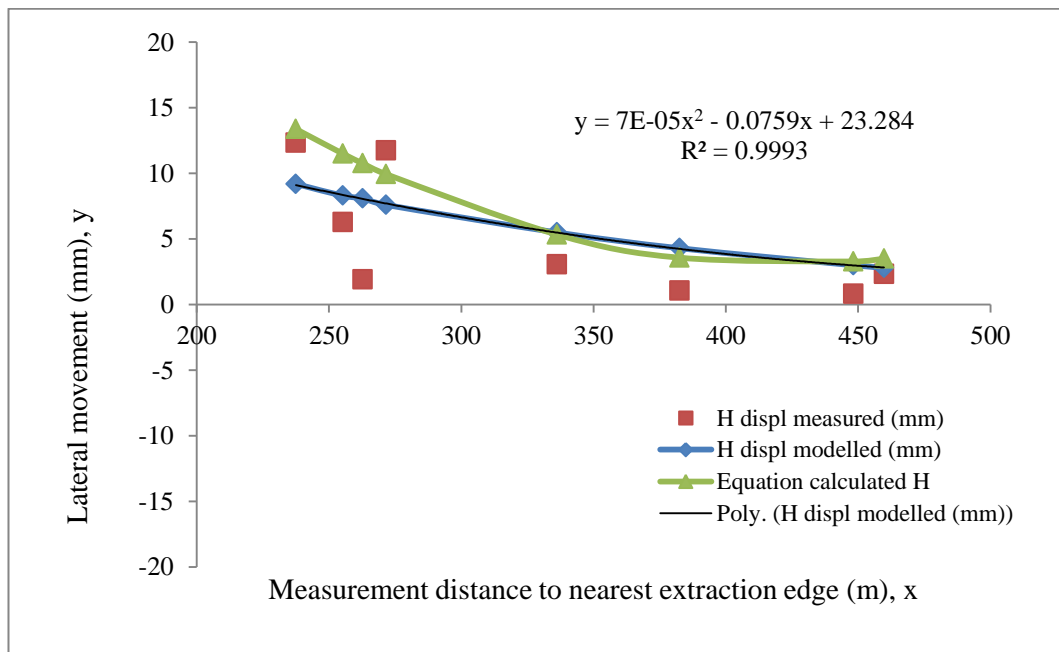


**Figure 7.17 The plots of the displacement from measurement, modelling and calculation at 135 m depth.**

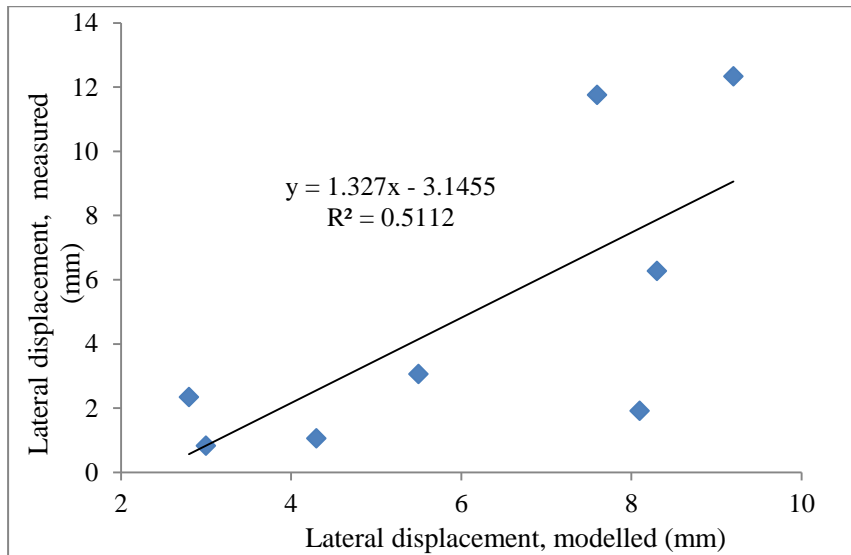


**Figure 7.18 Correlation between the measured and modelled lateral displacements at 135 m.**

Figure 7.19 shows the correlation between the modelled data and the calculated data at 135 m depth using the regression Equation 7.6. The trend line gives a high  $R^2 = 0.9535$ . Therefore, the Equation 7.9 may be used as the predication equation for determining the distance between the measurement locations to the nearest extraction edge at 135 m depth.

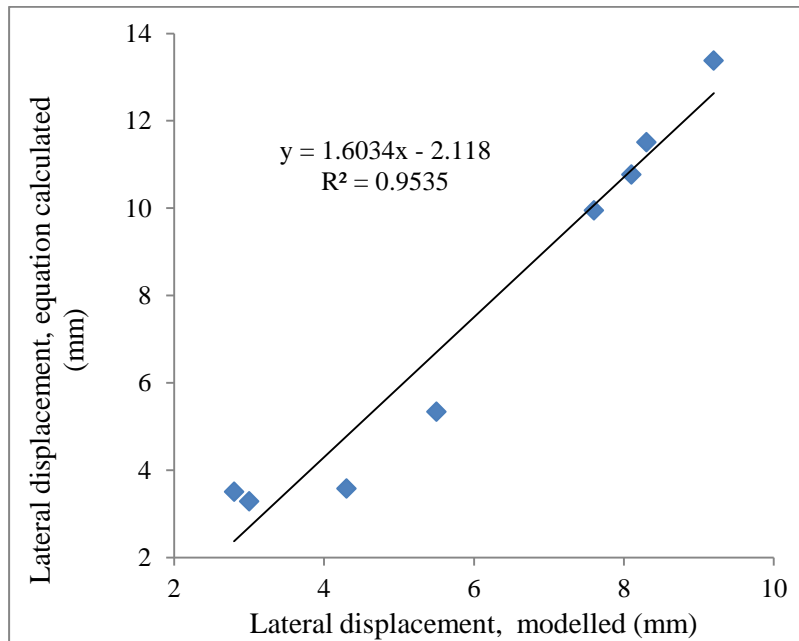


**Figure 7.19 Correlation between the calculated and modelled lateral displacements at 135 m.**

- **Displacement plots at 166 m**

Figure 7.20 compares the displacement plots of data from modelling and calculation by equation  $y = 392.3e-0.049x$  (Equation 7.7). The curved lines by calculation and modelling agree well. The equation from the modelled trend line were obtained as Equation 7.10,

$$y = 2E-05x^2 - 0.0304x + 11.131 \quad R^2 = 0.9967 \quad (7.10)$$

Figure 7.21 indicated the correlation between the modelled data and measured data. The lower  $R^2$  of 0.4906 is possibly due to the too small measured lateral displacements of -1.3 mm comparing with modelled displacement of -4.8 mm for the number 3-3 measurement at 166 m depth, which was measured at a distance of 263 m from the nearest edge (Table 7.17).

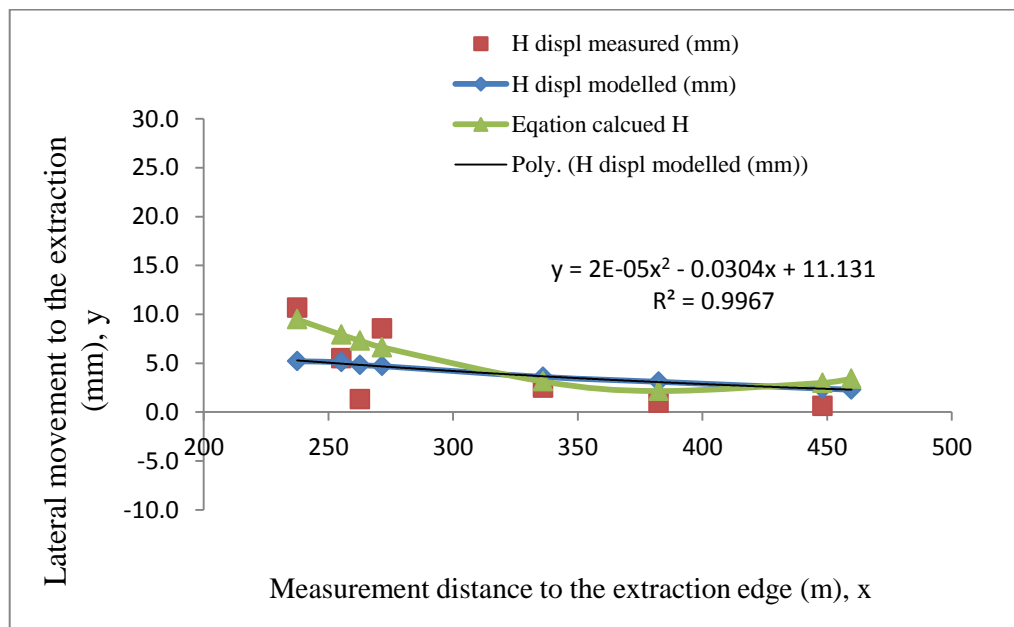


**Figure 7.20 The plots of the displacement from measurement, modelling and calculation at 166 m depth.**

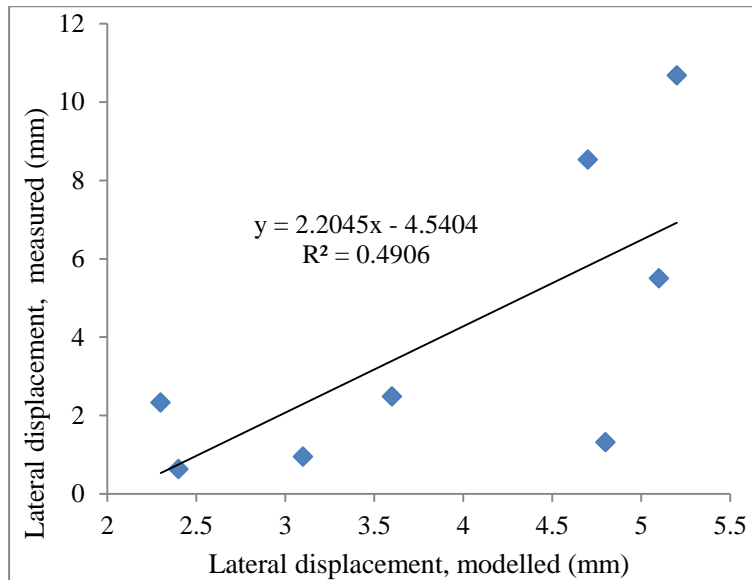


**Figure 7.21 Correlation between the measured and modelled lateral displacements at 166 m.**

Figure 7.22 shows the correlation between the modelled data and the calculated data at 166 m depth using the regression Equation 7.7. The trend line gives a  $R^2$  value of 0.8209. The Equation 7.10 may be used as the predication equation for determining the distance between the measurement locations to the nearest extraction edge at 166 m depth.

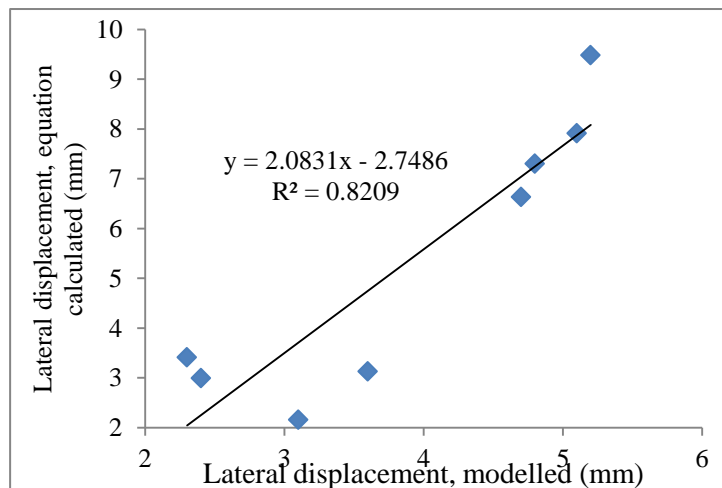


**Figure 7.22 Correlation between the calculated and modelled lateral displacements at 166 m.**

Then, some significant cut-off data can be initially obtained using the Equations 7.8, 7.9 and 7.10 (Table 7.18). The data suggest that for a 5 mm lateral

displacement at a measurement point the maximum distance from the nearest extraction edge to the measurement location should be not less than 374 m at 1 m depth, 360 m at 135 m depth, and 239 m at 166 m depth.

**Table 7.18 Some cut-off distances of extraction and cut-off horizontal movement of strata at surface, 135 m, and 166 m, North 5, the Huntly East Coalmine.**

Depth	Borehole horizontal movement (mm)		Extraction nearest distance to BH (m), calculated by equations				
			Phase2 modelled	Nonlinear regressed	Linear regressed	Difference	
	mm		m	m	m	m	m
			d1	d2	d3	d1-d2	d1-d3
1m	X= 0	Y=	438	553	433	-115	5
	X= 2	Y=	408	468	416	-60	-8
	X= 5	Y=	374	376	390	-2	-16
	X= 10	Y=	329	295	348	34	-19
135 m	X= 0	Y=	*	453	396	*	*
	X= 2	Y=	*	368	370	*	*
	X= 5	Y=	360	289	331	71	29
	X= 10	Y=	219	248	266	-29	-47
166 m	X= 0	Y=	615	392	396	223	219
	X= 2	Y=	412	356	365	56	47
	X= 5	Y=	239	307	317	-68	-78
	X= 10	Y=	38	240	237	-202	-199

\* The equation had no root.

## 7.4 Summary and Conclusions

### 7.4.1 Model Development and Regression Equations

This chapter has analysed the correlation between the lateral movement and the distance from the nearest extraction edge to the borehole, and then developed three regression equations.

- It was assumed that the only varying factor controlling the borehole movement in the North 5 project area was the nearest edge distance to the Borehole. Other factors were constant or stable.

- The delay time from completion of extraction to completion of subsidence was identified as approximately 18 months using the method of matching the correlation between the extraction and subsidence data.
- The correlation between the extraction nearest edge and the lateral movement was initially represented by three nonlinear equations 7.5, 7.6 and 7.7.

$$y = -0.05x^3 + 2.6829x^2 - 47.299x + 553.33 \quad R^2 = 0.8573 \quad \text{at 1m} \quad (7.5)$$

$$y = -0.0889x^3 + 3.8153x^2 - 49.711x + 452.91 \quad R^2 = 0.5513 \quad \text{at 135 m} \quad (7.6)$$

$$y = 392.3e^{-0.049x} \quad R^2 = 0.4953 \quad \text{at 166 m} \quad (7.7)$$

Of which equation 7.5 gave the best correlation between the extraction and the lateral movement at 1 m depth. At other two depths investigated (135 m and 166 m) correlations were not so strong as the overall direction of movement towards the ENE while the extraction was towards the ESE.

## 7.4.2 Numerical Modelling

This chapter then modelled the strata movement using Phase2. The regression equations in model development were verified and corrected using numerical modelling, and three new theoretical equations were obtained for calculating the lateral displacement by inputting the extraction edge distance to the borehole. The numerical Equations are:

$$y = 0.0003x^2 - 0.3216x + 83.306 \quad R^2 = 0.9994 \quad \text{at 1 m} \quad (7.8)$$

$$y = 7E-05x^2 - 0.0759x + 23.284 \quad R^2 = 0.9993 \quad \text{at 135 m} \quad (7.9)$$

$$y = 2E-05x^2 - 0.0304x + 11.131 \quad R^2 = 0.9967 \quad \text{at 166 m} \quad (7.10)$$

Where: x, the nearest distance from extraction edge to the Borehole, m.

y, the lateral movement distance of the Borehole at a depth over a month, mm.

Using the above three equations the maximum distances from the measurement point to the nearest edge of the extraction can be computed by inputting the limit of the lateral movement. The data suggest that for a 5 mm lateral displacement the maximum distance should be not less than 374 m at 1 m depth, 360 m at 135 m depth, and 239 m at 166 m depth.

The angle of draw in the inclinometer project area was  $35^{\circ}$  determined by the numerical model.

Apparently, the three equations above do not directly contain parameters or factors of geological, geotechnical properties or tectonic stresses in the computation. However the constants and function rule in the equations imply the influence of the effects of geological, geotechnical properties or tectonic stresses in the studied area of Huntly East Mine.

The results of the modelling should be considered to represent the best estimate on data currently available, and correction methods applicable rather than an exact prediction. The modelling was also based on estimated or averaged hydrological, geological settings and material properties. On-going monitoring of both surface and subsurface movements are required to provide validation and refinement in the properties used in the model, consequently provide more accurate outcomes of predictions.

Both the numerical model and the modelled equations require further calibration with future field observation, monitoring and third party reviews before application.



### 7.4.3 Discussions

In Tale 7.18 three datasets of the measured lateral displacement may be abnormal and contributed to the lower  $R^2$  values, they are:

- two equal measured lateral displacements of -12.5 mm for the number 1-2 and 1-3 measurements that were measured at two different distances of 255 m and 263 m;
- the too small measured lateral displacements of -1.9 mm (The modelled is -8.1 mm) for the number 2-3 measurements at 135 m depth, which was measured at a distance of 263 m from the nearest edge;
- the too small measured lateral displacements of -1.3 mm comparing with modelled displacement of -4.8 mm for the number 3-3 measurement at 166 m depth, which was measured at a distance of 263 m from the nearest edge.

The above three abnormalities may come from the random errors or errors by the probe casing bottom that may be possibly instable because the casing bottom was installed in the strata 50 m above roof of the extracted coal seam. The other limitations and assumptions were to be discussed in Section 8.5.

# Chapter 8 Summary and Conclusions

## 8.1 Summary of Literature Review

### 8.1.1 Findings and Implications from the Literature Review

Ground subsidence is a dynamic, spatial and temporal process. The final, static subsidence troughs have permanent impacts on surface structures located near the edges of a subsidence basin formed as a result of strains.

Dynamic subsidence applies both tensile and compressive strains to the structures as mining progresses. The structures in a subsidence domain may be damaged by both tension and compression.

The concept of 'the Negative Additional Vertical Friction' originates from China and is largely published in the Chinese literature. However over ten of the papers on the negative additional vertical friction have been published in International Journals or presented in International Conferences in English. Up to now I have not found any peer oppositions or questions in papers from other countries or international society, which have caused us to attention concerning this concept.

Where there is a relative displacement between the shaft lining and the surrounding strata, there may exist the negative additional vertical friction acting on the external surface of the lining, whatever factors lead to the displacement. This friction will cause vertical downwards stress within the shaft lining and damage the lining at a depth when the resultant stress is larger than the strength of the lining.

It is evident that the negative additional friction is an essential part of adverse effects from the ground subsidence onto the shaft lining, whether the subsidence is

from the underground mining or water withdrawal or other factors. Though the geology at Huntly is not quite the same as for the Xuhuai region, there may exist some similarities, such as in coal seam depths, hydrology, and geotechnical properties of the materials. Up to July 2011, none of the reports, designs or documents on the proposed shaft has mentioned the negative additional friction and its impacts. It is possible that we can use the negative additional friction concept to benefit us in this research project in help with the project of the 4m diameter, 300 m deep shaft, as a guidance and reference for the design, construction and even later maintenance and protection over the duration of mining production. Therefore, this review could be likely to be of some assistance and experience for the shaft sinking project above the N55 panel in Huntly East Mine (Details refer to Appendix B)

### **8.1.2 Potential Outstanding Features of This Study**

The potential outstanding features of this study are summarised (from section 2.4.4.2) as below:

- The installation of an inclinometer borehole deeper than 120 m has not been found in around 100 literature articles reviewed.
- Reports of use of inclinometer monitoring of ground movement induced by underground extraction were not found in the literature reviewed.
- All reviewed cases have the bottom of casing installed in stable strata below the movement zone, but the bottom of the casing in borehole 20091 may be not in the stable strata because the Borehole bottom is around 50 m above the seam extracted, that means that the bottom of the casing in borehole 20091 might move as well, therefore the plotted displacement may not be representative of the movement that occurred.

This borehole inclinometer monitoring project, therefore, has outstanding aspects that are more complicated and comprehensive than all the examples reviewed.

According to ASTM (2005), no standards are available yet for evaluation against precision and bias issues arising from use of borehole inclinometer (Machan & Bennett, 2008). Therefore, the inclinometer borehole in my research project may be one of the most complicated cases for monitoring and measurement of the strata movement induced by underground extraction in New Zealand.

## **8.2 Discussion**

### **8.2.1 Main Borehole Observations and Movement Interpretation**

In sections 5.5.1, three major events, such as probe kicking, probe jamming and borehole water level changes, were discussed and analysed. Those events were most likely to have the related connections with the inclinometer measurements, and influenced the veracity of the interpretation results of the strata movements. For example, the extreme checksum readings occurred at the joints or  $\pm 0.5$  m from the joints and or at a depth where casing deformation was evident.

The probe kicking, probe jamming and borehole water level changes may have all resulted from one casing rupture problem at a depth of about 38 m in the borehole. At first, the casing at around 38 m might have a large lateral differential movement in the weak and porous grout cement, which was induced by the vertical stretching and compression due to the differential layer subsidence and upsidence. Consequently, the significant differential deformation at around 38 m contributed to the tangled cumulative displacement plot before 03/02/2011, then the casing rupture occurred when deformation increased, but was small leading to groundwater from out of the enclosed borehole entering the casing, raising water

levels observed from 03/02/2011; meanwhile the rupture resisted the probe traversing or even kicked the probe leading to the occurrence of the two abnormal surveys on 12/11/2010 and 18/01/2011. As the rupture increased to a level, the probe was not able to traverse through and got jammed on 11 March 2011. The rupture kept increasing and became large enough to let the probe shift between A and B grooves in the casing in the trials of dummy probe and lowering in the B grooves on 02/06/2011.

An investigation by CCTV camera down the probe casing was suggested to locate the casing cracks and depth, consequently identifying the reason for probe jamming.

Nearly 2/3 of the mining area had been extracted around the inclinometer borehole up to March 2011 when the probe traversing was stopped at 38.53 m. The data measured might be approximately half of what the inclinometer research project should get.

It is expected that more measurements may yield more accurate interpretation results of strata movement; the repetition of inclinometer measurement can provide more accurate and reliable results.

### **8.2.2 Shortcoming of Traversing Inclinometer Method**

Compared with embedded in-place multi-probes, a traversing method using one probe can save investment. However, when the deformation rises to a level where the probe cannot be lowered through, continued use of the probe became impossible. Therefore the traversing inclinometer method could not measure for as long as desired.

When the probe traversing was stopped at 38.53 m in March 2011 the strata movement was just in its early stage considering that 2/3 of the extraction had been completed and the delay characteristics of ground movement vs. the extraction advancing (90% occurs within 6 months of the first instance of subsidence). Therefore, the data measured might be approximately half of what the inclinometer research project should get.

### **8.2.3 Replication of Measurement**

Checksums can be checked on site just after one traversing of probe is completed. But it is unlucky that the advice for repeating the measurement was not undertaken due to the first time application of the inclinometer in borehole monitoring in Huntly East Mine.

The inclinometer manual only recommends repetition of measurement when the checksums are beyond a certain limitation (i.e.5 mm). If the measurement was repeated two or three times on one day more accurate and reliable results would have been obtained. However, the repetition would have cost more and consumed more time, repetition in every second or several time measurements should be recommended for a deep borehole monitoring.

### **8.2.4 Suggestions for Further Work**

#### **8.2.4.1 Alternative software options**

ABAQUS was initially chosen as the modelling code, but was found too time-consuming because it is advanced software having large software package and thick user manual. Phase2 is available in University Laboratory and is simple to use. Considering the time limit of the research work, the Phase2 software was

finally selected for the modelling work in this study. In the future the code of ABAQUS could be tried to model the strata movement in Huntly East Coalmine when the resources of the time, cost and software for using ABAQUS are practicable.

#### **8.2.4.2 Inclinometer calibration**

The inclinometer system should be regularly calibrated to ensure that the readings taken with the system are accurate. Soil Instruments recommends calibration on an annual basis by the inclinometer manufacturer or an inclinometer expert (SOIL, 2009). The inclinometer system is used weekly for the inclinometer borehole monitoring and slope monitoring in Rotowaro Opencast Mine. The time spent on a trip and for calibration will take nearly 6 weeks if sending to the UK headquarters of SOIL Company, leading to influence of continuous monitoring. Therefore one more inclinometer system should be purchased to solve this problem.

#### **8.2.4.3 Continuing the monitoring**

The inclinometer monitoring was stopped in March 2011 when the seam extraction was just underneath the inclinometer borehole. Considering the requirement of further data for validating the results of this research, and the Borehole continuous use as a costly structure, the recommendation for extending capacity of the inclinometer method and further monitoring of strata movement in the Borehole was proposed, but it was not practically possible to carry out for the monitoring work.

#### **8.2.4.4 Attention to the Far Field Subsidence Movements**

Normally, the settlements and surface strains are considered to be confined to a ‘subsidence bowl’ above coal-mine extraction. The boundary of this bowl is delineated by ‘angles of draw’ measured from the edges of the area of extraction.

However, significant horizontal ground movements well occurred outside the expected subsidence bowl which has implications in the design of the proposed shaft when the distances between the shaft and the nearest extraction edge are calculated using Equations 7.8, 7.9, and 7.10. This is because the horizontal stress is higher than the vertical stress in the studied area in this research which is in accordance with the statement in Section 2.3.8, that the high horizontal stresses are ‘typically 2 to 3 times the overburden pressure’ (Pells, 2008). Details about the far field subsidence movements are included in Appendix A-11.

#### **8.2.4.5 Vertical movement data of the Borehole opening**

Vertical movement data of the Borehole opening may be insufficient for analysing the vertical movement in detail because of few datasets available and the relatively low accuracy of the GPS at  $\pm 40$  mm compared to the measured magnitude of the rise and drop of the borehole opening (section 6.6.1). There were only two (out of eight) results larger than calculation uncertainty of  $\pm 56.7$  mm in Table 6.14.

However, the available data suggested that the strata had heaved and subsided following extraction of the underground coal seam. Further monitoring of the vertical movement of the opening should be continued for interpreting the correlation between the ground vertical movement and underground extraction.



## 8.3 Conclusions

### 8.3.1 Conclusions on Data Error Correction

- There were 13 inclinometer measurements undertaken over approximately 2 years.
- The data errors in the 13 inclinometer datasets included the extreme checksum values, might contain bias-shift errors but were uncertain to determine the level of it, and may consist of minor rotation error, depth error and spiral error.
- Through evaluation of the checksum quality by the Coefficient of Variation (CV), two measurement datasets were discarded due to their abnormalities, then 11 datasets were analysed for error correction and data interpretation.
- Several spikes (extreme values) on the checksum plot in each survey have been corrected by averaging the neighbouring readings. The resulting amended mean checksums gave CV values of the corrected readings for each axis all less than 10%.
- Because the Borehole bottom was not installed in a stable stratum, the extraction induced movement and the Bias-shift error may have both contributed to the leaning lines in the bottom section of the cumulative plots. However the relative weighting of the two contributions is unknown.
- No major rotation errors, depth errors, or spiral errors were detected in the datasets. However, small errors of the above three error types might exist, consequently not corrected in this study.

### 8.3.2 Conclusions on Movement Interpretation

- There were three movement zones presented, two ‘shear zones’ from 135.0 to 135.5 m and from 166.0 to 170 m, and one ‘creeping zone’ from surface (1 m) to 115 m. From 135.0 to 135.5 m there was a thin, minor, shear zone. The shear zone at depths from 166 to 170 m was the major shear zone evident in the inclinometer data.
- The Borehole movement was presented by the trajectory of the intersection of the borehole at depths of surface (1 m), 135 m, and 166 m.
- The trajectories of the borehole lateral movement show that the movement was non-linear, and the trajectories varied with depth, having a varying movement rate and direction.
- The two shear zones were located on strata bedding planes of the Te Kuiti Group. The creeping movement occurred in the soft Tauranga Group and within the upper Te Kuiti Group.
- GPS measurements of the ground at the borehole location had a vertical raise and drop movement. The maximum range in vertical raise and drop was 15 cm (approximately  $\pm 6$  cm) from March 2009 to February 2011.
- The cumulative displacements along the trajectory of borehole movement were 58.3 mm at 135 m depth, 45.6 mm at 166 m depth, and 157.6 mm near the ground surface (1 m depth). However, the cumulative displacements between the initial measurement (No.0, undertaken on 29/03/2009) and the final measurement (No. 10, undertaken on 22/02/2011) were 29 mm at  $64^{\circ}$  (ENE) at 135 m depth, 22.8 mm at  $64^{\circ}$  (ENE) at 166 m depth, and 127.2 mm at  $134^{\circ}$  (ESE) at 1 m depth. Therefore, the casing top was moving in the general direction of coal extraction, but at depths of 135

m and 166 m the overall movement was towards ENE. The detailed discussion is undertaken in Chapter 7 using the comparison between the borehole movement trajectories and the extraction trajectory.

- The trajectory of the extraction advancing was not in a straight line. The trajectory of the borehole lateral movement was also a non-linear movement having a varying movement rate and direction.

To conclude, the three movement zones had different movement directions and rates along depth and over time. Therefore the three zones had different movement behaviours over depth which may have been responding to dynamic extraction locations in the mining operation.

The correlation between the completion of extraction and the completion of subsidence has been initially analysed in this study. However the correlation, especially their vector correlation (the patterns of movement trajectory and the extraction trajectory) needs further study to obtain a better trajectory matching.

### **8.3.3 Conclusions on Movement Modelling**

- The only varying factor controlling the borehole movement in the North 5 project area was the nearest edge distance to the Borehole. Other factors were considered to be stable.
- The best estimate of the delay time from extraction to subsidence was identified as approximately 18 months using the method of matching the correlation between the extraction and subsidence data.
- The correlations between the nearest extraction edge and the lateral movement were represented by non-linear equations. The non-linear Formulas 7.5, 7.6 and 7.7 showed the non-linear correlation between the

horizontal movement at depths of surface (1 m), 135 m, and 166 m, and the nearest edge distance from extraction to the Borehole. Revised equations were developed using numerical modelling, and finalised as:

$$y = 0.0003x^2 - 0.3216x + 83.306 \quad R^2 = 0.9994 \quad \text{at 1 m} \quad (7.8)$$

$$y = 7E-05x^2 - 0.0759x + 23.284 \quad R^2 = 0.9993 \quad \text{at 135 m} \quad (7.9)$$

$$y = 2E-05x^2 - 0.0304x + 11.131 \quad R^2 = 0.9967 \quad \text{at 166 m} \quad (7.10)$$

where:

x: the nearest distance from extraction edge to the Borehole, m.

y: the lateral movement distance of the Borehole at a depth over a month, mm.

Then the cut-off distance to avoid 5 mm lateral displacement at 1 m depth was computed as 376 m (Table 7.18).

## 8.4 Limitations

### 8.4.1 Limitations of Monitoring Operation

Appendix C lists 11 helpful precautions for minimising the data errors in the inclinometer monitoring and measurement. However, 4 of 11 were not true in the inclinometer borehole for this research project:

- The casing was not inserted into stable strata, the base of the borehole and the bottom of the casing was 50 m above the seam roof.
- Only one survey was used to determine the reference measurement.
- When checksums were not constant, the probe was not recalibrated before subsequent measurement.

- Sometimes, the probe might have been left less than 10 minutes at the borehole bottom for warm-up and getting stabilisation.

#### **8.4.2 Limitation of Literature on Inclinometer Monitoring**

On summary of the major documents and literature on inclinometer borehole monitoring for the reviewed approximately 100 references, no references discussions about installations of an inclinometer borehole deeper than 120 m have been found. Only a few applications of inclinometers use in monitoring movement induced by underground extraction have been found and all less than 120 m deep. All reviewed cases have the bottom of casing in stable strata below the movement zone. But the inclinometer Borehole in this study had a bottom level about 50 m above the extracted seam roof. Furthermore, no standards are available yet for evaluation against precision and bias issues arising. Our inclinometer borehole had a depth of 250 m and the borehole bottom might have potential movement. Therefore few similar cases were available as my research reference, and data measured from a potential moving datum (the borehole bottom) may disadvantage the accuracy of the prediction of the subsidence using the modelled equations.

#### **8.4.2 Limitation on Inclinometer Calibration in Laboratory**

Though the probe (1678) was calibrated in the Laboratory at Huntly Coalmine by the operators, the regular calibration by manufacturers or experts is still suggested to ensure that the readings taken with the system are accurate.

### **8.4.3 Modelling Limitation**

#### **8.4.3.1 “All Models Are Wrong But Some Are Useful” (Box, 1979).**

The numerical modelling of the geological and geotechnical problems often exist with uncertainties, not only about the selection of the model and modelling code but also the option of the input parameters and ‘quite often assumptions made without proper justification’(Keilich, 2009). The principles of the numerical modelling that ‘numerical modelling itself is not the most important aspect, but the conceptualisation of the problem, material properties and parameters should be paramount in any investigation’ (Keilich, 2009).

Therefore, the results of the modelling in this thesis should be considered to represent the best estimate on data currently available, and correction methods applicable rather than an exact prediction. The modelling was also based on estimated or averaged hydrological, geological and material properties.

On-going monitoring of the surface and subsurface is required to provide validation and refinement in the properties used in the model (SCT, 2003).

#### **8.4.3.2 Limitation of option of software**

The Phase 2 software cannot be used to model shear movement in the Axisymmetric Analysis type (section 4.4.2.4). ABAQUS can model the shear movement, but has complex complexity, while Phase2 is comparatively simple (Section 2.5.3). ABAQUS may give a more accurate modelling outcome. In the future the code of ABAQUS could be tried to model the strata shear movement in Huntly East Coalmine when the resources of the time, cost and software for using ABAQUS are practicable and available.

#### **8.4.4 Insufficient Vertical Subsidence Data**

Lateral movement has been analysed and interpreted in this thesis, but vertical subsidence has only been identified to exist and is not discussed in detail due to the less dataset available and the small GPS accuracy compared to the initial measured values of the vertical drop and rise at the borehole opening. Further monitoring and measurement are needed to determine the correlation between the vertical movement and extraction underneath.

What we are mostly concerned with for the negative vertical additional friction as to damage to the shaft lining is the occurrence of the vertical subsidence, not the magnitude of it. The vertical subsidence was proved to exist, and then the designers can tailor the design of the proposed shaft with different approach by considering that the shaft may suffer impacts of vertical subsidence once sunken.

#### **8.4.5 The 0.336 m Outstanding Casing above the Ground Surface**

The inclinometer casing had a 0.336 m length standing out of the inclinometer borehole above the ground surface (Figure 4.3 in Chapter 4). The inclinometer measurement depth used in my thesis started from the top of the casing, so the real depths of the three movement zones should be minus the 0.336 m. In the data analysis and interpretation, this 0.336 m was thought over, and had a minor or no influence to the mechanism of subsidence, and correlations between the extraction and the results of the lateral movement. To simplify the analysis and interpretation, therefore, this 0.336 m was not used in the relative calculations in my research.

## **8.5 Epilogue**

To conclude the discussion and conclusions, this research report has been prepared for my qualification of Master of Earth Science and also for Solid Energy North for the particular objectives described in the thesis and the collaborative agreements. The thesis was based on data acquired during the project and other published and non-published sources, internal and or external. The research findings and conclusions were based on interpretations of those data and are limited by the interpolations and assumptions made. The information contained in the thesis should not be used by anyone else or for any other purposes. All the results of this study should be regarded as interim until further site confirmation is available and assessed on the basis of local experience, field observations, and monitoring.





## References

- Alonso, E.E., Josa, A. & Ledesma, A. (1984). Negative skin friction on piles: a simplified analysis and prediction procedure, *Journal of Geotechnique*, 34, No. 3, 341-357.
- Ambrozic, T & Turk, G. (2003). Prediction of subsidence due to underground mining by artificial neural networks, *Computers & Geosciences* 29 (2003), 627–637, doi:10.1016/S0098-3004(03)00044-X.
- ASTM (The American Society for Testing and Materials) (2008). *Geotechnical Engineering Standards ASTM D4644 – 08, Standard Test Method for Slake Durability of Shales and Similar Weak Rocks*, USA.
- Aston, T.R.C. Tammemagi, H.Y. & Poon A.W. (1987). A review & evaluation of empirical and analytical subsidence prediction techniques. *Mining Science and Technology*, 5 (1987), 59-69. Retrieved from Elsevier Science Publishers.
- Bahuguna, P.P. Srivastava, A.M.C. & Saxena, N.C.(1991). A critical review of mine subsidence prediction methods, *Mining Science and Technology*, 13 (1991), 369-382. Retrieved from Elsevier Science Publishers.
- Bi, S. (1996). The Research on the deformation mechanism and counter measurement of shaft failure. *Earth Science Frontiers* (China University of Geosciences, Beijing), Vol. 3 No.1, 1996 (in Chinese).
- Bi, S., Lou, X., & Xu, B. (1997). On the Mechanism of Coal Mine Shaft Damage caused by Subsidence in Xuhuai Area, Southeast China. *Communications in Nonlinear Science & Numerical Simulation*, Vol.2, No.2. doi:10.1016/S1007-5704 (97)90043-5, Retrieved from [http:// www.elsevier.com/locate/jcumt](http://www.elsevier.com/locate/jcumt).
- Blodgett, Steve, M.S. & Kuipers, James R., P.E (2002). *Technical Report on Underground Hard-Rock Mining: Subsidence and hydrologic Environmental Impacts*. The Center for Science in Public Participation (CSP2), USA, pp.50.
- Box, George E.P, (1979). *A great quote, Robustness in the strategy of scientific model building*. Page 202 of *Robustness in Statistics*, R.L. Launer and G.N. Wilkinson, Editors. 1979. Retrieved from <http://ukpmc.ac.uk/>.
- Bozozuk, M. & Andre, L. (1969). Downdrag measurements on 270-Ft composite piles performance of deep foundation. S TM S T P 434. *American Society for Testing and Materials*, 1969, 15-40.
- Bozozuk M. (1972). Downdrag measurements on a 160-Ft floating pipe test pile in marine clay. *NRC Publications Archive (NPARC), Canadian Geotechnical Journal*, 9, 127 (1972), 127-136. Retrieved from Geotechnical Section. Division of Building Research, Canada.

- Bozozuk M. (June, 1981). *Bearing capacity of pile preloaded by downdrag*. NRC Publications Archive (NPArc). National Research Council Canada, Proceedings, 10th International Conference on Soil Mechanics and Foundation Engineering Stockholm, 15 - 19 June 19, 631 – 636.
- Brady, B.H.G. & Brown, E.T. (2004). *Rock Mechanics for underground Mining*, pp. 628, 3rd edition, Kluwer Academic Publishers, the Netherlands.
- Brown University (2011). *Advanced Mechanics of Solids, ABAQUS Tutorial*. Retrieved from <http://www.brown.edu/> on 10/10/2011.
- Brownlee, G. (2009). *Opening Address to Australasian Institute of Mining and Metallurgy, 2009*. Retrieved from <http://www.beehive.govt.nz/speech/opening-address-australasian-institute-mining-and-metallurgy-2009>.
- Cai, Y.Q. & Geng, X. (2007). The analysis of the compaction of strata surrounding shaft under Multi-loads. *Journal of Wenzhou University (Natural Sciences)*, Vol. 28, No 1 (in Chinese).
- Cao et al. (2008). Coal mine land subsidence monitoring by using space-borne Insar data - a case study in Fengfeng, Hebei Province, China. *The International Archives of the Photogrammetry, Remote Sensing and Spatial Information Sciences*. Vol. XXXVII. Part B8. Beijing.
- Capasso, G. & Mantica, S. (2006). *Numerical Simulation of Compaction and Subsidence Using ABAQUS*. 2006 ABAQUS Users' Conference. Exploration and Production Division, Milan, Italy.
- Chai, J. Liu, J. X, & Qiu, B. (2011). Detecting deformations in uncompacted strata by fiber Bragg grating sensors incorporated into GFRP. *Tunnelling and Underground Space Technology*, 26 (2011), 92–99, doi: 10.1016/j.tust.2010.06.009.
- Chen, X.F. et al. (2010). Numerical model research of super deep shaft sidewall destruction. *Chinese Journal of Underground Space and Engineering*, Vol. 6, 2010 (in Chinese).
- China Safety. (2007). Research and Technology of Shaft Lining Rupture in Coalmine. China Bureau of Safety and Supervision, Retrieved from [http://www.chinasafety.gov.cn/zhuantibaodao/2007-04/25/content\\_234210.htm](http://www.chinasafety.gov.cn/zhuantibaodao/2007-04/25/content_234210.htm), (in Chinese) on 02 August 2011.
- China Ministry of Construction. (2002). *Code for design of concrete structures, GB 500102002*. The Press of China Ministry of Construction, Beijing (in Chinese).
- Chow, Y.K., Lim, C.H. & Karunaratne G.P. (1996). Numerical Modelling of Negative Skin Friction on Pile Groups. *Computers and Geotechnics*, Vol. 18, No. 3, 201-224.

- Chrzanowski, A. & Secord, J. M. (2000). Tilt Measurement, University of New Brunswick, CRC Press LLC, Retrieved from <http://www.engnetbase.com>.
- Cornforth, Derek H. (2005). *Landslide in Practice: investigation, analysis and Remedial / preventative options in soil*, John Wiley & Sons, pp. 616.
- Crampton, N. (Oct. 2010). Hydrogeology and Interconnection, Solid Energy. Thick Seam Mining Huntly Coalfield Workshop, 2010, Pattle Delamore Partners Ltd (PDP).
- Crowell, D.L. (2010). Mine subsidence, Ohio Department of Natural Resources. Retrieved from <http://www.dnr.state.oh.us/>.
- Desai, C.S. & Cheistian, J.T. (1977). *Numerical methods in geotechnical engineering*. McGraw-Hill Book Company, USA, pp.783.
- Daemen, Jaak J.K (1972). The Effect of Protective Pillars on the Deformation of Mine Shafts. *Springer-Verlag Rock Mechanics* 4, 89 -113 (1972).
- Debono, P. (2007). *Introduction to Longwall Mining and Subsidence*. Mine Subsidence Engineering Consultants. Retrieved from [www.minesubsidence.com](http://www.minesubsidence.com).
- Ding, M. (2005). *Failure Forecast of the Underground Structure under Complicated Load* (Master's dissertation, Shandong University of Science and Technology, China) (in Chinese). Retrieved from <http://eng.cnki.net/grid2008/index.htm>.
- Emilios, M.C. & Spyridoula, V. B. (2005). Evaluation of Negative Skin Friction effects in pile foundations using 3D nonlinear analysis. *Computers and Geotechnics* 32 (2005), pp. 210–221. Retrieved from [www.elsevier.com/locate/compgeo](http://www.elsevier.com/locate/compgeo).
- Fellenius, B.H. (1971). Downdrag on piles in clay due to Negative Skin Friction. *Canadian Geotechnical Journal*, Vol. 9, No. 4, 323 - 337.
- Gale, W. (2001). *East mine seam extraction options, CNZ1963B*. Internal report by SCT Operations Pty Ltd, Solid Energy.
- Gale, W. (2003). *Review of computer model Outcomes of N51 Panel and layout options for N52 Panel, CNZ2543*, Internal report by SCT Operations Pty Ltd, Solid Energy.
- Gale W. (2006). *Huntly north geotechnical characterisation*, internal report by SCT Operations Pty Ltd, Solid Energy.
- Gale, W. (2007). *Background and process of subsidence prediction used for Huntly North design*, internal report by SCT Operations Pty Ltd, Solid Energy.

- Ge, X. (2002). Engineering properties of two grouting techniques in mending shaft lining ruptures. *Journal of China Coal Society*, Vol. 27, No. 1, pp. 4 (In Chinese). Retrieved from <http://eng.cnki.net/grid2008/index.htm>.
- Geotechnics Co. (2009). *Geotechnical testing results for borehole 20097*, internal reports provided by Geotechnics Co., Solid Energy.
- Golder Kingett Mitchell (2007). *Huntly North Project surface water management*. Internal report by Golder Kingett Mitchell Ltd for Solid Energy.
- Gutierrez, Juan J. Vallejo, Luis E. & Lin, J.S. (2010). *A study of highway subsidence due to Longwall mining using data collected from I-79 FINAL REPORT*, April 30th, 2010, University of Pittsburgh, USA.
- Guy, G. et al. (2006). *An investigation into underground mine interaction with overlying aquifers, Huntly East Mine, New Zealand*, Coal Operators' Conference, University of Wollongong Year 2006. Retrieved from <http://ro.uow.edu.au/coal/44> on 02 April 2011.
- HACIOSMANOĞLU, M. Esenay (2004). *Development of a subsidence model for Cayirhan Coal Mine*. (Master's thesis of Middle East Technical University, Turkey). Retrieved from <http://etd.lib.metu.edu.tr/upload/12605481/index.pdf>.
- Hauraki District Council (2002). *Waihi underground mines report to the people of Waihi*. Hauraki District Council, New Zealand. Retrieved from <http://www.hauraki-dc.govt.nz/news/Mining-issues/mineworkingsreport/Summary/default.htm>.
- He F. et al. (2003). The policies and measures on prevention and mitigation to the surface subsidence in coal mine. *Engineering of Coal Mining*, 3rd edition, 2003, China (in Chinese).
- Howard L.H. et al. (1992). *Mining engineering*, Society for Mining Metallurgy & Exploration. 2nd Revised edition Handbook, pp.2394, USA.
- Hsieh, W.W. (2009). *Machine Learning methods in the environmental science: Neural Networks and Kernels*. Cambridge University Press, UK. Retrieved from [http://assets.cambridge.org/97805217/91922/frontmatter/9780521791922\\_frontmatter.pdf](http://assets.cambridge.org/97805217/91922/frontmatter/9780521791922_frontmatter.pdf).
- Huang, D., Yu, H. & Ma, J. (1991). The influence of land subsidence on the rupture of shaft lining in Linhuai coalfield. *Journal of Coal Science and Technology*, China (in Chinese). Retrieved from <http://www.zgmtkj.com/Techs.aspx>
- Huang, Q. (2009). Simulation of clay aquifuge stability of water conservation mining in shallow-buried coal seam. *Chinese Journal of Rock Mechanics and Engineering*, Vol.28 No.5, May, 2009 (in Chinese).

- Itasca (2011). *FLAC overview*. Itasca International Inc. Retrieved from <http://www.itascacg.com/flac/features.html> on 12/04/2011.
- Jing, L.W., Liu, F. & Gai, Q. (2004). Rupture stress of shaft lining in mine due to ground subsidence. *Chinese Journal of Rock Mechanics and Engineering*, Vol. 23, No19, pp. 3274~ 3280 (In Chinese). Retrieved from [http://english.whrsm.cas.cn/sp/200909/t20090904\\_35796.html](http://english.whrsm.cas.cn/sp/200909/t20090904_35796.html).
- Jing, L.W., Zhang, T.Y. & Xu, H.D. (2005). Relation between the seepage sedimentation mechanism of soil in mining area and shaft rupture. *Journal of Coal Geology and Exploration of China*, Vol.33, No.3, June, 2005 (In Chinese).
- Johnson, A. I. (May 1991). *Land subsidence*. Proceedings of the Fourth International Symposium on Land Subsidence May 1991 held at Houston, Texas, 12-17. Retrieved from <http://catalogue.nla.gov.au/Record/701477>.
- Karmis, M., Agioutantis, Z. & Andrews, K. (2008). *Enhancing mine subsidence prediction and control methodologies*. The 27th International Conference on Ground Control in Mining, USA. Retrieved from <http://www.techtransfer.osmre.gov>.
- Kennedy, Edward M. (2008). *Report on the August 6, 2007 Disaster at Crandall Canyon Mine United States Senate*, pp.75. Health, Education, Labour and Pensions Committee. Retrieved from <http://www.infomine.com/publications/docs/CrandallCanyonReport2008.pdf>.
- Kim, H. J. & Mission, L.J.C. (2009). Negative skin friction on piles based on Finite Strain consolidation theory and the nonlinear load transfer method. *KSCE Journal of Civil Engineering* (2009) 13(2), 107-115, Geotechnical Engineering. Retrieved from [www.springer.com/12205](http://www.springer.com/12205).
- Keilich, W. (2009). *Numerical modelling of mining subsidence, upsidence and valley closure using UDEC*. (PhD thesis, University of Wollongong, Australia). Retrieved from <http://www.uow.edu.au/index.html>.
- Kelsey, P.I. (1986). *An engineering geological investigation of ground subsidence above the Huntly East Mine area*. (Master thesis, University of Canterbury, pp.280, 1986). Retrieved from [www.ir.canterbury.ac.nz](http://www.ir.canterbury.ac.nz).
- Kumar, B. R. Deb, D. & VNS Prasad, M. (2010). *Numerical modelling – an effective tool for strata control in coal mines*. National Seminar on Underground Coal Mining, India, 152-162.
- Lawless, J., Okada, W. & Terzaghi, S. (2003). *Two dimensional subsidences modelling at Wairakei-Tauhara, New Zealand*. International Geothermal Conference, Reykjavík, Sept. 2003 Session #12
- Larratt, P. (2009). *Huntly North Shaft geotechnical baseline report*, 2009. pp.36, unpublished internal report by Coffey Mining Pty Ltd Australia, for Solid Energy.

- Larratt, P. et al. (2010). *Permanent lining analysis part A: Design assumption*, pp.14, unpublished internal report by Coffey Mining Pty Ltd Australia for Solid Energy.
- Leng, Y. et al. (2005). *Handbook of technologies, standards, and specifications on projects of Tunnels and Shafts in mines*, Jilin Electronic Press, Jilin, China (in Chinese), pp1777.
- Li, W.X, Zhao, S.T. & Liang, X.L. (2006). Influence of underground mining on shaft towers in Luzhong Mining areas. *Chinese Journal of Rock Mechanics and Engineering*, Vol. 21, No1, 74~ 78 (In Chinese).
- Li, W.X., Liu, L.& Dai, L.F. (2010). Fuzzy probability measures (FPM) based Non-symmetric membership function: Engineering examples of ground subsidence due to underground mining. *Engineering Applications of Artificial Intelligence*, 23 (2010), 420–431. Retrieved from [www.elsevier.com/locate/engappai](http://www.elsevier.com/locate/engappai).
- Liang et al. (2009). In-site monitoring and analysis of shaft lining's additional strain in failure and formation grouting. *Procedia Earth and Planetary Science* 1 (2009): 503–511, and the 6th International Conference on Mining Science & Technology. Retrieved from [www.elsevier.com/locate/jcumt](http://www.elsevier.com/locate/jcumt).
- Liu, X. (2010). *Six modern standards of operation & technology of mining*. pp.2101, Jilin Science Press, Changchun, China (in Chinese).
- Liu, H.Y., Chen, W.Z.& Wang, Z.M. (2007). Theoretical analysis of shaft lining damage mechanism of Yanzhou mine. *Chinese Journal of Rock Mechanics and Engineering*, Vol.26 Supp.1 (In Chinese).
- Liu, H.Y., Wang, S.J. & Zeng, Q.B. (2005). An artificial neural network forecast model for Shaft lining non-mining fracture. *Chinese Journal of Hydrologic and Engineering Geology*, Vol 2, 2005 (In Chinese).
- Liu, Y. (2010a). *Dynamic processes of the mining subsidence, and its subsidence model based on the key layers* (PhD thesis, Chongqing University, China, pp139, in Chinese).
- Lv, H.L. & Cui, G.X. (2001). Study on the coupling mechanism between reinforced concrete Shaft lining and thick surrounding rock (soil). *Journal of China Coal*, Vol.26 No.5, October.2001, China (in Chinese).
- Lv, T.H.& Dai, H.Y. (1998). The mechanism of deformation and damage of the shaft lining in land subsidence by non-underground extraction. *Journal of Mine Survey*, Vol. 4, pp.1 –16.
- Machan, G. & Bennett, V.G. (2008). *Use of inclinometers for geotechnical instrumentation on transportation projects, state of the practice*, Transportation Research, Number E-C129, October 2008, USA.



- Mikkelsen, P. E. (2003). Advances in Inclinometer Data Analysis. *Symposium on Field Measurements in Geo-mechanics*, Norway, Sept. 2003, pp.13. Retrieved from [www.slopeindicator.com/pdf/papers/advances-in-data-analysis.pdf](http://www.slopeindicator.com/pdf/papers/advances-in-data-analysis.pdf).
- Mikkelsen, P. E. (2007). *Inclinometer Data & Recognition of System Errors* [Course notes]: University of Florida, Short Course, March 19, 2007, pp.22.
- Mine Subsidence Engineering Consultants (2007). *Introduction to Longwall Mining and Subsidence*. Mine Subsidence Engineering Consultants. Retrieved from [www.minesubsidence.com](http://www.minesubsidence.com), revision A.
- Minerals Council of Australia (1997). Minesite Water Management Handbook. Australia, pp.9. Retrieved from [www.minerals.org.au/\\_data/assets/pdf\\_file/.../MWMH\\_Content.pdf](http://www.minerals.org.au/_data/assets/pdf_file/.../MWMH_Content.pdf).
- MCRC (Ministry of Coal Resources, China). (2000). *National Specification on coal mining and pillar sizes for working under buildings, water-bodies and railways*, Ministry of Coal Resources, China, National Coalmine Industry Publish Ltd, 2000, pp.304 (in Chinese).
- Ministry of Construction of China (MCC). (1991). *The Code for construction, inspection and acceptance of mine Tunnels and Shafts, GBJ213-90 1991*, pp.122, Beijing, China (in Chinese).
- Ministry of Construction of China (MCC). (2007). *Design specification of the Shafts and Underground Chamber in coal mine*, GB 50384-2007, Beijing, China (in Chinese).
- Ministry of Economic Development. (2011). *Coal resources: Waikato region, New Zealand*. Retrieved from <http://www.nzpam.govt.nz>, on 02 August 2010.
- Mitre Software Co. (2003). *Inclinometer software, GTILT v2.18a*, Canada.
- Moon, V. & Roy, T. (2004). Geological controls on rock mass classification of coal from Huntly East Mine, New Zealand. *Engineering Geology* 75 (2004), 201–213. Retrieved from [www.elsevier.com/locate/enggeo](http://www.elsevier.com/locate/enggeo).
- New York State (2007). *New York State Hazard Mitigation Plan*, USA. Retrieved from [www.dhSES.ny.gov/oem/](http://www.dhSES.ny.gov/oem/).
- New Zealand Government. (1991). *Resource Management Act, 1991*. New Zealand.
- Novikov, F.Y. (1979). Pressure of thawing soils on the concrete lining of vertical mine shafts. *Engineering Geology*, 13 (1979), 277-286, Elsevier Scientific Publishing Company, Amsterdam.
- Page, P. (2009). *Geotechnical Information Report Drillhole 20097*, internal report, Solid Energy, New Zealand, pp.18.



- PDP (PATTLE DELAMORE PARTNERS LTD). (2006). *Huntly North PAG 4 – Report on Tauranga Group Interconnection Study - Stage 1*, Internal reports, Solid Energy, Huntly, pp. 31.
- PDP (PATTLE DELAMORE PARTNERS LTD). (2009). *Huntly North Shaft Borehole Testing – Factual Report*, Internal reports, Solid Energy, Huntly, 2011.
- Poorooshasb, H.B., Alamgi, M. & Miurab, N. (1996). Negative skin friction on rigid and deformable piles. *Computers and Geotechnics*, Vol. 18, No. 2, 109-126. Retrieved from [www.sciencedirect.com](http://www.sciencedirect.com).
- Puertas, J.J. G. (2010). *Estimating highway subsidence due to Longwall mining*. (PhD thesis, University of Pittsburgh). Retrieved from <http://d-scholarship.pitt.edu/8170/>.
- Queen's University (2009). *Mine Shaft Development*. Retrieved from <https://wiki.queensu.ca/display/mine448/Mine+Shaft+Development>, on 10/11/2010.
- RockScience Inc. (2011). *Phase2 Tutorials*. Retrieved from <http://www.roscience.com/downloads/phase2/webhelp/tutorials/Phase2Tutorials.htm>.
- RST Instruments Ltd. (2010). *RST MEMS Digital Inclinometer System Instruction Manual*, USA, pp.54.
- Sheorey, P.R., Loui, J.P. & Singh, K.B. (2000). Ground subsidence observations and a modified influence function method for complete subsidence prediction. *International Journal of Rock Mechanics and Mining Sciences* 37 (2000): 801-818.
- Singh, T. N. & Singh, B. (1985). Model simulation study of coal mining under river beds in India. *International Journal of Mine Water*, Vol.4, (3), (1985): 1-10. Retrieved from <http://www.springerlink.com>.
- Slope Indicator Company. (2000). *Slope Indicator Training, Data Reduction and Error Correction*, 13-15, Slope Indicator Company, Mukilteo, Washington, USA.
- Slope Indicator Company. (2001). *Slope Indicator Training, Data Reduction and Error Correction 2001 - graph types*. Slope Indicator Company, Mukilteo, Washington, USA.
- Slope Indicator Company. (2002). *Slope indicator spiral-sensor datasheet 2002*. Slope Indicator Company, Mukilteo, Washington, USA.
- Slope Indicator Company. (2003). *Slope Indicator DigiPro for windows 2003*, pp.38, Slope Indicator Company, Mukilteo, Washington, USA.

- Slope Indicator Company. (2004). *Slope Indicator guide-to-instrumentation 2004*, pp. 52, Slope Indicator Company, Mukilteo, Washington, USA.
- Slope Indicator Company. (2006). *Slope Indicator Digitilt Probe Manual*, pp.16, Slope Indicator Company, Mukilteo, Washington, USA.
- Slope Indicator Company. (2011). *DMM for Windows 50310970, Slope Indicator*, pp50, Company, Mukilteo, Washington, USA.
- SOIL (Soil Instruments Limited). (2007). *SOIL C9-4 Quick Drive Inclinometer Casing Rev01.4 2007*, pp4, Soil Instruments Limited, UK.
- SOIL (Soil Instruments Limited). (2008). *Vertical Digital Bluetooth Inclinometer System with TDS Recon 200 PDA User Manual*, Soil Instruments Limited, UK.
- SOIL (Soil Instruments Limited). (2009). *In-Site Inclinometer Data Presentation Software (Dongle Version)*. Soil Instruments Limited, UK, pp.25.
- SOIL (Soil Instruments Limited). (2010). *Vertical Digital Bluetooth Inclinometer System MkII with Archer PDA User Manual*. Soil Instruments Limited, UK, pp.34.
- Solid Energy. (2006). *N55/57 Project Area Draft Geological Interpretation*. September 2006, internal report, pp.91, Solid Energy, New Zealand.
- Solid Energy. (2007). *Huntly East Mine Fact Sheet*, Solid Energy. Retrieved from <http://www.coalnz.com/index.cfm/3,205,429/huntly-east-factsheet.pdf>, viewed on 09 August 2011.
- Solid Energy. (2007a). *Huntly North project assessment of environmental effects*, August 2007. Internal report, pp125, Solid Energy, New Zealand
- Solid Energy, (2009). *Solid Energy Operations*. June 2009. Retrieved from [www.coalnz.com/index.cfm/3,463,992/se-operations.pdf](http://www.coalnz.com/index.cfm/3,463,992/se-operations.pdf), 08 August 2011
- Solid Energy. (2009a). *Borehole 20091 Chip Photographs*, Internal data, Solid Energy.
- Solid Energy. (2009b). *Borehole 20091 Strip Logs – overview*, internal data, Solid Energy.
- Solid Energy. (2009c). *Borehole 20091 Drillers logs*, internal data, Solid Energy.
- Solid Energy. (2009d). *Borehole 20091 geophysical logs*, internal data, Solid Energy.
- Solid Energy. (2011). *New Zealand Coal - The Waikato coal region – Geology*. Retrieved from <http://www.coalnz.com/index.cfm/1,198,0,49.html>, on 4/09/2011.

- Solid Energy. (2011a). *The data from the Vulcan database of the Huntly East Mine, including the location of inclinometer borehole, extraction outlays and parameters, and cross sections across the inclinometer borehole*, internal data, Solid Energy, 2011.
- Stark, T. D. & Choi, H. (2008). Slope inclinometers for landslides, *Technical Development, Landslides* (2008) 5: 339–350, Springer-Verlag 2008.
- Su, J. & Cheng, H. (2000). Analysis on additional forces of shaft with drainage of stratum. *Chinese Journal of Rock Mechanics and Engineering*, Vol. 19 (No3): 310~ 313 (In Chinese). Retrieved from <http://english.whrsm.cas.cn/>.
- Su, M., Zhao, Z. & Li, D. (2003). Application of grey system theory model in mining subsidence. *West-China Exploration Engineering*, series No. 83, Apr. 2003 (in Chinese).
- Tan J.K. & St. George J.D. (1989). Geomechanics of underground coal mining under very weak overburden rocks at Huntly East Mine, *New Zealand, Mining Science and Technology*, 9 (1989): 253-265.
- Tan, Z.X., Li, P.X. & Yan, L. L. (2009). *Study of the method to calculate subsidence coefficient based on SVM*, The 6th International Conference on Mining Science & Technology Procedia Earth and Planetary Science 1 (2009): 970–976. Retrieved from <http://eng.cnki.net/grid2008/index.htm>.
- Texas A&M University. (2011). *University Physics I, Mechanical Equilibrium*, <http://physics.tamuk.edu/~suson/html/2325/>, viewed on 20 August 2011.
- The New Zealand Government. (2010). *Statement to Parliament*. Retrieved from <http://beehive.govt.nz/feature/statement-parliament>, 9 February, 2010.
- Ti, K. S., Huat, B.B.K. & Noorzaei, J. (2009). A review of basic soil constitutive models for geotechnical application, *The Electronic Journal of Geotechnical Engineering* Retrieved from <http://www.ejge.com/2009/Ppr0985/Ppr0985ar.pdf>, on 03/04/2011.
- Tobar, T. & Meguid, M.A. (2010). Comparative evaluation of methods to determine the earth pressure distribution on cylindrical shafts: a review. *Tunnelling and Underground Space Technology*, 25 (2010): 188–197.
- UWA (The University of Western Australia). (2010). *Numerical Methods in Rock Mechanics*, DEER (Deep Extraction of Earth Resource), the University of Western Australia (UWA).
- Vardoulakis, I; Vairaktaris E.& Papamichos, E. (2004). Subsidence diffusion convection: I. The direct problem. *Computer Methods in Applied Mechanics and Engineering*, 193 (2004): 2745–2760. Retrieved from <http://www.sciencedirect.com/>.

- Wang, C.Q. (2007). New type of shaft structural design of vertical shaft in the area of goaf and subsidence. *Chinese Journal of Coal Technology*, V01. 26. No. 1 January, 2007 (In Chinese).
- Wang, J.J., Luo, N.H. & Bai, Z.M. (2003). On the relation between interlayer glide caused by coal extraction and the shaft rupture occurring in coal mines in Huanghuai area. *Chinese Journal of Rock Mechanics and Engineering*, 22(7): 1072~1077 (in Chinese).
- Wang, Y.S., Zhang, C. & Xue, L.B..(2010). Prediction and safety analysis of Additional Vertical Stress within a shaft wall in an extra-thick alluvium. *Mining Science and Technology* 20 (2010): 0350–0356.
- Wang, Z.Q., Lu, Z.Y. & Zhang L.M. (2009). The inverse analysis of the Vertical Additional Force and stability forecast of shaft lining for thick alluvium. *Journal of Shandong University (Engineering Science)*, Vol. 39, No. 4 (in Chinese).
- Whittaker, B.N. & Reddish, D.J. (1989). *Subsidence: Occurrence, Prediction, and Control*. Elsevier Science Pub, Co., Amsterdam, Netherlands (Interloan 4557745), pp528.
- Widener University. 2012, *Error Analysis*, Retrieved from <http://science.widener.edu>, on 08 January 2012.
- Wikipedia. (2011). *Drucker–Prager yield criterion*, [http://en.wikipedia.org/wiki/Drucker%E2%80%93Prager\\_yield\\_criterion](http://en.wikipedia.org/wiki/Drucker%E2%80%93Prager_yield_criterion).
- Yang, W.H., Li, F. & Wang, Z.S. (2007). Field measurements for strains in shaft lining in alluvium during drainage and grouting. *Chinese Journal of Rock Mechanics and Engineering*, Vol.26 Supp.1: 2713-2717, July, 2007, (in Chinese).
- Yao, Z.S. & Li, R.J, (1997). Calculation method for stress of shaft wall under Vertical Additional Force. *Coal Technology of Northeast China*, No. 2, 1997 (In Chinese).
- Zhao, Z. M. & Chen, X. (2009). Surface movement and deformation simulated by Verhulst model, 978-1-4244-4520-2/09 2009. *IEEE (Institute of Electrical and Electronics Engineers)*. Retrieved from <http://www.ieee.org>.
- Zhao, G.S., Zhou, G.Q. & Zhong, G.R. (2009). *Analysis of stratum grouting influence on shaft lining stress with the methods of simulation and in Site Measurements*. The 6th International Conference on Mining Science & Technology, Procedia Earth and Planetary Science 1 (2009): 497–502. Retrived from [www.elsevier.com](http://www.elsevier.com).

- Zhou, J., Zhou, G.Q. & Shang, X.Y. (2009). *Numerical simulation on shaft lining stresses analysis of operating mine with seasonal temperature change*. The 6th International Conference on Mining Science & Technology, *Procedia Earth and Planetary Science* 1 (2009): 550–555. Doi:10.1016/j.proeps.2009.09.087.
- Zhou, J., Zhou, G.Q. & Shang, X.Y. (2010). Numerical simulation on structure optimization of double-layer shaft lining with Vertical Additional Force and thermal stress. *Journal of Xi'an University of Architecture & Technology (Natural Science Edition)*, Vol. 42 No.2 April. 2010 (In Chinese). Retrieved from <http://www.cnki.net/>.
- Zhou Z. & Yang, W.M. (2003). The analysis of the lateral resistance on the fractured shaft lining. *Coal Geology and Exploration Journal of China*, Vol 31, No. 5 (in Chinese). Retrieved from <http://www.cnki.net/>.

## Contents of Appendices

<b>1</b>	<b>Appendix A: Literature Review Supplements.....</b>	<b>315</b>
	A-1 Subsidence Deformation Indices and Concepts .....	315
	A-2 Factors Affecting Mine Subsidence.....	319
	A-3 Empirical Prediction Method of Subsidence - Graphical method .....	325
	A-4 Empirical Prediction Method of Subsidence - Profile functions .....	328
	A-5 Empirical Prediction Method of Subsidence - Influence functions.....	332
	A-6 Prediction Method of Subsidence - Numerical Techniques .....	335
	A-7 Physical Models.....	341
	A-8 State of Art on Prediction of Subsidence .....	347
	A-9 In-Situ Horizontal Stress, Yassien’s Study (2003) .....	354
	A-10 Prevention of Subsidence .....	354
	A-11 Far Field Subsidence Movements.....	357
	A-12 Safety Pillars for Shaft .....	359
<b>2</b>	<b>Appendix B: The Negative Additional Vertical Stress .....</b>	<b>366</b>
	B-1 Introduction.....	366
	B-2 Rupture Characteristics .....	367
	B-3 Negative Additional Vertical Friction.....	372
	B-4 Examples for Calculations.....	376
	B-5 Prevention, Protection and Repair of Shaft Lining .....	384
	B-6 Contribution and Supports .....	388
	B-7 Interesting Finding – Novikov’s paper.....	390
	B-8 Discussions .....	391
	B-9 Conclusions.....	393
<b>3</b>	<b>Appendix C: Precautions for Minimising the Data Errors.....</b>	<b>394</b>
<b>4</b>	<b>Appendix D: Original Inclinometer Measurement Data (electronic copy in CD)</b>	<b>395</b>
<b>5</b>	<b>Appendix E: The Incremental Displacement Data after Error Correction (CD</b>	<b>396</b>
	<b>file) 396</b>	
<b>6</b>	<b>Appendix F: Calculations for the Weighted Extraction Parameters (CD file)</b>	<b>397</b>
<b>7</b>	<b>Appendix G: Cross Sections of Strata across the Inclinometer Borehole (CD file)</b>	<b>398</b>



## List of Figures in Appendices

Figure A 1 The surface subsidence indices and concepts (from Puertus, 2010; Debono, 2007).....	315
Figure A 2 Strata Movement (from Puertus, 2010; Debono, 2007). ....	316
Figure A 3 Critical extraction width on subsidence (from Howard et al. 1992). 319	
Figure A 4 Schematics of displacement and strain curves for various working widths (a) Subcritical width. (b) Critical width. (c) Supercritical width (Howard L. et al., 1992, p940).....	320
Figure A 5 Relationship of subsidence to extraction width and depth (Whittaker and Reddish, 1989). ....	326
Figure A 6 Correction graph for limited face advance (Whittaker and Reddish, 1989). ....	326
Figure A 7 Design graph for prediction of subsidence profiles (after SHE, 1975, cited by Whittaker and Reddish, 1989).....	327
Figure A 8 Design graph for prediction of strain profiles (Whittaker & Reddish, 1989). ....	327
Figure A 9 Graph of the three principal types of strain profile after SEH 1975 (Whittaker and Reddish, 1989). ....	328
Figure A 10 Monographs developed by NCB: (a) the influence of width/depth on subsidence, (b) The influence of extraction width (from Bahuguna et al., 1991). ....	329
Figure A 11 Calculation of subsidence by integration grid method (Bahuguna et al 1991). ....	332
Figure A 12 Representation of Bals' influence function (Whittaker and Reddish, 1989). ....	334
Figure A 13 (a) elemental excavation (three-dimensional problem) and (b) cross section of elemental excavation (x o z), (Li et al., 2010).....	334
Figure A 14 Keinhorst's influence function (Whittaker and Reddish 1989). ....	335
Figure A 15 Numerical Methods Relationship (after Desai and Christian, 1977, p2). ....	337
Figure A 16 The locations of the point P and excavation underground (Li et al, 2010). ....	338
Figure A 17 Physical model shows the dropped beds into the extracted zone (Whittaker and Reddish, 1989). ....	341
Figure A 18 Overburden and coal seam simulated by physical model (Huang, 2009). ....	342
Figure A 19 Physical model and roof caving after the first slice mining (Huang, 2009). ....	342
Figure A 20 Roof caving after the second slice mining (Huang, 2009). ....	343
Figure A 21 Roof caving laws of mining face (Huang, 2009).....	343
Figure A 22 Roof and clay aquifuge subsidence laws (Huang, 2009).....	344
Figure A 23 Axisymmetric trap-door mechanism in small-scale model test with dry sand (Vardoulakis et al. 2004). ....	344
Figure A 24 The trap-door mechanism—the model (Li et al, 2010, p424). ....	345
Figure A 25 Equivalent Material Mine Modelling (Sign and Singh, 1985). ....	346
Figure A 26 Harmonic mining studies for mining under HFL (Sign and Singh, 1985). ....	346
Figure A 27 Observed and predicted subsidence in Xiaoli mining area (Li et al., 2010). ....	348
Figure A 28 Subsidence growth. a. amount of subsidence growth; b. accumulated amount of subsidence growth (after Zhao and Chen, 2009). ....	350



Figure A 29 Subsidence by prediction and measurement (mm) (After Su et al, 2003).....	351
Figure A 30 Far field movements, Douglas Park (From Pells, 2008). .....	358
Figure A 31 Far field horizontal movements in the NSW Southern Coalfield (from mine subsidence engineering consultants, 2008, cited by Pells, 2008). .....	358
Figure A 32 Predicted far field movements in metres (Pells, 2008). .....	359
Figure A 33 Coordinate system for the study of the influence on the shaft of mining and area A in a seam at depth H (from Daemen 1972). .....	361
Figure A 34 Vertical strain along the shaft, $R=0.3 H$ . A seam of 10 ft. thick at a depth of 1000 ft. is mined out except for a protective pillar of 300 ft. radius. Z: depth, $\nu$ : Poisson's ratio (From Daemen 1972).....	362
Figure A 35 Tilt along the shaft. A seam of 10 ft. thick at a depth of 1000 ft. is mined out over the entire (planar) region on one side of the shaft, except for a protective pillar of 300 ft. radius. Z: depth, $\nu$ : Poisson's ratio (From Daemen 1972).....	362
Figure A 36 Vertical strain along the shaft for four different pillar radii (Daemen 1972).....	363
Figure A 37 Tilt along shaft for five different pillar radii (Daemen 1972). .....	363
Figure A 38 Pillar radius R required with increasing seam depth to keep the ...	364
Figure A 39 Pillar radius R required with increasing seam depth to keep the maximum tilt along the shaft less than $1.3 \times 10^{-3}$ , or $3.0 \times 10^{-3}$ or $5.5 \times 10^{-3}$ (Daemen 1972). .....	364

## List of Tables in Appendices

Table B 1 Shaft damage classification in Xuhuai area (From Bi, 1996).....	368
Table B 2 The shaft rupture information of part frozen shafts in China (Jing et al., 2005).....	372
Table B 3 The calculated results of additional force on surface of lining in Linhuan Coal Mine (kpa) (Su and Cheng, 2000). .....	381
Table B 4 Analysis results of stress composition (from Jing et al., 2004). .....	383

# Appendices

## 1 Appendix A: Literature Review Supplements

### A-1 Subsidence Deformation Indices and Concepts

Subsidence generally possesses both vertical and lateral displacements. Surface subsidence shows itself in three major ways in nature: Cracks, fissures, or step fractures; pits or sinkholes; troughs or sags (Howard et al., 1992, Li et al., 2010).

Theoretically, surface subsidence is a complicated spatial and temporal process mostly characterized in three-dimensional profile to illustrate its vertical settlement and horizontal displacements, tilting, curvature (convex and concave), and tensile and compressive strains (Figures A1 and A2) (Whittaker and Reddish 1989; Debono, 2007; Puertus, 2010).

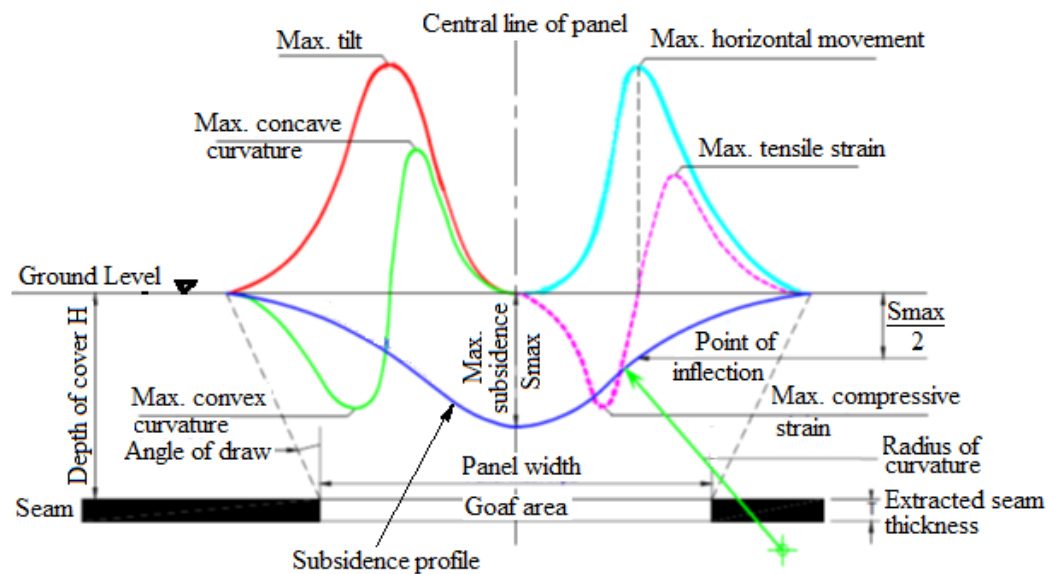


**Figure A 1** The surface subsidence indices and concepts (from Puertus, 2010; Debono, 2007).

These deformation parameters and concepts are defined as below:

#### Subsidence

The terminology of subsidence represents the whole phenomenon of surface deformations in a broad meaning. However, it is also frequently meant for the

vertical displacement of the surface anywhere within a subsidence trough in practice (Figure A-1). It has the units of length, mostly in meter or millimetre (Debono, 2007; Puertuas, 2010; Whittaker and Reddish, 1989).

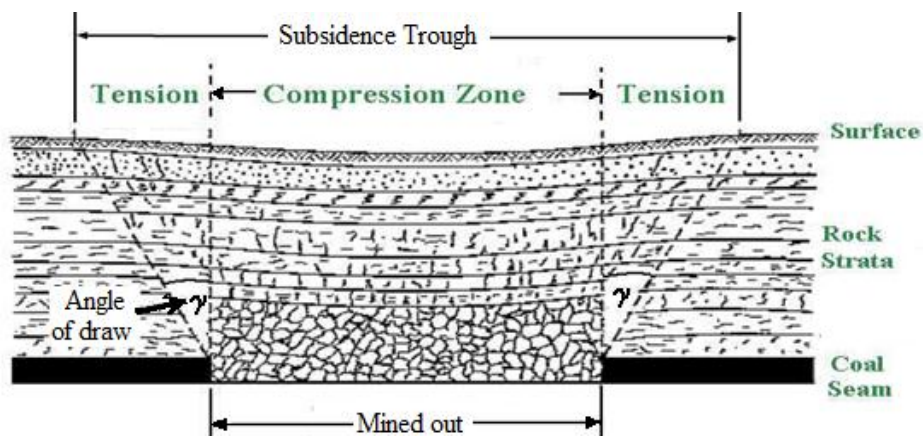


Figure A 2 Strata Movement (from Puertus, 2010; Debono, 2007).

### Tilt or slope

Tilt or slope in the subsidence surface is measured by instrument or mathematically calculated as the first derivative of subsidence and reaches its maximum magnitude at the point of inflection of the subsidence profile, where the curvature changes from convex to concave. It is given in units of length over length, usually expressed in millimetres per metre (Figure A1) (Debono, 2007; Puertuas, 2010).

But on the definition by Chrzanowski and Secord (2000), tilt is the angular amount that the orientation has varied in a vertical plane, from a previous or a reference direction. In strata movement monitoring, the angle change to vertical is called tilt and measured by the inclinometer (Slope Indicator Co., 2006; SOIL, 2010; RST Instruments Ltd, 2010).

### Horizontal displacement

Along the subsidence curve, there are three points with zero horizontal displacement at two edges of depression curve, and the middle point of the subsidence sink. The maximum displacement took place at the inflection point of the subsidence curve, where the curvature transmits from convex to concave and the slope also reaches its maximum (Figure A1) (Debono, 2007). The horizontal displacements can be measured by survey methods or by linear correlation to

slope computation. Its unit is the length unit as meter or millimetre (Puertuas, 2010).

### **Curvature**

Curvature is computed by the second derivative of subsidence or the first derivative of slope. It is convex from the inflection point towards the edge of the depression and concave towards the panel centre (Figure A1). Its unit is 1 over length (Debono, 2007; Puertuas, 2010). Radius of Curvature is used to define magnitude of curvature in a subsidence (Whittaker and Reddish, 1989).

### **(Horizontal) strain**

Strain is created by linear, volumetrical or shape deformation by bending, compression and tension. Horizontal measured strain is from survey data by calculating the horizontal change in length of a section of a subsidence profile, divided by the initial horizontal length of that section. If the ground is in tension the resulting strain is positive, if the ground is in compression the resulting strain is negative (Figure A1). The unit of strain is generally millimetres per metre. The maximum strains occurs where of the maximum curvature, thus the maximum tensile strains is created towards the sides of the panel while the maximum compressive strains occur at the bottom of the subsidence trough (Debono, 2007). Horizontal strain is theoretically from the first derivative of horizontal displacements (Puertuas, 2010). Changes in length relative to an original dimension are also called Shortening (-) or lengthening (+), (Whittaker and Reddish, 1989; Debono, 2007).

### **Angle of draw**

The angle of draw is the angle formed between a vertical line and an inclined line that is projected from the panel edge to the ground surface point next to the subsidence area with the limit of subsidence or experiencing no subsidence (Figures A1, A2). Its unit is degree (Whittaker and Reddish, 1989; Debono, 2007).

### **Subsidence area**

Subsidence area is defined as the whole area of one continuous depression of the ground. It describes the suffering area of the land subsidence. Its unit is square meters or square kilometres.

### **Subsidence rate**

Subsidence rate is the ratio of the vertical settlement divided by the time consumed as the settlement has occurred. Its units are mm/day or mm/year.

### **Subsidence coefficient**

Subsidence coefficient is one of the key parameters in subsidence prediction when mining under the building, water, and railway or the shaft. Magnitude of subsidence coefficient  $q$  can be calculated by the average consistence coefficient  $f$  of overburden strata by Formula (MCRC, 2000):

$$q=0.5*(0.9+f),$$

$$f = \frac{\sum_{i=1}^n m_i Q_i}{10 \sum_{i=1}^n m_i}$$

Where  $m_i$  is normal thickness of  $i$ -th Rock layer (m) and  $Q_i$  is uniaxial compression strength of the strata sample (MPa).

### **Subsidence factor**

The Subsidence factor is a ratio of complete subsidence to extracted seam height (S/M) without dimension (Whittaker and Reddish, 1989).

### **Subcritical, critical and supercritical area**

If the mining width,  $W$ , of a panel is small in respect to the depth of the panel,  $H$ , an arching effect may occur in the strata above the roof, which produces a stable dome and reduces the magnitude of surface subsidence. This condition is called subcritical (Figure A3) (Gutierrez et al., 2010).

As the mining width increases, the strata above the goaf are no longer able to arch or bridge and the collapse starts, finally causing the maximum potential subsidence to take place. The panel width where maximum potential subsidence is formed is called critical width. If the width is further extended, no larger vertical subsidence increases. Any width above that critical width is called supercritical (Figure A3) (Whittaker and Reddish 1989; Debono, 2007; Gutierrez et al, 2010).

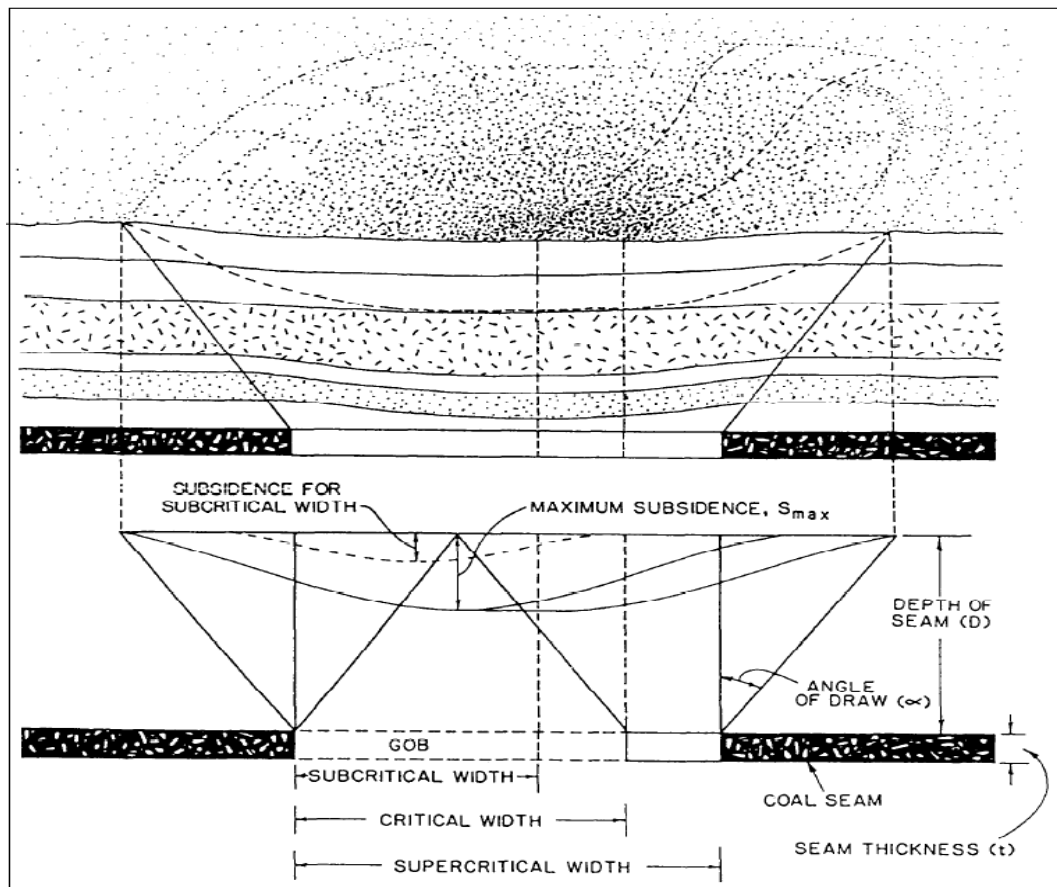
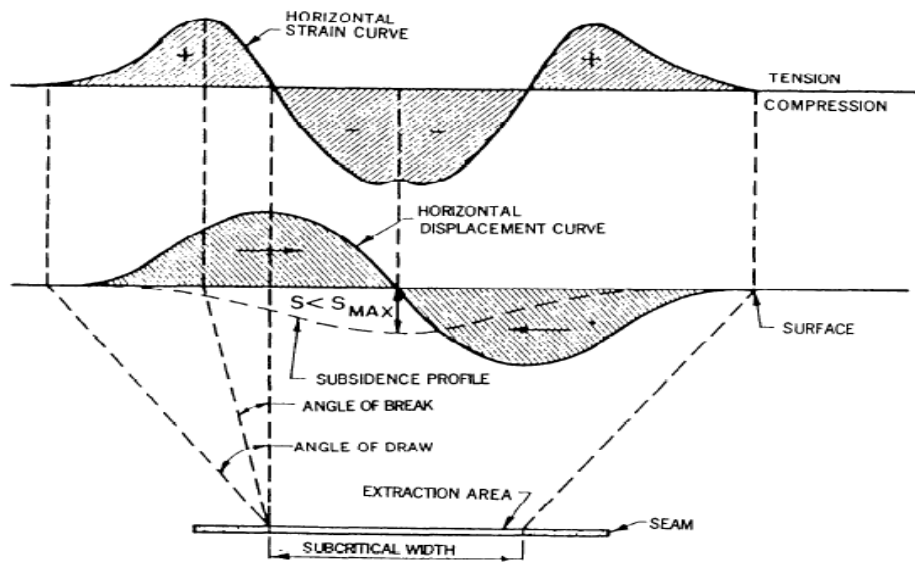


**Figure A 3 Critical extraction width on subsidence (from Howard et al. 1992).**

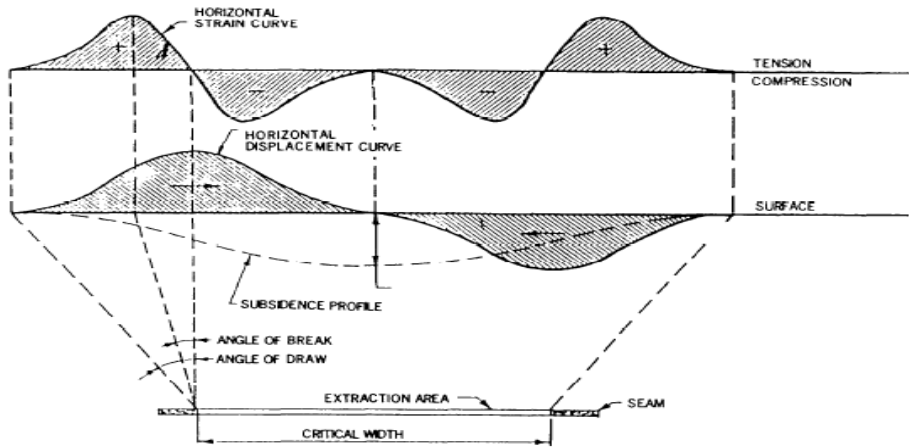
Figure A4 displays the different strains and displacement in above three conditions. Therefore, the Critical Area is the area of working just sufficient to cause the complete subsidence of one point on the surface; Sub-critical area is an area of working not sufficient to cause complete subsidence of one point on the surface; and the Super-critical area is an area of working causing complete subsidence of part of, not just one point, of the surface (Whittaker & Reddish, 1989).

## **A-2 Factors Affecting Mine Subsidence**

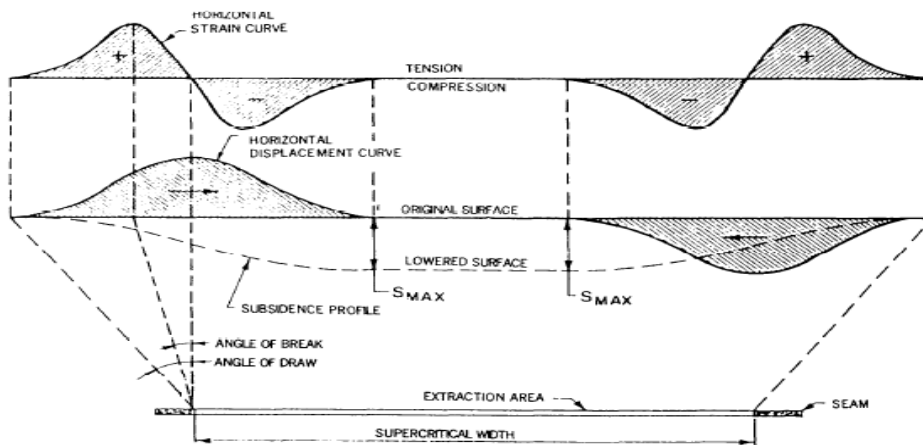
The subsidence is the resultant result of the complicated affecting factors that are from the geologic, hydrological and mining characteristics, and determine the magnitude and extent, subsiding temporal features of the ground subsidence due to coal extraction (Howard L. et al., 1992, Whittaker and Reddish, 1989).



(a)



(b)



(c)

Figure A 4 Schematics of displacement and strain curves for various working widths (a) Subcritical width. (b) Critical width. (c) Supercritical width (Howard L. et al., 1992, p940)

**Competence of Mine Roof and Floor:** Subsidence induced by coal mining commences from the goaf. The characteristics of the goaf roof and floor are as critical in initiating subsidence movements by caving as pillars. The major characteristic of the goaf roof is the roof strength, also called bridging or spanning strength (Gale, 2006).

Weak goaf floors, such as fireclay, are prone to heave and to cause pillar punching. Weak roofs, such as strata of shale, siltstone, and limestone, have relatively low bridging strength, then are high likely to collapse. Competent roof strata tend to prop the overburden longer and hence delay the subsidence, also occupy a higher bulk volume than weaker strata once caving (Howard L. et al., 1992). When both the roof and floor are competent, the pillars incline to spalling and crushing once over stressed (Gale, 2006; Li et al, 2010).

**Degree (ratio) of Extraction:** Higher extraction ratio tends to accelerate and aggravate subsidence. Lower ratio wastes the coal resource. Therefore, the right extraction ratio is desirable and vital in enhancing the resource exploitation and controlling the subsidence (Li et al, 2010).

**Dip of Seam:** When extracting the inclined coal seam, the subsidence basin formed will be asymmetric and skewed toward the rise with the bigger limit angle on the dip side of the workings. Pillars in dipping seams are less stable (Li et al, 2010).

**Extraction Height:** The thicker the seam is mined, the deeper may be the ground subsidence. In thick coal seam the entire seam may not be extracted out. Pillars may be left in place to increase the extraction height of the seam. But slender pillar is more prone to failure. The amount of complete subsidence at the centre is a linear function of the mining height (Li et al, 2010).

**Geologic Discontinuities:** The geologic discontinuities including faults, folds, and joints increase subsidence potential. Mining breaks the equilibrium state of strata and may lead to creeping or movement along an adjacent fault plane, resulting in settlement or up-thrust of the ground beside the fault. Structures on surface, which straddle fault planes, or structures is sunken underground nearby the fault, like shaft and tunnels, are prone to be severely damaged. Small joints



and fissures in strata have less impact than the folds and faults on subsidence behaviour (Howard et al., 1992; Li et al, 2010).

**Gob Backfilling:** Gob backfilling to goaf mitigates, but does not eliminate, subsidence. The effect of subsidence controlled by backfilling is contingent on the type and extent of backfilling used. Gob backfilling may be achieved by hand packing, pneumatic stowing or hydraulic backfilling (Howard L. et al., 1992).

**Groundwater and water head:** Strata deformation from caving subsidence may modify groundwater gradients by draining or seeping water into goaf. Consequently the aquifers suffer depressurization and compaction leading to the above strata settling down. The settlement around shaft may apply a drag-down force on the shaft lining, ultimately damage the lining. The erosion of flow can create voids surrounding the shaft and thus reduces the strength of the lining. The erosion and lubrication effects also lead to strata sliding causing shearing failure. Not only rocks may be softened by saturation, also water remarkably decreases the strength, hardness and consistency of pillars, roof and floor. Softened floor tends punching, leading to instability and subsidence. Water in the joints reduces the strength of rock mass then endangers the stability of the rock mass; cause the strata movement (Howard et al., 1992).

**In Situ Stresses:** The arch stability and height in head-rock are susceptible to the ratio of vertical to horizontal stresses. High horizontal stresses tend to detain surface subsidence by arching the immediate mine roof (Lee & Abel, 1983, cited by Li et al, 2010). However, highly stressed arches may collapse violently (Howard L. et al., 1992; Li et al, 2010).

**Method of Mining:** Subsidence is about 70–95% of the excavated thickness since immediate layers collapse and has a bulking effect as breaking up. Ming method mostly determines the type of subsidence profile, namely pit or trough.

- In room and pillar mining and Bord and Pillar mining the subsidence may exist as pit or hole, but the ultimate failure of pillars may cause occurrence of trench or trough.
- In longwall mining nearly immediate but predictable subsidence occurs in the shape of trough or trench.

- Harmonic mining is used adjacent to longwalls in the same seam or superposed panels in different seams. Harmonic mining is used to protect surface structures as the resultant compressive and or tensile strains can be effectively neutralized. But, harmonic mining is only applied where ‘mining costs become subservient to historical or social demands’ (Howard L. et al., 1992, Li et al, 2010).

**Mined Area:** To achieve the maximum subsidence the critical width needs to be exceeded to improve the extraction ratio within the subsidence control. This is particularly crucial if the head-rock present in the overburden has high bridging strength across the goaf (Howard et al., 1992).

**Multiple Seams:** In mine with multi-seams the goaf roof collapse, in any one of the seams, normally increases the likelihood of subsidence occurrence due to adjacent interference, particularly when initial mining start from the upper seam (Li et al, 2010).

**Nature of Overburden:** Strength and type of overburden, as the major factors, affect the magnitude and extent of subsidence. Caving height of overburden is controlled by rock properties and stratigraphic sequence. Hard and brittle strata are more likely to crack than the soft and plastic strata. Fractures in soft and plastic strata, such as clayey strata, trend to close up with time.

The characteristics of the seam roof and floor are critical in initiating subsidence movements (Li et al, 2010). Soft floor, especially if sensitive to further weakening due to moisture, leads to pillar punching or floor heaving. Weak roof, consisted of shale, siltstone, is prone to fall, which is deteriorated if punching also occurs. Strong and thick head-rock above the mine void avoids goaf caving and collapse or tends to support the overburden for a longer period and postpone the occurrence of subsidence (Howard L. et al., 1992). Also, strong rock occupies a larger bulking volume than weaker strata when fracturing (Li et al, 2010).

**Rate of Face Advance:** Surface subsidence tracks the advancing face of extraction underground. If the coal extraction rate varies extremely, the subsidence profile and strains also vacillate, this leads to very irregular settlements. A reasonably fast, steady rate of face advance is most preferable (Legget, 1972, cited by Howard et al., 1992).

**Seam Depth or Mining Depth:** the depth of seam controls the velocity and time of period of the strata subsiding from the goaf to the surface (Li et al, 2010). It was recognised that when the seam depth is deeper than a certain amount there may be no subsidence events due to strata arching effects. However, this has been gradually refuted in recent years, because of the time period elapsed before subsidence effects being much prolonged. But the total amount of subsidence does not change; that is, subsidence amount may be independent of depth (Whittaker and Reddish, 1989).

**Structural Characteristics:** The extent of damage to a structure both on the ground, like buildings and hoisting houses, and in ground such as shaft and tunnels, is determined by the structure type and its size, shape, age, foundation style, used materials and techniques in construction, measures of maintenance (Chen et al., 1974, cited by Howard et al., 1992). The large in size and or length structure bodies, for example edifice and deep shaft lining, are more prone to damage by subsidence because of its relatively lower strength than the smaller structure (Howard et al., 1992).

**Surface Topography:** Subsidence in rolling or hilly area is more complicated than in flat plain where the seam also lies relatively flat. Inclining ground tends to move downward due to gravity. More tensile strains occur on upslope and more compressive strains display down valleys. In fairly flat land the subsidence may be simplified in symmetric two dimensions. But in mountainous terrace it is better to illustrate the subsidence in three dimensions for better representative (Li et al, 2010).

**Time Elapse:** Subsidence develops as a function of time. All the subsidence indices vary in a time series. In partial mining (room and pillar) no surface effects may be observed in a certain period of time after extraction of coal, until the pillars fail or punch into the floor. In longwall mining, the surface may start settling almost immediately after the heading passes below an area (Howard L. et al., 1992). But the occurrence of thick rock head could deter the sagging. In longwall mining, ground subsidence complete within several years. However, this may take decades if pillars are left intact for support (Howard L. et al., 1992). When the head-rock is weak the subsidence may take place within much shorter time, for example, at Huntly Mine, 90% of subsidence generally occurs within the

first 6 months from notice of subsidence after partial extraction (Golder Kingett Mitchell, 2007; Solid Energy, 2007a).

### **A-3 Empirical Prediction Method of Subsidence - Graphical method**

Graphical methods are simply based on ‘compilation and summary of case histories’ in graphical form, where a prediction of subsidence might be made (Bahuguna et al 1991). The earliest and best known examples of graphical empirical methods were published in Subsidence Engineer’s Handbook (SEH) by the UK National Coal Board (NCB, 1965, 1975, cited by Bahuguna et al., 1991). Subsidence parameters are graphically plotted to present some certain relationships (Figure A5) with the mining variables, such as: extraction thickness, seam depth, seam dip and panel outlay (Bahuguna et al., 1991).

The graphical method is based on observations at approximately 200 sites from different coalfields in UK, which are mainly published twice in 1965 and 1975 (Whittaker and Reddish, 1989).

#### **Prediction of maximum subsidence**

Maximum subsidence can be determined by referring to the two graphical tools (Figures A5 and A6) from SEH 1975 Handbook. Figure A5 is used when the panel length is at least 1.4 times the depth of excavation. Figure A6 gives the correction factors to correct the subsidence magnitudes in Figure A5, when the panel length is greater than 1.4 times the depth of excavation. The SEH (1975) also announces that ‘when considering workings of any w/h value in a virgin area the prediction from Figure A5 (which was derived from cases of multi-seam working) should be reduced by a multiplying factor of 0.9’ (Cited by Gutierrez et al., 2010).

#### **Prediction of complete subsidence profiles**

Figure A7 presents a normalized graph of subsidence contours. The normalised subsidence is the function of the ratio of width/depth (w/h), and the distance from the centre of the panel in terms of the depth (d/h). Therefore, complete subsidence

profiles with respect to magnitude, shape and extension can be worked out by the use of Figures A5, A6, and A7.

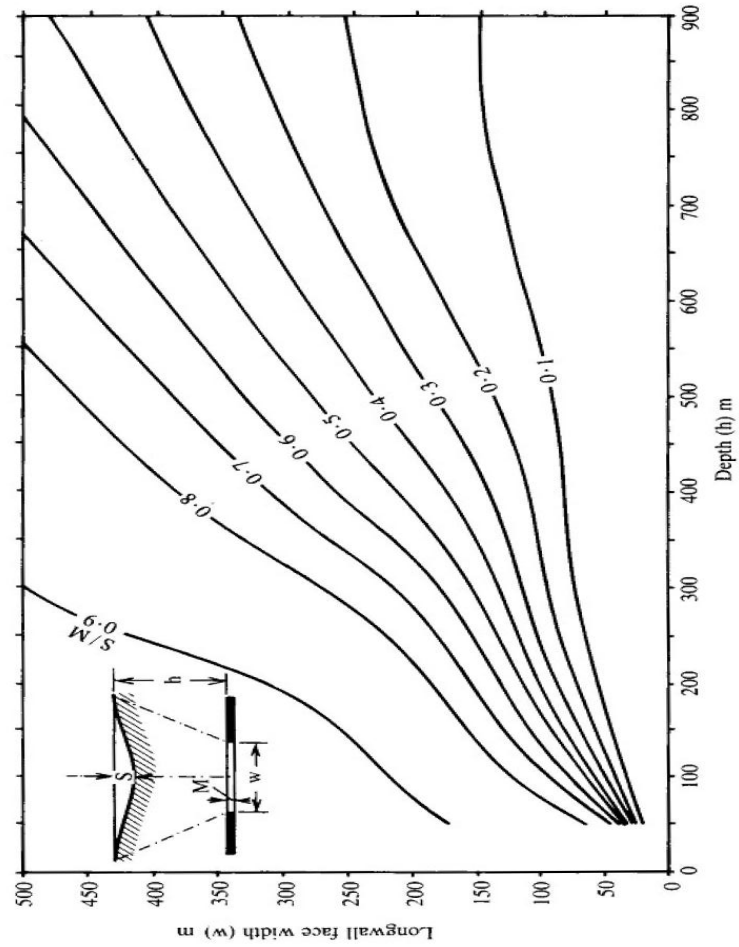


Figure A 5 Relationship of subsidence to extraction width and depth (Whittaker and Reddish, 1989).

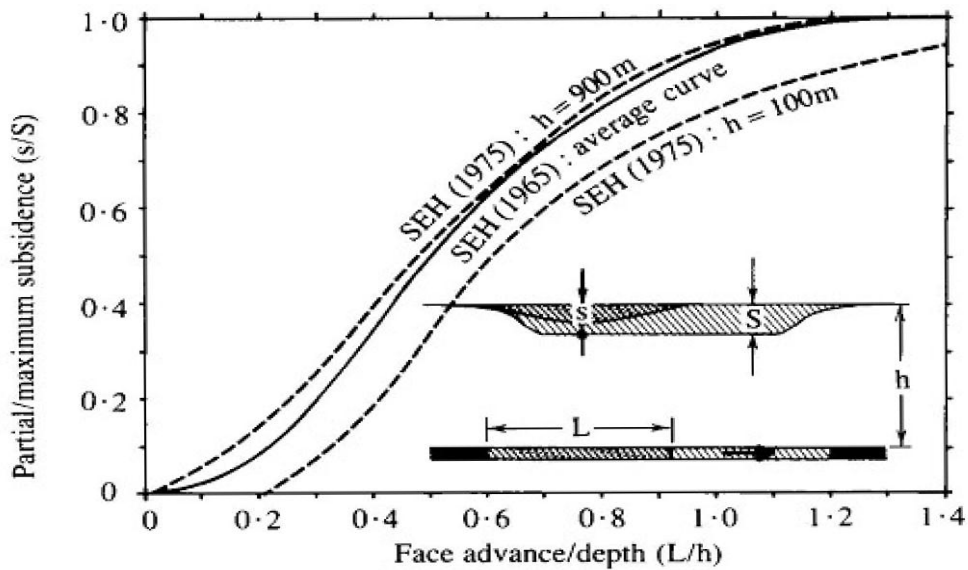


Figure A 6 Correction graph for limited face advance (Whittaker and Reddish, 1989).

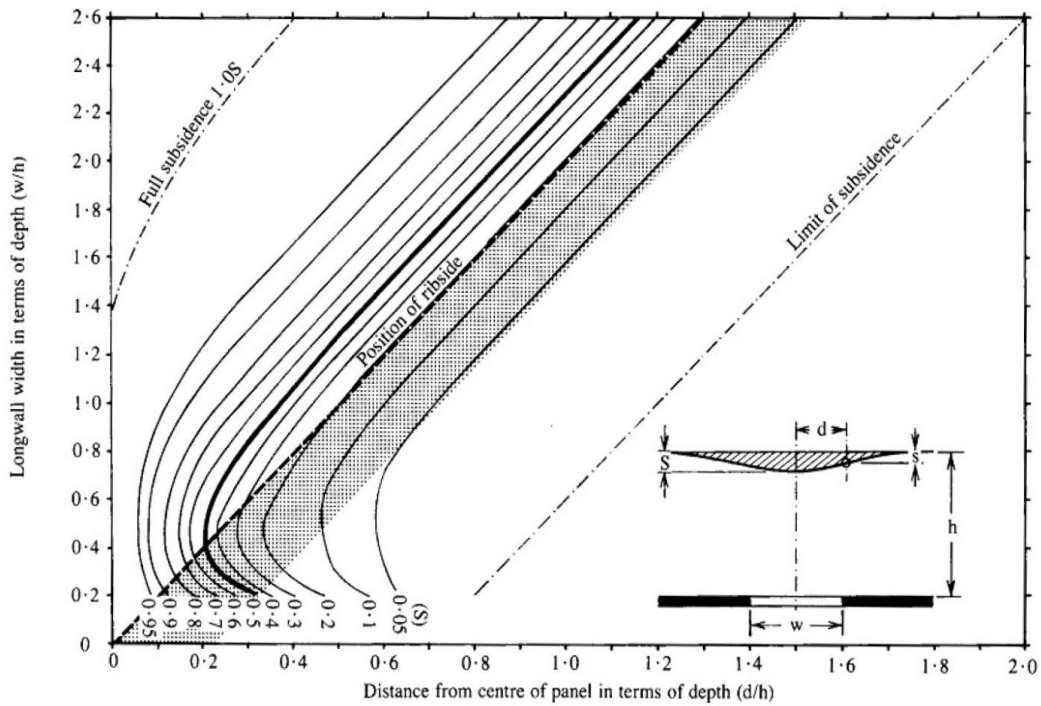


Figure A 7 Design graph for prediction of subsidence profiles (after SHE, 1975, cited by Whittaker and Reddish, 1989).

### Prediction of strain profiles

Figure A8 is used to evaluate the maximum strains, where the subsidence to depth ratio is a function of the width to depth ratio. Maximum slope is also determined from Figure A8. As maximum strains are determined, a relative contour of strain can be found in Figure A9.

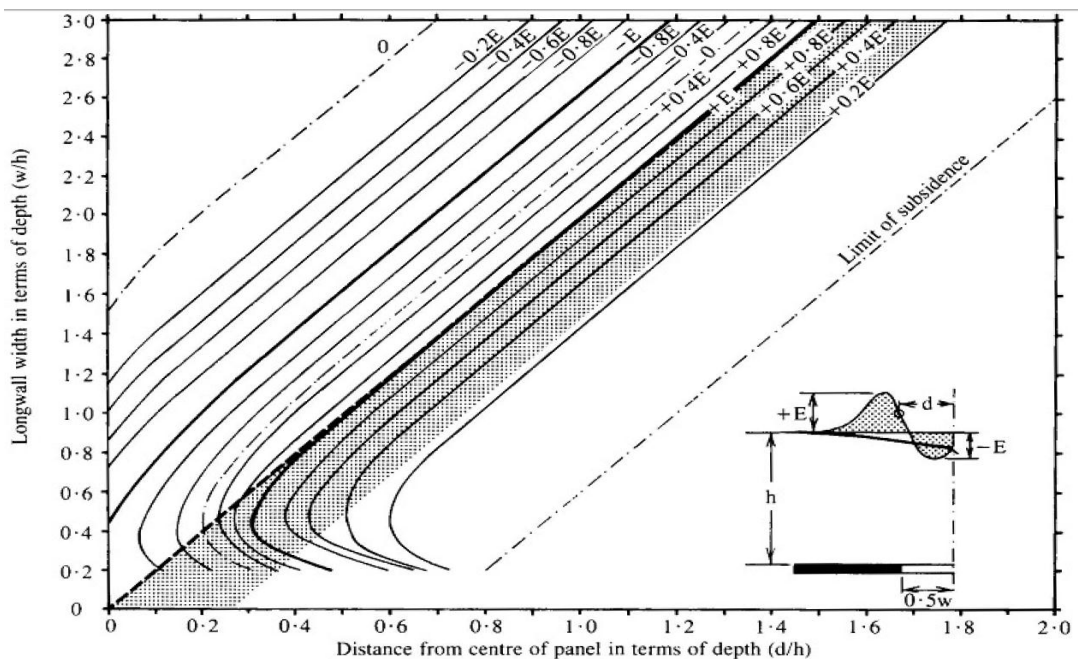


Figure A 8 Design graph for prediction of strain profiles (Whittaker & Reddish, 1989).

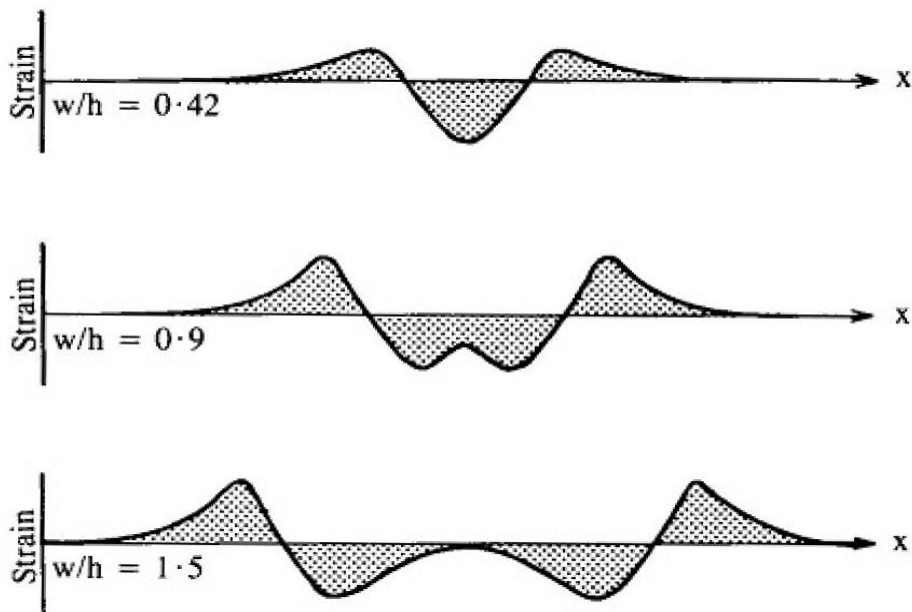


Figure A 9 Graph of the three principal types of strain profile after SEH 1975 (Whittaker and Reddish, 1989).

#### A-4 Empirical Prediction Method of Subsidence - Profile functions

In Profile functions, longitudinal or transverse profile for subsidence or strains generally can be evaluated by the uses of a number of standard functions related to the excavation geometry, equations and tables of data. The constants for the equations and the nomograms are site-specific constants, and ‘derived empirically from local observations’ (Gutierrez et al, 2010; Li et al, 2010).

As subsidence is expressed by a mathematical function, it often specifies vertical subsidence as a function of horizontal distance (Gutierrez et al, 2010). With the help of graphical charts like Figure A10, the magnitude and profile of the subsidence can be predicted. Also other related values, such as horizontal displacements, tilt, curvature and strains can be calculated from the subsidence profile curves or formula.

The empirical profile function methods are ‘basically curve fitting techniques for matching the predicted profiles with measured profiles to obtain a mathematical formula for the profile curve’ (Bahuguna et al 1991, p371). This method can be used for square or other simple geometric shape of stopes (Li et al, 2010). The major disadvantage is that they are too site-specific; therefore, their use is only

applied to areas with identical or very close geology and underground mining conditions (Bahuguna et al, 1991; Puertas, 2010).

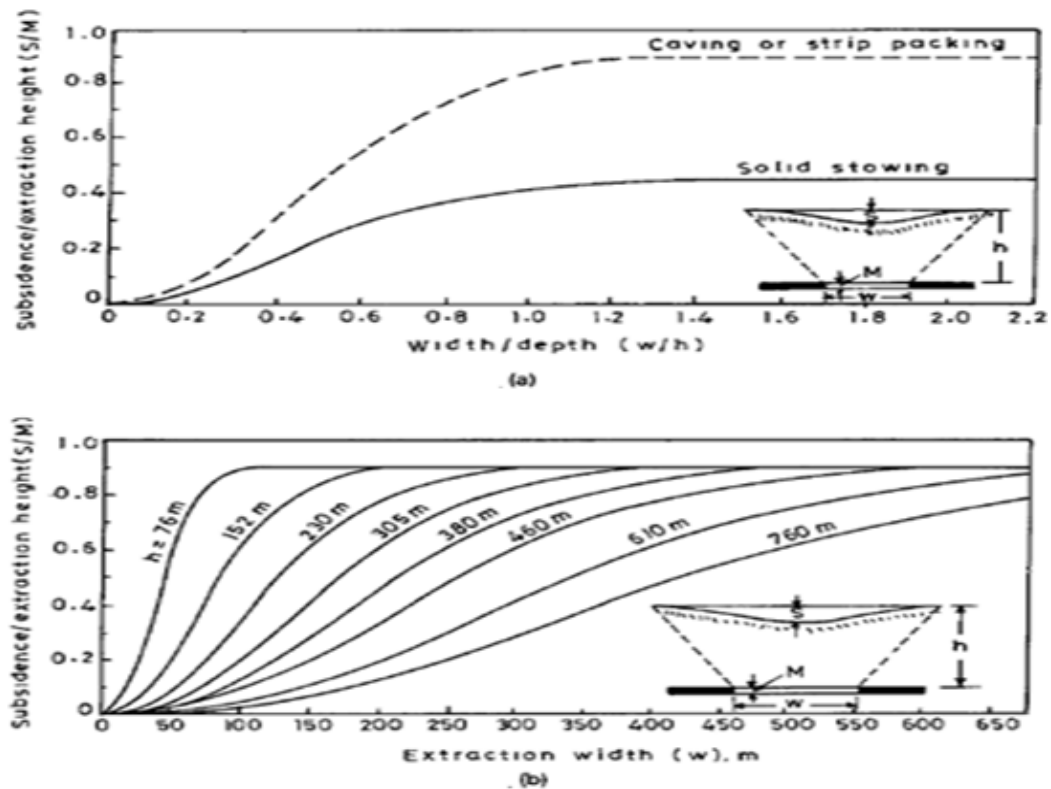


**Figure A 10 Monographs developed by NCB: (a) the influence of width/depth on subsidence, (b) The influence of extraction width (from Bahuguna et al., 1991).**

There is a number of profile functions developed in the world (Gutierrez et al, 2010). The following are some typical profile functions formulas:

**Typical profile functions formulas:**

(1) Donetz Trigonometrical Formula: the following profile equation was developed by VNIMI (General Institute of Mine Surveying, Leningrad, 1958, cited by Bahuguna et al 1991) to predict subsidence (s) in Donetz basin.

$$s = S \left[ 1 - \frac{x}{L} + \frac{1}{2\pi} \sin\left(2\pi \frac{x}{L}\right) \right]$$

and peak value of subsidence, S, is calculated by:

$$S = aM \cos \alpha \sqrt{n_1 n_2}$$

Where:

x and L = distances of calculation point and trough margin from the centre of the subsidence trough (m);

a = subsidence factor;



M= thickness of seam (m);

$\alpha$ = dip of seam;

$S_{\max}$ =maximum possible subsidence occurring at critical width (m);

S=maximum subsidence at the centre (m);

s= subsidence at any point P along the profile (m);

$A_{\text{sub}}, A_{\text{crit}}$ = subcritical and critical areas of extraction ( $\text{m}^2$ );

$n_1, n_2$ = constants for the particular mine geometry.

These equations were derived from an empirically-obtained data and its predictive results have yielded fairly confident agreement with in situ subsidence values in Donetz and some other European coalfields (Bahuguna et al 1991).

(2) Polish Profile Function: The profile formula was developed by Kowalczyk in Poland based on numerous data in upper Silesian coalfields. The subsidence: S at one point in the profile is given by:

$$S = S_{\max} \exp(-nx^2)$$

Where,

$$n = \frac{S_{\max}}{R^2 \bar{c}}$$

Where R: the radius of critical area.  $\bar{c}$ : The average roof settlement. Others are the same with before description (Bahuguna et al 1991).

(3) Hungarian Profile Function developed by Martos is represented by:

$$s = S_{\max} \exp\left(\frac{-x^2}{2l^2}\right)$$

For critical and supercritical widths,

$$s = S \exp\left(\frac{-x^2}{2l^2}\right)$$

For subcritical widths, where

$$S = S_{\max} \frac{W}{2R} \quad (\text{Howard L. et al., 1992, p945})$$

$$S(x) = S_{\max} \exp\left[-\left(\frac{1}{2}\right) \frac{(x + B)^2}{B^2}\right]$$

Where

$x$ ,  $l$ : the distances of calculation point and transition point from the centre of the panel

$w$ : the subcritical width of the panel.

This function predicts a relatively flatter and wider subsidence trough because the observations in Hungarian Coalfields show ‘the transition point to be not over the face edge but over the margin zone of the stowed goaf’ (Bahuguna et al 1991).

(4) Niederhofer's Profile Function. It is mathematically-obtained formula with several empirically - determined factors used. This Function is widely used in calculation of subsidence profiles for inclined seams and complicated mining geometry with the help of computer technology (Bahuguna et al 1991).

$$s = S \left[ 1 - \left( \frac{x}{p} \right)^2 \right]^2$$

Where:  $p$  = half width of subsidence profile, i.e.:

$$p = \frac{w}{2} + R$$

(5) Indian Profile Function: The profile function used in Indian coalmines makes use of a constant  $n$  and is given by:

For subcritical widths:

$$s = S e^{-\left[ \frac{nx^2}{p^2 - x^2} \right]}$$

For critical widths:

$$s = S e^{-\left[ \frac{nx^4}{p^4 - x^4} \right]}$$

This method tends broader subsidence trough than observed in situ of mine (Bahuguna et al 1991).

(6) Hyperbolic Function developed by King and Whetton gives quite satisfactory results for British coalfields (Bahuguna et al 1991):

$$s = \frac{S}{2} \left[ 1 - \tan h \left( \frac{2x}{R} \right) \right]$$

(7) Trigonometrical Profile Function established by Hoffman only predicts confident results for some of the European coalfields

$$s = S \sin^2 \left[ \frac{\pi}{4} \left( \frac{x}{R} - 1 \right) \right]$$

This method is simpler to use and need less input. The profile formulas are easy to calibrate with physical data and provides satisfactory prediction. However this Trigonometrical Profile Function can only be used to simple two-dimensional prediction of rectangular extraction (Bahuguna et al 1991).

### A-5 Empirical Prediction Method of Subsidence - Influence functions

The principle for Influence function methods is based on the influence of extraction of infinitesimal elements of area. Subsidence at any point on the influenced surface is the sum of the influence of every extracted element by superposition (Figure A11).

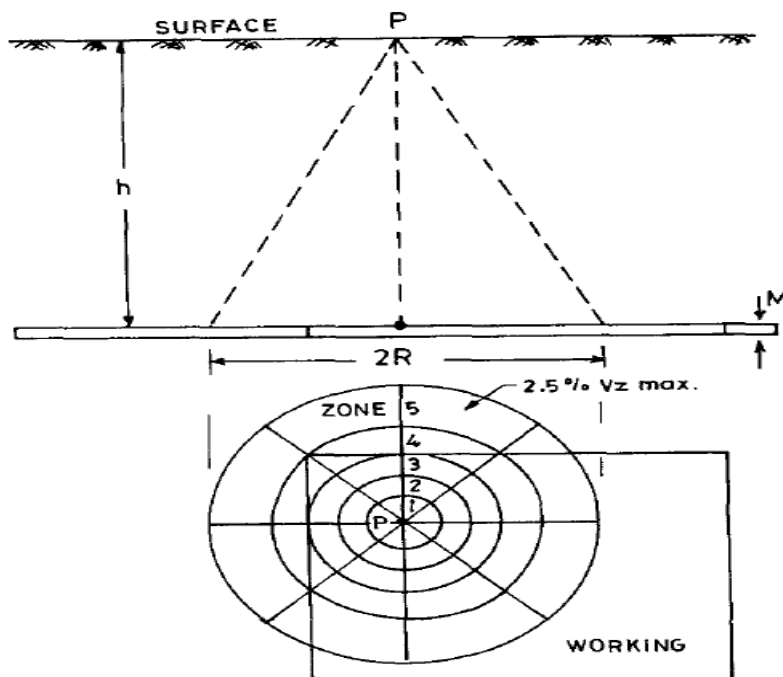


Figure A 11 Calculation of subsidence by integration grid method (Bahuguna et al 1991).

Influence functions cannot be obtained directly by measurement as profile functions do. Besides, this method supposes overburden materials as homogeneous and isotropic. Consequently, its accuracy is limited. Influence

functions are especially useful for subsidence prediction in mines with irregular outlay or complex geometries (Bahuguna et al 1991).

Some of the selected influence functions are introduced as following:

(1). Knothe's method. The function developed by Knothe is based on a Gaussian distribution of probabilities:

$$k_z = \frac{1}{R} \left[ e^{-\left(\frac{\pi x^2}{R^2}\right)} \right]$$

And the equation for the normal subsidence profile in polar form is:

$$s = S \left[ e^{-\left(\frac{\pi r_2^2}{R^2}\right)} - e^{-\left(\frac{\pi r_1^2}{R^2}\right)} \right]$$

$k_z(r)$ : influence function to stand for the elementary subsidence of point P moving radially within an elementary trough (Bahuguna, et al., 1991).

(2) Keinhorst's method. This method uses a formula which presents a simplified subsidence profile. The profile function is given as (Bahuguna et al 1991):

$$k_z = \frac{\tan^2 \beta}{3\pi(\tan^2 \beta - \tan^2 \gamma)} \cdot \frac{S}{R^2}$$

Where:

$\gamma$  = angle of influence of the outer zone (angle of draw);

$\beta$  = angle of break of the inner zone;

$R = h \cdot \cot \gamma$ ;

$h$  = depth of extraction.

(3) Bals' method. Bal's formula is based on the Newtonian gravitational law. The influence on the surface is in inverse-proportion to the square of distance of the particular element (Whittaker and Reddish, 1989).. The function is expressed in usable form by:

$$k_z = \frac{C}{h^2} \frac{1}{4} (\sin^2 \alpha_m + 2 \alpha_m)$$

Where

$C$  = constant,

$\alpha_m$  = angle of influence measured to the vertical (Figure A12).

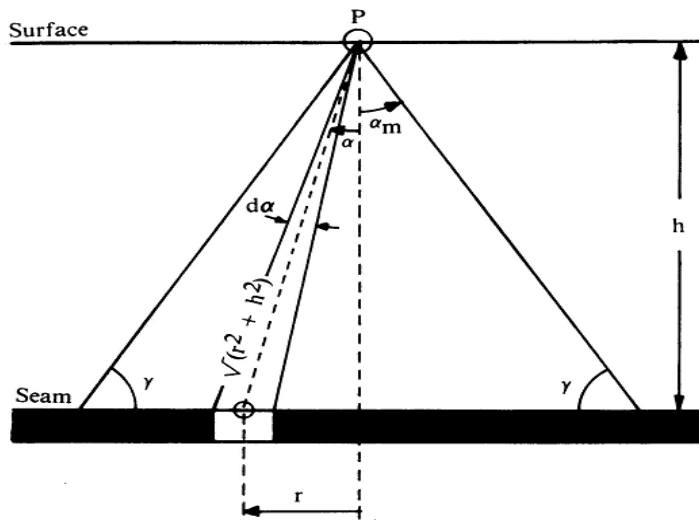


Figure A 12 Representation of Bals' influence function (Whittaker and Reddish, 1989).

(4) Stochastic medium theory (SMT) dominated function

Figure A13 illustrates an elemental excavation with dual coordinate systems: one for global coordinate  $(x, y, z)$  and the other for local coordinate  $(\xi, \zeta, \eta)$ . The elemental excavation has dimensions of  $d\xi$  by  $d\zeta$  by  $d\eta$  as shown in a and b. based on the stochastic medium theory of Litwiniszyn (1957, cited by Li et al, 2010), the ground surface subsidence,  $S(x)$ , due to underground mining can be expressed as:

$$S(x) = \iint_{\Omega} \frac{\tan \beta}{\eta} \exp \left[ -\frac{\pi \tan^2 \beta}{\eta^2} (x - \xi)^2 \right] d\xi d\eta$$

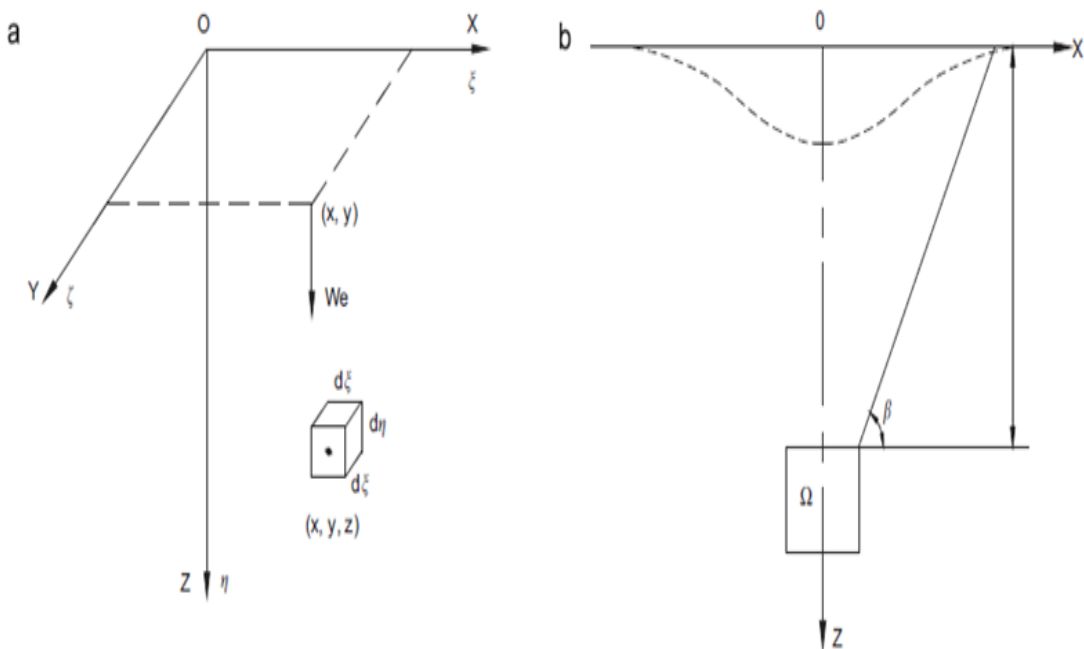


Figure A 13 (a) elemental excavation (three-dimensional problem) and (b) cross section of elemental excavation (x o z) (Li et al., 2010).

(5) Keinhorst's method

This influence function method was proposed in 1928 and 1934 (Figure A14).

$$k_z = \frac{2 \tan^2 \beta}{3\pi \tan^2 \gamma} \frac{S}{R^2}$$

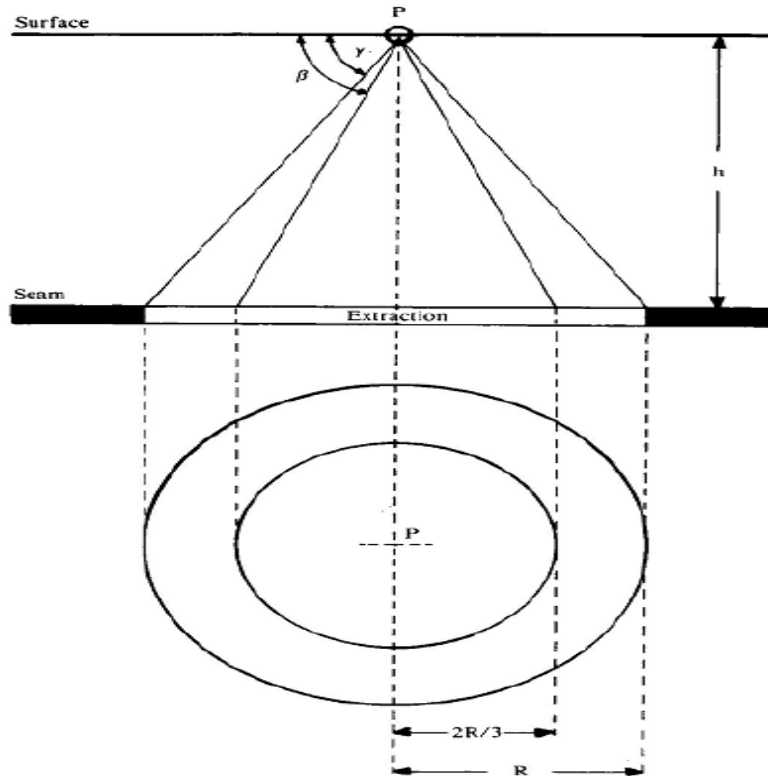


Figure A 14 Keinhorst's influence function (Whittaker and Reddish 1989).

Apparently, from the whole equations above, empirical methods do not directly need parameters or factors of geological, mechanical properties or tectonic stresses in the computation. However the constant or function rule in the equation should imply the influence of the effects of geological, mechanical properties or tectonic stresses. Consequently, the empirical techniques can be only used where the data were gained or to very similar areas (Szostak-Chrzanowski, 1988, cited by Puertas, 2010).

## A-6 Prediction Method of Subsidence - Numerical Techniques

Numerical models, also called theoretical models (UWA, 2010). Numerical modelling is the process of solving the equations representing a mechanical process by a step-wise approximation, to reach the final satisfying solutions (Minerals Council of Australia, 1997). The numerical methods have the advantage

that, once the model is established, then, a number of associated scenarios may be investigated by simulation with fewer efforts. However, it should be aware that numerical models may create wrong judgement in application.

There has been significant development in numerical methods as the extremely powerful tools in solving geochemical, hydrological problems following the fast and advanced development of computer technology. A number of commercial numerical analysis codes have become relatively user friendly in recent times, such as ABAQUS, ADINA, ANSYS, FLAC, RocScience and UDEC.

Several theoretical or numerical techniques have been utilised to problems in subsidence prediction. The computerized numerical modelling methods include the Finite Element Method (FEM), Boundary Element Method (BEM) and Distinct (or discrete) Element Method (DEM), and Finite Difference Method (FDM) (UWA, 2010).

Numerical models are based on statistical and mechanistic rules treating the material of the overburden as a 'model of either a cohesionless stochastic or elastic or even plastic, isotropic or anisotropic medium' (Bahuguna, et al., 1991). The numerical modelling methods are used in modelling overburden and simulation of mine geometry to predict subsidence over mine panels. Finite difference (FDM) and finite element (FEM) models are currently popular. FE models are more suitable for problems with complicated boundaries, but the methods are somewhat more complicated than FD models.

Numerical or theoretical model methods are using analytical or mechanistic characteristics of nature and base on the rheology and mechanics of subsiding materials and their response to changing extraction geometries (Bahuguna et al., 1991). Numerical methods work on modelling principles by using mathematical representation of idealized materials in the application of continuum mechanics (Blodgett & Kuipers, 2002). The numerical methods are summarised in Figure A15.

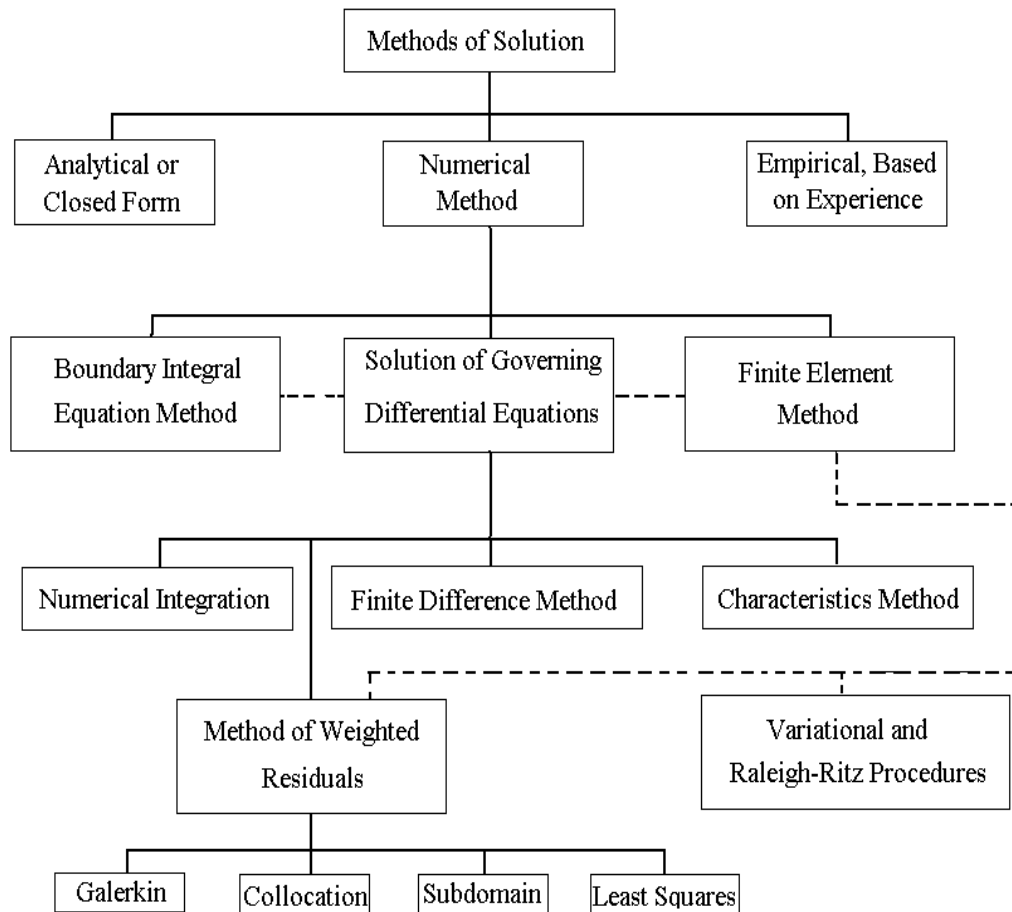


**Figure A 15 Numerical Methods Relationship (after Desai and Christian, 1977, p2).**

It needs to point out that the prediction work by both empirical methods and numerical methods can be computer-based or handwriting-paper-based. The choice of the subsidence prediction models depends primarily on the mining ‘situations being simulated and on the information sought’ (Whittaker and Reddish, 1989, p133).

Computer application for solving very complicated equations in various initial and boundary conditions with different material behaviours have made numerical methods more popular in the prediction of subsidence. Different software has been developed to contemplate inhomogeneous and anisotropic behaviours of rock mass worldwide, such as ABAQUS and FLAC (Li et al, 2010).

The ‘calibration’ and verification is an integral part of numerical modelling because of the simplifications, formulisations, assumptions used in describing the physical processes (UWA, 2010). By verification the modeller can tune the



parameters and indices against an observed event. The practicability of simpler models should be scrutinized first because complex models may have a larger opportunity for errors both judgementally and numerically. Finally, the restrictions of the model should always be clearly understood (UWA, 2010; Minerals Council of Australia, 1997).

### Theoretical analysis methods

Theoretical analysis methods are mainly based on continuum mechanics principles for prediction of the magnitude of subsidence. A number of behavioural models for immediate roof and strata above, such as elastic, plastic, visco-elastic, and elasto-plastic ones, have been used for predicting the surface subsidence in different situations. Szpetkowski (1972, cited by Li et al, 2010) introduced a theoretical model for calculation of surface subsidence at point P(x, y) when excavating an area of a, b, c and d at a depth of H and thickness of m (Figure A16),

$$S = \frac{am}{4\pi BH} \int_a^b \exp\left[-\frac{(x-\xi)^2}{4BH}\right] d\xi \times \int_c^d \exp\left[-\frac{(y-\eta)^2}{4BH}\right] d\eta$$

where a is the subsidence factor, symbols  $\xi$  and  $\eta$  are coefficients of the working conditions, and B can be calculated from

$$\frac{1}{\sqrt{2B}} = \frac{k\sqrt{2\pi}}{1000}$$

where k is a characteristic quantity of the overburden strata ( Li et al, 2010).

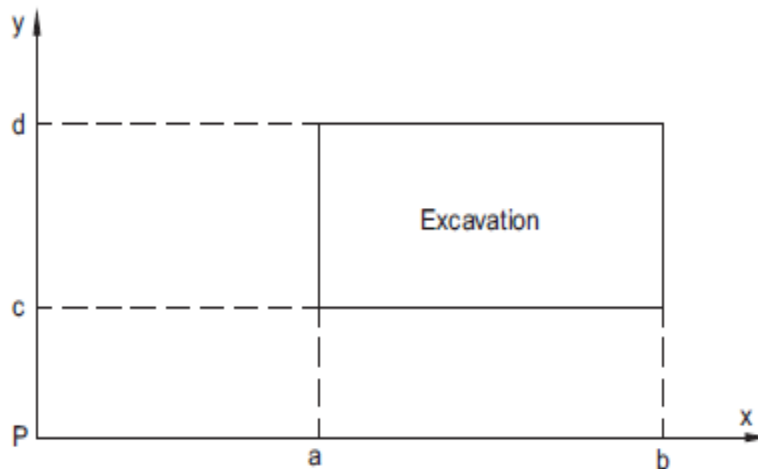


**Figure A 16** The locations of the point P and excavation underground (Li et al, 2010).

### **FEM: Finite element method**

Unlike empirical methods based on experience and observed data, the numerical techniques work on the basis of a 'reliable knowledge of the mechanical properties, in-situ stresses and tectonics of the area' (Puertas, 2010). Finite element (FEM) is the most widely used numerical method for geological mechanics and rock engineering, which does not need detailed programming experience to make efficient use of the finite element approach to problem solving in rock mechanics (UWA, 2010).

FEM undertakes the structural analysis of the overburden and gob (goaf) by dividing and subdividing it into a set of finite individual structural elements, also called sub-domains (UWA, 2010; Haciosmanoglu, 2004). Under the stresses in the overburden body, the nodes of the mesh, as elements of strata, suffer strains and get displaced.

The magnitudes of displacement of each element are dependent on the values of stress and material properties of each element. The factors of geological discontinuities such as joints, faults, bedding planes, and different types of overlying layers, can be put into FEM for prediction of the subsidence.

In FEM the element mesh is spread all over the body of the overburden. Handling very large scale and complex equation systems will make the FEM method more voluminous and time consuming (Haciosmanoglu, 2004). The FEM software currently used are Phase2, ANSYS, Plaxis (Lawless et al, 2003) ADINA, Abaqus FEA (formerly ABAQUS) (Brown University, 2011).

### **BEM: boundary element method**

The boundary element method (BEM) is much simpler to use. In the BEM of subsidence simulation, the element mesh is 'not spread all over the body of the overburden but only at the boundary' (Bahuguna et al., 1991; Haciosmanoglu, 2004). Therefore, BEM is more useful for situations where geological discontinuities are comparatively less as it is simpler than FEM. The BEM treats the rock mass as a 'discontinuous system of interacting blocks' (Bahuguna et al, 1991).

BEM is mainly suitable for modelling a jointed rock mass with deformation mechanism of separation of blocks, rotation of mass, or slip associated with large relative movements. Boundary element method has yet to develop its credit in confident subsidence prediction.

### **FDM: Finite differential method**

In finite differential method, the problem domain, such as a geological feature or manmade structure is discretised into a set of sub-domains or elements (UWA, 2010). This method demands physical or mathematical approximations made throughout an enclosed region. Solution procedure works on ‘numerical approximations of the governing equations, i.e. the differential equations of equilibrium, the strain displacement relations and stress-strain equations, as in classical finite difference methods’ (UWA, 2010). Instead, this procedure may also use approximations to the connectivity of the elements, and continuity of displacements and stresses between elements, as in finite element method (UWA, 2010).

Itasca International Incorporate has developed numerical modelling codes for solving problems in geomechanics and hydrology for the past 30 years.

- The finite difference programs (FDM), advanced continuum modelling codes (FLAC and FLAC3D) are suitable for geotechnical analysis of rock, soil, and structural support in [two](#) and three dimensions.
- Distinct element modelling (DEM) codes, PFC 2D and PFC 3D are applied for micromechanical analysis of geo-materials and particulate systems in two and three dimensions.
- Distinct element modelling (DEM) software UDEC and 3DEC are programmed for geotechnical analysis of rock, soil, and structural support in [two](#) and three dimensions (Itasca, 2011).

FEM, BEM, FDM, including displacement discontinuity (DDM), are all continuum methods. They may fail in modelling with elasto-plastic analysis performed by using realistic rock mass strengths inputs. Then DEM will possibly be the best method in dealing with rock characterization of each bed (Haciosmanoglu, 2004). Numerical modelling may ignore the possibility of each bed having different horizontal in situ stresses (Sheorey et al., 2000).

## A-7 Physical Models

Physical Models are the small scale simulation of the extraction area in different mining situations for observing the subsidence behaviours and profiles inducing by the mine extraction. The physical models are mostly established in laboratory by using a range of model materials such as sand, gelatine and plaster to represent the real strata. The outstanding strength of the physical modelling is the fact that ‘the actual mechanism of deformation and failure can be observed’ (Whittaker and Reddish, 1989). Physical models can be utilised in simulating the simple and complicated geological and mining situations, and especially advantageous to studying new situations in mining subsidence. Physical models have proved beneficial in complementing the other prediction methods in empirical and numerical techniques (Whittaker and Reddish, 1989).

### Physical Model by Whittaker and Reddish

Whittaker and Reddish (1989) reported a physical model to study the bridging (or arching) ability of the strong overburden. Figure A17 shows that the dropped beds into the extracted zone are nearly intact; the fracture voids and gaps may work as the flow paths for water and gas from upper strata to access into the goaf; the bridging capacity of the strata depends on the strength of competence of the head rocks.

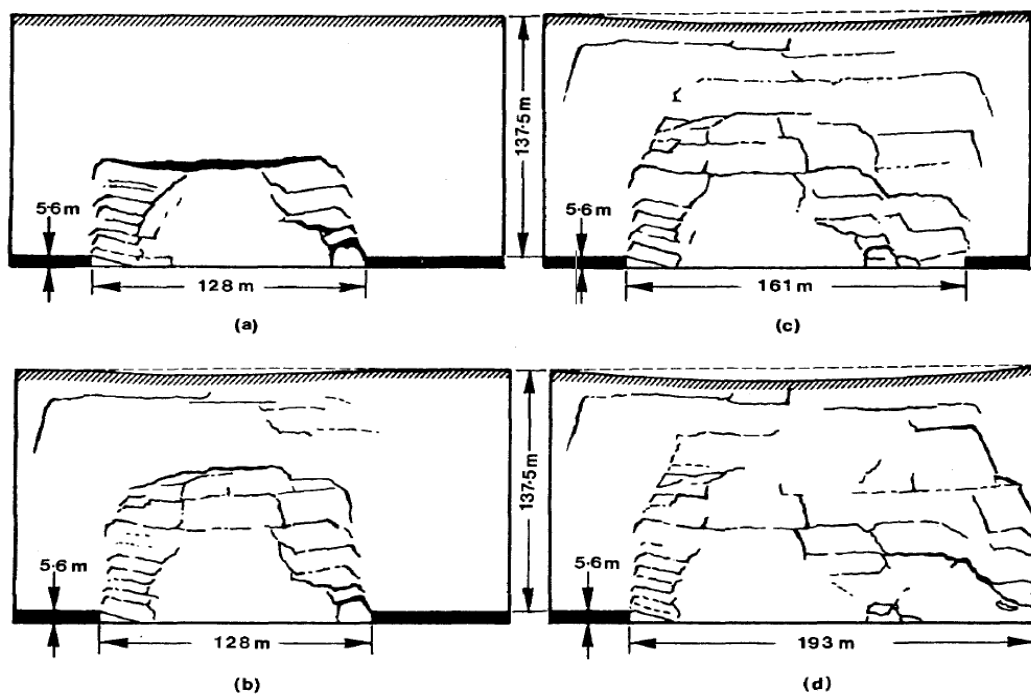


Figure A 17 Physical model shows the dropped beds into the extracted zone (Whittaker and Reddish, 1989).

### Physical Model by Huang (2009)

Huang established a new simulation physical model in 2009 to research the clay aquifuge stability in mining shallow seam. The modelled coalmine is Yushuwan Coal Mine. The brief overburden geology is illustrated in Figure A18. The reddish soil (75 m) and yellowish (25 m) soil are clayey soil that constitutes the aquifuge (100 m thick). Headrock (100 m) is consisted of mud rock, median sand rock and fine sand rock. The weathered layer is 20 m thick. The thickness of the seam is 11.5 m. Coal seam has an average depth of 230 m.

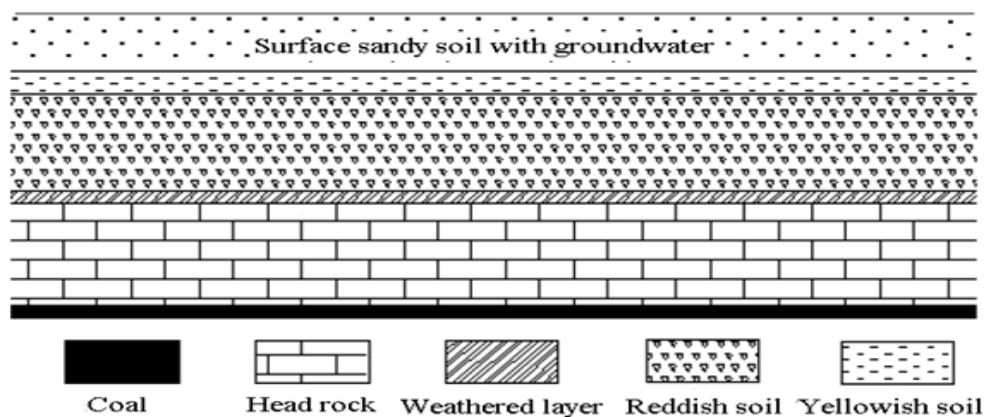


Figure A 18 Overburden and coal seam simulated by physical model (Huang, 2009).

The lab model is built on a 1:200 scale of the field dimensions 5810 m long, 250 m wide and 241.6 m deep of the studies geological strata. The aggregate materials and proper agent for materials compose of sand and soil at a ratio 1:1, oil and soil ratio 1: 4.0-4.5. The strength of the modelled material is around one 10th of the intact sample in situ. Figure A19 displays the physical model and the caving of the roof after the first slice mining. Figure A20 indicates the roof caving after the second slice mining. The caving height is much higher than the first slice mining.

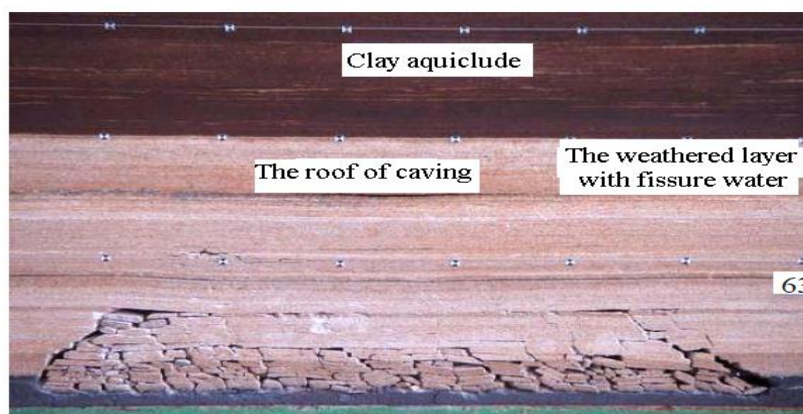
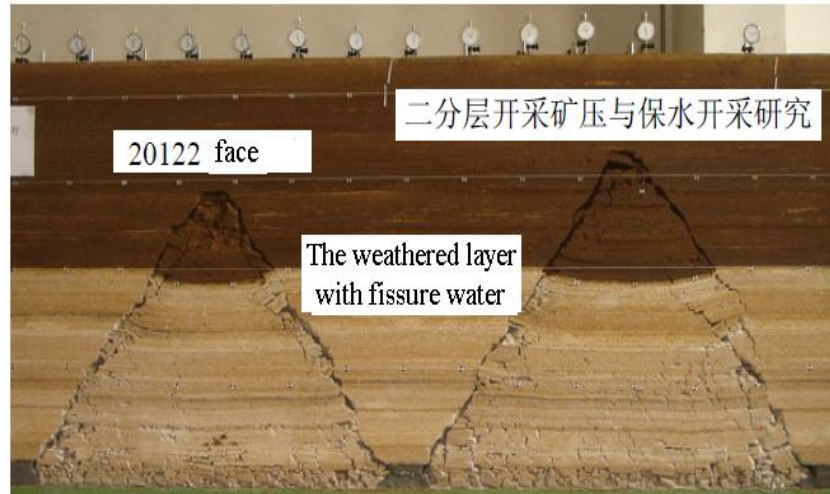
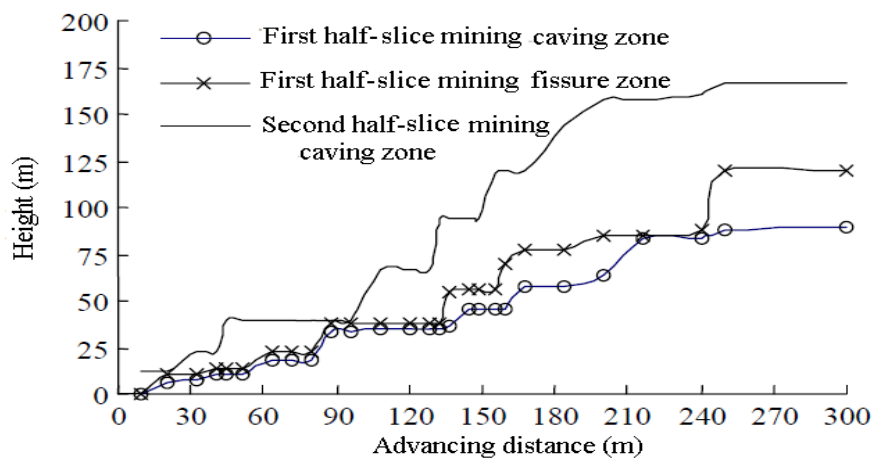


Figure A 19 Physical model and roof caving after the first slice mining (Huang, 2009).



**Figure A 20 Roof caving after the second slice mining (Huang, 2009).**

Through transferring the above simulation into the site features of overburden, the roof caving and fissure extent are plotted in Figure A21.



**Figure A 21 Roof caving laws of mining face (Huang, 2009).**

Figure A19 presents that the caving height is approximately 90 m after the first slice mining in a big extent; the fissure height is around 120 m, close to the weathered layer. After the second slice mining, the caving height reaches 166 m by an increase of 76 m from the first slice mining. The caved height into the clayey layer is 46 m, nearly half of the aquifuge stratum, where the aquifuge is still very stable to ensure the safety of extraction.

Through the physical modelling, the subsidence of head rock and aquifuge developed following the mining face advancement (Figure A22).

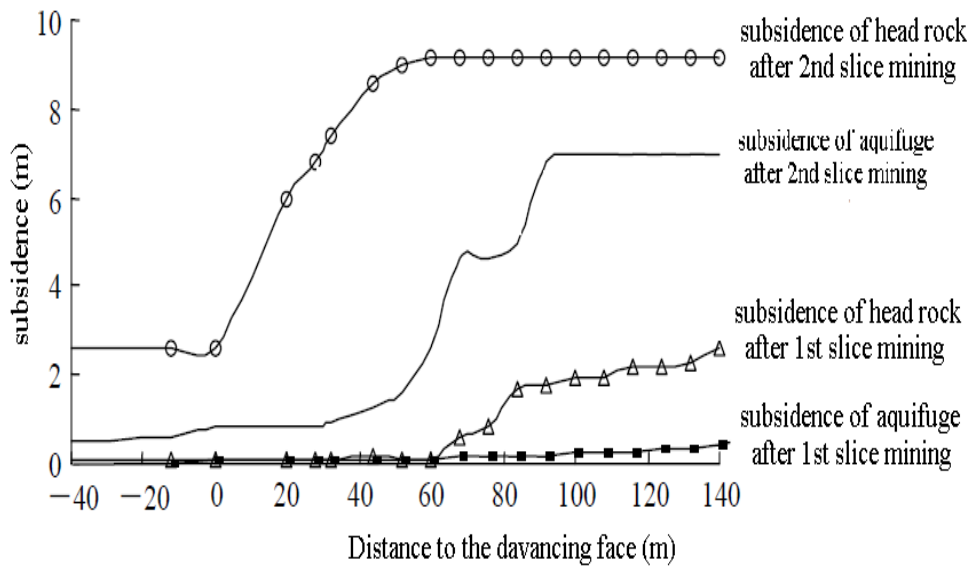


**Figure A 22 Roof and clay aquifuge subsidence laws (Huang, 2009).**

### Trap-door (TD) mechanism experiments

Trap-door experiments with sand layer model (Vardoulakis et al. 2004) have certified that trap-door displacement migrates vertically upwards above the trap-door (Figures A23 and A24).



**Figure A 23 Axisymmetric trap-door mechanism in small-scale model test with dry sand (Vardoulakis et al. 2004).**

The edges of the subsidence trough are shear bands, which incline inwards in vertical direction. The angle  $\beta$  of the trough boundaries varies as a function of trap-door vertical displacement, and being positive proportional to the trap-door displacement (cited by Vardoulakis, 2004, p2749; Li et al, 2010, p424).



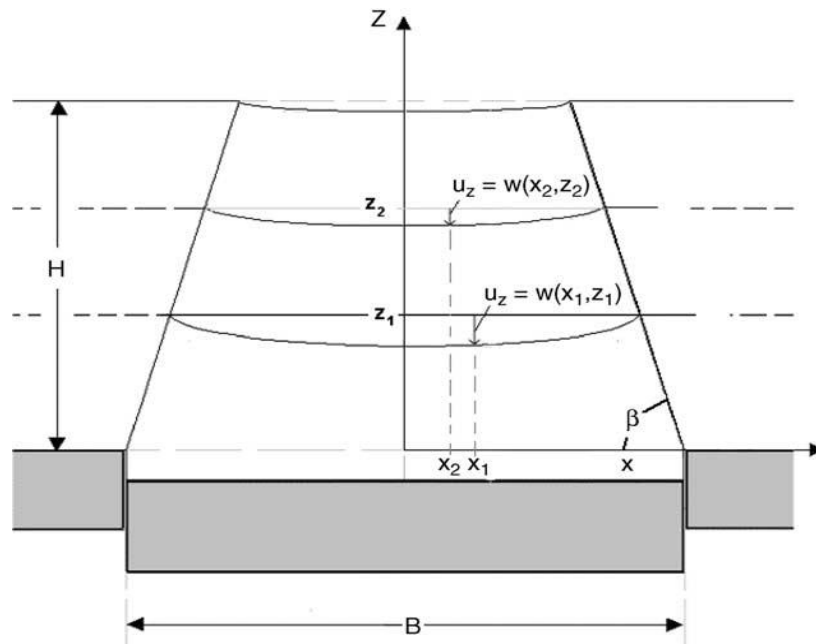


**Figure A 24 The trap-door mechanism—the model (Li et al, 2010, p424).**

In the simple trap door (TD) physical experiments Papamichos et al. (2001, cited by Li et al, 2010) researched the reservoir compaction and found that the reservoir compaction can change the stress regime in the overburden formations due to arching effects. Even a slight induction of the vertical stress is monitored, from small TD displacements, and before the formation of shear faults in the overburden. The horizontal stresses have increased above the TD. The surface subsidence bowl is formed above the TD area. Here  $H/B$  is the ratio of the overburden height  $H$  to the TD diameter  $B$  varying within a range of values representative of an oil field.

#### **Physical model by Singh and Singh (1985)**

For studying the suitable mining geometry under Indian geo-mining conditions under the high flood level (H.F.L.) of Kanhan River, Sigh and Sign (1985) reported an indirect technique - Equivalent Material Mine Modelling that was conducted under idealised laboratory condition. Indian coal measure formation in area of Kanhan River constitutes an approximately 70% medium-grained calcareous/arenaceous brittle sandstone which are prone to develop open cracks when the strain is larger than 5 mm/m. In the absence of fine clay particles, its wall swelling and subsequent sealing tendency, the fractures tend to form channel for water inflow or even interconnect water bodies in case of thick/multiple seam caving (Figure A25) (Sign and Singh, 1985).



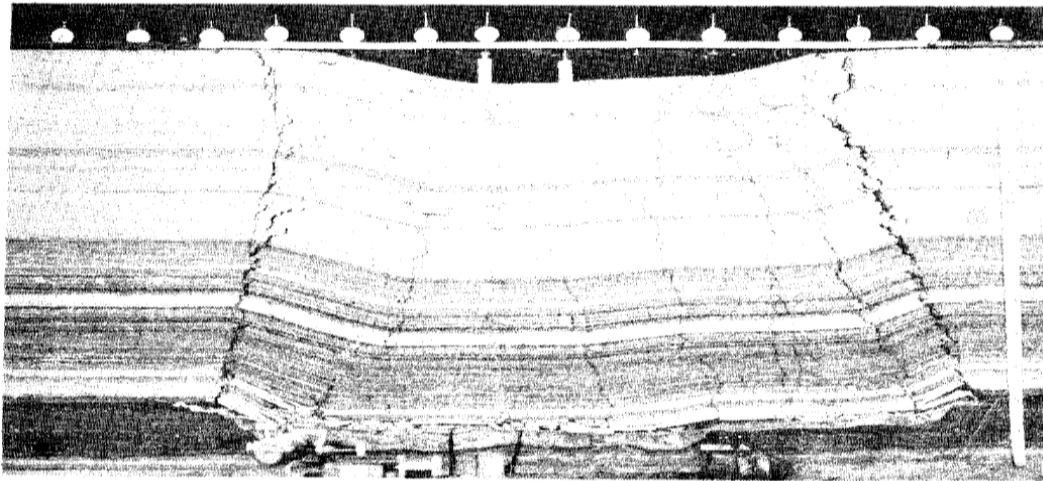


**Figure A 25 Equivalent Material Mine Modelling (Sign and Singh, 1985).**

For controlling the magnitude of strain the following methods were recommended:

- Control the geometry and layout of the panel or heading development so that ‘the crack planes remained below the water body, leaving at least 60 m thick formation as impermeable mass’ (Sign and Singh, 1985).
- ‘Reduce the effective working height of the seam by way of goaf stowing and thereby subsidence factors’ (Sign and Singh, 1985).
- ‘Adopt harmonic system of mining in conjunction with hydraulic stowing for mining of multiple seams under shallow depth cover’ (Sign and Singh, 1985). This effect was physically observed in a set of model experiments (Figure A26).

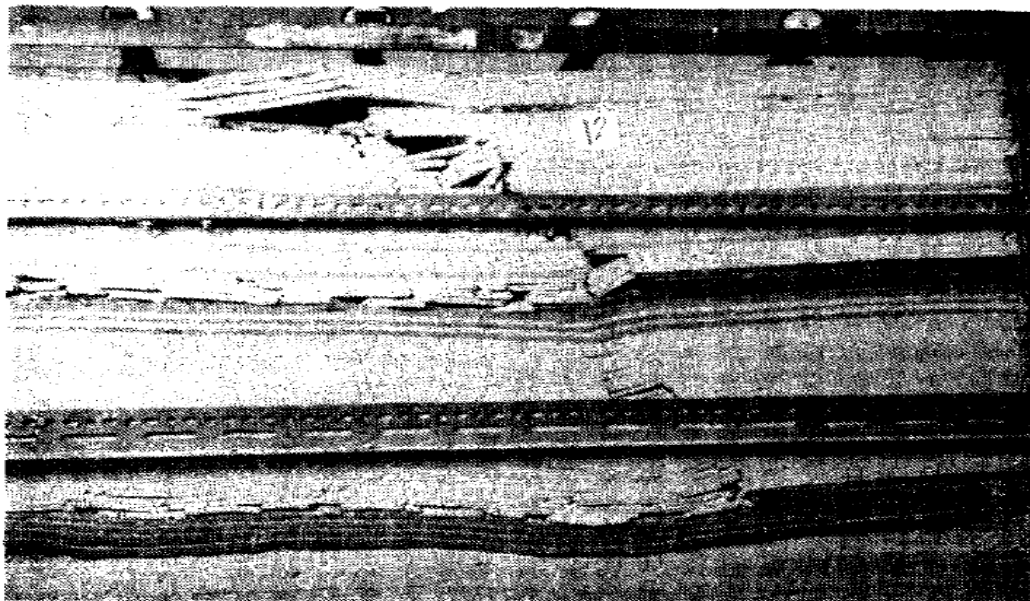


**Figure A 26 Harmonic mining studies for mining under HFL (Sign and Singh, 1985).**

## A-8 State of Art on Prediction of Subsidence

### Fuzzy probability measure (Li et al., 2010):

In past 30 years the term ‘‘fuzzy probability’’ has been used in various areas of science and engineering, such as slope stability assessment (Giasi et al., 2003 ; Li et al., 2005, cited by Li et al., 2010); Risk assessment system of natural hazards (Iman and Eyke, 2007, cited by Li et al., 2010); Reliability assessment for pressure piping (Zhou (2005, cited by Li et al., 2010); Application of fuzzy probabilistic method in the general evaluation of regional atmosphere environment, water environment (Wang et al., 2007, cited by Li et al., 2010). Li et al., (2010) reported that Fuzzy Probability also can be used to analyse rock mass displacements induced by mining, especially in coal and metal extraction. By the Fuzzy probability theory, the equation for expression of the fuzzy probability of ground subsidence is educated as follows:

$$M(A_1) = \int_D a(x/z)^{2b} \exp[-2c(x/z)^d] dx$$

Where, D is the mining range,  $D \in [0, x_n]$ ,  $n \rightarrow \infty$ .

Then the mining thickness and subsidence factors must be taken into account for computing the practical surface subsidence S.

$$S = k_i M(A_1)$$

Where, S is the practical ground subsidence;  $k_i$  ( $i=1, 2$ ) is the parameter which are determined by the mining method, the rock properties, and the measured data of mining site. For example, given the fuzzy probability of surface subsidence in a mine,  $M(A_1) = 0.7$ ,  $k_1 = 2.5$ ,  $k_2 = 0.6$ , then

$$S_{\xi} = 0.7 \times 2.5 \times 0.6 = 1.05 \text{ m.}$$

A case was introduced as in Xiaoli coal mine. The Mining conditions and Fuzzy Probability factors in Xiaoli area are listed in Tables A1 and A2.

**Table A 1 Mining conditions in Xiaoli mining area (L et al., 2010).**

Parameter	Value
Seam dip angle	21°
Seam thickness $k_2$	1.8 m
Working length $L$	340 m
Mining depth $z_{min}$ (average)	158 m
Working depth $z$ (minimum)	96 m

**Table A 2 Fuzzy model parameters in Xiaoli Mining area (Li et al., 2010).**

Parameter	Value
$k_1$	0.8873
$a$	0.3210
$b$	1.0533
$c$	1.1121
$d$	2.6502

By inputting the parameters (Tables A1 and A2) into the Equation A-1, the following formula can be obtained for Xiaoli mining area:

$$S(x) = k_1 k_2 M(A_1) = 0.7328 \times 1.8 \times \int_0^{x_n} 0.3210 \times \left(\frac{x}{96}\right)^{2.1066} \times \exp \left[ -2.2242 \times \left(\frac{x}{96}\right)^{2.6502} \right] dx$$

The monitored subsidence and the plotted curves from the above mathematical model are presented in Figure A27. The predicted values by the fuzzy probability method are in good agreement with the measured data in survey.

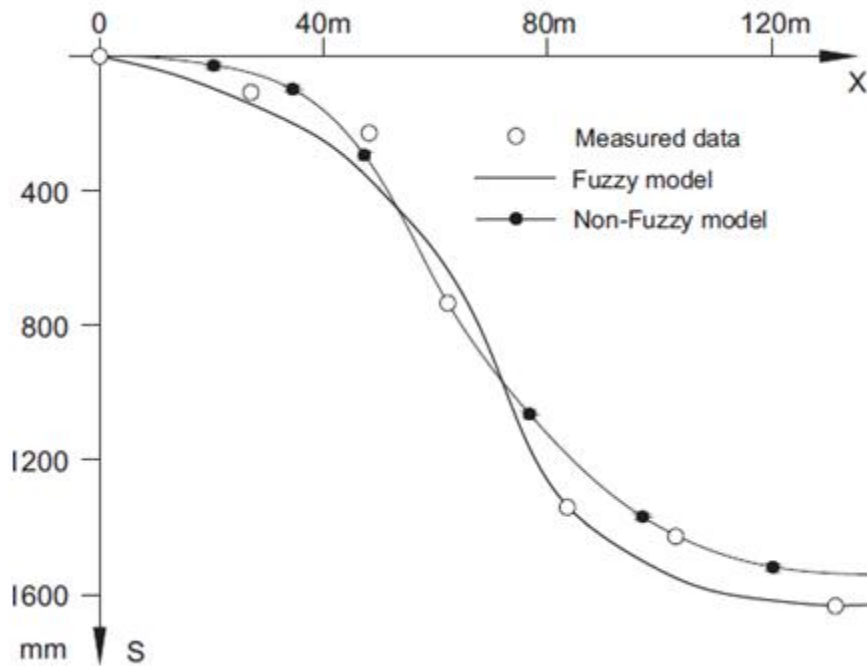


**Figure A 27 Observed and predicted subsidence in Xiaoli mining area (Li et al., 2010).**

The fuzzy probability method has the advantages below:

- ‘it is simple, and theoretical prediction results can be obtained by numerical integral;
- it is suitable for the study of ground subsidence due to flat and inclined coal seam mining; and

- Results are presented to demonstrate the advantages of the proposed method over traditional influence function procedures in terms of accuracy and stability’ (Li et al, 2010).

**Surface Movement Simulated by Verhulst Model (Zhao & Chen, 2009).**

There are number of factors affecting ground movement and deformation, such as geological structure, properties of overlying rock, hydrological features and mining methods. It is difficult to accurately describe these characteristics by the limited parameters and factors. In Verhulst Model mining subsidence is treated as a grey system, the effects of the above factors on mining subsidence are reflected in the time series growth of surface movement for predicting mining subsidence.

Verhulst model is one of special models in grey system, which is used when the available data are not plentiful or detailed and exact understanding of the physical mechanism of a system has not been made. Zhao and Chen (2009) used the characteristics of Verhulst model for processing some initial data to establish a grey differential equation model as the time response model of surface movement.

By inputting observation data from point No.12 on section 12101 in Xinfeng No.1 Mine, China to the established Verhulst model of surface movement is as follows:

$$W(t) = \frac{3982.294}{1 + 188.633e^{-0.4737 \frac{t}{40}}}$$

Using the above equation, the calculation results are shown as Table A3 (starting from October 9, 1992 and the time interval is 30 days).

**Table A 3 Calculation results of surface subsidence using the Verhulst Model equation (after Zhao and Chen, 2009).**

Time interval(d)	30	60	90	120	150	180	210	240	270	300	330	360	390	420	450	480
Monthly subsidence (mm)	4.9	6.9	9.6	13.3	18.4	24.9	33.2	43.0	53.7	63.5	69.9	69.3	58.5	36.7	6.9	
Accumulated subsidence (mm)	11.7	16.6	23.5	33.1	46.4	64.8	89.7	122.9	165.9	219.5	283.0	353.0	422.2	480.7	517.4	524.3

The plotted curves of magnitudes of subsidence growth and accumulated amount of subsidence growth in time series are presented in Figure A28.

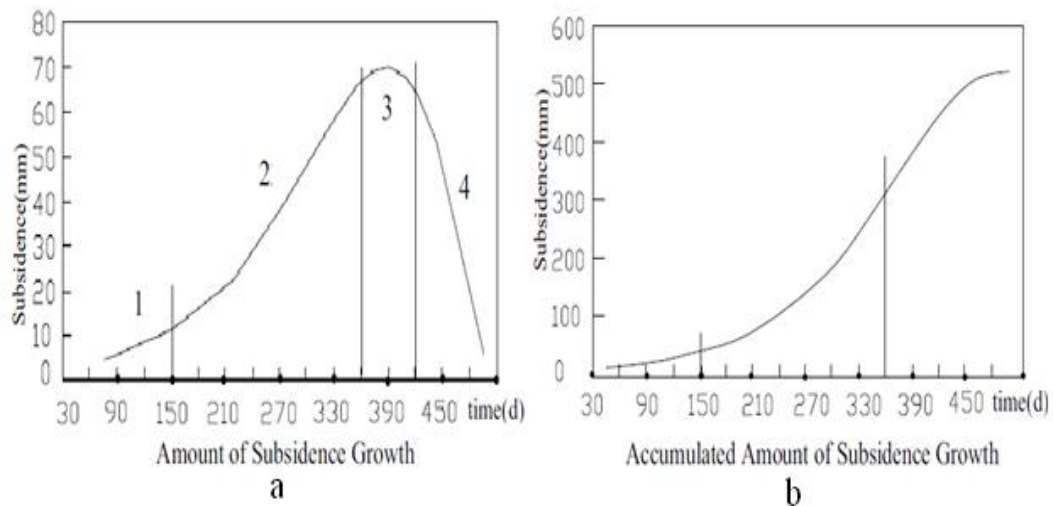


**Figure A 28 Subsidence growth. a. amount of subsidence growth; b. accumulated amount of subsidence growth (after Zhao and Chen, 2009).**

Surface movement and deformation process are divided into 4 phases which is helpful for taking measures in preventing the damage of mining subsidence to surface structure and in-ground facilities. The four stages are: 1) Detention adaptation phase, from 0 to 150 days. 2) Logarithmic growth phase, from 151 to 360 days (Figure A28), at this stage, intensive surface observation and some measures are undertaken, and then the damage of surface building induced by surface subsidence and deformation can be prevented or reduced. 3) Maximum growth phase, from 360 to 420 days, 4) Decline phase, its growth curve declines quickly (Figure A28), when the time reaches 480 days, the monthly subsidence is less than 10mm, i.e. daily subsidence less than 0.3mm, in this stage it can be regarded that surface movement has basically ceased.

In the same mine at No 46 observation station, Su et al (2003) used Versulst model to deduct the equation with corrected factor  $\delta$  as:

$$W(t) = \frac{7173.235}{1 + 447.3272e^{-0.4378951t/40}} + \frac{2078.558}{1 + 3.744655e^{-0.8994t/40}} \delta(t-290)$$

Through calculation by the above equation the calculated subsidence values and the measured data are listed in Table 2.9. The errors of prediction by the Versulst Model are less than 2.5% in this case.

The comparison curves are plotted in Figure A29 (after Su et al, 2003). The predicted results with Verhulst Model are very confident with the surveyed magnitude of subsidence.

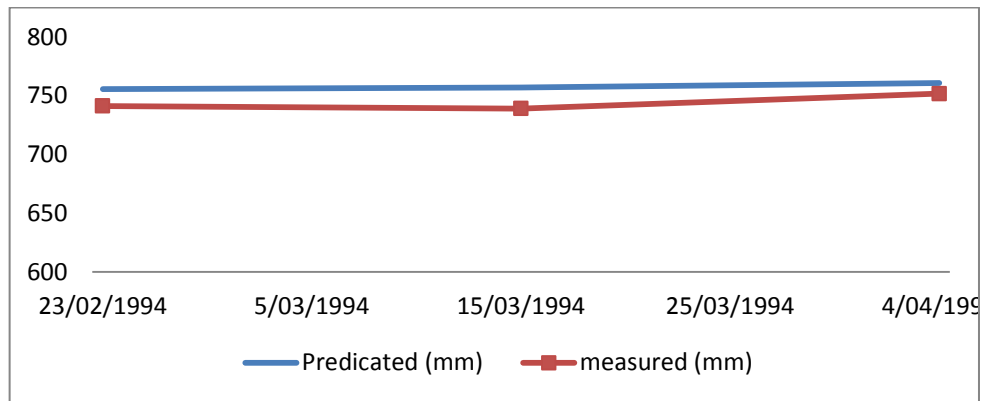


**Figure A 29 Subsidence by prediction and measurement (mm) (After Su et al, 2003).**

### **Dynamic Subsidence: Enhancing Prediction Methodologies (Karmis, 2008; Liu, 2010a)**

Ground subsidence is a dynamic process temporally, spatially and three-dimensionally. Dynamic subsidence is different from final subsidence, and is the subsidence movement processing along with mining approaching toward, beneath, and past one point of interest on the surface or in the subsurface. Contrastively, final subsidence is a static situation representing the degree of subsidence that has been induced at a specific point on or under the surface after the extraction has passed that point and no further subsidence movements occurring. However the degree of damages from the subsidence are not only basing on the final subsidence, but also the dynamic values of subsidence (Liu, 2010a). Distinguishing dynamic subsidence from static one is very vital as ‘the distribution of strains, and therefore damage potential, for each condition is different’ (Karmis et al, 2008). Therefore, it is important that the damage potential should be assessed from both dynamic and static subsidence. Structures on surface (i.e. buildings on ground) or under surface (i.e. mine shafts) may be damaged by both tension and compression (Karmis et al, 2008; Liu, 2010a).

Karmis (2008) concludes the enhanced prediction and control methodologies developed by the current research include:

- Dynamic ground deformation prediction for longwall mining situations provides the approach to predict the development of ground deformations at any point against the advancing longwall face with requirement of only a few simple parameters.

- Strain is one of the best and reliable indicators of subsidence-related damage in subsidence prediction. Ground strain is better than horizontal strain to present the ground deformation due to its inclusion of the slope features in it. Ground strain is more realistic as predictor of strain affecting a surface structure.
- In model calibration with measured subsidence data, different regional parameters may be used to cross-correlate predictions for ensuring that calibration results from two different procedures are ‘tied and considered as independent processes’ (Karmis et al, 2008).

### **Machine Learning Methods: Neural network methods**

Machine learning is a branch of artificial intelligence or computational intelligence. Its main objective is to allow computers to extract information from empirical data (such as sensor data or databases). Machine learning includes some sub-fields, such as neural networks and support vector machine. Neural Network methods formed the first wave of discovery in machine learning, and became popular in late 1980s. Support vector machine (SVM) have become popular in nonlinear classification and regression problems since mid-1990s (Hsieh, 2009). Some software packages for machine learning are Matlab series (Spider, Netlab, etc).

The use of artificial neural networks (ANN or NN) in engineering and science has become widespread recently, including for the surface subsidence prediction in mining industry. The first step to use ANNs is the training and testing of neural network based on the available data. Input variables consist of geological, extraction parameters and coordinates of the points of interest while the output variable will be surface subsidence data. After successful training of ANNs, the performance is tested on the specific separated sets of testing data. Finally, the surface subsidence profile above the extraction is predicted by the trained neural network. The reliability of ANN for the prediction of subsidence is validated in different subsidence models (Appendix A-3 to A-6) and ultimately proved on actual measured data (Ambrozic and Turk, 2003).

An important advantage of neural network method is that the geological and geo-mechanical conditions of the overburden above the mining are not required to

input. However, the data on extractions and the displacements of points on ground surface, even the data on the subsidizing causes are needed to input and are much easier to obtain. Multi-layer feed-forward is one type of the neural network, and is 'appropriate for the approximation of an unknown function' (Ambrozic and Turk, 2003), such as the prediction of subsidence. The predictive results of subsidence resulted from a 350 m wide and 400m long excavation with the excavating thickness of 4.0 m and average buried depth of 325 m. Compared to results predicted by Stochastic models, the correlation coefficient  $r$  equals to 0.997. Practicability of the prediction of subsidence is quite satisfied (Ambrozic and Turk, 2003).

### **Machine Learning Methods: Support vector machine**

Support vector machine (SVM) is small sample studying method and recently developed algorithm in machine learning supported by statistical learning theory. The key idea of the SVM is to minimize empirical risk, improve the generalization ability of study machine and effectively solve the problems over processes of machine learning. Compared to traditional methods, SVM, therefore, can be effectively used in conditions of deficient samples, abnormal result of observation, nonlinear and high dimensional pattern recognition (Tan et al., 2009).

Subsidence coefficient is one of major parameters for predicting ground movement and deformation, especially when mining under the buildings, water bodies, railways and shafts. Factors, influencing subsidence coefficient, consist of mechanical characteristics of overburden; thickness of strata, ratio value of mining depth to seam thickness, mining methods and roof control method, etc. Magnitude of subsidence coefficient  $q$  can be calculated by the average consistence coefficient  $f$  of overburden strata by Formula A-1 in Section A-1 (MCRC, 2000, p104, p105).

Tan et al (2009) established a regression relation model of SVM between subsidence coefficient and associated factors, analysed data from tens of typical observation stations as training samples. Radial basis function (RBF) is chosen as a kernel function, for assuring the accuracy of regression model, the insensitive loss factor is defined as 0.01(Tan et al., 2009).



The model prediction of coefficient is verified by 69~74th samples of data. The comparison between test results to the measured data is displayed in Table A4. The maximum absolute error predicted by SVM is 0.010026 and the maximum relative error is 1.28%. Thus, SVM is very confident in prediction of the subsidence coefficient (Tan et al., 2009).

**Table A 4 Comparison of the prediction results and measured results (Tan et al., 2009).**

Sequence number	Measured	Calculated by SVM	Absolutely error	Relative error
69	0.807	0.797019	-0.009981	1.24%
70	0.843	0.833011	-0.009989	1.18%
71	1	0.990008	-0.009992	0.99%
72	0.8	0.789974	-0.010026	1.25%
73	0.83	0.820004	-0.009996	1.20%
74	0.78	0.789993	0.009993	1.28%

## **A-9 In-Situ Horizontal Stress, Yassien’s Study (2003)**

In mine stability studies both horizontal and vertical stresses are to be deliberated. Field measurements have indicated that horizontal stresses are much larger than vertical stresses; the magnitude of the maximum horizontal stress may be three times greater than the vertical stress (Mark and Mucho, 1994, cited by Yassien, 2003).

Most of the horizontal stress is maintained by the roof layers, whereas the vertical stress is retained by the pillar. The high horizontal stress may affect entrance stability. The roof of the entries are oriented parallel to the direction of maximum horizontal stress to avoid its damage in a weak and laminated roof (Yassien, 2003). In this study the effects of horizontal stress and vertical stress will be discussed in the section 2.3.3 of the review on negative additional friction, also used in the Phase2 modelling.

## **A-10 Prevention of Subsidence**

Singh (1985) provided four types of measures to control subsidence (Howard et al. 1992): a. Alteration of mining techniques; b. Post-mining stabilization; c. Architectural and structural design for building associated with subsidence; d. Comprehensive planning methods. Each of those four measures comprises of several methods.

## Alteration of Mining Techniques

- **Partial Mining:** This method is one of the measures in Huntly East Mine to mitigate the subsidence. Partial mining may be completed in ways of leaving protective zones; use of sized pillars; mining subcritical widths, so that the maximum subsidence is reduced. Leaving protective zones is the most commonly methods for protecting the important manmade or natural structures. The zone may be protected by:
  - a. Leaving the entire pillar unmined beneath structures,
  - b. Partially extracting the pillar and backfilling
  - c. Room and pillar mining, with up to 50% extraction (Howard L. et al., 1992)

Partial mining includes the three methods: Strip pillar mining method; Room and pillar method; Limiting thickness mining (Guo et al., 2009).

- **Strip pillar mining:** Strip pillar mining is the most widely used technique to control ground subsidence in coal mining for protecting the buildings, railways and water bodies in China. In strip pillar mining the coal seam is divided into regular strips separated by the extracted space alternatively. The strips left behind, having a high length to width ratio, called strip pillars, are designed to prop the overburden and control surface subsidence (Guo et al., 2009, p141).

The advantage of strip pillar mining is to decrease the surface subsidence effectively without altering mining technology. Mining height is generally less than 6m, and the recovery ratio varies from 40% to 60%. The surface subsidence factor increases with recovery ratio and mostly less than 0.2 (Table A5) (Guo et al., 2009).

**Table A 5 Relationship between subsidence factor and recovery ratio in strip pillar mining (Guo et al., 2009).**

recovery/%	hard stratum		medium-hard stratum		soft stratum	
60	0.09	0.11	0.13	0.17	0.17	0.21
50	0.05	0.06	0.08	0.10	0.10	0.12
40	0.026	0.032	0.03	0.05	0.05	0.06

- **Room and pillar method also called bord and pillar:** The room and pillar mining is widely used in America, Australia, Canada, India, China and South

Africa. This method is the current mining method in Huntly East Coalmine. Its subsidence factor is between 0.35 and 0.68 (Guo et al., 2009).

- **Limiting thickness mining:** Limiting thickness mining can reduce the reverse effects of surface subsidence on the surface structures. This method is rarely used, because ‘its recovery ratio is quite low if no surface structure damage is allowed’ (Guo et al., 2009). The permitted extracted thickness  $M$  is calculated by,

$$M \leq \frac{\varepsilon_y \cdot H}{1.52 \cdot b \cdot q \cdot \tan \beta}$$

Where:  $\varepsilon_y$  is the allowed surface horizontal strain;  $H$  is mining depth in meters;  $q$  is subsidence factor;  $b$  is horizontal movement coefficient; and  $\tan\beta$  is tangent of major affected angle (Guo et al., 2009).

In Huntly East Mine the typical thickness of coal seam is 20 m. The extraction height ranges from 6 to 8 m currently in the partial mining area.

- **The Longwall Mining:** A typical longwall mining panel of coal has a width of around 150 to 300 metres, length of 1000 to 3500 metres and mining height at 2 to 5 metres. That dimension is totally extracted out by longwall shearing machinery. When coal is extracted in longwalls, the roof immediately above the seam may collapse immediately into the void (called goaf or stope) after the hydraulic shield moved. Consequently, the fractures and displacement of the overburden progress upwards, leading to sagging and bending of the near surface strata and subsidence of the ground above the goaf (Debono, 2007).

### Prevention Measures

In area with requirement of protection of the important manmade or natural structures the longwall mining is not preferred; methods by leaving protective zones are most commonly used instead.

- **Backfilling with mining:** It is a very effective method for reducing subsidence effects by both minimizing the strata deformation forces and ‘conserves the hydrologic regime’ (Howard L. et al., 1992, p964). This method can not only mitigate the subsidence but also make good use of the

waste materials such as coal gauge or refuses (e.g. in The Netherlands; Yanzhou, China).

- **Harmonious Mining:** This technique focuses on the end results of the superimposing compressive strains and the tensile strains both induced by different mining faces. This may be a superposition from two simultaneously mining faces that advance at the same rate, Time factors and advance speed must be known to successfully apply the Harmonious Mining method (Howard L. et al., 1992, p964).
- **Mine Layout or Configuration:** Layout or mining patterns controls the strains thus as one of factors to determine the subsidence (Howard L. et al., 1992, p964).
- **Extraction Rate:** A faster heading rate is preferable in unfractured, visco-elastic strata as it reduces the tensile summit and ‘moves it closer toward the working face’ (Howard et al., 1992, p964). However, in fractured, clastic rocks, rapid face advance may intensify displacements and strains and consequently lead to greater subsidence.

## **A-11 Far Field Subsidence Movements**

Normally, the settlements and surface strains are largely confined to a ‘subsidence bowl’ above the coal-mine extraction. The boundary of this bowl is delineated by ‘angles of draw’ measured from the edges of the area of extraction (Figure A30).

However, from the 1990s, significant horizontal ground movements well outside the expected subsidence bowl have been reported from the NSW southern coalfields. The longwall mining in those coalfields were at depths of approximately 400 m to 500 m, and movements were measured 1 km or more away from an active longwall. Figure A30 shows that lateral movements of 40 mm were measured 1.5 km away from a longwall panel being worked at a depth of about 480 m. There was no noticeable vertical settlement at that distance. These lateral movements are defined as ‘far field subsidence movements’ (Mine Subsidence Engineering Consultants, 2008, cited by Pells, 2008).

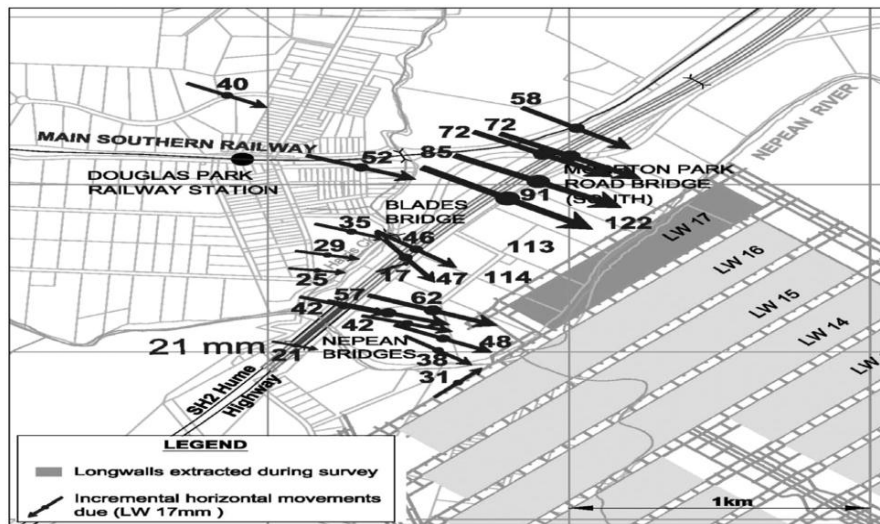


Figure A 30 Far field movements, Douglas Park (From Pells, 2008).

Figure A31 summarises far field movement in the Sydney Basin. The maximum lateral movement is around 50 mm at 500 m away from the edge of the panel. The furthest distance is about 2800 m away from the extraction boundary, giving the maximum lateral displacement of 25 mm.

The far field movements originate from redistribution of the high horizontal stress field overburden that overlies the Permian coal-seams. ‘These horizontal stresses are typically 2 to 3 times the overburden pressure’ (Pells, 2008).

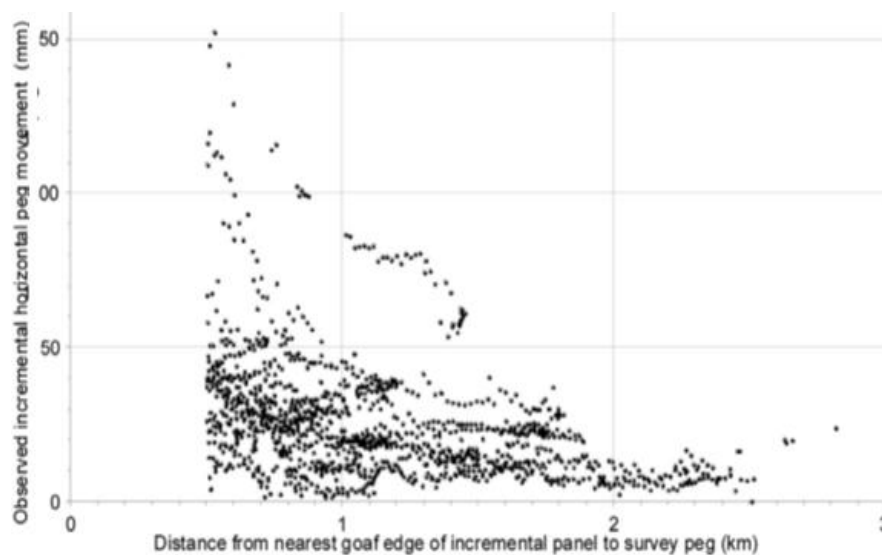
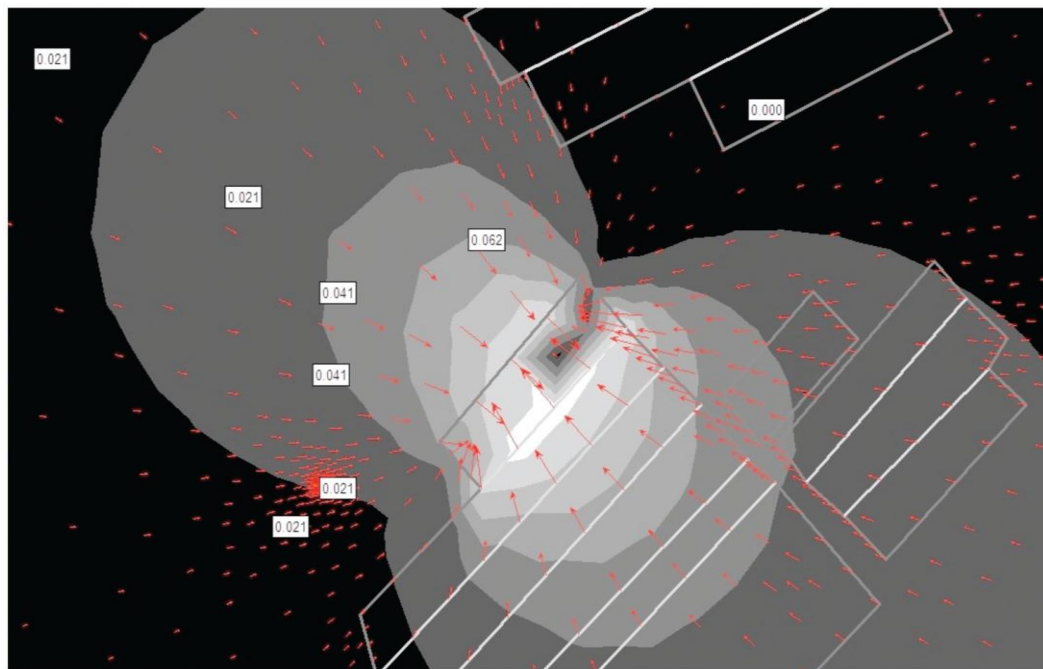


Figure A 31 Far field horizontal movements in the NSW Southern Coalfield (from mine subsidence engineering consultants, 2008, cited by Pells, 2008).

These movements are pseudo-elastic movements far away from the goaf zone where composite ‘3D non-linear fracturing is taking place’ (Pells, 2008). When stress or displacement well away from the point of action is analysed, what happened at that action point doesn’t matter, as long as the analysis obeys the laws of equilibrium and elasticity (St Venant, 1855, cited by Pells, 2008). Secondly, the coal-seam extracted was a soft horizon, most of the regional stress redistribution happened above seam level. Therefore, the far field movements can be analysed in a 2D bird’s-eye view in finite element model (Figure A32) that shows the model prediction for the real situation from Figure A30 (Pells, 2008).



**Figure A 32 Predicted far field movements in metres (Pells, 2008).**

## **A-12 Safety Pillars for Shaft**

The need to protect structures from the adverse effects of ground subsidence induced by mining has resulted in the practice of leaving blocks of ore in situ, called “safety pillars” immediately surrounding and beneath the shaft. Using the safety pillars or protective pillars is the main measure to protect shafts. The dimensions of the pillars may be determined by many empirical methods, theoretical method or modelling techniques. These methods are based upon simplified descriptions of the relationship between safety pillar and subsidence (Cheng, 1989; Daemen, 1972). This thesis only studies the relationship between the vertical shaft and the safety pillars.

Safety pillar dimensions are pillar radius, thickness and pillar geometry. Though shaft pillar has been commonly used for protecting shaft, the empirical rules quietly vary in respect to the pillar radius and shaft depth (Daemen, 1972). In European coal mines, the recommend equation to compute the shaft pillar radius (R)  $R = 0.7 H$ , here the H is shaft depth. In South African in the much deeper gold mines, the shaft pillar can be calculated by  $R = 0.1 H$  (Daemen, 1972).

When considering the radius of the protective pillar, the far field effects must be taken into account. Keilich (2009) found that there are a number of the cases where the river closure and upsidence have been reported above unmined mine. Those events mean the more stand-off distances may be reserved in mine layout to ensure the safety of the shaft protection pillars.

- **Application of the Face Element Principle to the Study of Shaft Pillars**

Salamon (1964) introduced the ‘face element principle’ to compute values of tilt, distortion, horizontal and vertical strain, curvature, and vertical stress along a shaft by inputting various parameters of Poisson's ratio, seam depth, pillar radius, mining geometry, and closures over the mined area. This homogeneous isotropic model supposes that the rock mass behaves as a linearly elastic material (cited by Daemen 1972).

In the mathematical functions derived by Salamon for the isotropic case, the influence of seam depth, extent of mining, and pillar radius on the deformations of the shaft can be calculated to obtain the vertical strain, the vertical stress, the vertical displacement, the horizontal strain, the tilt, the radius of curvature, and the distortion along the axis of the shaft as in the following equations. In the calculations the shaft is assumed as a straight line; the origin of a rectangular coordinate system is placed at the intersection of shaft and surface (Figure A33).

Vertical displacement (Daemen, 1972):

$$w = S_m \cdot f_1 \left( \frac{R_1}{H}, \frac{R_2}{H}, \frac{z}{H}, \nu \right) \cdot g_1 (\theta)$$

Vertical strain:

$$\frac{\partial w}{\partial z} = \frac{S_m}{H} \cdot f_2 \left( \frac{R_1}{H}, \frac{R_2}{H}, \frac{z}{H}, \nu \right) \cdot g_2 (\theta)$$

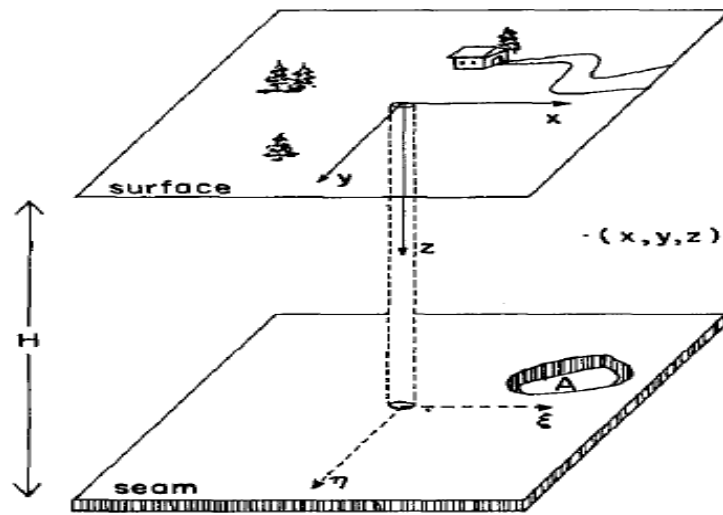


Figure A 33 Coordinate system for the study of the influence on the shaft of mining and area A in a seam at depth H (from Daemen 1972).

Vertical stress:

$$\sigma_z = E \cdot \frac{S_m}{H} \cdot f_3 \left( \frac{R_1}{H}, \frac{R_2}{H}, \frac{z}{H}, \nu, \theta \right)$$

Tilt:

$$\frac{\partial u}{\partial z} = \frac{S_m}{H} \cdot f_4 \left( \frac{R_1}{H}, \frac{R_2}{H}, \frac{z}{H}, \nu \right) g_4 (\theta)$$

Distortion:

$$\gamma_{xy} = \frac{\partial u}{\partial y} + \frac{\partial v}{\partial x} = \frac{S_m}{H} \cdot f_5 \left( \frac{R_1}{H}, \frac{R_2}{H}, \frac{z}{H}, \nu \right) \cdot g_5 (\theta)$$

Horizontal strain:

$$\frac{\partial u}{\partial x} = \frac{S_m}{H} \cdot f_6 \left( \frac{R_1}{H}, \frac{R_2}{H}, \frac{z}{H}, \nu, \theta \right)$$

Radius of curvature:

$$\frac{1}{\frac{\partial^2 u}{\partial z^2}} = \frac{H^2}{S_m} \cdot \frac{1}{f_7 \left( \frac{R_1}{H}, \frac{R_2}{H}, \frac{z}{H}, \nu \right) \cdot g_7 (\theta)}$$

These above equations indicate effects of mining a zone defined by radii R1, R2 and the angle  $\theta$ , over which a ground subsidence S has come into places. On the basis of above functions, Figures A34 to A35 illustrate the strains, tilts as the depth varying with 3D sketches of shaft and pillar. Figures A36 and A37 indicate the vertical strain and tilt with different pillar radius (Daemen 1972).



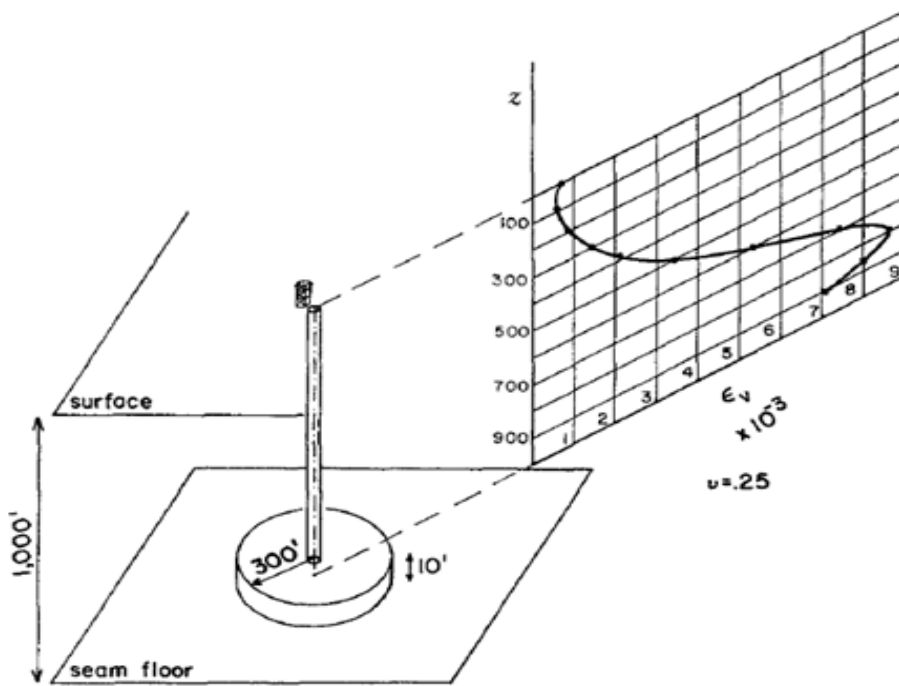


Figure A 34 Vertical strain along the shaft,  $R=0.3 H$ . A seam of 10 ft. thick at a depth of 1000 ft. is mined out except for a protective pillar of 300 ft. radius.  $Z$ : depth,  $\nu$ : Poisson's ratio (From Daemen 1972).

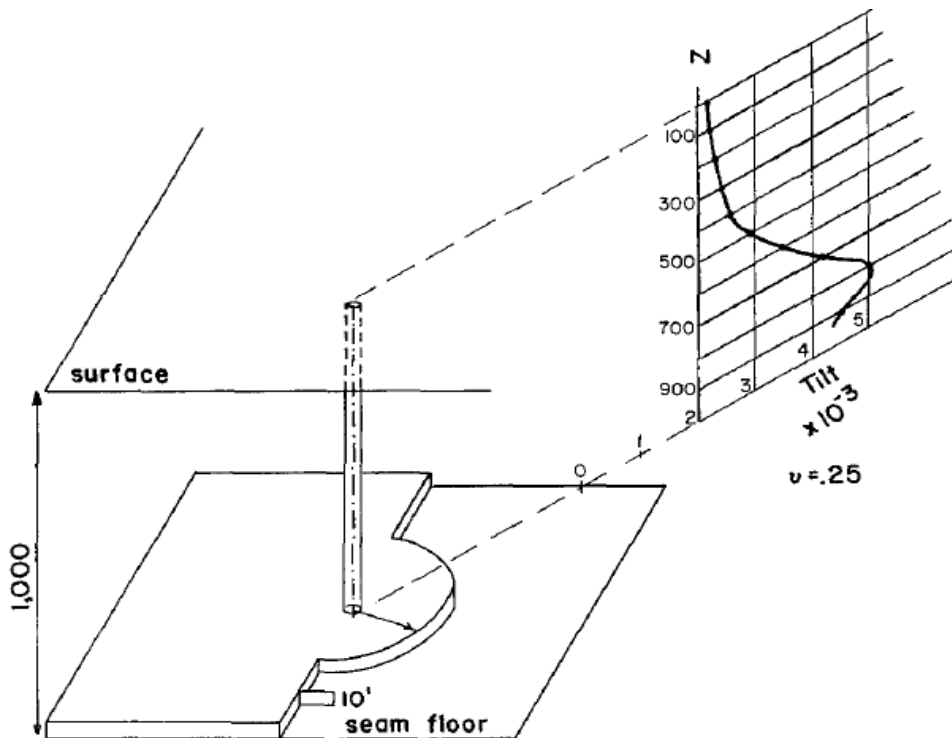
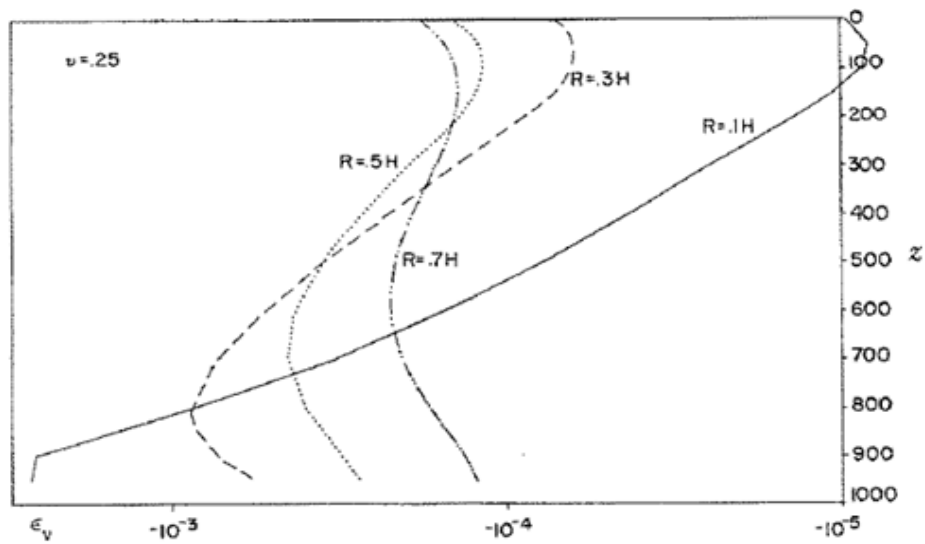


Figure A 35 Tilt along the shaft. A seam of 10 ft. thick at a depth of 1000 ft. is mined out over the entire (planar) region on one side of the shaft, except for a protective pillar of 300 ft. radius.  $Z$ : depth,  $\nu$ : Poisson's ratio (From Daemen 1972).



The depths along the shaft and seam depth,  $H=1000$ , are given in units of closure, i. e.:  $\frac{\text{Seam depth}}{\text{Closure}} = \frac{H}{S_m} = 1,000$   $S_m$  convergence.

Figure A 36 Vertical strain along the shaft for four different pillar radii (Daemen 1972).

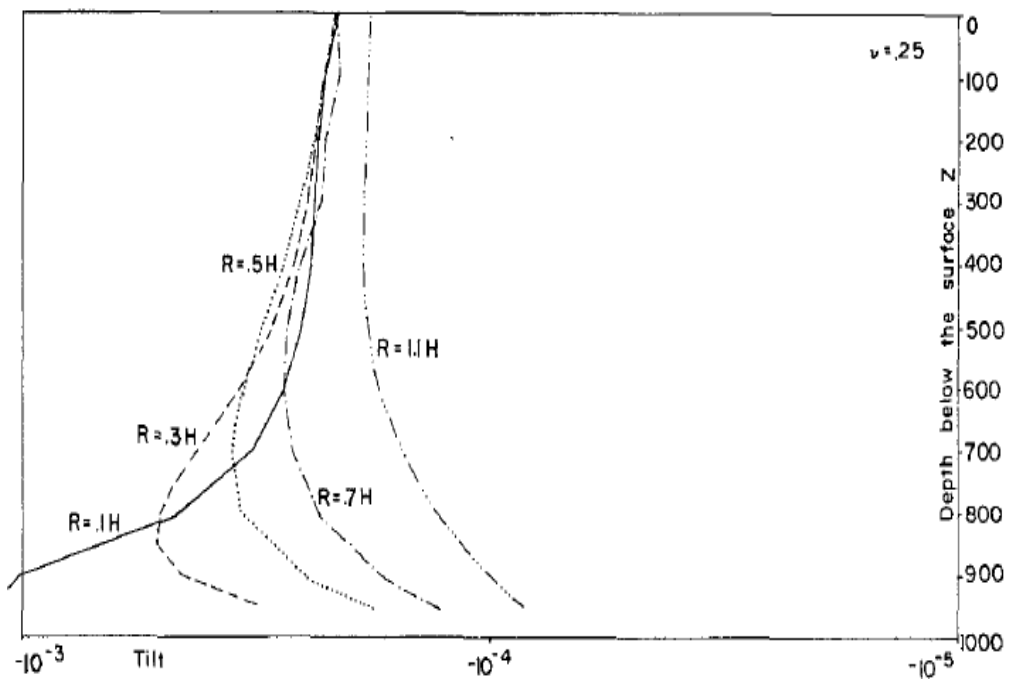
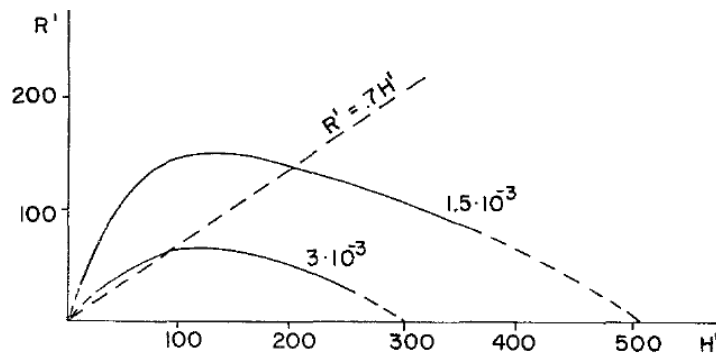
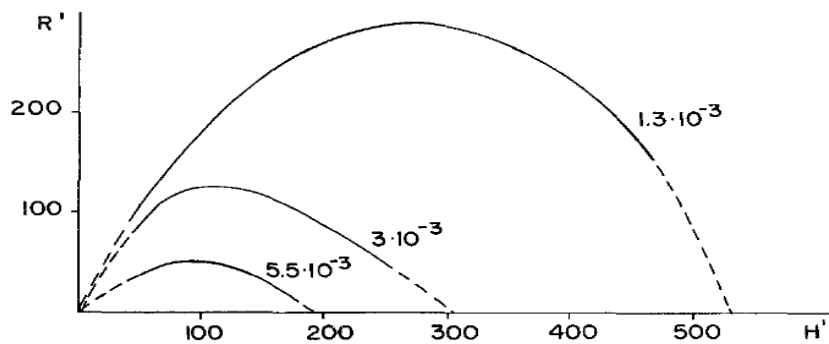


Figure A 37 Tilt along shaft for five different pillar radii (Daemen 1972).

To control the distortion, radius of curvature, and tilt less than the reference values, the absolute value of the pillar radius decreases as depth increases. The radii requirement following the increase of depth can be found in Figures A39 and A40.



**Figure A 38** Pillar radius  $R$  required with increasing seam depth to keep the maximum tilt along the shaft less than  $1.5 \times 10^{-3}$ , or  $3.0 \times 10^{-3}$  (Daemen 1972).



**Figure A 39** Pillar radius  $R$  required with increasing seam depth to keep the maximum tilt along the shaft less than  $1.3 \times 10^{-3}$ , or  $3.0 \times 10^{-3}$  or  $5.5 \times 10^{-3}$  (Daemen 1972).

- **The effect of protective pillars on the deformation of mine shafts**

Pillars may fail due to under-sizing, corrosion of cast iron and steel, erosion of concrete and rock behind the lining, water pressure, pressure due to extremely plastic clay, bad construction procedures, particularly in connections in the shaft linings and subsidence and temperature caused vertical friction (Chen et al, 2010; Zhou et al 2010; Wang et al 2009; Bi 1996; Bi et al., 1997). Therefore, clearly analysing the possible failure causes and taking the right precaution is one of the tasks in a shaft and protection pillar design.

Spickernagel (1965) studied subsidence at different levels above mine openings and concluded that the theory of the angle of draw are not at all suitable for displacements inside the rock mass and the differences are significant. Spickernagel's conclusion was widely supported, particularly in relation to the

‘loading conditions to which a shaft support is subjected’ in the choice of a steel, cast-iron, or concrete shaft lining (cited by Daemen 1972).

- **The safety pillars under the shaft and associated production ground**

In Specification on coal mining and pillar size of working under buildings, waterbodies, railways and shafts of China, launched by Ministry of Coal Resources of China in 2000, in Chapter 5, the safety pillars under the shaft and its associated production ground are detailed in its definition and design (MCRC, 2000).

When designing the pillars for protecting the shaft, the protected objects should include shaft surface tower, hoisting house and its surface barriers. There are five types of the vertical shafts in respect to the depth, use, seam features and geological characteristics (MCRC, 2000):

- The major and auxiliary shafts that is deeper than 400m or sinking through the seams.
- The major and auxiliary or ventilation shafts with depth are less than 400m.
- The shaft that sinks through the steep seam and its roof and floors.
- The shaft that insert through the strata that may slide in soft strata, soft coal or steep fault.
- The shaft that is adjacent to the hilly slope with the landslide hazard.

The design is commonly undertaken by using the vertical cross section method. According to the geology features in N55 panel for shaft sinking, the proposed shaft will be categorised into the second type as the major and auxiliary or ventilation shafts with depth are less than 400m. For common structures the maximum values permitted in the design are:

Maximum tilt  $T=3\text{mm/m}$

Maximum Curvature  $K= 0.2 \times 10^{-3}/\text{m}$

Maximum Horizontal strain = 2 mm/m

In the design of the protective pillar for the new installations, factors that should be considered include the angle of draw, topography of the site, the building patterns in situ etc. In addition the reinforcement measures may be applied to the

existing building to strengthen its structure and minimise the size of the leaving coal as safety pillar to enhance the coal extraction rate (MCRC, 2000).

## **2 Appendix B: The Negative Additional Vertical Stress**

### **B-1 Introduction**

Since 1987, there have been a number of large-diameter shafts in the Xuhuai region, China (Figure B1), suffering from the shaft lining rupture damage, which has threatened the safety of underground mining production, and even caused production to be stopped (Bi, 1996; Wang et al., 2003; Zhou et al., 2010). In the Xuhuai region (area of approx. 200 km times 400 km), there are 7 Coal Bureaus with 173 shafts.

Up to 1996 the ruptured shafts summed 86, including 53 occurred during shaft construction, 33 after construction of shaft, i.e. in the mining production period (Bi, 1996). Up to Dec. 2005 93 shaft linings ruptured across China (China Safety, 2007). On estimation over 150 shaft lining will suffer rupture in following ten years if no further mitigation measures taken (Ding, 2005). The depth of fracture in the shaft mostly was located near the interface between the soft overburden and the hard bedrock. Since 1996, researchers have investigated the mechanism and reasons for shaft rupture in that region.

The shafts in the Xuhuai region have hollow cylindrical lining inserted in the shaft holes. The linings have open ends, 5 - 8 m in outer diameter, a lining thickness of approximately 0.5 - 1 m, are generally constructed with concrete, and have a lining height (i.e. shaft depth) of approximately 200 – 500 m. The internal diameter of lining ranges around 4 m to 7 m. The ruptures manifested are damage to the lining of concrete bodies, not the strata wall (Ding, 2005).

In this review I will introduce the new definition of negative vertical additional stress, its mechanism, the development of the related research and studies, and finally present the implication and significance of the issues that might be a useful reference for the incoming shaft sinking project above the N55 panel at Huntly

East Mine, considering there are some similar geological and hydrological characteristics between the Huntly and Xuhuai regions (Ding, 2005).

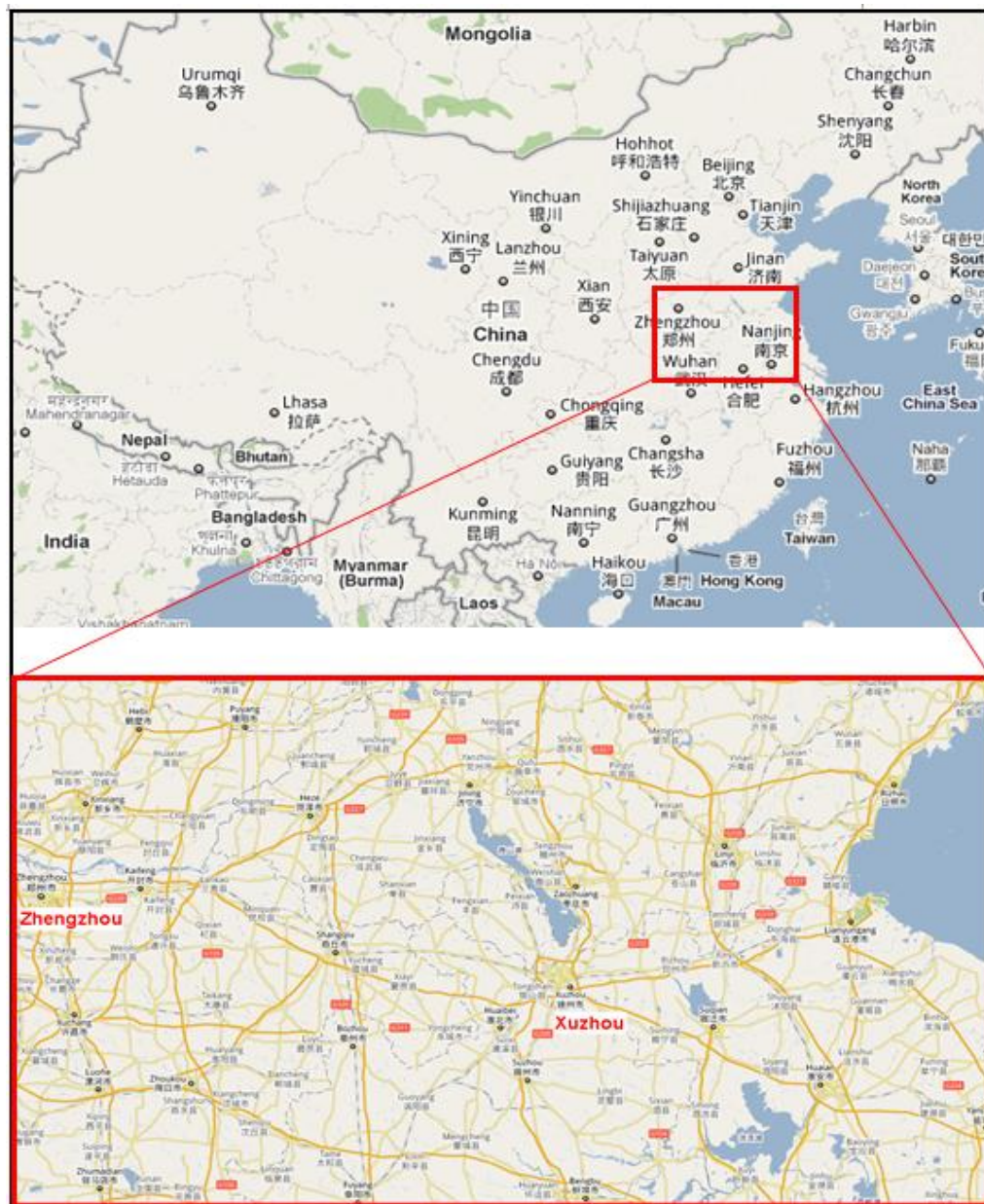


Figure B 1 The location of Xuhuai region in China (Google, 2010).

## B-2 Rupture Characteristics

The common features of rupture in shaft lining in the Xuhuai region are:

- The shafts are all sunk in or through the overburden with rich aquifers, which lie on the bedrock or seam formation and have hydraulic interconnection with seam formation. Especially the lowest aquifer above the seam is normally under a clayey aquitard/ aquiclude (Table B1) (Ding, 2005).

**Table B 1 Shaft damage classification in Xuhuai area (From Bi, 1996).**

Mine Shaft No.	Shaft name	Rupture Damage features	Alluvium thick (m)	Rupture Depth (m)	Height, rupture area (m)	Location to interface (m)	Interface Strata features
1	Zhang Asso.	1 layer, irregular, uncontinous blocky	103.5	104.2-108.5	4.3	-0.7 to -5.0	weathered shale
2	Zhangji Main	diametric shrinkage	105.25	101.0-102.6	1.6	4.25 to 2.65	clayey sandstone
3	Zhangji Asso.	diametric shrinkage	104.9	104-108	4	0.9 to -3.1	weathered shale
4	Jiahe Main	irregular rupture	78.6	100-104	4	-21.4 to -25.4	weathered sandy shale
5	Han Asso.	rupture and offset	30	-	-	-	interface
6	Dahuang Asso.	rupture by squeezing and offset	40	-	-	-	interface
7	Zhangsh Asso	2 layers, continous, irregular band rupture	243.5	225-230.5	5.5	18.5 to 13.0	clay and sand
8	Zhangsh Main	irregular, uncountinous blocky	242.5	240-244	4	2.5 to -1.5	sand and weathered sandstone
9	kongzh Vent	perimeter, irregular band-chain shape	156.35	151.7-155.8	4.1	4.65 to 0.55	clayey sandstone
10	Kongzh Asso	perimeter-oriented fractures, with some blocky	158.65	142-145	3	16.65 to 13.65	clayey sandstone
11	Long Main	6 layers irregular continous blocky-chain	212	162.6-246.9	83	49.4 to -34.0	clay
12	Zhangsh Vent	blocky	252	245-247	2	7.0 to 5.0	clayey sandstone
13	Long Vent	3 layers irregular, linear rupture	159.21	150-162	12	-2.8 to 9.2	clayey sandstone
14	Linhuang Asso	inclined enclosed perimeter band	239.17	229-245	16	10.17 to 5.83	weathered clay sandstone
15	Linmei Asso	2 to 3 layers of irregular, uncontinous, chain	247.2	232.8-237.5	4.7	14.4 to 9.7	clayey sandstone
16	Linmei Main	2 layer, irregular, uncontinous blocky	247.2	211.7-219.7	8	35.5 to 27.5	clay stone
17	Linmei xi Vent	huge area irregular falling, uncontinous damage	240.9	231.5-237.5	6	9.4 to 3.4	clayey sandstone
18	Linmei Vent	2 layers regular continous-uncontinous band	245	226.7-236.5	9.8	18.3 to 8.5	clayey sandstone
19	Luling Asso	2 layers uncontinous irregular blocky	202.75	212.1	-	-9.75	weathered shale
20	Luling Main	one side flat-sheet, uncontinous spalling	203.35	202.5-209.5	-	0.85 to -6.15	clayey sandstone weathered
21	Tongting Main	circumstance spalling	230.4	230.4	-	0	interface
22	Tongting Asso	perimeter blocky spalling	230.5	160-270	110	70.5 to -39.5	clayey sandstone weathered
23	Tongting Vent	perimeter uncontinous rupture	225.3	240	-	-14.7	weathered sandy shale
24	Linhuang vent	perimeter sheet spalling	244.4	227	-	17.4	clayey sandstone
25	Qianling Vent	irregular blocky	96.2	112.6-113.9	1.3	-16.4 to -17.7	sandy shale
26	Xieqiao Vent	flat pieces spalling	421	475-478.5	3.5	-54 to -57.5	sandy shale
27	Kongji Vent	irregular, uncountinous blocky	156.35	151-155.8	4.8	5.35 to 0.55	clayey sandstone
28	Pansan Vent	bunny swell off lining	440.82	444.4-447.9	3.5	-3.58 to -7.09	weathered sandy shale
29	Pandong Vent	irregular, uncountinous band	292.46	292.46	-	0	interface

- In the time between shaft construction and fracture occurrence the groundwater all had significant decline, level dropping by a range from 30 m to 90 m.
- Ground above underground mining had subsided 100 to 500 mm and the shaft also got minor subsidence.
- The rupture events mostly took place during summer from June to August every year since 1987 (Ding, 2005). From June to August it is summer in China when it is hot and the water use is in peak. So aquifers are actively lowered and temperature in lining is high.
- The location of rupture mostly happened at the interface between the overburden and the hard bedrock. The height of the crack area in the lining range from 1 meter to some tens of meters (Bi, 1996). The rupture horizontal depth into lining concrete was from 50 mm to 200 mm. Water seepage was often observed from the rupture, even with sand.
- Reoccurrence: repeated rupture occurs after first rupture was repaired (Ding, 2005).
- The rebars bent towards lining centre; the vent tube deformed. Beams across lining in shaft bent upwards; Skips got stuck at severely deformed section of lining (Ding, 2005).

In her MSc thesis, Ding (2005) concluded that the negative additional vertical friction may be created in the following five conditions when:

- After shaft sunk with freezing method where the surrounding strata were frozen to stop water ingress and stabilise the very fractured or soft strata, the thawing strata subsides and applies the downwards friction on the lining.
- The varying temperature results in the expanding and contracting of the lining that is confined by the surrounding strata.
- The surface ground water seeps downwards.
- Drainage and depressurizing of aquifers leads to consolidation and subsidence of strata.
- Underground mining caused strata subsidence and possible significant inflow into goaf.

Condition 1 happens in the shaft construction period with freezing technique or in production in the district of extreme climates with soil thawing problems.



Condition 2 may be a background affect and exist in every shaft lining. Condition 3 mostly occurs in rainy seasons, the seepage depth is very limited. Its affect could be neglected. Condition 4 and 5 were regarded as the major reason to cause the lining ruptures in the Xuhuai region, by the majority of the scientists and researchers. However, in a case of one specific shaft lining, all or several of the above five aspects may take actions together to produce the resultant downwards additional friction.

The resultant stress within a shaft lining at a depth is from the resultant vertical forces and the resultant horizontal forces. At a certain depth, as the resultant stress increases to above the strength of the lining the shaft lining starts rupturing. The load acting on or in the lining include self-weight of lining, lateral pressure from strata, load from temperature variation, horizontal additional pressure, vertical additional forces, load from soil freezing and thawing and seismic load. However the rupture stress is regarded mainly from the negative additional vertical forces in the Xuhuai (Ding, 2005).

During mine production, the damage to the lining include rupture, spalling, diametric shrinkage, lining rupture, and offset, most of the damage is irregular and discontinuous with blocky-break patterns. Most damage was likely to be compressive failure (Ding, 2005), except two incidences were found where shear failure led to rupture and offset. Figure B2 displays the two layers of an irregular continuous, and a discontinuous band, rupture at depth from 226 m to 234 m in the lining of Haizi Coal Mine (Wang et al., 2003).

The photo in Figure B3 shows a type of damages in shaft lining as the perimeter band-spalling. The rebars bent towards the centre of lining, displaying compressive damage. Table B2 classifies the shaft damage types and profiles in Xuhuai region with 29 lined shafts ruptured during the production phase. There were at least 8 shafts with blocky rupture, 5 with spalling damage, 5 with continuous or discontinuous band-rupture, 2 with diametric shrinkage, and 2 with rupturing and offsetting,. Most rupture heights were less than 10 m. Only 4 ruptures were higher than 10 m, they are No. 11, 13, 14 and 22, at 83 m, 12 m, 16 m, and 110 m respectively. The interface strata were mainly clayey sandstone and shale (Bi, 1996).

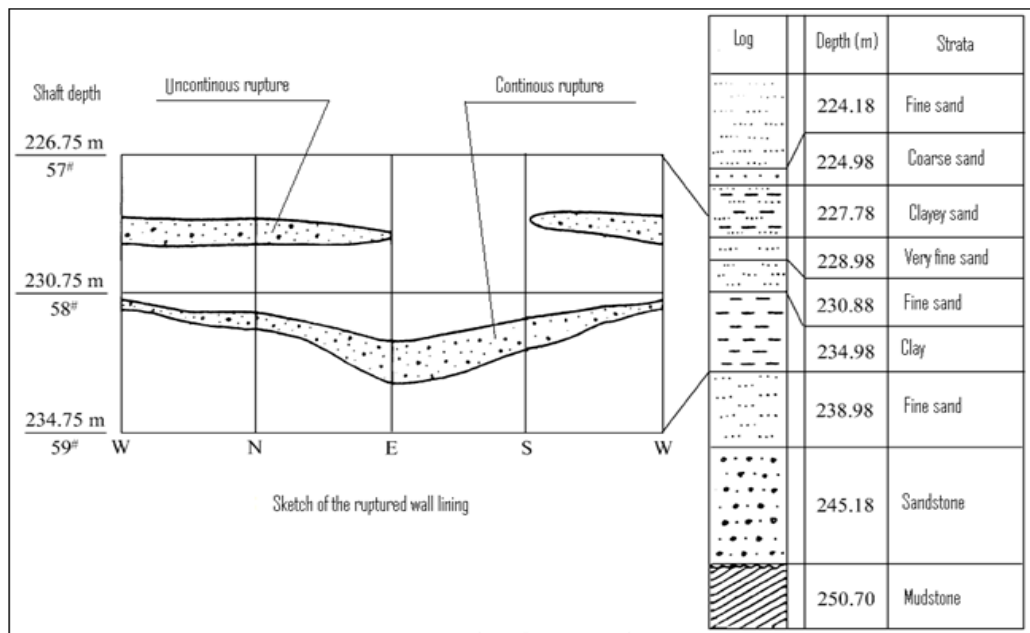


**Figure B 2 Sketch of the ruptured wall of the central ventilation shaft Haizi Coal Mine, Huaibei (from Wang et al., 2003).**



**Figure B 3 One of damage conditions of shaft lining (from Liu et al., 2007).**

Table B2 shows that the shaft rupture usually occurred after some year's use for production. The production duration lasted from 4 to 20 years until the lining ruptured. 4 out of 15 shafts (ZF, HF, HZ and HMF) had been used for less than 10 years; the other 11 served 12 to 19 years. The 15 shafts were all built by freezing method. Water table dropped by a range from 90 to 100 m when linings got damaged (Jing et al., 2005). No papers have been found to further analyse what are the proportions of contribution of over withdrawal of water and inflow into

goaf to compose the final water table decline. The freeze depth is the depth of boreholes to circulate the freezing agents to stabilising the strata surrounding shaft sinking location.

**Table B 2 The shaft rupture information of part frozen shafts in China (Jing et al., 2005).**

Shaft name	Built time/damage	Coverage (m)	Freeze depth(m)	Water level when damage(m)	Rupture depth(m)
ZF 张双楼副井	1982.12.31/1987.07.29	243.15	285	91.05	225.0, 229.3 - 230.5
HF 海孜副井	1983.03/1987.08.21	247.24	285	85.74	232.8 - 237.5
HZ 海孜主井	1982.08/1988.10.06	248.69	258	97	211.79 - 219.79
HMF 海孜中央风井	1980.05/1988.06	245.18	285	93	226.79 - 234.75
XZ 兴隆主井	1977.08.13/1997.06.23	189.31	216.4	93.57	150,184
XF 兴隆副井	1978.09/1997.06.26	190.41	221.75	93.57	154
XXF 兴隆西风井	1976.08/1995.10	183.9	219.45	89.17	165.6 - 171.6
XDF 兴隆东风井	1977.05.31/1997.06.07	176.45	204.95	93.572	157
YZ 杨村主井	1984.12/1997.02.29	185.42	206.94	95.03	176.5
YF 杨村副井	1985.01.23/1997.12.02	184.45	212.44	96.99	160,176
YBF 杨村北风井	1984.10.31/1997.02.04	173.4	212.8	95.03	150 - 156.6
BZ 鲍店主井	1979.05.14/1995.07.12	148.69	256	88.7	136 - 144
BF 鲍店副井	1979.11.26/1995.06.05	148.6	256	88.7	126.9
BNF 鲍店南风井	1979.08.01/1996.08.09	157.92	189	89.78	158.1 - 159.3
BXF 鲍店西风井	1979.10.21/1996.08.02	202.56	234	93.2	168.4,180,204

### B-3 Negative Additional Vertical Friction

A negative additional vertical force against a shaft lining is defined as a negative friction force applying on the external surface of the shaft lining and is resulting from subsidence movement of surrounding strata that have a relative displacement to shaft lining. The negative additional vertical friction can be distinguished off the conventional vertical upwards friction caused by the weight of the shaft lining and shaft equipment that move or have a trend to move against non-subsidence surrounding strata. The vertical stress, resulting from that additional vertical friction, on the cross section across the lining length can be defined as a negative additional vertical stress (Wang et al., 2003).

The negative vertical additional friction is a contact friction between subsiding ground and a rigid shaft lining, created by the strata downwards movement against the stable shaft lining. There may be a slight settlement of the shaft lining, but it is generally much smaller than the ground subsidence around the shaft lining due to the solid shaft lining sitting on hard bedrock or a large base stand underneath the bottom of shaft lining. The subsidence of strata may be caused by

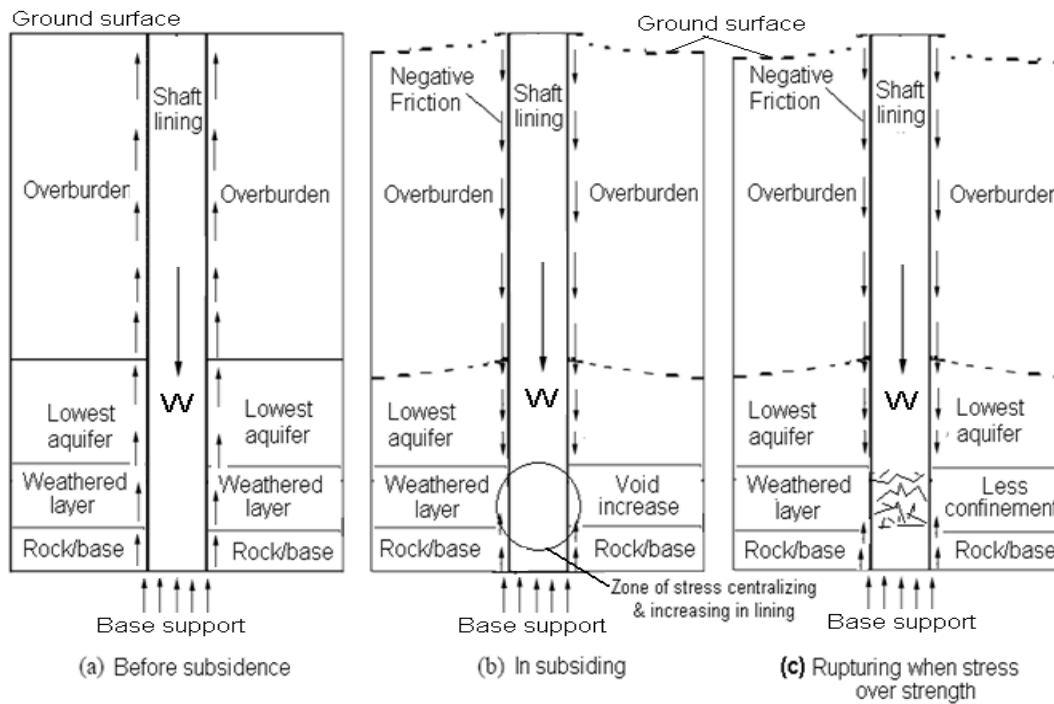
both underground caving of goaf and /or depressurization and consolidation of aquifer or soft layers (Bi, 1996; Ding, 2005) and or soil thawing (Novikov, 1979). However the downwards displacement of around-strata along the outer surface of concrete lining is the necessary factor to create the negative additional friction.

The negative additional vertical friction was proposed in 1991 by University of Mineral Resources of China (Ding 2005; Huang et al., 1991), as one of the theories to explain the mechanism of the massive and convergent occurrence of the shaft lining rupture in Xuhuai region and now it is the mostly recognised major cause to result in that shaft lining rupture, which has been accepted by the majority of scientist and researchers across Asia, particularly in China. That concept was most likely imported and used by referring to the experience of negative skin friction effects in pile foundations, because the vertical shaft lining and pile have very similar principal of suffering the friction from the surrounding subsiding strata (Bi et al., 1997; Yao and Li, 1997).

I have searched and found that the negative skin friction effects in pile foundations have been used in piling practice for over 40 years from 1969 (Bozozuk & Andre, 1969), also called downdrag or drag force (Fellenius, 1971; Bozozuk, 1972, 1981; Alonso et al., 1984; Chow et al., 1996; Poorooshasb, et al., 1996; Emiliou & Spyridoula, 2005). Also in some literature the authors addressed that the principal of negative skin friction effects also can be applied in the shaft practice, for example Kim and Mission (2009). Bozozuk (1981) discussed shaft friction in analysis of bearing capacity of pile preloaded by downdrag. In the review of Comparative evaluation of methods to determine the earth pressure distribution on cylindrical shafts by Tobar and Meguid (2010), they noticed the additional friction on the cylindrical shaft lining but have not discussed it further.

Huang and Chen (1991, cited by Liu et al. 2007) pointed out that the subsidence caused by underground mining and water table decline applies a downwards friction force onto the outer face of the shaft lining by the subsiding strata (Figure B4).

This downwards friction results in the downwards stress within lining wall, it is also called Negative Additional Stress (Wang et al., 2010). The downwards arrows stand for negative additional friction.



W: weight of lining & equipment attached to lining

**Figure B 4 Sketch on subsidence development and shaft lining rupture (after Liu et al. 2007).**

Negative Additional Friction is different from the conventional upwards friction resulting from strata to resist the lining downwards displacement (in Figure B4, the upwards arrows stand for the conventional friction). The accumulation of stress in the lining at the interface depth will reach the maximum because in the vertical direction from the interface the friction force is downwards above the interface and upwards below the interface, due to that in the bedrock the shaft is hold tight and no relative movement occurs between the contact of lining and bedrock strata. If there is no hard bedrock below the interface to hold the shaft lining then the lining may directly sit on the stable base stand to bear the lining weight and the downwards friction force from subsidence.

From the description above it is evident that the subsidence around the shaft lining leads to ‘Double Adverse Effects’ on the lining. The subsidence not only has vanished the upwards friction that holds up the lining by share  $\frac{3}{4}$  of the lining weight plus  $\frac{1}{4}$  with base support (Ding, 2005, p4), but also applied a downwards friction on lining to make the stress situation worse. In traditional design before these events of rupture from negative additional friction, the designers always knew the upwards holding friction in its static mechanics calculation in conventional hard rock ground, however never thought of that the upwards

holding friction could disappear in surrounding ground subsidence. Even worse, the land subsidence then applies an adverse downwards friction to worsen the situation of stress within the shaft lining, especially at the bottom of the lining (Ding, 2005).

The stress and strain caused by temperature change in the lining are also part of the reasons leading to rupture of the shaft lining. The strain and stress within the lining varies with the change of the atmospheric temperature via the ventilated air. Zhou et al. (2010) found that the measured lining strain and the modelled data that varied with the fluctuation of the temperature in the shaft by the ventilation air. In tested shaft in Xuzhou district has an inner diameter of 5.5 m with dual layer lining; overburden depth of 164.36 m. In 2003 the four sets of strain sensors were buried in inside lining at depth of 100 m, 125 m, 145 m, and 165 m respectively. Figure B5 illustrates that the airflow temperature in the shaft is higher in winter and lower in summer than the atmospheric temperature in situ. They used the ABAQUS software to simulate the temperature and strains within the shaft and plotted the data in Figure B6 to compare the results.

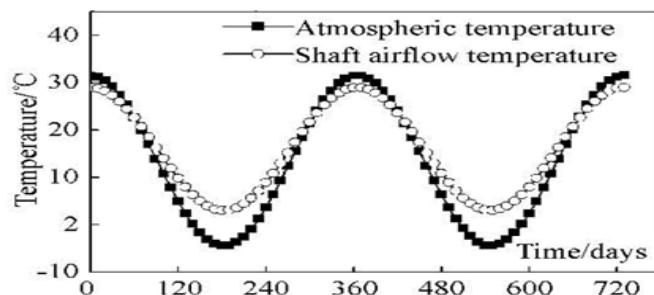


**Figure B 5 Atmospheric temperature and airflow fluctuation law (from Zhou et al., 2010).**

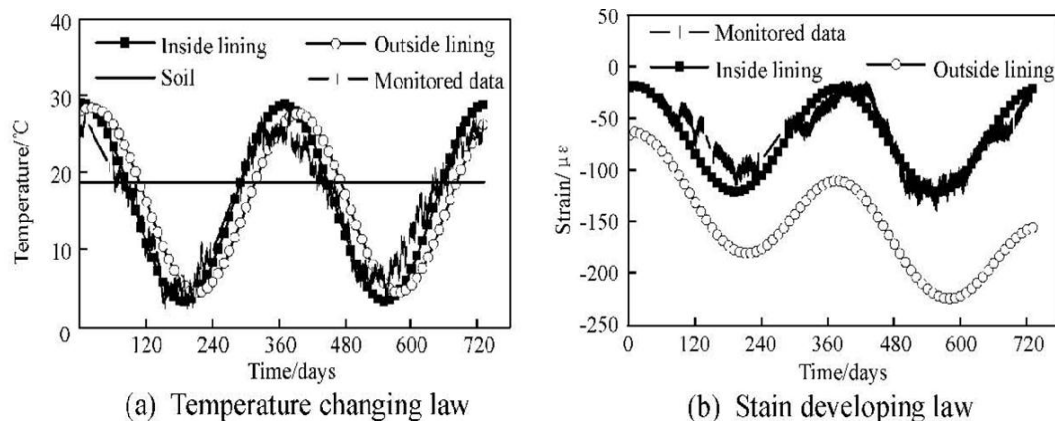


**Figure B 6 Comparison between the simulated and monitored data (from Zhou et al., 2010).**

Figure B6 (a) indicates that the monitored curve is quite close to the modelled curves of the temperature. The simulated outside lining has a narrower changing range of temperature and an approximate 10 days delay than the temperature of inside lining. The mean temperature is 19 degrees. Figure B6 (b) shows the comparison of the monitored vertical strain and the modelled vertical strain within two years. For inside lining of the dual lining the monitored and modelled data are matching well in both magnitude and time series with a regular changing wave. The simulated outside lining suffered much higher compressive strain, approximately are twice the inside lining, by comparing two groups of bottom data of 180/110, 230/120 on 200 days and 580 days respectively. However the strain of the outside lining increase dramatically as the time goes, from 180 to 230  $\mu\epsilon$  within 380 days. Unfortunately the modelled outside strain cannot be compared without the monitored data due to no sensors being installed in the outside lining after shaft construction in this field measurement.

On the 7 years' monitoring and measurement in situ, Zhou et al. (2010) concluded that under the resultant effects of self-weight of the lining, horizontal strata pressure, vertical addition forces and the periodic effect of the atmospheric temperature, the strain in the shaft lining varies in a law of sine (or cosine) function and have the increasing trend in time series (Zhou et al., 2010).

## **B-4 Examples for Calculations**

There are number of literature have provided methods or approaches to compute the values of negative additional stress (friction), its depth and predict the rupture time. Lv and Chui (2001) used ANSYS software to simulate the model of the rupture of the single layer lining and obtained the varying laws of the stress and strain in the lining. According to the principal of the effective stress, Zhou and Yang (2003) found that in different stratum there may exist different resistance vectors, in terms of negative stress, positive stress and zero stress, on the basis of their geo-hydrological features, thus the resultant effects of the different vectors determine the final rupture location, magnitude and features of compression or tension.

- **Stress calculation by Wang et al. (2010)**

The design value of C80 concrete uniaxial compressive strength is 35.9 MPa (Wang et al. 2010; Ministry of Construction of China, 1991, 2007). The maximum biaxial compressive strength is 1.2 times the uni-axial compressive strength, which reached 43.08 MPa. The tri-axial compressive strength depends primarily on the ratio of radial stress/ the maximum compressive stress, let the ratio = 0.25, then the tri-axial compressive strength is 140.01 MPa (Wang et al., 2010).

Figure B7 shows us one of the scenarios for quantifying negative additional vertical stress for the main shaft in the Zhangshuanglou Coal Mine. Wang et al. (2010) found that the vertical additional stress within shaft lining at depth of 530m could reach 48 MPa when the ground water level declined by over 100 m. That stress of 48 MPa is much lower than the uniaxial compressive strength of 140.01 MPa. However when the interface got enough void created by the inflow to carry the particles from the interface bedding into the goaf and the confinement of the strata is then not significant, consequently the shaft lining strength at interface depth will be dropped to maximum biaxial compressive strength of 43 MPa that is less than the vertical additional stress of 48 MPa. Therefore it is most likely that the shaft lining commences rupture (Wang et al., 2010). The shaft lining built with lower grade concrete are going to be much easier to rupture than this described C80 lining. If there is not this kind of interface underneath, the shaft is still in high risk to rupture when a section of the bottom end of the shaft is exposed to the mine goaf.

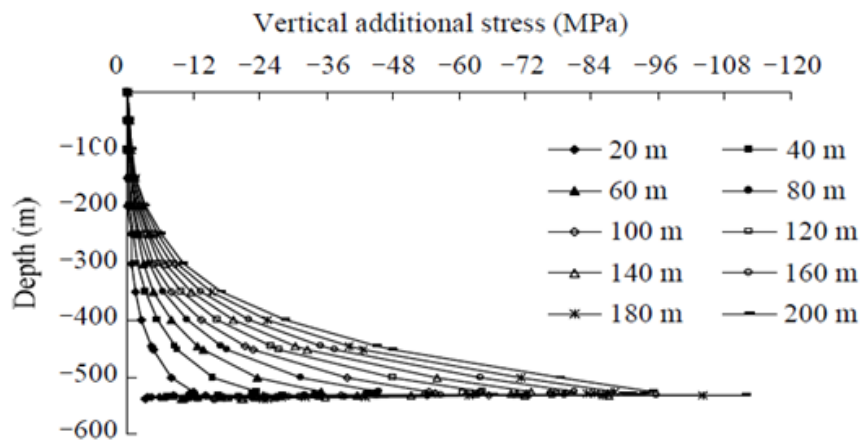


**Figure B 7 Curves of additional vertical stress within lining vs. depth (Wang et al., 2010).**



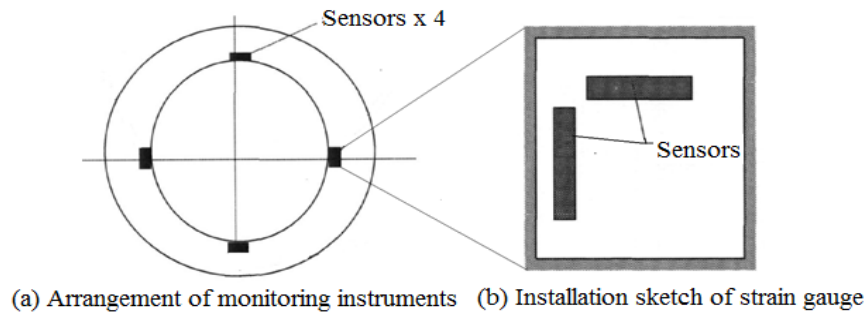
In the above case, the development of voids and loss of confinement is just one of the major causes and processes of rupture damage to the shaft lining, not the only conditions. As the above case, if no confinement loss, it could be anticipated that at a depth assumed 900m, the negative stress might be over 140 MPa, and then the lining still suffers rupturing. Ding (2005, p15) concluded in her MSc thesis, the negative additional vertical friction could be created when: strata thawing; varying of temperature in the lining; surface groundwater seepage; Drainage and depressurizing of aquifer leads to the consolidation and subsidence of strata; Underground mining caused strata subsidence and possible significant inflow. However, in a case of one specific shaft lining, all or several of the above five aspects may take actions together to produce the resultant downwards additional friction.

The resultant stress within lining at a depth could be resulted from the resultant vertical forces including negative additional friction and weight of lining and the attachments on shaft lining, plus resultant horizontal forces. As the resultant stress increases up to over the strength of the lining at a certain depth, the shaft lining starts rupturing.

Therefore, the development of voids, and loss of confinement is just one of the causes and processes of rupture damage to the shaft lining.

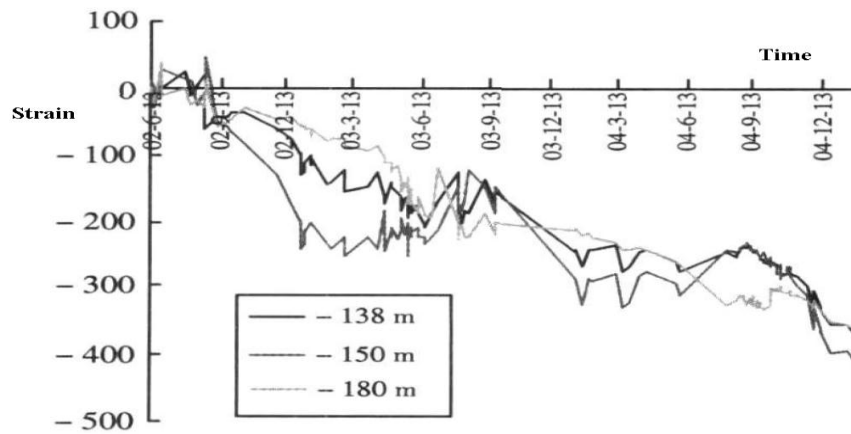
- **In situ test and prediction of rupture time**

A strain measurement was undertaken by Wang et al. (2009) in shaft of Jining No3 Mine in 2002. The Shaft is 395 m deep with inner diameter of 8 m, built by poured concrete at Grade C40 for internal lining, C30 for external lining as dual layer shaft lining. The soft overburden strata over hard rock have an average thickness of 184.57 m, surrounding the shaft. The shaft was completed in Dec. 1996 by freezing sunk techniques. The subsidence was mainly caused by the severe drainage of the aquifers due to inflow and over withdrawal of water. During the measurement the water head in lowest aquifer dropped by 12.7 m. The strain gauges were buried in the lining at 4 depth levels of 138 m, 150 m, 168 m, and 180 m, respectively. At every level there were 2X4 sensors arranged in 4 locations shown as in Figure B8 (a) & (b). In a group of 2 gauges one measured the vertical strain; the other measured the horizontal strain.



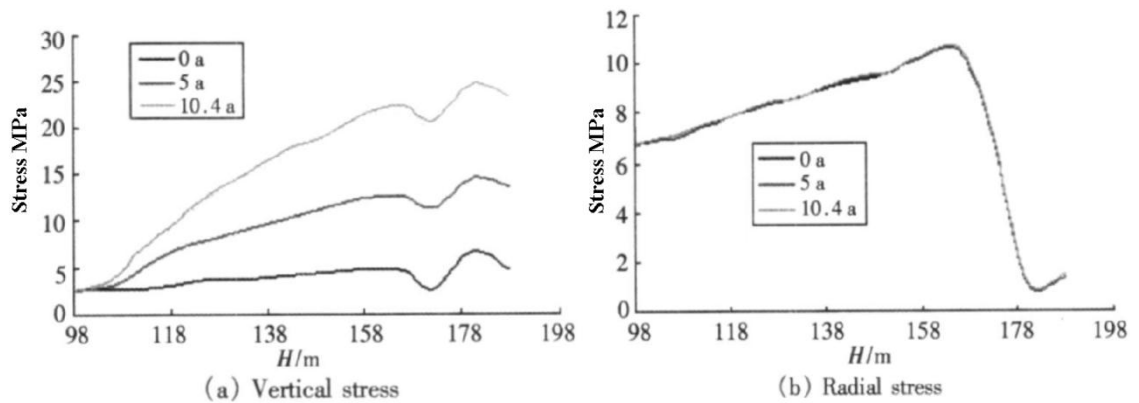
**Figure B 8 Sketch of strain sensors installation (after Wang et al., 2009).**

Figure B9 displays the strain-time curves obtained from monitoring of the three levels of sensors at depth of 138 m, 150 m, and 180 m. At the first 2 months the strain were tensile and then became compressive and increased fast to approximately  $400 \mu\epsilon$  on 13 Dec 2004.



**Figure B 9 The strain-time curves of monitoring data (after Wang et al., 2009).**

Then they used the adverse analysis technique to predict the rupture time and the stress development in the shaft lining and their results are presented in Figure B10.



**Figure B 10 Vertical and radial stress along the shaft length (Wang et al., 2009).**

From Figure B10 (b), the radial stress only changed with depth with a peak of 11 MPa at about 160 m deep, then dramatically decreased to approximately 1 MPa at depth of 183 m. However the radial stress kept stable following the time in expression by the overlapping of the three curves of the data from beginning, 5th years, and 10.4th years respectively in the monitoring. Figure B10 (a) displays the vertical stress, at depth of approximate 180 m, reaches 25 MPa in the 10.4 years, which is higher than the design strength value 19.1 MPa of C40 concrete (China Ministry of Construction, 2002, p21). Consequently, the shaft lining ruptures at 180 m in the 10.4 years after construction (Wang et al., 2009).

- **The generalized shearing displacement method and theory of pile foundation**

Su and Cheng (2000) used the generalized shearing displacement method and the theory of pile foundation, combining the drainage time of the aquifers, strata properties, and the depth of formations, the theoretical value of the negative additional forces on the lining can be computed. The assumption they made for the prediction are:

- The shaft structure, geological features, and subsidence of the strata are all symmetric along the shaft axis.
- There is the relative displacement existing between the lining and surrounding strata.
- The material of the lining and strata behaviours are accomplice with the Mohr-Coulomb Criteria.
- The relationship between the shear stress and shearing strain of the soil strata is a hyperbolic curve.

Through the deduction work the equation for the maximum negative friction:

$$f_n(z) = \frac{\Delta S}{a(z) + b(z) \Delta S} \quad (f_n(z) < f_{n, \max})$$

$$f_n(z) = p' \tan \varphi + c \quad (f_n(z) \geq f_{n, \max})$$

$\Delta S$ , the displacement between the lining and strata at depth  $Z$ , equal to  $w-w_t$ ;  $a(z)$  is the reciprocal of the initial shear strength;  $b(z)$  is the reciprocal of the maximum negative additional friction;  $p'$ : the effective pressure on the lining from the strata,  $p' = 0.013 z$ .  $\varphi$ : the inner friction angle;  $c$ : the cohesion.

For instance, the Linhuan Ventilation Shaft was built in 1979, ruptured in 1993. This shaft has a pure diameter of 6 m, concrete grade C38, and overburden depth at 240 m. The lowest aquifer is 12 m; the aquitard above the lowest aquifer is 50 m. The internal angle  $\phi$  is  $15^\circ$ , cohesion  $C = 0.06$  MPa. The calculating results are given in Table B3.

**Table B 3 The calculated results of additional force on surface of lining in Linhuan Coal Mine (kpa) (Su and Cheng, 2000).**

Depth /m	3 a	6 a	9 a	12 a	13 a
10	25.9	40.9	50.2	55.9	57.4
50	29.2	50.8	67.0	79.3	82.6
90	30.7	55.6	76.6	93.7	98.5
130	31.6	58.6	82.3	103.0	109.3
170	32.2	60.7	86.5	109.9	116.8
210	32.5	61.9	89.5	114.7	122.5
230	32.8	62.5	90.4	116.5	124.9
$\sigma_z$ /MPa (z = 240)	13.32	19.36	24.56	29.03	30.36

The permitted strength of the reinforced concrete  $R_z$  can be computed as  $R_z = R_c + \mu R_g$

Where:  $R_t$ : concrete uniaxial strength, for C38 concrete  $R_t = 23.0$  MPa;  $R_g$ : design strength of the reinforce bars,  $R_g = 340$  MPa;  $\mu$  is the minimum rebar ratio, here  $\mu = 0.02$ .

$$\text{So } R_z = 23.0 + 0.02 \times 340 = 29.8 \text{ MPa.}$$

From Table B3, when the time of lining use is 13 years the negative additional stress in lining reaches 30.36 MPa at depth of 240 m. Therefore the prediction of shaft lining rupture starts in 13rd years of production, the same as the occurrence of the practical damage of the lining (Su and Cheng, 2000).

- **Temperature change caused negative friction by (Jing et al., 2004)**

Jing et al. (2004) found that the stress from temperature-change caused negative stress could contribute 80 % to the damage of the shaft lining in their cases. When lining temperature increases, the shaft lining expands and lengthens upwards due to its bottom-end being tightly held on the base stand and the lining body being tightly enclosed by the surrounding strata, that is it is the only way for the lining

body to expand relatively easily. When the shaft lining lengthens upwards there will be a relative sliding displacement between the lining and the surrounding strata, therefore this displacement is one of scenarios for the negative vertical additional friction to take place. Another scenario is when the lining is stable and the strata subside due to underground mining or aquifer depressurization and compaction. In practice the displacement is most likely to occur resulting from the combination of the two scenarios in varying proportion of contribution. This theory has well explained why most shaft rupture took place in summer when the lining expands and the aquifers are actively lowered.

On the Physical Thermal theory, Solid Mechanical thermal–elastic theory, Jing et al. (2004) deduced the following functions for computing the temperature change caused negative stress:

$$\sigma_r'' = \frac{\alpha_f E T_a - T_b}{1-u} \cdot \frac{b}{2 \ln \frac{b}{a}} \cdot \left[ -\ln \frac{b}{r} + \frac{a^2}{b^2 - a^2} \left( \frac{b^2}{r^2} - 1 \right) \ln \frac{b}{a} \right] - \frac{b^2 r^2 - a^2 b^2}{b^2 r^2 - a^2 r^2} q_b$$

$$\sigma_\theta'' = \frac{\alpha_f E T_a - T_b}{1-u} \cdot \frac{b}{2 \ln \frac{b}{a}} \cdot \left[ 1 - \ln \frac{b}{r} - \frac{a^2}{b^2 - a^2} \left( \frac{b^2}{r^2} + 1 \right) \ln \frac{b}{a} \right] - \frac{b^2 r^2 + a^2 b^2}{b^2 r^2 - a^2 r^2} q_b$$

$$\sigma_z'' = \frac{\alpha_f E T_a - T_b}{1-u} \cdot \frac{b}{2 \ln \frac{b}{a}} \cdot \left( 1 - 2 \ln \frac{b}{r} - \frac{2a^2}{b^2 - a^2} \ln \frac{b}{a} \right) - \frac{2(f_D + \gamma_\epsilon z_D \lambda k_0 \pi D) y}{\pi(D^2 - d^2)} \cdot \frac{y}{z_D} - \frac{2\mu b^2}{b^2 - a^2} q_b \quad (y \leq z_D)$$

$$\sigma_z'' = \frac{\alpha_f E T_a - T_b}{1-u} \cdot \frac{b}{2 \ln \frac{b}{a}} \cdot \left( 1 - 2 \ln \frac{b}{r} - \frac{2a^2}{b^2 - a^2} \ln \frac{b}{a} \right) - \frac{R(H - z_B) - \frac{1}{2} f_y (H - y)^2 (f_B + \gamma_\epsilon z_D \lambda k_0 \pi D)}{\frac{\pi}{4} (D^2 - d^2) (H - z_B)} - \frac{2\mu b^2}{b^2 - a^2} q_b \quad (H \geq y \geq z_D)$$

By applying the above equations to analyse the stresses in a mine shaft that is 7 m in inner diameter, buried in 160 m overburden. The design strength of the lining concrete:  $\sigma_c = 19.6 \text{ MPa}$  ;  $E = 25.48 \text{ GPa}$  , thermal expanding factor:  $\alpha_f = 10 \times 10^{-6} \text{ 1/}^\circ\text{C}$  ; temperature in shaft:  $30^0 \text{ c}$ ; temperature in shaft wall:  $17^0 \text{ c}$ ; Figure B11 shows the structure of shaft lining and the 4 typical depth at A, B, C, D as neutral point of force, temperature influence depth, bottome of the lining and overburden depth respectively. The calculation results and the analysis results of stress composition are given in Table B4.

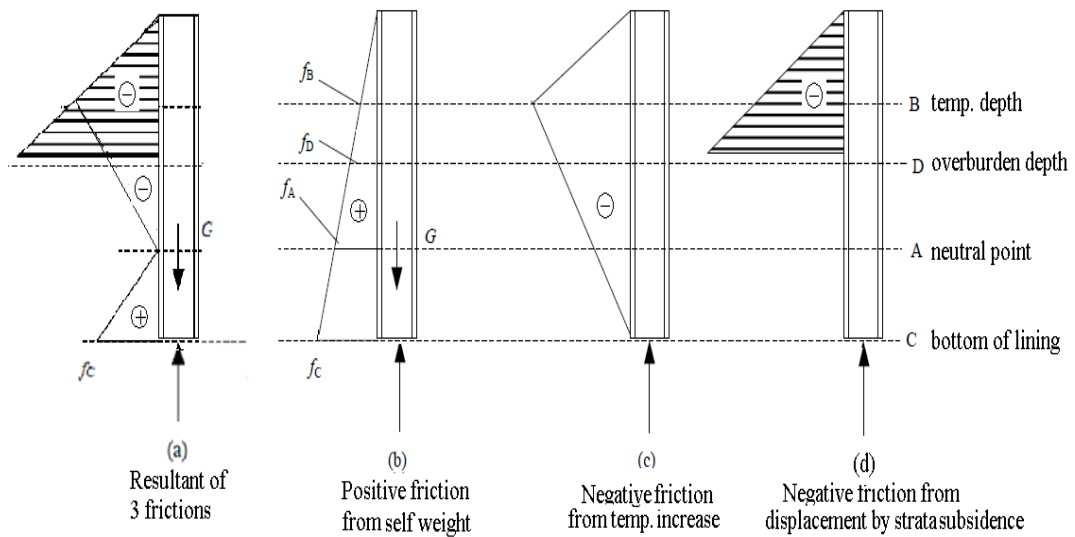


**Figure B 11 Formation laws of the friction between shaft lining and strata (from Jing et al., 2004).**

**Table B 4 Analysis results of stress composition (from Jing et al., 2004).**

Lining depth (m)	stress by weight /MPa (%)			stress by lateral pressure of strata /MPa (%)			stress by temperature increase /MPa (%)			Total stress /MPa		
	<i>r</i>	$\theta$	<i>z</i>	<i>r</i>	$\theta$	<i>z</i>	<i>r</i>	$\theta$	<i>z</i>	<i>r</i>	$\theta$	<i>z</i>
Support depth (m)	0 (0)	0 (0)	0.762 (4.08)	0 (0)	4.101 (28.7)	0.738 (3.95)	0 (0)	10.189 (71.3)	17.178 (91.97)	0	14.29	18.678
End of lining (m)	0 (0)	0 (0)	0 (0)	0 (0)	5.513 (35.1)	0.992 (5.24)	0 (0)	10.189 (64.89)	17.94 (94.76)	0	15.702	18.932

Table B4 displays that the negative vertical stress from the friction caused by displacement from temperature increase takes up over 90% of the total negative vertical stress. This 90% high proportion of the temperature change caused stress may be very specific to this studied shaft lining, however the significance of the studies has given researcher a brand new finding of the components in the negative vertical stress.

To conclude, the negative vertical stress can be created in the following three friction situations: dragging down friction on the shaft lining by subsiding strata due to underground mining and aquifers' compaction; dragging down friction on the shaft lining by the thawing and subsiding strata; sliding friction due to temperature increase in shaft causing the lining expansion and lengthening

upwards to lead to the sliding displacement of lining against strata. Figure B12 illustrates the analysis of the three situations summarised from the literature.

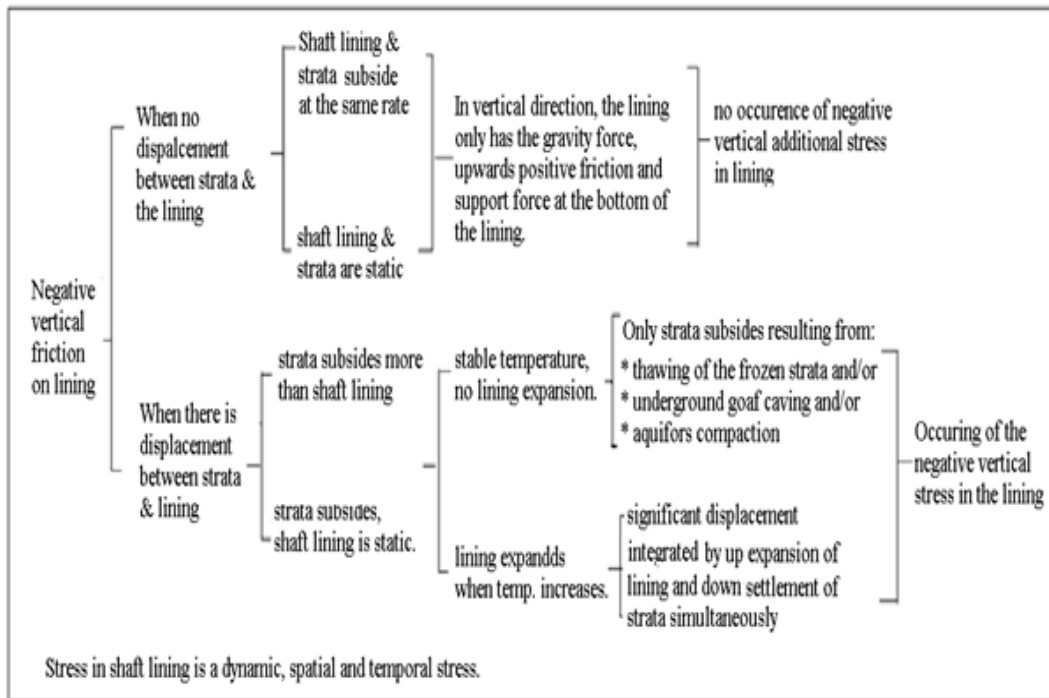


**Figure B 12 Three situations of occurrence of the negative vertical additional stress.**

## **B-5 Prevention, Protection and Repair of Shaft Lining**

The first step is to check if the geology and hydrology of the proposed site have the characteristics to cause the negative additional friction problems. For example, in the overburden the weak (or soft) strata are not neglectable because it is very prone to cause the strata moving, deforming and creeping under the influence of the underground extraction (Li et al., 2006). The design for the right structure of lining and shaft is the most efficient way to prevent the lining rupture. It is recommended that the location of the shaft should be chosen where without or low connectivity aquifer (Wang et al., 2003). Some techniques and approaches to prevent lining rupture are given below.

- **Design of shaft and lining structure:**

The right design of shaft lining in the strata that is easy to create and apply the negative additional friction on the lining is the most important thing in the shaft sinking projects. According to the geological and hydrological features to cause the negative additional friction and the mechanism of the rupture of the lining the

shaft lining structures could be chosen from the structure styles of the shaft lining (Figure B13) (Ding, 2005; Leng et al., 2005).

There are three principals in tackling the rupture problems in the shaft lining. They are: Bearing method: by making the lining strong enough for bearing the stress; Releasing method: by releasing stress in lining, thirdly the combination approach: by the integration of bearing and releasing methods. Bearing approach is performed by using high ratio rebars, high grade concrete and make the lining thick, and then will dramatically increase the cost and construction difficulty.

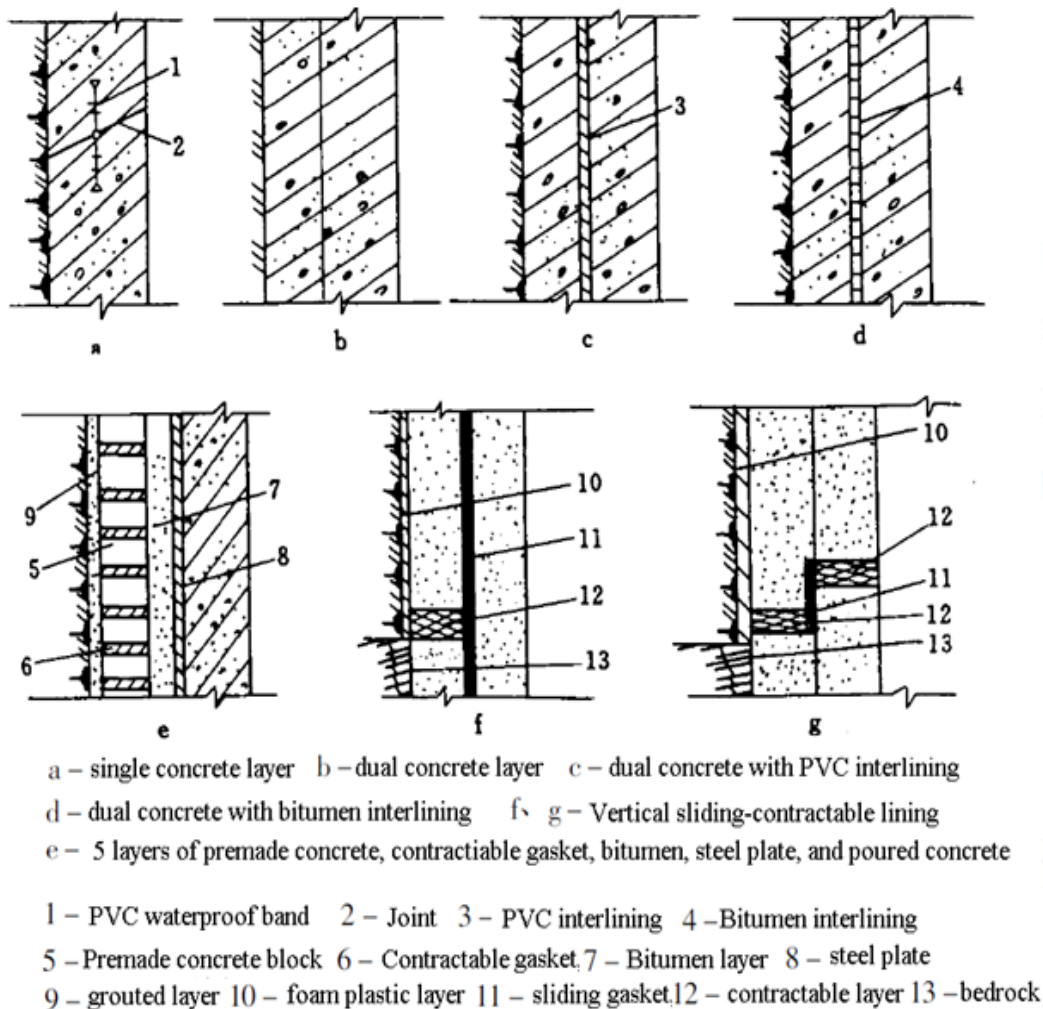


**Figure B 13 The structure styles of the shaft lining (Leng et al., 2005).**

Releasing method is applied by inserting the contactable gaskets or staining the bituminous layer between the lining and strata wall of shaft to reduce the effects of the negative additional forces (Cai and Geng, 2007). The bituminous layer is suitable for lining made of premade concrete blocks. Though the lining will not rupture, it does subside. Therefore, this method can avoid the lining level



changing, and the contactable gaskets need replaced when it is compacted to the least thickness. The combination method has both the advantages of the first and second approaches and is applied as the composite shaft lining as in c, d, e, f, and g in Figure 13. The combination method is widely used in freezing shaft sinking projects (Ding, 2005; Leng et al., 2005).

- **Pre-dewatering the bottom aquifer:**

Dewatering is one of effective measures to prevent the rupture, assure the fast construction of the shaft. Before construction the aquifer water is pumped through by boreholes and tunnel draining (Wang et al., 2003; Bi, 1996). For example, in sinking the auxiliary shaft in Zhangxiaolou Mine, the pre-dewatering led to the subsidence around the site area 266 to 368 mm, implying the significant effect of dewatering. Combining the pre-dewatering before and dewatering in shaft sinking the negative additional friction acting on the lining was dramatically reduced to successfully avoid the lining rupture (Bi, 1996).

- **Grouting to repair or prevent shaft rupture:**

Grouting is the very efficient technique to control and or prevent the lining damage. The existing aquifers behind the lining, which reduced the confinement of concrete lining, can be filled and stabilised by grouting cement into the voids in aquifers or at the interface depth before or after rupture occurs (Liu et al., 2005; China Safety, 2007). Ge (2002) introduced several grouting projects for repairing the ruptured shaft lining of South Vent shaft by drilling boreholes to the void depth and injecting cement to fill the voids in 1992 at Zhangshuang Coal Mine. After injection the consolidated cement bodies to fill the void was surveyed as approximately 8 meters thick behind surrounding the lining. The rupture was controlled (Figure B14).

Yang et al. (2007) reported a similar injection project to repair a ruptured shaft lining (Figure B15). The main shaft at Baodian Coal Mine has a 6.5 m inter diameter, 240 m depth, lining thickness 1m, overburden thickness 148 m, rupture depth 136~143 m (Yang et al., 2007). Totally around 6000 tons of mixture of cement and coal dust was injected into the zone at depth from 80 m to 150m within 180 days, through the 10 drillholes around the shaft at a diameter of 30 meters (Yang et al., 2007).

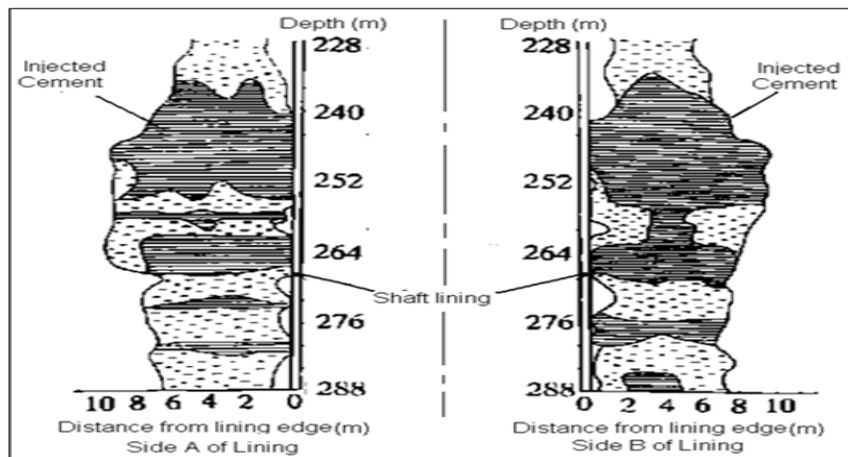


**Figure B 14 Profile of grouted cement curtain (After Ge, 2002).**

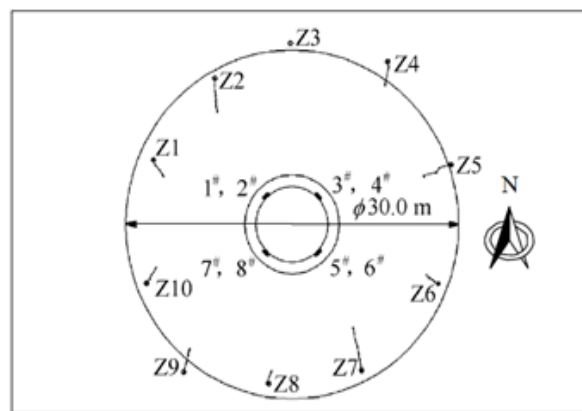


**Figure B 15 Injection borehole pattern around the repaired shaft Site of the grouting holes No. Z1 – Z10 and the layout of concrete strain meters, No. 1 – 8, Baodina Coal Mine, China (From Yang et al., 2007).**

- **The buffering gaskets and unloading grave:**

The buffering gasket placed at several critical depths in design is one of the most effective methods and has three advantages: reducing the negative additional friction by absorbing the lining strain caused by downwards friction; buffering and releasing the effects from the strata pressures; and make the lining waterproof, mitigate pressure and expansion resulted from freezing (in Figure B13 components 6 and 12 are gaskets) (Bi, 1996, Lv & Dai, 1998).

The unloading grave is made at the interface between the overburden and the hard-rock i.e. the location with maximum compressive stress in the lining to prevent further rupture. The grave is filled with treated 400 mm high timber to absorb the strain from the above section of the shaft lining; the timber will gradually compacted shorter and shorter. Therefore there needs several times of

replacement of the timber and every time the lining need a 400 mm high cut-off in the life period of the lining. Also the shaft lining becomes shorter and shorter and its reduced level of its opening on ground surface is getting lower and lower that will remarkably cause some problems in hoisting and some lining attachment distress. Though the direct cost is only 7% of the cost of grouting technique, the unloading grave method is a temporary technique and has some obvious disadvantages through it can avoid rupture problems (China Safety, 2007).

- **Monitoring:**

Monitoring is one of the necessary approaches to protect shaft and prevent the lining rupture and other incidents. To bury the sensors in lining when construction or inserting monitoring gauges in existing lining to set up an automatic monitoring system is the standards way to monitor the shaft conditions in mine production ( Bi, 1996). The intensive monitored shaft section is 40 m long across the interface of the overburden and bedrock (Wang et al., 2003).

- **Others:**

Optimising the extraction outlays, controlling the heading speed when approaching the safety pillars reduce the scale of the strata lateral sliding and decrease the influenced extent of ground (Wang et al., 2003). Reinforcing the lining with attached steel rings or casing can strengthen the ruptured or prone ruptured linings (Wang et al., 2003).

## **B-6 Contribution and Supports**

The Negative Additional Friction model has been supported by the experiment and test through testing model in the laboratory by Mr Bi in 1995 (Bi, 1996); by numerical modelling of Bi et al. in 1997 (Bi et al., 1997); by the 7 years measurement and monitoring by inserting sensors and cells into the shaft wall ( Zhou et al., 2010).

Some of the papers referred in this review have used FDM (finite difference method), or FEM (finite element method) software, namely FLAC (2D or 3 D) and ANSYS to stimulate the mechanism of damage of shaft lining under the negative stress. The results of rupture prediction from the software simulation

have contributed high confidence to the practical occurrence of lining rupture (Liu et al., 2005; Liu et al., 2007; Zhou et al., 2010; Chen et al., 2010; Wang, 2007).

In the Xuhuai region subsidence is caused by two main factors: underground mining and regional lowering of water table through over withdrawal of groundwater. But there are no papers analysing what is the magnitude of the contributions respectively from both causes. This review thinks that the mining caused subsidence would be the major trigger and subsidence from over withdrawal of groundwater is the preliminary and background factor. Underground mining results in strata migration downwards to the goaf, compaction and depressurisation of aquifers due to drainage for inflow into goaf. Inflow, meanwhile, erodes the lowest aquifer to create the voids to form less or zero confinement around the shaft lining. Though there were protective pillars underneath the damaged shafts, the sizes and or the layouts might be incomplete to fully control the subsidence or failed to predict some unexpected effects in the design.

There are several other hypotheses of mechanisms of shaft rupture, such as the bedding- plane-glide-dominant theory; the horizontal-movement-of-strata-dominant theory and geological-tectonic-movement-dominant assumption etc., where each of them considered itself a major factor to cause the ruptures (Wang et al., 2003). They all have not had enough support from theory analysis, modelling simulation and experiments to verify it as the common cause. Therefore, my literature review concludes that the Negative Additional Stress is generally the principal cause of shaft rupture, combining with the listed other factors above. Of course there are some other factors in effecting the stress distribution in lining, such as temperature variation around and within the shaft, lining quality, the construction quality etc. They may all or partially act together with the negative additional friction, however not dominantly (Ding, 2005). Therefore, the shaft lining is most likely working under a very complicated load environment where the negative additional vertical stress is dominant to lead to rupture of lining in the majority of cases of shaft damage in Xuhuai region (Ding, 2005).

Up to now I have not found cases reporting and describing the Negative Additional Friction, from the countries out of China, but do not think there are not these kinds of occurrence about rupture of shaft lining there. It is just because the

events of shaft rupture in Xuhuai of China were so massive, convergent and outstanding that has caused enough attention for the researchers and scientists to study. For example in New Zealand there are a few vertical shafts used mainly in coal mines and gold mines. The negative vertical additional friction has not drawn attentions to the mining industry.

## **B-7 Interesting Finding – Novikov’s paper**

Up to now, one of the earliest and most valuable papers touching the contents of the negative additional friction was written by Novikov (1979, pp10). In fact, fortunately, Novikov found the phenomena of downwards friction caused by subsidence of thawing soil. He described that ‘While the thawing soil is being consolidated due to gravity, because of friction and cohesion it transmits loads on to the walls’; ‘After one mine had been in operation for seven years, a shaft distortion, caused by this subsidence, was detected’; ‘Substantial vertical loads from the soil on the mine-shaft lining may occur only under certain conditions, the main one being that the soil around the mine shaft should be settled after thawing’ (Novikov, 1979, p277, 279). He clearly illustrated the occurrence of the rupture and distortion resulted from the subsidence of the thawing soil. Unfortunately, at that time he did not create an apparent concept as of negative additional vertical friction.

More valuably, Novikov established a test model to validate his hypothesis and quantifying the drag-down friction force (Figure B16) (Novikov, 1979). By freezing the clayey soil below  $-2^{\circ}\text{C}$ , then warming it up by the hot air blown through the vertical tube, the maximum pressure recorded on the dynamometer DS-1 was 189 kg and 231 kg by using waterproof tube and permeable tube respectively. The area of cross section of the tube equals to  $\pi/4*(0.18^2-0.15^2) = 0.007775\text{ m}^2$ . Then the vertical downwards stress caused by downwards friction will be 0.238 MPa and 0.291 MPa respectively. It is a quite high stress considering it only resulting from 1 meter thick soil to thaw and subside. Pitifully, Novikov did not dig further to find such as the relationship between vertical downwards friction and thawing soil depth by changing the scale of the device of testing model. Also he did not detail the used clay characteristics in his test.

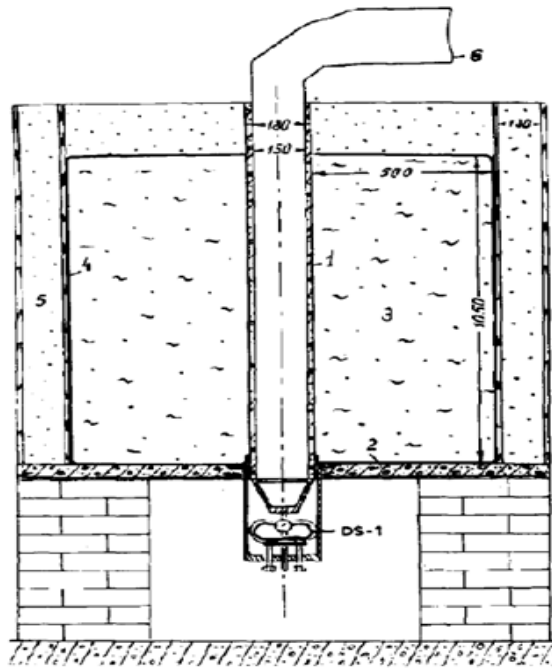


**Figure B 16 Model of mine shaft with air inflow: 1- concrete tube (lining); 2 - reinforced concrete slab; 3 - soil; 4 - hydraulic seal; 5 - heat insulation; 6 - ventilating duct (From Novikov, 1979).**

## **B-8 Discussions**

The concept of ‘Negative Additional Vertical Friction (stress)’ originated from China and largely published in the Chinese literature. However over ten of the papers on the negative additional vertical friction (stress) have been published in International Journals or presented in International Conferences in English (such as Bi et al., 1997; Liang et al., 2009; Tobar and Andre, 2010; Wang et al., 2010; Zhao et al., 2009; Zhou et al., 2009). Up to now I have not found any peer oppositions or questions in papers from other countries or international society that have caused us to attention concerning this concept.

It is evident that the negative additional friction is an essential part of adverse effects from the ground subsidence onto the shaft lining, whatever the subsidence is from the underground mining or water withdrawal or other factors. The study on the mechanism of this negative vertical additional friction is still under development. It is possible that we can use the negative additional friction concept to benefit us in this research project in help with the project of the 4m diameter, 300 m deep shaft, as an guidance and reference for the design, construction and even later maintenance and protection in the duration of mining production as the reviewed papers not only have analysed and certified the effect of negative

additional friction, but also submitted some constructive guidelines and techniques where how to avoid or minimise the adverse effect of negative friction during design, construction and production, with some successful practices and projects. Though the geology at Huntly is not quite the same with the Xuhuai region, there may exist some similarities. The quaternary strata at Huntly is less than 100 m, but the strata underneath quaternary are relatively weak and its hydrological condition is close to Xuhuai as well. Especially from inspection of rock core of the shaft pilot borehole 20097 on 10 December, the majority of layers are siltstone, mudstone or claystone, which are prone to be activated by disturbance to increase numerous joints, consequently easy to contribute high conductivity and migrant towards goaf. The intact conductivity of all the strata at N55 area is within the order of  $10^{-7}$  m/s to  $10^{-8}$  m/s, but become  $10^{-3}$  to  $10^{-5}$  m/s within the disturbed radius of 150 m away from rib edge of goaf edge (Crampton, 2010). There is a thousand times increase of the strata hydraulic conductivity if disturbed. Up to July 2011, none of the reports, designs or documents on this proposed shaft has mentioned the negative additional friction and its impacts. Therefore, this review could be likely to be of some assistance and experience for the shaft sinking project above N55 panel.

There are some problems that require further work to clarify and study:

1. The reviewed papers did not give detailed analysis and description on the 53 rupture cases occurring within construction duration. There may be very few first hand data or records to trace.
2. If we could find some literature or data about the shaft sinking in New Zealand, especially in coal mine. That would be remarkably helpful for our project.
3. The negative additional friction concept has been adopted for less than 10years from 1991. The reviewed papers may have its specific applying mines and regions, and may have the errors and shortcomings in individuals of the cited literature. However, this review may supply us the big picture and profile of the negative additional friction for the practical reference and further research.

Where there is the relative displacement between the shaft lining and the adjacent strata, there exists the negative additional vertical friction acting on the external

surface of the lining, whatever factors lead to the displacement. The significance of this concept in our shaft sinking project lies in that the research attention is probably focusing on not only the affects from the lateral movement of the strata onto the lining and shaft, but also being aware of the adverse vertical affect caused by the negative vertical friction, that is, to consider the their resultant effects on the shaft and its lining, in underneath pillar design, shaft design, shaft construction and their later maintenance in production.

In the existing inclinometer shaft, the lining is PVC casing, is not the simulation of the rigid concrete or metal lining. However in the research we could realize and receive the concept by reviewing whether there are any relation and concerns in our shaft sinking with the negative additional friction problem. If yes, then we might try to understand its potential local mechanism and possible affects, submit the prediction and mitigation advice for the design, construction even future maintenance of the shaft and its lining.

## **B-9 Conclusions**

Where there is the relative displacement between the shaft lining and the surrounding strata, there may exist the negative additional vertical friction acting on the external surface of the lining, whatever factors lead to the displacement. This friction will caused vertical downwards stress within shaft lining and damage the lining at a depth when the resultant stress is larger than the strength of the lining. The stress in the lining is of dynamic, spatial and temporal features. The shaft lining is most likely working under a very complicated load environment where the negative additional vertical stress might be dominant to lead to rupture of lining in a majority of cases of shaft damage. Considering the geology features, this review could be likely to be of some reference for the shaft sinking project above N55 panel.



### 3 Appendix C: Precautions for Minimising the Data Errors

To avoid or minimise the systematic errors some precautions for inclinometer monitoring are summarised mostly after Mikkelsen (2003, 2007) and Stark and Choi (2008), and are listed as follows:

- 1) Try best to use the same probe, the same cables by same operators during measurement and data work in one installation.
- 2) The borehole is to be drilled as vertical and straight as possible and casing is grouted as vertical and straight as possible.
- 3) Casing is flexible enough to detect movement (polyvinyl chloride PVC casing is currently used.)
- 4) Casing is as large as possible, because larger diameter casing has bigger precision of the movement, and allow more shear deformation to occur before traversing of probe is stopped by distressed segment of casing.
- 5) At least 6 m casing is inserted into stable strata, that is, casing is fixed from translation in order to:
  - a. check instrument
  - b. Detect and correct systematic errors
  - c. Calculate total deformation accurately
- 6) The cement-sodium bentonite-water mixture is the best grout for backfilling the annular space between casing and borehole walls.
- 7) After 1 to 3 days curing of grout to take zero readings
- 8) At least the first 2 surveys are used for determine the reference measurement (or zero readings).
- 9) Never hit the probe onto the bottom of the borehole.
- 10) Leaving at least 10 minutes for probe to get warm-up and for sensors to stabilise after lowering down to the bottom of casing.
- 11) If checksums are inconstant, i.e. displayed as leaning line in plots, probe must be recalibrated before subsequent measurement.

## **4 Appendix D: Original Inclinometer Measurement Data (CD copy)**

## **5 Appendix E: The Inclinometer Data after Data Error Correction (CD file)**

The Inclinometer Data after Data Error Correction, for the 11 inclinometer measurements.

## **6 Appendix F: Calculations for the Weighted Extraction Parameters (CD file)**

## **7 Appendix G: Cross Sections of Strata across the Inclinator Borehole (CD file)**

The cross sections of geological formations across the inclinometer borehole showing the strata are relatively flat and the thickness of the strata within the model were assumed as even.